

WL-TR-96-3057



**AN EXPERIMENTAL INVESTIGATION
OF NONLINEAR BEHAVIOUR OF BEAMS
AND PLATES EXCITED TO HIGH LEVELS
OF DYNAMIC RESPONSE**

**HOWARD F. WOLFE
CYNTHIA A. SHROYER
DANSEN L. BROWN
LARRY W. SIMMONS**

OCTOBER 1995

FINAL REPORT FOR OCTOBER 1989 - OCTOBER 1995

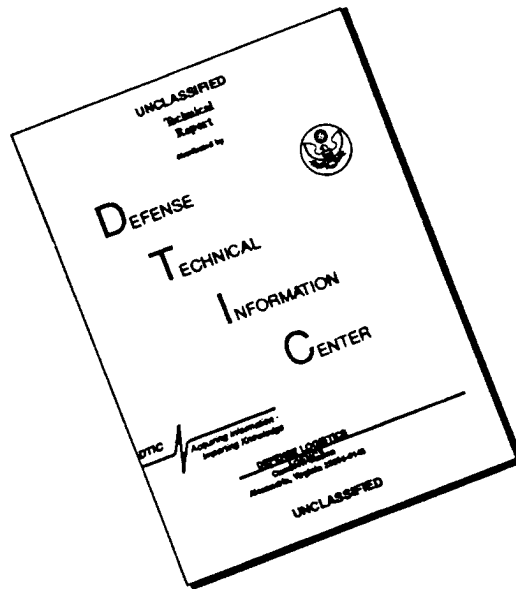
Approved for public release; distribution unlimited

19960603 112

**FLIGHT DYNAMICS DIRECTORATE
WRIGHT LABORATORY
AIR FORCE MATERIEL COMMAND
WRIGHT-PATTERSON AIR FORCE BASE, OH 45433-7006**

DTIC QUALITY INSPECTED 1

DISCLAIMER NOTICE



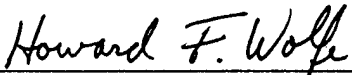
THIS DOCUMENT IS BEST QUALITY AVAILABLE. THE COPY FURNISHED TO DTIC CONTAINED A SIGNIFICANT NUMBER OF PAGES WHICH DO NOT REPRODUCE LEGIBLY.

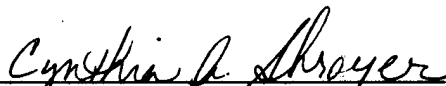
NOTICE

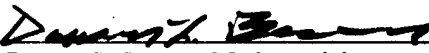
When Government drawings, specifications, or other data are used for any purpose other than in connection with a definitely Government-related procurement, the United States Government-incurs no responsibility or any obligation whatsoever. The fact that the government may have formulated or in any way supplied to said drawings, specification, or other data, is not to be regarded by implication, or otherwise in any manner construed, as licensing the holder, or any other person or corporation; or as conveying any rights or permission to manufacture, use, or sell any patented invention that may in any way be related thereto.


This report is releaseable to the National Technical Information Service (NTIS). At NTIS, it will be available to the general public, including foreign nations.

This technical report has been reviewed and is approved for publication.

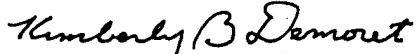

Howard F. Wolfe, Aerospace Engineer
Vibration and Acoustics Section

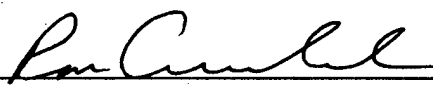

Cynthia A. Shroyer, Computer Scientist
Dynamic Test and Analysis Section

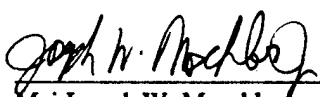

Dansen L. Brown, Mathematician,
Dynamic Test and Analysis Section


Larry W. Simmons, Electronic Technician
Technology Scientific Services Incorporated

Coordination:


Capt Kimberly Demoret, Tech Manager
Vibration and Acoustics Section


Ron Crumbacher, Technical Manager,
Dynamic Test and Analysis Section


Maj Joseph W. Moschler
Structural Dynamics Branch
Structures Division

If your address has changed, if you wish to be removed from our mailing list, or if the addressee is no longer employed by your organization, please notify WL/FIBGQ, Wright-Patterson AFB, OH 45433-7006 to help maintain a current mailing list.

Copies of this report should not be returned unless return is required by security considerations, contractual obligations, or notice on a specific document.

REPORT DOCUMENTATION PAGE

Form Approved
OMB No. 0704-0188

Public reporting burden for this collection of information is estimated to average 1 hour per response, including the time for reviewing instructions, searching existing data sources, gathering and maintaining the data needed, and completing and reviewing the collection of information. Send comments regarding this burden estimate or any other aspect of this collection of information, including suggestions for reducing this burden, to Washington Headquarters Services, Directorate for Information Operations and Reports, 1215 Jefferson Davis Highway, Suite 1204, Arlington, VA 22202-4302, and to the Office of Management and Budget, Paperwork Reduction Project (0704-0188), Washington, DC 20503.

1. AGENCY USE ONLY (Leave blank)		2. REPORT DATE 31 OCTOBER 1995	3. REPORT TYPE AND DATES COVERED Final Technical Report 1 OCT 89-31 OCT 95	
4. TITLE AND SUBTITLE An Experimental Investigation of Nonlinear Behaviour of Beam and Plates Excited to High Levels of Dynamic Response			5. FUNDING NUMBERS Program Element: 62201F Project: 2401 Task: LE Work Unit: 00	
6. AUTHOR(S) Howard F. Wolfe, Cynthia A. Shroyer, Dansen L. Brown, and Larry W. Simmons				
7. PERFORMING ORGANIZATION NAME(S) AND ADDRESS(ES) Flight Dynamics Directorate Wright Laboratory Air Force Materiel Command Wright-Patterson Air Force Base, OH 45433-7006			8. PERFORMING ORGANIZATION REPORT NUMBER WL-TR-96-3057	
9. SPONSORING / MONITORING AGENCY NAME(S) AND ADDRESS(ES) Flight Dynamics Directorate Wright Laboratory Air Force Materiel Command Wright-Patterson Air Force Base, OH 45433-7006			10. SPONSORING / MONITORING AGENCY REPORT NUMBER WL-TR-96-3057	
11. SUPPLEMENTARY NOTES				
12a. DISTRIBUTION / AVAILABILITY STATEMENT Approved for public release: distribution is unlimited.			12b. DISTRIBUTION CODE	
13. ABSTRACT (Maximum 200 words) Dynamic tests were conducted utilizing clamped aluminium and composite beams and plates excited by shakers and acoustic progressive wave tubes. The total strains and the components, bending and axial and the displacements were measured with increasing levels of excitation. Bistable behaviour is observed with sinusoidal excitation for both the beams and plates. The beams randomly excited exhibit a slight frequency shift and peak broadening, which can be attributed to an increased stiffening or hard spring geometric nonlinearity. The plates randomly excited exhibit a greater frequency shift and peak broadening than the beams. The implications of nonlinear behaviour of beams and plates relative to fatigue lives are studied. The Miles single mode model is modified to account for multimodal response. Trends in the strain peak probability densities at low level and high levels of excitation are analyzed to determine the effects of axial strain on their shape. An effective multimodal cyclic frequency model is developed. A method to incorporate the effects of multimodal response of simple structures is presented with fatigue life estimates.				
14. SUBJECT TERMS Nonlinear vibrations, acoustic fatigue, clamped beams, clamped plates, dynamic testing, dynamic analysis.			15. NUMBER OF PAGES 466	
			16. PRICE CODE	
17. SECURITY CLASSIFICATION OF REPORT UNCLASSIFIED	18. SECURITY CLASSIFICATION OF THIS PAGE UNCLASSIFIED	19. SECURITY CLASSIFICATION OF ABSTRACT UNCLASSIFIED	20. LIMITATION OF ABSTRACT SAR	

LIST OF CONTENTS

I	INTRODUCTION.....	1
1.1	LITERATURE REVIEW.....	1
1.1.1	REVIEW OF DESIGN GUIDES	2
1.1.2	CLASSICAL AND FINITE ELEMENT APPROACHES.....	4
1.1.3	TIME DOMAIN METHODS APPLICABLE TO ACOUSTIC FATIGUE.....	6
1.1.4	DAMPING CONSIDERATIONS.....	9
1.1.5	REVIEW OF RANDOM PROCESSES.....	9
1.1.6	REVIEW OF BEAMS AND PLATES SINUSOIDALLY EXCITED.....	12
1.1.7	REVIEW OF BEAMS AND PLATES RANDOMLY EXCITED.....	14
1.1.8	IDENTIFICATION TECHNIQUES.....	15
1.1.9	MODAL ANALYSIS METHODS.....	16
1.1.10	RANDOM FATIGUE METHODS.....	17
1.2	OBJECTIVE AND OUTLINE OF THE STUDY.....	19
II	BEAM EXPERIMENTAL INVESTIGATIONS.....	21
2.1	INTRODUCTION.....	21
2.1.1	MEASUREMENT TRANSDUCERS.....	24
2.1.1.1	DISPLACEMENT TRANSDUCERS.....	24
2.1.1.2	ACCELEROMETER TRANSDUCERS.....	26
2.1.1.3	STRAIN GAUGES AND BRIDGE AMPLIFIERS.....	26
2.1.1.4	MICROPHONES.....	27
2.1.2	DATA ACQUISITION AND PROCESSING.....	27

2.2 C-C ALUMINIUM ALLOY BEAM EXPERIMENTS.....	31
2.2.1 INTRODUCTION.....	31
2.2.2 LINEAR MODE SHAPES.....	32
2.2.3 NONLINEAR STATIC DEFLECTION SHAPES.....	35
2.2.4 NONLINEAR ALUMINIUM ALLOY BEAM SINUSOIDAL EXPERIMENTS.....	36
2.2.5 NONLINEAR ALUMINIUM ALLOY BEAM RANDOM EXPERIMENTS...	38
2.3 C-C CFRP BEAM EXPERIMENTS.....	41
2.3.1 INTRODUCTION.....	41
2.3.2 LINEAR CFRP BEAM MODE SHAPES.....	41
2.3.3 STATIC CFRP BEAM MEASUREMENTS.....	41
2.3.4 NONLINEAR CFRP BEAM SINUSOIDAL EXPERIMENTS.....	42
2.3.5 NONLINEAR CFRP BEAM RANDOM EXPERIMENTS.....	44
2.4 P-P ALUMINIUM ALLOY BEAM EXPERIMENTS.....	45
2.4.1 INTRODUCTION.....	45
2.4.2 LINEAR P-P ALUMINIUM ALLOY BEAM MODE SHAPES.....	45
2.4.3 NONLINEAR P-P ALUMINIUM ALLOY BEAM STATIC MEASUREMENTS.....	46
2.4.4 NONLINEAR P-P ALUMINIUM ALLOY BEAM SINUSOIDAL EXPERIMENTS.....	47
2.4.5 NONLINEAR P-P ALUMINIUM ALLOY BEAM RANDOM EXPERIMENTS.....	47
 III PLATE EXPERIMENTAL INVESTIGATIONS.....	 48
 3.1 BASE EXCITATION METHOD.....	 48
3.1.1 INTRODUCTION.....	48
3.1.2 C-C-C-C ALUMINIUM ALLOY PLATE SHAKER EXPERIMENTS.....	49

3.1.2.1 LINEAR MODE SHAPES.....	50
3.1.2.2 NONLINEAR ALUMINIUM ALLOY SINUSOIDAL SHAKER EXPERIMENTS.....	50
3.1.2.3 NONLINEAR ALUMINIUM ALLOY RANDOM EXPERIMENTS.....	51
3.1.3 C-C-C-C CFRP PLATE SHAKER EXPERIMENTS.....	53
3.1.3.1 LINEAR MODE SHAPES.....	54
3.1.3.2 NONLINEAR CFRP SHAKER SINUSOIDAL EXPERIMENTS.....	54
3.1.3.3 NONLINEAR CFRP SHAKER RANDOM EXPERIMENTS.....	55
3.2. APWT PLATE EXPERIMENTAL METHODS.....	57
3.2.1 INTRODUCTION.....	57
3.2.2 C-C-C-C ALUMINIUM ALLOY PLATE APWT EXPERIMENTS.....	60
3.2.3 C-C-C-C CFRP PLATE APWT EXPERIMENTS.....	64
3.2.3.1 LINEAR MODE SHAPES.....	64
3.2.3.2 CFRP APWT NONLINEAR RANDOM EXPERIMENTS.....	64
IV EVALUATION OF EXPERIMENTAL RESULTS.....	68
4.1 INTRODUCTION.....	68
4.2 STATIC BEAM TEST COMPARISONS.....	68
4.3 NONLINEAR DYNAMIC DISPLACEMENT SHAPES.....	74
4.3.1 C-C ALUMINIUM ALLOY BEAM NONLINEAR DISPLACEMENT SHAPES.....	74
4.3.2 C-C CFRP BEAM NONLINEAR DISPLACEMENT SHAPES.....	80
4.3.3 P-P ALUMINIUM ALLOY BEAM NONLINEAR DISPLACEMENT SHAPES.....	81
4.3.4 C-C-C-C ALUMINIUM ALLOY SHAKER PLATE NONLINEAR DISPLACEMENT SHAPES.....	82

4.3.5 C-C-C-C CFRP SHAKER PLATE NONLINEAR DISPLACEMENT SHAPES.....	84
4.4 LINEAR FREQUENCY COMPARISONS.....	85
4.4.1 BEAM LINEAR FREQUENCY COMPARISONS.....	85
4.4.2 PLATE LINEAR FREQUENCY COMPARISONS.....	86
4.5 COMPARISONS OF INTEGRATING ACROSS THE STRAIN SPECTRAL DENSITIES.....	88
4.6 NONLINEAR RANDOM BEAM COMPARISONS.....	89
4.7 NONLINEAR RANDOM SHAKER PLATE COMPARISONS.....	90
4.8 NONLINEAR RANDOM APWT PLATE COMPARISONS.....	90
4.9 COMPARISON OF STRAIN STATISTICAL MOMENTS.....	92
4.10 COMPARISONS OF THE RESULTS WITH ANALYTICAL METHODS.....	94

V IMPLICATIONS OF NONLINEAR BEHAVIOUR IN RELATION TO FATIGUE LIFE.....98

5.1 INTRODUCTION.....	98
5.2 MULTIMODAL FATIGUE MODEL.....	99
5.3 COMPARISON OF PEAK PDFs AND DAMAGE MODEL.....	102
5.3.1 CLAMPED ALUMINIUM ALLOY BEAM PPDFs.....	102
5.3.2 CLAMPED ALUMINIUM ALLOY SHAKER PLATE PPDFs.....	103
5.3.3 CLAMPED CFRP SHAKER PLATE PPDFs.....	104
5.3.4 CLAMPED ALUMINIUM ALLOY APWT PLATE PPDFs.....	104
5.3.5 CLAMPED CFRP APWT PLATE PPDFs.....	105
5.4 FATIGUE MODEL APPLICATION.....	105

5.5 DAMAGE ASSESSMENT.....	107
5.6 SUMMARY.....	110
 VI CONCLUSIONS AND RECOMMENDATIONS.....	 111
 REFERENCES.....	 124

APPENDICES

APPENDIX A

COIL CALIBRATION.....	137
Fig A-1 Coil calibration testing arrangement.....	139
Fig A-2 Exciter coil calibration curves, DC, 19 mm.....	140
Fig A-3 Exciter coil calibration curves, sine, 19 mm.....	141
Fig A-4 Exciter coil calibration curves, random, 19 mm.....	142
Fig A-5 Exciter coil calibration curves, DC, 38 mm.....	143
Fig A-6 Exciter coil calibration curves, sine, 38 mm.....	144
Fig A-7 Exciter coil calibration curves, random, 38 mm.....	145

APPENDIX B

TABLE OF COEFFICIENTS, TABLE B-2.1.....	146
---	-----

APPENDIX C

TABLES OF CURVE FITTING FUNCTIONS AND COEFFICIENTS FOR

CHAPTER IV.....	147
-----------------	-----

TABLE C-4.1 CURVE FITTING FUNCTIONS STATIC BENDING TEST, C-C AL BEAM, 2.5 N FORCE	147
--	-----

TABLE C-4.2 CURVE FITTING FUNCTIONS STATIC BENDING TEST, C-C AL BEAM, 13.8 NEWTON FORCE.....	149
TABLE C-4.3 COEFFICIENTS FOR DISPLACEMENT SHAPES IN FIG 4.26.....	151
TABLE C-4.4 COEFFICIENTS FOR DISPLACEMENT SHAPES IN FIG 4.29.....	152
TABLE C-4.5 CURVE FITTING FUNCTIONS, SINE EXCITATION, 0.086 N.....	153
TABLE C-4.6 CURVE FITTING FUNCTIONS, SINE EXCITATION, 0.60 N.....	155
TABLE C-4.7 COEFFICIENTS FOR DISPLACEMENT SHAPES IN FIG 4.52.....	157
TABLE C-4.8 COEFFICIENTS FOR DISPLACEMENT SHAPES IN FIG 4.55.....	157
TABLE C-4.9 COEFFICIENTS FOR DISPLACEMENT SHAPES IN FIG 4.63.....	158
TABLE C-4.10 COEFFICIENTS FOR DISPLACEMENT SHAPES IN FIG 4.67.....	158
TABLE C-4.11 COEFFICIENTS FOR DISPLACEMENT SHAPES IN FIG 4.72.....	159
TABLE C-4.12 COEFFICIENTS FOR DISPLACEMENT SHAPES IN FIG 4.76.....	159

LIST OF TABLES

TABLE 3.1 MEASURED LINEAR MODAL FREQUENCIES.....	160
TABLE 4.1 BEAMS AND PLATE SIZES.....	161
TABLE 4.2 MATERIAL PROPERTIES.....	162
TABLE 4.3 STATIC TESTS, COMPARISON OF MEASURED DATA WITH CURVE FITTING FUNCTIONS.....	163
TABLE 4.4 SINE TESTS, COMPARISON OF MEASURED DATA WITH CURVE FITTING FUNCTIONS.....	164
TABLE 4.5 COMPARISON OF MEASURED DATA WITH LINEAR BEAM THEORY.....	165
TABLE 4.6 COMPARISON OF MEASURED DATA WITH LINEAR PLATE THEORY.....	166
TABLE 4.7 STRAIN STATISTICAL MOMENTS, BEAM AND SHAKER PLATES.....	167
TABLE 4.8 STRAIN STATISTICAL MOMENTS, APWT PLATES.....	168
TABLE 5.1 CALCULATIONS FOR CYCLIC MULTIMODAL FREQUENCIES.....	169
TABLE 5.2 FATIGUE CALCULATIONS CANTILEVERED BEAM.....	170
TABLE 5.3 FATIGUE CALCULATIONS C-C ALUMINIUM BEAM.....	171

TABLE 5.4 FATIGUE CALCULATIONS FLEXIBLE RIVETED ALUMINIUM	
COUPON.....	172
TABLE 5.5 FATIGUE CALCULATIONS FLEXIBLE RIVETED ALUMINIUM	
COUPON (K MODIFIED).....	173
TABLE 5.6 FATIGUE LIFE CALCULATIONS, C-C AL BEAM.....	174
TABLE 5.7 FATIGUE LIFE CALCULATIONS, C-C-C-C AL SHAKER PLATE.....	177
TABLE 5.8 SUMMARY OF FATIGUE LIFE CALCULATIONS.....	180
TABLE 5.9 CURVE FITTING OF PPDF, C-C-C-C AL SHAKER PLATE.....	181

LIST OF FIGURES

Fig 2.1	Constant current modifier schematic for beam tests.....	183
Fig 2.2	Photograph of testing arrangement for clamped straight beams.....	184
Fig 2.3	Scanning laser vibrometer diagram.....	185
Fig 2.4	Video holography test arrangement diagram.....	186
Fig 2.5	Clamped beam size and strain gauge locations.....	187
Fig 2.6	Beam testing arrangement diagram.....	188
Fig 2.7	Photograph of mode shape test arrangement, C-C aluminium alloy beam.....	189
Fig 2.8	Displacement time history, 10-400 Hz random excitation, C-C aluminium beam	190
Fig 2.9	Displacement spectral density, centre of C-C aluminium beam, acoustic excitation concentrated at $1/4 \ell$	191
Fig 2.10	Displacement spectral density, centre of C-C aluminium beam, acoustic excitation concentrated at $1/8 \ell$	192
Fig 2.11	Displacement spectral density, centre of C-C aluminium beam, acoustic excitation concentrated at $1/6 \ell$	193
Fig 2.12	Strain spectral densities, SG 1, 2, 4 and 5, acoustic excitation at the centre.....	194
Fig 2.13	Mode shapes, acoustic excitation, a=85 Hz, b=207 Hz, c=380 Hz, d= 612 Hz, e=765 Hz and f=898 Hz.....	195
Fig 2.14	Slow sine sweep, low level coil excitation, 45- 60 Hz, C-C aluminium beam.....	196
Fig 2.15	Nonlinear static transverse displacement shapes, C-C aluminium beam.....	197
Fig 2.16	Total static strains for increasing and decreasing forces, C-C aluminium beam..	198
Fig 2.17	Total static strains compared with linear theoretical results, C-C aluminium beam.....	199
Fig 2.18	Nonlinear centre displacements for slow sine sweeps increasing from 35-63 Hz and decreasing from 70-35 Hz, C-C aluminium beam.....	200

Fig 2.19 Total, axial and bending strains for sine dwell tests, C-C aluminium beam.....	201
Fig 2.20 Sinusoidal strain vs displacement, C-C aluminium beam.....	202
Fig 2.21 Nonlinear displacement shapes fundamental resonance, unsmoothed data, C-C aluminium beam.....	203
Fig 2.22 Nonlinear displacement shapes, 3rd mode, 7th order polynomial fit, C-C aluminium beam.....	204
Fig 2.23 Force spectral densities, 10-1000 Hz random excitation, C-C aluminium beam.	205
Fig 2.24 Total strain spectral densities, 10-1000 Hz random excitation, SG 3, C-C aluminium beam.....	206
Fig 2.25 Total strain spectral densities, 10-1000 Hz random excitation, SG 1, C-C aluminium beam.....	207
Fig 2.26 Axial strain time history, 10-400 Hz random excitation, SG 3 and 6, C-C aluminium beam.....	208
Fig 2.27 Total axial bending strain spectral densities, 10-400 Hz random excitation, SG 1, 1 & 4, C-C aluminium beam.....	209
Fig 2.28 Total, axial and bending strains, 10-400 Hz random excitation, SG 3, C-C aluminium beam.....	210
Fig 2.29 Normalised force amplitude PDFs, 10-1000 Hz random excitation, C-C aluminium beam.....	211
Fig 2.30 Normalised strain amplitude PDFs, 10-1000 Hz random excitation SG 1, C-C aluminium beam.....	212
Fig 2.31 Normalised strain amplitude PDFs, 10-1000 Hz random excitation, SG 3, C-C aluminium beam.....	213
Fig 2.32 Photograph of test arrangement for linear mode shape, C-C CFRP beam.....	214
Fig 2.33 Total static strains, C-C CFRP beam.....	215
Fig 2.34 Static stain vs displacement, SG 1 and 3, C-C CFRP beam.....	216

Fig 2.35 Nonlinear centre displacements for slow sine sweeps increasing from 41-93 Hz and decreasing from 90-41 Hz C-C, CFRP beam.....	217
Fig 2.36 Slow sine sweeps, increasing 40-90 Hz, C-C CFRP beam.....	218
Fig 2.37 Slow sine sweeps, decreasing 90-40 Hz, C-C CFRP beam.....	219
Fig 2.38 Slow amplitude sweeps, increasing excitation force 0.5-6N at constant frequency, C-C CFRP beam.....	220
Fig 2.39 Slow amplitude sweeps, decreasing excitation force 0.5-6N at constant frequency C-C CFRP beam.....	221
Fig 2.40 Total, axial and bending strains for sine dwell tests C-C CFRP beam.....	222
Fig 2.41 Nonlinear displacement shapes fundamental resonance, unsmoothed data, C-C CFRP beam.....	223
Fig 2.42 Nonlinear displacement shapes 2nd mode, 370 Hz, unsmoothed data, C-C CFRP beam.....	224
Fig 2.43 Nonlinear displacement shapes, 3rd mode, 389 Hz, unsmoothed data C-C CFRP beam.....	225
Fig 2.44 Nonlinear displacement shapes, 4th mode, 899 Hz, unsmoothed data C-C CFRP beam.....	226
Fig 2.45 Nonlinear displacement shapes, 5th mode, 1028 Hz, unsmoothed data C-C CFRP beam.....	227
Fig 2.46 Force spectral densities, 10-1300 Hz, random excitation, C-C CFRP beam.....	228
Fig 2.47 Strain spectral densities, 10-1300 Hz random excitation, SG 1, C-C CFRP beam.....	229
Fig 2.48 Strain spectral densities, 10-1300 Hz random excitation, SG 3, C-C CFRP beam.....	230
Fig 2.49 Displacement spectral densities, 10-1300 Hz random excitation, C-C CFRP beam.....	231
Fig 2.50 Total, axial and bending strains, 10-600 Hz, SG 3 and SG 3& 6, random excitation, C-C CFRP beam.....	232
Fig 2.51 Normalised force amplitude PDFs, 10-600 Hz random excitation, C-C CFRP beam.....	233

Fig 2.52 Normalised strain amplitude PDFs, 10-600 Hz random excitation, SG 1, C-C CFRP beam.....	234
Fig 2.53 Normalised strain amplitude PDFs, 10-600 Hz random excitation, SG 3, C-C CFRP beam.....	235
Fig 2.54 P-P aluminium alloy beam design.....	236
Fig 2.55 Total static strains and displacements, P-P aluminium beam.....	237
Fig 2.56 Total static strains, P-P aluminium beam.....	238
Fig 2.57 Nonlinear displacement shapes fundamental resonance unsmoothed data, P-P aluminium beam.....	239
Fig 3.1 Shaker rated performance curves.....	240
Fig 3.2 Photograph of shaker testing arrangement.....	241
Fig 3.3 Shaker flat plate size and strain gauge locations.....	242
Fig 3.4 Schematic of shaker test arrangement.....	243
Fig 3.5 Mode shapes using video holography, a=208 Hz, b=365 Hz, c=485 Hz, d=618 Hz, e=623 Hz, f=864 Hz and g=966 Hz , C-C-C-C aluminium alloy shaker plate.....	244
Fig 3.6 Total strains and displacements for sine dwell tests, C-C-C-C aluminium shaker plate.....	245
Fig 3.7 Nonlinear displacement shapes, fundamental resonance width direction, unsmoothed data, C-C-C-C aluminium shaker plate.....	246
Fig 3.8 Nonlinear displacement shapes, fundamental resonance length direction, unsmoothed data, C-C-C-C aluminium shaker plate.....	247
Fig 3.9 Excitation spectral densities, 100-1000 Hz, C-C-C-C aluminium shaker plate....	248
Fig 3.10 Strain spectral densities, 100-1000 Hz, SG 1, C-C-C-C aluminium shaker plate	249
Fig 3.11 Strain spectral densities, 100-1000 Hz, SG 2, C-C-C-C aluminium shaker plate	250
Fig 3.12 Strain spectral densities, 100-1000 Hz, SG 3, C-C-C-C aluminium shaker plate	251
Fig 3.13 Strain spectral densities, 100-1000 Hz, SG 4, C-C-C-C aluminium shaker plate	252

Fig 3.14 Strain spectral densities, 100-1000 Hz, SG 5, C-C-C-C aluminium shaker plate	253
Fig 3.15 Displacement spectral densities, 100-1000 Hz, C-C-C-C aluminium shaker plate.....	254
Fig 3.16 Total, axial, bending strain spectral densities, 1.46g random excitation, C-C-C-C aluminium shaker plate.....	255
Fig 3.17 Total, axial, bending strain spectral densities, 14.4g random excitation, C-C-C-C aluminium shaker plate.....	256
Fig 3.18 Total strains and displacements, C-C-C-C aluminium shaker plate.....	257
Fig 3.19 Total strain vs displacement, C-C-C-C aluminium shaker plate.....	258
Fig 3.20 Axial strains and displacements, C-C-C-C aluminium shaker plate.....	259
Fig 3.21 Bending strains and displacements, C-C-C-C aluminium shaker plate.....	260
Fig 3.22 Total, axial and bending strains and displacements, SG 1 and 1 & 6, C-C-C-C aluminium shaker plate.....	261
Fig 3.23 Total, axial and bending strains and displacements, SG 2 and 2 & 7 C-C-C-C aluminium shaker plate.....	262
Fig 3.24 Total, axial and bending strains and displacements, SG 3 and 3 & 8 C-C-C-C aluminium shaker plate.....	263
Fig 3.25 Normalised integrals of strain PSDs, SG 2, C-C-C-C aluminium shaker plate...	264
Fig 3.26 Normalised excitation amplitude PDFs, 100-1000 Hz random, C-C-C-C aluminium shaker plate.....	265
Fig 3.27 Normalised strain amplitude PDFs, 100-1000 Hz random, SG 2, C-C-C-C aluminium shaker plate.....	266
Fig 3.28 Normalised strain amplitude PDFs, 100-1000 Hz random, SG 2, 12 s and 25 s time histories, C-C-C-C aluminium shaker plate.....	267
Fig 3.29 Mode shape, video holography method, a=156 Hz, b=246 Hz, c=352 Hz, d=449 Hz and e=535 Hz, C-C-C-C CFRP shaker plate.....	268
Fig 3.30 Mode shape, video holography method, a=587 Hz, b=674 Hz, c=825 Hz, d=981 Hz and e=1110 Hz, C-C-C-C CFRP shaker plate.....	269

Fig 3.31	Total strains and displacements, SG 3, sine dwell tests, C-C-C-C CFRP shaker plate.....	270
Fig 3.32	Nonlinear displacement shapes, fundamental resonance width direction, unsmoothed data, C-C-C-C CFRP shaker plate.....	271
Fig 3.33	Nonlinear displacement shapes, fundamental resonance length direction, unsmoothed data, C-C-C-C CFRP plate.....	272
Fig 3.34	Excitation spectral densities, 100-1000 Hz, C-C-C-C CFRP shaker plate.....	273
Fig 3.35	Strain spectral densities, 100-1000 Hz, SG 1, C-C-C-C CFRP shaker plate.....	274
Fig 3.36	Strain spectral densities, 100-1000 Hz, SG 3, C-C-C-C CFRP shaker plate.....	275
Fig 3.37	Strain spectral densities, 100-1000 Hz, SG 4, C-C-C-C CFRP shaker plate.....	276
Fig 3.38	Strain spectral densities, 100-1000 Hz, SG 7, C-C-C-C CFRP shaker plate.....	277
Fig 3.39	Displacement spectral densities 100-1000 Hz, C-C-C-C CFRP shaker plate.....	278
Fig 3.40	Axial and bending strain spectral densities, 1.45g random excitation, C-C-C-C CFRP shaker plate.....	279
Fig 3.41	Axial and bending strain spectral densities, 14.4g random excitation, C-C-C-C CFRP shaker plate.....	280
Fig 3.42	Total strains and displacements, C-C-C-C CFRP shaker plate.....	281
Fig 3.43	Total strain vs displacement, C-C-C-C CFRP shaker plate.....	282
Fig 3.44	Axial strains and displacements, C-C-C-C CFRP shaker plate.....	283
Fig 3.45	Bending strains and displacements, C-C-C-C CFRP shaker plate.....	284
Fig 3.46	Total, axial and bending strains and displacements, SG 1 and 1 & 6, C-C-C-C CFRP shaker plate.....	285
Fig 3.47	Total, axial and bending strains and displacements, SG 2 and 2 & 7, C-C-C-C CFRP shaker plate.....	286
Fig 3.48	Total, axial and bending strains and displacements, SG3 and 3 & 8, C-C-C-C CFRP shaker plate.....	287
Fig 3.49	Normalised integrals of strain PSDs, SG 7, C-C-C-C CFRP shaker plate.....	288

Fig 3.50 Normalised excitation amplitude PDFs, 100-1000 Hz random, C-C-C-C CFRP shaker plate.....	289
Fig 3.51 Normalised strain amplitude PDFs, 100-1000 Hz random, SG 7, C-C-C-C CFRP shaker plate.....	290
Fig 3.52 Photograph of C-C-C-C aluminium alloy plate installation in APWT.....	291
Fig 3.53 C-C-C-C aluminium APWT plate size and strain gauge location.....	292
Fig 3.54 Schematic of C-C-C-C aluminium APWT plate testing arrangement.....	293
Fig 3.55 Total strain vs pressure, C-C-C-C aluminium APWT plate testing arrangement	294
Fig 3.56 Pressure spectral densities, 158 dB OSPL, C-C-C-C aluminium APWT plate....	295
Fig 3.57 Strain spectral densities, four OSPLs, SG 10, C-C-C-C aluminium APWT plate.....	296
Fig 3.58 C-C-C-C Total, axial, bending strain spectral densities, 140 dB OSPL, SG 9 and 4&9, C-C-C-C aluminium APWT plate.....	297
Fig 3.59 C-C-C-C Total, axial, bending strain spectral densities, 158 dB OSPL, SG 9 and 4&9, C-C-C-C aluminium APWT plate.....	298
Fig 3.60 Normalised integrals of strain PSDs, SG 9, C-C-C-C aluminium APWT plate..	299
Fig 3.61 Normalised pressure amplitude PDFs, M 2, four OSPLs. C-C-C-C aluminium APWT plate.....	300
Fig 3.62 Normalised pressure amplitude PDFs, M 2, M 3, M 4, 158 dB OSPL, C-C-C-C aluminium APWT plate.....	301
Fig 3.63 Normalised strain amplitude PDFs, SG 9, C-C-C-C aluminium APWT plate.....	302
Fig 3.64 Normalised strain amplitude PDFs, SG 10, C-C-C-C aluminium APWT plate...	303
Fig 3.65 C-C-C-C CFRP APWT plate size and strain gauge location.....	304
Fig 3.66 Photograph of C-C-C-C CFRP APWT clamping arrangement.....	305
Fig 3.67 Schematic of C-C-C-C CFRP APWT plate mode shape testing arrangement.....	306
Fig 3.68 Mode shape, video holography method, a=59 Hz, b=77 Hz, c=107 Hz, d=139 Hz, e=160 Hz and f=187 Hz, C-C-C-C CFRP APWT plate.....	307

Fig 3.69 Mode shape, video holography method, a=194 Hz, b=220 Hz, c=266 Hz, d=281 Hz, e=355 Hz and f=405 Hz, C-C-C-C CFRP APWT plate.....	308
Fig 3.70 Photograph of C-C-C-C CFRP plate installation in APWT.....	309
Fig 3.71 Schematic of C-C-C-C CFRP APWT plate testing arrangement.....	310
Fig 3.72 Pressure spectral densities, M 3, five OSPLs, C-C-C-C CFRP APWT plate.....	311
Fig 3.73 Pressure spectral densities, M 5, five OSPLs, C-C-C-C CFRP APWT plate.....	312
Fig 3.74 Total strain spectral densities, five OSPLs, SG 2, C-C-C-C CFRP APWT plate	313
Fig 3.75 Total strain spectral densities, five OSPLs, SG 3, C-C-C-C CFRP APWT plate	314
Fig 3.76 Axial strain spectral densities, five OSPLs, SG 3&8, C-C-C-C CFRP APWT plate.....	315
Fig 3.77 Total, axial and bending strain spectral densities, 134 dB OSPL, SG 3 and 3&8, C-C-C-C CFRP APWT plate.....	316
Fig 3.78 Total, axial and bending strain spectral densities, 152 dB OSPL, SG 3 and 3&8, C-C-C-C CFRP APWT plate.....	317
Fig 3.79 Displacement spectral densities, five OSPLs, C-C-C-C CFRP APWT plate.....	318
Fig 3.80 Total strains and displacements, C-C-C-C CFRP APWT plate.....	319
Fig 3.81 Total strains and displacements vs pressure, C-C-C-C CFRP APWT plate.....	320
Fig 3.82 Axial strains and displacements, C-C-C-C CFRP APWT plate.....	321
Fig 3.83 Bending strains and displacements, C-C-C-C CFRP APWT plate.....	322
Fig 3.84 Normalised integrals of total strain PSDs, SG 2, C-C-C-C CFRP APWT plate..	323
Fig 3.85 Normalised integrals of total strain PSDs, SG 3, C-C-C-C CFRP APWT plate..	324
Fig 3.86 Normalised integrals of axial strain PSDs, SG 3, C-C-C-C CFRP APWT plate..	325
Fig 3.87 Normalised pressure amplitude PDFs, M 3, C-C-C-C CFRP APWT.....	326
Fig 3.88 Normalised strain amplitude PDFs, SG 2, C-C-C-C CFRP APWT.....	327

Fig 4.1 Static total strains compared with a second linear bending theory, C-C aluminium beam.....	328
Fig 4.2 Rank 1, logistic curve fit of displacement shape, 2.5 N static test, C-C aluminium beam.....	329
Fig 4.3 Rank 2, Gaussian curve fit of displacement shape, 2.5 N static test, C-C aluminium beam.....	330
Fig 4.4 Rank 3, Lorentzian curve fit of displacement shape, 2.5 N static test, C-C aluminium beam.....	331
Fig 4.5 Rank 7, sine curve fit of displacement shape, 2.5 N static test, C-C aluminium beam.....	332
Fig 4.6 Rank 15 classical curve fit of displacement shape, 2.5N static test, C-C aluminium beam.....	333
Fig 4.7 Rank 20 fourth order polynomial curve fit of displacement shape, 2.5 N static test, C-C aluminium beam.....	334
Fig 4.8 Rank 1 Gaussian curve fit of displacement shape, 13.7 N static test, C-C aluminium beam.....	335
Fig 4.9 Rank 2 sine curve fit of displacement shape, 13.7 N static test, C-C aluminium beam.....	336
Fig 4.10 Rank 5 logistic curve fit of displacement shape, 13.7 N static test, C-C aluminium beam.....	337
Fig 4.11 Rank 6 classical curve fit of displacement shape, 13.7 N static test, C-C aluminium beam.....	338
Fig 4.12 Rank 7 Lorentzian curve fit of displacement shape, 13.7 N static test, C-C aluminium beam.....	339
Fig 4.13 Rank 13 fourth order polynomial curve fit of displacement shape, 13.7 N static test, C-C aluminium beam.....	340
Fig 4.14 Second derivative of Fig 4.2, 2.5 N static test, C-C aluminium beam.....	341
Fig 4.15 Second derivative of Fig 4.3, 2.5 N static test, C-C aluminium beam.....	342
Fig 4.16 Second derivative of Fig 4.4, 2.5 N static test, C-C aluminium beam.....	343
Fig 4.17 Second derivative of Fig 4.5, 2.5 N static test, C-C aluminium beam.....	344

Fig 4.18 Second derivative of Fig 4.6, 2.5 N static test, C-C aluminium beam.....	345
Fig 4.19 Second derivative of Fig 4.7, 2.5 N static test, C-C aluminium beam.....	346
Fig 4.20 Second derivative of Fig 4.8, 13.7 N static test, C-C aluminium beam.....	347
Fig 4.21 Second derivative of Fig 4.9, 13.7 N static test, C-C aluminium beam.....	348
Fig 4.22 Second derivative of Fig 4.10, 13.7 N static test, C-C aluminium beam.....	349
Fig 4.23 Second derivative of Fig 4.11, 13.7 N static test, C-C aluminium beam.....	350
Fig 4.24 Second derivative of Fig 4.12, 13.7 N static test, C-C aluminium beam.....	351
Fig 4.25 Second derivative of Fig 4.13, 13.7 N static test, C-C aluminium beam.....	352
Fig 4.26 Seventh order polynomial fit of displacement shapes, sine excitation, C-C aluminium beam.....	353
Fig 4.27 First derivative of Fig 4.26, C-C aluminium beam.....	354
Fig 4.28 Second derivative of Fig 4.26, C-C aluminium beam.....	355
Fig 4.29 Fourth order polynomial fit of displacement shapes, sine excitation, C-C aluminium beam.....	356
Fig 4.30 First derivative of Fig 4.29, C-C aluminium beam.....	357
Fig 4.31 Second derivative of Fig 4.29, C-C aluminium beam.....	358
Fig 4.32 Normalised displacement shapes from Fig 4.29, C-C aluminium beam.....	359
Fig 4.33 Rank 1, sine curve fit of 0.086N sine excitation, C-C aluminium beam.....	360
Fig 4.34 Rank 2, sine squared fit of 0.086N sine excitation, C-C aluminium beam.....	361
Fig 4.35 Rank 5, fourth order polynomial fit of 0.086N sine excitation, C-C aluminium beam.....	362
Fig 4.36 Rank 8, classical fit of 0.086N sine excitation, C-C aluminium beam.....	363
Fig 4.37 Rank 1, fourth order polynomial fit 0.60N sine excitation, C-C aluminium beam.....	364
Fig 4.38 Rank 2, sine squared fit of 0.60N excitation, C-C aluminium beam.....	365

Fig 4.39 Rank 3, sine fit of 0.60N sine excitation, C-C aluminium beam.....	366
Fig 4.40 Rank 4, classical curve fit of 0.60N sine excitation, C-C aluminium beam.....	367
Fig 4.41 Second derivative of Fig 4.33, C-C aluminium beam.....	368
Fig 4.42 Second derivative of Fig 4.34, C-C aluminium beam.....	369
Fig 4.43 Second derivative of Fig 4.35, C-C aluminium beam.....	370
Fig 4.44 Second derivative of Fig 4.36, C-C aluminium beam.....	371
Fig 4.45 Second derivative of Fig 4.37, C-C aluminium beam.....	372
Fig 4.46 Second derivative of Fig 4.38, C-C aluminium beam.....	373
Fig 4.47 Second derivative of Fig 4.39, C-C aluminium beam.....	374
Fig 4.48 Second derivative of Fig 4.40, C-C aluminium beam.....	375
Fig 4.49 Rank 2 curve fit of data near clamp, fourth order polynomial, C-C aluminium beam.....	376
Fig 4.50 Second derivative of Fig 4.49, C-C aluminium beam.....	377
Fig 4.51 Coefficients 'a' for fourth order polynomial fits, C-C aluminium and CFRP beams.....	378
Fig 4.52 Fourth order polynomial fit of displacement shapes, sine excitation, C-C CFRP beam.....	379
Fig 4.53 First derivative of Fig 4.52, CFRP beam.....	380
Fig 4.54 Second derivative of Fig 4.52, CFRP beam.....	381
Fig 4.55 Fourth order polynomial fit of displacement shapes, sine excitation, P-P aluminium beam.....	382
Fig 4.56 Second derivative of Fig 4.55, P-P aluminium beam.....	383
Fig 4.57 Sixth order polynomial fit of displacement shapes, sine excitation, P-P aluminium beam.....	384
Fig 4.58 First derivative of Fig 4.57, P-P aluminium beam.....	385

Fig 4.59 Second derivative of Fig 4.57, P-P aluminium beam.....	386
Fig 4.60 Gaussian fit of displacement shapes, sine excitation 0.61 N, P-P aluminium beam.....	387
Fig 4.61 Lorentzian fit of displacement shapes, sine excitation 3.06 N, P-P aluminium beam.....	388
Fig 4.62 Second derivative of Fig 4.60, P-P aluminium beam.....	389
Fig 4.63 Fourth order polynomial fit of displacement shapes, width direction, C-C-C-C aluminium shaker plate.....	390
Fig 4.64 Normalised displacement shapes from Fig 4.63, C-C-C-C aluminium shaker plate.....	391
Fig 4.65 First derivatives of Fig 4.63, C-C-C-C aluminium shaker plate.....	392
Fig 4.66 Second derivatives of Fig 4.63, C-C-C-C aluminium shaker plate.....	393
Fig 4.67 Fourth order polynomial fit of displacement shapes, length direction, C-C-C-C aluminium shaker plate.....	394
Fig 4.68 Normalised displacement shapes from Fig 4.67 C-C-C-C aluminium shaker plate.....	395
Fig 4.69 First derivative of Fig 4.67, C-C-C-C aluminium shaker plate.....	396
Fig 4.70 Second derivative of Fig 4.67, C-C-C-C aluminium shaker plate.....	397
Fig 4.71 Coefficients 'a' for fourth order polynomial fits, C-C-C-C aluminium and CFRP shaker plates.....	398
Fig 4.72 Fourth order polynomial fit of displacement shapes, length direction, C-C-C-C CFRP shaker plate.....	399
Fig 4.73 Normalised displacement shapes from Fig 4.72, C-C-C-C CFRP shaker plate...	400
Fig 4.74 First derivative of Fig 4.72, C-C-C-C CFRP shaker plate.....	401
Fig 4.75 Second derivative of Fig 4.72, C-C-C-C CFRP shaker plate.....	402
Fig 4.76 Fourth order polynomial fit of displacement shapes, width direction, C-C-C-C CFRP shaker plate.....	403
Fig 4.77 Normalised displacement shapes of Fig 4.76, C-C-C-C CFRP shaker plate.....	404

Fig 4.78 First derivative of Fig 4.76, C-C-C-C CFRP shaker plate.....	405
Fig 4.79 Second derivative of Fig 4.76, C-C-C-C CFRP shaker plate.....	406
Fig 4.80 Comparison of the fundamental resonance contribution with increasing strain levels.....	406a
Fig 5.1 Strain time history, 0 to 12 seconds, 10-400 Hz random excitation, C-C aluminium beam.....	407
Fig 5.2 Expanded time history from Fig 5.1, a= 0-0.1 s, b=0.1-0.2 s, c=0.2-0.3 s.....	408
Fig 5.3 Expanded time history from Fig 5.1, a=0.3-0.4 s, b=0.4-0.5 s, c=0.5-0.6 s.....	409
Fig 5.4 Clamped aluminium shaker plate, time histories, 10-1000 Hz random excitation, a=0-0.1 s, b=0.1-0.2 s, c=0.2-0.3 s.....	410
Fig 5.5 Clamped aluminium shaker plate, time histories, 10-1000 Hz random excitation, a=0.3-0.4 s, b=0.4-0.5 s, c=0.5-0.6 s.....	411
Fig 5.6 Minor peaks, PPDF, run 21, SG2, C-C-C-C aluminium shaker plate.....	412
Fig 5.7 Major peaks, PPDF, run 19, SG2, C-C-C-C aluminium shaker plate.....	413
Fig 5.8 Normalised strain major peaks, PPDF, SG1, 10-400 Hz random, 0.50 and 6.46 N, comparison with Gaussian, C-C aluminium beam.....	414
Fig 5.9 Normalised strain major peaks, PPDF, SG3, 10-400 Hz random, 0.50 and 6.46 N comparison with Gaussian and Rayleigh, C-C aluminium beam.....	415
Fig 5.10 Normalised strain major peaks, PPDF, SG3, 10-1000 Hz random, 0.815 and 12.2 N compared with Gaussian, C-C aluminium beam.....	416
Fig 5.11 Normalised strain major peaks, PPDF, SG2, 10-1000 Hz random, 1.46 and 14.4 g compared with Gaussian, C-C-C-C aluminium shaker plate.....	417
Fig 5.12 Strain time history, 0 to 25 seconds, 10-1000 Hz random excitation, C-C-C-C aluminium shaker plate.....	418
Fig 5.13 Normalised strain APDF comparisons, from 12 and 25 seconds time histories with Gaussian, C-C-C-C aluminium shaker plate.....	418
Fig 5.14 Normalised strain PPDF comparison with Gaussian, SG 7, C-C-C-C CFRP shaker plate.....	419

Fig 5.15 Normalised strain PPDF comparison with Gaussian, SG10, C-C-C-C aluminium APWT plate.....	420
Fig 5.16 Normalised strain PPDF comparison with Gaussian, SG 9 and 10, C-C-C-C aluminium APWT plate.....	421
Fig 5.17 Normalised strain PPDF comparison with Gaussian, SG 2, C-C-C-C CFRP APWT plate.....	422
Fig 5.18 Characterization of S-N curve, DTD 5070 aluminium alloy.....	423
Fig 5.19 ϵ -N curves for BS 1470-NS3, aluminium alloy.....	424
Fig 5.20 ϵ -N curve comparisons.....	425
Fig 5.21 Damage accumulation for cantilevered and clamped beams.....	426
Fig 5.22 Damage accumulation for C-C aluminium beam.....	427
Fig 5.23 Damage accumulation for C-C-C-C aluminium shaker plate.....	428
Fig 5.24 Cumulative damage comparison, cantilevered and C-C beams.....	429
Fig 5.25 Cumulative damage comparison, C-C aluminium beam and C-C-C-C aluminium shaker plate.....	430
Fig 5.26 Rank 1, curve fit of PPDF, SG 2, C-C-C-C aluminium shaker plate.....	431
Fig 5.27 Rank 41, curve fit of PPDF, SG 2, C-C-C-C aluminium shaker plate.....	432
Fig 5.28 Rank 1 curve fit, part of PPDF data, SG 2, C-C-C-C aluminium shaker plate....	433
Fig 5.29 Linear mode shape comparison of C-C-C-C aluminium and CFRP shaker plates and CFRP APWT plate.....	434
Fig 5.30 Comparison of changes in cyclic multimodal frequencies.....	435

NOMENCLATURE

A	area
A_0	reference area
AGARD	Advisory Group in Aeronautical Research and Development
AL or ALUM	aluminium
APDF	amplitude probability density function
APWT	Acoustic Progressive Wave Tube
A/D	analogue to digital
C-C	clamped - clamped boundary conditions
C-C-C-C	clamped - clamped - clamped - clamped boundary conditions
CFRP	carbon fibre reinforced plastics
DOF	degrees of freedom
E	Young's modulus
ESDU	Engineering Sciences Data Unit
F	force
F_0	uniformly distributed static force
G/E	graphite epoxy
$G_x(f_n)$	sound power spectral density
G_{xy}	shear modulus
I	second moment of area of the cross-section
Hz	Hertz
ISVR	Institute of Sound and Vibration Research
M or MIC	microphone
M	number of peaks
K	constant
N	Newton
N	number of cycles to failure
N_i	number of cycles at stress level S_i
N_s	number of samples
N_t	total number of samples
N_t	total number of cycles to failure
OSPL	overall sound pressure level
PC	personal computer
P-P	pinned - pinned boundary conditions
PDF	probability density function
PPDF	peak probability density function
PWL	sound power level
R	test run number
S	stress
S-S-S-S	simply supported boundary conditions
S_{rms}	root mean square stress

SR	sampling rate
S_o	static stress
SPL	sound pressure level
SG	strain gauge
T	time period for one Fourier transform in seconds
T_n	number of Fourier non-overlapping transforms
T_t	total data record length in seconds
W	power in Watts
W_{ref}	reference power in Watts
WP or WPAFB	Wright - Patterson Air Force Base
a,b,c,d.....	coefficients
c	damping coefficient
c_c	critical damping coefficient
dB	decibel reference $20\mu Pa$
f	frequency
f_c	cyclic frequency
f_{cm}	cyclic multimodal frequency
f_{max}	highest frequency of interest
f_n	resonant frequency
f_q	Nyquist frequency
f_s	sampling rate
g	acceleration due to gravity
h	thickness
m	mean
p	probability density function
p_p	peak probability density function
\bar{p}	pressure rms
\bar{p}_{ref}	reference pressure= $20\mu Pa$
rms or RMS	root mean square
sd	standard deviation
t	time
α	slope of S-N curve plotted logarithmically
ϵ	strain
ϵ_a	axial strain
ϵ_b	bending strain
ϵ_t	total strain
ϵ	coefficient
Δf	frequency of resolution
κ	nonlinear parameter of the cubic stiffness
σ	standard deviation

ℓ
 ψ
 ζ

length
function
viscous damping ratio

ACKNOWLEDGMENTS

The authors wish to express their appreciation and gratitude to the friends and colleagues who have supported this lengthy project. A debt of gratitude is due to our previous supervisors, Jerome Pearson and Ralph Shimovetz, the staff at Wright Laboratory and the training staff for the award of a one year long term full time training program at ISVR. Without their financial assistance, the training abroad would not have been possible. The following list is by no means complete but special mention is appropriate:

At the Institute of Sound and Vibration Research:

Professor R G White for his guidance, encouragement, patience and council in helping to start and continue the program of study leading into the project. His hospitality at school, in his home and on the air field was greatly appreciated.

Dr Maurice Petyt for his guidance, advice, encouragement and help during this study.

Dr Neil Ferguson for his guidance, advice, encouragement and help during this study.

Professor J K Hammond for his help, encouragement and advice in signal processing and many other areas.

Sally Abrams for her friendship, administrative support, typing support and help in social activities.

Maureen Strickland for her friendship, encouragement and help during visits to England.

Professor Neil Halliwell and John Baker for their assistance and help in laser vibrometry.

John Hawke and Jim Baker for their help in building the test rig, instrumenting the test specimens and their assistance in the acoustic progressive wave tube tests.

At the Center for Structural Vibration and Acoustics, Old Dominion University:

Professor Chuh Mei and Dr. Roger Chen for their guidance, advice, encouragement and help with the finite element analysis.

At Wright Laboratory:

Dansen Brown and Cindy Shroyer for their help and advice with computers, signal processing and analysis of the test data.

Gene Maddux for his help and assistance with laser scanning vibrometers, laser holography and curve fitting techniques.

Arnel Pacia and Kevin Harris for their help with instrumentation and testing in the acoustic progressive wave tube.

Dr Jon Lee and Bob Gordon for their help and assistance in vibration theory and methods of analysis.

Dr George Sendeckyj, Dr Greg Schoeppner and Doug Dolvin for their help fabricating carbon fibre test specimens and the characterization of the composite material properties.

Larry Simmons and TSSI contractors for help, assistance and advice in acquiring all the equipment, fixtures and setting up and conducting the tests at Wright Laboratory.

FOREWORD

This technical report summarizes the information contained in M. Phil/Ph.D. Progress Reports submitted in 1990, 1991, 1992, 1993 and 1994 to Professor R.G. White, Academic Supervisor, at the Institute of Sound and Vibration Research (ISVR), University of Southampton, England. The work was performed under the supervision of Professor R.G. White and R.M. Shimovetz, Technical Manager, Acoustics and Sonic Fatigue Section, Structural Dynamics Branch, Wright Laboratory, Wright-Patterson Air Force Base (WPAFB). The initial work at ISVR, published in WL-TM-91-311-FIBG, has been continued at WPAFB. A second technical memorandum was published, WL-TM-92-352-FIBG. A third technical memorandum was published, WL-TM-94-3077. This report summarizes all the above work and the work continued to complete the project.

PREFACE

Acoustic fatigue failure in aerospace structures has been a concern for many years. New prediction techniques are needed for the new materials and structural concepts of interest and higher sound pressure levels encountered. The objective of this work is to improve the understanding of the nonlinear behavior of beams and plates excited from low to high levels of excitation and to develop multimodal fatigue models for aircraft structures. Tests were conducted utilizing a clamped beam statistically tested and shaker driven at increasing levels of excitation. Experiments were also conducted utilizing clamped plates excited by a vibration shaker and an acoustic progressive wave tube. Two types of materials were selected for the experiments, an aluminum alloy and a carbon fibre reinforced plastic. The total strains and the components, bending and axial and the displacements were measured with increasing levels of excitation. Bistable behaviour was observed with sinusoidal excitation for both the beams and plates. The measured axial or in-plane strains were very low compared to the bending strains. However, the axial strain lowered the bending strains from that predicted with linear bending theory. The randomly excited beams exhibited a slight frequency shift and peak broadening, which can be attributed to an increased stiffening or hard spring geometric nonlinearity. The randomly excited plates exhibited a greater frequency shift and peak broadening than the beams. The dynamic tests resulted in a nonlinear relationship between the response strains and displacements. The implications of nonlinear behaviour of beams and plates relative to fatigue lives has been studied. The Miles single mode model has been modified to account for the multimodal strain response of clamped straight beams and flat plates. Trends in the strain peak probability densities at low level and high levels of excitation were analyzed to determine the effects of axial strain on their shape. An effective multimodal cyclic frequency model has been developed. A method for incorporating the effects of multimodal response of simple structures is presented, together with their fatigue life estimates. The fatigue model developed gave reasonable estimates of the fatigue life of structures with multimodal response.

I INTRODUCTION

Acoustic fatigue¹ problems with military aircraft structures have continued to be expensive to solve. Results of modifications to older aircraft, changes in their usage to accommodate new weapons and equipment, extended usage and lifetimes have all had a significant cost impact. Increased performance capabilities also result in increased acoustic levels. Aircraft designs resulting in direct exhaust gas impingement on structural components have caused increased levels of excitation and high thermal loads. Flow separation and oscillating shock waves cause very high fluctuating pressure on the structures. Exposure of aircraft structures and equipment to these increasingly higher noise levels warrants the development of new prediction methods. Methods have been developed over the years to predict and reduce acoustic fatigue, but they have not kept pace with increasing requirements. In addition, future structural configurations with new materials and much higher stiffness-to-weight ratios are evolving. A better understanding of the nonlinear random vibrational response of structures is needed to improve the prediction of acoustic fatigue damage. The first part of this chapter contains a literature review. The second part contains the objectives and an outline of the study.

1.1 LITERATURE REVIEW

Acoustic fatigue life prediction methods generally include predicting the random acoustic loads, estimating the vibrational stress response of the structure and predicting the life from stress versus cycles to failure curves for the material and fastener configuration. As the acoustic load increases, the stress response becomes more nonlinear and more difficult to predict. Even in this regime the terminology *mode shape* is often used to describe the dynamic deflection shape in the neighbourhood of a resonant frequency. Strictly speaking, this is not the mode shape as there are small off-resonant contributions from other modes when measurements are made by the peak amplitude method. This terminology is commonly used throughout the published literature.

¹ The terminology *acoustic fatigue* is often found in the literature from the UK. The terminology *sonic fatigue* is often found in the literature from the USA. Both terms are used in this work to mean the same thing.

Modal analysis theory is generally based upon linear assumptions where mode shapes are amplitude independent and occur at a single frequency. In the nonlinear case, the displacement shapes and natural frequencies are dependent upon the boundary conditions, the level of the excitation force and the initial conditions. The terminology *linear mode shape* is used in this study to distinguish between the displacements measured at low levels of excitation and those obtained at high levels of excitation where the axial strains are formidable. In the latter case, the terms *nonlinear displacement shape* or *displacement shape* are used throughout this study.

1.1.1 REVIEW OF DESIGN GUIDES

Clarkson [1] recently reviewed the sonic fatigue technology evaluating the results of 170 publications on the subject. He discusses various design guides for predicting the acoustic fatigue life of metallic and composite plate-type structures. These are based on simplified theory and test data formulated into semi-empirical mathematical expressions. The predictions are based upon assuming the fundamental mode as the controlling parameter which accounts for most of the damage. Miner's [2] law and cumulative damage theory and a range of experimental results were utilized to predict the fatigue life. Single panel tests were conducted by Hess et al [3] in 1959. Lacking theoretical methods to predict acoustic fatigue lifetimes accurately, more testing of actual aircraft structures and standardized test structures evolved. These studies eventually evolved into simplified design guides in the form of nomographs by Belcher et al [4] in 1959, McGowan [5] in 1963, Ballentine et al [6] in 1968 and Rudder and Plumlee [7] in 1974. The successive developments extended into a wider range of structures both metallic and composite at room temperature and elevated temperatures. Early work at elevated temperatures is reported by Schneider and Rudder [8] in 1973. Design guides in the form of separate data sheets were published by Thomson and Lambert [9] in 1972 from data and information obtained by the Group on Acoustic Fatigue of the AGARD Structures and Materials Panel. The Engineering Science Data Unit [10] took over the early work produced by AGARD and continues updating these design guides periodically. A design guide for graphite epoxy structures was developed by Holehouse

[11] in 1984. The design guides are all based upon the simplifying single mode assumption that considers the fundamental panel mode as the only source of damage.

Multimodal effects were considered theoretically as early as 1958 by Powell [12], but it was not practical to pursue at that time. The S-N fatigue curves in references [7] and [9] are limited to narrow band random excitation around the fundamental resonance, thereby excluding higher frequency resonances. The experimental studies of van der Heyde and Kolb [13] used acoustic excitation of panels in the 50-800 Hz range. This included more than the fundamental resonance. Their comparisons of the multimodal response with the uni-modal prediction methods of references [7] and [9] show agreement in predicting fatigue life between 0.4 to 2.0. The experimental studies of Wolfe and Holehouse [14] of adhesively bonded aluminium and graphite epoxy panels and shaker beam coupons show a difference between single mode shaker coupon fatigue data and multimode panel data. In the case of the graphite epoxy experiments, the rms stress responses of the coupons were a factor of 2 or more greater than that of the panel data for the same time to failure. Mei and Paul [15] investigate the multimodal response of clamped rectangular plates to acoustic loading. This work eventually was incorporated into MSC/NASTRAN, a finite element program [16]. A comparison is made between the multimodal response of composite and aluminium alloy plates to random acoustic loads by White [17]. This shows the importance of the multimodal response of several peaks as the excitation level increases. The frequencies of the peaks increase and the peaks become much wider as the overall level increases. The paper introduces a new method of showing the contribution of each response frequency by integrating across the normalised strain spectral density.

Many tests were confined to simple beams and plates to concentrate on gaining a fundamental understanding of the behaviour of carbon fibre reinforced plastics² by White and his co-workers [18]. White and Mousley [19] compare overall plate response levels to predictions made using the uni-modal response method described by Clarkson [1 p 17]. As

² The terminology *carbon fibre reinforced plastic* is often found in the literature from the UK. The terminology *graphite epoxy* is often found in the literature from the USA. Both terms are used in this work to mean the same thing.

the in-plane compressive loads increase, plates approach the buckling condition and 'snap-through' occurs as shown by Ng and White [20]. The coupon tests used successfully to develop basic S-N data from metal structures are not as reliable for composites. The edge peeling problem makes it difficult to reproduce the type of failure that takes place in practical structures. Usually delamination failure occurs in practical structures. To overcome this problem, White [21] developed extra wide coupons using a half sine wave clamp for the cantilevered plate to yield representative delamination failures within the plate. Further investigations using this method were reported in Drew and White [22].

Acoustic load predictions are an essential ingredient to predict acoustic fatigue life. Clarkson [1 p33-35] reviewed the literature on the many aircraft sources of noise. Sources include jet noise, turbulent boundary layer noise, separated flow, oscillating shocks and cavity oscillations. Unger et al [23] developed a guide for estimating aeroacoustic loads. More recently, Hubbard (editor) [24] developed an aeroacoustic guide including theory and practice. Coe and Chyu [25] showed the large differences in the spectra from attached boundary layer noise, intermittent shock, separated flow and shock. More recently, Laganelli and Wolfe [26] discussed prediction methods for fluctuating pressures in attached and separated flows. The load predictions should include the overall sound pressure levels, the frequency spectra and the spatial correlation. These are important in the design of test facilities to simulate the acoustic loads of the aircraft. The acoustic properties of the test facilities can considerably affect the response of the test structure.

1.1.2 CLASSICAL AND FINITE ELEMENT APPROACHES

Clarkson [1 p33-35] presents a review of the developments by Chuh Mei and his co-workers in determining the nonlinear response of beams and plates using the equivalent linearization method. Mei and Wentz [27] and Mei and Prasad [28] consider the geometric nonlinearity of large deflection of composite panels including various lay up angles and numbers of plies. The theoretical development is given for single mode response using the equivalent linearization technique. Mei and Prasad [28- 30] considered the effect of transverse shear. Chiange and Mei [31] developed the equations for the multimodal

representation of a beam. Locke and Mei [32] extended the work to the multimodal response of thermally buckled plates. By including the in-plane stretching effect in the bending formulation, the nonlinear deflections and stresses were found to be much less than those predicted by linear theory at the higher levels of excitation. The total strain at the surface is based upon the sum of the bending and axial strains. Small deflection linear bending theory neglects the strain in the mid-plane. In cases where the deflections are small in comparison with the plate thickness, the linear bending theory of Timoshenko [33] is usually adequate. For higher load values, the rate of increase of the deflection with increasing load decreases due to the increased resistance by the tensile forces in the midplane of the plate.

The work of Chuh Mei and his co-workers was incorporated into MSC/NASTRAN version 67 r 2 by Robinson, Chiang and Rizzi [34]. A new main SUBDMAP, SEMELRR, and a significantly modified MSC/NASTRAN SUBDMAP SEDRCVR are compiled with the MSC/NASTRAN delivered library of SUBDMAPs to create the new solution sequence. The equivalent linear rms displacements, strains or stresses, and frequencies are calculated by an iterative solution method. The numerical results obtained were in good agreement with existing solutions. The output requests and the iterative solution method are controlled by several new user defined PARAMeters. The versatility of the implementation will enable the analyst to determine the nonlinear random responses for complex structures under combined loads.

Gordon [35] describes an approach for generating local area finite element models of aircraft structures numerically that are reasonable in size. Constant boundary stiffness is imposed on a finite element model of a local structural area and is updated with experimental modal data. The boundary stiffness updating is tuned using a model updating procedure to minimize the error between frequencies and mode shapes of the model and experiment. The method accurately predicted the plate-like modes of two similar structures: the top plate of an electronics chassis and the centre bay of a stiffened aircraft panel. However, the local model of the stiffened panel was no better at predicting mode shapes than a clamped plate. The method is unable to predict non-plate-like modes of the stiffened panel. Accurate

experimental frequencies and model shapes are required for setting up the model and updating the boundary stiffness parameters. Engineering judgment is required in selecting the boundary stiffness design variables and in determining which modes could be accurately reproduced by the method. The implementation of the boundary stiffness updating is adequate for this type of investigation but could be improved. The simplex search optimization method used converged very slowly. The proposed method should work equally well and converge much faster with proven optimization tools like ASTROS [36]. Finally, the local models tuned for minimum frequency error resulted in significantly better frequency agreement and only slightly lower mode shape correlation than those tuned for minimum mode shape error.

1.1.3. TIME DOMAIN METHODS APPLICABLE TO ACOUSTIC FATIGUE

Clarkson [1 p 35-37] presents a review of the development of the time domain method by Vaicaitis and his co-worker for structural dynamics problems of probabilistic nature, particularly acoustic fatigue problems. A brief summary is presented here. Vaicaitis et al [37] in 1972 developed a method to simulate a boundary layer pressure field. Vaicaitis [38] extends the work and shows the time history of the generalized random force, its probability density distribution of peaks and threshold crossings. Vaicaitis and Dowell used the method to compare two cases from acoustic progressive wave tube tests. The estimates were about twice that of the measured data. Vaicaitis [39] summarizes the basic concept of the simulation procedures, the time domain modal solutions of the nonlinear equation and the Monte Carlo method as used up to 1986. Vaicaitis and Choi [40] introduce the transfer matrix method to obtain the response solution for a stiffened plate array. Attempts were made to include many forcing functions including cavity oscillations, unsteady aerodynamic pressures, thermal loads and random pressure. Vaicaitis and Choi [41] extended the previous analysis to consider fatigue life. Maekawa [42] provides one completely independent check on the method. The results show the magnitude of the response is between 2 to 3 times that of experimental results of Van der Heyde and Kolb [13]. Choi and Vaicaitis [43] use the transfer matrix method for predicting the response of a stiffened panel and to solve the

response equation. The simulation method was used to determine the time history response. Very close agreement between theory and the experiments of Van der Heyde and Kolb was achieved for nonlinear response. Robinson and Mei [44] also use the time domain approach with the finite element method.

Vaicaitis [45] describes the general features of the time domain method. The key ingredient in this approach is the ability to simulate efficiently multi-dimensional and multi-variate random processes in the time-space domain [46-48]. The time domain Monte Carlo method consists of three basic steps: (1) realizations of random inputs and/or random system parameters are generated utilizing simulation procedures of random processes, (2) the equations of motion are solved numerically for each realization, (3) statistical moments, distributions and other quantities of the random response process are computed from the ensemble solutions. For the cases where the ergodicity condition is applicable, the ensemble statistics can be replaced with temporal averages thereby saving computation time. Thermal effects, buckling and snap through effects are included. The acoustic loads are digitally simulated using a multi-dimensional stationary and homogeneous Gaussian random surface pressure. The significant advantage of the time domain method is that it can be extended to regions involving nonlinear kinematic and nonlinear material behaviour. Nonlinear kinematic relationships are used to model the strain-displacement behaviour of flat homogeneous panels. Von Karman's theory of large deflection of thin plates is used to develop the equations of motion. A Galerkin like procedure is used to develop a system of nonlinear differential equations. Discretely stiffened homogeneous panels and composite panels are discussed. Research and design efforts for fatigue life estimation are basically proceeding along two lines: stress-type cumulative damage theories and fracture mechanics (crack growth) approaches. The fracture mechanics theories are nonlinear and deal with the stress intensity at the crack tip rather than the continuum state stress used in the cumulative damage approach. Even though significant gains have been achieved in damage estimation by fracture mechanics, there are many deficiencies such as proper models for random load spectra, predictions for crack initiation, accounting for material and manufacturing imperfections, and reliable knowledge of two or three-dimensional stress field states at the

crack tip. For composite and metallic materials, the fracture mechanics models seem to fail in reliable prediction of fatigue damage. In addition, the stress response of surface panels to random pressure is dominated by relatively high frequencies in the range of 100-1000 Hz. Thus, the crack growth stage for high cycle fatigue might be very short as compared to the crack initiation stage before a crack can be measured and assigned an initial crack size in the crack growth model. In the present time domain approach, it would be a straight forward procedure to incorporate the stress response time histories in the crack growth models and then estimate damage on a cycle-by-cycle basis. Due to the various uncertainties discussed earlier and computational difficulties for realistic structural models, such an approach is not undertaken in Vaicaitis' study. The earliest method of fatigue analysis based on constant amplitude fatigue tests is the Miles [49] cumulative damage model. Various tests [50-52] indicate a significant range in damage predictions. To improve on fatigue life predictions, cumulative damage theories that incorporate the nonlinearity of the damage rate [53 and 54] and stress interaction effects [55-58] have been proposed. Furthermore, the larger scatter of experimental data in fatigue tests has led to the general conclusion that fatigue damage is a random process. Numerous research efforts have been devoted to treating the fatigue damage as a stochastic model where the key random parameters are loading and material response to stress cycles [59-65]. A more refined cumulative damage rule for constant amplitude cycling and stochastic modeling of fatigue damage has been proposed by Kutt [66]. For the constant amplitude cumulative damage, an interaction function is introduced which accounts for the effect of the sequence of high-low and low-high cycle transitions. The stochastic model of fatigue damage is a function of random quantities such as loading and material properties. The nonlinear nature of the stress response leads to a non-Gaussian distribution of stress amplitudes. Analytical expressions to predict fatigue damage for non-Gaussian response are available for only a few limited cases [67]. A starting point in developing a damage theory that is consistent with the present time domain approach for nonlinear/non-Gaussian response is to utilize fatigue data from coupon testing. Size and mean stress effects, imperfections, local stress-strain relations of the material at bonds, connections, rivets, etc, could be built into the model utilizing experimental and empirical information. Vaicaitis [45] applied the cumulative damage method to an isotropic and discretely stiffened titanium panel and discussed the results.

1.1.4. DAMPING CONSIDERATIONS

Damping is a major factor in determining the resonant peak response of a structure. Since there are no theoretical methods to determine the damping factor of typical structures, measurements have been relied upon to estimate the frequency average values as discussed by Ranky and Clarkson [68]. A thorough review of the subject is found in a damping design guide, Soovere and Drake [69]. Many papers dealing with all aspects of damping and its influence on structural response were published in conference proceedings by Rogers in 1984 [70], 1986 [71], 1989 [72], 1991 [73] and 1993 [74], Ni and Adams [75] and White and Adbin [76] studied the damping properties of laminated plates and beams. Nonlinear damping is the next stage of sophistication. This is due to its inherent nonlinear behaviour at large amplitude displacements. Mei and Prasad [77-79] include nonlinear damping as well as large amplitude displacements in their theory. The purpose is to explain the observed broadening of the response peak and its increase in peak frequency of response. The first study using a single mode approach on a beam is extended to plates. The third study included additional modes. Clarkson [1 p 33] observed that the broadening does not look as great as that observed by White [17]. Schudt [80] and Zavodney studied the nonlinear response of beams excited by random excitation. The peak broadening is modelled by including cubic stiffness terms in the equations of motion. It can also be simulated by including higher damping factors.

1.1.5 REVIEW OF RANDOM PROCESSES

The theory of nonlinear random vibration has not reached a state of maturity. Ibrahim [81] indicates that although many methods of solution exist, there can be no general rule about the suitability of any method for a particular nonlinear system. Most theories for the dynamic response of beams and plates for geometric nonlinearities were based upon the Duffing equation or equations of motion with some nonlinear stiffness term or terms. Among the most widely used are the Fokker-Planck equation solutions, perturbation methods, equivalent stochastic

linearization, stochastic averaging, cumulant-neglect closure, energy dissipation balancing and the time domain Monte Carlo approach [45]. Two types of excitation are usually considered: deterministic and random excitation. The nonlinear deterministic or sinusoidal cases results in a jump phenomenon. The random excitation case usually results in stochastic chaos. Gleick [82] describes many interesting accounts of discovery in the field of chaos. Although highly mathematical in origin, chaos is a science of the everyday world. It offers a way of seeing order and patterns where formerly only the random, the erratic and the unpredictable had been observed.

Random processes are described by many others in the literature. Particularly applicable for acoustic fatigue is Rice's [83] mathematical analysis of random noise through physical devices, primarily vacuum tubes or from thermal agitation of electrons in resistors. His main interest is in the statistical properties of such noise contained in Part III [84], and he leaves to one side many of the physical results of which Nyquist's law may be given as an example. He first states the results, then shows that they were plausible by methods that are heuristic rather than rigorous. He shows that the distribution of peak values depends on a quantity $N_0 / 2M$ where N_0 is the number of zero crossings and $2M$ is the number of positive and negative peaks. Thompson [85] explains that for a sine wave or a narrow band process, N_0 is equal to $2M$ so that the ratio $N_0 / 2M = 1$. For a wide band random record, the number of peaks will greatly exceed the number of zero crossings so that $N_0 / 2M$ tends to approach zero. When $N_0 / 2M = 0$, the probability density distribution of peak values turns out to be Gaussian, whereas, when $N_0 / 2M = 1$, as in the narrow band case, the probability density distribution of the peak values tends to a Rayleigh distribution. When a wideband signal is put through a narrow band filter or a resonant system where the filter bandwidth is small compared to its central frequency, we have the third type of wave that is apparently of a constant frequency oscillation with slowly varying amplitude and phase. The probability distribution for its instantaneous values is the same as that for a wide band function namely Gaussian. However, the absolute values of its peak, corresponding to the envelope, will have

a Rayleigh distribution. This corresponds to peak probability distributions for the narrow band record. The Gaussian distribution is symmetrical about the mean value, assumed to be zero in this case, with the following equation,

$$p(x) = \frac{1}{\sigma\sqrt{2\pi}} e^{-x^2/2\sigma^2} \quad (1.1)$$

The standard deviation σ is a measure of the spread about the mean value. The total area under the curve is equal to one. Random variables restricted to positive values, such as the absolute values of the amplitudes often tend to follow the Rayleigh distribution, which is defined by the following equation,

$$p(x) = \frac{x}{\sigma^2} e^{-x^2/2\sigma^2} \quad x>0 \quad (1.2)$$

For a wideband record, the amplitude, phase and frequency all vary randomly and an analytical expression is not possible for its instantaneous value.

Newland [86] describes a stationary process as an ergodic process if, in addition to all the ensemble averaging being stationary with respect to time, the averages along any sample are the same as the ensemble averages. Strictly speaking, a random process cannot be precisely predicted in advance. If it changes with time, the process is generally nonstationary. For engineering purposes it usually is adequate to assume the process is stationary or weakly stationary. The random process is said to be stationary if the probability distributions obtained for the ensemble do not depend upon time.

Since there is a limit to the number of data points that can be fed into a computer, there is a limit to the length of the sample function that can be analyzed. This restricts the length of the samples and causes some loss in precision similar to that occurring in analogue data analysis with a finite averaging time. The accuracy depends on the length of the record in

time and the bandwidth. However, the bandwidth is not that of an analogue filter, but it must be interpreted in a different way when analyzing the data digitally.

1.1.6. REVIEW OF BEAMS AND PLATES SINUSOIDALLY EXCITED

Many theoretical and experimental analyses of nonlinear vibrations of beams and plates excited sinusoidally have been conducted. The following brief review mentions representative examples of the work performed. Many types of nonlinear behaviour are due to material properties, geometric effects, midplane stretching, nonlinear damping or any combination along with other types. The Duffing equation has been useful in describing cubic stiffness nonlinearity. The basic solutions of this equation is the backbone curve described by Nayfeh and Mook [87] and many others. The difficulty lies in the evaluation of the coefficients for various cases. The fundamental resonance and its stability were studied by Eisley [88], Srinivasan [89], Bennett [90] and Bennett and Eisley [91]. The problem was first reduced to that of a finite degree of freedom system by applying the Galerkin method to obtain the steady state solutions. The resulting equations were solved using the harmonic balance method. The experimental results of Bennett and Eisley compared favourably with their analytical results, but the accuracy of the experiments seemed insufficient for precise evaluation of the numerical results. Yamaki and Mori [92] and Yamaki, Otomo and Mori [93] also studied theoretically and experimentally nonlinear vibrations of clamped beams using the harmonic balance method. Discrepancies between theory and experiments were significant with increase in amplitude. These were attributed to insufficient rigidity of the base frame of the beam as well as to the restricted degrees of freedom of the beam assumed in the theory. A variety of nonlinear responses were found to occur in connection with the internal and combination resonances as well as dynamic snap-through for which the experimental results seemed to provide effective data. Nonlinear responses of a buckled beam under initial axial load have been studied by Tseng and Dugundji [94]. Ray and Bert [95] studied the nonlinear vibration of a beam with pinned ends. They compared their experimental results with three models: an assumed space model, an assumed time model and the Ritz-Galerkin method. The Ritz-Galerkin method coincides numerically with the

perturbation method and with the assumed-time-mode method. With all the simplifying assumptions made in the analyses, the results were considered validated by the experiments. The assumed-time-mode and the Ritz-Galerkin method were preferred over the perturbation method due to the ease in applying them. Caughey [96] showed the existence and stability of ultraharmonics and subharmonics in forced nonlinear vibrations. Countryman and Kannan [97] discussed the limitations of the harmonic balance method and used an iterative approach. Dickinson and Di Blasio [98] used orthogonal polynomials in the Rayleigh-Ritz method to study buckled rectangular plates. Chu and Herrman [99] studied beams and plates considering the possibility of modal interactions. Chaotic motions of systems with multi-positions of equilibria have been investigated by computer simulations and experiments by Moon [100], Chuster [101], Guckenheimer [102], Leven [103] and Maewal [104].

Nayfeh, Mook and Sridhar [105] illustrated the importance of considering internal resonance in nonlinear response of beams and plates excited sinusoidally. Nayfeh and Mook [87] defined internal resonances as frequency relationships in the presence of appropriate nonlinearities that lead to modal interactions when some of the natural frequencies are commensurate or nearly commensurate. They also describe the method of multiple scales for solving the equations. Nayfeh, Mook and Lobetiz [106] discuss the developments of nonlinear analysis of structural vibrations needed for a combined numerical and perturbation technique. A comprehensive review of previous work is discussed. Nayfeh [107] describes the perturbation method based on the method of multiple time scales and the techniques of using the method. Ibrahim, Afaneh and Lee [108] investigated nonstationary response characteristics of multimode interaction in a clamped beam axially loaded (compression) and harmonically excited. They examined the stochastic bifurcation of the unexcited modes of a clamped beam. They also discuss the developments of nonlinear analysis of structural vibrations. Benamar, White and Bennouna [109] studied the effect of large amplitudes on the fundamental mode shapes of fully clamped plates. They studied aluminium alloy plates both experimentally and theoretically which exhibited a high degree of geometrical nonlinearity. This was attributed to high in-plane stiffnesses inducing a higher contribution of the axial strain energy to the total strain energy at large displacement amplitudes. Even higher nonlinearities were obtained with composite plates.

1.1.7. REVIEW OF BEAMS AND PLATES RANDOMLY EXCITED

Many theoretical and experimental analyses of nonlinear vibration of beams and plates excited randomly have been conducted. The following brief review mentions representative examples of the work performed. Nayfeh and Serban [110] studied the effect of combined deterministic and random excitations on nonlinear systems. Lyon et al [111] considered narrow band random excitation of a hardening spring oscillator represented by the Duffing equation. The purpose was to find out if the well known jump phenomenon can occur under narrow band random excitation. The multivalued response characteristics had the same general appearance as those for sinusoidal forcing except that the peaks are much sharper. Similar results were also obtained by Lennox and Yusak [112], Rajan and Davies [113], Iyengar [114] and Roberts and Spanos [115]. Ibrahim, Lee and Afaneh [116] investigated stochastic bifurcation in moments of a clamped beam response to wide band random excitation. Schudt and Zavodney [80] studied the nonlinear response of beams to random excitation using an externally excited 'hardening Duffing oscillator'. The purpose was to study peak broadening by generating a family of typical response characteristics. These characteristics represent the effects of the damping and the cubic nonlinearity coefficients in the Duffing oscillator when subject to random excitation.

$$\ddot{x} + 2\epsilon\dot{x} + x + \kappa x^3 = F(t) \quad (1.3)$$

where ϵ , ζ and κ are coefficients. The nonlinear term is cubic or third order. The viscous damping ratio coefficient is ζ fixed at selected realistic values. The other coefficients are selected accordingly to study their effect on the response. The response is obtained by direct integration of the governing equation of motion using a fifth order Runge-Kutta-Verner algorithm. Bennouna and White [117] studied the effects of large vibration amplitudes on the dynamic fundamental resonance of clamped-clamped and cantilevered aluminium alloy thin beams excited sinusoidally and randomly. A limited set of fatigue experiments shows a considerable decrease in fatigue life of the C-C beam due mainly to the axial strain, compared to

that of a cantilevered beam of the same material and at the same rms strain level. Using a statistical approach, good correlation was achieved between predicted and measured fatigue life.

1.1.8 IDENTIFICATION TECHNIQUES

The identification of mathematical models to represent dynamic system in general has attracted considerable attention in recent years. Identification of nonlinear systems ranges from methods simply to detect the presence or type of a nonlinearity to those which seek to quantify the behavior via some mathematical models. Balachandran et al [118] studied identification of structures with internal resonances to highlight the difficulties posed by these resonances. The features of free oscillations of quadratically and cubically coupled pairs of oscillators are discussed. More information about nonlinear random vibration, probabilistic theory and stochastic methods can be found in Crandal and Mark [119], Lin [120], Caughey [121], Spanos [122], Roberts [123 and 124], Ibrahim et al [125], X. Zhang et al [126], Elishakoff and X. Zhang [127] and Cederbaum et al [128]. Cederbaum's book covers among other topics random vibration of laminated composite plates, nonstationary random excitation and micromechanics of fibre-reinforced composites. Shinozuka [129] shows the generation of sample functions of a homogeneous Gaussian vector process by using the Auto-Regressive-Moving-Average (ARMA) method. Stry and Mook [130] developed a technique based on the Maximum Model Error (MME) optimal estimation approach. The most significant feature of this work is the ability to identify nonlinear dynamic systems without prior assumptions regarding the form of the nonlinearities. This method is in contrast to existing nonlinear identification approaches which usually require detailed assumptions of nonlinearities. Model form is determined via statistical correlation of the MME optimal state estimates with the MME optimal model error estimates.

Many researchers have investigated peak broadening. Zavodney [131] demonstrates a procedure to identify several types of nonlinearity in structures exhibiting nonlinear behaviour. The limitations of random and impact excitation for the purposes of identifying nonlinear coupling of modes are discussed. A method for quantifying quadratic and cubic

nonlinearity using the jump-down bifurcation is discussed. The method uses commercially available instrumentation and modal analyzers and does not require state-space variables in the formulation. Miles [132] examined a single mode response of a plate subject to high intensity acoustic loading. He used a one-degree-of-freedom Duffing oscillator to model the temporal response of the spatial (one mode) shape function. The numerical simulation study showed broadening of the resonant peak in the stochastic power spectral density curve. Since he had only a positive cubic term and linear viscous damping, he concluded that the peak broadening behaviour can be effected by only a nonlinear stiffness term. Comparisons of stochastic response data to harmonic sweep data are also discussed for several levels of excitation. These studies show cases of close agreement with numerical simulation data.

1.1.9 MODAL ANALYSIS METHODS

The study of structural mode shapes has grown considerably over recent years as described in the proceedings of the International Modal Analysis Conferences (IMAC) and many other publications. One of the more recent publications is a keynote address by Allemang [133] at the Eleventh IMAC. Many experimental modal analysis packages of software and hardware are commercially available that are relatively inexpensive. Rost and Brown [134] give a brief history of the events that led to this development. Advances in electronics and computer technology made it practical to develop systems with a low cost per channel that can take hundreds of simultaneous measurements. These methods are especially useful in vibration analysis of complex structures. Modal analysis can be a powerful tool in the study of structural dynamics, but a number of assumptions and limitations are inherent. Dobson [135] describes the main requirements which are linear behaviour together with idealised forms of damping. Some developments in quantifying nonlinearity are described by Tomlinson [136]. Meirovitch [137] defines modal analysis as the procedure of solving the system of simultaneous differential equations of motion by transforming them into a set of independent equations by means of the modal matrix. The modal matrix is defined to be orthogonal with respect to the mass matrix and the stiffness matrix. Both matrices are uncoupled and orthonormal, all of which are linear

assumptions. Ewins [138] describes some of the practical theory for modal testing. Modal testing was originally used to define the natural frequencies and mode shapes of a structure. The extraction of frequencies and mode shapes is accomplished by many techniques. These range from selecting peaks or circle fitting, to time domain or frequency domain curve fits of frequency response functions or their transforms. Much simpler and less expensive methods are available with earlier techniques. These include the observation of sand patterns formed along the nodal lines of a flat structure sinusoidally excited, noting the frequencies. Accelerometer mapping of a vibrating structure at its resonant frequencies, yields mode shape after normalization. These suffer from being too time consuming and cumbersome to obtain the data in computer files.

1.1.10 RANDOM FATIGUE METHODS

Further fatigue work, other than that cited above, is included in this section. Lambert [139] develops equations for the multiple degree-of-freedom system randomly excited by adding both the stresses and effective frequencies of the multiple modes in the rms sense rather than the linear sense. His multiple mode treatment is for a 2 degree-of-freedom (DOF) system. The 2 DOF equations based on the linear summation and the rms summation are compared with the fibreglass experimental data of Brock [140]. The damage accumulated for each individual mode based on the linear summation is discarded because of the large disparity (factor of 10) with experimental results. The rms summation technique compared much more favourably (factor of 1.7) with experimental results. Later, Lambert [141] developed analytical expressions for the fatigue life of various random stress peak distributions. These included the Rayleigh, exponential, truncated exponential, skewed Rayleigh and the finite sample size Rayleigh distribution. Examples are worked out for aluminium alloy 7075-T6 using sinusoidal fatigue data for the distributions mentioned.

Bernstein [142] investigates a procedure for analytically comparing the fatigue damage under broad and narrow band random stress cycles. An approximate analytical expression is developed for fatigue damage as a function of stress levels and frequencies in multiple modes. This is used to determine the stress level required in a single mode to generate equivalent fatigue damage. He measures strains during sonic fatigue tests using both broad and narrow spectra to calculate damage per unit time. Small increases in the narrow band spectrum strain are required to make the damage equivalent to that from the broad spectrum.

Curtis and Morte [143] investigate the increase in average times to failure which may be expected due to the absence of stresses in excess of $\pm 3\sigma$ and the lack of fatigue damage for stress reversals less than the endurance limit. Only narrow band random loads are considered. A Rayleigh distribution of stress peaks is assumed. As the slope of the S-N curve increases, the time to failure decreases as expected. The point of damage for stresses in excess of $\pm 3\sigma$ is not conclusive since the author only investigated $\pm 3\sigma$.

Blevins [144] extends the formulation of Clarkson [145] to higher modes and complex shapes. Approximate analytical methods are developed for determining the response of plate and shell structures to coherent sound fields. The methods are based on separating the spatial and temporal aspects of the problem and then developing approximations for both. The method is most applicable to relatively uniform flat or curved panels which respond out of plane to these pressures. It can be used for simple direct calculation of the response of panels to random and harmonic surface pressure loads. The method requires that the natural frequencies and mode shapes of the panels be calculated. Either closed form, numerical or experimental methods of modal analysis can be used. The method also requires that the relationship between modal deformation and modal stress be known if stress predictions are desired. Damping and the magnitude of the applied pressures are also required inputs. The method does not require exact knowledge of the distribution of the applied surface pressures. Approximate distributions are generated which are consistent with the modal response of the panel. Corrections are then applied to allow for the influence of the acoustic wavelength

relative to the wavelength of the panel modes. The method is applicable to the fundamental and higher modes. Comparisons with the ESDU [10] methods show that the present method agrees exactly for the stress in flat panels and is within 12% for the stress in a curved panel. The advantage of this method over the ESDU method is that it is capable of predicting response of complex plates and shells, and it can predict higher mode response as well as response to both random and deterministic stationary surface pressures. Direct comparison is made with experimental data for the response of an integrally stiffened titanium panel. The results show that the theory agrees with the experimental results within the uncertainty of the experimental method.

1.2 OBJECTIVE AND OUTLINE OF THE STUDY

The objective of this study was to improve the understanding of the nonlinear behaviour of beams and plates excited to high levels of vibration. The prediction of aeroacoustic and thermal loads and fatigue failure are not included. The focus is the development of methods to predict the nonlinear response of simple structures and the implications of nonlinear behaviour on fatigue life.

A series of experimental investigations were conducted using beams and plates to understand the nonlinear dynamic behaviour. Clamped aluminium alloy and carbon fibre reinforced plastic (CFRP) beams, pinned beams, and clamped plates were investigated. Static tests were also conducted on beams. Linear mode shapes and nonlinear displacement shapes were studied together with jump phenomena. The response due to random excitation was investigated. For forced vibration studies of beams, electromagnetic coils and annular permanent magnets were used. For the plate studies, a large vibration shaker and acoustic progressive wave tubes (APWT) were used. Total, axial and bending strains and displacements were measured. Frequency responses and statistical properties are investigated. Fatigue models are developed to account for nonlinear bending response and multimodal effects.

Chapter II contains a discussion of beam testing methods and instruments to measure displacement and strain. The advantages and disadvantages are studied. Data acquisition and

processing are discussed. Static bending experiments were conducted measuring displacement and strain. Sine and random excitation experiments were conducted measuring displacement and strain. The results of the aluminium alloy and carbon fibre beam experiments are analyzed and discussed.

Chapter III contains a discussion of the plate testing methods. The base excitation methods and acoustic progressive wave tube methods are discussed. The advantages and disadvantages are studied. Sine and random excitation experiments were conducted measuring displacement and strain. The results of both types of plate experiments are analyzed and discussed.

Chapter IV contains an evaluation of the test results. Comparisons with linear bending theory are made. Comparisons and trends for each experiment are discussed. The nonlinear displacement shapes were measured accurately in great detail. The shapes are curve fitted with various functions and ranked according to their *goodness of fit*. The bending strains are determined from the second derivatives of the functions. The statistical properties are compared and discussed. The multimodal behaviour of the beams and plates are discussed.

Chapter V discusses the implications of nonlinear behaviour on fatigue life. The peak probability density functions are evaluated. Multimodal modal models to estimate the strain response and fatigue behaviour are presented. A multimodal fatigue model is developed and applied to the test data with reasonable results.

Chapter VI discusses the conclusions made from the study. Conclusions are made from the test and evaluation of the data collected and the multimodal fatigue model developed. Recommendations for further studies are also made.

II BEAM EXPERIMENTAL INVESTIGATIONS

2.1. INTRODUCTION

The objective of the beam experiments was to determine the nonlinear behaviour of beams excited sinusoidally and randomly and its effect on the displacements and the total, axial and bending strains. The behaviour was examined by measuring large transverse bending responses and the axial responses induced by large deflections. The tests were conducted at sufficiently low levels to prevent fatigue failure, which was beyond the scope of this study. The fatigue studies in Chapter V investigate fatigue modelling and use the limited fatigue data already available.

Many factors were evaluated to obtain the desired results. The driving equipment to produce well defined forcing functions should have sufficient travel to cover the desired displacement ranges of interest. The force should be linear as much as possible. The devices were grouped into three categories. These were the direct or indirect attachment method, base excitation and acoustic excitation. Ng [146] discusses the advantages and disadvantages of these experimental methods.

Using acoustic excitation for the nonlinear response of beams was eliminated because the levels of excitation required for the small area of the beam to be measured were not practical. Also, the unknowns in determining the amounts of acoustic coupling between the load and response complicate the analysis to a greater degree. Acoustic excitation was used, however, to determine linear mode shapes. This method provides a low power, inexpensive means with no direct attachment to alter the response. Only low level excitation is needed for linear modal analysis. The force should be applied off the node lines in order to excite the desired mode. Small acoustic drivers and horns provide a convenient means to excite many modes because they are easily moveable.

The base excitation method for beams was eliminated primarily due to cost of operation and manufacturing suitable fixtures. Shaker performance is another limitation. However, the base excitation method was used for the plate tests as discussed in further detail in Chapter III.

The last method evaluated is the direct or indirect attachment method. Indirect methods include inductive devices which generally are not powerful enough and suffer linearity problems. There are many direct attachment methods, such as attaching a commercially available shaker directly through a slender connecting rod sometimes referred to as a 'sting'. The resonant responses of the sting should be outside the frequency range of interest in the beam response. The mass of the shaker table or 'head' and the flexural suspension system can introduce unwanted stiffness, inertia and damping effects on the beam response. For these reasons, this method was not used.

Another direct method, a one-sided push-pull system, was selected for the beam tests. A simple coil and annular permanent magnet were selected for the driving system for the nonlinear beam experiments. Inexpensive coil-magnets are available for various commercially available loud speakers. Cylindrical coils were capped off by bonding discs on one of the ends. The disc was used to attach the coil to a beam, through a plastic screw bonded to the beam. These nonmagnetic materials are not affected by strong magnetic fields. A stiff disc was used to keep the resonant frequencies above the highest frequency of interest, 2000 Hz. Annular permanent magnets were aligned with the coil. This system does not require a suspension system since the coil is attached directly to the beam. A disadvantage is the added mass of the coil attached to the beam. The use of light weight material can minimize this effect.

A linear coil response over the frequency range of interest is needed with a force versus amplitude relationship proportional to the current through the coil. This was determined by driving the coil attached to a suspended mass through a force transducer described in Appendix A. A disadvantage to this method is the back e.m.f. generated when the beam responds around its resonant frequencies. This produces a negative peak or dip in the force

spectrum with band limited random excitation. The full magnitude of the resonant response peak of the beam cannot be determined unless the spectrum level (1 Hz bandwidth) is flat across the frequency band of interest. Commercially available constant current power amplifiers were tested and it was found that they did not maintain a truly flat band limited random spectrum. Therefore, a *constant current modifier* was designed and developed at the ISVR. Further constant current modifier developments were made at the WPAFB. The feedback loop, shown in Fig 2.1, provides a method of maintaining a flat force frequency spectrum as shown later in the data.

The sizes of the beams were selected to produce deflections exceeding their thickness for the nonlinear response region but below the strain levels that produce fatigue with the available exciter force. The width was sufficiently large to make the torsional resonant frequencies higher than the bending resonant frequencies of interest. The mild steel clamping blocks used were heavy and rigid with resonant frequencies well above the frequencies of interest. The clamped boundary condition requires that there be no displacement in the transverse direction, the in-plane or axial direction and no rotation. The fixture must be capable of applying high bending moments to the beam. Axial slippage can create compressive stresses that cause buckling. Although no clamping blocks can be built to produce exactly immovable boundary conditions, they can be designed to closely approximate them. Very high compressive clamping pressures are needed to prevent slippage, but must not exceed the elastic limit of the beam. A torque wrench was used to determine the optimum tightness without slippage. The edges in contact with the ends of the beam were rounded slightly to prevent stress concentrations causing early fatigue failure of the beam. A tensioning block connected by a threaded rod was added to apply a static strain to the beams to prevent buckling due to thermal changes. Aluminium alloys expand much more rapidly than steel due to their larger coefficient of thermal expansion. A slight increase in temperature can cause the beam to buckle in the fixture. All blocks were accurately aligned by using a tongue and groove system and bolted to a vibration isolated bed plate as shown in Fig 2.2.

2.1.1. MEASUREMENT TRANSDUCERS

Various measurement transducers were tested to determine their suitability for beam and plate nonlinearity tests at high excitation levels. An acceptable transducer must exhibit linearity over the range of interest or dynamic range, low signal-to-noise ratio and the desired frequency response.

2.1.1.1 DISPLACEMENT TRANSDUCERS

Many methods are available to measure linear mode shapes and nonlinear displacement shapes using various transducers and techniques. Large stand-off distances for displacement transducers are required to prevent the test specimen from contacting the transducer. Displacement transducers must achieve five beam thicknesses of dynamic peak displacement, thus using a 2 mm beam would require 10 mm peak-to-peak displacement. Also, a non-contacting device is needed to prevent mass loading the vibrating surface and to avoid attachment problems. Another consideration is the cost per channel for the measuring devices.

Optical vibration transducers were developed at the ISVR by Wright [147]. The intensity of the light incident on a photocell at the observation point is proportional to the distance between the cell and the vibrating surface. Static measurements indicated that the device was acceptably linear for large deflection measurements of up to approximately 20 mm but was nonlinear at 40 mm.

Fibre optical displacement methods were considered for the beam tests, but the linear range was considered to be too small. The distance from the fibre optic source and the photodetector was only 0.5 mm.

Laser vibrometer technology is growing at a rapid pace with more capabilities, but the equipment costs are very high. An ISVR developed laser vibrometer available in 1989 did

not have sufficient range to measure the beam displacements up to the desired level. Wave distortion was apparent at relatively low displacement levels. A B&K laser vibrometer available in 1990 was tested with a clamped beam arrangement. Up to 20 mm peak-to-peak displacements were obtained before reaching the limit of the instrument. Advances were made in 1991 in scanning laser Doppler sensor technology. The rapid scanning capability along with automatic data collection and display methods are particularly advantageous in measuring mode shapes and large amplitude surface velocities. The upper velocity limit of 1 m/s has been increased to 10 m/s which facilitates the measurement of displacement shapes to very high amplitudes of several beam thicknesses with a high degree of accuracy. The inherent accuracy of these sensors is due to small wavelengths of the light beam. These capabilities plus many other features have made the scanning laser Doppler sensor very favorable for obtaining accurate experimental surface velocities for high amplitude vibration of beams as well as many other structures of interest. The integration of the velocity amplitudes yields the displacement amplitudes. A diagram of the method used is shown in Fig 2.3. The vibrometer is based on an interferometer in which a laser beam is divided into reference and signal beams [148]. The signal beam is directed onto a vibrating surface. The back reflected light is re-combined with the internal reference beam. When the surface moves, the path difference between the reference and signal beams changes. This results in intensity modulation of the re-combined beam due to interference between the reference and the signal beams. The re-combined beam is split between two independent detection channels configured so that the two signals are phase shifted by $\pm 90^\circ$, depending on the direction of motion of the surface. Electronic mixing of these signals with the carrier frequency is used to derive a single frequency shifted Doppler signal. This is converted to an analog voltage directly proportional to the instantaneous velocity of the vibrating surface.

Video holography is sometimes referred to as TV- holography or Electronic Speckle Pattern Interferometry (ESPI). Small spatial details in the deformation pattern can be resolved within the field of a TV frame to detect small deformations or movements. This method was used to supplement the plate linear mode shape measurements. A laboratory was available at WPAFB with the necessary equipment. Tyrer [149] describes the theory and application of such devices.

The arrangement used to study linear mode shape is shown in Fig 2.4. Basically, the test object is illuminated by the object wave and imaged onto the target of the camera. The reference beam is combined in line with the object beam and the resulting interference pattern is detected by the camera. Video holography is limited to very small displacements.

Other displacement transducers using ultrasonic devices and infra-red devices are inexpensive and looked promising. The ultrasonic devices tested reached one phase shift in about 2 mm which was too small. Methods of multiple phase shifting were considered but needed further development. Linear Variable Differential Transformers (LVDT) and eddy current devices were also investigated but they too had insufficient range.

2.1.1.2 ACCELEROMETER TRANSDUCERS

Selection of the accelerometer transducers was based upon the desired frequency range, linearity over the desired range of acceleration and signal-to-noise ratio. Using small accelerometers, the measured acceleration was integrated twice to obtain displacement curves of the beams. Direct attachment of a mass to the vibrating surface affects the mass of the vibrating system and thus changes the response and the resonant frequency of the system. Because the laser vibrometer method is less intrusive and more accurate in obtaining displacement curves than the accelerometer transducers, it was used in most of the studies. Accelerometers were restricted to measuring the excitation levels of the shaker system described in Chapter III.

2.1.1.3 STRAIN GAUGES AND BRIDGE AMPLIFIERS

Strain gauges having little spurious effect when used in magnetic fields were desired. Suitable strain gauges were readily available and relatively inexpensive. Temperature compensating resistive wire gauges for aluminium were selected. Many advances have been made to improve the accuracy of strain gauge measurements including bonding techniques. Temperature compensation was built into the gauge by the manufacturer using a backing material suitable for the material attached. A gauge length of 1 mm was selected for low

mass loading and because it would be small enough to locate close to the clamping frame or clamping block for both the plate and beam tests. Larger lengths produce larger averaging areas for the measurement. The same types of strain gauges were used on the CFRP material. The excitation voltage was changed from 3 volts to 1 volt to keep the power density lower for the CFRP beams and plates since the CFRP material is less conductive than the aluminium alloy.

Most strain bridge amplifiers can be either AC coupled or DC coupled. DC coupling was selected since the in-plane stretching results in a DC offset or a mean value other than zero in the strain time histories. The in-plane stretching or axial strain was one of the primary effects of interest in this study. Many sources of electronic errors contaminate the strain data when the strain bridges are DC coupled. Any DC offset in the force excitation circuit can result in a DC shift in strain. The band pass filter, current modifier, current amplifier, the strain bridge amplifier and recording system are all possible sources of contamination. Each source was carefully checked before the start of a test to eliminate electronic DC offsets as much as possible.

2.1.1.4 MICROPHONES

The selection of microphones was based upon the desired frequency range, linearity up to the highest SPL of interest and the signal-to-noise ratio. Microphones were used to measure the SPLs in the progressive wave tube tests described in Chapter III.

2.1.2. DATA ACQUISITION AND PROCESSING

A few data acquisition systems using a PC were evaluated. A portable 386 PC based system was selected with 16 channels of analogue to digital (A-D) conversion, antialiasing filters, simultaneous sample and hold, many data conversion formats, and a wide range of data analysis capabilities.

Random, stationary, and ergodic processes were discussed briefly in Section 1.1.5 of Chapter I. Otnes and Enochson [150], Bendat and Piersol [151] and Randall [152] describe many engineering applications of digital time series analysis. DeJong [153] discusses converting analogue signals to useful digital data.

Analogue to digital conversion involves two processes, sampling and quantization. Sampling is the process of measuring the value of a continuous signal at a finite number of points over time. Quantization is the process of rounding or truncating the measured value so it can be represented by a finite number of digits. The collection of all time history records produced by an experiment is called the ensemble that defines a random process describing the phenomenon.

In order to preserve accurate frequency information when digitally sampling an analogue signal, the sample rate (SR) must be greater than *twice* the maximum frequency (f_{\max}) which is present in the signal or,

$$SR > 2 f_{\max} \quad (2.1)$$

If this condition is not met the signal content outside the frequency range $0 < f < SR/2$ will be confused with frequencies within this range. This phenomenon is called aliasing. The frequency $f_q = SR/2$ is called the Nyquist frequency. In these studies, the highest frequency of interest was 1000 Hz. So the time signals were low pass filtered with a cut-off frequency of 1500 Hz. A sampling rate of 4000 Hz, 4 times the maximum frequency present in the data, was selected to be conservative.

The record length is important when time averaging is required. It also controls the lower frequency limit in a frequency analysis of the data. If a signal is sampled at regular intervals over a time period T for one Fourier transform, then the frequency of resolution Δf that can be resolved by standard frequency analysis is,

$$\Delta f = 1/T \quad (2.2)$$

The frequency resolution Δf is related to the sampling rate SR and transform size N_s by,

$$\Delta f = SR / N_s \quad (2.3)$$

For most cases, the sampling rate was 4000 Hz and the transform size N_s was 4096 or 2^{12} .

Using Eq (2.3) the frequency resolution was 0.977Hz.

The total number of samples N_t is related to the transform size (4096) and the total record length in seconds T_t by,

$$N_t = (SR)T_t \quad (2.4)$$

Selecting a record length (T_t) of 12.5 seconds and a sampling rate (SR) of 4000Hz, yields a total number of samples of 50,000 using Eq 2.4. The selection of two digitizing parameters determines all the other parameters. In this case the sampling rate and the transform size were the determining parameters. The number of non-overlapping transforms T_n is related to the total record length T_t and the time per transform T by,

$$T_n = \frac{T_t}{T} = \frac{12.5}{1.024} \approx 12 \quad (2.5)$$

T is determined from Eq 2.2. Then the degrees of freedom are twice that of the number of transforms T_n ,

$$\text{DOF} = 2 T_n = 24 \quad (2.6)$$

A Hanning window with 50% overlap was used in the frequency analysis. The statistical properties including probability density functions were determined from the time history using a VAX 11/780 computer with software developed at WPAFB and described in more detail in reference [154].

When a statistical measure is evaluated for a data set that is only a subset of a longer signal, it is desirable to have some information about the accuracy of the measure in estimating the true value of the desired parameter of the signal. One approach is to assume that the signal has a certain statistical distribution and then evaluate the potential for errors in calculating the desired parameter of the distribution from a finite set of data. This approach leads to the specification of *confidence intervals* around the estimated statistical measures.

The confidence intervals of a statistical measure are based on the probability distribution of that measure when it is computed for a number of different sets of data taken from the same process. For instance, if a continuous random signal is digitally sampled and the mean value of a finite number of samples is evaluated, this mean value will be a random variable with a certain probability density function (PDF). If a certain form of the PDF is assumed, such as the Normal distribution, then confidence intervals can be set around the value of the mean based on the probable distribution of all possible values.

The characteristics of the Normal PDF can then be used to evaluate confidence intervals for the sample mean value. For example, the confidence interval at ± 1 standard deviation, σ , from the mean has a 68% confidence level. Therefore, based on the sample mean value of the numbers, it can be stated that the true mean is within a 68% confidence interval. For $\pm 3\sigma$, the mean has a 99.7% confidence interval. Generally, 90-95% confidence intervals are acceptable.

In order to use the sample variance, which is calculated from the number of values, it is necessary to use a slightly different PDF called the Student's T distribution. The confidence intervals grow dramatically when the number of statistical DOF are less than 10. Generally 20 degrees of freedom are satisfactory. Values greater than this do not significantly increase the accuracy.

The Chi-squared distribution can be used to obtain confidence intervals for the estimation of the variance. The computation of the sample power spectral density (PSD) from the FFT of a digitally sampled signal involves the summation of squared quantities. The characteristics of the Chi-squared distribution can then be used to determine the statistical errors in the PSD.

Two types of errors occur in the analysis of random data. The first called the *random error* is a haphazard scatter in the results from one analysis to the next of different samples of the same random data. Random errors are a direct result of the fact that averaging operations must be performed over a finite number of sample records or over a single sample record of finite length. It follows that all analyses will involve a random error. The second type of error called the *bias error* is a systematic error that will appear with the same magnitude and in the same direction from one analysis to the next. Bias errors generally evolve from windowing operations associated with the calculation of derivatives.

2.2 C-C ALUMINIUM ALLOY BEAM EXPERIMENTS

2.2.1 INTRODUCTION

Modal analysis theory is generally based upon the linear assumptions of amplitude independence and each mode occurring at a single frequency. In the nonlinear case, the displacement shapes and natural frequencies are dependent upon the boundary conditions, the level of the excitation force and the initial conditions. The study of structural mode shapes has grown considerably over recent years.

Clamped-clamped aluminium alloy 7075-T6 flat beam tests were performed first since the boundary conditions could be made to closely model mathematical models, and the homogenous, isotropic, elastic properties provide less complicated phenomena to be considered. The clamped beam size was 406 x 20 x 2 mm. Strain gauges were bonded back-to-back, as shown in Fig 2.5, to the beam to measure total, axial and bending strains. The back-to-back arrangement was selected to measure the bending strains only or the axial strain only by changing the wiring configuration on the Wheatstone bridges in the strain bridge amplifiers. Total strain was measured by using a single strain gauge in the bridge. The components of the total strain due to bending and axial strain were determined. Sinusoidal and random linear and nonlinear beam displacements were measured with a laser vibrometer. The laser vibrometer was directed at the centre of the beam perpendicular to the surface. It was scanned 203 mm left and right of centre. As the distance between the beam and the laser vibrometer is increased, the error resulting from the angular distance decreases. The distance selected was 850 mm which was close enough to maintain good signal return, yet far enough away so that the largest angular deflection was 14° resulting in a maximum error of 3%. Some of the tests were performed with static tension approximately 50 or 100 microstrain to prevent the possibility of buckling, others were performed with no pretension. The beam testing arrangement is shown in Fig 2.6. It is similar to that used by Bennouna [155]. The figure shows the set-up for the C-C beam tests, the excitation system, response measuring instruments, monitoring equipment and data acquisition system. The strain bridges were balanced before each testing sequence. Calibration of the data acquisition system removed any DC offsets. The displacement measurements were recorded from the electronic integrator, which converted the velocity to displacement with the proper engineering units. The dwell points were selected by sweeping the sinusoidal frequency of the drive coil from low-to-high since this method produced the largest displacements.

2.2.2 LINEAR MODE SHAPES

The term *linear* is used to distinguish between the tests described in this section and the nonlinear tests described in later sections. The scanning laser vibrometer method was selected to

measure the mode shapes since it was selected for the nonlinear tests and was capable of measuring small displacements. Methods using transfer function mapping, described in references [68-80], were not used since they require different equipment and processing.

For these tests the beam was pretensioned to 100 microstrain. Five bending vibration modes were found between 0-1000 Hz. Early testing with a moveable dynamic force indicated that the odd modes required less force than the even modes when the force was placed at a maximum deflection point on the beam. In later tests the mode shapes were measured with the beam excited by an acoustic driver without the exciter coil mass attached as shown in Fig 2.7. Various horn arrangements were tested. More consistent results were obtained using a horn, with a small diameter (1.5 mm) which could be moved away from the nodal lines to excite the mode of interest. Both symmetric and antisymmetric modes were obtained by moving the acoustic driver away from nodal points.

Filtered random excitation between 10-1000 Hz was used and the beam response examined to determine which frequencies to use for the sine dwell test to obtain the mode shapes. These were measured with a scanning laser vibrometer. A typical displacement time history is shown in Fig 2.8. The displacement spectral densities with the excitation concentrated at 1/4, 1/6 and 1/8 the length of the beam are shown in Figs 2.9, 2.10 and 2.11. The amplitudes of the peaks change with the driver location, but six distinct resonant peaks are clear at 85, 205, 380, 612, 765 and 898 Hz. The strain spectral densities are shown together in Fig 2.12. The same six peaks are clear except for the one at 765 Hz. The harmonics of the electrical supply noise (60 Hz in USA) in the strain measurements are clear at 180, 300, 420, 540, 660 and 780 Hz. The mode shapes associated with the six peaks are shown in Fig 2.13. The first mode occurred at 85 Hz, the second at 207 Hz, the third at 380 Hz, the fourth at 612 Hz and the fifth at 898 Hz. These follow the linear vibration theory in which higher order modes occur at higher frequencies. For example, the second mode occurs at a higher frequency than the first mode. The 765 Hz displacement response frequency occurs between the fourth and the fifth modal frequencies, which is unusual. Its shape appears similar to the first mode with a broader and lower amplitude peak. It is also slightly unsymmetrical about the centre of the beam. Lacking a better term, it is labelled as a *distorted first mode*. The 765 Hz mode was not a flexural mode of the beam since it does not fit

modal analysis theory which states that the first mode can only occur at a single frequency which is lower than the second and higher order modes. Strictly speaking, the *mode shapes* shown are not really mode shapes because there are small off resonance contributions from other modes as seen in the displacement power spectral densities. Considerable effort was devoted to determining the nature of this phenomenon. The shape observed was not a torsional mode of the beam nor a longitudinal mode. The nature of the behaviour was not established but could only be associated with a resonance of the whole structural system.

The beam was excited with slow sine sweeps at low levels to determine damping for the first mode using the half power point bandwidth method. The following relationship is used,

$$\zeta = \frac{c}{c_c} = \frac{\Delta f}{2f_o} \quad (2.7)$$

where ζ is the viscous damping ratio, c is the damping coefficient, c_c is the critical damping coefficient, Δf is the half power point frequency bandwidth, and f_o is the peak frequency. With the exciter coil attached to the beam, the viscous damping ratios measured were 1.89%, 1.85% and 1.92%. No measurable difference in damping for the beam was found with or without retro-reflective laser tape which is used to lower noise in vibrometer measurements. An example of response to a sine sweep is shown in Fig 2.14. A typical value for the material viscous damping ratio for aluminium alloys is 0.5%. A typical value for the structural damping of joints [156 p 81] is 1.0%, which is about one half of those measured. Acoustic radiation damping should be smaller than the measured values. The damping increase above 1% is attributed to the coil magnet arrangement, which acts like a piston with a large clearance.

2.2.3 NONLINEAR STATIC DEFLECTION SHAPES

Static deflection shapes were measured for the C-C aluminium alloy beam by applying DC current to the exciter coil and measuring the displacements with a dial gauge. The displacements measured and the loads applied at the centre of the beam are shown in Fig 2.15. The displacements increase with an increase in the applied force and are symmetrical about the centre of the beam. The centre displacement increases almost linearly from 0 to 7.2 N as shown in Fig 2.16. At higher loads, the displacements do not increase proportionally to loads. One bending 'rule-of-thumb' indicates applicability of linear theory for displacements up to 50% of the beam thickness. The measurements indicate that accuracy decreases for displacements higher than 34%. The shape of the displacement curve is similar to that of the strain curve.

The total strain measurements at six locations and the linear beam theory results are shown in Fig 2.17. Strain measurements were taken as the test loads increased and decreased. Very little hysteresis is observed in the data. Neither strain pair, at the centre of the beam and near the clamp are equal in magnitude. The tensile strains are higher than the absolute value of the compressive strains. None of the strains are as great as the linear pure bending theory. Linear theory 'A' shown in the figure is from Roark [157 p112]. For a rectangular C-C beam with the applied force at the centre, the maximum positive bending strain at the centre and the maximum bending strain near the clamp can be calculated using,

$$\epsilon_b = \frac{1}{8} \frac{F \ell (h/2)}{EI} = 333 \mu\epsilon, \quad \text{for } F=10 \text{ N}, \quad (2.8)$$

where ϵ_b is the bending strain, F is the force, h is the thickness, E is Young's modulus, and I is the second moment of the area of the cross-section. Using a force of 10 N yields 333 microstrain whereas the measured bending strain was 285 microstrain. Similarly, the compressive bending theory at 10 N indicates -333 microstrain compared with a measured value of -215 microstrain. The accuracy of pure bending theory decreases when the strains increase above 50 microstrain.

The measured strains are somewhat less than linear theory due to the stretching of the beam, which is one form of nonlinearity.

2.2.4 NONLINEAR ALUMINIUM ALLOY BEAM SINUSOIDAL EXPERIMENTS

In the nonlinear case, the displacement shapes and natural frequencies are dependent upon the level of the excitation force and the frequency as described in reference [86]. The modal analysis methods described briefly in Section 1.1.9, references [68-80], are not applicable because they are based upon linear theory. Superposition, which is based upon linear theory, also is not applicable. Strictly speaking, the term *mode* is not applicable, but will be used to describe the fundamental spatial response and higher order resonances. The term *nonlinear displacement shape* will be used to describe the shape of the resonant frequency response.

When the excitation frequency is increased slowly during sinusoidal excitation of a C-C aluminium alloy beam, jump phenomena are observed by a large drop in amplitude over a small increase in frequency. The fundamental resonant frequency increased from 44 Hz to 63 Hz as the excitation level increased as shown in Fig 2.18. The frequencies were noted from the display on the signal generator. Jump phenomena are also observed when the frequency is above resonance and slowly swept to lower frequencies. The resonant frequency changed from 51 Hz to 42 Hz. At lower excitation levels similar phenomena are observed with a smaller increase or decrease in range of resonant frequencies and lower amplitudes of vibration. The jump phenomenon exhibits the characteristics of a hardening Duffing oscillator Eq (1.3), a cubic nonlinearity. The *back-bone* curve described in reference [86] bends toward the right with the added cubic term in the equation of motion. If the curve bends toward higher frequency response, it is called a hardening spring nonlinearity. The dwell points were selected by sweeping the frequency from low to high. Six excitation levels were selected near the jump down frequency measuring the displacement at the centre and the total strains. The tests were repeated as closely as possible to measure the bending strains after changing the configuration of the strain bridge amplifiers. The axial strains were determined during the third set of tests after changing the configuration of the strain bridge amplifiers. If the frequency was too close to the jump frequency, the response would often jump

down during the recording, before acquiring the full time history. The excitation was reduced in 0.1 Hz increments until stability was achieved. The total, axial and bending strains for the six different force levels are shown in Fig 2.19. The total strain is usually the sum of the axial and bending strain components, however, for these tests the bending strain was slightly higher than the total strain. This was primarily due to conducting the tests near a jump point, an instability in the beam response that made it difficult to repeat the measurement more accurately. The total and bending strains are nonlinear with little increase in the driving force. The bending strain does not increase linearly with the excitation force. The axial strains are about 11% of the total strains at a higher excitation level, 2 N.

The displacements shown in Fig 2.20 were measured with a scanning laser vibrometer at the centre of the beam. Displacement amplitudes of slightly more than one beam thickness are shown in the figure. The strain versus displacement relationships are slightly nonlinear at the higher excitation levels. The strain measurements at the centre, SG 1 and 4, are nearly equal except for the highest displacement. The strain measurements near the edge of the clamping block where SG 3 and 6 are located are greater than those at the centre. The strain measurements near the edge of the clamping block, where the displacements are zero, are shown in the figure for comparison purposes. These strain measurement pairs are nearly equal.

The nonlinear displacement shapes were measured using a scanning laser vibrometer. The dwell points were selected by sweeping the frequency from low to high. Six excitation levels were selected near the jump down frequency. Examples of unsmoothed first mode nonlinear displacement shapes for a C-C aluminium alloy beam are shown in Fig 2.21. The frequencies increase from 54.8 Hz to 67 Hz from the smallest to the largest displacement shapes measured. The peak displacement amplitudes increase with increasing sinusoidal excitation levels. The displacement measurements along the length of the beam (raw data) contained some small variations from a smooth curve. The beam was essentially flat and uniform with no discontinuities that would cause variations in closely spaced measured displacements. The variations seem to be in the laser vibrometer. The displacements were limited to velocities less than 1 m/s for these tests due to the vibrometer range limitation. Also, RMS values were used for smoothing the curve since the peak option was not working properly on the newly developed

instrument. Many noise peaks were apparent when using the peak option on the instrument. The ends of the beam show large curvature due to the high bending moments at the clamp. This curvature reverses as expected around the centre region of the beam.

The third resonant response of the beam was also examined. Nonlinear displacement shapes, shown in Fig 2.22, result in a centre peak much lower in amplitude than the two on either side. The reduction in amplitude at the centre of the beam in the displacement shapes for the third mode is due to the mass of the coil (26.7 g) attached to the beam. In this case, the centre peak is inverted since the scanning vibrometer only measures peaks in a positive fashion and the phase could not be determined. From other tests, it was shown that the peaks are out of phase. The shapes shown in the figure were obtained from a seventh order polynomial fit of the displacement shape data. The coefficients for the fit are listed in Appendix B, Table B-2.1. Attempts to obtain the second derivatives of the third and fifth nonlinear displacement shapes were postponed until more accurate curve fitting techniques could be developed.

The motion of the clamping blocks was measured at the highest level of excitation with the laser vibrometer. The maximum displacement of the beam at the fundamental frequency was 1.65 mm rms. The corresponding displacement of the tensioned clamping block was 0.00716 mm rms. The displacements at the other block was 0.00507 mm rms. These displacements are 0.434% and 0.307% respectively of the displacement of the beam. While not perfect, the clamping blocks were reasonably effective in minimizing the motion of the beam at the ends.

2.2.5 NONLINEAR ALUMINIUM ALLOY BEAM RANDOM EXPERIMENTS

Random excitation tests were conducted with a C-C aluminium alloy beam by bandpass filtering the wide band random voltage output from the signal generator to include the first modal responses, the first and third modal responses and the first, third and fifth modal responses. Five excitation levels below the fatigue endurance level were selected to measure the displacement and the total strain. The tests were repeated twice to measure the bending and axial strain response, similar to that described for the sine dwell tests. The excitation spectra are shown in Fig 2.23 for

the 10-1000 Hz tests, which are nearly flat up to 1000 Hz. The strain spectral densities for the gauge near one clamp (SG 3) are shown in Fig 2.24. Well separated resonant peaks appear around 50 Hz and 300 Hz with nearly equal amplitudes. The next highest peak appears around 750 Hz, followed by 1450 Hz. It is interesting to note that a peak appears around 700 Hz at this location which almost vanishes in the strain spectral densities for the centre strain location (SG 1) shown in Fig 2.25. This frequency response could be the same response found in the mode shape studies which was denoted as a *distorted first mode*. It should be noted that the peaks contain some contribution of other off resonant peaks. The bending modal frequencies of vibration, of course are not harmonically related. The axial strain response is twice that of the bending frequency.

Excitation was band limited from 10-400 Hz for these tests. The axial strains remain positive as shown as in Fig 2.26 as expected, since the beam stretches twice for each bending cycle. An example of the total, axial and bending strain spectral densities is shown in Fig 2.27. The axial strain response is not a resonance but is due to the bending resonance producing a stretching effect. The axial strain results from the stretching of the beam when the beam deflects from its initial position. The longitudinal beam resonances are well above the frequencies of interest and do not affect the axial strains. The subharmonic (75 Hz) and the fundamental (150 Hz) peaks are of nearly the same amplitude. The 75 Hz axial peak is much lower than the 75 Hz total peak. The axial peak at 450 Hz and 700 Hz are evident. The axial fundamental frequency response and the harmonics add to the total strain spectrum filling in the gaps between the bending strain response. The higher the deflections, the higher are the axial strains.

The total, bending and axial overall rms strain levels obtained are shown in Fig 2.28. The total strain increases at a much lower rate than the axial strain. The bending strain rate follows that of the total strain minus the axial strain. The shape of the total strain curve seems to follow the characteristics of a parabola. As the excitation levels increase, the axial strain increases at a slightly higher rate than the excitation level. The axial strains are in tension adding to the tensile bending strains and subtracting from the compressive bending strains. This affects the mean value by shifting it toward the tensile side. Higher peak values tend to shorten fatigue life.

This shift in the mean and the reduction of the bending strains as the axial strain increase results in a nonlinear increase in the total strain as the excitation level increases. The axial overall rms strains are about 10% of the total strains at the 5.5 N excitation level. The axial strain would be a higher percentage of the total strain if a longer beam were utilized. The total strains exhibited some frequency increase and peak broadening as the excitation level increased. The bending strains without the effects of the axial component also exhibited some peak broadening.

The excitation force amplitude probability density functions (APDFs) were determined for the experimental tests. The program used computed the PDFs by taking out the mean values, assuming a zero mean. This results in the 'x' axis of force divided by the rms value. The mean values, were added back in which results in the 'x' axis of force divided by standard deviation. This method is used for all the force and strain APDFs. The APDFs for five different levels of 10-1000 Hz random excitation are shown in Fig 2.29. Most of the force APDFs follow that of a Gaussian distribution. Producing linear excitations is a prerequisite to examine nonlinear response. The lower levels of excitation indicate some symmetric offset which can be attributed to a slight DC offset in the recording system or the constant current modifier. The force was determined directly from the current applied to exciter coil, coming from the signal generator which should be Gaussian. The strain amplitude probability density functions (APDFs) for the five different excitation levels at the centre of the beam (SG 1) with 10-1000 Hz random excitation are shown in Fig 2.30. While the APDFs are close in shape, some characteristics are noted. One effect of the axial strain is to shift the mean to some positive value, but since the axial strains are small, this effect will be small. If this is the only effect, the amplitude APDFs would be symmetric about the mean. This is not observed in the APDFs. The APDFs approach zero at +3 sigma and -2.8 sigma, while the Gaussian function approaches zero around ± 3.5 sigma. The measured APDFs are not symmetrical about their mean value. More larger positive amplitudes occur than large negative amplitudes especially at the higher excitation levels, which is an indication that the beam response becomes more nonlinear at higher excitation levels. The strain APDFs for the strain near the clamp (SG 3) at the 12.2 N excitation level are shown in Fig 2.31. Similar characteristics are noted as those for SG 1. More larger positive amplitudes occur than large negative amplitudes.

2.3 C-C CFRP BEAM EXPERIMENTS

2.3.1 INTRODUCTION

Similar tests were conducted with a C-C CFRP beam (406 x 20 x 1.98 mm). The beam was fabricated using Hercules AS4 /3501-6 unidirectional prepreg tape with AS4 fibres in a 3501-6 matrix ($0^\circ / \pm 45^\circ / 90^\circ$). The fibre volume fraction was 58.7%. The beam size was essentially the same as that of the aluminium alloy beam as well as the test set-up and strain gauge locations. This permits some direct comparisons to be made between the behaviour of the aluminium alloy beam and the CFRP beam.

2.3.2 LINEAR CFRP BEAM MODE SHAPES

The beam was pretensioned to 50 microstrain. Mode shapes were measured with the beam excited by an acoustic driver without the exciter coil mass attached to the beam as shown in Fig 2.32. The modes were obtained by moving the acoustic driver away from nodal points. The amplitudes of the peaks changed with the driver location. The displacements were measured with a scanning laser vibrometer. The antisymmetric modes were not clear or well formed. The first mode occurred at 107 Hz, the third at 503 Hz and the fifth at 1201 Hz.

2.3.3 STATIC CFRP BEAM MEASUREMENTS

Static bending strain measurements were made with the C-C CFRP beam by applying DC current to the exciter coil in the same test rig as that used for the aluminium alloy beam tests. Similar results were obtained with the CFRP beam as shown in Fig 2.33. The observations made in Section 2.2.3 are applicable to the CFRP beam. The tensile strains at the centre of the beam and near the clamp are not equal in magnitude. The tensile strains are higher than the absolute value of the compressive strains due to the axial strain from the beam stretching. Both are not as high as those predicted by linear pure bending theory. Strain measurements were taken as the test loads increased and decreased. Very little hysteresis is observed in the data. The relationship

between the strains and displacements for two strain locations is shown in Fig 2.34. This relationship is nearly linear. The absolute magnitudes of the strains are lower at the centre of the beam than those near the clamp.

2.3.4 NONLINEAR CFRP BEAM SINUSOIDAL EXPERIMENTS

The frequency was slowly swept from low-to-high at a constant excitation level near the first resonant response. A summary of the frequency sweeps is shown in Fig 2.35. The shifts in the jump frequency cover a range of 53 to 91 Hz. Bistable response is observed when the frequency is slowly swept for each excitation level over the frequency range of 50 to 91 Hz. Five different levels were selected for each test recording the displacement responses from the vibrometer at the centre of the beam. These are shown in Fig 2.36 to observe the jump phenomena. The frequency response is not symmetrical even for the lowest level of excitation (0.025 N). As the force level increased from 0.826 to 1.77 N, the jump frequency increased from 65 to 91 Hz. The frequency was slowly swept from high -to- low as shown in Fig 2.37. At the higher excitation levels, the displacement jumps up to a higher value, then settles to a slightly lower value. As the levels decrease, the jump up frequencies decreased from 73 to 50 Hz. The amplitudes before and after the jump do not follow along the same deflection curve. Five frequencies were selected around the first resonant response and the amplitudes were slowly increased as shown in Fig 2.38. Jump up phenomena are noted at 2.8, 3.8, 4.5, 4.9 and 5.6 N. Five frequencies were selected around the first resonant response and the amplitudes were slowly decreased as shown in Fig 2.39. Jump down phenomena are noted at 3.8, 3.4, 3.0, 2.7 and 2.3 N. Bistable response was observed for changes in the excitation level at a constant frequency over the frequency range of 56 to 66 Hz.

Sine dwell tests were conducted near the jump point. The total, axial and bending strains measured for different excitation levels of the fundamental resonant frequency response along with the displacements from the vibrometer are shown in Fig 2.40. The frequencies increase from 56.6 Hz to 75.3 Hz which were similar to the aluminium alloy beam tests. The displacements are higher than those of the aluminium alloy beam tests, but the total strains are

lower. Also the axial strains are a larger percentage of the total strains, which increased with higher excitation levels.

The nonlinear peak displacement shapes were measured using a scanning laser vibrometer. The dwell points were selected by sweeping the frequency from low to high. Seven excitation levels were selected near the jump down frequency. Examples of the first mode unsmoothed nonlinear displacement shapes for a C-C CFRP beam are shown in Fig 2.41. The frequencies increase from 56.3 Hz to 74.0 Hz from the smallest to the largest displacement shapes measured. The peak displacement amplitude increases with increasing levels of sinusoidal excitation. The displacement measurements along the length of the beam (raw data) contained some small variations from a smooth curve. The beam was essentially flat and uniform with no discontinuities that would cause variations in the closely spaced displacements measured. The ends of the beam show large curvature due to the high bending moments at the clamp. This curvature reverses as expected around the centre region of the beam. Large curvature is observed around the central region of the beam.

Higher order resonant frequencies were examined for the peaks found at 370, 389, 899 and 1042 Hz. The 370 Hz nonlinear displacement shape is shown in Fig 2.42. The shape is similar to the theoretical linear second mode, two peaks and three nodes, but the amplitudes of the peaks are not equal and symmetrical about the centre of the beam. The lower peak is 73% of the higher peak. The 389 Hz nonlinear displacement shape is shown in Fig 2.43. The shape is similar to the theoretical linear third mode, three peaks and four nodes, but the amplitudes of the peaks are not equal and symmetrical about the centre of the beam. The lowest peak is affected by the mass of the exciter coil attached to the beam. The next lowest peak is 75% of the highest peak. The 370 Hz response peak (second mode) is very near to the 389 Hz peak (third mode). The 899 Hz nonlinear displacement shape is shown in Fig 2.44. The shape bears a slight resemblance to that of the theoretical linear fourth mode, four peaks and five nodes, but the amplitudes of the peaks are not all equal and symmetrical about the centre of the beam. The 1028 Hz nonlinear displacement shape is shown in Fig 2.45. The shape is similar to the theoretical linear fifth mode, five peaks and six nodes, but the amplitudes of the peaks are not equal and symmetrical about the centre of the beam. The lowest peak is affected by the mass of the exciter coil attached to the

beam. The next lowest peak is 69% of the highest peak. Two pairs of peaks appear on each side of the centre peak. Each pair is nearly equal in amplitude. The 889 Hz frequency peak is relatively close in frequency to the 1042 Hz peak. The closeness in frequency of the last two pairs of frequency peaks resulted in distortion of the displacement shapes.

2.3.5 NONLINEAR CFRP BEAM RANDOM EXPERIMENTS

Random excitation tests were conducted with a C-C CFRP beam similar to those with the aluminium alloy beam which included the first, third, and fifth resonant response frequencies. The excitation spectra are shown in Fig 2.46 with a flat excitation level from 10-1300 Hz. The strain spectral densities for the centre gauge are shown in Fig 2.47. Well separated resonances appeared around 60 Hz, 400 Hz and 1030 Hz. It should be noted that the peaks contain some contribution of other off resonant peaks. These were similar to those of the aluminium alloy beam but the frequencies were higher. Again the second harmonic of the fundamental appeared at a much lower level than the fundamental. The strain spectral densities for the gauge near the clamp are shown in Fig 2.48. Two additional peaks appeared around 365 and 895 Hz at this location along the beam length. These correspond to the 370 Hz resonance (second resonant response shape) and the 899 Hz (fourth resonant response shape) discussed earlier. The displacement spectral densities for the centre of the beam are shown in Fig 2.49. The displacement amplitudes for the third and fifth resonances are much lower than the fundamental which was not the case for the strain amplitudes. An example of the overall total, bending and axial strain levels together with the displacements at the centre of the beam are shown in Fig 2.50. The total strains are higher than the bending strains. Again the axial strains are much lower than the total strains and a higher percentage of the total strain than for the aluminium beam.

The excitation force amplitude probability density functions (APDFs) for five different levels of 10-1300 Hz random excitation are shown in Fig 2.51. Most of the PDFs followed that of a Gaussian distribution except the lower levels of excitation. Some symmetric offset occurs which can be attributed to a slight DC offset in the recording system or the constant current modifier. The APDFs shown in Fig 2.52 are similar to those for the clamped aluminium alloy beam tests.

The strain APDFs for the five different excitation levels are shown in Fig 2.53. The APDFs approach zero at +3.5 sigma and -2.7 sigma, while the Gaussian function approaches zero around ± 3.5 sigma. The measured APDFs are not symmetrical about their mean. More larger positive amplitudes occur than large negative amplitudes especially at the higher excitation levels, which is an indication that the beam response becomes more nonlinear at higher excitation levels. This effect is greater for the CFRP beam than that observed for aluminium alloy beam in section 2.25. The response of the CFRP beam is more non-Gaussian than that of the aluminium alloy beam.

2.4 P-P ALUMINIUM ALLOY BEAM EXPERIMENTS

2.4.1 INTRODUCTION

A pinned-pinned aluminium alloy 7075-T6 beam (405 x 218 x 2 mm) was machined as a single piece. The pins were 3.02 mm in diameter which rotated in brass bushings mounted in steel blocks as shown in Fig 2.54. The assembly was bolted to the same test rig used for the clamped beams described in section 2.2. A longer exciter coil was also fabricated in order to maintain a linear current-force relationship since the displacements were much higher for the P-P tests than the C-C tests. The mass of the new coil assembly was 66 g, 39.6 g heavier than the coil assembly for the C-C tests. Modifications were made to the current modifier for the higher currents required with the longer coil. The calibration curves for the longer coil and magnet assembly are shown in Appendix A. This was determined by driving the coil attached to a suspended mass through a force transducer.

2.4.2 LINEAR P-P ALUMINIUM ALLOY BEAM MODE SHAPES

The beam was pretensioned to 50 microstrain. Five bending vibration modes were found between 0-1200 Hz. The mode shapes were measured with the beam excited by an acoustic driver without the exciter coil mass attached to the beam. Both symmetric and antisymmetric modes were obtained by moving the acoustic driver away from nodal points. The displacements were measured with a scanning laser vibrometer. The amplitudes of the peaks changed with the driver

location, but five resonant peaks were clear. These occurred at 72, 174, 323, 538 and 789 Hz, which correspond to the first to the fifth modes of vibration.

2.4.3 NONLINEAR P-P ALUMINIUM ALLOY BEAM STATIC MEASUREMENTS

Static bending strain measurements were made with the P-P beam by applying DC current to the exciter coil in the same test rig as that used for the other beam tests. The total strain measurements are shown in Fig 2.55 except for the strain locations near the pins. Strain gauges 3 and 6 were located too near the stress concentrations produced by the pins to provide any meaningful data. The tensile strains at the centre of the beam are 488 microstrain at 17.5 N and the compressive strain, minus 333 microstrain. The tensile strains are higher than the absolute value of the compressive strains. Both are not as high as the linear pure bending theory. The strains at the $1/4 \ell$ position are both in tension, 109 and 46 microstrain. The strains near the pin location are 123 and minus 151 microstrain. This indicates that bending is present near the pins. Linear bending theory for pinned boundary conditions indicates that the strain at the pin should be zero. The compressive strains are not as high in magnitude as the tensile strains due to the stretching effect. Slightly more hysteresis is observed than in the results for the clamped beam tests. The shape of the strain curves in Fig 2.56 shows more curvature than the shape of the displacement curves for the clamped beams. Linear bending theory is accurate at very low force levels, but it does not describe the nonlinear behaviour at the higher load levels. These include a smaller displacement amplitude and strain level as the load increases and a shift in the neutral axis toward the tensile side of the beam. The stretching effects shift the neutral axis. It also causes a small reduction in the cross-sectional areas which reduces the second moment of area of the cross-section. Linear theory assumes the second moment of area of the cross-section to be constant.

2.4.4 NONLINEAR P-P ALUMINIUM ALLOY BEAM SINUSOIDAL EXPERIMENTS

The nonlinear displacement shapes were measured using a scanning laser vibrometer. The dwell points were selected by sweeping the frequency from low to high. Seven excitation levels were selected near the jump down frequency. Examples of the first mode unsmoothed nonlinear displacement shapes for the P-P aluminium alloy beam are shown in Fig 2.57. The frequencies increase from 27.9 Hz to 46.8 Hz from the smallest to the largest displacement shapes measured. The displacement measurements along the length of the beam (raw data) contained some small variations from a smooth curve. The beam was essentially flat and uniform with no discontinuities that would cause variations in closely spaced displacements measured. The peak displacement amplitude increases with increasing sinusoidal excitation. The ends of the beam show little curvature since the pins theoretically do not impart a bending moment. High curvatures are observed in the centre region of the beam. The P-P beam mode shape (low level of excitation) should have a sinusoidal shape, which is discussed in more detail in section 4.3.3.

2.4.5 NONLINEAR P-P ALUMINIUM ALLOY BEAM RANDOM EXPERIMENTS

Random excitation tests were conducted with a P-P aluminium alloy beam similar to those conducted for the other two beam tests. The bandwidths of the resonant peaks were wider than expected due to the friction of the pin-bushing arrangements. Also more damping from the longer coil was to be expected. The pins and coil added much more damping to the system than desired, which limits the usefulness of the data. For these reasons, this part of the study was not taken further.

III PLATE EXPERIMENTAL INVESTIGATIONS

3.1 BASE EXCITATION METHOD

3.1.1 INTRODUCTION

Base excitation methods are useful in studying geometrical nonlinear responses of plates. These methods use the inertia effects of a plate to provide the loads by exciting the clamping frame or fixture. Well defined forcing functions from accelerometer measurements can be determined. When the force measurement is simultaneously acquired with the strain or displacement measurements, the transfer functions can be determined. Other advantages of this indirect method of attaching the plate to the exciter are that it does not mass load the plate or contaminate the response with responses from attachment devices. The disadvantages of the capital investment and cost of operations of the shaker were within acceptable limits for this project since the shaker and operational support were readily available. The disadvantages of the fixture design and manufacturing costs were negligible since the fixture was already available and had been used by Ng [146] in his studies. The sizes of the plate and clamping arrangement were selected based upon the weight limitations of the shaker, the frequency response limitations and the prevention of fatigue damage during the response tests.

The base excitation method used a 6.53×10^7 N (12,000 lbf) electrodynamic shaker. The shaker performance limitations are shown in Fig 3.1. Choosing a 133 N (30 lbf) payload for the fixture design results in a low frequency roll-off at 180 Hz with 100 g acceleration sinusoidally. This was acceptable since the calculated first mode response was around 200 Hz for the aluminium alloy plate and higher for the CFRP plate. The clamping fixture consisted of a flat aluminium alloy 6061-T6 plate 19 mm thick and four clamping bars of equal thickness as shown in Fig 3.2. Eight bolts were used to fasten the fixture and plate to the shaker head. Aluminium alloy spacers were used at the eight locations to allow sufficient

space between the plate and shaker head to prevent radiation damping of the small volume of air from affecting the response.

The radius of curvature of the clamping edges was 4.76 mm to prevent early fatigue failure. A four bar clamping arrangement was selected to prevent buckling of the plate while torquing the clamping bolts. The corners of the clamping plate were cut off to save weight. The fixture rigidity was sufficiently high so that the resonant frequencies were well above the plate resonant frequencies of interest. The clamped boundary conditions require infinite bending and axial rigidity, which cannot be achieved exactly but can be closely approximated. The fixture design was a trade off among the shaker performance, the fixture rigidity and the total weight.

The shaker head was rotated to the vertical position. The panel resonant response motion was perpendicular to the direction of gravity. This method was selected to prevent the effects of gravity from affecting the strain and displacement measurements. Since the vibrometer at its lowest position on its tripod was slightly higher than the centre of the shaker head, the shaker head was rotated slightly to keep the vibrometer perpendicular to the plate being tested.

3.1.2 C-C-C-C ALUMINIUM ALLOY PLATE SHAKER EXPERIMENTS

Clamped aluminium alloy 7075-T6 flat plates were tested. The unclamped size was 254 x 203 x 1.30 mm which results in a 1.25 aspect ratio (length divided by width). Strain gauges were bonded back-to-back, shown in Fig 3.3, to measure total, axial and bending strains using the same methods as those used for the beam experiments. Edge strain gauges 2 and 7 were positioned to obtain the maximum strain response for the first mode. Edge gauges 1 and 6 were positioned to obtain for the third mode response. Displacements were measured with a scanning laser vibrometer as discussed in Chapter II. An accelerometer was mounted on the shaker head to determine the acceleration of the fixture. The plate testing arrangement is shown in Fig 3.4. The figure shows the set-up including the excitation system, response measuring instruments, monitoring equipment and data acquisition system. The same data acquisition and processing

methods used for the beam experiments, described in Chapter II, were used in the plate experiments.

3.1.2.1 LINEAR MODE SHAPES

The linear modal frequencies of the plate used in the shaker experiments were measured using low level excitation. The plate was excited sinusoidally in its clamping frame with an acoustic driver (loud speaker). With the plate bolted to the clamping fixture and lying on a vibration isolated block, mode shapes were measured using a scanning laser vibrometer. The vibrometer is previously described in more detail in section also 2.1.1.1. Low level excitation (below 90 dB overall SPL) was used to avoid nonlinear response. Additional mode shapes were determined using a video holography method, described in section 2.1.1.1. Both methods yielded frequencies with a 1 Hz accuracy for the fundamental mode. Using the video holography method, the fundamental mode occurred at 208 Hz. The seven measured mode shapes are shown in Fig 3.5. The frequencies are listed in Table 3.1. All the mode shapes up to the 4:1 mode were found in the 208-966 Hz frequency range. The 3:1 (617.6 Hz) and the 2:2 (623 Hz) modes are 5 Hz apart. This closeness is an indication that it would be difficult to determine which mode is contributing energy to the strain spectral density.

3.1.2.2 NONLINEAR ALUMINIUM ALLOY SINUSOIDAL SHAKER EXPERIMENTS

With the plate and fixture bolted to the shaker head, sine dwell tests were conducted near the fundamental resonant frequencies. The dwell tests were similar to those conducted for the beam described in Chapter II. The nonlinear displacement shapes were measured using a scanning laser vibrometer. The frequency range for the tests was selected by sweeping slowly from below the fundamental frequency to a frequency just below where the amplitude jumped down to a low level. The excitation was reduced in 0.1 Hz increments until stability was achieved. Four excitation levels, selected near the jump down frequency were used in measuring the displacement at the centre and the total strains. The jump phenomenon occurred when the fundamental frequency increased from 228.9 to 245.9 Hz, shown in Fig 3.6. This is indicative of a hardening spring type cubic nonlinearity. Displacement amplitudes of more than three plate

thicknesses are shown in the figure. The shape of strain and displacement relationships are quite similar, nonlinear at the higher excitation levels. The nonlinear displacement shapes (raw data) for the fundamental resonant responses are shown in Figs 3.7 and 3.8. The zero position is the centre of the plate. The displacement amplitude increases with increasing sinusoidal excitation. The edges of the plate near the clamping fixture show large curvature due to the high bending moments at the clamp. This curvature reverses as expected around the centre region of the plate. Large curvature is observed around the centre region of the plate. The maximum displacement measured near the clamps is 0.01 mm peak and is due to the shaker head motion and the clamping frame.

3.1.2.3 NONLINEAR ALUMINIUM ALLOY RANDOM EXPERIMENTS

Random response tests were conducted with a spectrum controller programmed for a flat spectrum shape from 100-1000 Hz. Examples of the excitation spectral densities are shown in Fig 3.9. This frequency band includes the 1:1 to 3:2 modes. Examples of the total strain spectral densities for gauges 1 to 5 are shown in Figs 3.10 to Fig 3.14. No appreciable differences are found comparing the front gauges (SG 1 to 5) with the back gauges (SG 6 to 10). The highest strain measured is along the clamped edge at the centre of the longer side of the plate near the clamping frame, strain gauge location 2. Large strain responses occurred around 220, 670 and 900 Hz with peak broadening and shifting to higher frequencies at the highest excitation level. This is indicative of geometrical nonlinearities described in more detail in section 2.2.4. Two peaks are apparent around 670 Hz at low levels of excitation that combine at high levels of excitation. The displacement spectral densities, shown in Fig 3.15, are quite similar to the strain spectral densities except for the relative amplitudes of the higher order modes.

Comparisons of the total, axial and bending strain spectral densities for gauge location 2 for the lowest (1.46 g) and the highest (14.4 g) excitation levels are shown in Figs 3.16 and 3.17. The axial overall rms strain is 4.56% of the total strain at the highest level of excitation. High strain responses occur first around 220-235 Hz, then 900-915 Hz, 635-660 Hz and 430-510 Hz. Peak broadening and frequency shifting to higher frequencies are evident. The axial or in-plane stretching effect occurs at twice the bending resonant frequencies. Over most of the frequency

band the bending and total strain spectral densities are about equal. The fundamental axial frequency is 440 Hz and the subharmonic is 220 Hz. The axial strain peak at 220 Hz is much lower than the bending peak. The axial strain response is higher than the bending strain around 460 Hz at the higher level of excitation. This results in a higher total strain response around the axial fundamental resonance, at twice the bending fundamental resonance.

The total strain overall levels for the five strain gauge locations and the displacements at the centre of the plate are shown in Fig 3.18. At the maximum excitation level (14.4 g), the highest total strain recorded is 425 microstrain rms at gauge location 2 followed by 282 microstrain at gauge location 5, then 240 microstrain at gauge location 3, 198 microstrain at gauge location 4 and 138 microstrain at gauge location 1. The shape of the displacement curve closely follows that of the total strain curve for strain location 2. The shape of the total strain curve seems to follow the characteristics of a parabola. The relationship between total strain and displacement is shown in Fig 3.19. This relationship is nonlinear even at small displacements. The axial strain overall levels for five gauge locations and the displacement at the centre of the plate are shown in Fig 3.20. As the excitation levels increase, the axial strain increases at a slightly higher rate than the excitation level. The bending overall strain levels are shown in Fig 3.21. These are quite similar to the total strain curves. The total, bending and axial overall strain levels for three gauge locations are shown in Figs 3.22, 3.23 and 3.24. The highest strain is measured at strain location 2, the centre of the length of the plate near the clamp. All three locations exhibit characteristics described in the four previous figures. The shape of the bending curve closely follows that of the displacement curve. The total strain is nearly equal to the sum of the axial and the bending strain.

An estimate of the individual resonance contributions to the total strain energy can be determined by integrating across the strain spectral densities and normalising by dividing by the overall level. Examples of integrating across four strain spectral densities for the gauge at location 2 are shown in Fig 3.25. The first resonance contributes approximately 82% of the total strain at the lowest level of excitation (1.46 g). As the level of excitation is increased, the first resonance contribution decreases from 82% to 76%. At the highest level of excitation (14.4 g), the higher order frequency peaks in the strain spectral densities contribute more significantly to

the overall strain response. Peak broadening at the highest level is evident from the shape of the curves.

The excitation force amplitude probability density functions (APDFs) were determined by incorporating the mean values in the PDF. This results in the 'x' axis of force divided by the standard deviation. This method is used for all the force and strain plate APDFs except for the microphone APDFs used in the APWT tests.

The acceleration AFDFs, shown in Fig 3.26, are compared with the Gaussian function. The shaker controller was programmed for ± 4 sigma, however, the shaker did not produce 4 sigma amplitudes. Theoretically, the APDFs should be Gaussian, however, some differences are noted. The APDFs for the highest excitation level approach zero near +2.5 sigma and -2.9 sigma. The lowest level APDFs approach zero at +2.5 sigma and -3.2 sigma. The strain APDFs for four different excitation levels are shown in Fig 3.27. The APDFs for the highest excitation level approach zero near +3.2 sigma and -2.8 sigma. The low level APDFs are more symmetric and approach zero at +2.7 sigma and -2.7 sigma. More large positive amplitudes occur than large negative amplitudes especially at the higher excitation levels. This is an indication that the beam response becomes more nonlinear at higher excitation levels. Very high sigma values, above 4 sigma, may not be observed if the time history is too short. Most of the tests conducted used a 12 second time history. Some tests used a 25 second time history which permits investigations of large sigma values. A comparison of the APDFs for SG 2 at the highest excitation level is shown in Fig 3.28. No appreciable difference is observed comparing the 12 second time history with the 25 second the history. The 3.2 sigma value is the highest amplitude response observed.

3.1.3 C-C-C-C CFRP PLATE SHAKER EXPERIMENTS

The CFRP plate was fabricated using Hercules AS4 /3501-6 unidirectional prepreg tape with AS4 fibres in a 3501-6 matrix $(0^\circ / \pm 45^\circ / 90^\circ)_s$. The fibre volume fraction was 58.7%. The unclamped size of the plate in the fixture was 254 x 203 x 1.09 mm which resulted in an aspect

ratio of 1.25. The test arrangement and strain gauge locations are the same as those used for the aluminium alloy shaker plate in section 3.1.2.

3.1.3.1 LINEAR MODE SHAPES

The linear modal frequencies of the composite plate used in the shaker tests were measured using low level excitation. Mode shapes were measured using the video holography method described in section 3.1.2.1 for the aluminium alloy plate test arrangement. The fundamental mode occurred at 156 Hz. The mode shapes measured are shown in Figs 3.29 and 3.30 and Table 3.1. The frequency range is 156 to 1110 Hz. The density and stiffness of the composite material are different from that of aluminium alloy producing different frequencies. The anisotropic properties of CFRP, as well as the thermal expansion problems, make it difficult to find well defined mode shapes. In addition, there are thermal expansion problems. More modes were found but they were lacking definition and symmetry. The same care in testing was used in both cases, such as torquing the bolts in the clamping frame, but more tests were required to obtain reasonable results. An increase in temperature of 1.11°C (2°F) resulted in a 16 Hz increase in the fundamental modal frequency. This was due to expansion of the aluminium alloy clamping frame which was much greater than that of the CFRP plate.

3.1.3.2 NONLINEAR CFRP SHAKER SINUSOIDAL EXPERIMENTS

Sine dwell tests were conducted near the fundamental resonant frequencies. The test procedures were identical to the aluminium alloy plate tests described in section 3.1.2.2. The jump phenomenon occurs when the fundamental frequency increases from 147.5 Hz to 188.7 Hz, shown in Fig 3.31. This is indicative of a hardening spring type cubic nonlinearity. Displacement amplitudes of slightly more than five plate thicknesses are shown in the figure. The shape of strain and displacement relationships are quite similar to those of the aluminium alloy plate, being nonlinear at the higher excitation levels. The nonlinear displacement shapes (raw data) for the fundamental resonant responses are shown in Figs 3.32 and 3.33. The zero position is located at the centre of the plate. The 'x' direction corresponds to the width (shorter

dimension) of the plate and the 'y' direction corresponds to the length (longer dimension) of the plate. The displacement amplitude increases with increasing sinusoidal excitation. The edges of the plate near the clamping fixture show large curvature due to the high bending moments at the clamp. This curvature reverses as expected around the centre region of the plate. Large curvature is observed around the centre region of the plate. The maximum displacement measured near the clamps is 0.06 mm peak and is due to the shaker head motion and the clamping frame.

3.1.3.3 NONLINEAR CFRP SHAKER RANDOM EXPERIMENTS

Examples of the excitation spectral densities for the CFRP plate are shown in Fig 3.34. The frequency band included the 1:1 to the 2:3 modes. Examples of the total strain response spectra are shown in Figs 3.35 to 3.38 for gauge locations 1, 3, 4 and 7. Large strain responses occurred around 155, then 310, 475, 810, 940 and 1140 Hz with peak broadening and shifting to higher frequencies which is indicative of geometrical cubic nonlinearities. Many more peaks were found in the CFRP plate tests than those found in the aluminium alloy plate tests over the same frequency range. The displacement spectral densities, shown in Fig 3.39, are similar to the strain spectral densities except for the relative amplitudes of the higher order modes.

Comparisons of the axial and bending strains for location 2 for the lowest (1.45 g) and the highest excitation levels (14.4 g) are shown in Figs 3.40 and 3.41. The axial overall rms strain is 7.47% of the total strain at the highest level of excitation. This is almost twice that of the aluminium alloy plate tests. The larger axial strain responses occur around 160 and 340 Hz for the low level test. The fundamental axial strain response (320 Hz) occurs near the 3:1 mode. For the high level tests, the bending strain responses occur first around 170-200 Hz, then 940-1000 Hz and 350-680 Hz. Peak broadening and frequency shifting to higher frequencies are evident and more so than with the aluminium alloy shaker plate.

The total strain overall levels for five strain gauge locations and displacements at the centre of the plate are shown in Fig 3.42. At the maximum excitation level (14.4 g rms), the highest total strain measurement is 394 microstrain rms overall at location 10, followed by 352 microstrain at

location 2, 227 microstrain at location 3, 205 microstrain at location 1 and 169 microstrain at location 4. The shape of the displacement curve closely follows the total strain curve for strain location 2. The shape of the total strain curve seems to follow the characteristics of a parabola. The relationship between total strain and displacement is shown in Fig 3.43. This relationship, as in the case of the aluminium alloy plate, is nonlinear at small displacements. The axial overall strain levels for five gauge locations and displacements at the centre of the plate are shown in Fig 3.44. As the excitation levels increase, the axial strain increases at a slightly higher rate than the excitation level. The bending overall strain levels are shown in Fig 3.45. These are quite similar to the total strain curves. The total, bending and axial overall strain levels for three gauge locations are shown in Figs 3.46, 3.47 and 3.48. The highest strain is measured at strain location 2, the centre of the length of the plate near the clamp. The shape of the bending curve closely follows that of the displacement curve. All four of the previous figures are very similar to those of the aluminium alloy plate tests.

An example of integrating across the strain spectral densities and normalising for strain location 7 is shown in Fig 3.49. Note that gauges 2 and 7 were positioned at the same location and installed back-to-back. Strain at location 7 was used in this case because the gauge at location 2 was not functioning. The first resonance contributes approximately 96% of the overall strain at the lowest level of excitation (1.45 g). As the excitation level increases, the first resonance contribution is less, from approximately 96% to 90%. At the highest level of excitation (14.4 g), the higher order frequency peaks in the strain spectral densities contribute more significantly to the overall strain. Peak broadening at the higher level is evident from the shape of the curves.

The acceleration amplitude probability density functions (APDFs) for four different excitation levels are shown in Fig 3.50. The APDFs for the highest excitation level approach zero near +2.5 sigma and -2.9 sigma. The lowest level APDFs approach zero at +2.5 sigma and -3.2 sigma. This result is identical to those from the aluminium alloy shaker plate tests, which is expected. However, slightly more scatter in the data is observed. The strain APDFs for four different excitation levels are shown in Fig 3.51. The APDFs for the highest excitation level approaches zero near +3.2 sigma and -2.8 sigma. The low level PDFs approach zero at +2.7 sigma and -3.2 sigma. More large positive amplitudes occur than large negative amplitudes at the higher

excitation levels. This is an indication that the plate response becomes more nonlinear at higher excitation levels. The high strain level contains smaller negative amplitudes. The strain APDFs are similar to those from the aluminium alloy shaker plate tests, but more scatter is observed. Also, the CFRP APDFs are more non-Gaussian than the aluminium alloy shaker plate APDFs.

3.2 APWT PLATE EXPERIMENTAL METHODS

3.2.1 INTRODUCTION

Acoustic progressive wave tubes (APWT) provide a convenient method of exciting plates to extremely high levels of excitation, similar to sound fields produced by high performance aircraft. Kinsler [158] describes a plane wave as a wavefront where all the acoustic variables are functions of one spatial coordinate. The phase of any variable is constant on any plane perpendicular to this coordinate.

Beranek [159] describes a one dimensional, plane free progressive wave produced by the motion of a piston vibrating in one end of a rigid tube of infinite length or a finite tube with a nonreflecting termination. Anechoic termination is practical since it absorbs most of the acoustic power before it is exhausted to the outside environment. The sound wave produced by the motion of a piston merely progresses down the tube with no backward travelling wave. The wavelengths should be larger than the duct cross-sectional dimensions to prevent standing waves from forming across the duct. The duct should have rigid walls to prevent resonance response of the duct from altering the plane progressive wave and to prevent the loss of acoustic power as the wave progresses down the duct. The relationship of sound power level (PWL), sound pressure level (SPL) at standard temperature and at sea level and the cross-sectional area (A) of the duct can be expressed as

$$\text{SPL} = \text{PWL} - 10 \log (A/A_0) + 0.5 \quad (\text{dB}) \quad (3.1)$$

where $PWL = 10 \log_{10} \frac{W}{W_{ref}}$ (dB), $W_{ref} = 10^{-13}$ watts (3.2)

and $SPL = 10 \log_{10} \frac{\bar{p}^2}{\bar{p}_{ref}^2}$ (dB), $\bar{p}_{ref} = 20 \mu Pa$ (3.3)

A is the surface area in square feet through which the sound power is radiated. A_0 is the reference area which was selected as 645 mm^2 (1 ft^2). The reference sound power level used here was chosen so that the $SPL \approx PWL$ when the area of the surface being considered was one square foot. It should be noted that the reference SPL used throughout these studies was $20 \mu Pa$.

In practice, a noise generator provides the acoustic power through a coupling horn to a test duct with anechoic termination. From Eq (3.1) for a given PWL, the SPL level decreases as the cross-sectional area of the duct increases. To obtain higher sound pressure levels for a given noise generator system, smaller cross-sectional area ducts are needed. The cross-sectional area of the duct should be larger than the area of the plate to prevent the duct from reducing the response of the plate through acoustic radiation damping. It is important to reduce discontinuities or steps in the walls of the duct to prevent generating reflecting waves which contaminate the wave front. Discontinuities result in sudden changes in impedance which reduce the power transmitted. The APWT produces grazing incidence excitation of panels installed in the side walls of the duct assuming plane progressive wave propagation.

The major advantage of this test method is that it closely simulates many of the excitation environments experienced in aircraft operations. The major disadvantages are the cost of manufacturing the system (capital investment) and the cost of operation including the air supply requirements.

Exact descriptions of the acoustic field and its forcing function on the plate installed in an APWT are controversial and difficult to produce with existing methods. It is complicated by the existence of standing waves and the determination of correlation lengths. Also, the determination of the amount of the force that the plate actually receives is not known for the nonlinear case. For the linear case, the joint acceptance theory is useful. Allen [160] studied methods of obtaining 180 dB in a large APWT and described nonlinear acoustic propagation effects. This is important in choosing the form of the input spectrum to a noise generator. Clipping the input spectrum will change the amplitude probability density function at the source. However, at the test plate location in the duct, the pressure amplitude probability density function remains nearly Gaussian as described in further detail in the next paragraphs.

A sound wave is a longitudinal wave in which the particles of air move forward as a pressure portion of the wave passes and move backward as the rarefied portion of the wave passes. Thus, although the particles of the air remain centered at their individual undisturbed positions as a train of waves passes, their movement involves an oscillating particle velocity in phase with the sound pressure as it oscillates above and below the ambient pressure.

Since the pressure and the particle velocity in a free progressive wave are in phase, the pressure portion of the wave propagates at the normal speed of sound plus a small amount due to the added particle velocity; the rarefied portion propagates at the speed of sound minus the particle velocity. Thus a sound wave, whatever its shape as it is generated, distorts and the pressure portions continually advance relative to the rarefied portions. Because the wave pressure changes are adiabatic (meaning that the heat of compression is conserved in the pressure zone and raises the temperature there) causing the local speed of sound to increase and conversely for the rarefied portion. This effect adds to the rate of that advancement of the pressure portion.

It is apparent that as the wave propagates, the pressurized portions continually travel faster than the rarefied portions of the wave while the uncompressed, intermediate portions

(that remain at atmospheric pressure and temperature) travel at the normal speed of sound. This becomes easily observable at levels of 160 dB and higher.

High intensity waves, such as those associated with jet engines and rockets, distort so rapidly they may form shock fronts in a distance of a few wave lengths. Actually, the most intense wave trains that the ambient atmosphere can carry may develop shock fronts within a fraction of one wave length from the source.

Studying various wave forms led to the following conclusions. The most efficient sound generation by an air flow modulator (whether it be with a reciprocating valve or a siren) is accomplished by producing a substantially square wave form. Such a wave can approach 100% efficiency in utilizing the available energy from the air stream. A sine wave generator, on the other hand, can approach only 50% efficiency because energy is lost in the partially open phases of the valving process. A sawtooth wave generator is limited to even lower theoretical efficiency. Actual attainable efficiencies are much less; half the theoretical value is generally considered a good practical output. Any wave form generated at the source will become a sawtooth wave at some distance from the source. It will be composed of the fundamental frequency and all of its harmonics (odd and even). This leads directly to the recommendation to put aside any attempts to simulate at the source, the spectrum required at the test panel. Instead, use an efficient generator of a high level low frequency wave train. Such a wave train, during its travel, will create the broad spectrum of high level sounds needed for the required fatigue testing.

3.2.2 C-C-C-C ALUMINIUM ALLOY PLATE APWT EXPERIMENTS

Two heavy mild steel clamping plates bolted together with rectangular holes cut in the centre were used to clamp the aluminium alloy plate. The openings in the plates were 450 x 300 mm. The frame on the sound side of the test plate was 18mm thick. The other frame was 15 mm thick. This produced an 18 mm step in the APWT cross-section at the test plate location which affects the sound field. Since this is only a 6% increase in the width of the

duct (305 mm), the effects are small. The test plate was 450 x 300 x 1.22 mm L71 18 SWG aluminium alloy.

The aluminium alloy plate and steel frame were heated from 23°C to 37°C before torquing the bolts clamping the plate to the frame. This provided a light tension (50 microstrain) to the panel as long as the environment did not exceed 37°C. There was sufficient hole clearance space to prevent the panel from buckling when heated. The panel frame was suspended by two chains in the plywood opening in the side of the duct. This plate installation is shown in Fig 3.52. The APWT, located at ISVR, was rectangular in cross-section, 610 x 305 mm (1 x 2 ft), with a 30 KW Wyle WAS 3000 air modulator. For full acoustic power 3000 scfm at 25 psig is required. The plate was instrumented with 10 strain gauges. Pairs of strain gauges were mounted back-to-back, shown in Fig 3.53, similar to the shaker plate arrangement. The plate test arrangement, the instrumentation and the data acquisition and monitoring equipment are shown in Fig 3.54. Since no signal clipper was available, peaks up to $\pm 5\sigma$ were used to drive the air modulator valve, which provides a nearly Gaussian APDF in the drive signal. At the plate location the pressure APDF was also nearly Gaussian. The disadvantage of this method is that it results in a much lower sound pressure level limit in the test duct.

The spectrometer produced outputs between 0 and 100 volts, whereas, the PC data acquisition system was limited to 1 volt. A voltage reducer was used to keep the voltages in the required ranges. The microphones were orientated for grazing incidence and calibrated with a pistonphone. Strain bridge amplifiers were balanced before each testing sequence. The same procedure was used to measure total, bending and axial strains. The overall sound pressure levels used were 140, 146, 152 and 158 dB. From Eq (3.3), each 6 dB represents a doubling of sound pressure.

The air modulator random signal was shaped by a 1/3 octave spectrum shaper from 100-630 Hz to yield a relatively flat pressure spectral density at the microphone opposite the plate, M 2. With this shape, equal energy is available over the desired frequency range. The microphone was located at the centre of the plate and midway across the duct. Microphone 3

was upstream from the panel at the edge of the side wall and Microphone 4 was downstream from the panel at the edge of the side wall. Example spectra from these three microphones are shown in Fig 3.55. Differences occur in the spectrum levels due to many factors. The standing waves in the duct, due to parallel walls, have wavelengths in the frequency band of interest. The panel response interacts with the plane waves travelling down the duct. Frequencies higher than the 630 Hz input are contained in the measurements. As discussed in the introduction, section 3.2, this is due to the nonlinear propagation effects or the finite amplitude effects.

Only three strain gauges survived the highest level of excitation. These were two centre gauges and an edge gauge located on the shorter side of the plate. Since the overall SPLs (OSPLs) are logarithmic, they were changed to pressures, as shown in Fig 3.56, to examine nonlinearity of the overall levels. As the excitation levels increased the total strains increased linearly up to 600 Pa as well as the displacements. Most of the measurements were limited to 158 dB (1620 Pa) and below to prevent damage to the strain gauges and to remain in the elastic region of the material. The SPL is not high enough for this size of plate to be in the nonlinear range of excitation. Some similarities between the plate response strain time history characteristics and the C-C beam case with random excitation are noted. The plate time histories are more complex. A composite plot of the strain spectral densities obtained for an edge strain gauge location is shown in Fig 3.57. The results are similar to those obtained from the C-C beam. However, the peak broadening effect is greater than in the beam case and more resonances are exhibited as expected for a plate.

The total, bending and axial strain spectral densities for a centre gauge location with a low level of acoustic random excitation are shown in Fig 3.58. At this location the response amplitude of the third resonance is higher than that of the fundamental. The bending strain spectrum levels are generally a little lower than those for the total strain. The peaks in the axial strain spectrum are higher at the fundamental frequency. The total, bending and axial strain spectral densities for a centre gauge location with the highest level of excitation are shown in Fig 3.59. The axial strain spectrum levels are much lower than those for the bending strain. Peak broadening and shifting to higher frequencies are noted.

An example of integrating across the spectral densities and normalising for a low and a high level centre strain gauge location (SG 9) is shown in Fig 3.60. The first resonance contributes approximately 5% of the overall strain at the lowest level of excitation, 140 dB OSPL. The first and the second peaks contribute 90%. At the higher excitation level, 158 dB OSPL, the first and second resonance contribution is less, approximately 74%. Higher order resonances contribute more to the total energy. Peak broadening at the higher level is evident from the shape of the curves. The first resonant peak of the response is much lower than the second resonance. Near the clamp, strain location 10, the first resonance is the highest contribution.

The pressure APDFs for microphone 2 (across from the test plate) at four different OSPLs are shown in Fig 3.61 and compared with the Gaussian function. The air modulator controller signal was amplified from the random signal generator without a clipper. The APDFs for most excitation levels approach zero near ± 3.5 sigma and -3.5 sigma. The APDFs between -2 and $+2$ sigma deviate from the Gaussian function. The lower the OSPL, the greater is the deviation. The three microphone locations (across from the plate, upstream and downstream of the plate) are examined as shown in Fig 3.62 for the 158 dB OSPL tests. All three microphone APDFs are similar. The strain APDFs for SG 10 (near the clamp) at four different OSPLs are shown in Fig 3.63. The APDF for the 146 dB OSPL test is more symmetric and near zero at ± 3.5 sigma, nearly Gaussian. The APDFs are shifted to the negative side at the other OSPLs. The offset does not increase as the OSPL increases, which is puzzling. More large positive amplitudes should occur than large negative amplitudes especially at the higher excitation levels, which is an indication that the plate response becomes more nonlinear at higher excitation levels. The negative APDF results could be due to an inverted sign of the signal in the signal processing. For example, some digital filters invert the sign of the signals. However, the time histories do not show large negative mean values, but do show positive mean values. With the exception of the 146 dB data, a shift toward the positive amplitudes is noted as the excitation level increases. The strain APDFs for SG 9 (centre location) for the 140 dB and 158 dB OSPLs are shown in Fig 3.64. The APDF for the high OSPL approaches zero near $+3.3$ sigma and -3.1 sigma. The APDF for the low OSPL approaches zero near $+2.8$ sigma and -3.9 sigma.

3.2.3 C-C-C-C CFRP PLATE APWT EXPERIMENTS

The CFRP plate was fabricated using Hercules AS4 /3501-6 unidirectional prepreg tape with AS4 fibres in a 3501-6 matrix ($0^\circ / \pm 45^\circ / 90^\circ$)_S. The size of the panel, clamping frame and strain gauge locations are shown in Fig 3.65. The unclamped size of the plate in the fixture was 514 x 387 x 1.09 mm which results in an aspect ratio of 1.33. The plate was attached to the heavy mild steel clamping frame using screws and flat stainless steel washers. Thin CFRP strips were inserted underneath the washers. This arrangement was used to reduce the effects of a thick clamping plate inside the APWT from affecting the acoustic plane wave progression across the panel. Since the first attempts resulted in extruding the washers into the holes in the plate, larger clamping washers were used as shown in Fig 3.66. No pretension was applied to the plate since this method was useful in preventing buckling due to the clamping arrangement.

3.2.3.1 LINEAR MODE SHAPES

The modal frequencies of the composite plate used in the APWT experiments were determined from low level tests. The plate, in its clamping frame suspended on bungy cords, was excited sinusoidally with an acoustic driver, as shown in Fig 3.67. The fundamental mode at 59 Hz along with higher order modes are shown in Figs 3.68 and 3.69. The higher order modes are listed in Table 3.1. The range of frequencies covered was 59 to 405 Hz which includes modes up to 5:3. The 1:2, 2:3 and 3:3 modes were not found.

3.2.3.2 CFRP APWT NONLINEAR RANDOM EXPERIMENTS

The CFRP APWT nonlinear random experiments were performed using an APWT at the Wright Laboratory. The plate was instrumented with 10 strain gauges. Pairs of strain gauges were mounted back-to-back similar to the shaker plate and the aluminium alloy APWT test arrangement. The plate was suspended in the side wall of an APWT of rectangular cross-section 1219 x 304.8 mm (4 x 1 ft) shown in Fig 3.70. Two 30 KW Wyle WAS 3000 air modulators were used. The test rig was actually designed for two test panels. The panel of

interest was located further downstream from the air modulators than the other panel. The plate test arrangement, the instrumentation and the data acquisition and monitoring equipment are shown in Fig 3.71 . The random input signal to the air modulators was clipped at a crest factor of 1.4. Random acoustic excitation was utilized with a relatively flat spectrum level from 50-500 Hz at five levels. The microphones were AC coupled. Examples of spectra from two microphone locations are shown in Figs 3.72 and 3.73. Microphone 3 (M 3) was upstream of the panel and microphone 5 (M 5) was located in the wall of the duct across from the panel. Microphone 3 was utilized to shape the spectrum. A relatively flat spectrum level, with some peaks, was obtained with M 3. Larger peaks are observed around 400 and 450 Hz, possibly do to standing waves in the duct. The peaks change considerably in the spectrum levels for M 5. A slight increase in the spectrum levels is observed for M 5 in the range of 50-500 Hz.

Examples of the total strain spectral densities for gauges 2 and 3 are shown in Figs 3.74 and 3.75. The peaks for the fundamental response are much higher than the higher order responses for the strain near the clamp (SG 2). The peaks at 100 and 340 Hz at the centre of the plate (SG 3) are nearly equal for the 152 dB OSPL test. The highest strain is along the clamped edge at the centre of the longer side of the plate. Peak broadening and shifting to higher frequencies are noted. Many more resonant responses occur than for the aluminium alloy APWT plate tests. The axial strain response spectra are shown in Fig 3.76. The highest peak is at approximately 320 Hz. As the excitation levels increase the response becomes broadband and nearly flat from 50-1000 Hz. Comparisons of the total, axial and bending strain spectral densities for strain gauge 3 for the lowest and the highest excitation levels are shown in Figs 3.77 and 3.78. For the low level tests (134 dB OSPL) many narrow band peaks occur with the highest at 59 Hz. Note, this is not electronic noise since the band widths are much broader. The fundamental bending mode occurred at 59 Hz. The axial fundamental strain component occurred at 118 Hz with a subharmonic at 59 Hz. No higher order harmonics appear above the noise floor. For the high level tests, the axial strains are broadband and nearly flat from 50-1000 Hz. The total and bending strains contain four distinct peaks at 100, 325, 740, and 900 Hz. An example of the displacement spectral densities is shown in Fig 3.79. The displacements include the clamping frame motion since the frame was vibration isolated from the test duct. At 162 dB OSPL, considerable frame displacement was measured, 3.8 mm peak overall compared with 4.4 mm

peak overall at the centre of the plate. The fundamental resonance occurred at 100 Hz for the 152 dB OSPL tests. Similar characteristics as those from the strain responses are noted. However, the higher order peaks are much smaller in amplitude. Peak broadening and frequency shifting are evident.

The total strain overall levels for seven strain gauge locations and the displacement at the centre of the plate are shown in Fig 3.80. The highest total strain measured is 578 microstrain at strain gauge location 2 at 156 dB overall SPL. The displacements increase as the excitation levels increase. Since the OSPLs are logarithmic, they were changed to pressures, shown in Fig 3.81, to examine nonlinearity of the overall levels. As the excitation levels increase the total strains increase linearly up to 600 Pa as well as the displacements. Most of the measurements were limited to 152 dB (840 Pa) and below to prevent damage to the strain gauges and to remain in the elastic region of the material. Higher levels, up to 162 dB OSPL (2234 Pa), were selected to obtain a failure point for the plate, but after 8 hours, the test was terminated with no visible signs of fatigue failure. The displacements are clearly nonlinear at the 162 dB level. The axial strain overall levels for three gauge locations are shown in Fig 3.82. All three are practically the same. Comparisons of the total, axial and bending overall strain levels are shown in Fig 3.83. The axial strain was approximately 10.8% of the total strain at 151 dB OSPL. The total and bending strains are nearly equal with curvature similar to the displacement curve.

Examples of integrating across the five strain spectral densities (total strain) for the gauge at location 2 are shown in Fig 3.84. The first resonance contributes approximately 35% of the total strain at the lowest level of excitation. At the highest level of excitation, the first resonance contribution increases slightly to approximately 50%. Examples of integrating across five strain spectral densities for the gauge at location 3 are shown in Fig 3.85. The first resonance contributes approximately 50% of the total strain at the lowest level of excitation. At the highest level of excitation, the first resonance contribution decreases to approximately 30%. The integrals of the axial strain spectral densities for gauge location 3 are shown in Fig 3.86. Vibration resonances are not distinguishable. The lowest level response is fairly well distributed over the 0-2000 Hz frequency range, whereas, the highest level is spread over the 0-1000 Hz range. At the higher level of excitation, the higher order frequency peaks in the strain spectral

densities contribute more to the overall strain than the first resonant response. Peak broadening at the higher level is evident from the shape of the curves. These results are quite different than those from the aluminium alloy APWT tests where three distinct peaks were observed.

The pressure APDFs for microphone 3 (across the duct from the test plate) at five different OSPLs are shown in Fig 3.87 and compared with the Gaussian function. The air modulator controller was programmed to clip the random signals at approximately ± 2 sigma (crest factor =1.4). However, the amplitudes produced downstream of the air modulator contain much higher sigma amplitudes due to the finite amplitude effects in the propagation waves. The APDFs for most excitation levels approach zero near +3 sigma and -3.2 sigma, slightly skewed. The strain APDFs for five different OSPLs are shown in Fig 3.88. The low level APDF is more symmetrical near zero at ± 3.5 sigma, nearly Gaussian. The APDFs are shifted to the negative side at higher OSPLs. The offset does not increase as the OSPL increases, which is more puzzling. More large positive amplitudes should occur than large negative amplitudes especially at the higher excitation levels, which is an indication that the plate response becomes more nonlinear at higher excitation levels. The negative APDF results could be due to inverting the sign of the signal in the signal processing. For example, some digital filters invert the sign of the signal. However, the time histories do not show large mean values at the lower OSPLs.

IV EVALUATION OF EXPERIMENTAL RESULTS

4.1 INTRODUCTION

This chapter contains further evaluation of the experimental results. Comparisons are made of the two beams of different materials and two boundary conditions. Likewise, comparisons are made of the two clamped shaker flat plates and the APWT flat plates. A summary of the beam and plate sizes is given in Table 4.1. The sizes are of the unclamped areas are listed. For the pinned tests, the distance between pins is listed. The material properties are shown in Table 4.2. The aluminium alloy properties are from a handbook. The carbon fibre material data were computed from the manufacturer's data sheets.

Nonlinear effects due to mid plane stretching are studied here. Curve fitting of the nonlinear displacement shapes and their derivatives are investigated to determine the beam and plate strains for both the dynamic excitation tests and the static load tests. The nonlinear static displacements are compared with static bending theory. Comparisons of the bending, axial and total strains are made. Frequency response measurements are compared with linear theory. Comparisons are made of the normalised integrals across the strain spectral densities. The strain statistical moments are compared.

4.2 STATIC BEAM TEST COMPARISONS

The C-C aluminium alloy beam static test results show an offset, a shift of the neutral axis, towards the positive strain side due to the axial strains. Adding the axial strain to the bending strain equation (Eq 2.8) yields the total strain,

$$\epsilon_t = \frac{1}{8} \frac{F \ell (h / 2)}{E I} + \epsilon_a \quad (4.1)$$

where ϵ_t is the total strain and ϵ_a is the axial strain. With a 10 N force, the measured strain is 28 microstrain at the $1/4 \ell$ location. Substituting this into Eq (4.1) results in 361 microstrain and -305 microstrain, labelled theory 'B' in Fig 4.1. The figure shows an offset in the linear theory due to stretching, which also appears in the measurements. If the axial strains are subtracted from the total strains, then the tensile and compressive strains at the centre and near the clamp will be nearly equal in magnitude. For example, with a 10.4 N applied force, subtracting the axial strain at the centre location ($282-30 = 252$ microstrain) and subtracting it from the compressive strain near the clamp ($-225-30 = -255$ microstrain) results in near equality. The $1/4 \ell$ location seems to be the location of zero bending strain and only axial strain is present.

The beam is much more stiff in axial loading than in transverse bending loading as shown in the following example. The C-C transverse static strain is given in Eq 2.7 and repeated here for comparison purposes,

$$\epsilon_b = \frac{1}{8} \frac{F \ell (h/2)}{EI} = 333 \mu\epsilon, \quad \text{for } F=10 \text{ N}, \quad (4.2)$$

where ϵ_b is the bending strain, F is the force, h is the thickness, E is Young's modulus, and I is the second moment of area of the cross-section. The axial strain is given by,

$$\epsilon_a = \frac{F}{E w \ell} = 3.43 \mu\epsilon, \quad \text{for } F=10 \text{ N}, \quad (4.3)$$

where ϵ_a is the axial strain and w is the width of the beam. The bending strain is 97 times that of the axial strain for a 10 N static force.

The stretching effect shifts the neutral axis. It also causes a reduction in the cross-sectional area which reduces the second moment of area. Linear theory assumes the second moment of area to be constant and does not account for the reduction in the bending stiffness (EI). The compressive strains are not as high in magnitude as the tensile strains due to the stretching effect.

Linear bending theory is accurate at very low force levels, but it does not describe the nonlinear behaviour at higher load levels. This behaviour includes a smaller displacement amplitude and strain level as the load increases and a shift in the neutral axis toward the compressive side of the beam.

The C-C CFRP beam static test results are very similar to those for the aluminium alloy beam. The length, width and thickness of the CFRP beam are the same as the aluminium alloy beam, but the bending stiffness (EI) is slightly smaller. This should slightly increase the strains for a given force level, but the results indicate that they are nearly equal. The stretching effect shifts the neutral axis. It also causes a reduction in the cross-sectional areas which reduces the second moment of area.

The P-P aluminium alloy beam static test results have some different characteristics than those from the clamped beam tests. This is expected due to the change in boundary conditions. Larger deflections cause more stretching. Increasing the load level results in a smaller increase in the strain level. More hysteresis was observed in the strain measurements as the loads increase and decrease.

If a mathematical function can be determined that accurately describes the nonlinear deflection shape, the nonlinear bending strain can be calculated at any point along the length of the beam. This can be determined by calculating the second derivatives of the functions discussed in this section. Bending and axial strains are defined by Timoshenko [33]. Curvature in beams is related to the bending strain by,

$$\epsilon_b = \frac{h}{2} \frac{d^2 w}{dx^2} \quad (4.4)$$

and the axial strain by,

$$\epsilon_a = \frac{1}{2\ell} \int_0^\ell \left(\frac{dw}{dx} \right)^2 dx = \frac{\Delta \ell}{\ell} \quad (4.5)$$

where ϵ_b is bending strain, ϵ_a axial strain, h is thickness and ℓ is the length of the beam.

The static nonlinear displacement shapes are compared with functions used for dynamic mode shapes. The displacements for the lowest static force level (2.5 N) and the highest level (13.7 N) shown in Fig 2.15 are compared. A commercially available curve fitting PC computer program was used. The program rank orders mathematical functions in its library according to the best statistical fit. Up to two *user defined* functions can be included in the library of functions. One user defined function was added, the linear classical mode shape function, for comparison purposes. The linear classical mode shape function for the first mode of a clamped-clamped beam from reference [163 p108] is

$$\cosh \frac{\lambda x}{\ell} - \cos \frac{\lambda x}{\ell} - \beta (\sinh \frac{\lambda x}{\ell} \sin \frac{\lambda x}{\ell}) \quad (4.6)$$

where
$$\beta = \frac{\cosh \lambda - \cos \lambda}{\sinh \lambda - \sin \lambda} \quad (4.7)$$

and λ is the modal coefficient. The fundamental resonant displacement shape is studied. Eq (4.6) is multiplied by a constant 'A' to increase accuracy when the amplitudes are greater than one,

$$A [\cosh \frac{\lambda x}{\ell} - \cos \frac{\lambda x}{\ell} - \beta (\sinh \frac{\lambda x}{\ell} \sin \frac{\lambda x}{\ell})] \quad (4.8)$$

Another approach is to normalise the length of the beam. Eq (4.8) is selected in order to evaluate the second derivatives by directly scaling the curvature plots. The form of the user defined function added to the library of functions is,

$$y = a \{ \cosh(bx) - \cos(bx) - c [\sinh(bx) - \sin(bx)] \} \quad (4.9)$$

A partial listing of the functions and the ranking for the 2.5 N excitation force is shown in Appendix C, Table C-4.1. The table also shows a goodness of fit for each of the functions.

The complete list contains 203 functions. The highest ranking (1) is a logistic function, followed by a Gaussian function (2). The Lorentzian function is ranked third, the sine function seventh, the classical function fifteenth and the fourth order polynomial, twentieth. The goodness of fit ranges from 0.99589 to 0.99040 for the first to the twentieth, which is a small range. The curve fit test data for these six functions are shown in Figs 4.2 to 4.7. The curve fits are shown beyond the length of the beam (0-406 mm) to examine the shape of the functions beyond the finite boundaries. Generally, these six appear to be reasonable fits. The logistic, Gaussian, and Lorentzian functions fit the peak displacements better than the displacements near the clamp. Theoretically for clamped beams, the slope near the clamp should approach zero, however these functions asymptotically approach negative displacements rather than zero displacements. The other three functions overcome this problem but lose accuracy in fitting the peak displacement.

A partial listing of the functions and the ranking for the 13.7 N excitation force is shown in Appendix C, Table C-4.2. The complete list contains 206 functions. The highest ranking is the Gaussian function (1), followed by the sine function (2), the logistic function (5), the classical function (6) the Lorentzian (7), and the fourth order polynomial function (13). The goodness of fit ranges from 0.99712 to 0.99537 for the first to the thirteenth, which is a smaller range than for the 2.5 N test data. The curve fit test data for these six functions are shown in Figs 4.8 to 4.13. Generally, these six appear to be reasonable fits. Similar features as those for the 2.5 N test data are found for the Gaussian, logistic, and Lorentzian functions. These three functions asymptotically approach negative displacements. The other three functions are lower at the highest amplitudes than the test data, more so than those for the 2.5 N test.

The second derivatives were calculated by the PC curve fitting computer program. The second derivatives of the logistic, Gaussian and Lorentzian functions for 2.5 N force have similar shapes over the length of the beam as shown in Figs 4.14 to 4.19 (the solid squares in the figures indicate the length of the beam). The strains calculated using Eq 4.1 at the centre of the beam are -34, -32, and -37 microstrain respectively, shown in Table 4.3. The measured strain (SG 4) is -70 microstrain. The low values calculated are due to the fitted

function falling below the measured displacements. All three are meaningless since the curvature near the clamp is decreasing instead of increasing. Likewise, the second derivative of the sine function at the centre of the beam is -27 microstrain compared with the measured value of -70 microstrain (SG 4). The second derivative of the sine function at the clamp is 26.9 microstrain compared with the measured value of 69 microstrain (SG 6). The second derivative of the classical function at the centre of the beam is -22 microstrain compared with the measured value of -70 microstrain (SG 4). The second derivative at the clamp is 36.7 microstrain compared with the measured value of 69 microstrain (SG 6). The second derivative of the fourth order polynomial function at the centre of the beam is -20 microstrain compared with the measured value of -70 microstrain (SG 4). The second derivative at the clamp is 42.3 microstrain compared with the measured value of 69 microstrain (SG 6). Although the discrepancies using these last two functions are large, the shape of the curves follow the expected behaviour more closely.

The second derivative functions for the 13.7 N force, shown in Fig 4.20 to 4.25, have similar shapes along the length of the beam as those for the 2.5 N tests. The second derivative of the fourth order polynomial function at the clamp is 211 microstrain compared with 326 microstrain measured with SG 6. This function is the best of the six evaluated as shown in Table 4.3. The second derivative of the classical function at the clamp is 200 microstrain. The second derivatives for the remaining functions at the clamp are much smaller than the two preceding functions.

The ranking of the functions for the 13.7 N force changed from that for 2.5 N force. This is due to the small changes in the goodness of fit which is less important than the curvature near the clamps and the centre of the beam. The ranking is based upon the whole displacement shape. The accuracy of the curve fit is very important to obtain acceptable second derivatives.

A literature search for nonlinear static beam theory produced some articles of interest. Wei-Zang and Kai-Yaun [161] studied the problem of a uniformly loaded static clamped rectangular plate under large deflection using the Ritz energy method and double Fourier series method.

They compared their experimental results with the theory developed. At low static pressure loads (20 psi) the results compared favourably with the theory, but the theory under predicted the experimental results at the higher pressure loads (60 psi). Since static load testing was not conducted on the plates in this study, no comparison could be made. Mei studied large deflections of beams using the Von Karman- Herman equation to determine nonlinear multimodal dynamic response of beams and plates. More theoretical development is needed to account for the reduction in bending strains as the axial strain increase for increasing transverse bending loads.

4.3 NONLINEAR DYNAMIC DISPLACEMENT SHAPES

If a mathematical function can be determined that accurately describes the nonlinear dynamic deflection shape, the nonlinear bending and axial strains can be calculated at any point along the length of the beam. This can be determined by calculating the first and second derivatives of the function, the slopes and curvature, as discussed in this section.

4.3.1 C-C ALUMINIUM ALLOY BEAM NONLINEAR DYNAMIC DISPLACEMENT SHAPES

The selection of the function is based upon how well the function fits the data and how the derivatives behave. Smoothing of the fundamental resonant response was accomplished with a seventh order polynomial curve fitting routine,

$$y = C + ax + bx^2 + cx^3 + dx^4 + ex^5 + fx^6 + gx^7 \quad (4.10)$$

where C and a to g are constants. Once a continuous function is found for the nonlinear displacement shapes, the axial and bending strains at any point along the beam can be found.

A seventh order polynomial fit of the raw data is shown in Fig 4.26. The coefficients obtained for the seventh order polynomial fit of the displacement shape data and the excitation levels are listed in Appendix C, Table C-4.3. The peak displacement amplitudes increase with increasing sinusoidal excitation. The ends of the beam show large curvature due to the high bending moments at the clamp. This curvature reverses as expected around the centre region of the beam. Large curvature is observed around the centre region of the beam. The slopes and curvatures increase with increasing levels of excitation and can be calculated from the first and the second derivatives with respect to distance along the length of the beam. The first derivatives are shown in Fig 4.27. The slopes do not go to zero at the clamps as required by the clamped boundary conditions. The slope is zero as expected at the centre of the beam. The second derivatives are shown in Fig 4.28. Errors in the second derivatives are noted near the clamps. The curvatures decreases toward the clamp, when they should be increasing. The resulting curvatures near the clamp are not accurate.

A fourth order polynomial fit is shown in Fig 4.29 and the coefficients are listed in Appendix C, Table C-4.4. The first and second derivatives are shown in Figs 4.30 and 4.31. The fourth order fit seems to yield more reasonable results for these boundary conditions. The maximum curvature is about 3.4×10^{-4} per millimeter which corresponds to 340 microstrain using Eq (2.7) where $h/2 = 1$ for a 2 mm thick beam. This is comparable to the bending strain measured. The normalised displacement shapes are shown in Fig 4.32. Curvature near the clamps increases with larger sinusoidal forces.

The response for the lowest level of sinusoidal excitation (0.086 N) and the highest (0.60 N), shown in Fig 2.21, were compared. A curve fitting computer program was used. Two user defined functions are added including a fourth order polynomial,

$$y = a + bx + cx^2 + dx^3 + ex^4 \quad (4.11)$$

A partial listing of the functions and the ranking for the 0.086 N excitation force is shown in Appendix C, Table C-4.6. The complete list contains 206 functions. The highest ranking

is a sine function, followed by a sine squared function. The fourth order polynomial is ranked fifth and the classical solution, eighth. The curve fit test data for these four functions are shown in Figs 4.33 to 4.36. Generally, these four appear to be reasonable fits. The inaccuracies appear at the peak displacement and near the clamps in the first three functions. The asymmetrical shape of the data compared with the classical solution and the inaccuracies at the peak are the reasons that it is ranked lower than the others.

A partial listing of the functions and the ranking for the 0.60 N excitation force is shown in Appendix C Table C-4.6. The complete list contains 135 functions. The highest ranking is the fourth order polynomial, followed by a sine squared function. The sine function is ranked third and the classical solution, fourth. The curve fit test data for these four functions are shown in Figs 4.37 to 4.40. Generally, these four appear to be reasonable fits. The inaccuracies appear at the peak displacement at the centre of the beam, near the clamps and in the asymmetrical shape of all four functions.

The classical solution ranking moves from eighth place in the 0.086 N tests to fourth place for the 0.60 N tests. It is not expected that the classical solution has a lower ranking for the lower excitation level. At the lower excitation level, the displacement shape should be nearly linear and better fit the classical solution. The constant 'b' in Eq (4.9) is shown in Table 4.4. The constant increases from 0.0116756 to 0.0117559 with increasing displacement amplitude. The normalised classical solution from reference [163] is 0.0118251 for the first mode. While the numbers may appear to be close in value, small changes produce large changes in the curve fit. This is the reason for the six significant numbers. Increasing the amplitude into the nonlinear region slightly improved the accuracy of the classical solution to predict the nonlinear displacement shape. The strain part of the table will be discussed in subsequent paragraphs.

The second derivatives of the functions for the 0.086 N tests are shown in Figs 4.41 to 4.44. Using Eq (4.5) one half of the thickness of a 2 mm beam is 1 mm. The bending strain can be determined directly from the second derivatives of the curve fitting functions without using a scaling factor. A high degree of precision in the displacement shape is essential for

essential for determining bending strain from the second derivative. Both sine functions lose accuracy near to the clamps and the centre of the beam due to the inaccuracies of the fit in these regions. The curvature decreases instead of increasing near the clamps. The derivative of the fourth order polynomial is higher (90 microstrain) than the measurement (70 microstrain) at the clamp due to the function increasing curvature more than the measurement. The derivative of the classical function is the most accurate near the clamps (67 microstrain). The curvature at the centre of the beam is nearly the same for the four functions analyzed (about 40 microstrain). All four are lower than the measured value (60 microstrain). The curve fit is lower in amplitude near the centre of the beam than the measured displacements, which is the reason for the differences.

The second derivatives of the functions for the 0.60 N tests are shown in Figs 4.45 to 4.48. Both sine functions lose accuracy near the clamps and the centre of the beam due to the inaccuracies of the fit in these regions. The curvature decreases instead of increasing near the clamps. Comparisons of the strains determined by calculating the derivatives are also shown in Table 4.4. The derivative of the fourth order polynomial at the clamp (375 microstrain) is higher than the measurement (300 microstrain) due to the function increasing curvature more than the measurement. Derivatives of the classical function are the most accurate near the clamps (280 microstrain). Derivatives of both sine functions at the centre of the beam are nearly the same (195 microstrain). The derivative of the fourth order polynomial is 175 microstrain. The derivative of the classical function is 170 microstrain. All four are lower than the measured value (235 microstrain) due to the inaccuracy of the fit. No clear trends are found in these comparisons, but the strains determined from the classical solution and the fourth order polynomial fit are more promising.

The ranking of the curve fitting functions is based upon the whole length of the beam. Increased accuracy is gained by curve fitting a small part of the data near the clamp as shown in Figs 4.49 and 4.50. Only fourteen amplitudes were used near the clamp. The classical function was used with good accuracy. The bending strain (70 microstrain) determined from the second derivative was identical to the measured value (70 microstrain also). The best fit of the derivatives of the whole function was the classical solution with appropriate constants

for large amplitudes. The next best fit was a fourth order polynomial. The Gaussian function (rank 7) is ranked higher than the classical function (rank 8) for the 0.086 N excitation. It was ranked sixth for the 0.60 N excitation and the classical function is ranked fourth. Many other functions shown in the tables have reasonable displacement shape fits.

The three constants in the classical Eq (4.9) are examined for the clamped aluminium alloy beam. The constant 'a' significantly affects the amplitude of the curve fit but not the symmetry about the centre of the beam. The constant 'b' tends to shift the peak of the curve off centre. The constant 'c' tends to alter the entire shape. The five constants in the fourth order polynomial Eq (4.11) are examined. The coefficients primarily affect the shaping and, to a lesser degree, the amplitude. The constant 'a' affects the displacement shapes significantly. Examples of the coefficient 'a' for both aluminium alloy and CFRP clamped beams are shown in Fig 4.51. The CFRP beam example shown in the figure will be discussed in section 4.3.2. All the coefficients from Table C-4.2 generally increase with increasing excitation levels as expected, since the measured amplitudes increase. The rate of increase of the coefficients with excitation level is irregular or not smooth. The curve is similar to the nonlinear strain curves. The coefficients do not increase linearly with the excitation force. If the peak amplitude can be estimated for the nonlinear clamped beam, coefficients can be estimated by trial and error, starting with the coefficients listed in the table. The measurements show an increase in the peak amplitudes as the excitation level increases. The measured displacement shapes remain symmetrical at the high levels, but the curve fitting becomes more asymmetric the higher the level of excitation.

Other functions were studied to improve the accuracy of the second derivatives. A cosine function with another coefficient is added to the sine function,

$$y = a + b \sin(2\pi x / d + c) + e \cos(2\pi x / d + c) \quad (4.12)$$

This did not improve the accuracy of the derivatives. Extra hyperbolic sine and sine terms multiplied by another constant are subtracted from the classical equation,

$$y = a\{\cosh(bx) - \cos(bx) - c[\sinh(bx) - \sin(bx)] - d[\sinh(bx) - \sin(bx)]\} \quad (4.13)$$

This did not improve the accuracy of the derivatives. Higher order polynomials were studied up to the seventh order. The fifth and higher orders did not improve the accuracy of the derivatives. Third order polynomials are useless for this application, since the second derivative of a third order polynomial is a first order function, a straight line. The second derivative of a fourth order polynomial is a second order function which is the order expected from linear bending theory.

It is interesting to note that the linear classical mode shape function for the first mode of a pinned-pinned beam is,

$$\sin \frac{\lambda x}{\ell} \quad (4.14)$$

This function ranked high on the goodness of fit in the tables. The pinned-pinned aluminium alloy beam curve fitting is discussed in section 4.3.3. The Gaussian function is the best fit for the lowest excitation level. The Lorentzian function is the best fit for the highest level of excitation.

Another useful feature of nonlinear displacement shapes is determining the axial strain from Eq (2.10) or other methods of determining the change in length due to stretching of the deflected beam shape. The axial strain can be determined from the first derivative of the displacement shape. Another useful feature of the displacement shapes is correcting the strain measurement close to a clamping block. A strain gauge cannot be exactly at the clamp due to distortion of the gauge and its adhesive. The strain gauge averages the strain over the length and width of the active element.

4.3.2 C-C CFRP BEAM NONLINEAR DISPLACEMENT SHAPES

The fourth order polynomial fits are shown in Fig 4.52. The coefficients obtained for the polynomial fits of the displacement shape data and excitation forces are listed in Appendix C, Table C-4.7. Results similar to those from the clamped aluminium beam tests in section 4.3.1 were obtained. The first derivative is shown in Fig 4.53 and the second in Fig 4.54. The shape of the slopes and the curvatures are quite similar to those from the clamped aluminium beam tests. The coefficients 'a' for the fourth order polynomial fit are shown in Fig 4.51 and compared with those obtained from the aluminium alloy beam. The CFRP beam was tested to higher displacements since a vibrometer with an increased range was available. The coefficients increase with increasing excitation levels, but not in a linear fashion. The shape of the curve shown is similar to the strain and displacement curves. Larger coefficients were obtained for the CFRP beam than the aluminium alloy beam, due to the larger displacements. A form of the bending equation is given by Meirovitch [165 p161],

$$\frac{d^2}{dx^2} \left[EI(x) \frac{d^2 \psi(x)}{dx^2} \right] = \omega^2 m(x) \psi(x) \quad (4.15)$$

where E is the modulus of elasticity, I is the second moment of area of cross-section, ω is the frequency and m is the mass density. The stiffness (EI) of the CFRP beam is slightly lower than that of the aluminium alloy beam, due to the lower modulus of elasticity. The second moments of area of the cross-section are essentially the same. The resonant frequencies from Blevins [163] are given by,

$$\omega_n = \frac{\lambda \pi^2}{\ell^2} \sqrt{\frac{EI}{\rho}} \quad (4.16)$$

As the density increases, the frequency decrease. The density of the CFRP beam is 51.8% of the aluminium alloy beam, however the lowest sine dwell frequencies are essentially equal (54.8 Hz for the aluminium alloy beam and 56.6 Hz for the CFRP beam). This is due to the lower pretension in the CFRP beam (50 microstrain) than the aluminium alloy beam (100 microstrain). The remaining term in Eq (4.16) is the mass density. The larger mass density of the aluminium

alloy beam lowers the deflection for the same force. The fourth order polynomial fit seems to yield reasonable results.

4.3.3 P-P ALUMINIUM ALLOY BEAM NONLINEAR DISPLACEMENT SHAPES

Theoretically, the S-S and P-P mode shapes should be sinusoidal as defined in Eq 4.14. The mode shape of the simply supported beam is amplitude independent, which is the conclusion often assumed in the literature, for example Ray and Bert [95]. Bennouna and White [162] show that the mode shapes of the simply supported beam is not affected by nonlinear vibration created by large deflections. The resonant frequency increases with an increase of deflection amplitude. The mode shape of the pinned beam should be sinusoidal. The nonlinear displacement shapes should be affected by the axial strain present from the stretching effect.

A fourth order polynomial fit is shown in Fig 4.55. The coefficients and excitation forces are listed in Appendix C, Table C-4.8. The second derivatives are shown in Fig 4.56. Since the polynomial fit altered the shape to that similar to the clamped tests, the derivatives were meaningless. Theoretically, the slope should be zero at the centre of the beam and maximum at the ends for the pinned boundary conditions. A sixth order polynomial fit of the data is shown in Fig 4.57. These fit the raw data better, especially near the pins where theoretically, no bending should occur, only stretching. The first and second derivatives are shown in Figs 4.58 and 4.59, which again are practically meaningless. Other commercially available curve fitting routines were found to be useful. Examples of two that were used for the lowest nonlinear displacement shape and the highest are shown in Figs 4.60 and 4.61 with the raw data. Close agreement with the raw data is found with a Gaussian equation,

$$y = a + b \exp\left[-0.5\left(\frac{x - c}{d}\right)^2\right] \quad (4.17)$$

and a Lorentzian equation,

$$y = a + \frac{b}{1 + \left(\frac{x - c}{d}\right)^2} \quad (4.18)$$

where a , b , c , and d are constants. The constants are listed in the figures. A slight curvature in the nonlinear displacement shapes is noted near the pins and the bushings. More favourable results were obtained with the second derivative of the Gaussian equation shown in Fig 4.62, where the maximum curvature occurred at the centre of the beam as expected. The maximum curvature is about 7.5×10^{-5} per millimeter which corresponds to 75 microstrain for a 2 mm thick beam using Eq (2.7). This was somewhat comparable to the measured strain. The figure also shows some curvature at the pins. Pinned boundary conditions assume the bending moment at the boundary to be zero. A possible source of the curvature at the boundary is the friction between the pin and the bushing in the fixture.

For the smallest displacement shape, the goodness of fit was 0.99864 with the Gaussian fit and 0.99794 with the sine fit. While the Gaussian function was the highest ranking fit, the sine function was not ranked very much lower than other functions. For the largest displacement shape, best fit was the Lorentzian function and the sine function ranked slightly lower. The sine fit was slightly better with the largest displacement shape than with the smallest displacement shape, due to the better fit with the data near the pins (less curvature). The friction between the pins and the bushing in the fixture would be expected to be less, since the angular velocity was greater even though the normal force (axial force) was larger. The only noticeable difference in the two displacement shapes (high and low) was the curvature near pins, which, if neglected, agrees with simply supported beam theory. The resonant frequency increases with an increase in deflection amplitude, since the axial strain increases. This agrees with linear simply supported beam theory.

4.3.4 C-C-C-C ALUMINIUM ALLOY SHAKER PLATE NONLINEAR DISPLACEMENT SHAPES

The nonlinear displacement shapes for the fundamental resonant responses were obtained using a fourth order polynomial curve fit are shown in Fig 4.63. The coefficients obtained for the fourth order polynomial fits of the displacement shape data in the 'x' direction are listed in Appendix C, Table C-4.9. The 'x' direction in the figure corresponds to the width of the

plate, the shorter dimension. The 'y' direction corresponds to the length of the plate, the longer dimension. The peak displacement amplitudes increase with increasing sinusoidal excitation. The ends of the plate show large curvature due to the high bending moments at the clamp. This curvature reverses as expected around the central region of the plate. Large curvature is observed around the centre region of the beam. The slopes and curvatures increase with increasing levels of excitation and can be calculated from the first and the second derivatives with respect to distance along the width of the plate. The motion of the shaker head was not subtracted from the plate measurements since it was considered small, 0.01 mm peak maximum. The normalised displacement shapes are shown in Fig 4.64. This shows more clearly the different curvatures near the clamps. The first derivatives are shown in Fig 4.65. This shows more clearly the differences between the slopes at the clamped edges of the plate. The displacements near the clamps are not quite zero as desired for a clamped boundary condition. The other parts of the curves appear more promising. The slope is zero as expected at the centre of the plate. The second derivatives are shown in Fig 4.66. The curvature at the clamped edges is not accurate due to the small displacements of the shaker head. The strain from the second derivative is 600 microstrain at the clamp and the measured value is 400 microstrain. The strain from the second derivative at the centre of the plate is 425 microstrain and the measured strain is 300 microstrain. The bending strains and the axial strains can be determined from the second derivatives and the first derivatives of the nonlinear displacement shapes as discussed in the beam section (4.2).

The nonlinear displacement shapes and their derivatives for the 'y' direction are shown in Figs 4.67 to 4.70. The coefficients for the fourth order polynomial fit of the displacement shape data in the 'y' direction are listed in Appendix C, Table C-4.10. Results similar to those from the test in the 'x' direction were obtained.

The coefficients 'a' for the fourth order polynomial fit are shown in Fig 4.71 and compared with those obtained from the CFRP plate. The CFRP plate studies will be discussed in section 4.3.5. The coefficients increase with increasing excitation levels, but not in a linear fashion. The shape of the curve shown is similar to the strain and displacement curves.

4.3.5 C-C-C-C CFRP SHAKER PLATE NONLINEAR DISPLACEMENT SHAPES

The nonlinear displacement shapes for the fundamental resonance using a fourth polynomial curve fit are shown in Fig 4.72. The coefficients obtained for this fit of the displacement shape data in the 'y' direction are listed in Appendix C, Table C-4.11. The peak displacement amplitudes increase with increasing sinusoidal excitation. The ends of the plate show large curvature due to the high bending moments at the clamp. This curvature reverses as expected around the central region of the plate. Large curvature is observed around the central region of the plate. The slopes and curvatures increase with increasing levels of excitation. The motion of the shaker head was not subtracted from the plate measurements since it was considered small, 0.06 mm peak maximum. The normalised displacement shapes are shown in Fig 4.73. The first derivatives are shown in Fig 4.74. The slopes do not go to zero at the clamps as required for a clamped boundary condition. This is due to the small displacements at the clamps. The slopes are not quite zero at the centre of the plate. The asymmetrical shape is also noted in the linear mode shapes and the normalised displacement shapes. This could be due the non-homogenous material properties. The second derivatives are shown in Fig 4.75. The curvature at the clamped edges is not accurate due to the small displacements of the shaker head. The strain from the second derivative at the centre of the plate is 430 microstrain and the measured strain is 315 microstrain.

The nonlinear displacement shapes and their derivatives for the 'x' direction are shown in Figs 4.76 to 4.79. The coefficients for the fourth order polynomial fit of the displacement shape data in the 'x' direction are listed in Appendix C, Table C-4.12. The results obtained are similar to those from the measurements in the 'x' direction. The asymmetrical shapes are apparent from the normalised displacement shapes and the derivatives of the fourth order polynomial fit.

The coefficients 'a' for the fourth order polynomial fit are shown in Fig 4.71 and compared with those obtained from the aluminium alloy plate. The coefficients increase with increasing

excitation levels, but not in a linear fashion. The shape of the curve shown is similar to the strain and displacement curves. For the CFRP plate, much higher excitations levels were required to reach a 5 mm displacement level than were required for the aluminium alloy plate. This is due to the much lower density of the CFRP material, 51.8% of the aluminium alloy.

4.4 LINEAR FREQUENCY COMPARISONS

4.4.1 BEAM LINEAR FREQUENCY COMPARISONS

The first five linear, transverse bending natural frequencies for a C-C and a S-S beam were calculated using two methods, Blevins [163] and a finite element method (FEM) developed by Chen [164]. The frequencies are compared with sine and random low level excitation test data as shown in Table 4.5. The frequencies are greatly affected by the initial strain tension applied to the beam and by the mass of the exciter coil. A two Hz difference between the random test data and that calculated is seen for the C-C beam. This may be attributed to small temperature variations during the test which were less than 1°C . The thermal coefficient of linear expansion is much greater for aluminium alloys than steel. For the first and third modes, the random test results are almost equal to the FEM theoretical results for the C-C condition. The frequencies for the S-S condition are always less than those for the C-C condition. Since the test results are close to the theoretical results, the clamping fixture is considered effective in simulating the clamped boundary conditions. The sine test results are not quite as favourable. The resonant frequencies are very sensitive to the boundary conditions, pre-tensioning and mass added to the beam which makes it difficult to compare the results.

The C-C aluminium alloy beam linear mode shapes are well defined and symmetrical about the centre. They closely resemble the linear theory except for the distorted first mode shape found between the fourth and fifth modes. The C-C CFRP beam linear mode shapes are well defined and symmetrical about the centre only for the first mode. The second and third modes are distorted and occur at two closely spaced frequencies, 370 and 389 Hz. The fourth and fifth modes likewise are distorted and occur in the same region, 899 and 1025 Hz.

4.4.2 PLATE LINEAR FREQUENCY COMPARISONS

The first and the third linear modal frequencies for a C-C-C-C and a S-S-S-S plate were calculated using a method from reference [7 p 285] and compared with the modal test data as shown in Table 4-6. The fundamental natural frequencies for a flat rectangular specially orthotropic plate with C-C-C-C boundary conditions is given by,

$$f_{11}^2 = \frac{3.8325}{\rho h} \left[3.307D_1 / a^4 + 3.307D_2 / b^4 + 2D_3 / a^2b^2 \right] \text{ Hz}^2 \quad (4.19)$$

where
$$D_1 = \frac{E_{11}h^3}{12(1-\nu_{12}\nu_{21})} \quad (4.20)$$

$$D_2 = \frac{E_{22}h^3}{12(1-\nu_{12}\nu_{21})} \quad (4.21)$$

$$D_3 = \frac{\nu_{21}E_{11}h^3}{12(1-\nu_{12}\nu_{21})} + \frac{1}{6}G_{12}h^3 \quad (4.22)$$

where D is the stiffness parameter, f is the frequency, ρ is the density, h is the thickness, a is the width of the plate, b is the length of the plate, ν is Poisson's ratio, E is Young's modulus and G is the shear modulus. The fundamental natural frequency for a flat plate with S-S-S-S boundary conditions is given by,

$$f_{11}^2 = \frac{\pi^2}{4\rho h} \left[D_1 / a^4 + D_2 / b^4 + 2D_3 / a^2b^2 \right] \text{ Hz}^2 \quad (4.23)$$

Modal frequencies for practical boundary conditions usually are found between the clamped and the simply supported boundary conditions.

Reasonable agreement is obtained comparing the first natural frequency of the aluminium alloy shaker plate theoretical result (221.7 Hz) with the test results (207.8 Hz). Since both the clamping frame and the test plate were of aluminium alloy, thermal stress is not a factor in pretensioning the plate. The slight decrease in the measured results is an indication of the effectiveness of the clamping arrangement. The frequency is far from the simply supported boundary conditions, 114.9 Hz. Comparing the clamped third modal frequencies shows a difference of 24.5 Hz, larger than the 13.9 Hz difference for the first mode. This comparison is reasonable considering the higher modes are usually more difficult to predict.

Reasonable agreement is obtained comparing the first natural frequency of the CFRP shaker plate theoretical result (221.8 Hz) with the test result (156 Hz). Since the clamping frame and the test plate are very dissimilar in their thermal coefficients of expansion, thermal stress is a major factor in tensioning or compressing the plate. Comparing the clamped third modal frequencies shows a difference of 287 Hz, much larger than the 66 Hz difference for the first mode. This comparison is not reasonable until the thermal effects are factored into the results.

Comparing the first natural frequency of the aluminium alloy APWT plate theoretical results (90.4 Hz) with the test result (180 Hz) indicates a large difference in frequency. Since the test plate was pretensioned, the experimental frequency is expected to be greater than that predicted. This comparison is not reasonable until the thermal effects are factored into the results. Comparing the third modal frequencies shows a difference of 127 Hz, larger than the 90 Hz difference for the first mode.

Comparing the first mode of the CFRP APWT plate theoretical result (59 Hz) with the test result (59 Hz) indicates, surprisingly, an exact match. Comparing the third modal frequencies shows a difference of 40 Hz, larger than the 0 Hz difference for the first mode. This comparison is reasonable considering the higher modes are usually more difficult to predict.

The C-C-C-C aluminium alloy shaker plate linear mode shapes are well defined and symmetrical about the centre. They closely resemble the linear plate theory. The C-C-C-C CFRP shaker plate linear mode shapes are slightly less symmetric about the centre of the plate than those found in the aluminium alloy plate tests. The 1:2, 2:3 and 3:3 modes were not found for the CFRP shaker plate, leaving a gap in the modal responses.

4.5 COMPARISONS OF INTEGRATING ACROSS THE STRAIN SPECTRAL DENSITIES

Comparisons have been made of the integrals across the strain spectral densities. The first resonance at an edge gauge location of the aluminium alloy shaker plate at the highest excitation level (14.4 g) contributed 76% of the total strain compared with 93% for the CFRP shaker plate tests. The CFRP plate first resonant response is dominant, more so than that of the aluminium alloy shaker plate. The first two resonances at a centre gauge location of the aluminium alloy APWT plate at the highest excitation level (158 dB OSPL) contributed 70% of the total strain. The first resonance at an edge gauge location of the CFRP APWT plate at the highest excitation level (152 dB OSPL) contributed 30% of the total strain. The CFRP APWT plate tests indicate the importance of higher order resonant responses. Approximately 55-70% of the overall strain levels come from higher order resonances. The size of the two APWT plates is a major factor. The CFRP plate was larger with a smaller thickness than that of the aluminium alloy plate. Also the gauge location is important since the resonant peak amplitudes are different at the centre of the plate than that at the edge of the plate.

Similar characteristics are observed for the integrals across of strain spectral densities to those obtained by White [17 p 255]. At the low excitation levels (130 dB OSPL), the first resonance contributed 60% of the total. At the high excitation levels (154 dB OSPL), the first resonant response contributed 50% of the total strain. At the highest excitation level the resonant phenomenon almost disappears. The modal contributions are not very distinguishable. It appears that the nature of the response changes from that of a multi-resonant system to that of a non-resonant system strongly forced system.

4.6 NONLINEAR RANDOM BEAM COMPARISONS

Both clamped beams exhibited a slight frequency shift and peak broadening in the resonant responses. Bistable frequency response (jump phenomenon) is obtained with sinusoidal excitation of structures made of both types of material. This occurs when the excitation amplitude is constant and the frequency is swept upward or downward around the fundamental resonant frequency. Bistable amplitude response (jump phenomenon) occurs when the frequency is constant (near the fundamental resonant frequency) and the amplitude is increased or decreased. The total strains and the components, bending and axial and the displacements were measured with increasing levels of excitation. The measured axial strains are much lower than the measured bending strain at the centre of the beam and near the clamp. The axial strain significantly reduces the bending strain at high excitation levels. The beam is much stiffer in stretching than in bending. The frequency of the in-plane strain component is always twice the frequency of the annotated flexural resonance. Or, the response at the fundamental frequency is one half the frequency axial strain component. The amplitude of the axial strain component is always positive. When randomly excited, both beams exhibited a slight resonant frequency shift and peak broadening, which can be attributed to an increased stiffening or hard spring nonlinearity described in reference [86]. With a longer beam of the same cross-section, such as that studied by Bennouna [155], the axial strain is a larger percentage of the total strain. The static strain response of both CFRP beams did not exhibit a nonlinear response as great as the dynamic case with sinusoidal and random excitations.

The aluminium alloy beam APDFs were nearly Gaussian for all levels of excitation. Slightly more positive amplitudes are present than negative amplitudes at high sigma values. At low sigma values, slightly more negative amplitudes are present than positive values. These same characteristics are found in the CFRP beam APDFs.

4.7 NONLINEAR RANDOM SHAKER PLATE COMPARISONS

Both clamped shaker plates exhibited a large frequency shift and a large peak broadening. The total strains and the components, bending and axial, and the displacements were measured with increasing levels of excitation. The measured axial strains are much lower than the measured bending strains at the centre of the beam and near the clamp. The axial strain significantly reduces the bending strain at high excitation levels. The plate is much stiffer in stretching than in bending. The frequency of the in-plane strain component is always twice the frequency of the annotated flexural resonance. The amplitude of the axial strain component is always positive. When randomly excited, both shaker plates exhibited a large resonant frequency shift and peak broadening, which can be attributed to an increased stiffening or hard spring nonlinearity as described in reference [86].

The clamped aluminium alloy shaker plate APDFs differ from a Gaussian distribution at high sigma values. More positive amplitudes are present than negative amplitudes at high sigma values. At low sigma values, more negative amplitudes are present than positive values. These same characteristics are found in the CFRP shaker plate APDFs. No significant changes are found in comparing the aluminium alloy APDFs with those from the CFRP structures. These same characteristics were found in the APDF obtained by Ballentine [156 p 255] for an aluminium alloy panel.

4.8 NONLINEAR RANDOM APWT PLATE COMPARISONS

For high level acoustical excitation of a clamped plate, the responses at resonant frequencies are less pronounced (larger bandwidth) than for low level excitation. Responses at resonant frequencies higher than the fundamental resonance contribute significantly to the overall induced response. Multimodal effects become more significant at high levels of excitation.

Both clamped APWT plates exhibited a large resonant frequency shift and a large peak broadening. The total strains and the components, bending and axial, and the displacements were

measured with increasing levels of excitation. The measured axial strains were much lower than the measured bending strains at the centre of the plate and near the clamp. The axial strain significantly reduces the bending strain at high excitation levels. The frequency of the in-plane strain component is always twice the frequency of the annotated flexural resonance. When randomly excited, both shaker plates exhibit a large frequency shift and peak broadening, which can be attributed to an increased stiffening or hard spring nonlinearity described in reference [86].

The aluminium alloy plate APDFs differed from a Gaussian distribution at high sigma values. More positive amplitudes were present than negative amplitudes at high sigma values. At low sigma values, more negative amplitudes are present than positive values. A shift in the mean value occurred for the lowest excitation level (140 dB OSPL) for SG 9, more than expected from the axial strain. This should be corrected before any further evaluation can be made. Shifts in the mean values were also present in the SG 10 data. The same characteristics were also found in the clamped CFRP shaker plate APDFs. No significant changes were found in comparing the aluminium alloy APDFs with those from the CFRP tests.

The aluminium alloy plate was tested in the ISVR AWPT, with no clipping of the input signal to the coil of the air modulator valve. The CFRP plate was tested in the WL AWPT, with heavy clipping of the input signal to yield a crest factor of 1.4. The microphone and strain APDFs at the plate location do not indicate any significant changes due to clipping the input. The APDF of the input signal resembles that of a sine wave, but as this waveform propagates down the coupling horn and into the test duct, the APDF of the pressure changes to that similar to a Gaussian distribution. This can be explained as acoustic finite amplitude effects develop within a fraction of one wave length from the source, as described in more detail in section 3.2.1. Both unclipped and clipped random input signals produce the desired APDF at the test plate location.

Different characteristics are found in the APDFs obtained by White [17 p 255]. Higher negative amplitudes occurred at large sigma values than positive amplitudes at high OSPLs. The CFRP plate used was only four plies thick ($0^\circ, 90^\circ, 90^\circ, 0^\circ$) fabricated from DX 210 resin with HT-S carbon fibres, which is different than that used in this study. A major parameter in the

nonlinearity of composite plates is thickness. It is recognized in ESDU design charts that linear prediction methods are not applicable to composite plates with less than six plies.

4.9 COMPARISON OF STRAIN STATISTICAL MOMENTS

Strain statistical moments are calculated to determine trends in response data. Results from the aluminium alloy beam and shaker plate tests and the CFRP beam and shaker plate tests are summarized in Table 4.7. For a Gaussian probability density function, the mean is zero, the skewness is zero and the kurtosis is three. The mean values increase as the excitation levels increase. This is expected since the axial strain increases which adds to the bending strain amplitudes. The neutral axis is not on the centre line of the structure. The means are low compared with the rms levels which makes the mean values difficult to determine. The mean values of the two beams at approximately 6 N are about equal. The skewness of the probability density function of the random response of the aluminium alloy beam under the excitation of a 6 N force was 0.187; that for the CFRP beam was 0.311. The skewness for the aluminium alloy plate follows approximately that of the aluminium alloy beam. The skewness is higher (0.311) for the CFRP beam at 6.54 g than that of the aluminium alloy beam (0.187) excited at 6.24 g. No clear trend is observed in examining the kurtosis for the four test specimens. The range is 2.53 to 3.04. The moments for the shaker plates are calculated from the same time history as the 12 second time duration, but extending the analysis to include a total of 25 seconds at the highest level of excitation (14.4 g). The skewness and kurtosis increased very slightly.

The statistical moments calculated for the CFRP APWT plate are shown in Table 4.8. Generally, the absolute value of the mean value increases with increasing OSPL. The mean values are negative for strain location 2 and positive for strain location 3. For both locations the skewness increases. At location 2, the skewness increases from 0.059 to 0.316. The kurtosis seems to have an increasing trend from 2.96 to 3.59. The moments calculated using the 25 second time history are shown in the table. Comparing the data from the 12 second record with that from the 25 second time history, the rms value and the kurtosis value decreased slightly. The skewness increase slightly. Small differences are noted in the comparisons of the minimum and

maximum amplitudes, the rms values and the standard deviations. Higher values are obtained near the clamp (location 2) than the centre (location 3) of the plate as expected. The skewness values of the strain response obtained for the CFRP APWT plates are significantly higher than those for any of the aluminium alloy test specimens.

Similar tests on a CFRP plate were conducted in a progressive wave tube by White [17 p 256] and the statistical moments were calculated. The mean values for three strain gauges were all negative increasing in absolute value as the OSPL increased. The mean value computed in this section for the CFRP APWT plate were positive at one strain location and negative at another location. The skewness values obtained by White are all negative (-0.012 to -0.930) and not necessarily increasing with the OSPL. The skewness in this thesis for SG 2 are 0.059 to 0.316 and all positive. The kurtosis values obtained by White are 2.91 to 3.11, 3.31 to 4.85 and 2.65 to 3.02 with no obvious trend due to an increase in OSPL. The kurtosis values in this thesis are 2.96 to 3.59 with a weak trend toward increasing with increasing OSPLs. Considering the size of the plates, number of plies and their lay-up and the uncertainty in interpreting negative mean values, the comparisons are reasonably close. An aluminium alloy plate was also tested in reference [17]. The skewness values were much higher for the CFRP plate than the aluminium alloy plate tested. This observation also agrees with the results of this study.

More information is available from the strain and force normalised APDFs. The strain APDFs are found in chapters I and II. The excitation signals should be linear and nearly Gaussian in order to study nonlinear response characteristics of beams and plates. The normalised force APDFs for the C-C aluminium alloy beam fit almost perfectly a Gaussian distribution except at the lowest two levels of excitation, 0.815 N and 1.47 N. A small amount of offset occurs probably due to a small amount of DC drift, which is difficult to prevent because of the signal-to-noise ratio at low signal levels. The normalised force APDFs for the C-C CFRP beam fit almost perfectly a Gaussian distribution except at the lowest two levels of excitation, 1.08 N and 2.14 N. The normalised force APDFs for the C-C-C-C aluminium alloy shaker plate nearly fit a Gaussian distribution except at the lowest two levels of excitation, 1.46 g and 5.64 g. The normalised force APDFs for the C-C-C-C CFRP shaker plate nearly fit a Gaussian distribution except at the lowest two levels of excitation, 1.45 g and 5.64 g. The normalised force APDFs for the C-C-C-C

aluminium alloy APWT plate are close to a Gaussian distribution in the range of -3.5 and -2 sigma and +2 to +3.5 sigma. The normalised force APDFs for the C-C-C-C CFRP APWT plate are nearly Gaussian but slightly skewed towards the negative amplitudes. Since the kurtosis of the strain responses is nearly 3, any small deviations in the kurtosis of the excitation did not appreciably influence the results.

4.10 COMPARISONS OF THE RESULTS WITH ANALYTICAL METHODS

Most analytical methods studied require a great deal of work to implement the lengthy computer programs successfully or require the development of new software to model and validate the nonlinear characteristics desired. While neither were successfully completed, many features and short comings became apparent.

Commercially available programs studied included ANSYS, COSMOS/M, ABACUS, ALGERIA, MSC NASTRAN and MACRO. The types of nonlinearities which are possible to model using structural FEM programs seem to be material, plastic region crash dynamics, buckling, and temperature dependent material properties. PATRAN PLUS pre and post processing and ANSYS V were available for use. The code needs to be analyzed to determine how the stretching nonlinearity is formulated. The formulations used to produce these computer programs require a great amount of time to locate and analyze. A multimodal nonlinear FEM program developed by Mei was incorporated into MSC/NASTRAN [34], discussed in section 1.1.2. Further work will be required to evaluate the program.

The literature search for work on the nonlinear response of C-C and P-P flat thin beams and C-C C-C flat rectangular plates composed of both homogeneous and laminated materials produced many papers cited in Chapter I. Most papers introduce an in-plane strain as the beams and plates deflect from their initial positions. This nonlinearity is introduced by the

force due to mid-plane stretching at large deflections. Linear assumptions that plane sections remain plane and a linear stress-strain law seem to be prevalent.

Many of the equations of motion reduce to the well known Duffing equation. Other solutions of superharmonic and subharmonic component amplitudes exist, near the *shifted backbone curve*, found in Nayfeh and Mook [87]. They allow for nonplanar motions, longitudinal inertia and stretching. Transverse shear and rotary inertia terms are neglected. A case for coupled longitudinal and transverse oscillations is made. There is a continual exchange of energy back and forth between the longitudinal and transverse motions due to vanishing coupling coefficients leading to *internal resonance*. The idea is to study the transfer of energy between modes. This is applicable for parametric oscillations. The formulations studied are applicable only for sinusoidal excitation. While the transfer of energy from one mode to another is a very important phenomena for some cases, it did not seem to occur under the conditions tested for the C-C beam.

Multimodal nonlinear plate response for elevated thermal environments is formulated by Lee [166]. His modal differential equations contain an inertia term, viscous damping, external forcing, a linear stiffness term, two cubic nonlinear stiffness terms arising from the quasi-linear contribution and the product of the W and F functions, a global thermal expansion due to uniform temperature, one for temperature variation and a term for the moment due to the temperature gradient across the plate. He solves the equations for the pinned plate case and the clamped plate case. The temperature effects can be neglected for the room temperature case. The stresses are separated into bending and membrane. Neglecting the temperature terms for the pinned plate case, the rms membrane and bending stresses are,

$$\bar{\sigma}_x^m = \frac{\beta^2 + \nu}{2(1 - \nu^2)} w_{11}^2 - \frac{\beta^2}{2} w_{11}^2 \cos 2\pi x \quad (4.24)$$

$$\bar{\sigma}_x^b = \frac{z\beta^2 + \nu}{(1 - \nu^2)} w_{11}^2 \psi_1(x) \psi_1(y) \quad (4.25)$$

where $\beta = b/a$, $Z = z/h$, $\bar{\sigma}$ is the rms stress, 'm' superscript is membrane and 'b' is bending, W and ψ are plate functions and ν is Poisson's ratio. For the clamped plate case,

$$\bar{\sigma}_x^m = \frac{2\beta^2 + \nu}{3(1 + \nu^2)} W_{11}^2 - \frac{32}{9} W_{11}^2 \left[\frac{\beta^2}{4} \cos 2\pi y - \frac{\beta^2}{16} \cos 4\pi y - \frac{\cos 2\pi x \cos 2\pi y}{2(\beta + \beta^{-1})^2} + \frac{\cos 2\pi x \cos 4\pi y}{(\beta + 4\beta^{-1})^2} + \frac{\cos 4\pi x \cos 2\pi y}{4(4\beta + \beta^{-1})^2} \right] \quad (4.26)$$

$$\bar{\sigma}_x^b = \frac{2Z}{(1 - \nu^2)} W_{11}^2 a_{11} [\beta^2 \cos 2\pi \psi_1 y + \nu \psi(x) \cos 2\pi y] \quad (4.27)$$

It is noted that both membrane stresses are functions of W_{11}^2 and both bending stresses are functions of W_{11} . The membrane stresses are squared functions, whereas, the bending stresses are the first power of the functions. This appears contrary to the test results of the C-C aluminium alloy plate results which do not indicate rapid increasing membrane stresses compared with bending stresses as excitation levels increase. The formulations seem to agree with those published by other authors. Further work will be needed to compare with the experimental results.

Schudt and Zavodney [79] studied peak broadening by generating a family of typical response characteristics. These represented the effects of the damping and the cubic nonlinearity coefficients in the Duffing oscillator when subject to random excitation. An externally excited 'hardening Duffing oscillator' is used,

$$\ddot{x} + 2\epsilon \dot{x} + x + \epsilon \kappa x^3 = F(t) \quad (4.28)$$

where ϵ , ζ and κ are coefficients. The damping ratio coefficient is ζ fixed at selected realistic values. The other coefficients are selected accordingly to study their effect on the response. The response is obtained by direct integration of the governing equation of motion

using a fifth order Runge-Kutta-Verner algorithm. The selection of coefficients is the key element in the usefulness of the method and prior knowledge of the system characteristics is advantageous. This method and others studied seem to yield good approximations of the peak broadening phenomena, but require a considerable amount of work to implement. A modified form of the nonlinear equation of motion is given by,

$$[m]\ddot{x} + [c]\dot{x} + [k]x + b[k]x^a = F(x, t) \quad (4.29)$$

where $[m]$ is the mass matrix, $[c]$ is the damping matrix, $[k]$ is the stiffness matrix, F is the force and 'a' and 'b' are nonlinear coefficients to be determined. If the stiffness (EI) is changing, then the potential energy (PE) is changing producing a nonlinear force. Applying Newton's second law ($F=ma$), the acceleration should change as the force produced by a nonlinear spring changes. The kinetic energy ($KE=1/2 mV^2$) should also change in a similar fashion as the PE. The acceleration term in the equation should change in order for the conservation of energy to be maintained. Incorporating the kinetic energy into the equation of motion results in an additional acceleration term in addition to the additional stiffness term,

$$[m]\ddot{x} + d[m](\ddot{x})^e + [c]\dot{x} + [k]x + b[k]x^a = F(x, t) \quad (4.30)$$

where $[m]$ is the mass matrix, $[c]$ is the damping matrix, $[k]$ is the stiffness matrix, F is the force and a , b , d and e are nonlinear coefficients to be determined. The solution of the nonlinear equation of motion above would be a formidable task. A more practical approach would be to formulate set of empirical guidelines to estimate the nonlinear displacement shapes and the maximum rms stress response.

V IMPLICATIONS OF NONLINEAR BEHAVIOUR IN RELATION TO FATIGUE LIFE

5.1 INTRODUCTION

Many fatigue models are found in the literature. The Miner single mode model is selected for further investigation to develop a multimodal nonlinear model. Miner's linear cumulative damage rule [2] proposed that fatigue damage of a metallic material under cyclic stress is related to the net work absorbed by the material and that the rate of damage accumulation is linearly proportional to the number of cycles at a stress level, independent of the stress level. The incremental damage resulting from n_i cycles at a stress level S_i is then $n_i/N(S_i)$ where $N(S_i)$ is the number of cycles to failure at the stress level S_i as given by a constant amplitude S-N curve or a constant life fatigue diagram.

$$\sum_i \frac{n_i}{N(S_i)} \equiv 1 \quad (5.1)$$

Miner's rule has been used to predict random loading fatigue life by Bennouna and White [117] and Rudder and Plumblee [7],

$$N_t = \left[\sum \frac{P_p(\epsilon)}{N} \right]^{-1} \quad (5.2)$$

where N_t is the total number of cycles, $P_p(\epsilon)$ is the strain peak probability density and N is the total number of cycles to failure at incremental strain levels (derived from a strain versus cycles to failure curve). The maximum mean square stress in an acoustically excited plate from Clarkson [1] is expressed as,

$$\overline{S}^2(t) \approx \frac{\pi}{4\zeta} f_n G_p(f_n) \left[\frac{S_0}{F_0} \right]^2 \quad (5.3)$$

where S_0 is the static stress, \overline{S} is the rms stress, $G_p(f_n)$ is the sound power spectral density, f_n is the resonant frequency, ζ is the viscous damping factor, F_0 is a uniformly distributed static force

(assumed to be equal to one) and t is time. This equation uses only the first mode response and assumes that the static and dynamic deflected shapes are identical and that the acoustic pressures are in phase over the whole panel. Rather than referring to the modes as *deflections in space at the nonlinear resonant responses*, the simple terms *mode* or *multimode* are used, which is more familiar but strictly speaking, not precise. The first, third and fifth vibration modes seemed to be the predominant modes found from the results of the acoustic progressive wave tube test of plates. Assuming that the first, third and fifth modes are the major contributing sources of response, an estimate of the total mean square stress may be expressed as,

$$\overline{S}^2(t) \approx A_1 \frac{\pi}{4\zeta_1} f_1 G_p(f_1) S_1^2 + A_3 \frac{\pi}{4\zeta_3} f_3 G_p(f_3) S_3^2 + A_5 \frac{\pi}{4\zeta_5} G_p(f_5) S_5^2 \quad (5.4)$$

where A is a coefficient and $A_1 + A_3 + A_5 = 100\%$. The static pressure assumption for the first mode is dependent upon the length, width and thickness of the plate, upon which the natural frequencies are dependent. The critical part is determining the contributions of the higher order vibration modes with the coefficients A_3 and A_5 . These can be estimated from the normalised integration of the strain spectral densities as discussed in the experimental sections. Another difficult part is the estimation of the strain power spectral densities for the first, third and fifth modes. Further investigation is needed to evaluate this model.

5.2 MULTIMODAL FATIGUE MODEL

The statistical nomenclature used herein is,

$$\text{rms}^2 = \sigma^2 + m^2 \quad (5.5)$$

where rms is the root mean square, σ is the standard deviation (sd), σ^2 is the variance and m is the mean. Rewriting Eq (5.5) yields,

$$\text{rms}^2 = (\text{sd})^2 + m^2 \quad (5.6)$$

where sd and σ are the same. Standard deviation is used here to avoid confusion when the mean value is assumed to be zero. Then the rms value is equal to the standard deviation. However, these studies include the mean value which is not zero. This non-zero mean value is the result of the axial strain in nonlinear transverse bending response of clamped beams and plates. Using

Miner's rule for the assessment of fatigue life for a single mode response, the following equation was used to estimate the time to failure,

$$N_t(\text{hours}) = \left[\sum \frac{P_p(\text{sd})}{N_c} 3600 f_c \right]^{-1} \quad (5.7)$$

where $P_p(\text{sd})$ is the peak standard deviation probability density, N_t is the total number of cycles to failure at a specified strain level and f_c is the cyclic frequency. The standard deviation is used to compute the time to failure. Most of the S-N curves or ϵ -N curves are approximated as a straight line on a logarithmic graph. The relationship between strain and the cycles to failure is then,

$$N_c = \left[\frac{K}{\epsilon} \right]^\alpha \quad (5.8)$$

where K is a constant and α the slope of a straight line on a log-log graph. Equation (5.7) can be written as,

$$N_t = \left\{ \left[\sum \frac{P_p(\text{sd})}{(K/\epsilon)^\alpha} \right] 3600 f_c \right\}^{-1} \quad (5.9)$$

The cyclic frequency f_c for a single mode case is the natural frequency of the mode. Given a particular peak probability density curve from an experiment, the number of peaks and the sample time t_s can be used to determine the effective multimodal cyclic frequency,

$$f_{cm} = \text{number of peaks} / t_s \quad (5.10)$$

where f_{cm} is the effective multimodal cyclic frequency. Substituting in equation (5.8) for the multimodal case,

$$N_t = \left\{ \left[\sum \frac{P_p(\text{sd})}{(K/\epsilon)^\alpha} \right] 3600 f_{cm} \right\}^{-1} \quad (5.11)$$

Strain peak probability densities for the multimodal case are dependent upon the model used to define a peak in the time history. A sample strain time history (12 s) for the C-C aluminium alloy beam excited at a high level (10-400 Hz) is shown in Fig 5.1. The rms value is 336 microstrain, the mean value is 26.4 microstrain, and the maximum peak is 1450 microstrain. The history is

expanded in increments of 0.1 seconds as shown in Figs 5.2 and 5.3. The 'average' frequency is determined from a time history by taking the reciprocal of the time for one complete cycle. A number of combinations of the two superimposed response frequencies 55 and 320 Hz can be observed. During the same time intervals only the high frequency appears and other intervals both appear. The highest level appears when both peaks are high. The highest peak and the crest factor (CF) are important when considering cumulative damage. The crest factor is the peak value divided by the rms level. The statistical values change with each short time interval including the crest factor. A sample time history for the C-C-C-C aluminium alloy shaker plate excited (10-1000 Hz) at a high level (425 microstrain) is shown in Figs 5.4 and 5.5. More natural frequencies were noted due to the two dimensional nature of the modes.

Two types of peak probability density techniques are investigated from multimodal nonlinear strain responses. These are called major peaks and minor peaks. The major peaks are counted for the largest peaks between zero crossings. The minor peaks are counted for all stress reversals or a positive slope in the time history followed by any negative slope. Examples of these two extremes in the peak counting are shown in Figs 5.6 and 5.7. The effective cyclic frequency is much higher for the major peak count than the minor peak count. However, the peak probability density functions or PPDFs compared for these two cases are almost the same. The major peak method was selected for further study. The cyclic multimodal frequency is determined for three test cases from each major peak PDF as shown in Table 5.1. In general, the cyclic multimodal frequency increases as the standard deviation (microstrain) increases. The cyclic multimodal frequency for the aluminium alloy beam at the highest level resulted in $f_{cm} = 600$ Hz, the CFRP beam, 390 Hz and the C-C-C-C aluminium alloy shaker plate, 902 Hz. Considering the modal frequencies involved, these frequencies are high compared with the fundamental resonant frequencies. If the minor peak method is used, the frequencies would be much higher. The major peak PDF is used in this study. Rewriting equation 5.11 in terms of standard deviation yields,

$$N_t = \left\{ \left[\sum \frac{P_p(sd)}{[K/(sd)]^\alpha} \right] 3600 f_{cm} \right\}^{-1} \quad (5.12)$$

This model accounts for the axial strains where the mean is not zero. If the mean is zero, then the standard deviation is equal to the rms value.

5.3 COMPARISON OF PEAK PDFs AND DAMAGE MODEL

Rice [84] discusses the peak probability distribution which depends greatly on the signal bandwidth. For a wide band random process, the number of peaks exceeds the number of zero crossings and the PPDF is a Gaussian distribution. In the narrow band case the PPDF is a Rayleigh distribution. In all random tests conducted, the bandwidth was wide enough to include two or more resonant frequencies. While (10-400 Hz) is not a narrow band process, it is more toward a wide band process (0-10,000 Hz) in its characteristics. Other bandwidths were used, for example 10-1000 Hz and 50-1000 Hz, which more closely resemble the characteristics of wide band rather than narrow band process.

5.3.1 CLAMPED ALUMINIUM ALLOY BEAM PPDFs

The strain major peak probability density functions (PPDF) were determined for the experimental test cases. The computer program used computed PDFs by removing the mean values, assuming a zero mean. This results in the 'x' axis of strain divided by the rms value. The mean values were added back in using Eq (5.6) which resulted in an 'x' axis of strain divided by the standard deviation. Since the mean is nonzero the 'x' axis or sigma is the strain divided by the standard deviation. The major peak probability density functions are determined for the C-C aluminium alloy beam at the centre strain location for the low level test (0.50 N) and high level test (6.46 N) with random excitation from 10-400 Hz. The PPDFs were compared with a Gaussian distribution as shown in Fig 5.8. The low level case followed the Gaussian distribution closely for the positive sigma values and slightly exceeded the values for the negative values of sigma between -0.75 to -2.25. The high level case also followed the Gaussian distribution closely for the positive sigma values, but changed considerably for a negative value. A higher concentration of peaks above the Gaussian distribution was noted around -1 sigma and a lower concentration of peaks was noted around -2 sigma. The larger values of sigma represent the high level peaks which can cause larger amounts of damage. The major peak probability density functions for the strain

location near the clamp, for the low level test (0.50 N) and high level test (6.46 N) are shown in Fig 5.9. These are compared with the Gaussian and the Rayleigh distribution functions. The Rayleigh distribution function theoretically describes the peak probability densities of a single mode response case. It is not useful for the multimodal case since the response of the beam more closely resembles that of a Gaussian function. Comparing PPDFs for SG 1 and SG 3 indicates a high shift in the number of peaks around -1 sigma for the high level case. This results in few peaks around -2.2 sigma and much fewer around 0 sigma. The results obtained with the 10-1000 Hz excitation are shown in Fig 5.10 for the strain location near the clamp, where three resonant frequencies respond. Increasing the bandwidth from 10-400 Hz adds a third resonant response which results in a PPDFs following more closely a Gaussian distribution and the previously noted effects in the regions of -1 and 0 sigma did not occur.

5.3.2 CLAMPED ALUMINIUM ALLOY SHAKER PLATE PPDFs

The strain major peak probability densities were determined for the low level (1.46 g) and high level (14.4 g) excitation of the C-C-C-C aluminium alloy shaker plate with random excitation from 10-1000 Hz as shown in Fig 5.11. A lower concentration of peaks is noted around +2 sigma and -2 sigma. Higher concentrations of higher sigma values are obtained for the high level excitation than those of the low level excitation. A comparison with the high level beam case (10-1000 Hz) indicates that both have very similar characteristics except for the number of peaks around +1.75 and -1 sigma. The shaker plate case shows an increased number of peaks in these regions and a shift toward more negative peaks but fewer peaks around -2 sigma.

Most of the time histories analyzed were of 12 seconds time duration. Some test records were 25 seconds long, which were also analyzed. With longer records, the statistical properties may change. A sample 25 second time history for the clamped aluminium alloy shaker plate is shown in Fig 5.12. The mean value is 20.7 microstrain, the standard deviation is 424 microstrain, the maximum peak is 1800 microstrain and the minimum peak is -1420

microstrain. For the 12 seconds case, the mean value is 28.5 microstrain, the standard deviation is 428 microstrain, the maximum peak is 1770 microstrain and the minimum peak is -1440 microstrain. The maximum peak increased from 1770 to 1800 microstrain. The minimum peak increased from -1420 to 1440 microstrain. Very little accuracy is gained by analyzing the 25 second time records instead of the 12 second records, but the computer time and storage is significantly higher. A comparison of the 12 second strain amplitude PDFs for 12 and 25 seconds time histories is shown in Fig 5.13. Very little changes are observed at the higher sigma values.

5.3.3 CLAMPED CFRP SHAKER PLATE PPDFs

The strain major peak probability densities were determined for low level (1.45 g) and high level (14.4 g) excitation of the C-C-C-C CFRP shaker plate with random excitation from 10-1000 Hz as shown in Fig 5.14 and compared to the Gaussian distribution. The low level excitation peaks are close to the Gaussian distribution at values of sigma larger than 2. However, at other values of sigma, the PPDFs do not resemble a Gaussian distribution. A high concentration of peaks is noted between 1 to 2 and -1 to -2 sigma. At the high level of excitation, the peaks between 1 to 2 and especially -1 to -2 are significantly larger than the Gaussian distribution. No evidence of buckling is found in examining the time histories. The frequency response of this plate contains more resonant response peaks than that of the aluminium alloy shaker plate for the same frequency range.

5.3.4 CLAMPED ALUMINIUM ALLOY APWT PLATE PPDFs

Aluminium alloy APWT plate strain major peak probability densities for four levels of excitation are shown in Fig 5.15 for the strain location at the centre of the width of the plate (SG 10). For all test conditions, some shifts around zero are noted. Significant changes from the Gaussian distribution are found from 0 sigma to -1 sigma. No consistent pattern is found comparing the PPDFs for different sound pressure levels. The centre strain location (SG 9) is compared with the edge gauge location (SG 10) as shown in Fig 5.16 for

140 dB and the 158 dB test conditions. No new consistent patterns are found in these comparisons. However, the patterns of the PPDFs are quite different from the previous cases. On the positive side more peaks are noted close to zero sigma. Fewer peaks are noted in the 0 to -1 sigma range and a significant increase in peaks occurs between -1 to -2 sigma.

5.3.5 CLAMPED CFRP APWT PLATE PPDFs

The strain major peak probability densities for five levels of excitation of the CFRP APWT plate are shown in Fig 5.17. For all test conditions, some shifts around zero are noted. Significant changes from the Gaussian distribution are found from 0 sigma to -1 sigma. No consistent pattern is found comparing the PPDFs for different sound pressure levels. Larger peak concentrations are noted for values of sigma between 1 and 1.25 and -1.75 and -2.5. Similar patterns of the PPDFs occur for this case as for that of the aluminium alloy APWT plate.

5.4 FATIGUE MODEL APPLICATION

The terms K (a constant) and α (the slope of a straight line on a log-log graph of S-N data) are obtained from the S-N data for DTD 5070 aluminium alloy [7 p 488] as shown in Fig 5.18. The rms stress is changed to rms strain using Hooke's Law ($S=E\epsilon$). For this material $K = 7.116 \times 10^{20}$ and $\alpha = -0.2033$. The stress was measured on the test specimen halfway between two rivets along the centre line between the rivets described in more detail in reference 1. The data were obtained from cantilevered coupon specimens with transverse random vibratory base excitation introduced to the 'rib' specimen through a riveted joint with the 'skin'. The strain gauge location, stress concentrations, and boundary conditions greatly affect the strain level measurements. Correction factors are needed for a different set of conditions.

Two other strain versus cycle curves for BS 1470-NS3 aluminium alloy were obtained from [117 Fig 8] as shown in Fig 5.19 for sinusoidal excitation of a cantilevered beam and a

C-C beam. As noted in the reference, failure occurred much earlier for the C-C beam than the cantilevered beam for the same strain level. This was attributed to the influence of a large axial strain. These two curves together with the DTD 5070 riveted coupon curve and a 7075-T6 aluminium alloy curve are shown in Fig 5.20. The two coupon curves are essentially equal. The two BS1470 (lower strength aluminium alloy) curves are different. The cantilevered beam slope is -0.560 and the C-C beam is -0.162. The two higher strength aluminium alloy curves are nearly the same with slopes of -0.203 and -0.210. This suggests that assuming α is constant for a given material, the constant K would be more sensitive to changes in stress concentration. This same property has been observed by Holehouse [11] with similar results comparing coupon data with APWT panel data.

The fatigue life is computed for a series of test cases with different ϵ - N curves to determine the damage characteristics. A cycle is defined as a response amplitude with one positive peak, one negative peak and two zero crossings. If the mean value is significantly high, then a more appropriate definition would be to define the peaks above and below the mean. The time to failure was computed from Eq 5.9 for the cantilevered beam single mode case as shown in Table 5.2. The failure time was 16.7 hours compared with 16.7 hours from reference 117 using only positive peaks. If the negative peaks are included, the time to failure is one half or 8.3 hours. The time to failure for the C-C beam case was 3.04 hours as shown in Table 5.3 compared with 2.53 hours from reference 117 for positive peaks. The negative peaks contributed little to the damage due to high axial strains shifting the mean to a high positive value. Using an aluminium alloy ϵ - N curve for 7075-T6 riveted flexible coupon data resulted in a time to failure of 4.51 hours as shown in Table 5.4. The actual fatigue failure times obtained for the two tests were 5.25 and 5.29 hours. These are surprisingly close considering the boundary conditions and stress concentration differences. The slope seems to be relatively constant and independent of changes in stress concentrations. A larger K value increases the fatigue life. Modifying K from 1.31×10^{20} to 1.50×10^{20} increased the fatigue life from 4.51 to 5.14 hours. Changing K to 1.70×10^{20} increased the fatigue life to 5.82 hours. Using the same slope for the 7075-T6 curve, the K

value of 1.50×10^{20} resulted in a time of 5.14 hours shown in Table 5.5. This is closer to the actual failure times than the 2.53 hours from reference 117.

The time to failure is computed using Eq 5.12 for the C-C aluminium alloy beam multimodal test data as shown in Table 5.6. The failure time is 0.803 hours using both positive and negative peaks. Modifying K to 1.70×10^{20} increased the fatigue life to 1.05 hours. The time to failure for the C-C-C-C aluminium shaker plate test is 0.304 hours using the same $K = 1.30 \times 10^{20}$ as shown in Table 5.7. Since these last two cases were not tested until failure, no comparisons could be made. The predicted times to failure appear to be a little short in duration. The cases studied in the last two paragraphs are summarized in Table 5.8.

5.5 DAMAGE ASSESSMENT

The data from the tables in section 5.4 are used to determine the damage accumulation by plotting the $PPDF/N_c$ or $PPDF/N_{cm}$ for various sigma values (strain/sd). The results from two cases in reference 117 together with the 7075-T6 fatigue data are shown in Fig 5.21.

The rms strains were approximately the same for all three cases. Larger $PPDF/N_c$ values results in shorter times to failure. The damage for the single mode C-C beam case (BS1470) was much higher than that of the cantilevered beam. This is attributed to the large axial strain resulting in much higher total positive strain peaks. The single mode C-C aluminium (7075) beam case produced more damage than the other two cases. The multimodal C-C aluminium beam case is shown in Fig 5.22. The axial strain produced more damage in the positive peak domain than the negative peaks. The highest values are obtained around sigma equal to 2. The multimodal C-C aluminium alloy shaker plate test is shown in Fig 5.23 which is quite similar to the multimodal beam case. The axial strain produced more damage in the positive peak domain than the negative peaks. The highest values are obtained around sigma equal to 2.

The constants K and α were obtained from the S-N curve for DTD 5070 aluminium alloy [7 p 488] as shown in Fig 5.18. The rms stress (S) is changed to rms strain using Hooke's Law ($S=E\epsilon$). Using this method $K=9.77 \times 10^{10}$ and $\alpha = -0.2033$. The stress was measured half way between two rivets along the centre line between the rivets on the test specimen.

The cumulative damage is determined by normalising the peak probability functions divided by the cycles to failure ($PPDF/N_c$) and plotting it versus sigma. The results for the positive peaks for the clamped and cantilevered beam cases from reference 117 are shown in Fig 5.24. The normalised values show the most damage occurs between 0.5 and 3 sigma. Normalising provides a method for estimating the percentage of the damage. Higher damage is accumulated in the clamped beam case. The largest slope occurred around 1 to 2 sigma. Approximately 75% of the damage occurred between 0 and 2 sigma. For the cantilevered case, the largest slope occurred around two to three sigma with 82% of the damage in that range. The normalised values for the single mode cantilevered beam case result in the most damage occurring between 1 and 3.5 sigma.

The same procedures were used for the multimodal C-C aluminium alloy beam and the C-C-C-C aluminium alloy shaker plate tests at high levels of excitation as shown in Fig 5.25. More damage occurs with the positive peaks than the negative peaks. For the same beam, approximately 37% of the damage occurred between -2.4 and -1 sigma with the remaining damage occurring between 1 to 3 sigma. Little or no damage occurred between -1 and +1 sigma. Similar results are obtained with the clamped aluminium alloy shaker plate. Approximately 39% of the damage occurred over a similar negative sigma range with the remaining damage occurring in a similar positive sigma range.

A curve-fitting routine was used to determine a mathematical function for the high level PPDF for the clamped shaker plate from Fig 5.11. The most important part of the fit is outside the range of -1 to 1 sigma, since most of the damage accumulation occurs outside this range. A partial listing of the functions and their goodness of fit are rank ordered

accordingly in Table 5.9. The highest ranking function is a tenth order polynomial followed by ninth and eighth order polynomial fits. The goodness of fit from 1 to 14 range from 0.9775 to 0.9625, which are very close statistically. The tenth order polynomial shown in Fig 5.26 is,

$$y=a+bx+cx^2+dx^3+ex^4+fx^5+gx^6+hx^7+ix^8+jx^9+kx^{10} \quad (5.13)$$

where $a=0.346$, $b=-0.0148$, $c=-0.137$, $d=-0.054$, $e=0.090$, $f=0.043$, $g=-0.0400$, $h=-0.00976$, $i=0.00722$, $j=6.85 \times 10^{-4}$, $k=-4.36 \times 10^{-4}$. Ranked fourteenth is a natural logarithmic function as shown in Fig 5.28. The function and its coefficients are,

$$\ln y=a+bx+cx^2+dx^3+ex^4+fx^5 \quad (5.14)$$

where $a=-1.088$, $b=-0.1191$, $c=-0.1302$, $d=0.0104$, $e=-0.0653$, and $f=0.0079$. The function fits the test data similar to the tenth order polynomial and may be easier to use.

Ranked forty-first is a Gaussian function as shown in Fig 5.27. The function and its coefficients are,

$$y=a+b \exp\{-0.5[(x-c)/d]^2\} \quad (5.15)$$

where $a=-0.0968$, $b=0.4485$, $c=-0.050$ and $d=1.45$. The function fits better for sigma values of 2 or greater than those of -2 sigma and greater. This is due to the axial strains shifting the peaks to higher positive values. A constant coefficient is used to fit the Gaussian function to permit shifting the function to fit the test data. This equation can be used to replace the Rayleigh equation to determine multimodal fatigue damage for clamped plates by substituting eq 5.15 into Eq 5.12,

$$N_t = \left\{ \left[\sum \frac{a + b \exp\{-0.5[(x-c)/d]^2\}}{[K/(sd)]^\alpha} \right] 3600 f_{cm} \right\}^{-1} \quad (5.16)$$

where $a=-0.0968$, $b=0.4485$, $c=-0.050$ and $d=1.45$. Using only the positive values of the PPDF in the curve fitting program resulted in a natural logarithmic function ranked first as shown in Fig 5.28. The function and its coefficients are,

$$\ln y=a+bx^2 \ln x \quad (5.17)$$

where $a=-1.383$ and $b=-0.4275$. This function fits the test data more closely than that shown previously for the positive peaks. The positive peaks are higher than the negative peaks which are expected to produce more damage.

The equivalent cyclic multimodal frequency is needed to predict the fatigue life. Prediction of the linear modal frequencies is obtainable from a variety of sources. Usually the first mode prediction is the most accurate. The measured modal frequencies for three test cases were shown in Fig 5.29. The modal frequencies increase as the modal number increases. The cyclic multimodal nonlinear frequencies are studied for four test cases as shown in Fig 5.30. These cases are based upon the PPDFs where the peaks were counted for a specific time interval and from which the nonlinear cyclic multimodal frequencies are calculated. Generally the resonant frequencies increased with the excitation level. The equivalent cyclic multimodal frequencies for the two beam cases increased more rapidly than those for the two plate cases. Very little change was noted for the plate cases.

5.6 SUMMARY

A multimodal model is suggested extending the single mode model to include the third and fifth modes. Further development is needed to estimate the coefficients and the third and fifth strain power spectral densities. The coefficients can be estimated from the normalised integrals across the strain spectral densities.

Another multimodal model is suggested that extends the single model, based upon Miner's linear cumulative damage rule, to include more resonant response frequency peaks. The Rayleigh distribution function was replaced by a Gaussian function to incorporate the multimodal effects of plate response as shown in Eq 5.16. This function was based upon the PPDFs analyzed using a major peak counting technique. Appropriate ϵ -N curves for the boundary conditions of the plate are needed to apply the model. A fatigue curve can be characterized logarithmically by a constant and the slope of a straight line. The multimodal frequency can be estimated by dividing the number of peaks determined from the PPDFs by the length of the time history. With test data, the fatigue life can be calculated using Eq. 5.12. A number of test cases have been calculated with reasonable accuracies. For the clamped aluminium alloy beam and shaker tests, the most damage occurs between - 2 to - 1 sigma and between 1 and 3 sigma.

VI CONCLUSIONS AND RECOMMENDATIONS

As new materials and structural concepts evolve and are applied to aircraft, a better understanding of their nonlinear vibrational response and acoustic fatigue life is needed to prevent premature failure of these structures. New methods and techniques are needed to prevent expensive acoustic fatigue failures.

A considerable amount of research work has been conducted in this field. Acoustic fatigue design guides have been developed for older metallic alloys, composite structures and older structural configurations. Acoustic fatigue life prediction methods generally include predicting the random acoustic loads, estimating the vibrational stress response of the structure and predicting the life from stress or strain versus cycles to failure curves for the material and fastener configuration. These are based on simplified theory and test data formulated into semi-empirical mathematical expressions. The predictions are based upon the assumption that response in the fundamental mode causes most of the damage. The importance of the multimodal response where several peaks in the frequency response spectrum broaden as the excitation level increases has been stressed by many researchers. By including the [↙] in-plane stretching effect in the bending formulation, the nonlinear deflections and stresses were found to be much less than predicted by linear theory at the higher levels of excitation. Many of the analytical methods available lack validation with good experimental data.

The literature search for studies of the nonlinear response of clamped, simply supported and pinned flat thin beams and clamped flat rectangular plates of both homogeneous and laminated materials produced many papers. Most papers introduce an in-plane strain as the beams and plates deflect from their initial positions. This nonlinearity is introduced by the force due to stretching. Many of the equations of motion reduce to the well known Duffing equation. The effects of the damping and the cubic nonlinearity coefficients in the Duffing oscillator when subjected to random excitation have been investigated. The selection of coefficients is the key element in the usefulness of the method. It requires a great deal of knowledge of the system in order to characterize the coefficients. This method and others

studied seem to yield approximations of the peak broadening phenomenon, but require a considerable amount of effort to implement.

With this background, a study of the nonlinear behaviour of simple flat beams and plates was begun. Careful experiments were conducted to provide a data base to evaluate the nature of nonlinear structural response and its effect on predicting acoustic fatigue lifetimes. Linear mode shapes, nonlinear displacement shapes, frequency responses and strain responses were studied and measured with sinusoidal excitation. The jump phenomenon was observed and described for both the aluminium alloy and carbon fibre reinforced beams and plates. Curve fitting of nonlinear displacement shapes with mathematical functions was investigated using the measured data to determine which functions fit the nonlinear responses. The spatial derivatives of the more accurate functions found were calculated. The bending strains were calculated from the second derivative and compared with measured data. The band limited random strain and displacement responses were studied and compared with linear theory. Multimodal peak broadening effects in the strain frequency response data were also studied with increasing levels of random excitation. The contribution of each mode to the total multimodal response was determined. The four statistical moments were calculated and compared with theory and other experimental data. A multimodal fatigue model was developed and checked with a limited amount of fatigue failure data. Damage accumulation was defined and studied. The principle findings, general characteristics of these studies and suggestions for future studies are described in subsequent paragraphs.

Beams and plates were tested using an older aluminium alloy for a baseline and an older carbon fibre composite material. Newer carbon fibre beams fabricated did not remain flat. The more reliable carbon fibre materials were used in this study. The boundary conditions selected for the beam tests were clamped and pinned. Three test methods selected were the direct shaker attachment method, the base excitation method on a large shaker and the acoustic progressive wave tube method. The boundary conditions selected for the shaker plate tests were clamped. The boundary conditions selected for the high intensity acoustic tests were clamped. Sine and band limited random excitations were used in these tests.

Laser vibrometer technology is growing at a rapid pace with increased capabilities to study nonlinear displacement shapes. Advances were made in 1991 in the scanning laser Doppler sensor technology. The upper velocity limit has been increased to 10 m/s which makes it possible to measure dynamic structural displacement shapes to very high amplitudes with a high degree of accuracy. The rapid scanning capability together with automatic data collection and display methods are particularly advantageous in measuring mode shapes and large amplitude surface velocities. The inherent accuracy of these sensors plus many other features have made the scanning laser Doppler sensor very favourable for carrying out high amplitude vibration measurements on beams and plates, as well as many other structures of interest. The scanning laser vibrometer along with proven software and hardware provides a powerful tool for nonlinear displacement shape analysis. Since the vibrometer output is a voltage indicating surface velocity, integration with respect to time yields the displacement. An electronic integrator (hardware) provided these data much more conveniently than using software. The laser Doppler sensors used provided non-contacting nonlinear high amplitude displacement shapes of the beams and plates with excellent accuracies. These were used to calculate nonlinear bending and axial strains from the smoothing functions determined from the raw data measured.

The stretching effect shifted the neutral axis in the static nonlinear bending experimental results. This was due to the addition of an axial tensile force to the bending tensile and compressive components, resulting in a total strain which was larger in tension than compression. The stretching effect also causes a reduction in the cross-sectional areas which reduces the second moment of area of the cross-section. Linear theory assumes that the neutral axis is at the centre of the cross-sectional area and the second moment of area of cross-section is constant. It does not account for the reduction in the bending displacement amplitudes at high load levels. Linear bending theory was accurate at very low force levels, but it does not describe the nonlinear behaviour at the higher load levels. Nonlinear theory usually assumes that the second moment of area of cross-section is constant or varies as some function of length and does account for the reduction in the bending displacement amplitudes at high load levels. The carbon fibre beam static and dynamic test results were very similar to those of the aluminium alloy beam. The

length, width and thickness of the carbon fibre beam were the same as for the aluminium alloy beam, but the Young's modulus of elasticity was smaller and the mass density was considerably smaller. The accuracy of static bending theory decreased rapidly for displacements greater than 34% of the beam thickness. The *rule of thumb* often cited in the literature of displacement up to 50% of the beam thickness was shown to be conservative, since deviation from linear theory was found when the displacements were greater than 34% of the thickness. The static strain of both clamped aluminium and carbon fibre beams did not exhibit a nonlinear response as great as the dynamic case with sinusoidal and random excitations. This is due to the resonant phenomenon which amplifies the response of the beams under dynamic excitation.

The clamped aluminium alloy beam and shaker linear mode shapes were well defined and the mode shapes were symmetrical about the centre of the structure. They closely resembled their predicted shapes from linear theory except for the distorted first beam mode shape found at a frequency between the fourth and fifth modes. Considerable effort was devoted to determining the nature of this phenomenon. The shape observed was not a torsional mode of the beam nor a longitudinal mode of the beam. The nature of the behaviour was not established but could only be associated with a resonance of the whole structural system. Since the distorted first mode amplitude was relatively small, it was insignificant in the band limited random response. The clamped carbon fibre reinforced beam and shaker linear mode shapes were not quite as well defined and symmetrical about the centre except for the first mode of the beam. The same test rig, clamping arrangement and axial tension were used for both types of material, however the linear mode shapes for carbon fibre reinforced specimens were more difficult to measure than those for the aluminium alloy test specimens. Considerable effort was devoted to the plate clamping fixture fasteners and their torque sequence and magnitude to prevent load distortion and prestress in the plate. The distortion in the carbon fibre reinforced structure mode shapes may be due to the non-homogeneous material property of the composite specimens including small voids in the material. The small imperfections in the composite structure linear mode shapes did not seem to change significantly the expected results of the band limited random tests.

Mathematical functions were used to fit the linear and nonlinear measured displacement shapes. If a mathematical function can be determined that accurately describes the nonlinear deflection shape, the nonlinear bending can be calculated at any point along the length of the beam. This can be determined by calculating the second derivatives with respect to distance along the length of the beam. Taking derivatives of the displacement shapes was quite sensitive to instrument noise and ripple effects in the raw data, since the displacement amplitudes were very small compared with the length of the beam. Accuracy was dependent upon how closely the selected curve fitting function fitted the measured data. The axial strain can be determined by calculating the nonlinear displacement shape function from the first derivative or simply by determining the amount of elongation due to stretching. The static nonlinear displacement shapes were compared with the functions used to characterize the dynamic mode shapes. Six curve fit functions were compared with the lowest force level displacement shape and that obtained for the highest force level. These were the logistic, Guassian, sine and Lorentzian functions, the classical solution and a fourth order polynomial fit, which yielded reasonable fits with the data. The ranking of the functions, based upon the whole displacement shape, for the highest force level changed from that of the lowest force level. This is due to the small changes in the *goodness of fit* which is less important than the maximum and the minimum curvatures, near the clamps and the centre of the beam. The strain calculated from the second derivative of the fourth order polynomial function at the clamp was the most accurate, followed closely by the classical function for both low and high levels of force.

The purpose of studying the nonlinear displacement shapes was to determine the maximum rms stress response. The clamped aluminium alloy beam dynamic nonlinear displacement shapes were compared with five functions used for the dynamic mode shapes. The maximum strain occurred near the clamp. The strains calculated from the derivatives of the classical function were the most accurate near the clamps for both low and high level excitation. With low level excitation, the best fit expected theoretically is with the classical function, which is the closest to the linear case. For the nonlinear case the classical solution still produced excellent results. Increased accuracy was gained by curve fitting a small part of the data near the clamp. For this case, the classical function produced good accuracy.

The bending strain determined from the second derivative of the classical function was close to the measured value. The clamped carbon fibre beam dynamic nonlinear displacement shapes were compared with functions used for the dynamic mode shapes. Similar results were obtained as those from the clamped aluminium alloy beam tests. The shapes of the slopes and the curvatures of the nonlinear displacement shapes were quite similar to the clamped aluminium beam test data. The first coefficients for the fourth order polynomial fit were compared with those obtained from the aluminium alloy beam. The coefficients for structures of both materials increased with increasing excitation levels, but not in a linear fashion. The coefficients obtained from the carbon fibre reinforced beam were higher due to higher displacements. The aluminium alloy and carbon fibre shaker dynamic nonlinear displacement shapes were curve fitted with fourth order polynomial functions. The strain calculated from the second derivative near the clamp was less than the measured strain. Many curve fitting functions approximate the nonlinear displacement shapes of beams and plates. Among these were the classical, sine, sine squared functions and the fourth order polynomial. For the clamped boundary conditions, the maximum strains occurred at the clamp where the curvature should be zero. The curvature of all these is zero at the ends of the structures, which is assumed in linear theory. Further study of these functions with a small amount of data near the clamp is recommended. The other functions, the Gaussian, logistic, and Lorentzian resulted in a good fit along almost the whole length of the structure, but lacked accuracy in computing the strain response near the clamp. These functions loose accuracy because the curvature does not approach zero at the clamp, but approaches zero beyond the length of the structure. These functions are not recommended for further studies of nonlinear clamped beam displacement shapes.

The three constants in the classical equation were examined for the clamped aluminium alloy beam. The first constant significantly affects the amplitude of the curve fit but not the symmetry about the centre of the beam. The second constant tends to shift the peak of the function off centre. The third constant tends to alter the entire shape. The coefficients increase with increasing excitation levels as expected, since the measured amplitudes increased. The rate of increase of the coefficients with excitation levels did not increase linearly with the force excitation level. Other functions were studied to improved the accuracy of the second derivatives. A cosine function with another coefficient was added to

the sine function. Extra hyperbolic sine and sine terms multiplied by another constant were subtracted from the classical equation. Higher order polynomials were also investigated. All of these did not improve significantly the accuracy of the derivatives already studied.

The linear transverse bending natural frequencies for a clamped and a simply supported beam were calculated and compared with sine and random test resonant frequency data. The linear resonant frequencies theoretically are independent of the type of excitation, sine or random. For the first and third modes, the random test results were almost equal to the finite element method results for the clamped boundary condition. Since the test results were close to the theoretical results, the clamping fixture was considered effective in simulating the clamped boundary conditions. The sine test results were not quite as favourable. The resonant frequencies were very sensitive to the boundary conditions, pre-tensioning and mass added to the beam. The linear modal frequencies for a clamped and a simply supported plate were calculated. Reasonable agreement was obtained comparing the first mode of the aluminium alloy shaker plate theoretical results with the test results. Since both the clamping frame and the test plate were of aluminium alloy, thermal stress was not a factor in pretensioning the plate. The slight decrease in the measured results compared with theoretical values was an indication that the clamping arrangement was effective. The fundamental frequency was far from that associated with simply supported boundary conditions, but close to that for clamped boundary conditions. Reasonable agreement was obtained comparing the first mode of the carbon fibre shaker plate theoretical results with the test results. Since the clamping frame and the test plate were very dissimilar in their thermal coefficients of expansion, thermal stress was a major factor in tensioning or compressing the plate. Comparing the theoretical first mode natural frequency of the carbon fibre plate used in the acoustic tests with experimental results indicated, surprisingly, an exact match.

With sinusoidal excitation of clamped beams and plates, jump phenomena were observed. Bistable response occurred when the excitation amplitude was constant and the frequency was swept upward or downward around the fundamental resonant frequency and when the frequency was constant and the amplitude was increased or decreased. Chaotic structural behaviour was not observed with sinusoidal excitation. The fundamental resonant frequency range for the clamped aluminium beam was small and for the clamped carbon fibre

reinforced beam, slightly larger. For the clamped aluminium alloy shaker plates, the fundamental frequency range increased to four times that of the clamped aluminium alloy beam. For the carbon fibre reinforced shaker plate, the fundamental resonant frequency range increased to twice that of the clamped carbon fibre beam. The nonlinear frequencies were dependent upon the amplitude of excitation. A comparison between the aluminium alloy shaker plate sinusoidal response in the frequency region of the fundamental mode and that of the carbon fibre reinforced plate indicated a greater hardening spring nonlinearity in the composite plate. The jump phenomenon exhibited the characteristics of a Duffing oscillator with a cubic nonlinearity. Since the back-bone curve bends towards the higher frequency region, the behaviour observed was associated with a hardening spring nonlinearity. The stretching effect lowers the bending strain below the linear theoretical results as the axial strains increase.

Large dynamic displacements of beams, greater than one half of the thickness, created high axial strains in addition to the bending strains for increasing levels of random excitation. The measured axial strains were low compared to the bending strains for high levels of random excitation for both the aluminium alloy and carbon fibre beams. The stretching effect lowers the bending strain below the linear theoretical results as the axial strains increase. Higher axial strains are expected for a larger length beam than those tested. The carbon fibre reinforced beam exhibited higher axial strain responses than the aluminium alloy beams. This was expected since the Young's modulus for the carbon fibre material was slightly lower than that of the aluminium alloy material. Both clamped beams exhibited a slight frequency shift and peak broadening, which can be attributed to an increased stiffening or hard-spring nonlinearity. The randomly excited carbon fibre reinforced shaker plate exhibited a greater number of modal response frequencies and more peak broadening than exhibited by the aluminium alloy shaker plate. The contribution of higher order modes to plate response was greater as the level of excitation increased. For high level acoustical excitation of both clamped aluminium alloy and carbon fibre plates, the modal resonances were less pronounced than for low level excitation. Higher modes than the fundamental were significant in the response. The carbon fibre plate exhibited more modal responses than the aluminium alloy plate in the same frequency range. Multimodal effects become more

significant at high levels of excitation. The reductions in the total strain response due to stretching effects have been determined experimentally. More theoretical developments are needed to account for the reduction of bending strain as the axial strain increases for increasing transverse bending loads. Further work is needed to investigate nonlinear displacement effects and the nonlinear displacement-strain effects as excitation levels increase.

Peak broadening was observed in all the dynamic tests as the excitation level increased from low to high. The clamped aluminium alloy shaker plate exhibited more peak broadening than that of the clamped aluminium alloy beam. This was attributed to the two dimensional effects or Poisson's effects. The carbon fibre reinforced shaker plate exhibited an even greater peak broadening than that of the aluminium alloy shaker plate. The acoustically excited carbon fibre reinforced plate exhibited less peak broadening than that of the acoustically excited aluminium alloy plate. The sizes of the plates affect the modal response frequencies and their closeness in frequency. Many more resonant frequencies were found with the composite plate than that found with the other test specimens.

Normalised probability density functions were calculated from the time histories of the band limited random excitation force and the strain response. Both normalised peak and amplitude probability density functions were studied. The amplitude probability density function for a narrow band random signal and a wide band random signal are Gaussian functions. For the Gaussian function large amplitude occurrences become small near plus and minus 3.5 sigma for reasonable time history lengths. Generally, the occurrence of the largest excitation force amplitudes measured were approximately plus and minus 3 sigma, although the input signal generators produced up to 5 sigma amplitudes. Some loss in the amplitude magnitude occurrences was found between the input and the electrodynamic shaker response. The largest normalised strain amplitude occurrences generally were found at approximately plus 3 and minus 2.5 sigma. Some losses in the occurrence of high amplitude strain magnitudes were found, resulting in an amplitude probability more non-Gaussian than the excitation time histories. More large strain positive amplitude occurrences than large negative amplitude occurrences were found especially at the higher excitation levels, which is an indication that the beam response becomes

more nonlinear at higher excitation levels. The carbon fibre reinforced plastic structure, generally was more non-Gaussian in its behaviour than the aluminium alloy structure. The normalised peak probability density function of a narrow band random signal is a Rayleigh function. The normalised peak probability density function of a wideband random signal is a Gaussian function. The largest strain positive peak occurrence measured was approximately 2.5 sigma and the negative peak occurrence was approximately minus 2 sigma, being neither Rayleigh nor Gaussian in form. The shape of the normalised Gaussian function more closely resembled the normalised strain peak probability function resonant response than the normalised Rayleigh function. A best fit Gaussian function was defined for the peak probability densities measured.

An estimate of the individual resonant contributions to the total strain energy can be determined by integrating across the strain spectral density and normalising by dividing by the overall level. The beam strain at the edge near the clamp was the most important to consider since it was the highest level. Generally, the first resonance contributes the most to the overall level at low excitation levels and decreases as the excitation level increases. For the clamped aluminium alloy shaker plate test, the first resonant contribution was 82% for the low level excitation and 76% for the high level. The clamped carbon fibre reinforced shaker plate first resonant contribution varied from 96% to 90%. The clamped carbon fibre reinforced acoustic test plate varied from 35 to 45%, increasing as the excitation level increased. This was attributed to the many resonant responses in the carbon fibre shaker and acoustic plate tests. Strain location was important when analyzing the multimodal contributions of the overall response spectrum. Comparing the centre gauge location integrals across the strain spectral densities for the clamped aluminium plate tests indicated that the first resonance contributed only 5% decreasing to 3%. The clamped carbon fibre acoustic plate test indicated a decrease from 50 to 30%. At the highest excitation level the sharp resonant peak phenomenon almost disappeared. The modal contributions were not very distinguishable. The response changes from that of a discrete resonant vibration response to some kind of forced smeared resonant response. The integrals across the strain spectral densities provide information for the selection of coefficients to determine multimodal fatigue life.

The strain statistical moments were calculated to determine trends in the response data. For a Gaussian probability density function, the mean is zero, the skewness is zero and the kurtosis is three. The mean values increased as the excitation level increased. This was due to the axial strain increasing which adds to the nonlinear bending amplitudes. More detailed information about the mean and skewness values was obtained from the amplitude probability density functions. The normalised force amplitude probability density functions were nearly Gaussian for most tests studied. The normalised strain amplitude probability density functions consistently indicated more positive amplitudes were present than negative amplitudes at high sigma values.

A multimodal fatigue model has been developed to predict the fatigue life of aluminium alloy clamped plates excited randomly by shaker base excitation. The method includes selecting a suitable peak probability density function which was dependent upon the boundary conditions, strain concentrations, strain locations, and the shift in the mean value due to axial strain. The Rayleigh distribution function was replaced by a Gaussian function to incorporate the multimodal effects of plate response. A Gaussian function with four coefficients was determined for clamped aluminium alloy plates. This function was based upon the peak probability density functions analyzed using a major peak counting technique. The Rayleigh distribution is appropriate for a narrow band random process where one mode is excited. The peak probability density function for a wide band process is Gaussian. The multimodal model developed incorporates a Gaussian peak probability density function, which seems compatible with published theory. Appropriate strain versus cycles curves for the material and boundary conditions of the plate are needed to apply the model. A fatigue curve can be characterized logarithmically by the slope of the curve which is usually approximated by a straight line and the slope. The multimodal frequency can be estimated by dividing the number of peaks determined from the peak probability density function by the length of the time history in seconds. A number of test cases were calculated with reasonable accuracies.

Most of the nonlinear studies indicated a hardening spring stiffness nonlinearity. Both static and dynamic tests conducted with increasing and decreasing loads did not produce

hysteresis or material nonlinearity within the measurement accuracy. No significant change was found in Young's modulus with strain amplitude.

The fatigue curves in the literature consist of sinusoidally and randomly excited rms stress or rms strain data. Although methods to convert sinusoidal data to random exist, they are not considered as accurate as actually testing with random excitation. The random test methods are used more often to define the structural fatigue curves, since large shaker and high intensity random noise facilities are available. Generally, the peak to rms ratios or crest factors for random response fatigue data are not reported. For random rms strain data, knowledge of the crest factor is essential, since higher crest factor tests produce earlier fatigue failures. The crest factor can change from shaker to shaker or on a single shaker. The crest factor can change from one acoustic progressive wave tube to another or in a single acoustic progressive wave tube. It is one of the parameters to select when using a shaker controller or an acoustic progressive wave tube controller that affects the fatigue life. There is a lack of amplitude probability density function data in the literature for near field jet noise, separated flow noise and shock interaction flow noise needed to simulate in shaker and acoustic progressive wave tube testing. Generally, it is assumed to be Gaussian, as well as the rms strain response.

Most analytical methods studied require a great deal of work to implement the lengthy computer programs successfully or require the development of more efficient software to model and validate the nonlinear characteristics desired. While neither were successfully completed in these studies, many features and short comings became readily apparent. The test results can be used to validate more analytical models. Another approach is to formulate a set of empirical guidelines to estimate the parameters needed to predict acoustic fatigue life. Further development of the multimodal fatigue models and the cyclic multimodal frequencies can extend the application to more practical structures with flexible boundary conditions. Cantilevered beam coupon testing produces pure bending strain results. The ends of a beam must be restrained from moving in order to incorporate the axial strain effects. Base shaker excitation of clamped beams which incorporate the nonlinear bending effects is recommended for future work. More strain versus cycles to failure curves for beams, beam

coupons and plates are needed. Standardized methods are needed for the strain versus cycles to failure curves. The semi-empirical approach requires costly tests to provide the necessary data. Any method requires fatigue curves which can only be obtained as a result of testing. Further work is needed to develop the guidelines and a multimodal fatigue model.

The following are recommendations for future studies. The reduction in the multi-modal total strain responses due to the stretching effects has been determined experimentally for clamped beams and plates. More complex structures such as skin stiffened panels can be modelled as plates with flexible end constraints. More theoretical developments are needed for flexible boundary conditions to account for the reduction of bending strain as the axial strain increases for increasing transverse bending loads. From these developments the maximum RMS strain response of more practical structures can be predicted for a given acoustic load. The multi-modal effect of shifting energy from the fundamental response to higher modes was demonstrated for high excitation levels. A mathematical model for the prediction of the RMS stress response that includes the effects of higher order modes was presented. The development of higher order modal coefficients is needed for more flexible boundary conditions. A multi-modal fatigue model has been developed with a modified Gaussian peak probability function. More development is needed to incorporate peak probability distribution functions of flexible structures. It is useful to use these experimental results with clearly well defined boundary conditions for a validation exercise for numerical approaches.

REFERENCES

1. B.L. Clarkson, April 1994, 'Review of sonic fatigue technology', NASA contractor report 4587, NASA Langley Research Center, Hampton, Virginia.
2. M.A. Miner, 1945, 'Culmulative damage in fatigue', *ASME Journal of Applied Mechanics*, 12, A159-A164.
3. R.W. Hess, R.W. Herr, and W.H. Mayes, 1959, 'A study of the acoustic fatigue characteristics of some flat and curved aluminum panels exposed to random and discrete noise' NASA TN D1.
4. P.M. Belcher, J.D. Van Dyke, and A.L. Eshleman, 1959, 'Development of aircraft structure to withstand acoustic loads', *Aerospace Engineering* 18 No 6.
5. P.R. McGowan, 1963, 'Structural design for acoustic fatigue' ASD TDR 63-820, Wright-Patterson AFB Ohio.
6. J. R. Ballentine, F. F. Rudder, J. T. Mathis and H.E. Plumblee, 1968, 'Refinement of sonic fatigue structural design criteria', AFFDL TR 67-156, AD831118, Wright-Patterson AFB, Ohio.
7. F.F. Rudder, and H.E. Plumblee, May 1975, 'Sonic fatigue design guide for military aircraft', AFFDL-TR-74-112, AD-B004-600L, Wright Patterson AFB, Ohio.
8. C.W. Schneider and F.F. Rudder, 1973, 'Acoustic fatigue resistance of aircraft structures at elevated temperatures', AIAA paper, 73-994.
9. A.G.R. Thomson and R.F. Lambert, 1972-1975, 'Acoustics fatigue design data', NATO AGARD-AG162-Part I, II, III, and IV, Advisory Group for Aerospace Research and Development (AGARD), Seine, France.
10. ESDU Engineering Data; Acoustic Fatigue Series, Vol 1 General, endurance under acoustic loading, Vol 2, Loading actions, Damping, Vol 3, Stress/strain response to acoustic loading, Vol 4, Natural frequencies of plate structures, Vol 5, Natural frequencies of shell structures; Vol 6, Natural frequencies of sandwich panels and box structures, ESDU, International Ltd London.
11. I. Holehouse, 1984, 'Sonic fatigue design guide techniques for advanced composite airplane structures', PhD Thesis, University of Southampton.
12. A. Powell, 1958, 'On the fatigue failure of structures due to vibrations excited by random pressure fields', *Journal of Acoustical Society of America* 30, 1130-1135.
13. R.C.W. van der Hyde and A.W. Kolb, 1973, 'Sonic fatigue resistance of lightweight aircraft structures' AGARD CP 113, Seine France, 13-1 to 13-18.

14. H.F. Wolfe and I. Holehouse, July 1984, 'Acoustic fatigue life of adhesive bonded structures subjected to acoustic loads', *Recent Advances in Structural Dynamics, Proceedings of the Second International Conference, Southampton*, 763-773.
15. C. Mei and D.B. Paul, April 1984, 'Nonlinear multimode, response of clamped rectangular plates to acoustic loading', *Recent Advances in Structural Dynamics, Proceedings of the Second International Conference, Southampton*, 577-587.
16. J.H. Robinson, C. K. Chiang, and S.A. Rizzi, October 1993, 'Nonlinear random response prediction using MSC/NASTRAN', NASA Technical Memorandum 109029, Langley Research Center, Hampton, Virginia.
17. R.G. White, October 1978, 'A comparison of some statistical properties of the responses of aluminium alloy and CFRP plates to acoustic excitation', *Composites* 9(4), 125-258.
18. R.G. White, 1975, 'Some measurements of the dynamic properties of mixed, carbon fibre reinforced plastic beams and plates', *Aeronautical Journal of the Royal Aeronautical Society*, 318-325.
19. R.G. White and R.F. Mousley, July 1987, 'Dynamic response of CFRP plates Under the Action of Random Acoustic Loading', *Proceedings 4th International Conference on Composite Structures*, Paisley College of Technology, 1519-1535.
20. C.F. Ng, and R.G. White, 1988, 'Dynamic behaviour of postbuckled isotropic plates under in-plane compression', *Journal of Sound and Vibration* 120(1), 1-18.
21. R.G. White, 1988, 'The acoustic excitation and fatigue of composite plates', *Proceedings of 25th AIAA/ASME/ASCE/AHE Structures, Structural Dynamics and Materials Conference*, Williamsburg, AIAA paper, 88-2242, 253-260.
22. R.C. Drew and R.G. White, July 1987, 'An experimental investigation into damage propagation and its effects upon dynamic properties in CFRP composite material', *Proceedings 4th International Conference Composite Structures*, Paisley College of Technology, 245-256.
23. E.E. Ungar, J.F. Wilby, and D.B. Bliss, 1976, 'A guide for estimation of acoustic loads on flight vehicle surfaces', AFFDL-TR 76-91, Wright-Patterson AFB, Ohio.
24. H.H. Hubbard, August 1991, *Aeroacoustics of flight vehicles: theory and practice*, Vol 1: Noise sources and Vol 2: Noise control; NASA Reference Publication 1258, WRDC TR-90-3050, Wright Patterson AFB, Ohio.

25. C.F. Coe and W. J. Chyu, 1973, 'Pressure fluctuation inputs and response of panels underlying attached and separated supersonic turbulent-boundary layers', Section 5, AGARD CP-113, 962-970.
26. A.L. Laganelli and H.F. Wolfe, Dec 1993, 'Prediction of Fluctuating Pressure in attached and separated turbulent boundary-layer flow', *AIAA Journal of Aircraft* Vol 30, Nr 6, 962-970.
27. C. Mei and K.R. Wentz, 1982, 'Large amplitude random response of angle ply laminated composite plates', *AIAA Journal* 20, 1450-1458.
28. C. Mei and C.B. Prasad, 1985, 'Nonlinear random response of composite panels' NASA CR 176689.
29. C. Mei and C.B. Prasad, 1989, 'Effects of large deflection and transverse shear on response of rectangular symmetric composite laminates subjected to acoustic loading' *Journal of Composite Materials* 23, 606-639.
30. C. Mei and C.B. Prasad, 1987, 'Effects of large deflection and transverse shear on response of rectangular symmetric composite laminates', AIAA paper, 87-0933.
31. C.K. Chiang and C. Mei, July 1988, 'A finite element large deflection multiple-mode random response analysis of beams subjected to acoustic loading', *Proceedings of 3rd International Conference on Recent Advances in Structural Dynamics*, University of Southampton, AFWAL-TR-88-3034, Wright-Patterson AFB, Ohio, ISBN 0-85432-2298, 769-779.
32. J. Locke and C. Mei, 1989, 'A finite element formulation for the large deflection random response of thermally buckled plates', AIAA paper 89-110
33. S. Timoshenko, and S. Woinowsky-Krieger, 1959, *Theory of Plates and Shells*, McGraw-Hill, New York, 396-428.
34. J. H. Robinson, C. K. Chiang, and S.A. Rizzi, October 1993, 'Nonlinear random response prediction using MSC/NASTRAN', NASA Technical Memorandum 109029, Langley Research Center, Hampton, Virginia.
35. R.W. Gordon, 1994, 'Modeling a local structural area using artificial boundary stiffnesses', AIAA/ASME/ASCE/AHE 35th Structure, Structural Dynamics and Materials Conference, Hilton Head, South Carolina.
36. E. Johnson, and V. Venkayya, December 1988, 'Automated STructural Optimization System (ASTROS)' Air Force Wright Laboratory Technical Report, WL-TR-88-3028.

37. R. Vaicaitis, G.M. Jan and M. Shinozuka, 1972, 'Nonlinear panel response from a turbulent boundary layer', *AIAA Journal* 10 No 7, 895-899.
38. R. Vaicaitis, 1986, 'Non-linear reesponse - a time domain approach - with applications to acoustic fatigue, spacecraft and composite materials', AIAA paper 86-1934.
39. R. Vaicaitis, 1973, 'Generalised random forces for rectangular panels', *AIAA Journal* 11, No 7, 984-988.
40. R. Vaicaitis and S.T. Choi, 1987, 'Response of stiffened panels for applications to acoustic fatigue', AIAA paper 87-2711.
41. R. Vaicaitis and S.T. Choi, 1988, 'Sonic fatigue of stiffened panels', AIAA paper 88-2241.
42. S. Maekawa, 1982, 'On the sonic life estimation of skin structures at room and elevated temperatures', *Journal of Sound and Vibration* 80, 41-59.
43. S.T. Choi and R. Vaicaitis, 1989, 'Nonlinear response and fatigue of stiffened panels', *Probabilistic Engineering Mechanics* 4, 150-160.
44. J. Robinson and C. Mei, 1989, 'The influence of nonlinear damping on the random response of panels by time domain simulation,' AIAA 89-1104.
45. R. Vaicaitis, July 1991, 'Recent advances of time domain approach for nonlinear response and sonic fatigue', *Structural Dynamics: Recent Advances*. Proceedings of the Fourth International Conference, Southampton, Elsevier Applied Science, London, ISBN I-85-2660-670-2, 84-104.
46. M. Shinozuka and Y. K. Wen, 1972, 'Monte Carlo solution of nonlinear vibrations', *AIAA Journal*, 1972, 10.
47. M. Shinozuka and D. M. Jan, 1972, 'Digital simulation of random processes and its applications', *Journal of Sound and Vibration*, 111-128.
48. M. Shinozuka (ed), 1987, 'Stochastic Mechanics, Vol I and II, Department of Civil Engineering and Engineering Mechanics', Columbia University, New York.
49. J.W. Miles, 1954, 'On structural fatigue under random loading', *Journal of Aeronautical Sciences*, 21 No 11, 753-762.
50. G.W. Brown and R. Ikegami, August 1970, 'The fatigue of aluminum alloys subjected to random loading', *Experimental Mechanics*, 10.

51. J. Lucke and G.W. Brown, 1971, 'Prediction of fatigue lives on 2034-T3 and 6061-T6 aluminum alloys under broad band random loading', SCL-CR-71017, U.S. Department of Commerce.
52. S.R. Swanson, April 1968, 'Random load fatigue testing: a state of the art survey', *Materials Research and Standards*, Vol 8(4), 10-44.
53. S.M. Marco and W.L. Starkey, 1954, 'A concept of fatigue damage', *Journal of Applied Mechanics Transactions*, ASME, 76.
54. H.T. Corten and T.J. Dolan, 1956, 'Cumulative fatigue damage', IME and ASME Proceedings International Conference on Fatigue of Metals, 235-246.
55. S.S. Manson, J.C. Freche and C.R. Ensign, 1966, 'Application of a double linear damage rule to cumulative fatigue', *Fatigue and Crack Propagation*, ASTM, STP-415, 384-412.
56. K.J. Miller and K.P. Zachariah, 1977, 'Cumulative damage laws for fatigue crack initiation and stage I propagation', *Journal of Strain Analysis Engineering Design* 12, 262-270.
57. J. Martin, 1962, 'Simple stress fatigue properties - varying amplitudes', *Mechanical Behavior of Engineering Materials*, Prentice Hall, New York, 197-204.
58. Z. Hassin and A. Rotem, 1978, 'A cumulative damage theory of fatigue failure', *Material Science Engineering*, 34, 147-160.
59. P.H. Wirching, and M.C. Light, 1980, Fatigue under wide band random stresses, *ASCE Journal of the Structural Division*, 106, No ST7, 1593-1607
60. Z. Hashin, 1983, 'Statistical cumulative damage theory for fatigue life predictions', *ASME Journal of Applied Mechanics*, 50, 571-179
61. A.W. Powell, 1958, 'On the fatigue failure of structures due to vibrations excited by a random pressure field', *Journal of Acoustical Society of America*, 30, 1130-1135.
62. S.H. Crandall, W.D. Mark and G.R. Khabbaz, June 1962, 'The variance in Palmgren-Miner damage to random vibration', *Proceedings from the 4th U.S. National Congress of Applied Mechanics*, Berkeley, California, Vol 1, 119-126.
63. J.S. Bendat, 1964, 'Probability functions for random responses: prediction of peaks, fatigue damage and catastrophic failures', NASA CR-33, Measurement Analysis Corp.
64. E. Parzen, 1959, 'On models for the probability of fatigue failure of a structure', NATO AGARD Report 245.

65. J.L. Bogdanoff, 1978, 'A new cumulative damage model', *ASME Journal of Applied Mechanics*, 45, Part I, 246-250; Part II, 251-257; Part III, 733-739.
66. T.V. Kutt, 1985, 'Cumulative damage and fatigue life prediction', PhD Thesis, Department of Civil Engineering and Engineering Mechanics, Columbia University, New York.
67. S.R. Winterstein, 1985, 'Non-normal responses and fatigue damage', *ASCE Journal of Engineering Mechanics*, 110(10).
68. M. F. Ranky and B.L. Clarkson, 1983, 'Frequency average loss factors of plates and shells', *Journal of Sound and Vibration* 89, 309-323.
69. J. Soovere and M.L. Drake, December 1985, 'Aerospace structures technology damping design guide, Vol I - Technology Review, Vol II - Damping Guide, Vol III AFWAL-TR-84-3089, Wright -Patterson AFB, Ohio.
70. L. Rogers (editor), 1984, 'Vibration damping 1984 workshop proceedings', Dayton Ohio, AFWAL TR 84-3064, Wright-Patterson AFB, Ohio.
71. L. Rogers (editor), 1986, 'Proceedings Damping '86,' AFWAL TR 86-3059, Las Vegas Nevada, Wright-Patterson AFB, Ohio.
72. L. Rogers (editor), 1989, 'Proceedings Damping '89', West Palm Beach, Florida, WRDC-TR-89-3116, Wright-Patterson AFB, Ohio.
73. L. Rogers (editor), 1991, 'Proceedings Damping '91', AFWAL TR 91-3078, San Francisco, California, Wright-Patterson AFB, Ohio.
74. B.L. Portis (compiler), 1993, 'Proceedings Damping '93', San Francisco California, AFWAL TR-93-3103,4,5, Wright -Patterson AFB, Ohio.
75. R.G. Ni, and R.D. Adams, 1984, 'A rational method for obtaining the dynamic mechanical properties of lamina for predicting the stiffness and damping of laminated plates and beams', *Composites* 15, (3) 193-199
76. R. G. White and E.M.Y. Abdin, 1985, 'Dynamic properties of aligned short carbon fibre-reinforced plastics in flexure and torsion', *Composites* 16, 293-306.
77. C. Mei and C.B. Prasad, 1987, 'Effects of nonlinear damping on random response of beams to acoustic loading,' *Journal of Sound and Vibration* 117(1), 173-186.
78. C. Mei and C.B. Prasad, 1986, 'Response of symmetric rectangular composite laminates with nonlinear damping subjected to acoustic loading', AIAA paper, 86-1933.

79. C. Mei and C.B. Prasad, 1987, 'Multimode large deflection random response of beams with nonlinear damping subjected to acoustic loading', AIAA 87-2712.
80. J.A. Schudt, 1991, 'The response of nonlinear systems to random excitation', Masters Thesis, The Ohio State University, Ohio.
81. R. A. Ibrahim, July 1991, 'Nonlinear random vibration experimental results and research needs', *Structural Dynamics: Recent Advances*, Proceedings of the Fourth International Conference, Southampton, Elsevier Applied Science, London, ISBN I-85-2660-670-2, 58-83.
82. J. Gleick, 1987, *Chaos Making a New Science*, Viking Penguin New York.
83. S.O. Rice, 1944, 'Mathematical analysis of random noise', Bell System Technical Journal, Vol 23, 282-332.
84. S.O. Rice, 1945, 'Mathematical analysis of random noise (concluded)', Bell System Technical Journal, Vol 24, 46-156.
85. W.T. Thomson, 1981, 'Theory of vibration with applications', Prentice - Hall Inc.
86. D.E. Newland, 1981, 'An introduction to random vibrations and spectral analysis', Longman, London.
87. A.H. Nayfeh and D.T. Mook, 1979, *Nonlinear Oscillations*, John Wiley and Sons, New York.
88. J. G. Eisley, March 1964, 'Nonlinear vibrations of beams and rectangular plates,' Zeitschrift fur Angewandte Mathematik and Physik, Vol 15, No 2, 167-174.
89. A.V. Srinivasan, November 1966, 'Nonlinear vibration of beams and plates ', *International Journal of Nonlinear Mechanics*, Vol 1, No 3, 1789-191.
90. J. A. Bennett, 1969, 'A multiple mode approach to nonlinear beam vibrations', PhD thesis, University of Michigan, Ann Arbor, Michigan.
91. J.A. Bennett and J. G. Eisley, 1969, 'A multiple degree-of-freedom approach to nonlinear beam vibrations', *AIAA Journal* Vol 8 No 4, 734-739.
92. N. Yamaki and I. Mori, 1980, 'Nonlinear vibrations of a clamped beam with initial deflection and initial axial displacement part I: theory', *Journal of Sound and Vibration* 71(3), 333-346.
93. N. Yamaki, K. Otomo, and I. Mori, 1980, 'Nonlinear vibrations of a clamped beam with initial deflection and initial axial displacement, part II: experiment', *Journal of Sound and Vibration* 71(3)m 347-360.

94. W.Y. Tseng, J. Dugundji, 1970, 'Nonlinear vibrations of a buckled beam under harmonic excitation', *Journal of Applied Mechanics*, Vol 37, 292-297.
95. J.D. Ray and C.W. Bert, 1969, 'Nonlinear vibrations of a beam with pinned ends', *ASME Journal of Engineering for Industry*, 997-1004.
96. T.K. Caughey, December 1954, 'The Existence and Stability of Ultraharmonics and Subharmonics in Forced Nonlinear Oscillations', *ASME Journal of Applied Mechanics, Transactions*, Vol 75, 327-335.
97. M. Countryman and R. Kannan, March 1985, 'Nonlinear forced vibrations of beams', *Journal of Applied Mechanics*, Vol 52/163.
98. S.M. Dickinson and A. DiBlasio, July 1981, 'On the use of orthogonal polynomials in the Rayleigh-Ritz method for the study of the flexural vibration and buckling of isotropic and orthotropic rectangular plates', *Journal of Sound and Vibration* Vol 108, No 1, 51-62.
99. H.N. Chu and G. Hermann, 1956, 'Influence of large amplitudes on free flexural vibrations of rectangular elastic plates', *Journal of Applied Mechanics*, Vol 23, 532-540.
100. F.C. Moon, 1980, 'Experiments on chaotic motions of a forced nonlinear oscillator: strange attractor', *ASME Journal of Applied Mechanics* 47, 638-643
101. H.G. Chuster, 1984, *Deterministic Chaos - An Introduction*, Physik-Verlag, Weinheim.
102. J. Guckenheimer and P. Holmes, 1983, *Nonlinear Oscillations Dynamical Systems and Bifurcation of Vector Fields*, Springer-Verlag, New York.
103. R.W. Leven, B. Pompe, C. Wilke, and B.P. Koch, 1985, 'Experiments on periodic and chaotic motions of a parametrically forced pendulum', *Physics* 16d, 371-384.
104. A. Maewal, 1986, 'Chaos in a harmonically excited elastic beam', *Journal of Applied Mechanics*, Vol 53, 625-632.
105. A.H. Nayfeh, D.T. Mook, and S. Sridhar, 1974, 'Nonlinear analysis of the forced response of structural elements', *Journal of the Acoustical Society of America*, Vol 55, No 2, 281-291.
106. A.H. Nayfeh, D.T. Mook and D.W. Lobetiz, 1974, 'Numerical-perturbation method for the nonlinear analysis of structural vibrations', *AIAA Journal*, Vol 12, No 9, 1222-1228.

107. A.H. Nayfeh, 1981, *Introduction to Perturbation Techniques*, John Wiley and Sons, New York.
108. R.A. Ibrahim, A.Afaneh and B. Lee, 1991 'Nonlinear modal interaction in a clamped-clamped beam; part I - deterministic approach', *Vibration Analysis - Analytical and Computational*. ASME DE-Vol 37.
109. R.Benamar, R. G. White, and M. M. K. Bennouna, July 1991, 'The effects of large vibration amplitudes on the fundamental mode shape of a fully clamped, symmetrically laminated, rectangular plate', *Structural Dynamics: Recent Advances*. Proceedings of the Fourth International Conference, Southampton, Elsevier Applied Science, London, ISBN I-85-2660-670-2, 749-760.
110. A.H. Nayfeh and S.J. Serban, 1990, Response statistics of nonlinear systems to combined deterministic and random excitations', *International Journal of Non-linear Mechanics*, Vol 25, No 5, 493-509.
111. R.H. Lyon, M. Heckl, and C.B. Hazeigrove, 1961, 'Response of hardspring oscillator to narrow-band excitation', *Journal of Acoustical Society of America*, Vol 33, 1404-1411.
112. W.C. Lennox, and Y.C. Yusak, 1976, 'Narrow-band excitation of a nonlinear oscillator', *ASME Journal of Applied Mechanics*, Vol 43, 340-344.
113. S. Rajan and H.G. Davies, 1988, 'Multiple time scaling of the response of a Duffing oscillator to narrow-band random excitation', *Journal of Sound and Vibration*, Vol 123, 497-506.
114. R.N. Iyengar, 1989, 'Response of nonlinear systems to narrow-band excitation', *Structural Safety* Vol 6, 177-185.
115. J.B. Roberts and P.D. Spanos, 1990, *Random Vibration and Statistical Linearization*, John Wiley & Sons, New York.
116. R.A. Ibrahim, B.H. Lee, and A.A. Afaneh, 1991, 'Structural modal multifurcation with internal response part 2: stochastic approach', *International Journal of Non-linear Mechanics*.
117. M. M. Bennouna, and R. G. White, 1984, 'The effects of large vibration amplitudes on the dynamic strain response of a clamped-clamped beam with consideration on fatigue life', *Journal of Sound and Vibration*, 96 (3), 281-308.
118. B. Balachandran, A.H. Nayfeh, S.W. Smith and R.S. Pappa, 1992 'On identification of structures with internal resonances', AIAA-92-0491, 30th Aerospace Sciences Meeting and Exhibit, Reno, Nevada.

119. S.H. Crandall and W.D. Mark, 1963, *Random Vibration in Mechanical Systems*, Academic Press, New York.
120. Y.K. Lin, 1973, *Probabilistic Theory of Structural Dynamics*, McGraw-Hill, New York.
121. T.K. Caughey, 1971, 'Non-linear theory of random vibrations', *Advanced Applied Mechanics* 11, 209.
122. P.T.D. Spanos, 1981, 'Stochastic linearization in structural dynamics', *Applied Mechanics Review* 34, 1.
123. J.B. Roberts, 1981, 'Response of non-linear mechanical systems to random excitation; part I: Markov methods', *Shock and Vibration Digest* 13, 17.
124. J.B. Roberts, 1981, 'Response of linear mechanical systems to random excitation; part II: equivalent linearization and other methods', *Shock and Vibration Digest* 13, 15.
125. R.A. Ibrahim, 1985, *Parametric Random Vibration*, John Wiley and Sons, New York.
126. X. Zhang, I. Elishakoff and R. Zhang, 1990, 'A stochastic linearization technique based on minimum mean square deviation of potential energies', *Second International Conference on Stochastic Structural Dynamics*, Boca Raton, Florida.
127. I. Elishakoff and X. Zhang, 1992, 'An appraisal of different stochastic linearization techniques', *Journal of Sound and Vibration*, 153(2), 370-375.
128. G. Cederbaum, I. Elishakoff, J. Aboudi and L. Libreascu, 1992, *Random Vibration and Reliability of Composite Structures*, Technomic Publishing, Lancaster, Pennsylvania 17604, ISBN: 0-87762-865-3.
129. M. Shinozuka (ED, 1987, 'Stochastic Mechanics, Vol I and II, Department of Civil Engineering and Engineering Mechanics', Columbia University, New York.
130. G.I. Stry and D.J. Mook, February 11-13, 1991, 'Correlation techniques in robust nonlinear system realization/identification,' AAS/AIAA Spaceflight Mechanics Meeting, Houston Texas, February 11-13, 1991, AAS Paper 91-126.
131. L.D. Zavodney, October 1991, 'The Identification of Nonlinearity in Structural Systems: Theory, Simulation, and Experiment', *Applied Mechanics Review* Vol 44, 10, Part 2.
132. R.N. Miles, 1989, 'Effect of damping on the predicted fatigue life of a nonlinear plate', *Proceedings of Damping '89*, West Palm Beach, Florida, AFWAL TR 89-3116, Wright-Patterson AFB OH, FDA1-FDA21.

133. R. J. Allemang, April 1993, 'Keynote address: modal analysis - where do we go from here?', MAC 11, *Modal Analysis: The International Journal of Analytical and Experimental Modal Analysis*, Vol 8, No 2 (79-91).
134. R. Rost and D. Brown, 1988, 'Future trends in modal analysis', Proceedings of the third international conference on recent advances in Structural Dynamics, Southampton, England, AFWAL-TR-88-3034, Wright Patterson AFB, Ohio, ISBN 0-85432-2298, & 253-264.
135. B. J. Dobson, 1987, 'A straight-line technique for extracting modal properties from frequency response data', *Mechanical Systems and Signal Processing* 1(11,29-40).
136. G. R. Tomlinson, 1986, 'Detection, identification and quantification of nonlinearity in modal analysis - a review', *Proceedings of the Fourth International Modal Analysis Conference*, 837-843.
137. L. Meirovitch, 1986, '*Elements of vibration analysis*', McGraw-Hill, Inc, New York, 159.
138. D. J. Ewins, 1984, 'Modal testing, theory and practice', Research Studies Press Ltd, England and John Wiley and Sons, Inc, New York.
139. R. G. Lambert, September 1977, 'Fatigue analysis of multi-degree-of-freedom systems under random vibration, *Shock and Vibration Bulletin* 47, Part 2, Naval Research Laboratory, Washington, DC.
140. J.T. Brock, 1968, 'Peak distribution effects in random load fatigue', Bruell and Kjaer Technical Review 1.
141. R. G. Lambert, May 1982, 'Fatigue life prediction for various random stress peak distributions', *Shock and Vibrations Bulletin*, 52 Part 4, Naval Research Laboratory, Washington, DC.
142. M. Bernstein, March 1977, 'Single mode stress required for equivalent damage to multimodal stress in sonic fatigue', Dynamic Specialists Conference, San Diego, California, AIAA Paper 77-443.
143. A.J. Curtis and S.M. Morte, May 1982, 'The effect of endurance limit and crest factor on time to failure under random loading', *Shock and Vibration Bulletin* 52 Part 4, Naval Research Laboratory, Washington DC.
144. R. D. Blevins, 1989, 'An approximate method for sonic fatigue analysis of plates and shells', *Journal of Sound and Vibrations* 129(1), 51-71.

145. B.L. Clarkson, 1968, 'Stresses in skin panels subjected to random acoustic loads', J. Royal Aeronautical Society 72 1000-1010
146. C.F. Ng, November 1989, 'Experimental techniques for large amplitude vibration of curved plates', Shock and Vibration Bulletin 60, Part III, 19-34, Naval Research Laboratory, Washington DC.
147. G.C. Wright, 1971, 'The dynamic properties of fibre reinforced plastic beams', ISVR Technical Report No 51, University of Southampton, UK.
148. VPI Sensor Operator's Manual, 1991, Ometron Limited, Worsley Bridge Road, London SE26 5BX, England.
149. J. Tyrer, March 1987, 'Electronic speckle interferometry - theory and application', Tutorial T23, SPIE, Fourth International Symposium on Optical and Optoelectric Applied Science and Engineering.
150. R.K. Otnes and L. Enochson, 1972, '*Digital time series analysis*', John Wiley and Sons, New York, ISBN 0-471-65719-0
151. J.S. Bendat and A.G. Piersol, 1980, '*Engineering applications of correlation and spectral analysis*', John Wiley and Sons, New York, ISBN 0-471-05887-4.
152. R.B. Randall, September 1987, '*Frequency analysis*', Bruel and Kjaer, K. Larsen and Sons, Denmark, ISBN 87-87355-07-8.
153. R.G. DeJong, (editor), 1985, 'Compendium of methods for applying measured data to vibration and acoustic problems', AFWAL-TR-85-3080, Wright-Patterson AFB, Ohio.
154. D.L. Brown and C.A. Shroyer, 1988, '*Program for analysis of dynamics data*', AFWAL-TM-88-179-FIBG, Wright-Patterson AFB Ohio.
155. M. M. K. Bennouna, 1981, 'Nonlinear dynamic behaviour of a clamped-clamped beam with consideration of fatigue life', PhD thesis, University of Southampton, England.
156. J. R. Ballentine, F.F. Rudder, Jr., J. T. Mathis and H. E. Plumblee, Jr., January 1968, 'Refinement of the sonic fatigue structural design criteria, AFFDL-TR-67-156, Wright Patterson AFB, Ohio, AD 831-118
157. R. J. Roark, 1965, '*Formulas for stress and strain*', McGraw-Hill, New York.
158. L.E. Kinsler, A.R. Frey, A.B. Copens and J.V. Sanders, 1982, '*Fundamentals of acoustics*', John Wiley and Sons, New York.
159. L.L. Beranek, 1960, '*Noise reduction*', McGraw-Hill Company, New York.

160. C.H. Allen, October 1992, 'Sound source considerations for surface structure fatigue testing of the X-30 flight vehicle', Report No 1273.9210, The Clayton H. Allen Corporation, Chebeague Island, Maine.
161. Chen Wei-Zang and Yeh Kai-Yaun, 1957, 'On the large deflection of the rectangular plate', Proceedings of the 9th International Congress of Applied Mechanics, Vol 6, 403-413.
162. M.M. Bennouna and R.G. White, 1984, '*The effects of large vibration amplitudes on the fundamental mode shape of a clamped-clamped uniform beam*', Journal of Sound and Vibrations 96(3), 309-331.
163. R. D. Blevins, 1984, *Formulas for natural frequency and mode shape*, Krieger Publishing Company, Florida.
164. R. Chen, H. F. Wolfe, and C. Mei, 1995, 'Comparison of finite element nonlinear beam random response with experimental results, Journal of Sound and Vibration to be published.
165. L. Meirovitch, 1967, *Analytical methods in vibrations*, The Macmillan Company, London.
166. J. Lee, June 1992, 'Large-amplitude plate vibration in an elevated thermal environment', WL-TR-92-3049, Wright Patterson AFB, Ohio.

APPENDIX A COIL CALIBRATION

For forced vibration studies, various arrangements of voice coil and annular permanent magnets were available that are relatively inexpensive and have no suspension system between the coil and magnet assembly. This type shaker was utilized rather than a commercially available shakers with a rod attached to the shake table or a 'sting' attached to the beam. The coil and magnet from a loudspeaker were used with modifications of the coil assembly to attach to the beam.

To keep the drive force in the linear range of operation, the coil position in the magnet was analyzed statically to determine the linear range of displacements. The coil used for the clamped beam tests was capped off with a stiff aluminium alloy disc. The mass was 26.3 gm with a coil length of 19 mm. The natural frequency was 1925 Hz, from the ring modes of the disc. The current was recorded simultaneously with the responses for three types of experiments. The three types were static tests (DC), sinusoidal tests and band limited random tests. The test arrangement is shown in Fig A-1. The 9.85 Kg mass was suspended by thin wire ropes to permit free movement for the dynamic calibration. The force transducer and coil were attached to the mass using machine screws. The hanging mass was blocked against the steel frame to prevent movement during the static tests to build up the force required. A DC current was applied from 0-1200 ma as shown in Fig A-2. Both forces were applied inward and outward from the magnet. The outward curve was linear up to 1000 ma. The inward curve was similar, of opposite sign, with small deviations in the 400 to 900 ma range. The relationship between current and force can be determined from these curves.

The sinusoidal tests were conducted for five frequencies between 150 and 1200 Hz as shown in Fig A-3. The 150 and 300 Hz test data are identical and linear up to 1000 ma. The 600, 900 and 1200 Hz data are also linear up to 1000 ma. The 600, 900 and 1200 Hz curves increase in force as the current increases, more than that of the lower frequencies. This is due to the disc resonant frequency contribution, which becomes larger as the frequency increases toward the disc resonance. This was the second disc selected, thicker than the first, that

decreased the ring frequencies and increased the mass of the coil. Since the highest frequency of interest was approximately 1000 Hz, this disc was considered acceptable.

The random test data were conducted for two frequency ranges from 10-500 and 10-1200 Hz as shown in Fig A-4. The 10-500 Hz test data are linear up to 1200 ma, except for a slight variation at 600 and 800 ma. The 10-1200 Hz curve is also linear up to 1200 ma. The 10-1200 Hz curve shows an increase in force as the current increases, more than that of the 10-500 Hz curve. This is due to the disc resonance frequency contribution, which becomes larger as the frequency increases. Since the highest frequency of interest was approximately 1000 Hz, this disc was considered acceptable.

The second coil was designed and fabricated for the larger displacements needed for the pinned beam. It was 64.8 g and 38 mm in length with the lowest disc resonance frequency at 1445 Hz. A DC current was applied from 0-2500 ma as shown in Fig A-5. Both forces inward and outward from the magnet were recorded. The outward curve is linear up to 1000 ma. The inward curve is the same but with an opposite sign.

The sinusoidal tests were conducted with the longer coil for five frequencies between 150 and 1200 Hz as shown in Fig A-6. The 150 and 300 Hz test results are identical to the previous sine tests and linear up to 2400 ma. The 600, 900 and 1200 Hz curves are also linear up to 2400 ma. These curves increase linearly in force as the current increases, more than that of the lower frequencies. This is due to the disc off resonant frequency contribution, which becomes larger as the frequency increases toward the disc resonance. Since the highest frequency of interest was approximately 1000 Hz, this disc was considered acceptable.

The random tests were conducted for two frequency ranges from 10-1000 and 10-2000 Hz as shown in Fig A-7. Both curves are linear only up to 200 ma and nearly linear up to 800 ma. The curves are not linear from 800-5000 ma. The tests were conducted at a much higher current than that planned for the pinned beam test to check the full range available. This demonstrates the limitations in the linear performance of coil magnet arrangements. Since the highest current of interest was approximately 1000 ma, this was considered acceptable.

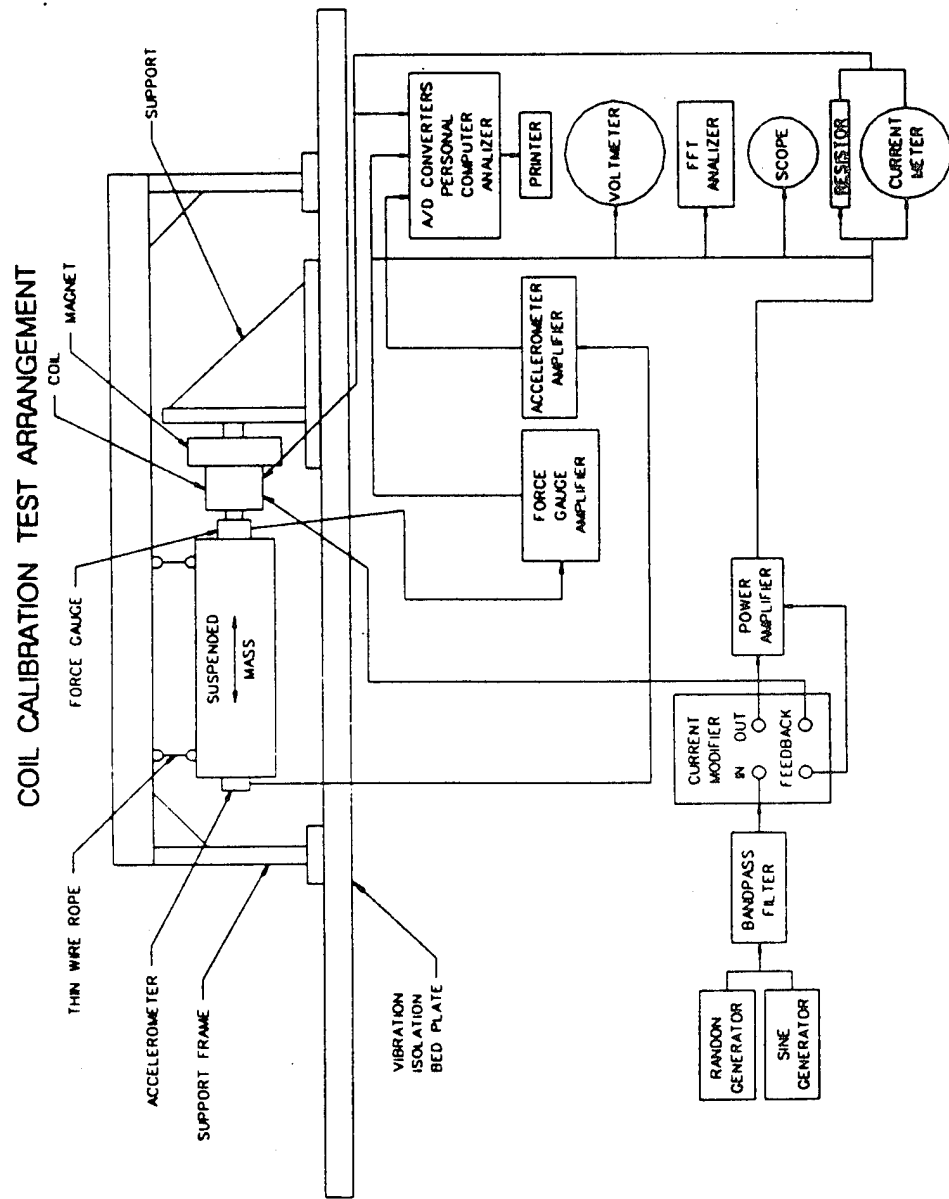


Fig A-1 Coil calibration testing arrangement.

19 mm EXCITER COIL CALIBRATION - DC

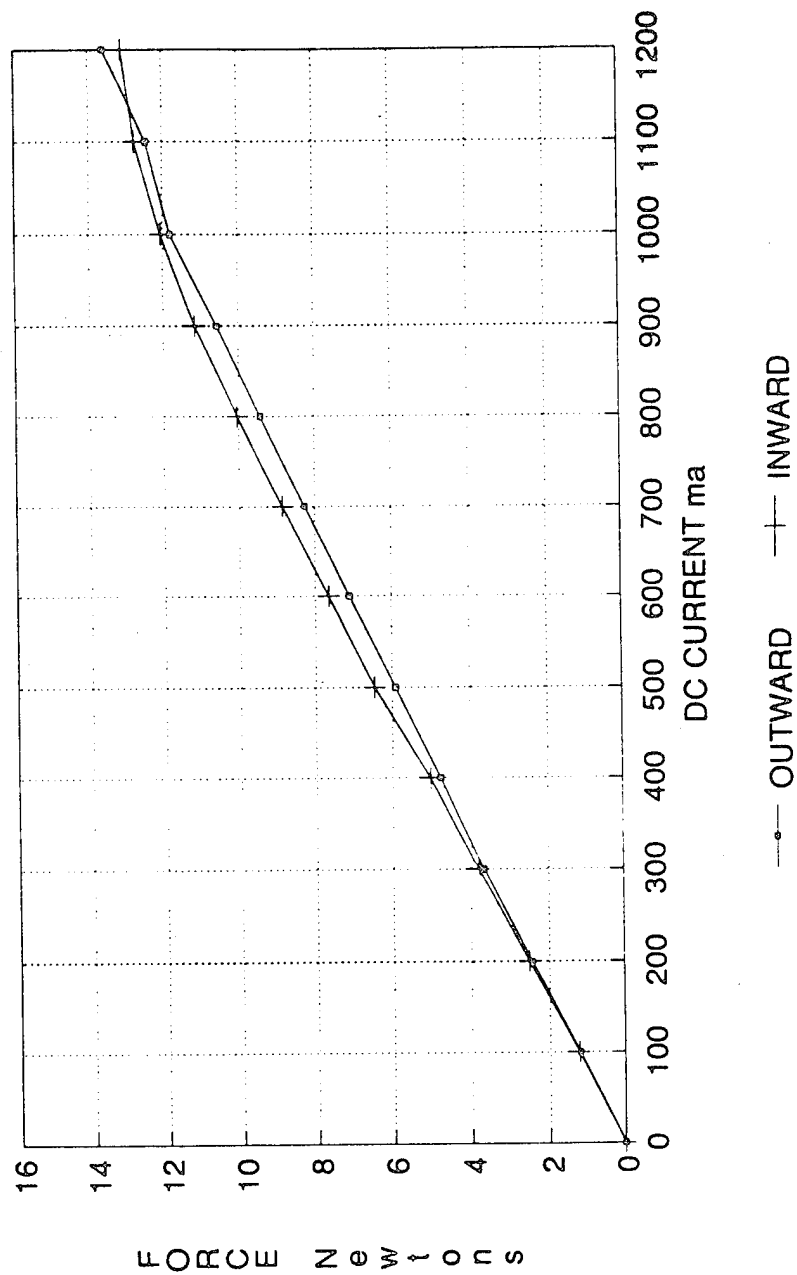


Fig A-2 Exciter coil calibration curves, DC, 19mm.

19 mm EXCITER COIL CALIBRATION - SINE

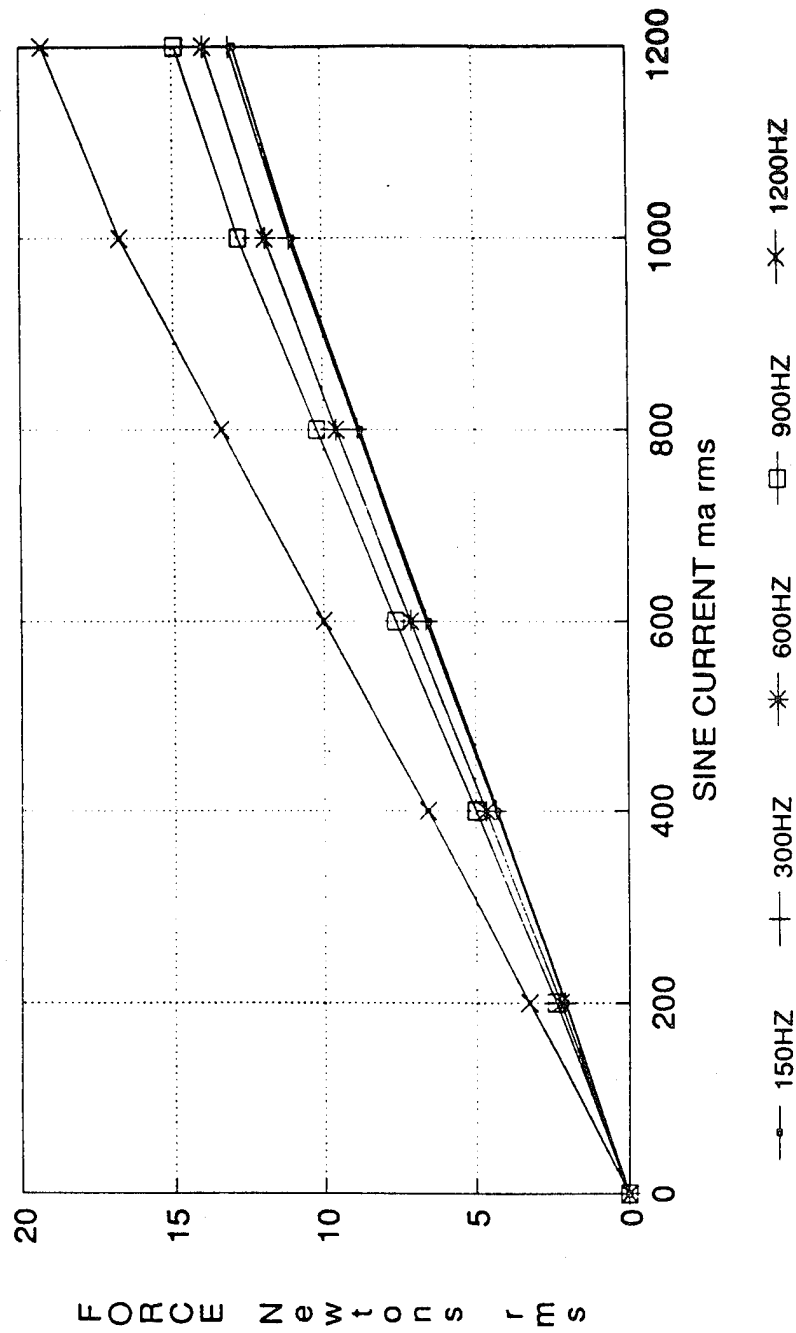


Fig A-3 Exciter coil calibration curves, sine, 19mm.

19 mm EXCITER COIL CALIBRATION - RANDOM

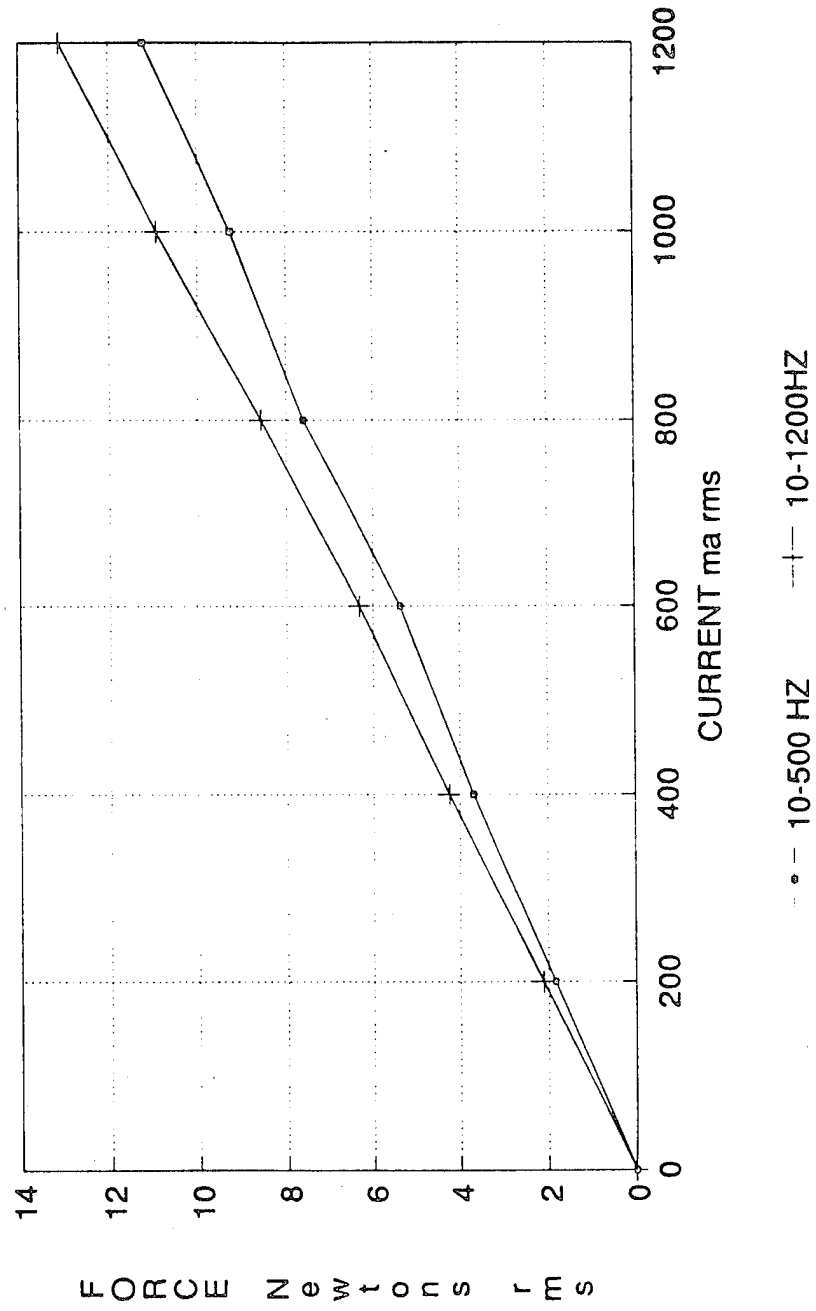


Fig A-4 Exciter coil calibration curves, random, 19mm.

38 mm EXCITER COIL CALIBRATION - DC

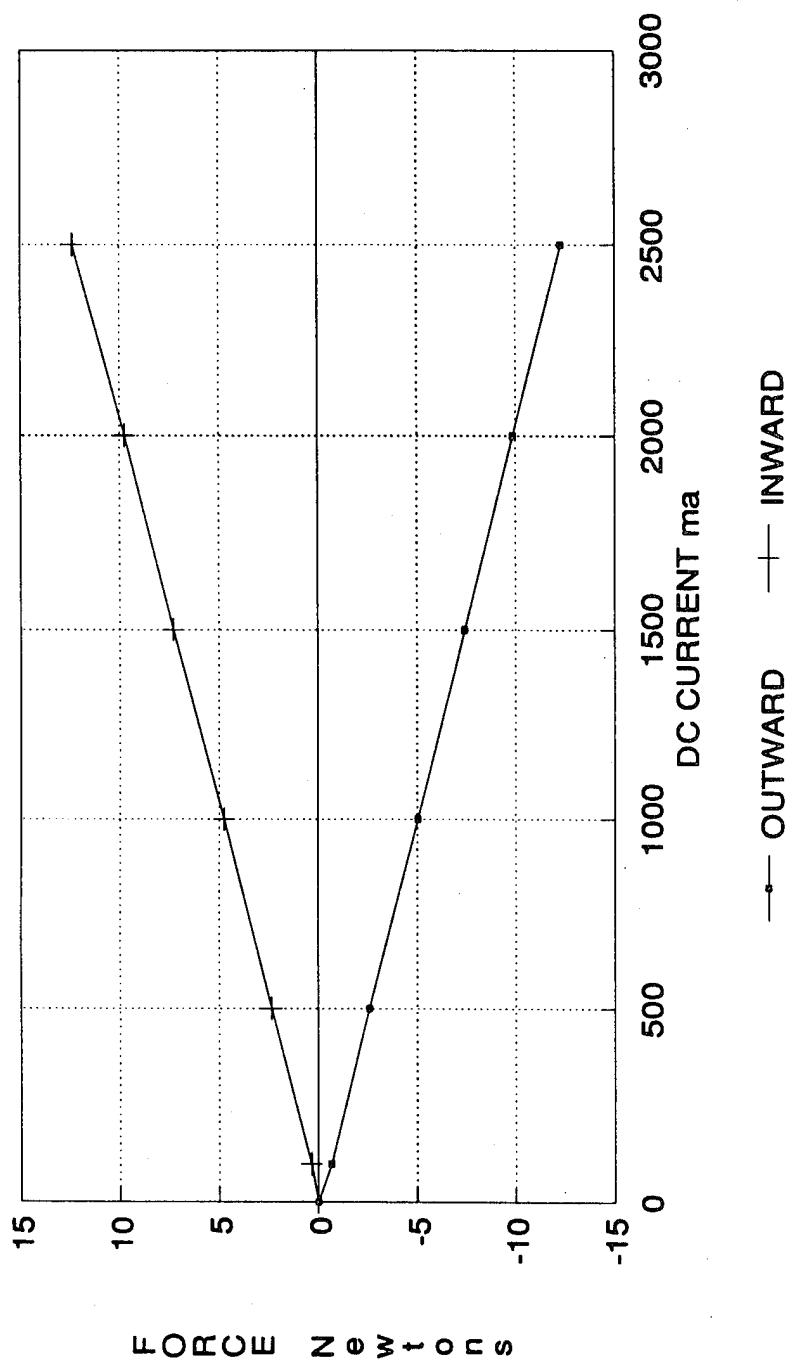


Fig A-5 Exciter coil calibration curves, DC, 38mm.

38mm EXCITER COIL CALIBRATION - SINE

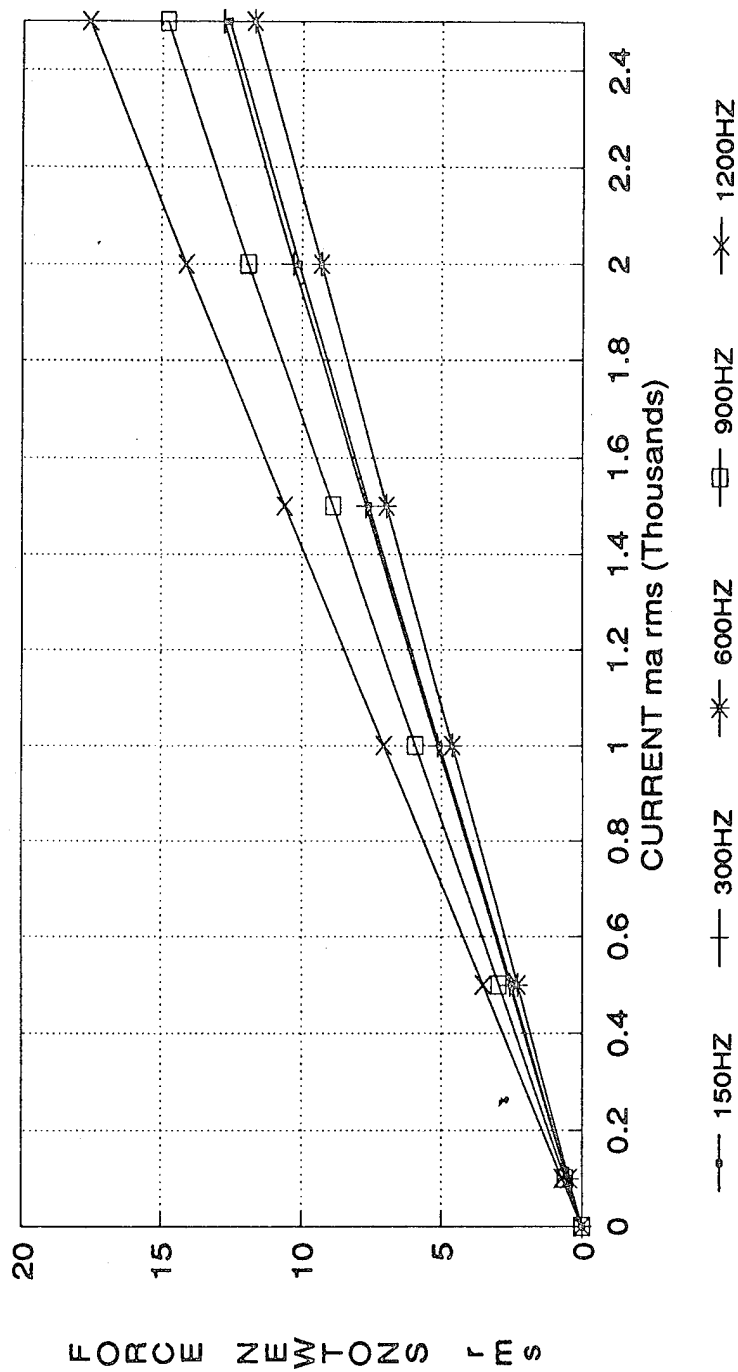


Fig A-6 Exciter coil calibration curves, sine, 38mm.

38 mm EXCITER COIL CALIBRATION - RANDOM

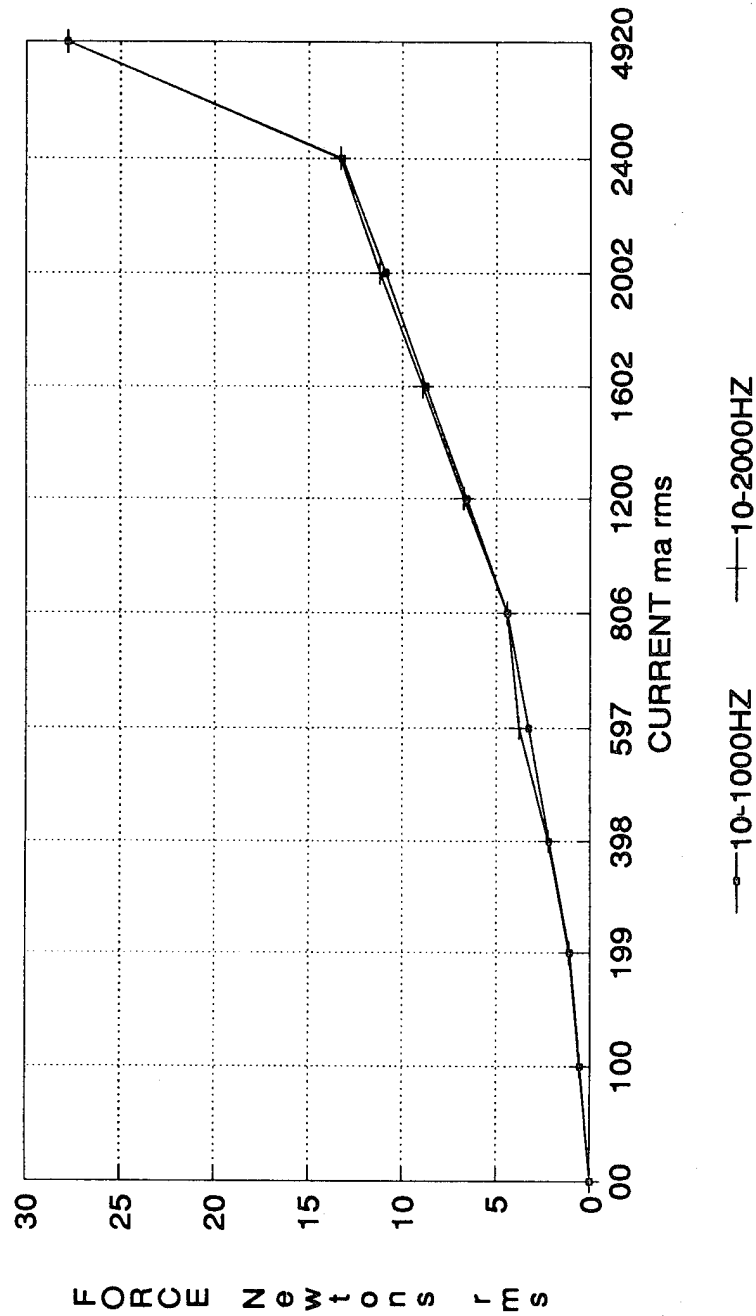


Fig A-7 Exciter coil calibration curves, random, 38mm.

APPENDIX B

TABLE OF COEFFICIENTS

TABLE B-2.1

Coefficients for Shapes in Chapter II Fig 2.22
C-C Al Beam - 3rd Displacement Shapes - Runs 16,18,19,20,23,24

$$y = C + ax + bx^2 + cx^3 + dx^4 + ex^5 + fx^6 + gx^7$$

0.053 N

C=1.5321310
a=1.79211484e-04
b=-8.22715212e-05
c=-3.83335898e-09
d=1.40499942e-09
e=-4.79644722e-15
f=-7.66567803e-15
g=-4.76221611e-19

0.110 N

0.38072481
-5.47066918e-05
-2.09604412e-05
3.10719848e-09
3.68412334e-10
-7.46252838e-14
-2.06672461e-15
7.79149548e-19

0.170 N

C=1.6413223
a=-3.88749739e-06
b=-8.82004536e-05
c=4.26603708e-09
d=1.53716695e-09
e=-1.97141394e-13
f=-9.11378594e-15
g=2.58123829e-18

0.23 N

0.51935807
1.26415632e-04
-2.86910834e-05
-6.33964521e-09
5.15720970e-10
1.77177478e-13
-3.13893450e-15
-2.58627820e-18

0.27 N

C=1.1523716
a=1.54486312e-04
b=-6.07732224e-05
c=-5.36977712e-09
d=9.76895890e-10
e=9.93394318e-14
f=-4.47772974e-15
g=-1.63526039e-18

0.30 N

0.78233449
-2.51150101e-05
-4.29423017e-05
5.12912235e-09
7.60357533e-10
-2.31337672e-13
-4.46852252e-15
3.11673419e-18

APPENDIX C

TABLES OF CURVE FITTING FUNCTIONS AND COEFFICIENTS FOR CHAPTER IV

TABLE C-4.1
CURVE FITTING FUNCTIONS
STATIC BENDING TESTS C-C AL BEAM 2.5 NEWTON FORCE
Partial Listing

Rank	Goodness of Fit	Function
1	0.9958900428	$y=a+b*4n/(1+n)^2$ $n=\exp(-(x-c)/d)$ [Logistic]
2	0.9958026288	$y=a+b\exp(-0.5((x-c)/d)^2)$ [Gaussian]
3	0.9957983374	$y=a+b/(1+((x-c)/d)^2)$ [Lorentzian]
4	0.9955376937	$y=a+b\exp(-0.5((x-c)/d)^2)$ [Gaussian]
5	0.9954418401	$y0.5=(a+cx+ex^2)/(1+bx+dx^2+fx^3)$
6	0.9951328460	$y0.5=(a+cx+ex^2)/(1+bx+dx^2)$
7	0.9949202615	$y=a+b\sin(2\pi x/d+c)$ [Sine]
8	0.9949202615	$y=a+b\sin^2(2\pi x/d+c)$ [Sine2]
9	0.9949057149	$y=(a+cx+ex^2)/(1+bx+dx^2)$
10	0.9943360535	$y=a+b*4n/(1+n)^2$ $n=\exp(-(x-c)/d)$ [Logistic]
11	0.9929319410	$y=a+b\sin(2\pi x/d+c)$ [Sine]
12	0.9927231060	$y0.5=a+bx+cx^2$
13	0.9925902485	$y=a+\operatorname{berfc}(((x-c)/d)^2)$ [Erfc Peak]
14	0.9924907551	$y=a+\operatorname{berfc}(((x-c)/d)^2)$ [Erfc Peak]
15	0.9924710258	$y=a\{\cosh(bx)-\cos(bx)-c[\sinh(bx)-\sin(bx)]\}$
16	0.9923140624	$\ln y=a+bx^3+cx0.5$
17	0.9921790932	$y=(a+cx+ex^2)/(1+bx+dx^2+fx^3)$
18	0.9921428385	$\ln y=a+bx^2.5+cx0.5$
19	0.9918436447	$y0.5=a+bx+cx^2+dx^3$
20	0.9904023524	$y=a+bx+cx^2+dx^3+ex^4$
21	0.9894567326	$\ln y=a+bx+cx^2$
22	0.9891521075	$y=(a+cx+ex^2+gx^3)/(1+bx+dx^2+fx^3)$
23	0.9880926934	$\ln y=a+bx^2+cx0.5$
24	0.9877476316	$\ln y=a+bx+cx1.5$
25	0.9876287867	$y=a+bx+cx^2+dx^2.5+ex^3$
27	0.9852880171	$\ln y=a+bx+cx^2.5$
28	0.9833246584	$\ln y=(a+cx+ex^2)/(1+bx+dx^2)$
29	0.9821824944	$y=a+bx+cx1.5+dx^2.5+ex^3$
30	0.9786834154	$\ln y=a+bx1.5+cx0.5$
31	0.9785193472	$\ln y=a+bx1.5+cx^2$
32	0.9778716727	$y=a+b/\ln x+c/(\ln x)^2+d/(\ln x)^3+e/(\ln x)^4+f/(\ln x)^5$
33	0.9771216925	$y=a+bx^2+cx^2.5+dx^3$
34	0.9764009717	$y=a+bx+cx1.5+dx^2+ex^3$
35	0.9760343547	$\ln y=a+bx+cx^3$

Table C-4.1 continued

36	0.9717929422	$y=a+bx+cx1.5+dx2+ex2.5$
37	0.9666323537	$y0.5=(a+cx)/(1+bx+dx2)$
38	0.9650501293	$y=a+bx+cx2.5+dx3+ex0.5$
39	0.9615817613	$\ln y=a+bx1.5+cx2.5$
40	0.9610885696	$\ln y=a+bx+cx0.5$
41	0.9610801108	$y=a+bx1.5+cx2.5+dx3$
42	0.9584042596	$y=a+bx+cx2+dx3+ex0.5$
43	0.9554425374	$y=a+bx+cx2.5+dx3+ee-x$
44	0.9550153908	$y=a+bx+cx2+dx2.5+ex0.5$
45	0.9519104676	$y=a+b\exp(-\exp(-(x-c)/d))-((x-c)/d)+1$ [ExtrVal]
46	0.9510161234	$y=a+bx+cx1.5+dx3+ex0.5$
47	0.9500919997	$y=a+bx1.5+cx2+dx3$
48	0.9495418795	$y=a+bx+cx1.5+dx2.5+ex0.5$
49	0.9491635713	$y=(a+cx+cx2+gx3)/(1+bx+dx2+fx3+hx4)$
50	0.9490009985	$y=a+bx+cx2+dx3+ee-x$
51	0.9483539538	$y=a+bx+cx1.5+dx2+ex0.5$
52	0.9477255119	$y=a+bx+cx1.5+dx0.5+ee-x$
53	0.9471990227	$y=a+bx+cx1.5+dx0.5$
54	0.9467676976	$y=a+bx+cx2+dx2.5+ee-x$
55	0.9450572147	$y=a+bx1.5+cx2+dx2.5$
56	0.9431203084	$y=a+bx+cx1.5+dx2+ee-x$
57	0.9423932553	$y=a+bx+cx1.5+dx2.5+ee-x$
58	0.9421163122	$y=a+bx+cx1.5+dx3+ee-x$
59	0.9421092964	$y=a+bx+cx1.5+de-x$
60	0.9413849137	$y=a+bx+cx2+dx0.5+ee-x$
61	0.9412765983	$y=a+bx+cx2+de-x$
62	0.9397265949	$y=a+b\exp(-0.5(\ln(x/c)/d)^2)$ [Log-Normal]
63	0.9394000448	$y0.5=a+bx+cx2+dx3+ex4$
64	0.9391435384	$y=a+bx+cx2+dx0.5$
65	0.9384195943	$\ln y=a+bx1.5+cx3$
66	0.9347896360	$y=a+bx+cx2.5+dx0.5+ee-x$
67	0.9345945334	$y=a+bx2.5+cx0.5+de-x$
68	0.9334877928	$y=a+bx2+cx0.5+de-x$
69	0.9310494573	$y=a+bx+cx2.5+dx3$
70	0.9287606290	$y=a+bx+cx1.5+dx2$
71	0.9284056073	$y=a+bx+cx3+dx0.5+ee-x$
72	0.9274072390	$y=a+bx+cx2.5+de-x$
73	0.9257926048	$y=a+bx1.5+cx2+de-x$
74	0.9256361700	$y=a+bx3+cx0.5+de-x$
75	0.9254857358	$y=a+bx1.5+cx2+dx0.5$
76	0.9251821567	$y=a+bx1.5+cx2$
77	0.9242444796	$\ln y=a+bx2+cx2.5$
78	0.9236789658	$y=a+bx+cx2+dx2.5$

TABLE C-4.2
CURVE FITTING FUNCTIONS
STATIC BENDING TESTS C-C AL BEAM 13.8 NEWTON FORCE
Partial Listing

Rank Goodness of Fit Function

1	0.9971217001	$y=a+b\exp(-0.5((x-c)/d)^2)$ [Gaussian]
2	0.9971189724	$y=a+b\sin(2\pi x/d+c)$ [Sine]
3	0.9971189724	$y=a+b\sin^2(2\pi x/d+c)$ [Sine2]
4	0.9970019433	$y0.5=(a+cx+ex^2)/(1+bx+dx^2)$
5	0.9967913645	$y=a+b*4n/(1+n)^2$ $n=\exp(-(x-c)/d)$ [Logistic]
6	0.9963925837	$y=a\{\cosh(bx)-\cos(bx)-c[\sinh(bx)-\sin(bx)]\}$
7	0.9963288625	$y=a+b/(1+((x-c)/d)^2)$ [Lorentzian]
8	0.9958512082	$y=a+\operatorname{berfc}(((x-c)/d)^2)$ [Erfc Peak]
9	0.9958485416	$y0.5=(a+cx+ex^2)/(1+bx+dx^2+fx^3)$
10	0.9957721533	$y0.5=a+bx+cx^2$
11	0.9956462644	$y0.5=a+bx+cx^2+dx^3$
12	0.9954495528	$y=a+b\exp(-0.5((x-c)/d)^2)$ [Gaussian]
13	0.9953724969	$y=a+bx+cx^2+dx^3+ex^4$
14	0.9952928421	$y=(a+cx+ex^2)/(1+bx+dx^2)$
15	0.9950006937	$y=a+\operatorname{berfc}(((x-c)/d)^2)$ [Erfc Peak]
16	0.9932787818	$y=(a+cx+ex^2)/(1+bx+dx^2+fx^3)$
17	0.9932376619	$\ln y=a+bx^3+cx0.5$
18	0.9928679897	$\ln y=a+bx^2.5+cx0.5$
19	0.9927104340	$y=(a+cx+ex^2+gx^3)/(1+bx+dx^2+fx^3)$
20	0.9924635782	$y=a+b\sin(2\pi x/d+c)$ [Sine]
21	0.9923433697	$y=a+b*4n/(1+n)^2$ $n=\exp(-(x-c)/d)$ [Logistic]
22	0.9916757313	$y=a+bx+cx^2+dx^2.5+ex^3$
23	0.9911029326	$\ln y=(a+cx+ex^2)/(1+bx+dx^2)$
24	0.9895978149	$\ln y=a+bx+cx^2$
25	0.9883733160	$\ln y=a+bx^2+cx0.5$
26	0.9879105224	$\ln y=a+bx+cx1.5$
27	0.9870902438	$y=a+bx+cx1.5+dx^2.5+ex^3$
28	0.9861977838	$y=(a+cx+ex^2+gx^3)/(1+bx+dx^2+fx^3+hx^4)$
29	0.9849547554	$\ln y=a+bx+cx2.5$
30	0.9845617991	$y=a+bx^2+cx2.5+dx^3$
31	0.9839134047	$y=a+b/\ln x+c/(\ln x)^2+d/(\ln x)^3+e/(\ln x)^4+f/(\ln x)^5$
32	0.9821434906	$y=a+bx+cx1.5+dx^2+ex^3$
33	0.9795887459	$y=a+b/(1+((x-c)/d)^2)$ [Lorentzian]
34	0.9782149567	$y=a+bx+cx1.5+dx^2+ex2.5$
35	0.9779571025	$\ln y=a+bx1.5+cx0.5$
36	0.9771393517	$\ln y=a+bx1.5+cx^2$
37	0.9749288488	$\ln y=a+bx+cx^3$
38	0.9723485757	$y=a+bx+cx2.5+dx^3+ex0.5$
39	0.9707677902	$y=a+bx1.5+cx2.5+dx^3$

Table C-4.2 continued

40	0.9664720215	$y=a+bx+cx^2+dx^3+ex^{0.5}$
41	0.9639754551	$y=a+bx+cx^{2.5}+dx^3+ee-x$
42	0.9635586548	$y=a+bx+cx^2+dx^{2.5}+ex^{0.5}$
43	0.9613693593	$y_{0.5}=(a+cx)/(1+bx+dx^2)$
44	0.9610053668	$a+bx^{1.5}+cx^2+dx^3$
45	0.9598609459	$y=a+bx+cx^{1.5}+dx^3+ex^{0.5}$
46	0.9586950121	$y=a+bx+cx^{1.5}+dx^{2.5}+ex^{0.5}$
47	0.9586207834	$\ln y=a+bx^{1.5}+cx^{2.5}$
48	0.9581757249	$y=a+bx+cx^2+dx^3+ee-x$
49	0.9579663223	$\ln y=a+bx+cx^{0.5}$
50	0.9578551673	$y=a+bx+cx^{1.5}+dx^{0.5}+ee-x$
51	0.9577850893	$y=a+bx+cx^{1.5}+dx^2+ex^{0.5}$
52	0.9570664859	$y=a+bx+cx^{1.5}+dx^{0.5}$
53	0.9564914978	$y=a+bx^{1.5}+cx^2+dx^{2.5}$
54	0.9562608509	$y=a+bx+cx^2+dx^{2.5}+ee-x$
55	0.9531289544	$y=a+bx+cx^{1.5}+dx^2+ee-x$
56	0.9523069558	$y=a+bx+cx^{1.5}+dx^{2.5}+ee-x$
57	0.9518955948	$y=a+bx+cx^{1.5}+dx^3+ee-x$
58	0.9518189010	$y=a+bx+cx^{1.5}+de-x$
59	0.9516926871	$y=a+bx+cx^2+dx^{0.5}+ee-x$
60	0.9516409679	$y=a+bx+cx^2+de-x$
61	0.9513810775	$y=a+b\exp(-\exp(-((x-c)/d)))-((x-c)/d)+1$ [ExtrVal]
62	0.9499898445	$y=a+bx+cx^2+dx^{0.5}$
63	0.9453017031	$y=a+bx+cx^{2.5}+dx^{0.5}+ee-x$
64	0.9449919625	$y=a+bx^{2.5}+cx^{0.5}+de-x$
65	0.9435975601	$y=a+bx+cx^{2.5}+dx^3$
66	0.9432363603	$y=a+bx^2+cx^{0.5}+de-x$
67	0.9411307680	$y=a+bx+cx^{1.5}+dx^2$
68	0.9391125614	$y=a+bx+cx^3+dx^{0.5}+ee-x$
69	0.9385535610	$y=a+bx+cx^{2.5}+de-x$
70	0.9374691370	$y=a+bx^{1.5}+cx^2+dx^{0.5}$
71	0.9369476711	$y=a+bx^{1.5}+cx^2+de-x$
72	0.9368740167	$y=a+b\exp(-0.5(\ln(x/c)/d)^2)$ [Log-Normal]
73	0.9367694679	$y=a+bx^3+cx^{0.5}+de-x$
74	0.9367652581	$y=a+bx^{1.5}+cx^2$
75	0.9367534773	$y=a+bx+cx^2+dx^{2.5}$
76	0.9363484632	$y=a+bx+cx^2+dx^3$
77	0.9363484629	$y=a+bx+cx^2$
70	0.9352111030	$y=a+bx+cx^{2.5}+dx^{0.5}$
79	0.9344914837	$y_{0.5}=a+bx+cx^2+dx^3+ex^4$
80	0.9342189798	$y=a+bx+cx^{1.5}+dx^{2.5}$
81	0.9336952565	$\ln y=a+bx^{1.5}+cx^3$
82	0.9333673066	$y=a+bx+cx^{2.5}$

TABLE C-4.3

C-C Al Beam - 1st Displacement Shapes - Runs 11,12,14,15,17,18

Coefficients for Displacement Shapes in Fig 4.26

$$y = C + ax + bx^2 + cx^3 + dx^4 + ex^5 + fx^6 + gx^7$$

0.086 N	0.09 N	0.17 N
C= 0.38072481	0.51935807	0.78233449
a = -5.47066918e-05	1.26415632e-04	-2.51150101e-05
b = -2.09604412e-05	-2.86910834e-05	-4.29423017e-05
c = 3.10719848e-09	-6.33964521e-09	5.12912235e-09
d = 3.68412334e-10	5.15720970e-10	7.60357533e-10
e = -7.46252838e-14	1.77177478e-13	-2.31337672e-13
f = -2.06672461e-15	-3.13893450e-15	-4.46852252e-15
g = 7.79149548e-19	-2.58627820e-18	3.11673419e-18
0.40 N	0.48 N	0.60 N
C= 1.1523716	1.5321310	1.6413223
a=1.54486312e-04	1.79211484e-04	-3.88749739e-06
b=-6.07732224e-05	-8.22715212e-05	-8.82004536e-05
c=-5.36977712e-09	-3.83335898e-09	4.26603708e-09
d=9.76895890e-10	1.40499942e-09	1.53716695e-09
e=9.93394318e-14	-4.79644722e-15	-1.97141394e-13
g=-4.47772974e-15	-7.66567803e-15	-9.11378594e-15
h=-1.63526039e-18	-4.76221611e-19	2.58123829e-18

TABLE C-4.4

C-C Al Beam - 1st Displacement Shapes - Runs 11,12,14,15,17,18

Coefficients for Displacement Shapes in Fig 4.29

$$y = C + ax + bx^2 + cx^3 + dx^4$$

0.086 N

C=0.37754706
a= -4.10821742e-05
b=-1.93481073e-05
c=1.09645527e-09
d=2.51653541e-10

0.09 N

0.51502419
1.05252996e-04
-2.64125771e-05
-2.62917095e-09
3.44688648e-10

0.17 N

C= 0.77584827
a=7.15210886e-06
b=-3.95879551e-05
c=-1.25423622e-10
d=5.12745826e-10

0.40N

1.1455797
1.47092740e-04
-5.73119833e-05
-3.65614421e-09
7.25097248e-10

0.48 N

C=1.5199174
a=1.87498558e-04
b=7.61431105e-05
c=-4.69703918e-09
d=9.66388880e-10

0.60 N

1.6278453
2.91810443e-05
-8.12715515e-05
-5.79369818e-10
1.02882533e-09

TABLE C- 4.5
CURVE FITTING FUNCTIONS - SINE EXCITATION
 C-C AL BEAM, R1st11, 0.086 Newton
 Partial Listing

Rank	Goodness of Fit	Function
1	0.9998652833	$y=a+b\sin(2\pi x/d+c)$ [Sine]
2	0.9998652833	$y=a+b\sin^2(2\pi x/d+c)$ [Sine2]
3	0.9998576525	$y_{0.5}=(a+cx+ex^2)/(1+bx+dx^2)$
4	0.9998199530	$y_{0.5}=(a+cx+ex^2)/(1+bx+dx^2+fx^3)$
5	0.9994199892	$y=a+bx+cx^2+dx^3+ex^4$
6	0.9993594340	$y_{0.5}=a+bx+cx^2$
7	0.9993359211	$y=a+b\exp(-0.5((x-c)/d)^2)$ [Gaussian]
8	0.9992222646	$y=a\{\cosh(bx)-\cos(bx)-c[\sinh(bx)-\sin(bx)]\}$
9	0.9991062370	$y=a+\operatorname{berfc}(((x-c)/d)^2)$ [Erfc Peak]
10	0.9988953079	$y_{0.5}=a+bx+cx^2+dx^3$
11	0.9988351832	$y=a+b*4n/(1+n)^2$ $n=\exp(-(x-c)/d)$ [Logistic]
12	0.9983638483	$y=a+\operatorname{berfc}(((x-c)/d)^2)$ [Erfc Peak]
13	0.9982308835	$y=a+b/(1+((x-c)/d)^2)$ [Lorentzian]
14	0.9976219358	$y=(a+cx+ex^2)/(1+bx+dx^2)$
15	0.9974685105	$y=a+bx+cx^2+dx^3+ex^4$
16	0.9967541563	$y=a+b\exp(-0.5((x-c)/d)^2)$ [Gaussian]
17	0.9957659676	$y=(a+cx+ex^2+gx^3)/(1+bx+dx^2+fx^3)$
18	0.9957359917	$y=a+bx+cx^2+dx^{2.5}+ex^3$
19	0.9953811913	$y=(a+cx+ex^2+gx^3)/(1+bx+dx^2+fx^3+hx^4)$
20	0.9945599183	$y=(a+cx+ex^2)/(1+bx+dx^2+fx^3)$
21	0.9930960334	$\ln y=a+bx^{2.5}+cx^{0.5}$
22	0.9928108239	$\ln y=a+bx^3+cx^{0.5}$
23	0.9920130040	$y=a+b*4n/(1+n)^2$ $n=\exp(-(x-c)/d)$ [Logistic]
24	0.9915466713	$y=a+bx+cx^{1.5}+dx^{2.5}+ex^3$
25	0.9894022574	$\ln y=a+bx+cx^2$
26	0.9886755263	$\ln y=a+bx^2+cx^{0.5}$
27	0.9877867969	$\ln y=a+bx+cx^{1.5}$
28	0.9866614430	$y=a+bx+cx^{1.5}+dx^2+ex^3$
29	0.9854075233	$y=a+b\sin(2\pi x/d+c)$ [Sine]
30	0.9849569400	$y=a+bx^2+cx^{2.5}+dx^3$
31	0.9844544988	$\ln y=a+bx+cx^{2.5}$
32	0.9826164375	$y=a+bx+cx^{1.5}+dx^2+ex^{2.5}$
33	0.9782497081	$\ln y=a+bx^{1.5}+cx^{0.5}$
34	0.9776221034	$\ln y=a+bx^{1.5}+cx^2$
35	0.9744155610	$y=a+b/(1+((x-c)/d)^2)$ [Lorentzian]
36	0.9740483812	$\ln y=a+bx+cx^3$
37	0.9706824452	$y=a+bx+cx^{2.5}+dx^3+ex^{0.5}$
38	0.9690437024	$y=a+bx^{1.5}+cx^{2.5}+dx^3$
39	0.9631592871	$y=a+bx+cx^2+dx^3+ex^{0.5}$
40	0.9614601643	$y=a+bx+cx^{1.5}+dx^{0.5}+ee-x$
41	0.9602035416	$\ln y=a+bx^{1.5}+cx^{2.5}$

Table C-4.5 continued

42	0.9600841223	$y=a+bx+cx^2+dx^{2.5}+ex^{0.5}$
43	0.9598935293	$\ln y=a+bx+cx^{0.5}$
44	0.9585781350	$y=a+bx^{1.5}+cx^2+dx^3$
45	0.9584354425	$y^{0.5}=(a+cx)/(1+bx+dx^2)$
46	0.9544863706	$y=a+bx^{1.5}+cx^2+dx^{2.5}$
47	0.9543252810	$y=a+bx+cx^{1.5}+dx^2+ex^{0.5}$
48	0.9541740831	$y=a+bx+cx^{1.5}+dx^3+ex^{0.5}$
49	0.9539594731	$y=a+bx+cx^{1.5}+dx^{2.5}+ex^{0.5}$
50	0.9539576147	$y=a+bx+cx^{1.5}+dx^{0.5}$
51	0.9514122911	$y=a+bx+cx^2+dx^{0.5}+ee-x$
52	0.9512130835	$y=a+bx+cx^2+dx^{0.5}$
53	0.9510273323	$y=a+bx+cx^{2.5}+dx^3+ee-x$
54	0.9463711773	$y=a+bx+cx^{1.5}+dx^2+ee-x$
55	0.9458836868	$y=a+b\exp(-\exp(-(x-c)/d))-((x-c)/d)+1$ [ExtrVal]
56	0.9443225439	$y=a+bx+cx^2+dx^3+ee-x$
57	0.9442877887	$y=a+bx+cx^2+dx^{2.5}+ee-x$
58	0.9442317113	$y=a+bx+cx^2+de-x$
59	0.9426174041	$y=a+bx+cx^{1.5}+dx^2$
60	0.9416296133	$y=a+bx+cx^{2.5}+dx^3$
61	0.9414238238	$y=a+bx+cx^{1.5}+dx^{2.5}+ee-x$
62	0.9404031325	$y=a+bx^{1.5}+cx^2+de-x$
63	0.9402499806	$y=a+bx^{1.5}+cx^2+dx^{0.5}$
64	0.9399314463	$y=a+bx^{1.5}+cx^2$
65	0.9384586024	$y=a+bx+cx^{2.5}+dx^{0.5}+ee-x$
66	0.9384177350	$y=a+bx+cx^{2.5}+de-x$
67	0.9372697084	$y=a+bx+cx^{1.5}+dx^3+ee-x$
68	0.9369317072	$\ln y=a+bx^{1.5}+cx^3$
69	0.9366830501	$y=a+bx+cx^{2.5}+dx^{0.5}$
70	0.9363668065	$y=a+bx+cx^2+dx^{2.5}$
71	0.9349139044	$y=a+bx+cx^2+dx^3$
72	0.9348058913	$y=a+bx+cx^{1.5}+dx^{2.5}$
73	0.9345243388	$y=a+bx+cx^{2.5}$
74	0.9341510613	$y=a+bx+cx^2$
75	0.9280155499	$y=a+bx+cx^{1.5}+dx^3$
76	0.9248423408	$y=a+bx+cx^{1.5}+de-x$
77	0.9245235432	$y=(a+cx+ex^2+gx^3+ix^4)/(1+bx+dx^2+fx^3+hx^4+jx^5)$
78	0.9244491660	$y=a+bx+cx^3+dx^{0.5}+ee-x$
79	0.9240225888	$\ln y=a+bx^2+cx^{2.5}$
80	0.9231203969	$y-1=a+bx^3+c/x^{0.5}$
81	0.9224897198	$y=a+bx^{1.5}+cx^{2.5}+dx^{0.5}$
82	0.9200629574	$y=a+bx^3+cx^{0.5}+de-x$
83	0.9173361890	$y=a+bx+cx^3+de-x$
84	0.9169029325	$y=a+bx+cx^3+dx^{0.5}$
85	0.9166494114	$y=a+bx^{2.5}+cx^{0.5}+de-x$

TABLE C - 4.6
CURVE FITTING FUNCTIONS - SINE EXCITATION
C-C AL BEAM, R1st18, 0.60 Newton
Partial Listing

<u>Rank</u>	<u>Goodness of Fit</u>	<u>Function</u>
1	0.9997580369	$y=a+bx+cx^2+dx^3+ex^4$
2	0.9996610568	$y=a+b\sin(2\pi x/d+c)$ [Sine2]
3	0.9996610568	$y=a+b\sin(2\pi x/d+c)$ [Sine]
4	0.9996239917	$y=a\{\cosh(bx)-\cos(bx)-c[\sinh(bx)-\sin(bx)]\}$
5	0.9993921247	$y=a+\operatorname{berfc}(((x-c)/d)^2)$ [Erfc Peak]
6	0.9991208055	$y=a+b\exp(-0.5((x-c)/d)^2)$ [Gaussian]
7	0.9986767960	$y=a+b*4n/(1+n)^2$ $n=\exp(-(x-c)/d)$ [Logistic]
8	0.9981162938	$y=a+b/(1+((x-c)/d)^2)$ [Lorentzian]
9	0.9977115261	$y=a+bx+cx^2+dx^{2.5}+ex^3$
10	0.9954143778	$y=a+bx+cx^{1.5}+dx^{2.5}+ex^3$
11	0.9927382164	$y=a+bx+cx^{1.5}+dx^2+ex^3$
12	0.9923566400	$y=a+\operatorname{berfc}(((x-c)/d)^2)$ [Erfc Peak]
13	0.9904141669	$y=a+bx+cx^{1.5}+dx^2+ex^{2.5}$
14	0.9896573869	$y=a+bx^2+cx^{2.5}+dx^3$
15	0.9859434735	$y=a+bx+cx^{2.5}+dx^3+ex^{0.5}$
16	0.9834197775	$y=a+b\sin(2\pi x/d+c)$ [Sine]
17	0.9818464054	$y=a+bx+cx^2+dx^3+ex^{0.5}$
18	0.9794743435	$y=a+bx+cx^2+dx^{2.5}+ex^{0.5}$
19	0.9782158529	$y=a+bx^{1.5}+cx^{2.5}+dx^3$
20	0.9781473464	$y=a+bx+cx^{2.5}+dx^3+ee-x$
21	0.9767724889	$y=a+bx+cx^{1.5}+dx^3+ex^{0.5}$
22	0.9753635354	$y=a+bx+cx^{1.5}+dx^{2.5}+ex^{0.5}$
23	0.9739822273	$y=a+bx+cx^{1.5}+dx^2+ex^{0.5}$
24	0.9737544699	$y=a+bx+cx^2+dx^3+ee-x$
25	0.9720030338	$y=a+bx+cx^2+dx^{2.5}+ee-x$
26	0.9712689767	$y=a+bx+cx^{1.5}+dx^{0.5}+ee-x$
27	0.9712275542	$y=a+bx+cx^{1.5}+dx^{0.5}$
28	0.9712158444	$y=a+bx^{1.5}+cx^2+dx^3$
29	0.9686580102	$y=a+bx+cx^{1.5}+dx^3+ee-x$
30	0.9686201462	$y=a+bx+cx^{1.5}+dx^2+ee-x$
31	0.9684992123	$y=a+bx+cx^{1.5}+dx^{2.5}+ee-x$
32	0.9684970274	$y=a+bx+cx^{1.5}+de-x$
33	0.9683281149	$y=a+bx^{1.5}+cx^2+dx^{2.5}$
34	0.9664914591	$y=a+bx+cx^2+dx^{0.5}+ee-x$
35	0.9662626991	$y=a+bx+cx^2+de-x$
36	0.9647128240	$y=a+bx+cx^2+dx^{0.5}$
37	0.9617053405	$y=a+bx+cx^{2.5}+dx^{0.5}+ee-x$
38	0.9615226694	$y=a+bx^{2.5}+cx^{0.5}+de-x$
39	0.9611163871	$y=a+bx^2+cx^{0.5}+de-x$
40	0.9589257280	$y=a+bx+cx^{1.5}+dx^2$
41	0.9588690280	$y=a+bx+cx^{2.5}+dx^3$

Table C-4.6 continued

42	0.9572607574	$y=a+bx+cx^3+dx^{0.5}+ee^{-x}$
43	0.9567684078	$y=a+bx+cx^{2.5}+de^{-x}$
44	0.9564761192	$y=a+bx^{1.5}+cx^2+dx^{0.5}$
45	0.9559348074	$y=a+bx^3+cx^{0.5}+de^{-x}$
46	0.9556482334	$y=a+bx+cx^2+dx^{2.5}$
47	0.9551774439	$y=a+bx+cx^{2.5}+dx^{0.5}$
48	0.9551669889	$y=a+bx^{1.5}+cx^2+de^{-x}$
49	0.9549982718	$y=a+bx^{1.5}+cx^2$
50	0.9549596248	$y=a+bx+cx^2+dx^3$
51	0.9546640500	$y=a+bx+cx^2$
52	0.9545962303	$y=a+bx+cx^{1.5}+dx^{2.5}$
53	0.9543123415	$y=a+bx+cx^{2.5}$
54	0.9538259408	$y=a+b\exp(-0.5((x-c)/d)^2)$ [Gaussian]
55	0.9509713574	$y=a+bx+cx^{1.5}+dx^3$
56	0.9501813813	$y=a+bx^{1.5}+cx^{0.5}+de^{-x}$
57	0.9466769660	$y=a+bx^{1.5}+cx^{2.5}+dx^{0.5}$
58	0.9447349692	$y=a+bx+cx^3+dx^{0.5}$
59	0.9439204911	$y=a+bx+cx^3+de^{-x}$
60	0.9439155086	$y=a+bx+cx^3$
61	0.9427360909	$y=a+b*4n/(1+n)^2$ $n=\exp(-(x-c)/d)$ [Logistic]
62	0.9392726692	$y=a+bx^{1.5}+cx^{2.5}+de^{-x}$
63	0.9388322324	$y=a+bx^2+cx^{2.5}+dx^{0.5}$
64	0.9372909032	$y=a+bx^{1.5}+cx^3+dx^{0.5}$
65	0.9367825843	$y=a+b/(1+((x-c)/d)^2)$ [Lorentzian]
66	0.9358081387	$y=a+bx+cx^{1.5}$
67	0.9331013801	$y=a+bx^{1.5}+cx^{2.5}$
68	0.9314031506	$y=a+bx^2+cx^3+dx^{0.5}$
69	0.9271309894	$y=a+bx^{2.5}+cx^3+dx^{0.5}$
70	0.9222980152	$y=a+bx^{1.5}+cx^3+de^{-x}$
71	0.9218932548	$y=a+bx+cx^{0.5}+de^{-x}$
72	0.9194917182	$y=a+bx^3+cx^{0.5}$
73	0.9180005502	$y=a+bx^2+cx^{2.5}+de^{-x}$
74	0.9089357714	$y=a+bx^{2.5}+cx^{0.5}$
75	0.9050737265	$y=a+bx^{1.5}+cx^3$
76	0.8992666347	$y=a+bx^2+cx^3+de^{-x}$
77	0.8877640477	$y=a+bx^2+cx^{2.5}$
78	0.8852063006	$y=a+bx^2+cx^{0.5}$
79	0.8781081195	$y=a+bx^{2.5}+cx^3+de^{-x}$
80	0.8464543179	$y=a+bx^2+cx^3$
81	0.8398065049	$y=a+bx^{1.5}+cx^{0.5}$
82	0.8134185425	$y=a+b\exp(-0.5(\ln(x/c)/d)^2)$ [Log-Normal]
83	0.7850485519	$y=a+bx^{2.5}+cx^3$
84	0.7588038036	$y=a+bx+cx^{0.5}$
85	0.7498332514	$y=a+b\exp(-\exp(-(x-c)/d))-((x-c)/d)+1)$ [ExtrVal]

TABLE C-4.7
C-C CFRP BEAM - 1st Displacement Shapes - Runs 1-6, 2314
Coefficients for Shapes in Fig 4.52

$$y = C + ax + bx^2 + cx^3 + dx^4$$

0.05 N	0.17 N	0.33N
C= 0.53495494	1.2316742	1.8345192
a=8.34808515e-05	-2.47798695e-04	-4.37880395e-04
b=-2.73201982e-05	-6.33232085e-05	-9.40954545e-05
c=-2.01157430e-09	7.34163042e-09	1.27819476e-08
d=3.63883300e-10	8.37968056e-10	1.23788958e-09
0.78 N	1.04 N	1.26 N
C=2.8277680	3.2241330	3.4965679
a=-8.45034026e-04	-9.86520532e-04	-1.11658164e-03
b=-1.43514640e-04	-1.62548857e-04	-1.75308403e-04
c=2.36327168e-08	2.72667752e-08	3.08939804e-08
d=1.86417621e-09	2.09455194e-09	2.24402750e-09
1.51 N	a=-1.24547019e-03	c=3.43851360e-08
C=3.7472703	b=-1.87146083e-04	d=2.38531802e-09

TABLE C-4.8
P-P Al Beam - 1st - Runs 34-37,40,41,43
Coefficients for Shapes in Fig 4.55

$$y = C + ax + bx^2 + cx^3 + dx^4$$

0.053 N	0.610 N	0.985 N
C=1.5994920	0.73249622	2.9270248
a= 9.64964167e-05	2.45090689e-05	1.43600130e-04
b= -6.07313048e-05	-3.14823460e-05	-1.16959209e-04
c=-1.89133025e-09	-3.43768670e-10	-3.21904929e-09
d=5.53022318e-10	3.48971568e-10	1.16400640e-09
1.55 N	2.02 N	2.49 N
C=3.9017898	4.3971350	4.6335057
a=5.60906090e-04	1.71102366e-04	-1.34190007e-04
b=-1.57999750e-04	-1.81160066e-04	-1.97157550e-04
c=-1.21168517e-08	-4.43143658e-09	3.90743641e-10
d=1.59964185e-09	1.89421164e-09	2.16237967e-09
3.06 N	a=-3.19015894e-04	c=8.61716716e-09
C=5.0187264	b=-2.05725477e-04	d=2.13766022e-09

TABLE C-4.9

C-C-C-C Al Plate - 1st Displacement Shapes - Runs 14,24,27,28
Coefficients for Shapes in Fig 4.63

X direction

$$y = C + ax + bx^2 + cx^3 + dx^4$$

0.111 g	0.309 g
C=0.18605322	0.50658390
a=4.80929236e-05	1.68623624e-04
b=-3.23016893e-05	-8.76216497e-05
c=-4.33407629e-09	-1.58920847e-08
d=1.41951031e-09	3.77657316e-09
0.694 g	1.23 g
C=0.90518525	C=1.2721722
a=3.09399684e-04	a=4.01432500e-04
b=-1.54638194e-04	b=-2.12125217e-04
c=-2.94181774e-08	c=-3.64499398e-08
d=6.43284926e-09	d=8.49601995e-09

TABLE C-4.10

C-C-C-C Al Plate - 1st Displacement Shapes - Runs 15,25,26,29
Coefficients for Shapes in Fig 4.67

Y direction

$$y = C + ax + bx^2 + cx^3 + dx^4$$

0.111 g	0.309 g
C=0.18510577	0.50291058
a=-2.15727482e-04	-1.97255793e-04
b=-1.99983855e-05	-5.59537957e-05
c=1.27114891e-08	1.20593351e-08
d=5.41844359e-10	1.55156880e-09
0.694 g	1.23 g
C=0.90023051	1.2702762
a=-3.34182756e-04	-4.61449662e-04
b=-1.02666874e-04	-1.45305131e-04
c=2.01552115e-08	2.80557163e-08
d=2.91477962e-09	4.15836928e-09

TABLE C-4.11
C-C-C-C CFRP Plate - 1st Displacement Shapes - Runs 48,51,52,55
Coefficients for Shapes in Fig 4.72

Y direction

$$y = C + ax + bx^2 + cx^3 + dx^4$$

0.4 g	1.35 g
C=0.19691269	0.63213456
a=7.76582726e-05	1.05624380e-03
b=-3.43349272e-05	-1.06701671e-04
c=-8.01449268e-09	-1.12736443e-07
d=1.54452587e-09	4.51276709e-09
2.18 g	6.95 g
C=0.97544980	1.4379342
a=1.95788219e-04	-4.71198599e-04
b=-1.67623230e-04	-2.33147117e-04
c=-1.41147326e-08	4.92541191e-08
d=7.28259903e-09	9.30904267e-09

TABLE C-4.12
C-C -C-C CFRP Plate - 1st Displacement Shapes - Runs 49,50,53,54
Coefficients for Shapes in Fig 4.76

X direction

$$y = C + ax + bx^2 + cx^3 + dx^4$$

0.4 g	1.35 g
C=0.19779860	0.62402380
a=5.63285628e-04	1.28890152e-03
b=-2.12759511e-05	-6.96398884e-05
c=-4.35215743e-08	-1.00695353e-07
d=5.67938711e-10	1.92995795e-09
2.18 g	6.95 g
C=0.97860655	1.4340610
a=1.36853617e-03	6.74334078e-04
b=-9.86510536e-05	-1.26206381e-04
c=-1.08817380e-07	-5.50096757e-08
d=2.31749075e-09	2.23560150e-09

TABLE 3.1

MEASURED LINEAR MODAL FREQUENCIES

MODE NUMBER	AL Shaker Plate 254 X 203 X 1.30 mm Frequency Hz	CFRP Shaker Plate 254 X 203 X 1.09 mm Frequency Hz	CFRP APWT Plate 514 X 387 X 1.09 mm Frequency Hz
1 : 1	208	156	59
2 : 1	365	246	77
1 : 2	485	449	
3 : 1	618	352	107
2 : 2	623	535	160
3 : 2	864	674	187
4 : 1	966	587	139
5 : 1		825	194
2 : 3		981	
3 : 3		1110	
4 : 2			220
5 : 2			266
1 : 3			281
4 : 3			355
5 : 3			405

TABLE 4.1

BEAMS AND PLATE SIZES

MATERIAL	STRUCTURE	SIZE	SIZE
BEAMS			
ALUMINIUM ALLOY	C-C	406x20x2 mm	15.98x0.787x0.0787 inch
ALUMINIUM ALLOY	P-P	405x21.8x2 mm	15.94x0.858x0.0787 inch
CFRP	C-C CFRP	406x20x2 mm	15.98x0.787x0.0787 inch
PLATES			
ALUMINIUM ALLOY	C-C-C-C SHAKER	254x203x1.30	10x8x0.0429 inch
CFRP	C-C-C-C SHAKER	254x203x1.09	10x8x0.0429 inch
ALUMINIUM ALLOY	C-C-C-C APWT	450x300x1.22	17.7x11.8x0.048 inch
CFRP	C-C-C-C APWT	584x387x1.09	23.0x15.25x0.0429 inch

TABLE 4.2

MATERIAL PROPERTIES

MATERIAL	E _{xx}		E _{yy}		G _{xy}		POISSONN RATIO	DENSITY		FIBRE FRACTION
	GPa	psi	GPa	psi	GPa	psi		Kg/m ³	lb/in ³	
ALUMINIUM ALLOY	71.6	10.5X10 ⁶	71.6	10.5X10 ⁶	47.4	6.88X10 ⁶	0.3	7196	0.2588X10 ⁻³	
CFRP*	56.1	8.148x10 ⁶	56.1	8.148x10 ⁶	21.6	0.3133x10 ⁷	0.30039	1400	0.0503X10 ⁻³	58.7

* Computed from laminate computer program,

Hercules AS4 /3501-6 unidirectional prepreg tape with AS4 fibres in a 3501-6 matrix (0°/±45°/90°)_{2s}, (16 plies) for the beams and (0°/±45°/90°)_s, (8plies) for the plates, the material properties are the same for both beams and plates.

TABLE 4.3
C-C ALUMINIUM ALLOY BEAM STATIC TESTS
COMPARISON OF MEASURED DATA WITH CURVE FITTING FUNCTIONS

FUNCTION NAME RANK	displacement function mm centre	displacement measured mm centre	$d^2F(x)/dx$ function microstrain centre	SG 1 measured microstrain centre	SG 4 measured microstrain centre	$d^2F(x)/dx$ function microstrain clamp	SG 3 measured microstrain clamp	SG 6 measured microstrain clamp
2.5 Newton								
1 LOGISTIC	0.228	0.231	-34	72	-70	8	-72	69
2 GAUSSIAN	0.228	0.231	-32	72	-70	10	-72	69
3 LORENTZIAN	0.229	0.231	-37	72	-70	6.4	-72	69
7 SINE	0.223	0.231	-27	72	-70	26.9	-72	69
15 CLASSICAL	0.22	0.231	-22	72	-70	36.7	-72	69
20 4th order poly	0.218	0.231	-20	72	-70	42.3	-72	69
13.8 Newton								
1 GAUSSIAN	1.174	1.243	-148	357	-256	50	-271	326
2 SINE	1.167	1.243	-131	357	-256	131	-271	326
5 LOGISTIC	1.181	1.243	-157	357	-256	41.7	-271	326
6 CLASSICAL	1.16	1.243	-117	357	-256	200	-271	326
7 LORENTZIAN	1.188	1.243	-169	357	-256	33.3	-271	326
13 4th order poly	1.15	1.243	-217	357	-256	211	-271	326

TABLE 4.4

C-C ALUMINIUM ALLOY BEAM SINE TESTS

COMPARISON OF MEASURED DATA WITH CURVE FITTING FUNCTIONS

EXCITATION	SINE	SINE SQUARED	4th POLY FIT	GAUSSIAN	CLASSICAL	CLASSICAL	MEASURED
FORCE Newton	rank	rank	rank	rank	rank	CONSTANT b	
0.086 0.600	1 3	2 2	5 1	7 6	8 4	0.0116756 0.0117559	
	$d^2F(x)/dx$ microstrain clamp	$d^2F(x)/dx$ microstrain clamp	$d^2F(x)/dx$ microstrain clamp				SG 3 microstrain clamp
0.086 0.600	40 190	40 190	90 375		67 280		70 300
	$d^2F(x)/dx$ microstrain centre	$d^2F(x)/dx$ microstrain centre	$d^2F(x)/dx$ microstrain centre				SG 1 microstrain centre
0.086 0.600	40 195	40 195	40 175		35 170		60 235

TABLE 4.5
COMPARISON OF MEASURED BEAM DATA WITH LINEAR BEAM THEORY
ALUMINIUM ALLOY BEAMS

λ_n C-C	λ_n S-S	THEORY* C-C Eq ¹ (4.14) Hz	THEORY* S-S Eq ¹ (4.14) Hz	FEM** C-C Hz	FEM** S-S Hz	TEST** C-C SINE Hz	FEM*** C-C Hz	TEST*** C-C RANDOM Hz
n=1,2,3...	$\lambda_n = n\pi$							
1=4.73	1=3.14	70.8	31.2	99.4	70.3	85	67	65
2=7.863	2=6.28	195.2				205		
3=10.1	3=9.42	382.6	281	431	339	380	350	348
4=14.14	4=12.6	632.8				612		
5=17.28	5=15.7	944.9	781	1000	842	898		

* NO PRELOAD, NO COIL MASS

** 100 MICROSTRAIN PRELOAD IN TENSION, NO COIL MASS

*** 100 MICROSTRAIN PRELOAD IN TENSION, 26.4 g COIL ATTACHED AT THE CENTRE
MORE THAN 3 BEAM THICKNESS - CONSIDER POISSON'S EFFECT WHICH INCREASES THE FREQUENCIES BY 4.8 %

$$^1 \text{ Equation (4.14) } \omega_n = \frac{\lambda_n \pi^2}{\ell^2} \sqrt{\frac{EI}{\rho}} \text{ from reference [162]}$$

TABLE 4.6

COMPARISON OF MEASURED PLATE DATA WITH LINEAR PLATE THEORY

ALUMINIUM AND CFRP SHAKER PLATE

TEST	FREQUENCY Hz	THEORETICAL C-C-C-C PLATE Hz	TEST DATA C-C-C-C PLATE Hz	THEORETICAL S-S-S-S PLATE Hz
ALUMINIUM- SHAKER	f_{11} f_{13}	221.7 642.1	207.8 617.6	114.9 447.7
CFRP-SHAKER	f_{11} f_{13}	221.8 669.3	156 382	119.8 489
ALUMINIUM-APWT	f_{11} f_{13}	90.4 223	180* 350*	47.6 164.6
CFRP-APWT	f_{11} f_{13}	59 147	59 107	31.5 108.4

*50 MICROSTRAIN PRETENSION

TABLE 4.7
STRAIN STATISTICAL MOMENTS
BEAMS AND SHAKER PLATES

TEST	EXCITATION RMS	TIME HISTORY seconds	MEAN microstrain	STANDARD DEVIATION microstrain	RMS microstrain	SKEWNESS	KURTOSIS	MAX microstrain	MIN microstrain
C-C ALUMINIUM BEAM SG 1	N								
	0.815	12	-0.98	33.4	33.4	0.0704	2.92	137	-119
	1.45	12	-0.629	68.2	68.2	0.103	2.99	267	-267
	3.15	12	0.602	135	135	0.135	2.91	545	-495
	4.61	12	8.46	178	178	0.157	2.68	659	-561
	6.24	12	13.3	230	231	0.187	3.01	987	-784
C-C CFRP BEAM SG 1	N								
	1.08	12	-5.82	40.7	41.1	0.107	3.04	168	-170
	2.14	12	-4.06	77.6	77.7	0.175	2.9	339	-292
	4.37	12	8.58	144	144	0.255	2.86	697	-470
	6.54	12	12.5	198	198	0.311	2.95	951	-731
	8.61	12	15.2	242	243	0.305	2.9	1060	-802
C-C-C ALUMINIUM SHAKER PLATE SG 2	g								
	1.46	12	-4.38	54.2	54.4	0.058	2.84	206	-193
	5.68	12	1.3	198	198	0.101	3.01	766	-800
	10.2	12	17.7	320	320	0.142	3	1290	-1080
	14.4	12	29	430	431	0.188	2.91	1770	-1400
	14.4	25	20.7	424	425	0.196	2.92	1800	1420
CFRP SHAKER	14.4	25	-21.6	349	350	0.273	2.53	1290	-991

TABLE 4.8

STRAIN STATISTICAL MOMENTS

APWT PLATES

TEST	EXCITATION RMS	TIME HISTORY seconds	MEAN microstrain	STANDARD DEVIATION microstrain	RMS microstrain	SKEWNESS	KURTOSIS	MAX microstrain	MIN microstrain
C-C-C-C CFRP APWT PLATE SG 2	OSPL dB 134 140 146 149 152	12	-1.38	52.3	52.3	0.059	2.96	226	-240
		12	-74.3	89.5	116	0.136	3.18	332	-452
		12	-79.7	188	205	0.277	3.35	967	-820
		12	-155	258	301	0.241	3.22	1290	-1350
		12	-123	426	444	0.312	3.59	2530	-1800
	152	25	-101	429	441	0.316	3.55	2550	-1780
C-C-C-C CFRP APWT PLATE SG 3	OSPL dB 134 140 146 149 152	12	40.9	20.3	45.7	0.075	2.92	139	-32.2
		12	20	32.9	38.5	0.091	3.14	182	-152
		12	50.4	687	852	0.192	3.15	474	-238
		12	106	191	140	0.192	3.25	630	-280
		12	124	155	198	0.284	3.4	965	-556

TABLE 5.1
CALCULATIONS FOR CYCLIC MULTIMODAL FREQUENCIES

RUN #	TEST	SG #	TIME HISTORY s	NUMBER OF SAMPLES	sd $\mu\epsilon$	f _{cm} Hz
2155	C-C ALUMINIUM	1	12	6359	40.1	530
56	BEAM 10-1000 Hz	1	12	6019	86.3	502
57		1	12	6959	174	580
58		1	12	7199	226	600
2346	C-C CFRP BEAM	1	12	3253	45.5	271
48	10-1300 Hz	1	12	3248	88.3	271
50		1	12	3898	160	325
52		1	12	4319	224	360
54		1	12	4690	273	390
17	C-C-C-C AL SHAKER	2	12	10,058	92.2	838
18	PLATE 100-1000 Hz	2	12	10,102	267	842
19		2	12	10,650	426	888
20		2	12	10,819	577	902

TABLE 5.2

FATIGUE CALCULATIONS USING EQUATION 5.9

CANTILEVERED BEAM BS 1470-NS3 (REF 117 FIG 8)

ϵ/sd	sd $\mu\epsilon$	ϵ $\mu\epsilon$	$N_c = (2.172 \times 10^{11} / sd)^{-0.560}$	PPDF	PPDF/ N_c	N_t hours
0.5	425	213	15079045.41	0.213	1.41256E-07	16.6885
1	425	425	4390936.857	0.31	7.06000E-07	
1.5	425	638	2125446.064	0.24	1.12917E-06	
2	425	850	1273261.536	0.138	1.08383E-06	
2.5	425	1063	854026.6252	0.06	7.02554E-07	
3	425	1275	617189.6449	0.018	2.91645E-07	
3.5	425	1488	468372.0662	0.005	1.06753E-07	
TOTAL				0.984	4.16121E-06	
neg peaks	$N_t/2$					8.34425

TABLE 5.3

FATIGUE CALCULATIONS USING EQUATION 5.9

C-C AL BEAM BS 1470-NS3 (REF 117 TABLE 1)

ϵ/sd	sd $\mu\epsilon$	ϵ $\mu\epsilon$	PPDF	$N_c = (9.61 \times 10^{14} / sd)^{-0.3187}$	PPDF/ N_c	N_t hours
0.5	427	213.5	0.07	4.71E+08	1.48602E-08	
1	427	427	0.118	5.35E+07	2.20517E-07	
1.5	427	640.5	0.195	1.50E+07	1.30067E-06	
2	427	854	0.26	6.08E+06	4.27725E-06	
2.5	427	1067.5	0.212	3.02E+06	7.02475E-06	
3	427	1281	0.105	1.70E+06	6.16531E-06	
3.5	427	1494.5	0.04	1.05E+06	3.80982E-06	
TOTAL			1		2.28132E-05	3.044048

TABLE 5.4

FATIGUE CALCULATIONS USING EQUATION 5.9

FLEXIBLE RIVETED COUPON AL 7075-T6 (REF 7 p 489)

ϵ/sd	sd $\mu\epsilon$	ϵ $\mu\epsilon$	PPDF	$N_c = (1.31 \times 10^{20} / sd)^{-0.21}$	PPDF/ N_c	N_t hours
0.5	427	213.5	0.07	1.06E+10	6.57318E-10	
1	427	427	0.118	3.92E+08	3.00652E-08	
1.5	427	640.5	0.195	5.69E+07	3.42581E-07	
2	427	854	0.26	1.45E+07	1.79746E-06	
2.5	427	1067.5	0.212	5.00E+06	4.24139E-06	
3	427	1281	0.105	2.10E+06	5.00522E-06	
3.5	427	1494.5	0.04	1.01E+06	3.97278E-06	
TOTAL			1		1.53902E-05	4.512265

TABLE 5.5

FATIGUE CALCULATIONS USING EQUATION 5.9

FLEXIBLE RIVETED COUPON (K modified) AL 7075-T6 (REF 7 p 489)

ϵ/sd	sd $\mu\epsilon$	ϵ $\mu\epsilon$	PPDF	$N_t = (1.5 \times 10^{20} / sd)^{-0.21}$	PPDF/ N_c	N_t hours
0.5	427	213.5	0.07	1.21E+10	5.77563E-10	
1	427	427	0.118	4.47E+08	2.64173E-08	
1.5	427	640.5	0.195	6.48E+07	3.01015E-07	
2	427	854	0.26	1.65E+07	1.57937E-06	
2.5	427	1067.5	0.212	5.69E+06	3.72677E-06	
3	427	1281	0.105	2.39E+06	4.39792E-06	
3.5	427	1494.5	0.04	1.15E+06	3.49075E-06	
TOTAL			1		1.35228E-05	5.135354

TABLE 5.6
FATIGUE LIFE CALCULATIONS FOR C-C AL BEAM 6.46 N SG 3 USING EQUATION 5.12

# data points 4696	Mean 131	RMS 489	sd 488.82	# pdf values 80		
ϵ/sd	sd $\mu\epsilon$	strain $\mu\epsilon$	$N_c=(1.3 \times 10^{20}/sd)^{-0.21}$	PPDF	PPDF/ N_c	Nt hours
-3.968704	489	1940.696515	28621.28561	0.00E+01	0	0.803482
-3.866418	489	1890.678564	32410.80843	0.00E+01	0	
-3.784589	489	1850.664202	35886.34308	0.00E+01	0	
-3.682303	489	1800.646251	40887.75881	0.00E+01	0	
-3.580016	489	1750.6283	46757.7697	0.00E+01	0	
-3.477730	489	1700.610348	53678.85108	0.00E+01	0	
-3.375444	489	1650.592397	61878.87838	0.00E+01	0	
-3.273158	489	1600.574445	71644.29575	0.00E+01	0	
-3.170872	489	1550.556494	83337.68432	0.00E+01	0	
-3.068585	489	1500.538542	97421.4075	0.00E+01	0	
-2.966299	489	1450.520591	114489.7346	0.00E+01	0	
-2.884470	489	1410.50623	130803.559	0.00E+01	0	
-2.782184	489	1360.488279	155341.929	2.13E-02	1.37117E-07	
-2.679898	489	1310.470327	185675.6981	0.00E+01	0	
-2.577612	489	1260.452376	223478.856	2.13E-02	9.53110E-08	
-2.475326	489	1210.434424	271004.8367	4.26E-02	1.57193E-07	
-2.373039	489	1160.416473	331323.34	8.52E-02	2.57151E-07	
-2.270753	489	1110.398521	408670.1812	1.07E-01	2.61825E-07	
-2.168467	489	1060.38057	508972.649	1.70E-01	3.34006E-07	
-2.066181	489	1010.362619	640652.6006	3.83E-01	5.97828E-07	
-1.974123	489	965.3464623	795942.8929	5.75E-01	7.22414E-07	
-1.873883	489	916.3288699	1020128.145	7.03E-01	6.89129E-07	
-1.773642	489	867.3112776	1325421.567	7.67E-01	5.78684E-07	
-1.673402	489	818.2936852	1748516.534	1.19E-00	6.80577E-07	
-1.573161	489	769.2760928	2346495.606	1.70E-00	7.24485E-07	

TABLE 5.6 continued					
-1.472921	489	720.2585004	3210580.971	1.85E-00	5.76220E-07
-1.372680	489	671.240908	4491054.593	2.22E-00	4.94316E-07
-1.274486	489	623.2236746	6395122.931	2.39E-00	3.73722E-07
-1.174245	489	574.2060823	9446317.614	2.83E-00	2.99588E-07
-1.074005	489	525.1884899	14447821.67	3.09E-00	2.13873E-07
-0.973764	489	476.1708975	23037569.93	3.68E-00	1.59739E-07
-0.873524	489	427.1533051	38645900.78	3.07E-00	7.94392E-08
-0.773283	489	378.1357127	69053393.27	2.73E-00	3.95346E-08
-0.673043	489	329.1181203	133756257.7	3.47E-00	2.59427E-08
-0.572802	489	280.1005279	288293220.8	3.58E-00	1.24179E-08
-0.472562	489	231.0829355	720577549.7	3.71E-00	5.14865E-09
-0.374367	489	183.0657022	2184785909	3.15E-00	1.44179E-09
-0.274127	489	134.0481098	9636690822	3.45E-00	3.58007E-10
-0.173272	489	84.7304097	85628862603	2.70E-00	3.15314E-11
-0.073236	489	35.81285321	5.17142E+13	3.00E-00	5.80111E-13
0.026798	489	13.10470327	6.20519E+15	2.85E-00	4.59293E-15
0.126834	489	62.02225976	3.78296E+12	3.05E-00	8.06247E-12
0.227075	489	111.0398521	23625061645	3.77E-00	1.59576E-10
0.327315	489	160.0574445	4141728419	3.37E-00	8.13670E-10
0.427556	489	209.0750369	1160551350	3.56E-00	3.06751E-09
0.527796	489	258.0926293	425664993.6	3.15E-00	7.40019E-09
0.625991	489	306.1098627	188884161.5	3.28E-00	1.73651E-08
0.726232	489	355.1274551	93113694.39	2.73E-00	2.93190E-08
0.826472	489	404.1450474	50305204.02	3.11E-00	6.18226E-08
0.926712	489	453.1626398	29164956.79	2.81E-00	9.63485E-08
1.026953	489	502.1802322	17883391.1	2.53E-00	1.41472E-07
1.127193	489	551.1978246	11477229.39	2.41E-00	2.09981E-07
1.227434	489	600.215417	7649705.59	1.96E-00	2.56219E-07
1.327674	489	649.2330094	5263707.274	1.77E-00	3.36265E-07
1.427915	489	698.2506018	3721872.169	1.73E-00	4.64820E-07
1.526110	489	746.2678351	2711556.63	1.17E-00	4.31486E-07

TABLE 5.6 continued					
1.626350	489	795.2854275	2002869.756	1.28E-00	6.39083E-07
1.726591	489	844.3030199	1506462.22	1.04E-00	6.90359E-07
1.826831	489	893.3206123	1151453.298	1.19E-00	1.03348E-06
1.927071	489	942.3382047	892833.704	7.88E-01	8.82583E-07
2.027312	489	991.3557971	701290.9472	5.32E-01	7.58601E-07
2.127552	489	1040.373389	557298.9357	2.98E-01	5.34722E-07
2.229839	489	1090.391341	445631.6132	3.62E-01	8.12330E-07
2.332125	489	1140.409292	359931.6798	1.07E-01	2.97279E-07
2.434411	489	1190.427244	293390.7013	1.49E-01	5.07855E-07
2.536697	489	1240.445195	241172.0143	1.92E-01	7.96112E-07
2.618526	489	1280.459556	207332.3642	2.13E-02	1.02734E-07
2.720812	489	1330.477508	172750.5589	4.26E-02	2.46598E-07
2.823099	489	1380.495459	144909.4693	4.26E-02	2.93977E-07
2.925385	489	1430.513411	122318.1109	2.13E-02	1.74136E-07
3.027671	489	1480.531362	103851.9574	0.00E+01	0
3.129957	489	1530.549313	88654.41774	0.00E+01	0
3.232243	489	1580.567265	76066.93674	0.00E+01	0
3.334530	489	1630.585216	65578.8208	2.13E-02	3.24800E-07
3.436816	489	1680.603168	56790.82475	0.00E+01	0
3.518645	489	1720.617529	50770.85898	0.00E+01	0
3.620931	489	1770.63548	44294.75266	0.00E+01	0
3.723217	489	1820.653432	38791.8977	0.00E+01	0
3.825503	489	1870.671383	34095.0432	0.00E+01	0
TOTAL				1.76687E-05	0.803482

TABLE 5.7
FATIGUE LIFE CALCULATIONS FOR C-C C-C AL SHAKER PLATE 14.4 g SG 2 USING EQUATION 5.12

# of samples 10819	Mean 2.12E+02	RMS 5.77E+03	sd 576.8094	# pdf values 80			
ϵ/sd	sd $\mu\epsilon$	strain $\mu\epsilon$	$N_c=(1.3 \times 10^{20}/sd)^{-0.21}$	PPDF	PPDF/ N_{cm}	N_t hours	
-3.96318	576.8094	2285.999478	23747.04649	0.00E+01	0	0.303880	
-3.86263	576.8094	2228.001293	26809.45909	0.00E+01	0		
-3.76381	576.8094	2171.000988	30297.97633	0.00E+01	0		
-3.66325	576.8094	2112.997035	34429.1398	0.00E+01	0		
-3.5627	576.8094	2054.998849	39262.52712	0.00E+01	0		
-3.46388	576.8094	1997.998544	44837.32873	0.00E+01	0		
-3.36333	576.8094	1940.000359	51525.75646	0.00E+01	0		
-3.26278	576.8094	1882.002174	59462.33389	0.00E+01	0		
-3.16396	576.8094	1825.001869	68752.11791	0.00E+01	0		
-3.0634	576.8094	1766.997916	80074.60875	0.00E+01	0		
-2.96285	576.8094	1708.999731	93736.06288	0.00E+01	0		
-2.8623	576.8094	1651.001546	110326.7479	0.00E+01	0		
-2.76348	576.8094	1594.001241	130227.4298	0.00E+01	0		
-2.66292	576.8094	1535.997287	155126.5034	0.00E+01	0		
-2.56237	576.8094	1477.999102	186031.6499	0.00E+01	0		
-2.46355	576.8094	1420.998797	223978.6427	0.00E+01	0		
-2.363	576.8094	1363.000612	272663.8491	9.24E-03	3.38879E-08		
-2.26245	576.8094	1305.002427	334783.0749	4.62E-02	1.38000E-07		
-2.16363	576.8094	1248.002122	413344.9089	4.62E-02	1.11771E-07		
-2.06307	576.8094	1189.998169	517452.4147	1.85E-01	3.57521E-07		
-1.96252	576.8094	1131.999984	655079.2093	3.33E-01	5.08335E-07		
-1.8637	576.8094	1074.999679	835990.9627	6.10E-01	7.29673E-07		
-1.76315	576.8094	1017.001494	1086153.017	9.71E-01	8.93981E-07		
-1.66311	576.8094	959.2974812	1430966.035	1.43E-00	9.99325E-07		
-1.56308	576.8094	901.599237	1917719.277	1.93E-00	1.00640E-06		

TABLE 5.7 continued					
-1.46322	576.8094	843.9990503	2618875.664	2.36E-00	9.01150E-07
-1.36319	576.8094	786.300806	3658222.858	2.46E-00	6.72458E-07
-1.26316	576.8094	728.6025617	5241949.665	2.79E-00	5.32245E-07
-1.16312	576.8094	670.8985493	7737997.34	2.81E-00	3.63143E-07
-1.06309	576.8094	613.200305	11829483.2	2.84E-00	2.40078E-07
-0.96323	576.8094	555.6001184	18843897.17	2.92E-00	1.54957E-07
-0.8632	576.8094	497.9018741	31617706.94	3.25E-00	1.02791E-07
-0.76316	576.8094	440.1978617	56549751.18	3.15E-00	5.57032E-08
-0.66313	576.8094	382.4996174	109756582.8	3.36E-00	3.06132E-08
-0.5631	576.8094	324.8013731	237472124.8	3.12E-00	1.31384E-08
-0.46324	576.8094	267.2011865	596721598.2	2.79E-00	4.67555E-09
-0.3632	576.8094	209.4971741	1881429560	3.22E-00	1.71146E-09
-0.26317	576.8094	151.7989298	8607174571	3.33E-00	3.86887E-10
-0.16319	576.8094	94.12952599	82122621998	3.64E-00	4.43240E-11
-0.06319	576.8094	36.44858599	7.23296E+13	3.93E-00	5.43346E-13
0.036806	576.8094	21.23004678	9.27343E+14	3.80E-00	4.09773E-14
0.136804	576.8094	78.90983316	1.88795E+12	3.73E-00	1.97569E-11
0.23682	576.8094	136.6000021	14161902133	3.30E-00	2.33020E-10
0.336853	576.8094	194.2999768	2684463771	2.86E-00	1.06539E-09
0.436713	576.8094	251.9001635	788225789.6	2.82E-00	3.57766E-09
0.536746	576.8094	309.6001382	297760793.3	2.98E-00	1.00080E-08
0.636779	576.8094	367.3001129	132907506.2	2.40E-00	1.80577E-08
0.736812	576.8094	425.0000876	66750227.29	2.76E-00	4.13482E-08
0.836845	576.8094	482.7000623	36600903.5	2.71E-00	7.40419E-08
0.936705	576.8094	540.300249	21498637.15	2.56E-00	1.19077E-07
1.036738	576.8094	598.0002237	13317373.07	2.23E-00	1.67450E-07
1.136771	576.8094	655.7001984	8621837.517	2.00E-00	2.31969E-07
1.236804	576.8094	713.4001732	5790501.364	2.18E-00	3.76479E-07
1.336837	576.8094	771.1001479	4011307.999	2.06E-00	5.13548E-07
1.436696	576.8094	828.6997577	2855052.386	1.77E-00	6.19954E-07

TABLE 5.7 continued						
1.536729	576.8094	886.3997325	2077959.757	2.02E-00	9.72107E-07	
1.636762	576.8094	944.0997072	1542995.318	1.52E-00	9.85097E-07	
1.737142	576.8094	1001.999835	1165074.277	1.23E-00	1.05573E-06	
1.835962	576.8094	1059.00014	897304.2389	1.03E-00	1.14788E-06	
1.936515	576.8094	1117.000055	697650.3925	7.86E-01	1.12664E-06	
2.037068	576.8094	1174.999971	549376.707	4.81E-01	8.75538E-07	
2.135887	576.8094	1231.999699	439305.7436	4.90E-01	1.11540E-06	
2.236441	576.8094	1290.000191	353561.6766	3.33E-01	9.41844E-07	
2.336994	576.8094	1348.000107	287284.6804	1.85E-01	6.43961E-07	
2.437547	576.8094	1406.000023	235482.249	9.24E-02	3.92386E-07	
2.536366	576.8094	1462.999751	195207.2986	7.39E-02	3.78572E-07	
2.636919	576.8094	1520.999666	162479.8393	1.85E-02	1.13860E-07	
2.737473	576.8094	1579.000159	136171.1364	4.62E-02	3.39279E-07	
2.836292	576.8094	1635.999887	115183.9295	1.85E-02	1.60613E-07	
2.936845	576.8094	1693.999802	97718.7458	0.00E+01	0	
3.037398	576.8094	1751.999718	83362.03171	0.00E+01	0	
3.136218	576.8094	1809.000023	71670.24019	0.00E+01	0	
3.236771	576.8094	1866.999938	61751.5422	0.00E+01	0	
3.337324	576.8094	1924.999854	53448.5605	0.00E+01	0	
3.436144	576.8094	1982.000159	46571.42516	0.00E+01	0	
3.536697	576.8094	2040.000075	40643.81409	0.00E+01	0	
3.63725	576.8094	2097.99999	35606.31644	0.00E+01	0	
3.736069	576.8094	2154.999718	31374.58961	0.00E+01	0	
3.836622	576.8094	2212.999634	27678.14542	0.00E+01	0	
3.937176	576.8094	2271.000126	24496.49414	0.00E+01	0	
TOTAL				1.00E+02	2.02777E-05	0.303880226

TABLE 5.8

SUMMARY OF FATIGUE LIFE CALCULATION

CONDITIONS	ϵ -N DATA SOURCE	ALUMINIUM ALLOY	K (ϵ -N curve) CONSTANT	alpha (ϵ -N slope)	METHOD OF EXCITATION	Nt hours	Nt (note 1) hours	Nt (note 2) hours
CANT BEAM	Ref 117 Fig 8	BS1470-NS3	2.17E+12	-0.56	SINE	16.69 pos	16.15	15.25 15.91
CANT BEAM	Ref 117 Fig 8	BS1470-NS3	2.17E+12	-0.56	SINE	8.34 pos & neg		
CANT BEAM	Ref 7 p 488	DTD 5070	7.17E+21	-0.203	RAND one mode	15.3 pos & neg		
C-C BEAM	Ref 117 Table 1	BS1470-NS3	9.61E+15	-0.3187	RAND one mode	3.04 pos	2.53	5.25 5.92
C-C BEAM	Ref 117 Fig 8	BS1470-NS3	3.98E+25	-0.1624	SINE	6.79 pos		
FLEX COUPON	Ref 7 p 489	7075-T6	1.32E+21	-0.21	RAND one mode	4.51 pos		
FLEX COUPON	Ref 7 p 489 modified	7075-T6	1.50E+21	-0.21	RAND one mode	5.14 pos		
FLEX COUPON	Ref 7 p 489 modified	7075-T6	1.70E+21	-0.21	RAND one mode	5.82 pos		
C-C BEAM	Ref 7 p 488	7075-T6	1.30E+21	-0.21	RAND multimodal	1.41 pos & neg		
C-C BEAM	Ref 7 p 488 modified	7075-T6	1.70E+21	-0.21	RAND multimodal	1.4 pos & neg		
C-C-C-C PLATE	Ref 7 p 488 modified	7075-T6	1.70E+21	-0.21	RAND multimodal	3.04 pos & neg		

note 1 Theoretical results from reference 117

note 2 Test results from reference 117

TABLE 5.9
CURVE FITTING FUNCTIONS OF PPDFs
C-C-C-C AL Shaker Plate R 20 SG 2
Partial Listing

Rank	Goodness of Fit	Function
1	0.9784536528	$y=a+bx+cx^2+dx^3+ex^4+fx^5+gx^6+hx^7+ix^8+jx^9+kx^{10}$
2	0.9740554290	$y=a+bx+cx^2+dx^3+ex^4+fx^5+gx^6+hx^7+ix^8+jx^9$
3	0.9724300537	$y=a+bx+cx^2+dx^3+ex^4+fx^5+gx^6+hx^7+ix^8$
4	0.9712823947	$y_{0.5}=a+bx+cx^2+dx^3+ex^4+fx^5$
5	0.9710257009	$y=a+bx+cx^2+dx^3+ex^4+fx^5+gx^6+hx^7$
6	0.9702265224	$y_{0.5}=a+bx+cx^2+dx^3+ex^4$
7	0.9698588213	$y=a+bx+cx^2+dx^3+ex^4+fx^5+gx^6$
8	0.9687897349	$y=a+bx+c/x+dx^2+e/x^2+fx^3+g/x^3+hx^4+i/x^4+jx^5$
9	0.9685721197	$y=a+bx+c/x+dx^2+e/x^2+fx^3+g/x^3+hx^4+i/x^4$
10	0.9674214501	$y=a+bx+c/x+dx^2+e/x^2+fx^3+g/x^3+hx^4$
11	0.9665260865	$y=(a+cx+ex^2+gx^3)/(1+bx+dx^2+fx^3+hx^4)$
12	0.9646339143	$y=a+bx+cx^2+dex+e/x^2$
13	0.963396113	$y=a+bx+cx^2+dx^3+ee-x$
14	0.9625290723	$\ln y=a+bx+cx^2+dx^3+ex^4+fx^5$
15	0.9624406469	$y=a+bx+cx^2+dx^3+ex^4+fx^5$
16	0.9623580240	$y=a+bx+c/x+dx^2+e/x^2+fx^3+g/x^3$
17	0.9614381348	$y=a+bx+cx^2+dx^3+ex^4$
18	0.9614317821	$y=a+b\exp(-\exp(-(x-c)/d))-((x-c)/d)+1$ [ExtrVal]
19	0.9606989190	$y=a+bx+cx^2+dex+ee-x$
20	0.9605540109	$\ln y=a+bx+cx^2+dx^3+ex^4$
21	0.9604978619	$y=a+bx^2+cx^3+de-x$
22	0.9601906898	$y=a+bx+cx^2+dex+e/x$
23	0.9601668987	$y=a+bx+cx^2+dx^3+eex$
24	0.9600361223	$y=a+bx+cx^2+dex$
25	0.9598795470	$y=a+bx+c/x+dx^2+e/x^2+fx^3$
26	0.9584708035	$y=a+bx+cx^2+dx^3+e/x^2$
27	0.9579770346	$y=(a+cx+ex^2)/(1+bx+dx^2)$
28	0.9568268513	$y=(a+cx+ex^2+gx^3)/(1+bx+dx^2+fx^3)$
29	0.9559956258	$y_{0.5}=a+bx+cx^2+dx^3$
30	0.9539661278	$y=(a+cx+ex^2)/(1+bx+dx^2+fx^3)$
31	0.9522638805	$y=a+bx+cx^2+dx^3+e/x$
32	0.9517573108	$y=a+bx+cx^2+dx^3$
33	0.9513985892	$y=a+\text{berfc}(((x-c)/d)^2)$ [Erfc Peak]
35	0.9431612386	$y=a+bx^2+cex+de-x$
36	0.9420260096	$y=a+\text{berfc}(((x-c)/d)^2)$ [Erfc Peak]
37	0.9414080466	$y=a+bx+cx^2+d/x^2+ee-x$
38	0.9406905220	$y=a+b\sin(2px/d+c)$ [Sine]
39	0.9406905220	$y=a+b\sin^2(2px/d+c)$ [Sine2]
40	0.9367484238	$y_{0.5}=a+bx^2$
41	0.9364111562	$y=a+b\exp(-0.5((x-c)/d)^2)$ [Gaussian]

TABLE 5.9 continued

42	0.9360144053	$y0.5=a+bx+cx^2$
43	0.9344709049	$y=a+b*4n/(1+n)^2$ $n=\exp(-(x-c)/d)$ [Logistic]
44	0.9327891259	$y=a+b/(1+((x-c)/d)^2)$ [Lorentzian]
45	0.9319625228	$y=a+bx+cx^2+d/x+ee-x$
46	0.9315120977	$y=a+bx+cx^2+de-x$
47	0.9288928519	$y=a+b\exp(-0.5((x-c)/d)^2)$ [Gaussian]
48	0.9283099154	$y=a+bx+cx^3+d/x^2+ee-x$
49	0.9268986789	$y=a+bx^2+cx^3+dex$
50	0.9265858409	$y=a+bx+cex+d/x^2+ee-x$
51	0.9237733407	$y=a+bx+cx^3+dex+ee-x$
52	0.9223936385	$y=a+bx^2+cx^3+d/x^2$
53	0.9205763517	$\ln y=a+bex+ce-x$
54	0.9192284995	$y=a+b*4n/(1+n)^2$ $n=\exp(-(x-c)/d)$ [Logistic]
55	0.9168242754	$y=a+bx+cx^3+d/x+ee-x$
56	0.9165493471	$y=a+bx+c/x+d/x^2+ee-x$
57	0.9157861895	$y=a+bx+cx^3+de-x$
58	0.9156574259	$y=a+bx+c/x^2+de-x$
59	0.9154668519	$y=a+bx^2+cex+d/x^2$
60	0.9150819733	$y=a+bx+cex+d/x+ee-x$
61	0.9143784224	$y=a+bx^2+cx^3+d/x$
62	0.9142570645	$y=a+bx^2+cx^3$
63	0.9138648498	$y=a+bx+cex+de-x$
64	0.9076699071	$y=a+bx+cx^2+d/x+e/x^2$
65	0.9074828624	$y=a+bx^2+cex+d/x$
66	0.9072889209	$y=a+bx^2+c/x^2+de-x$
67	0.9072768228	$y=a+bx^2+cex$
68	0.9071752212	$y=a+bx+cx^3+dex+e/x^2$
69	0.9048421291	$y=a+bx+c/x+de-x$
70	0.9024859375	$y=a+bx+ce-x$
71	0.9018485999	$y=a+bx^2+c/x+d/x^2$
72	0.9018180612	$y=a+bx^3+cex+d/x^2$
73	0.9002804198	$y=a+bx+cx^2+d/x^2$
74	0.8996330629	$\ln y=a+bx+cx^2+dx^3$
75	0.8979166817	$y=a+bx^2+c/x+de-x$
76	0.8978266571	$y=a+bx^2+ce-x$
77	0.8962599582	$y=a+bx^3+cex+de-x$
78	0.8962510333	$y=a+bx^2+c/x^2$
79	0.8945097660	$y=a+bx+cx^3+dex+e/x$
80	0.8935354853	$y=a+b/(1+((x-c)/d)^2)$ [Lorentzian]
81	0.8924828848	$y=a+bx+cx^3+dex$
82	0.8905209131	$y=a+bx+cx^2+d/x$
83	0.8904762856	$y=a+bx+cx^2$
84	0.8900634931	$y=a+bx^3+cex+d/x$
85	0.8893081185	$\ln y=a+bx+ce-x$
86	0.8889871584	$\ln y=a+bx+cx^2$

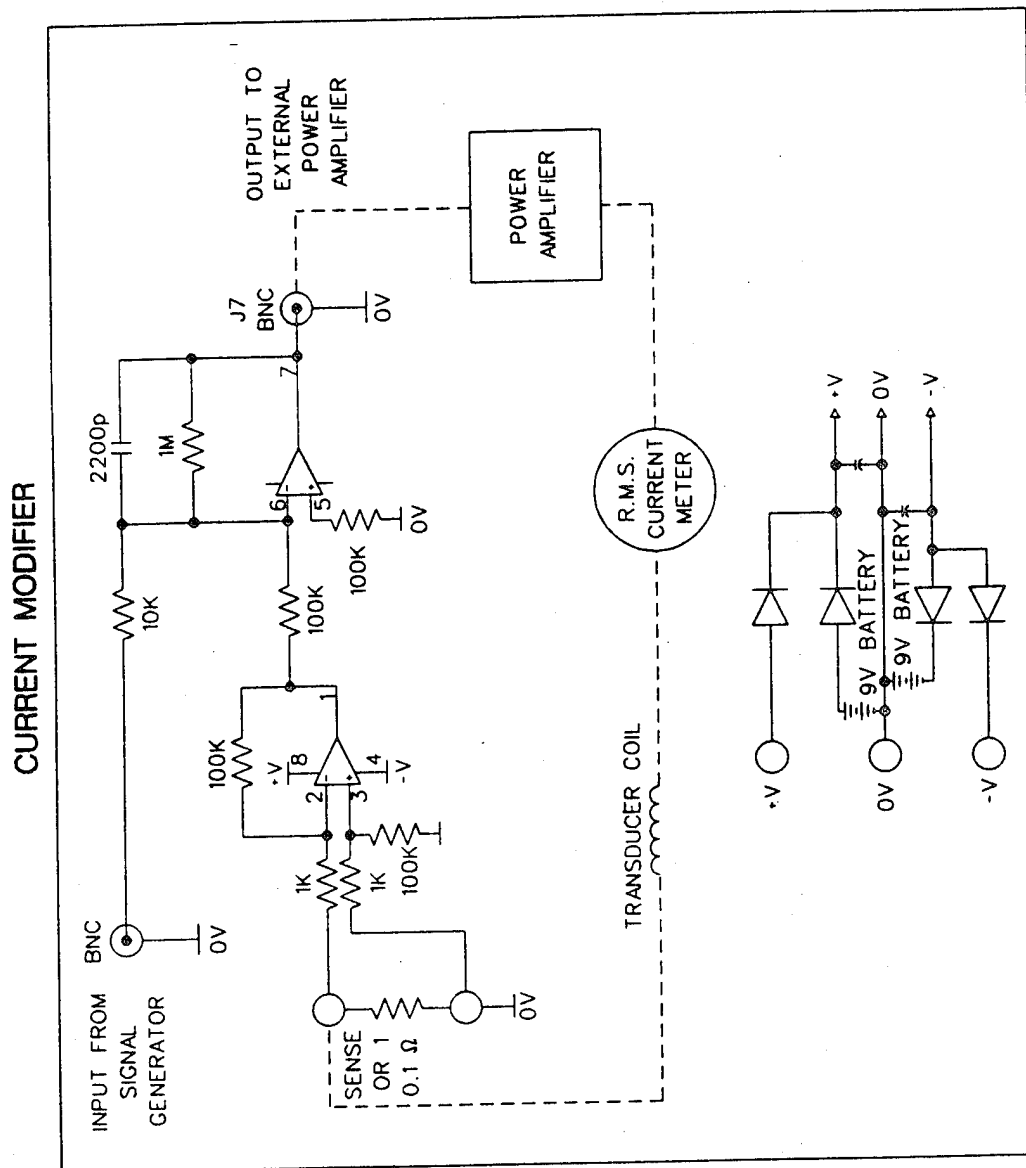


Fig 2.1 Constant current modifier schematic for beams tests.



Fig 2.2 Photograph of testing arrangement for clamped straight beams.

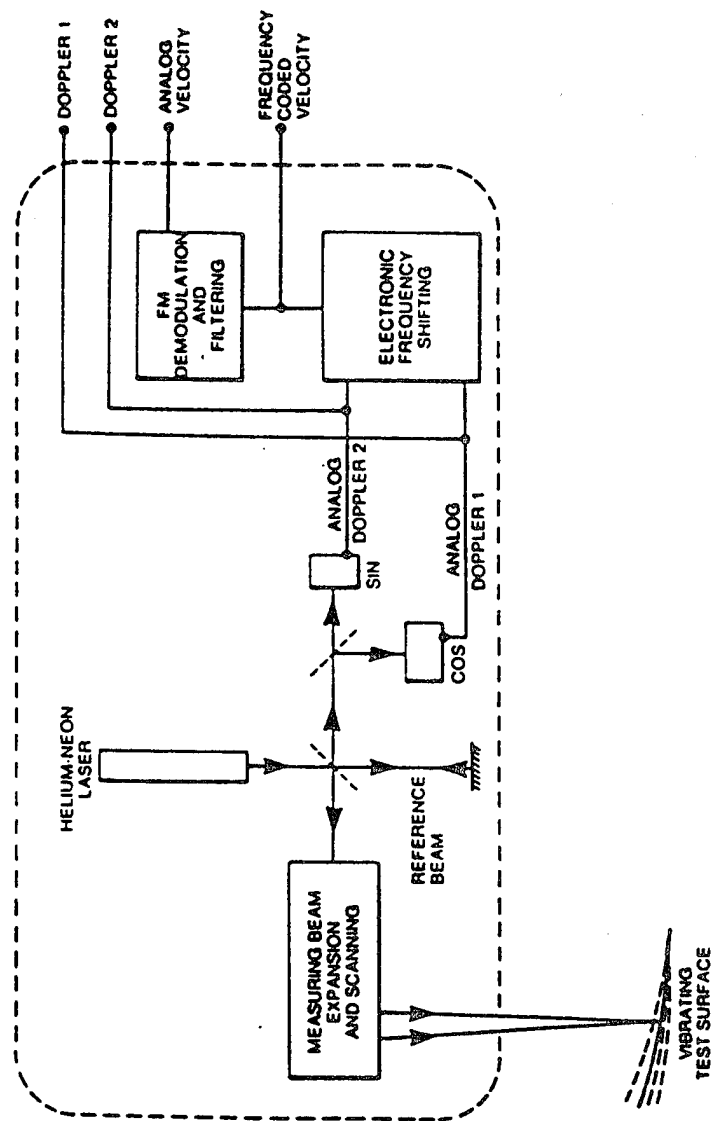


Fig 2.3 Scanning laser vibrometer diagram.

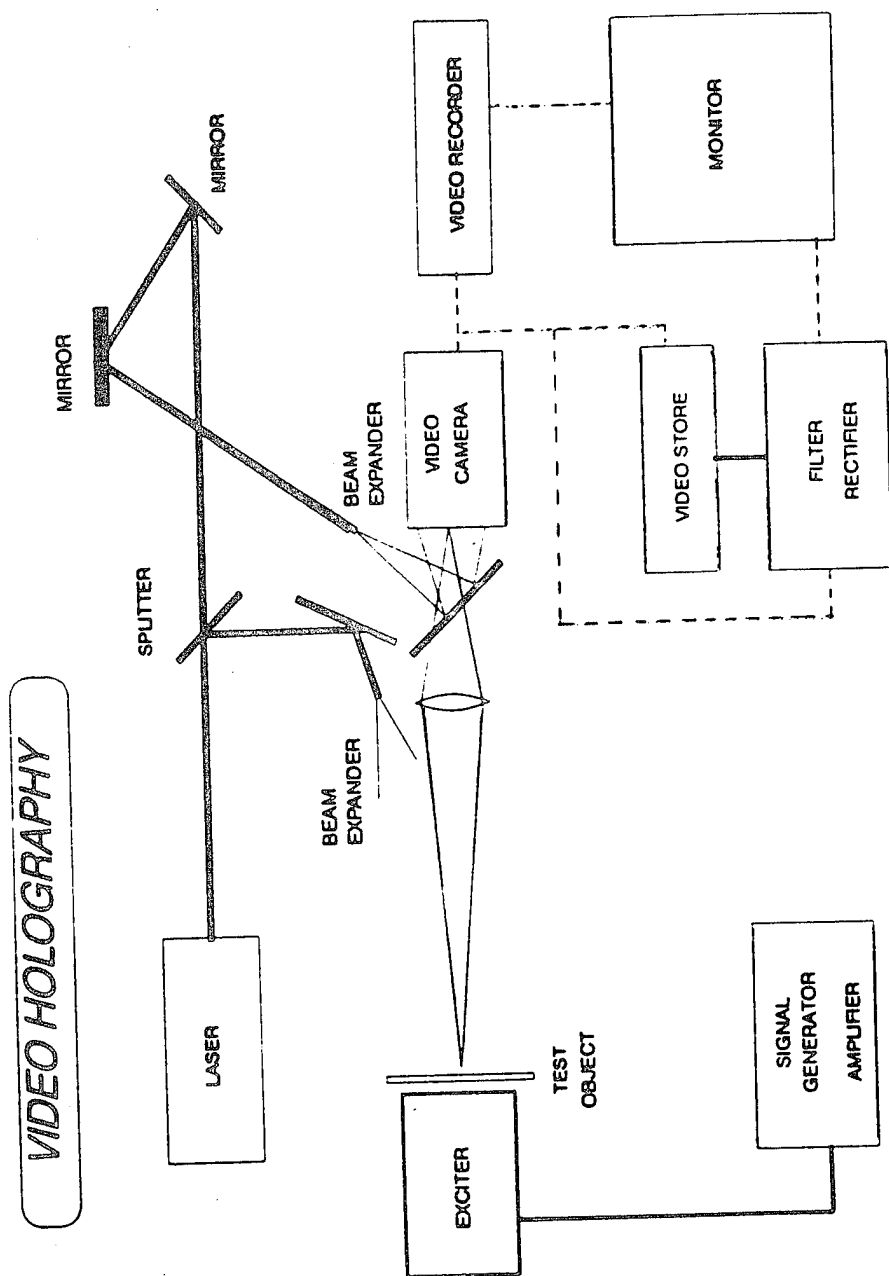


Fig 2.4 Video holography test arrangement diagram.

CLAMPED BEAM SIZE AND STRAIN GAUGE LOCATIONS

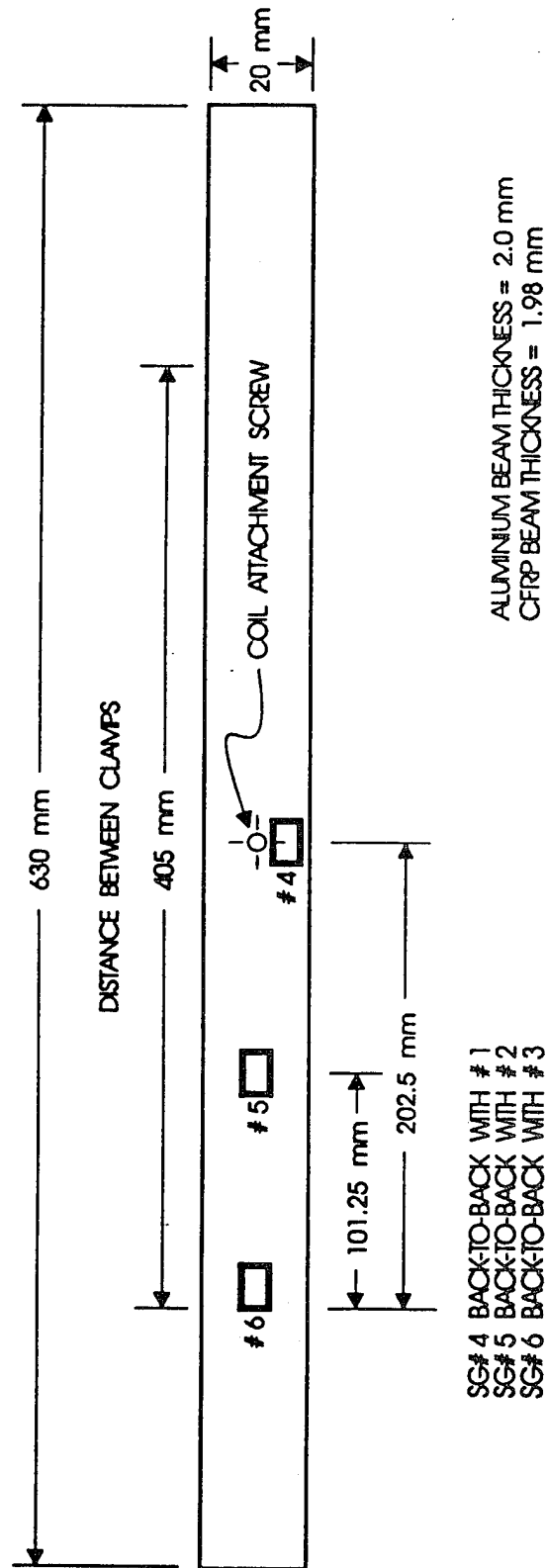


Fig 2.5 Clamped beam size and strain gauge locations.

BEAM TEST ARRANGEMENT

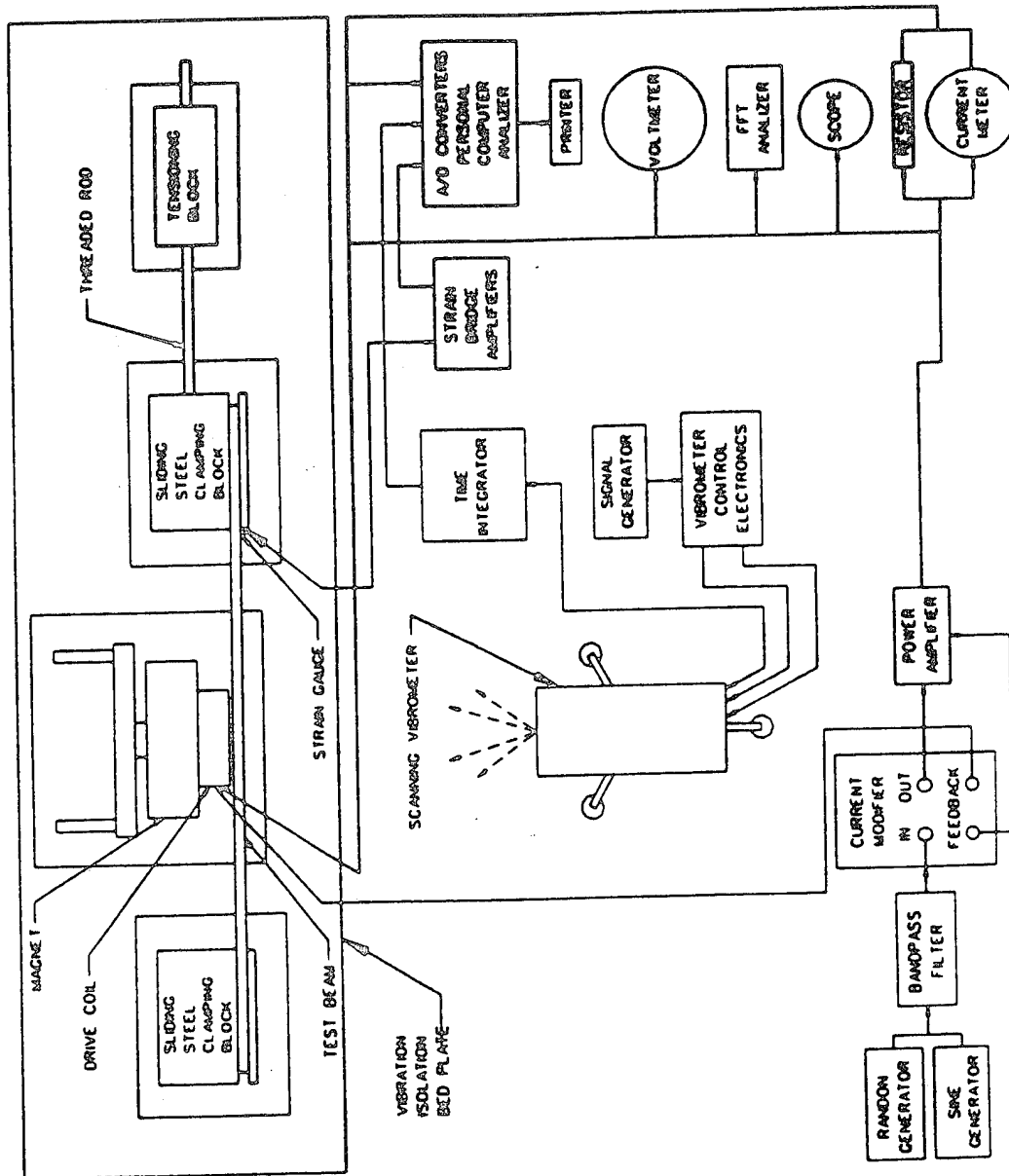


Fig 2.6 Beam testing arrangement diagram.

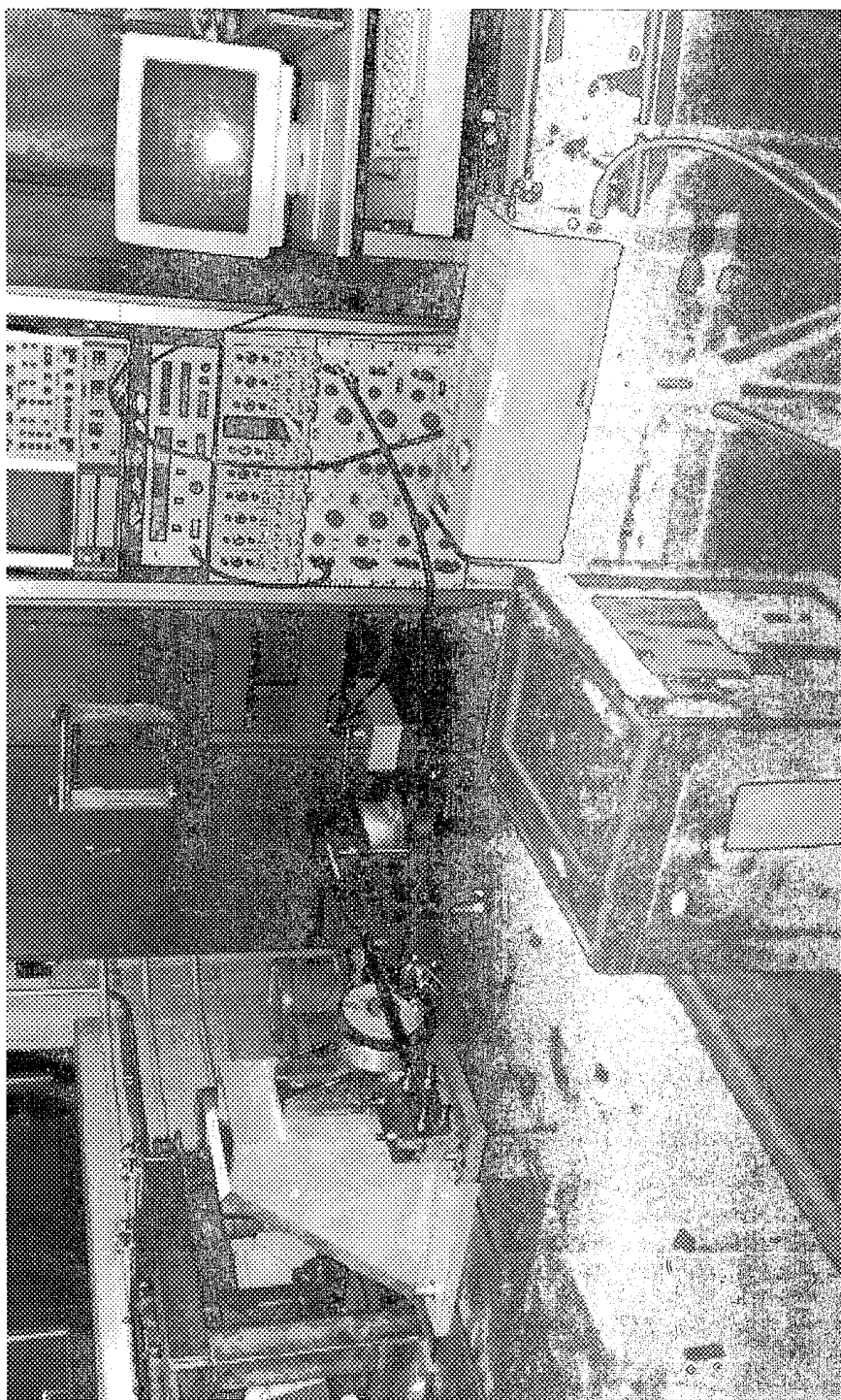


Fig 2.7 Photograph mode shape test arrangement, C-C aluminium alloy beam.

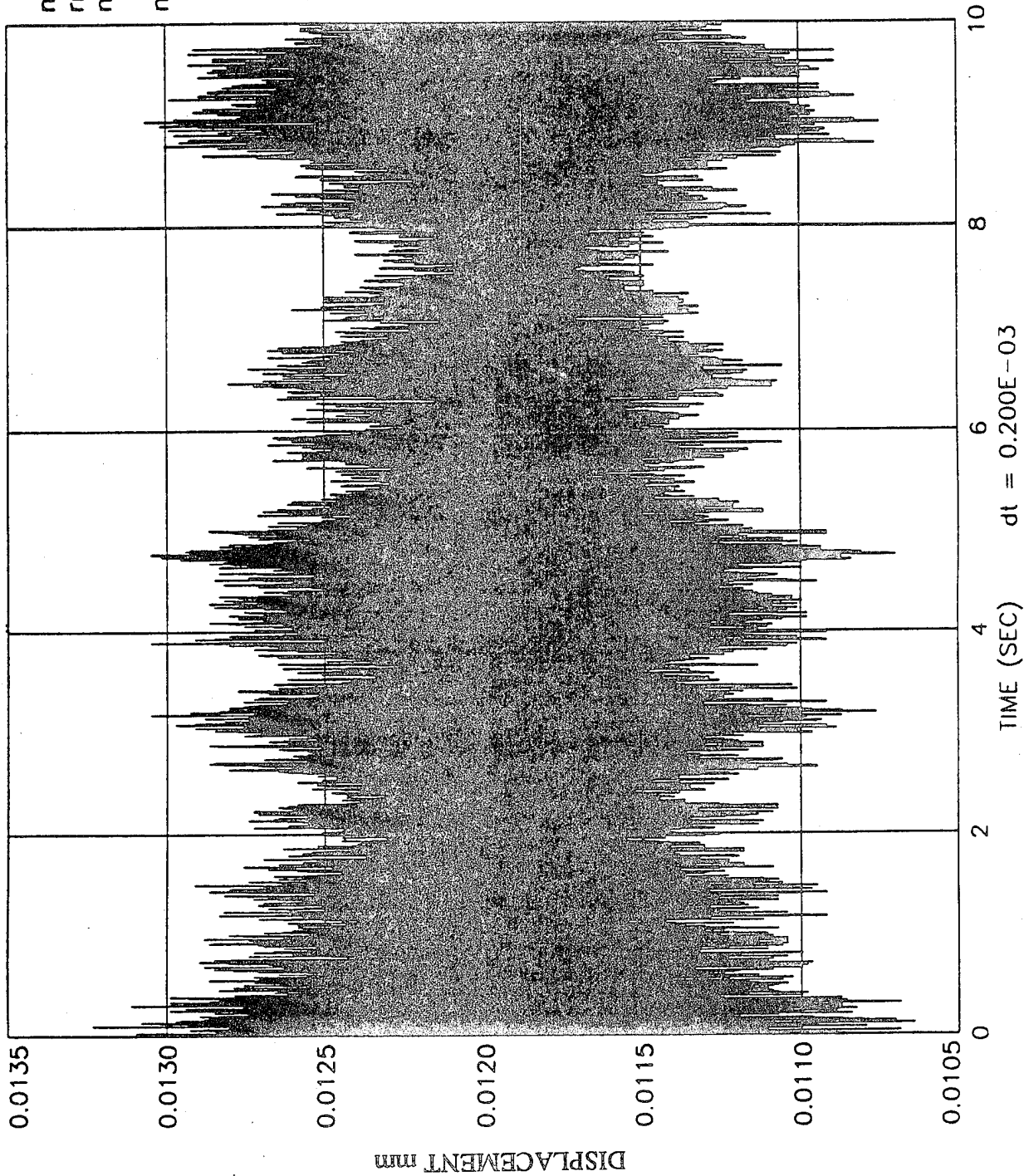


Fig 2.8 Displacement time history, 10-400 Hz random excitation, C-C aluminium beam.

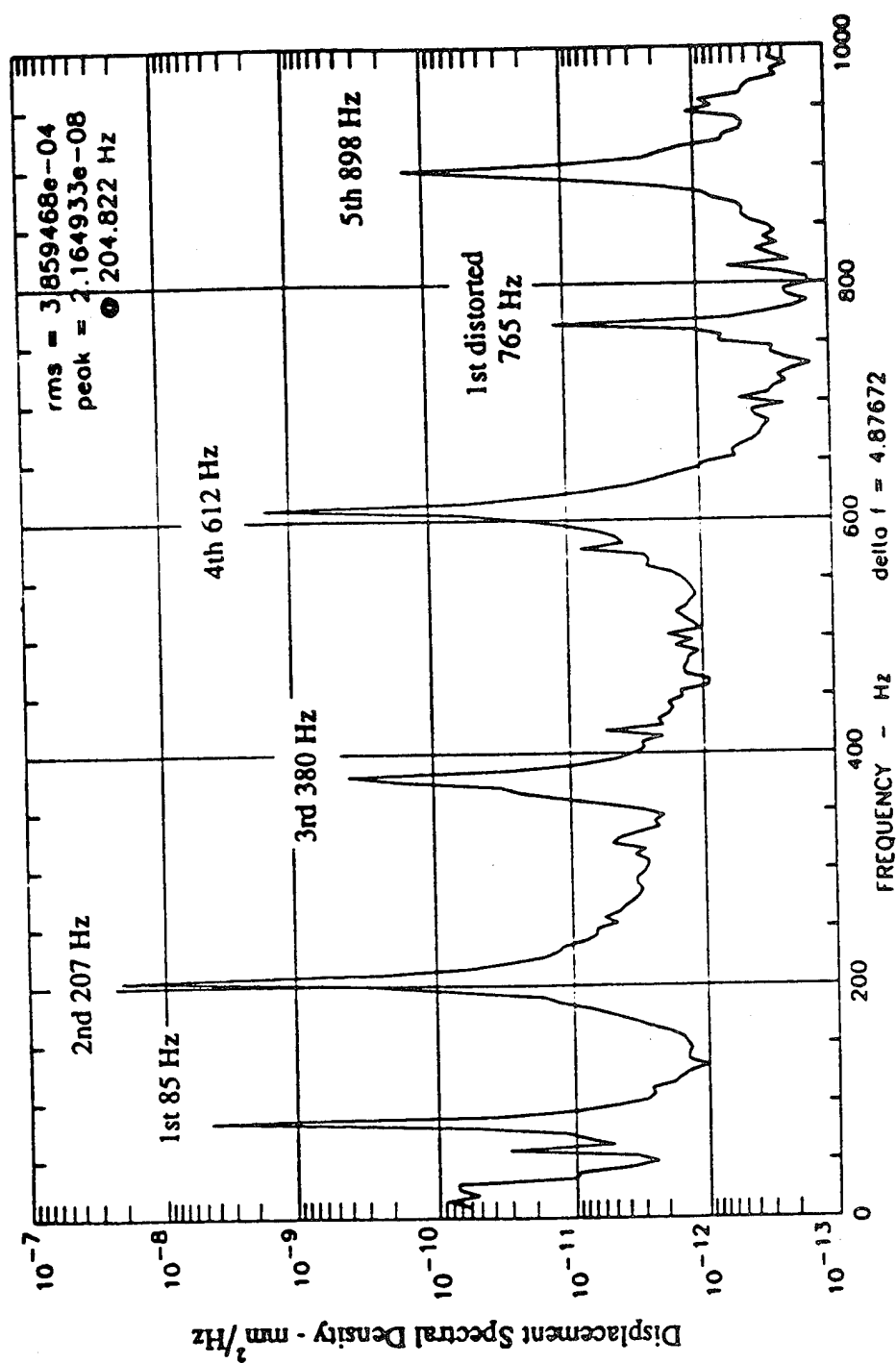


Fig 2.9 Displacement spectral density, centre of C-C aluminium beam, acoustic excitation concentrated at 1/4 ℓ .

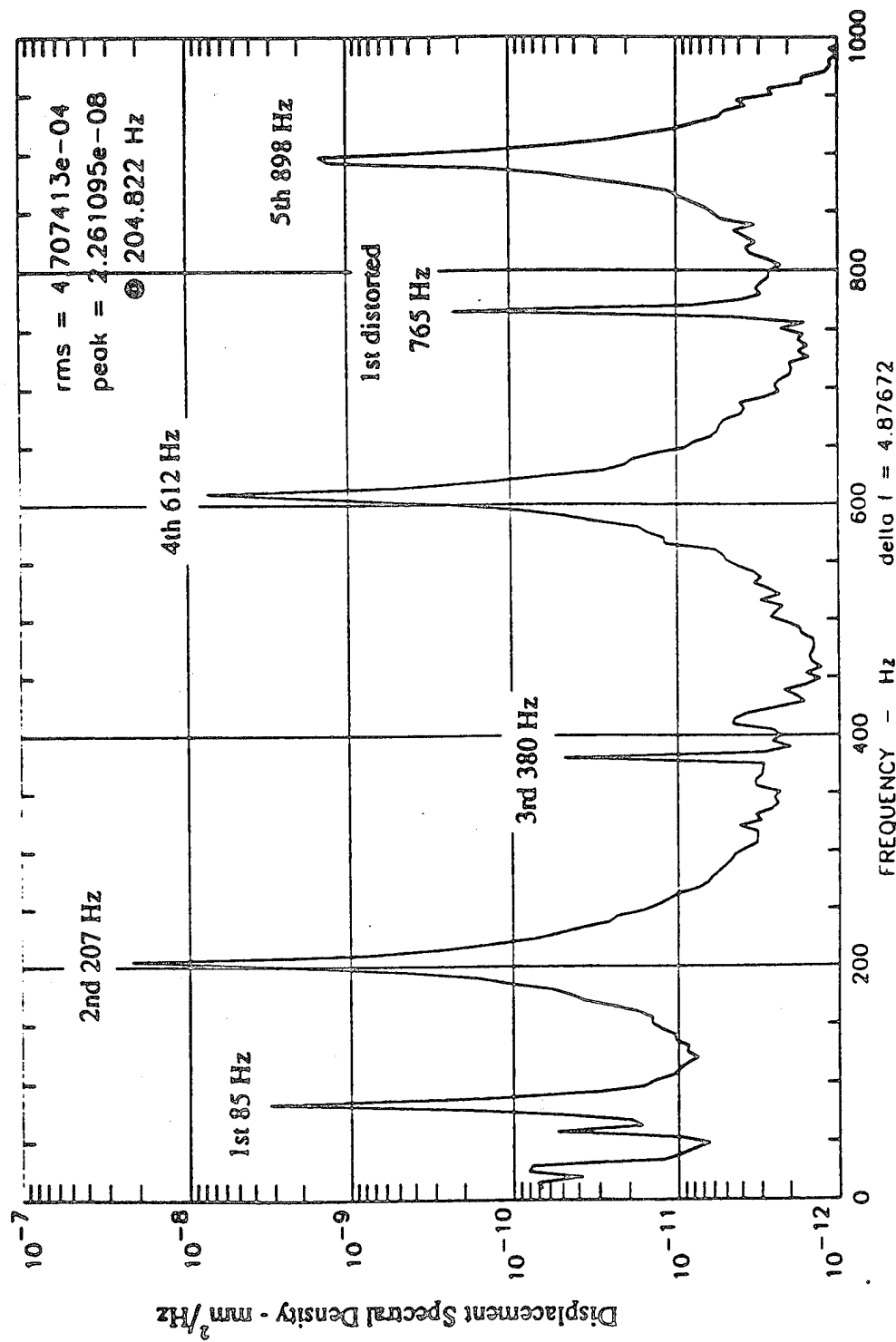


Fig 2.10 Displacement spectral density, centre of C-C aluminium beam, acoustic excitation concentrated at 1/8

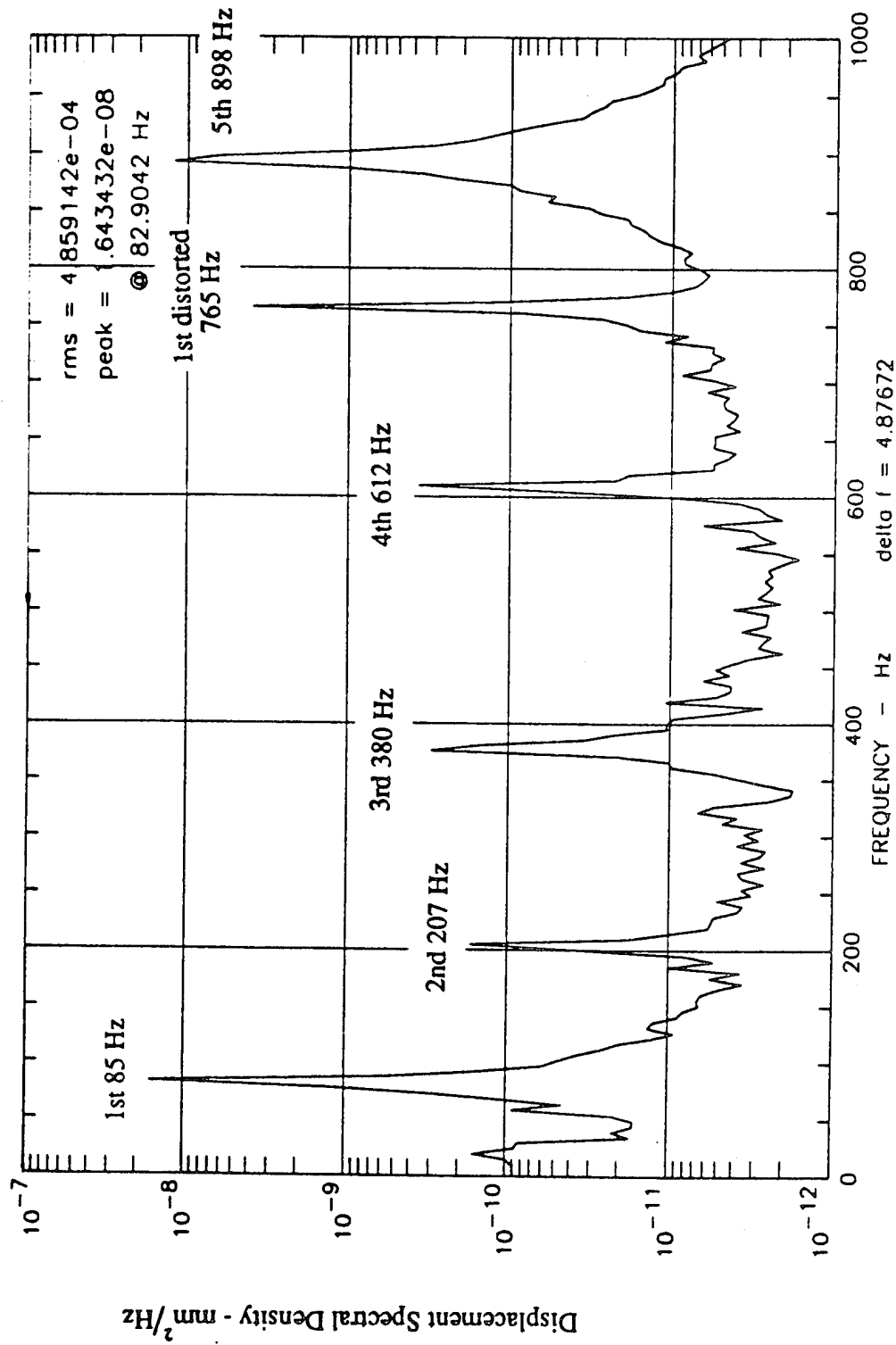


Fig 2.11 Displacement spectral density, centre of C-C aluminium beam, acoustic excitation concentrated at $1/6 \ell$.

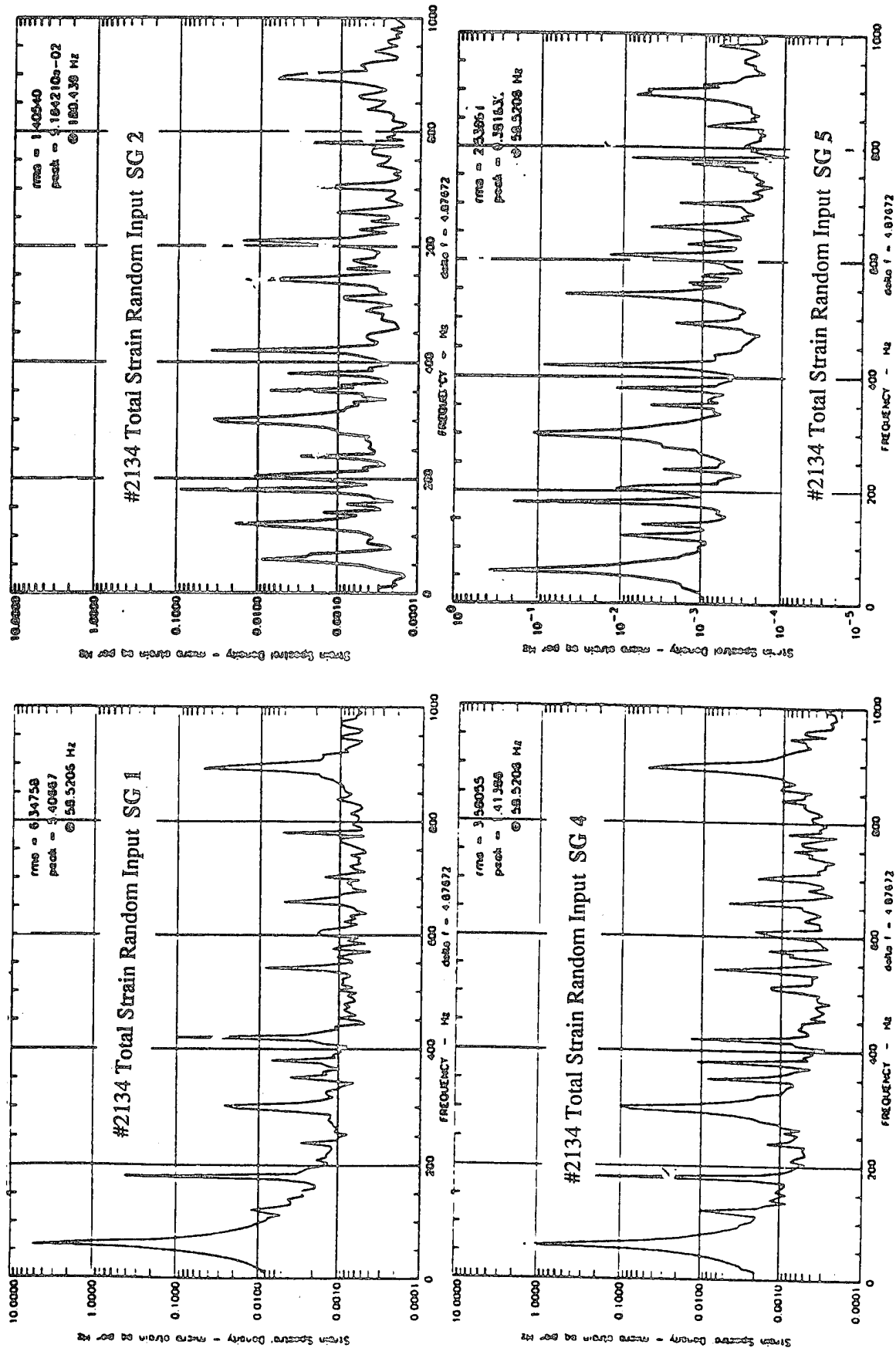


Fig 2.12 Strain spectral densities, SG 1, 2, 4 and 5, acoustic random excitation at the centre.

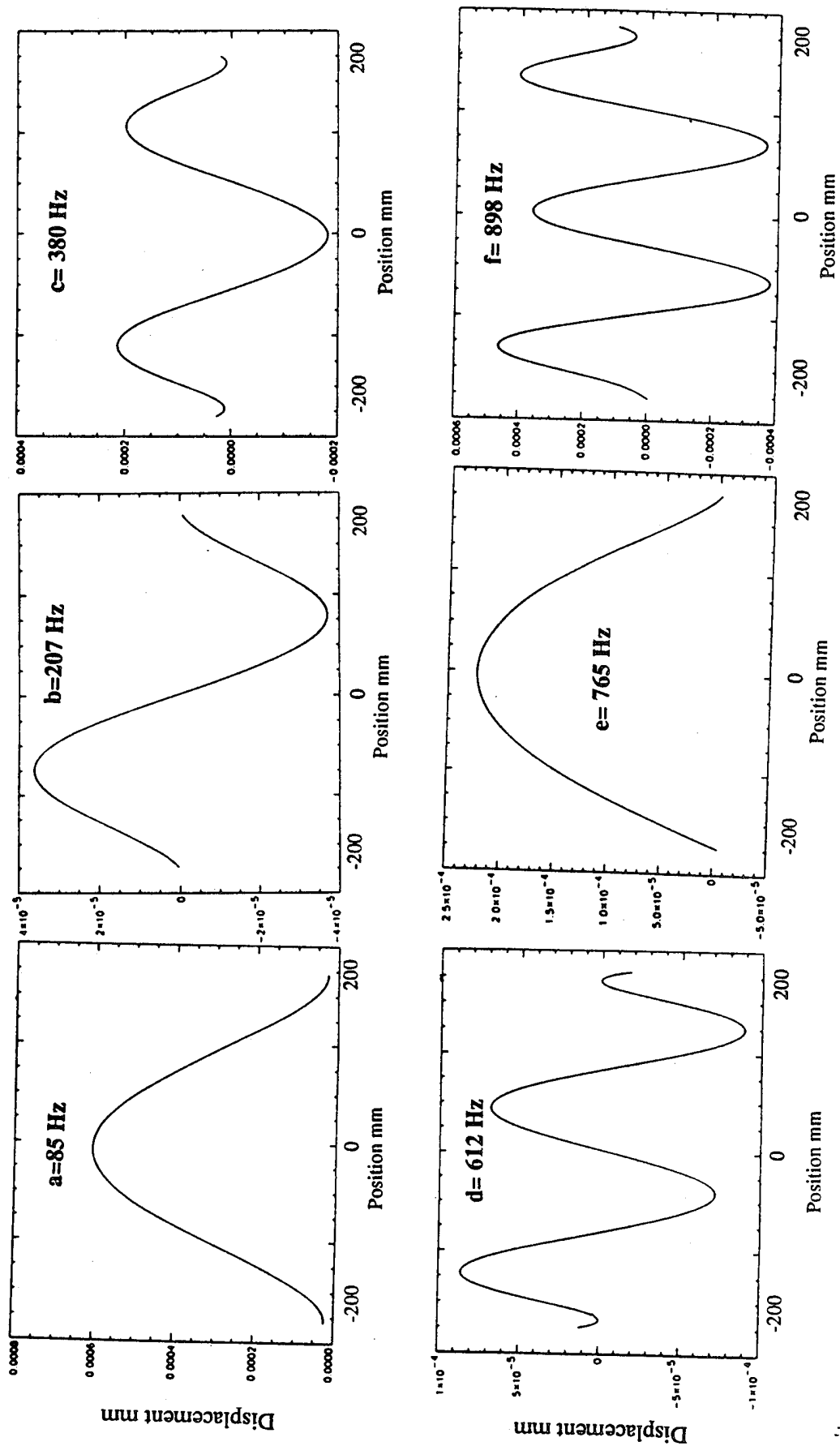


Fig 2.13 Mode shapes, acoustic excitation, a=85 Hz, b=207 Hz, c=380 Hz, d=612 Hz, e=765 Hz and f=898 Hz.

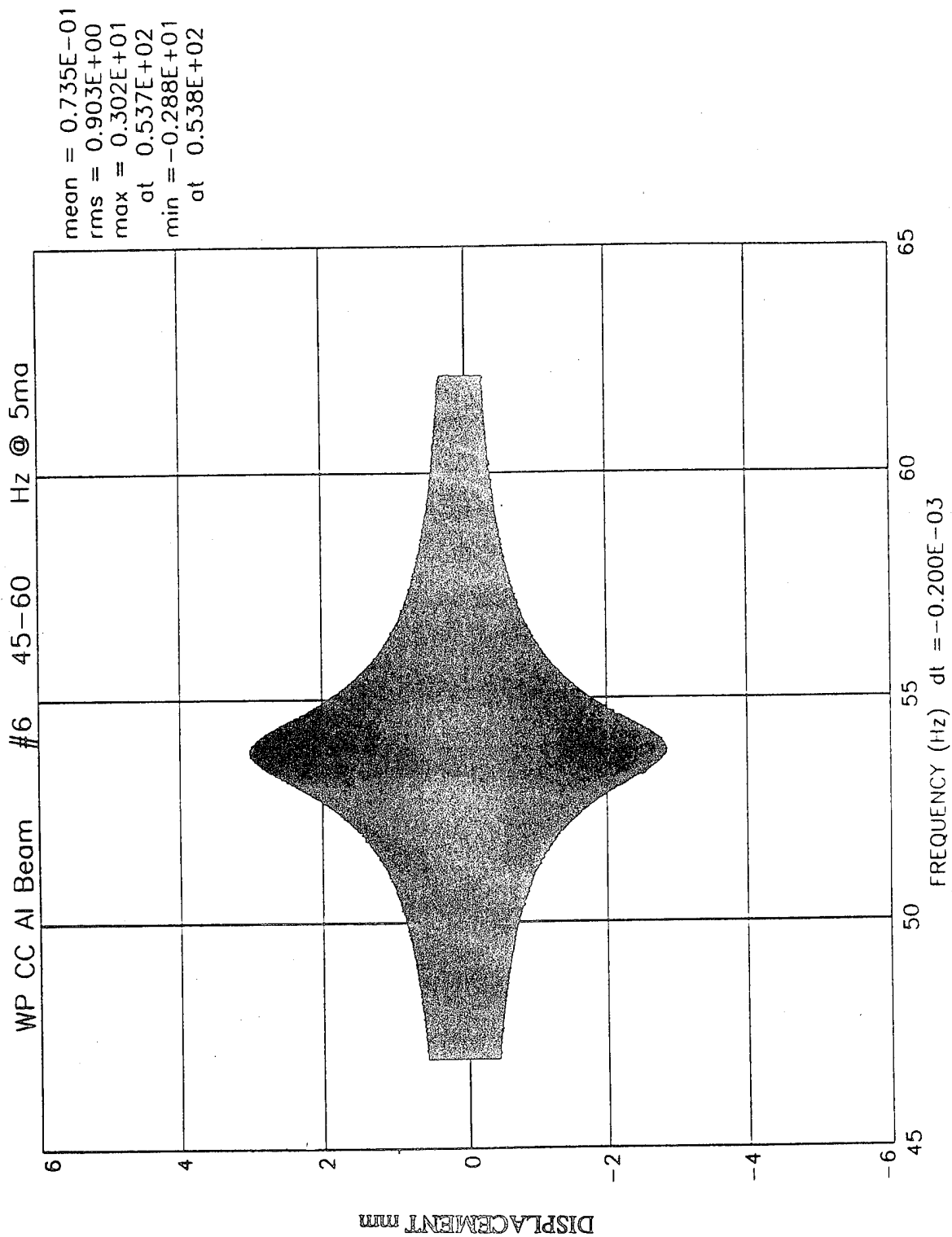


Fig 2.14 Slow sine sweep, low level coil excitation, 45- 60 Hz, C-C aluminium beam.

C-C AL BEAM STATIC DEFLECTIONS

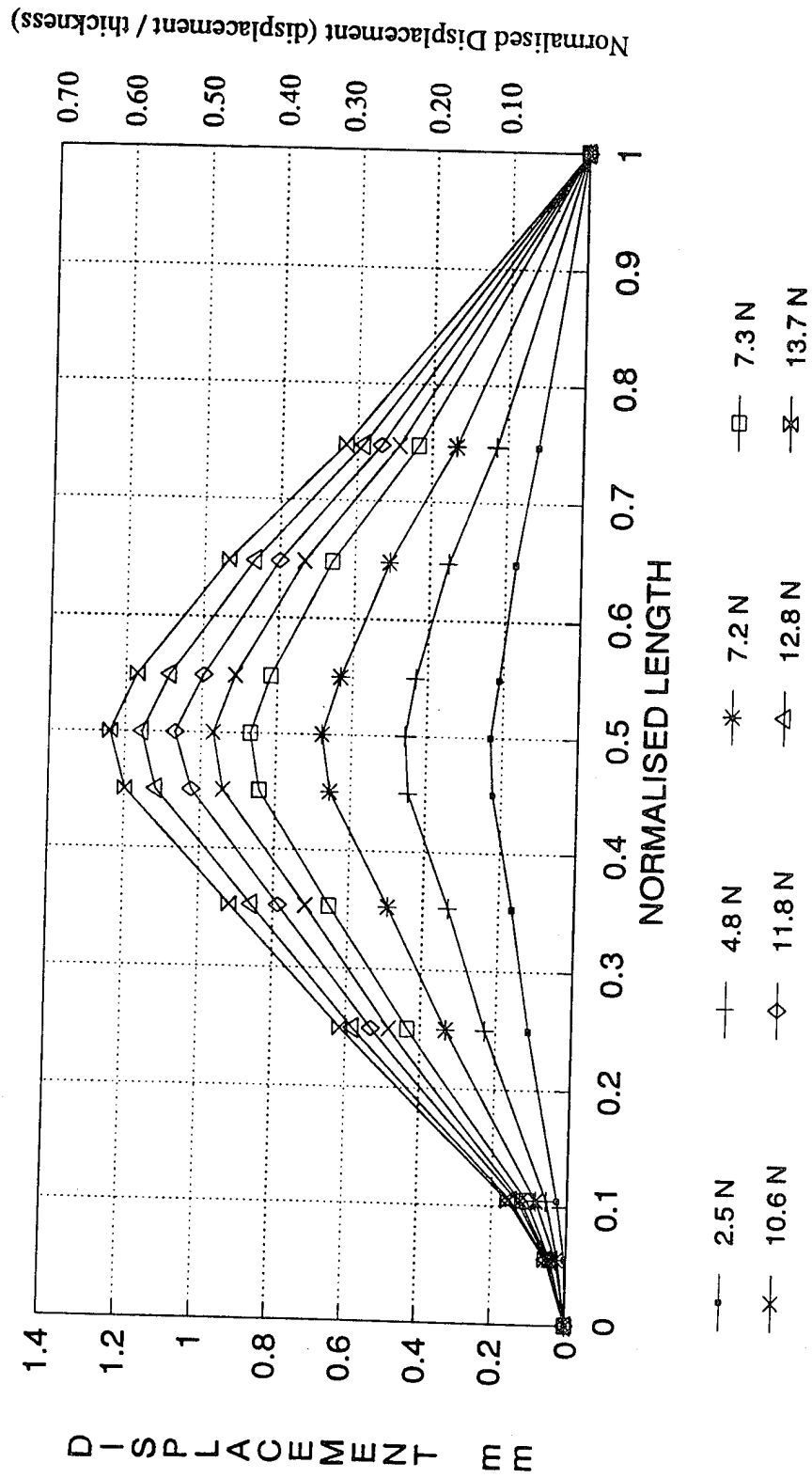


Fig 2.15 Nonlinear static transverse displacement shapes, C-C aluminium beam.

C-C ALUM BEAM STATIC TEST - BENDING

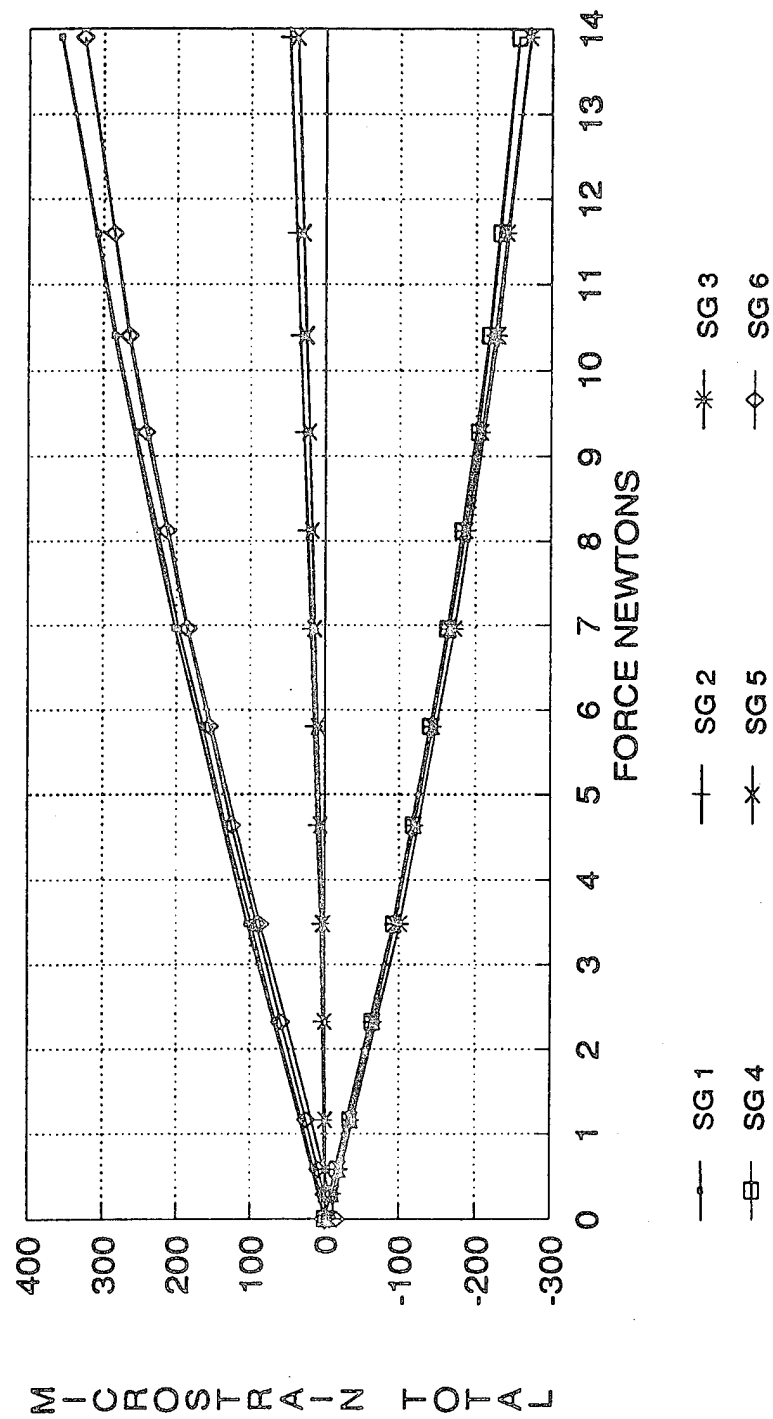


Fig 2.16 Total static strains for increasing and decreasing forces, C-C aluminium beam.

C-C AL BEAM STATIC TEST - BENDING

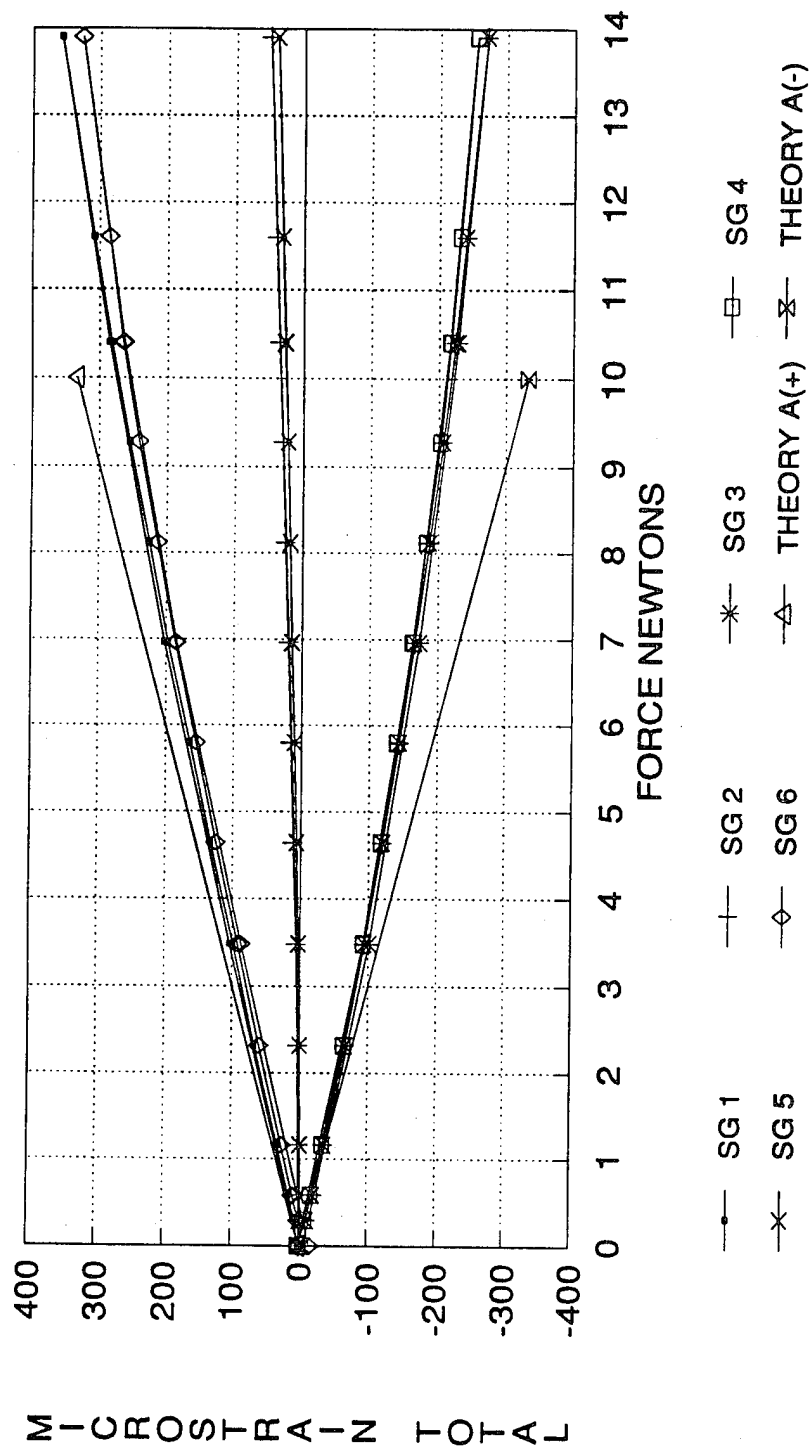


Fig 2.17 Total static strains compared with linear theoretical results, C-C aluminium beam

C-C AL BEAM SINE SWEEP

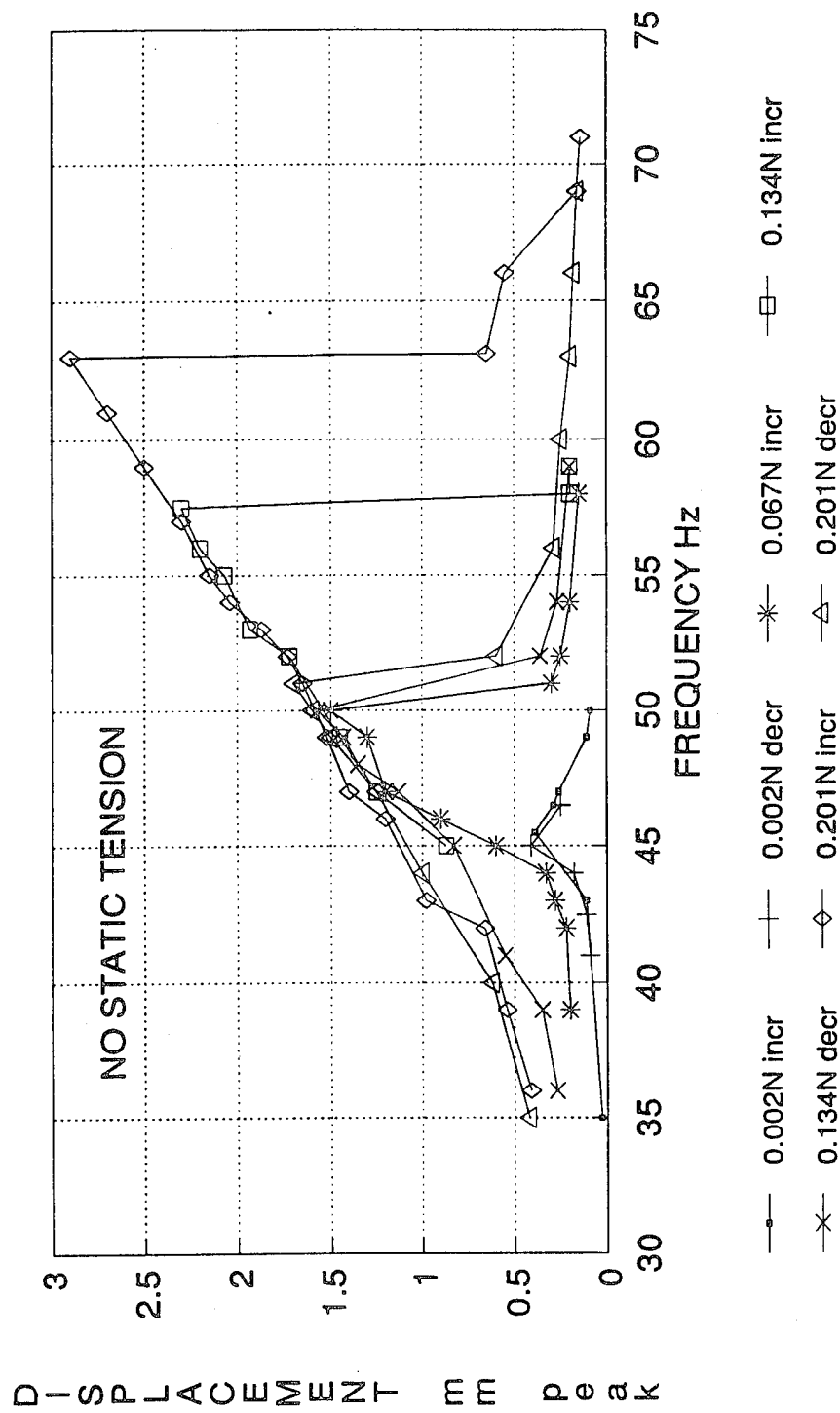


Fig 2.18 Nonlinear centre displacements for slow sine sweeps, increasing from 35-63 Hz and decreasing from 70-35 Hz, C-C aluminium beam.

C-C AL BEAM SINE DWELL

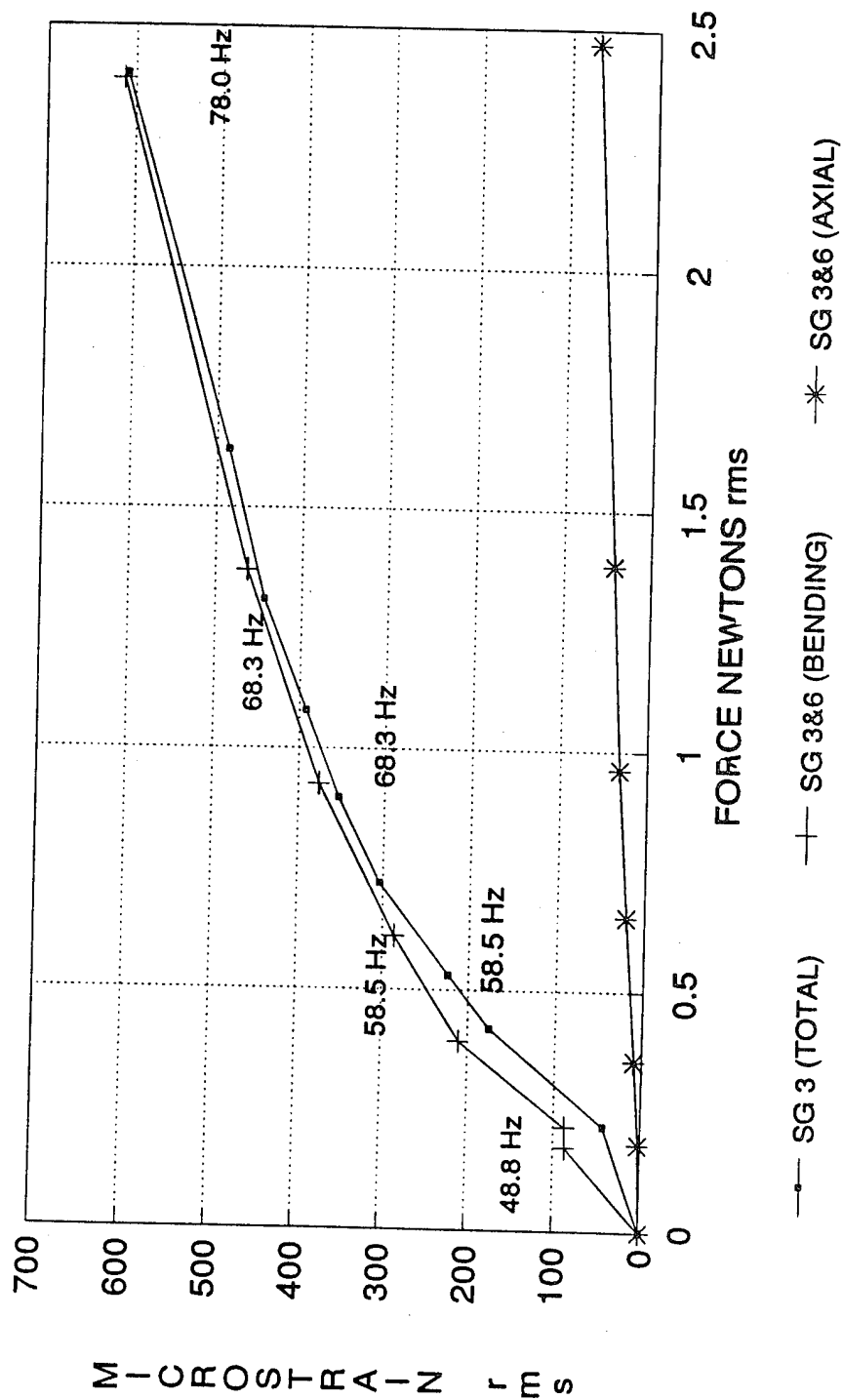


Fig 2.19 Total, axial and bending strains for sine dwell tests, C-C aluminium beam.

C-C AL BEAM SINE DWELL

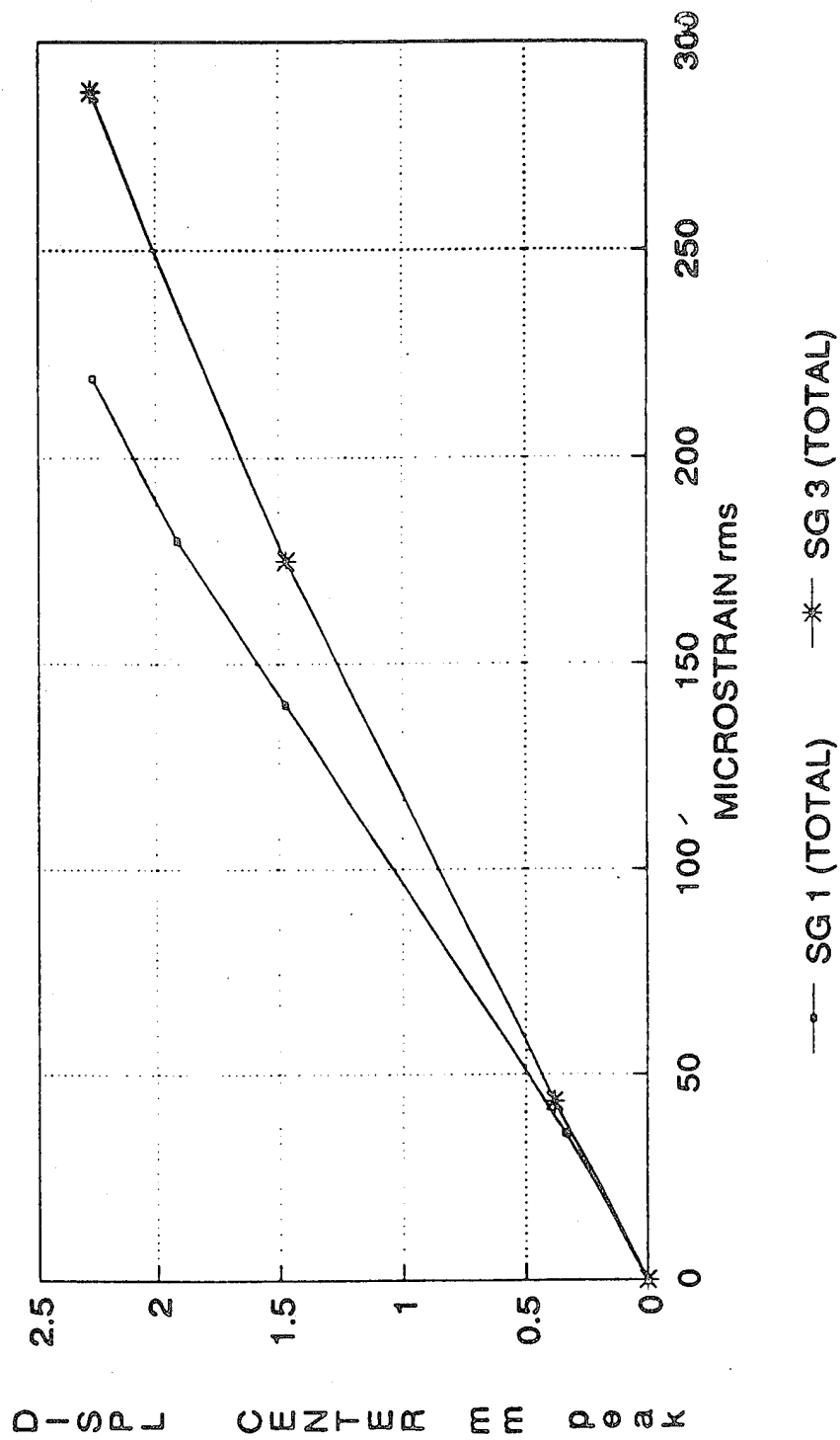


Fig 2.20 Sinusoidal strain vs displacement, C-C aluminium beam.

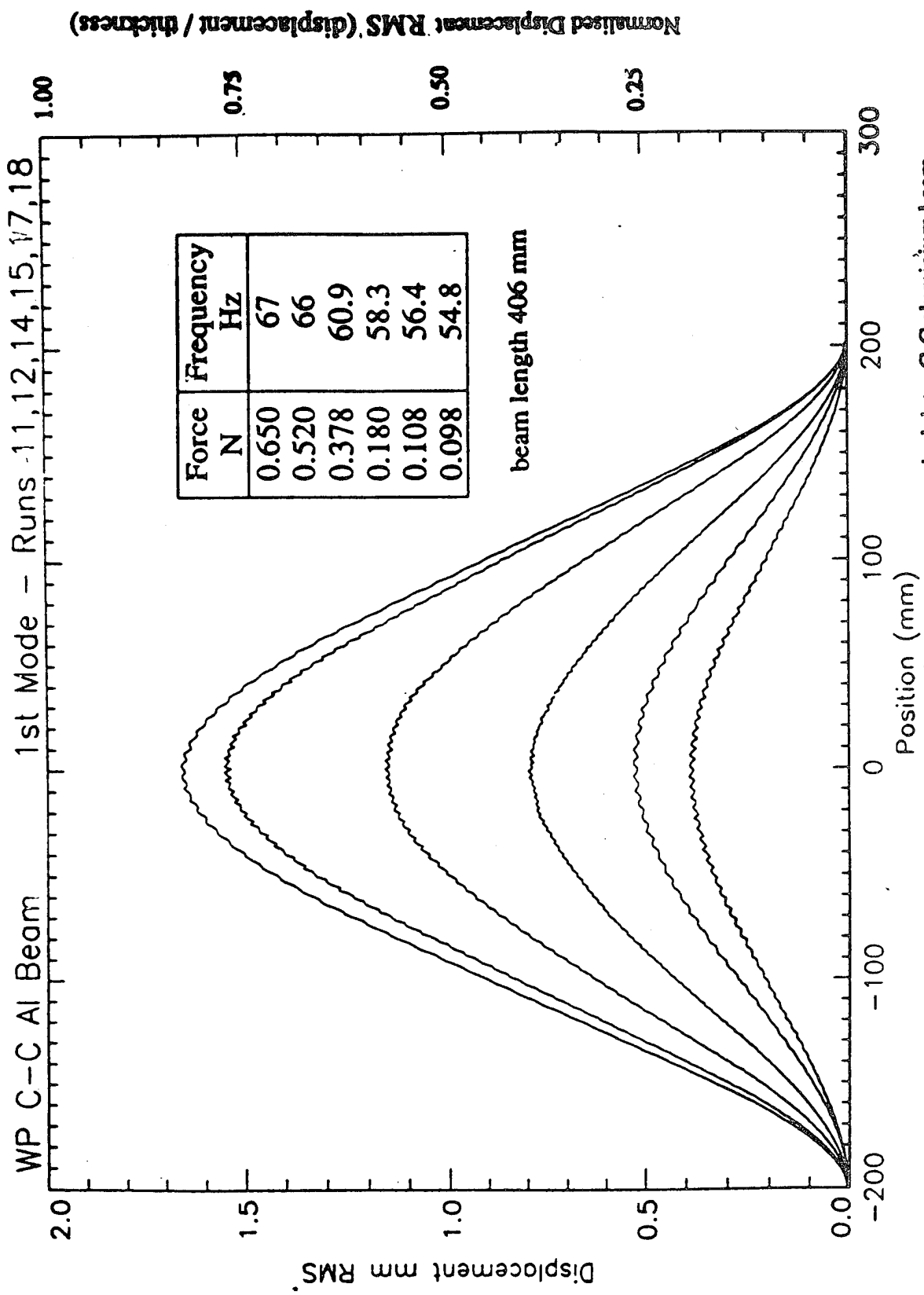


Fig 2.21 Nonlinear displacement shapes fundamental resonance, unsmoothed data, C-C aluminium beam.

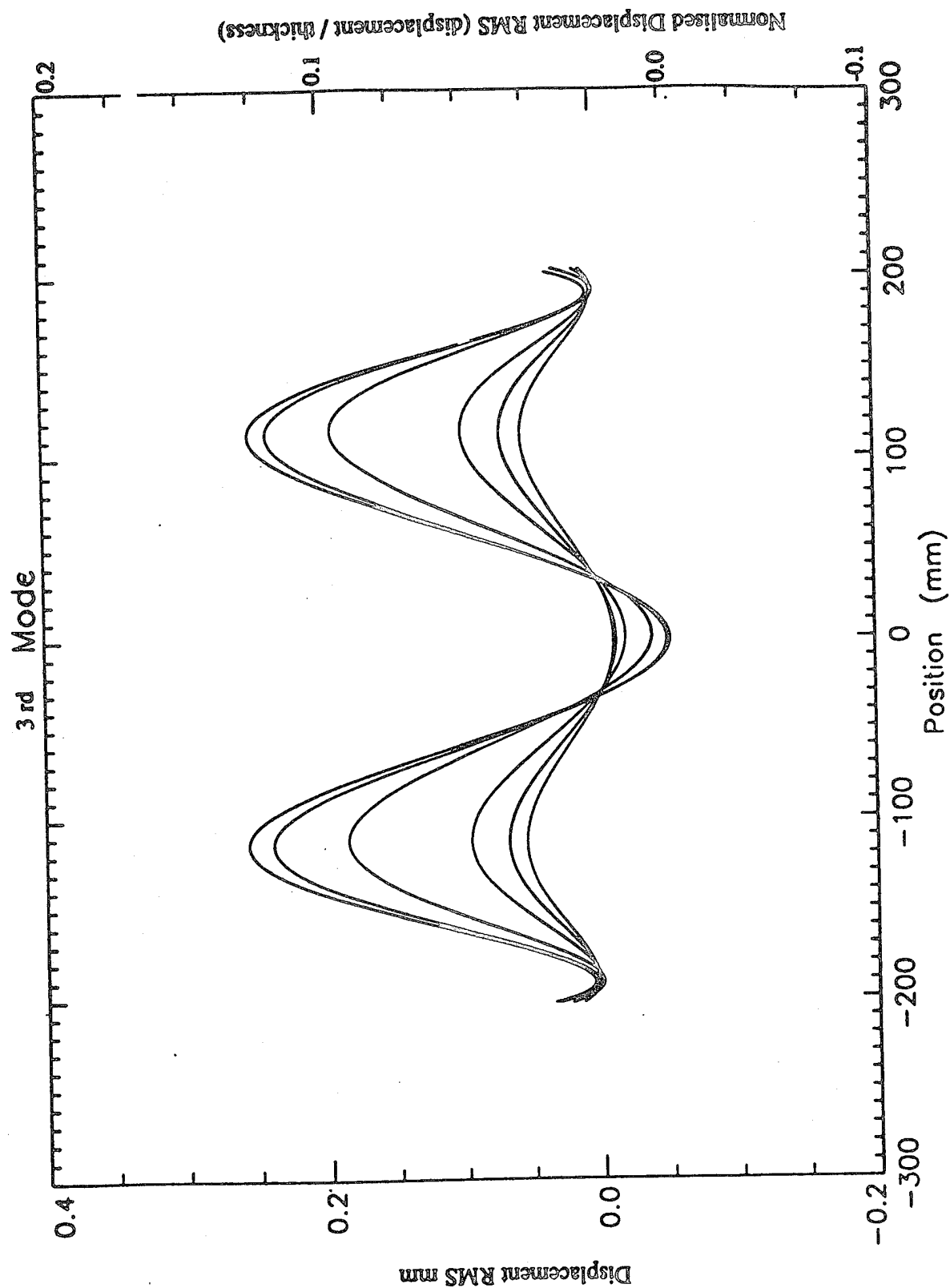


Fig 2.22 Nonlinear displacement shapes, third mode, seventh order polynomial fit, C-C aluminium beam.

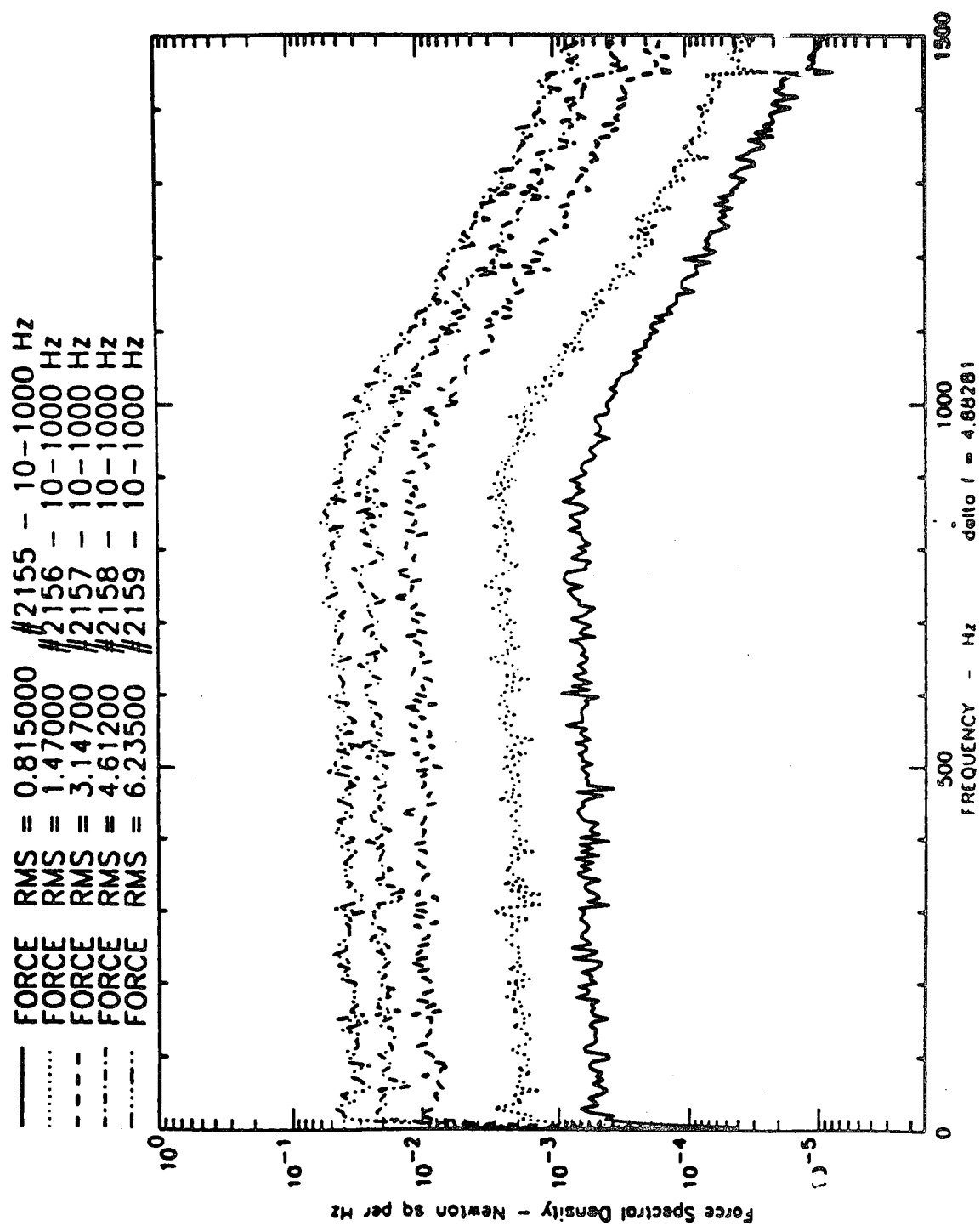


Fig 2.23 Force spectra densities, 10-1000 Hz random excitation, C-C Aluminium beam.

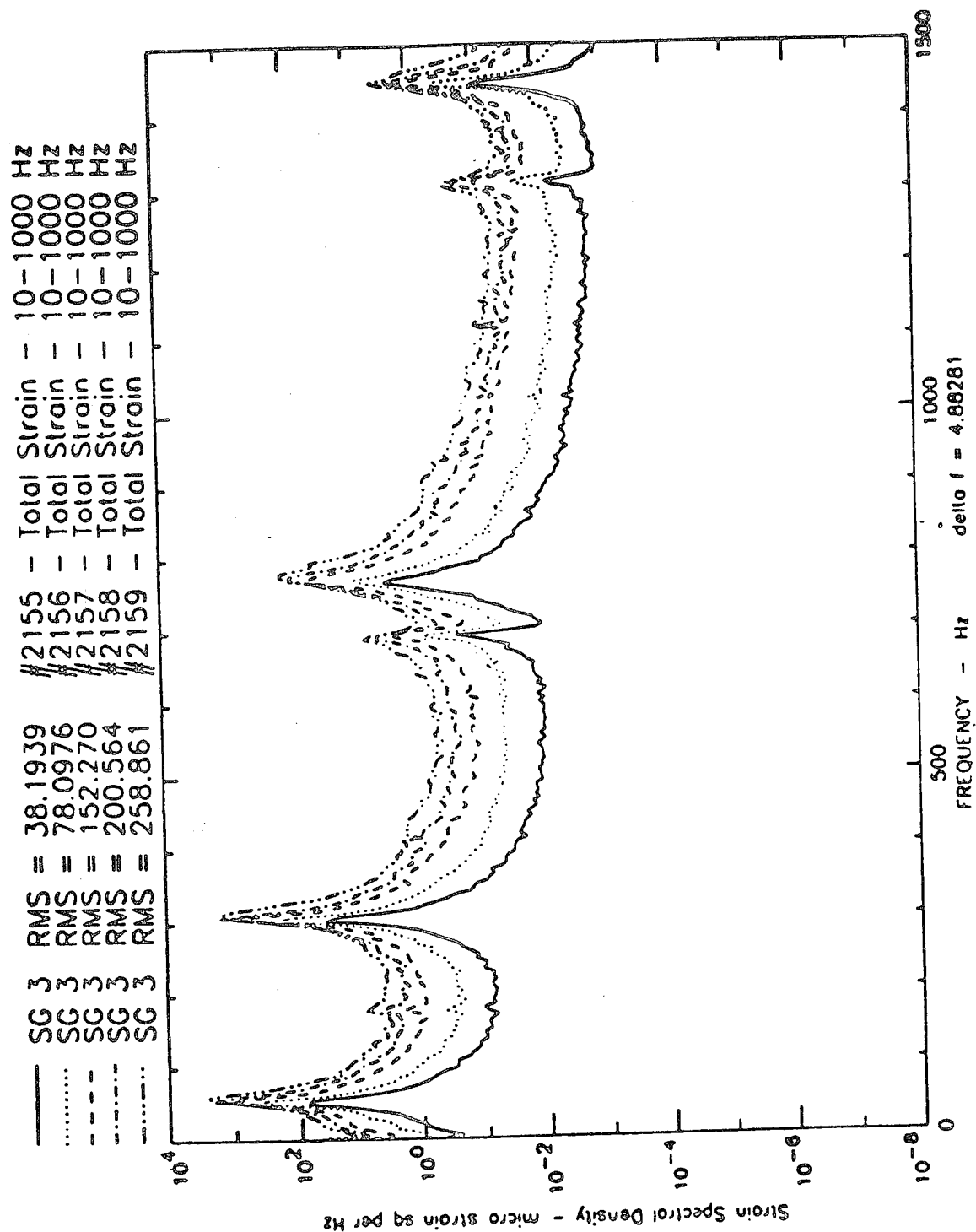


Fig 2.24 Total strain spectral densities, 10-1000 Hz random excitation, SG 3, C-C aluminium beam.

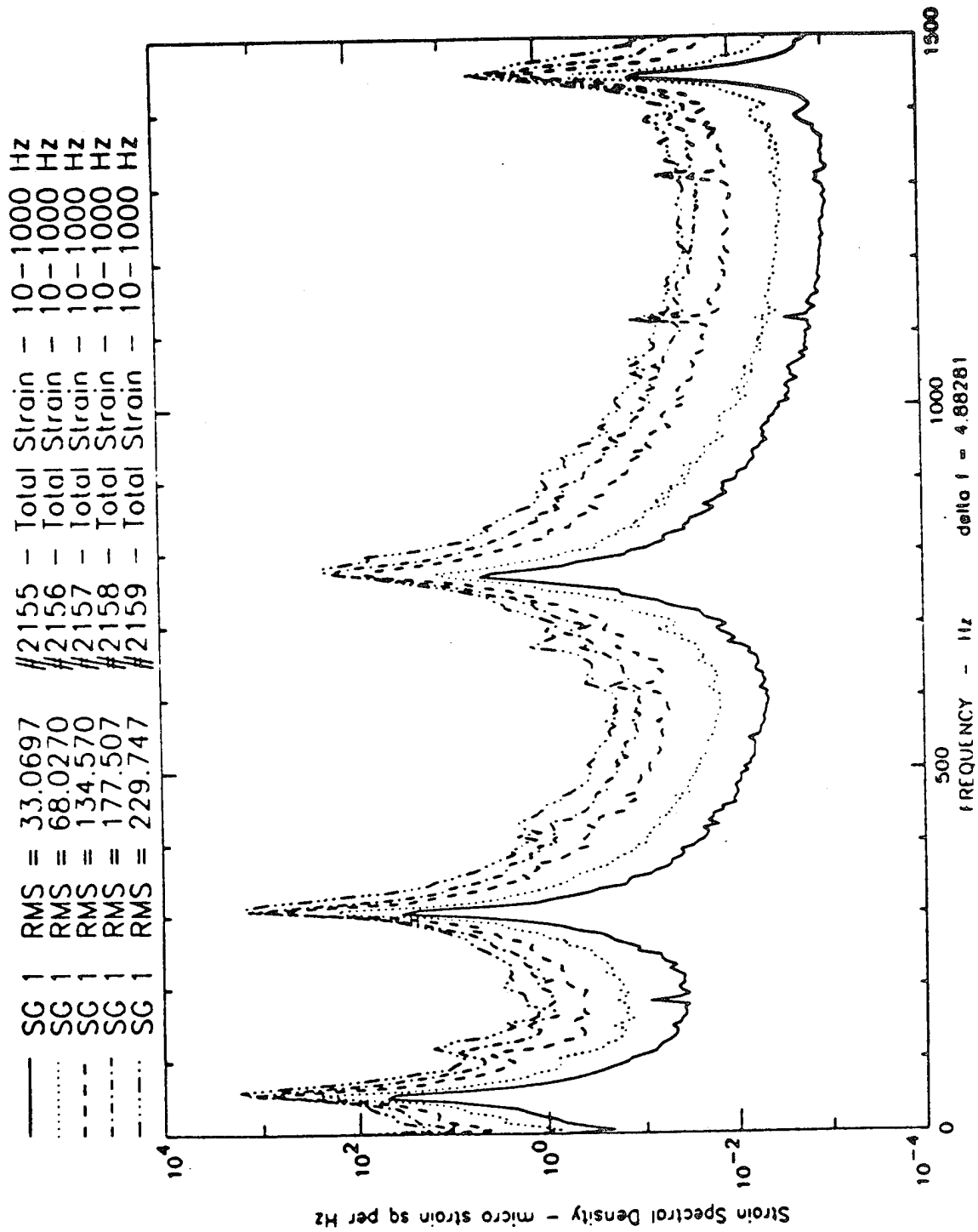


Fig 2.25 Total strain spectral densities, 10-1000 Hz random excitation, SG 1, C-C aluminium beam.

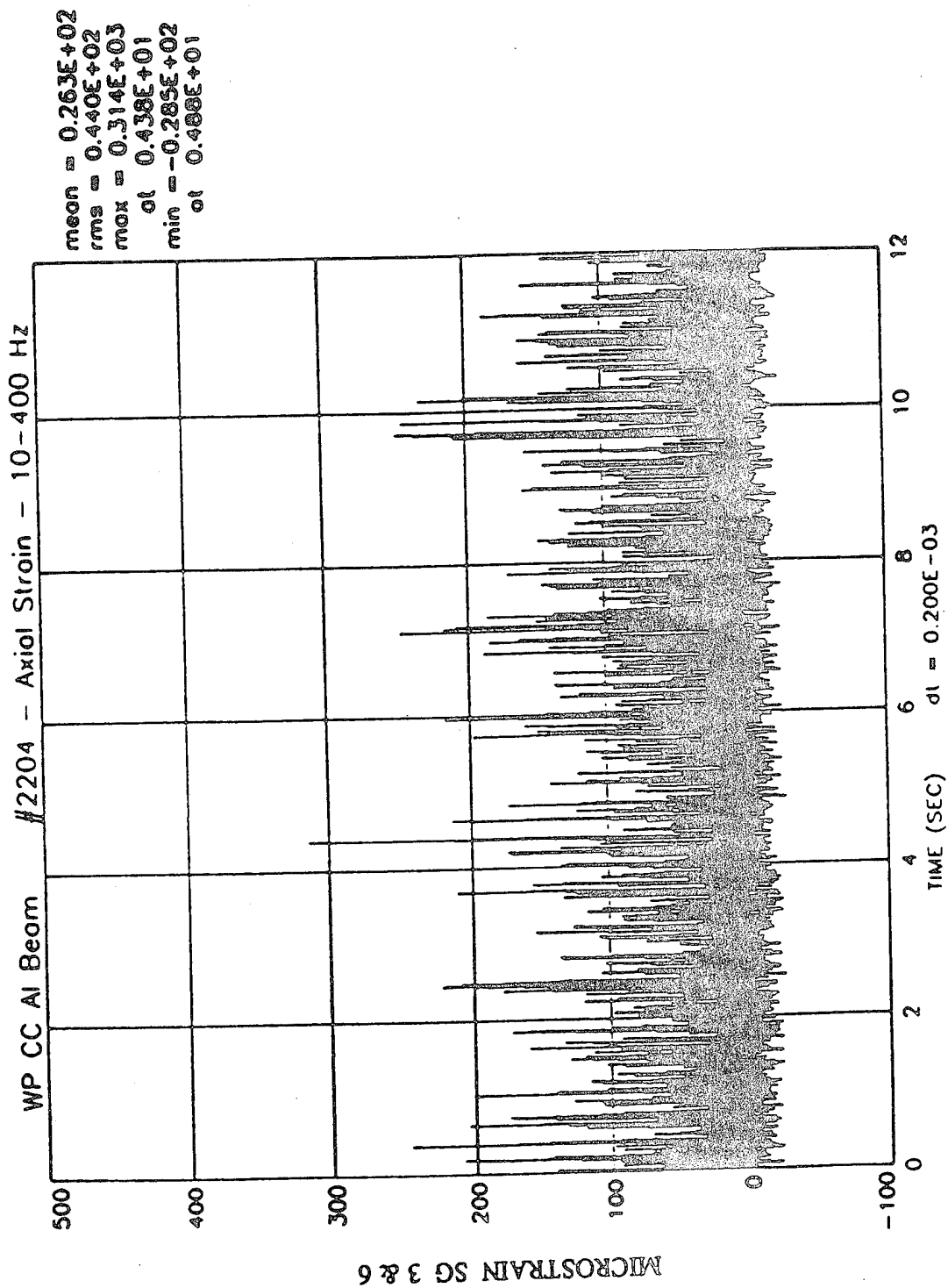


Fig 2.26 Axial strain time history, 10-400 Hz random excitation, SG 3 and 6, C-C aluminium beam.

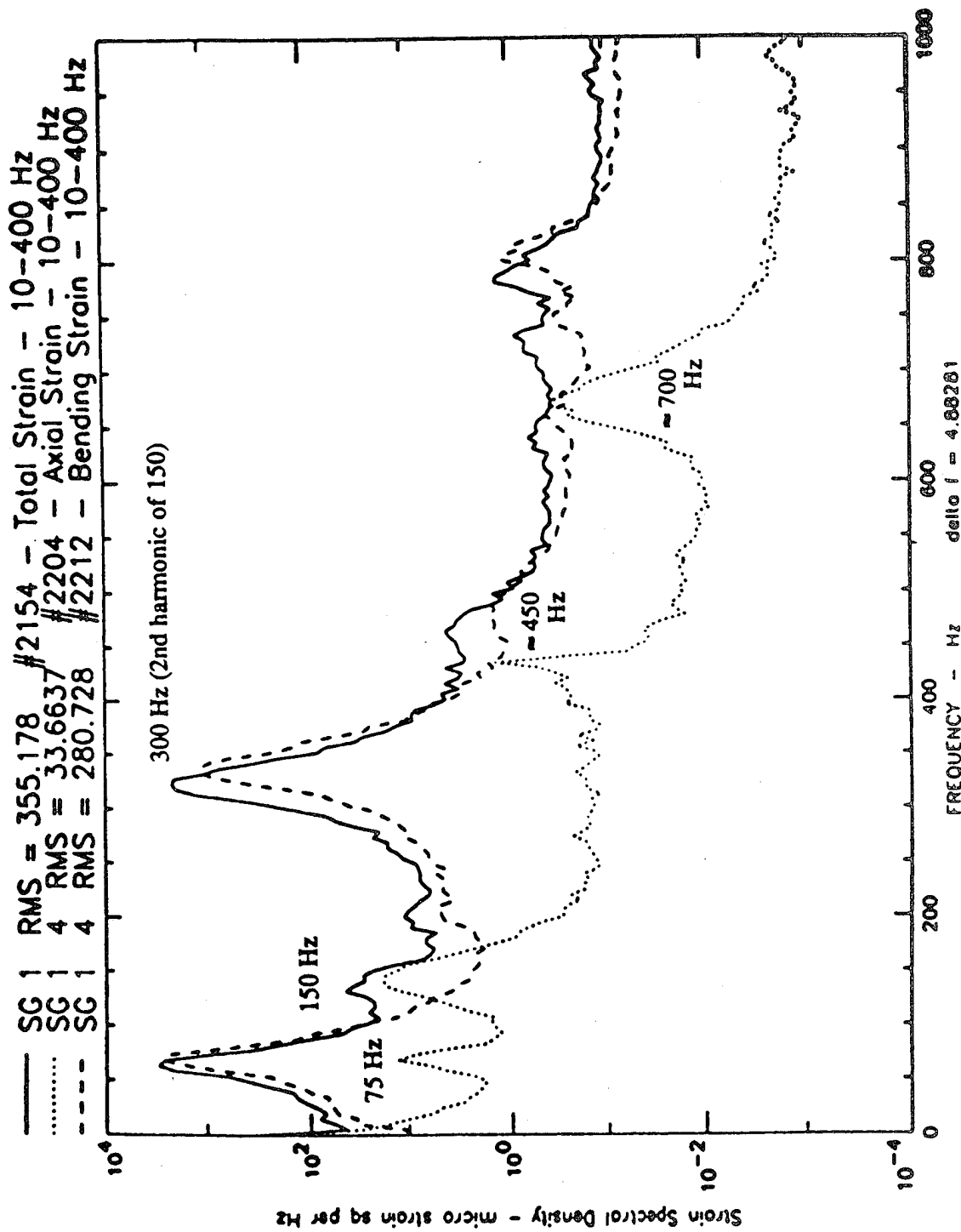


Fig 2.27 Total axial bending strain spectral densities, 10-400 Hz random excitation, SG 1, 1 & 4, C-C aluminium beam.

C-C AL BEAM
10-400HZ RANDOM

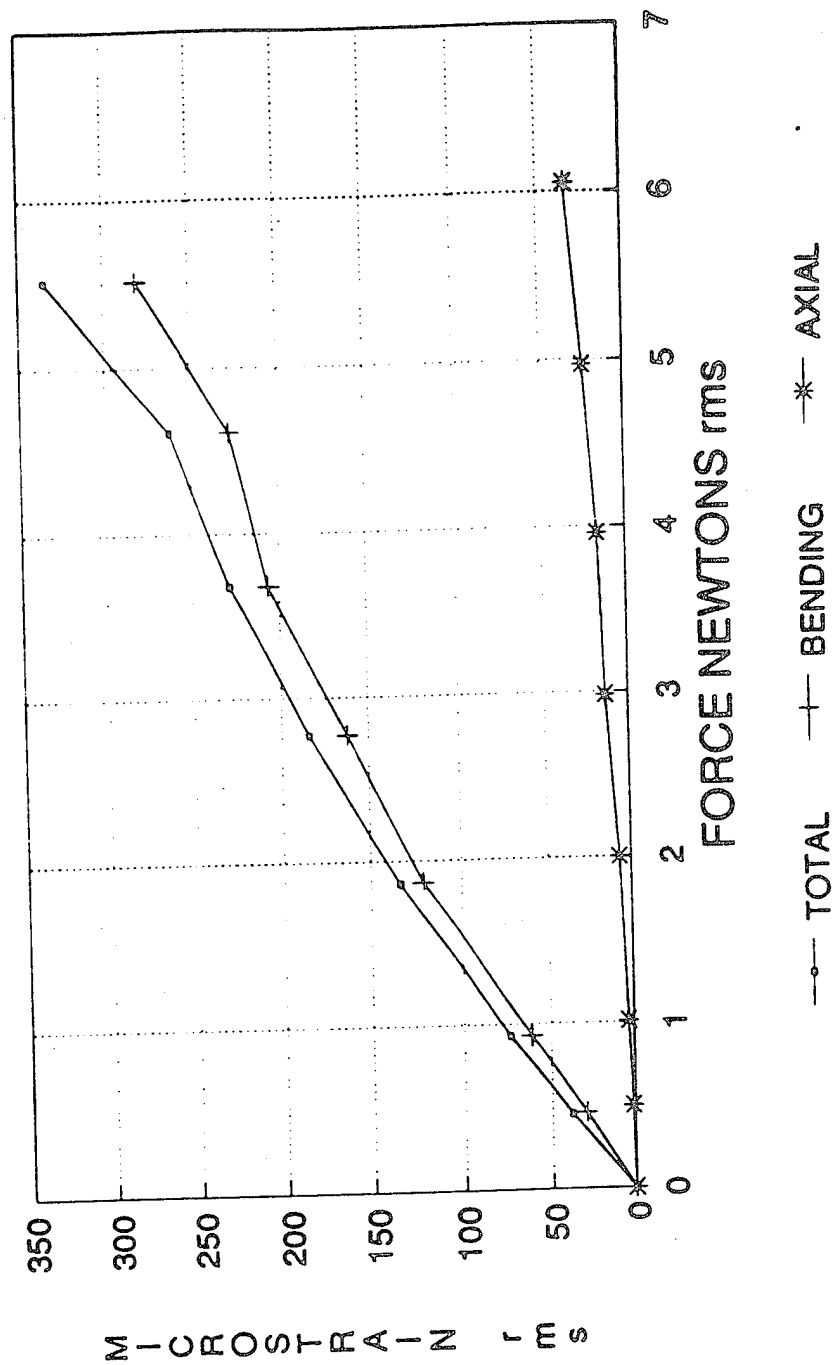


Fig 2.28 Total, axial and bending strains, 10-400 Hz random excitation, SG 3, C-C aluminium beam.

C-C Al Beam
Amplitude PDF Force Rec 2155-2159

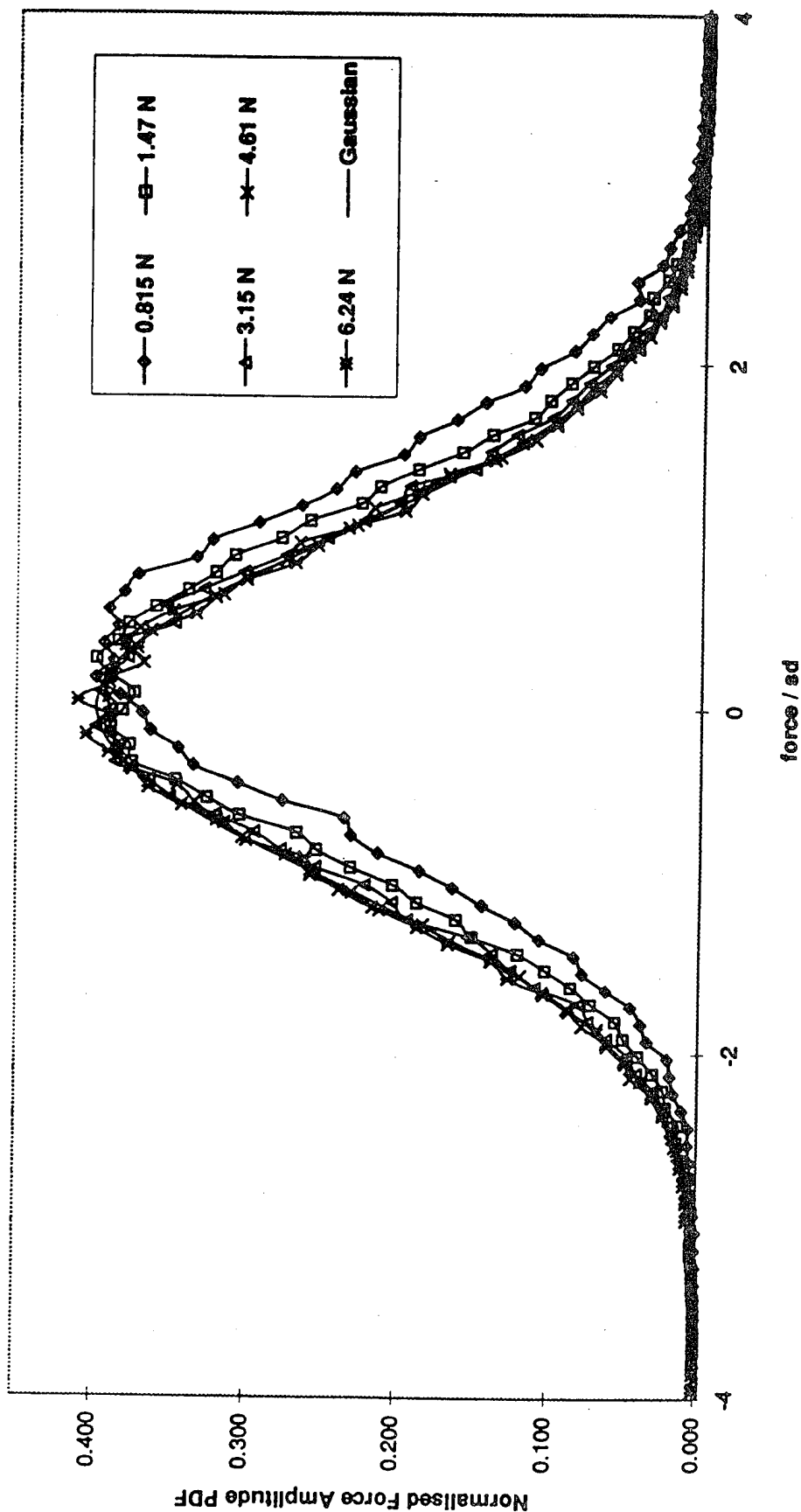


Fig 2.29 Normalised force amplitude PDFs, 10-1000 Hz random excitation, C-C aluminium beam.

C-C ALUM BEAM
Amplitude PDF SG 1 Rec 2155-2159

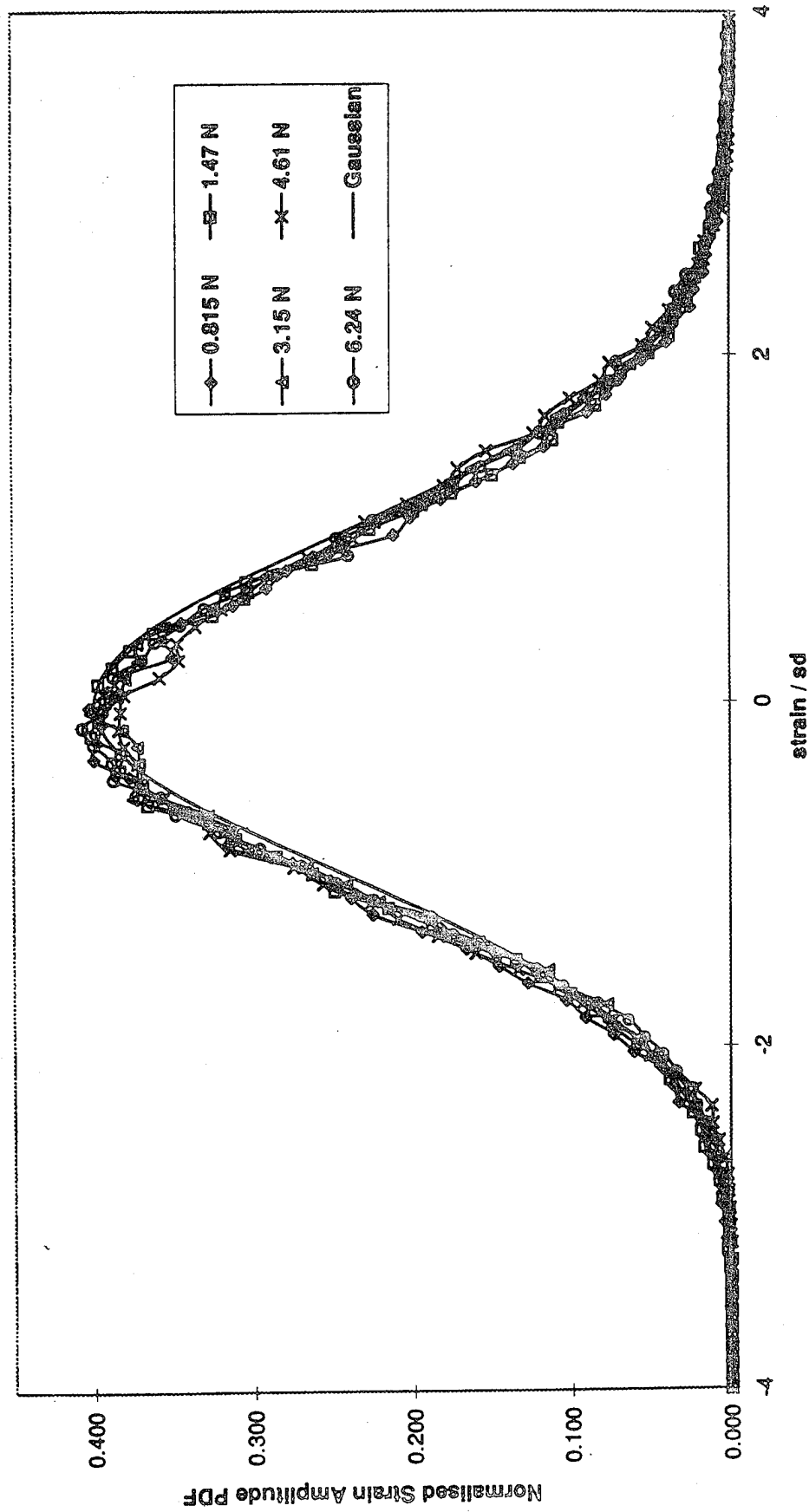


Fig 2.30 Normalised Strain amplitude PDFs, 10-1000 Hz random excitation, SG 1,C-C aluminium beam.

C-C AL BEAM
Amplitude PDF SG 3 Rec 2162

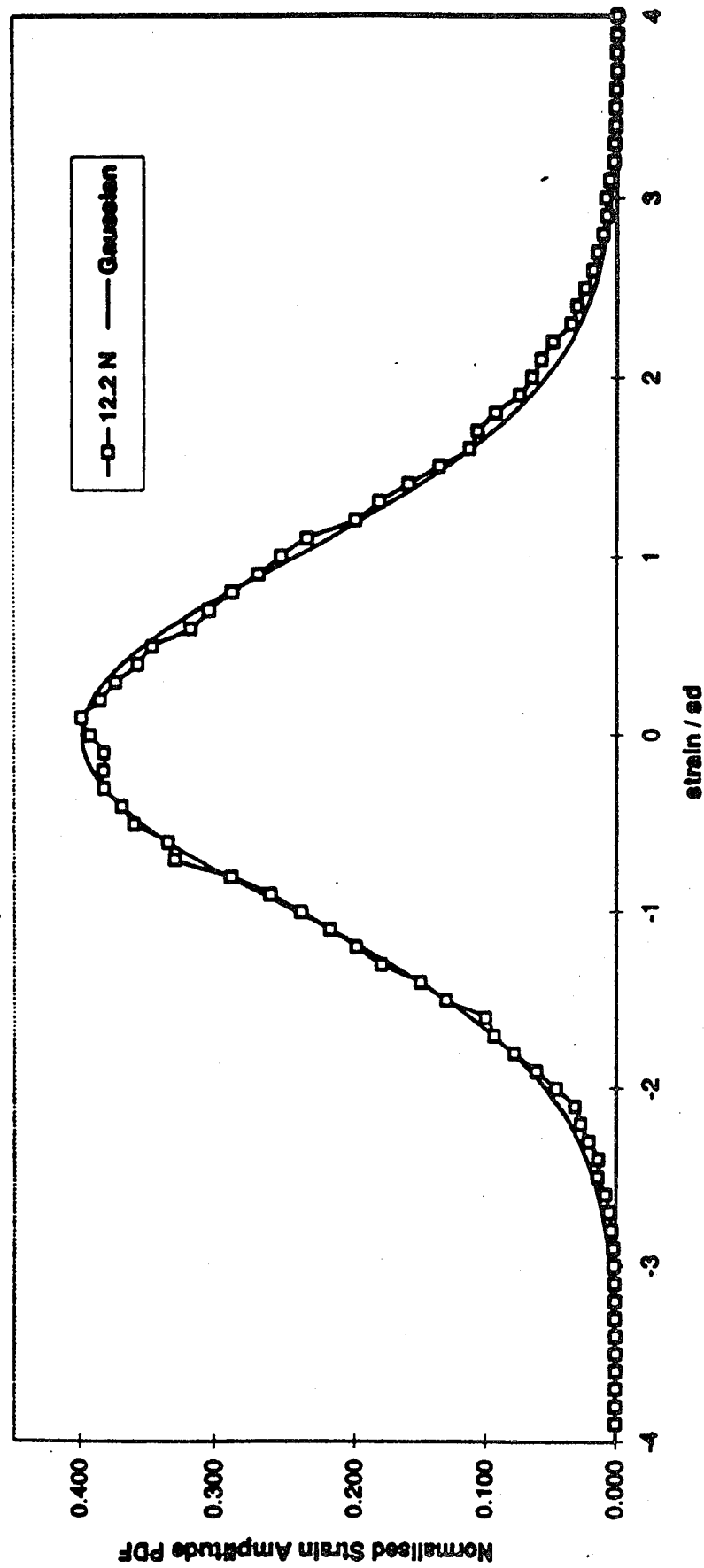


Fig 2.31 Normalised strain amplitude PDFs, 10-1000 Hz random excitation, SG 3, C-C aluminium beam.

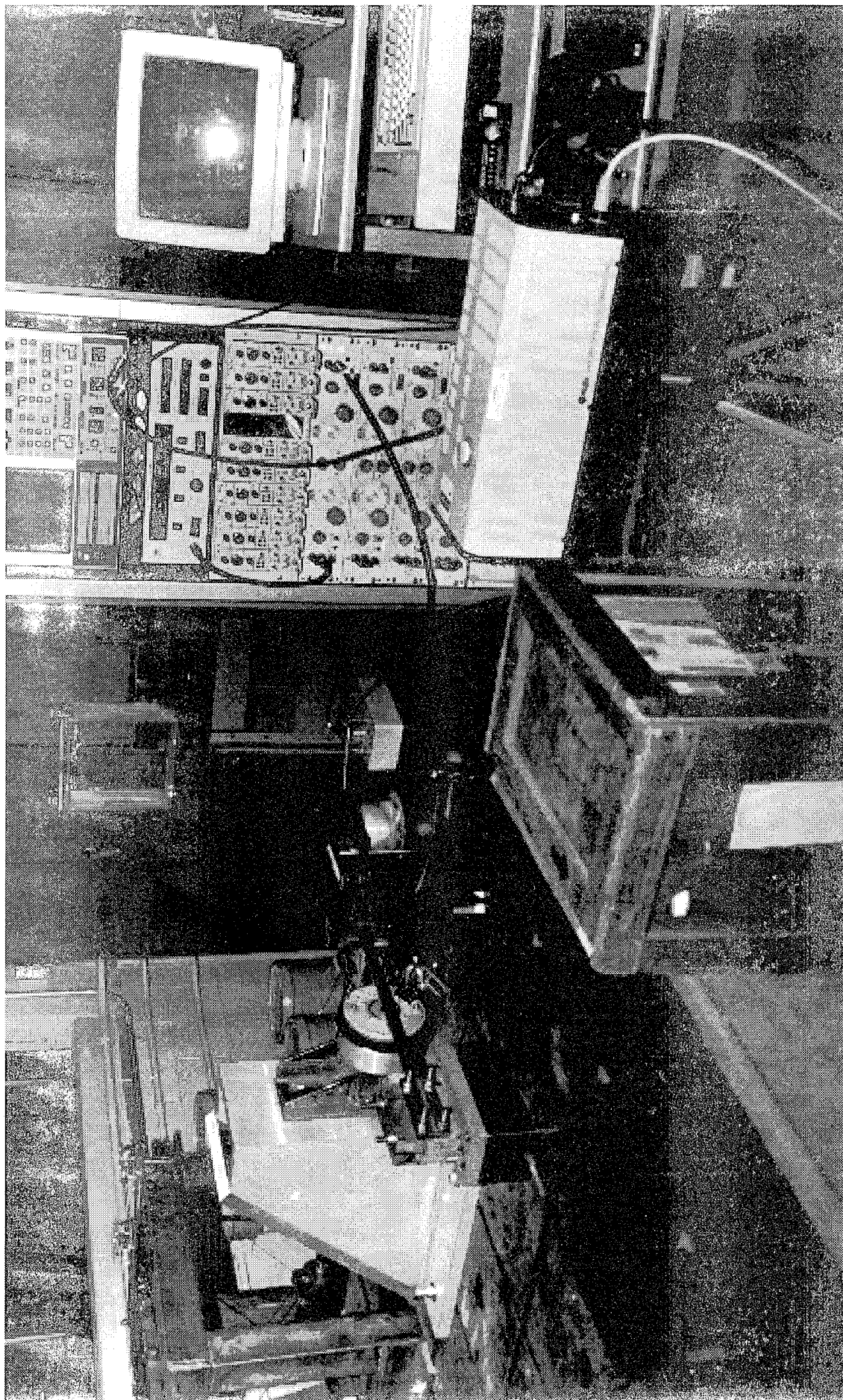


Fig 2.32 Photograph of test arrangement for linear mode shape, C-C CFRP beam.

C-C CFRP BEAM STATIC BENDING

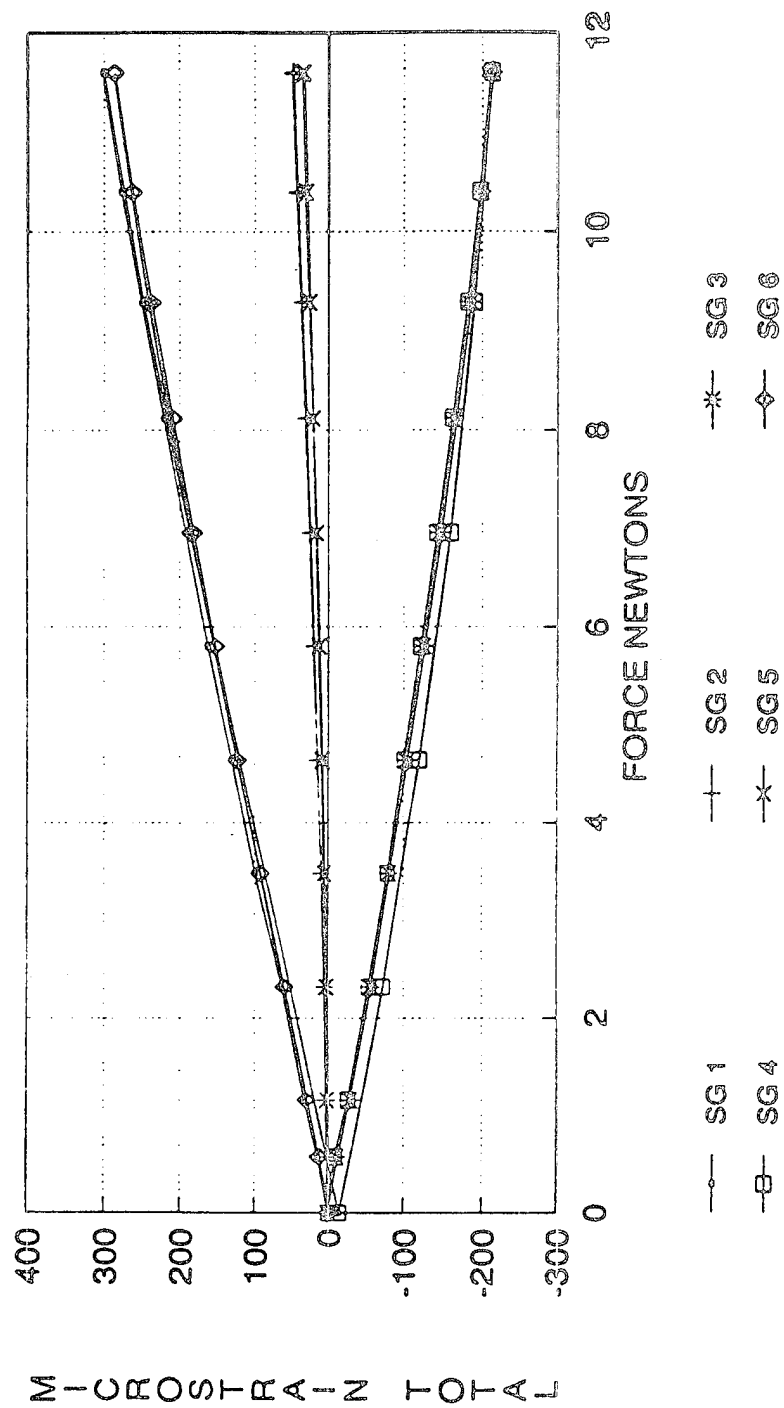


Fig 2.33 Total static strains, C-C CFRP beam.

C-C CFRP BEAM STATIC BENDING

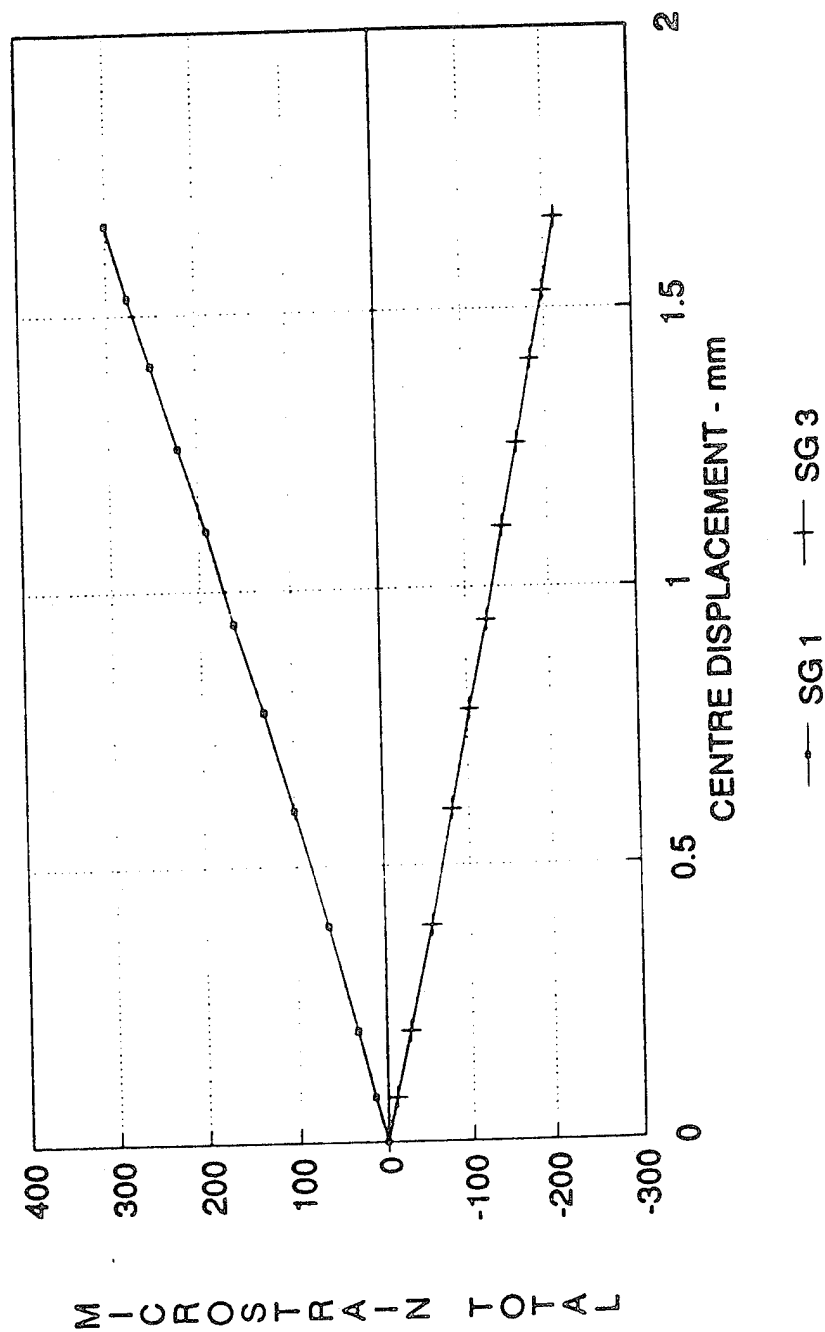


Fig 2.34 Static stain vs displacement, SG 1 and 3, C-C, CFRP beam.

C-C CFRP BEAM SINE SWEEP

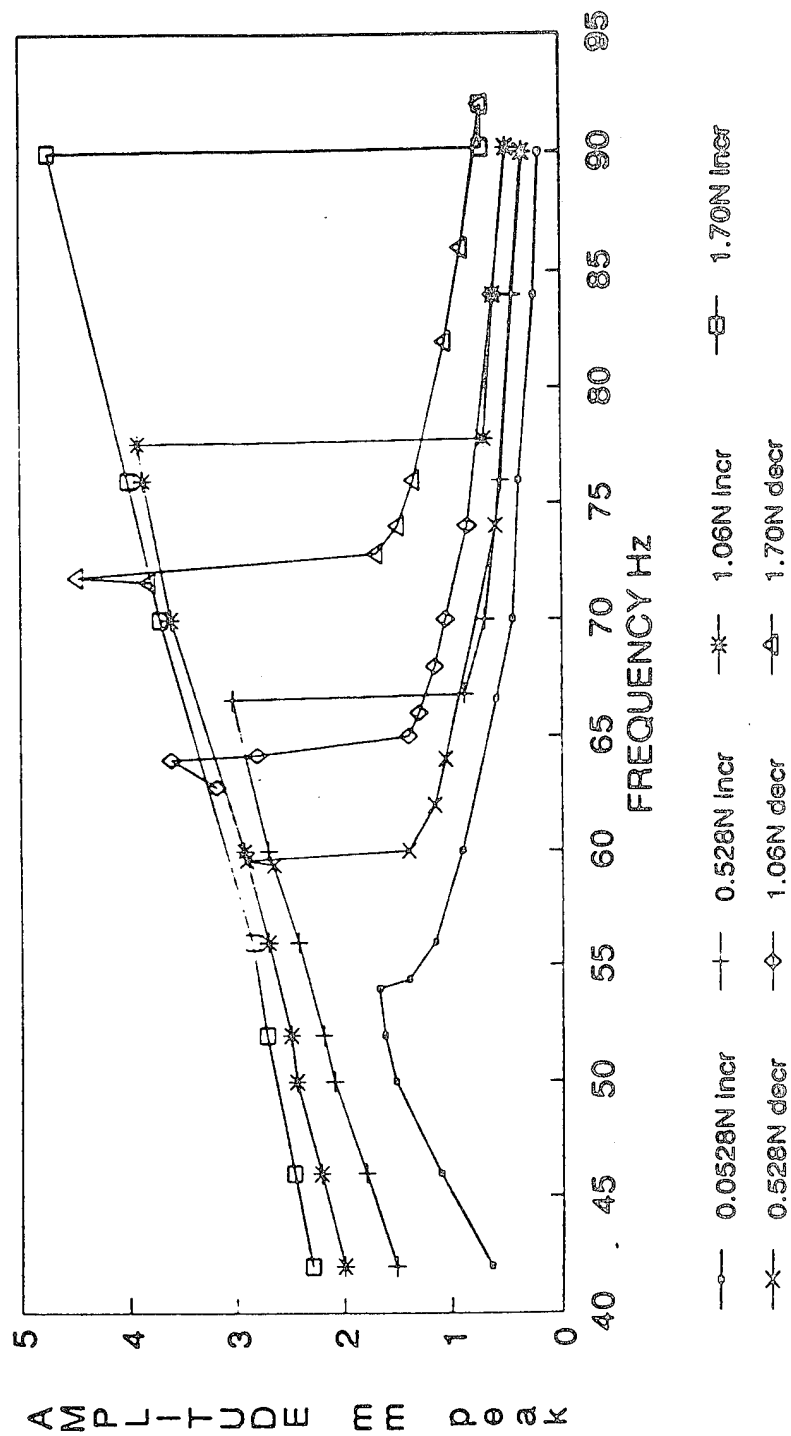


Fig 2.35 Nonlinear centre displacements for slow sine sweeps increasing from 41-93 Hz and decreasing from 90-41 Hz C-C, CFRP beam.

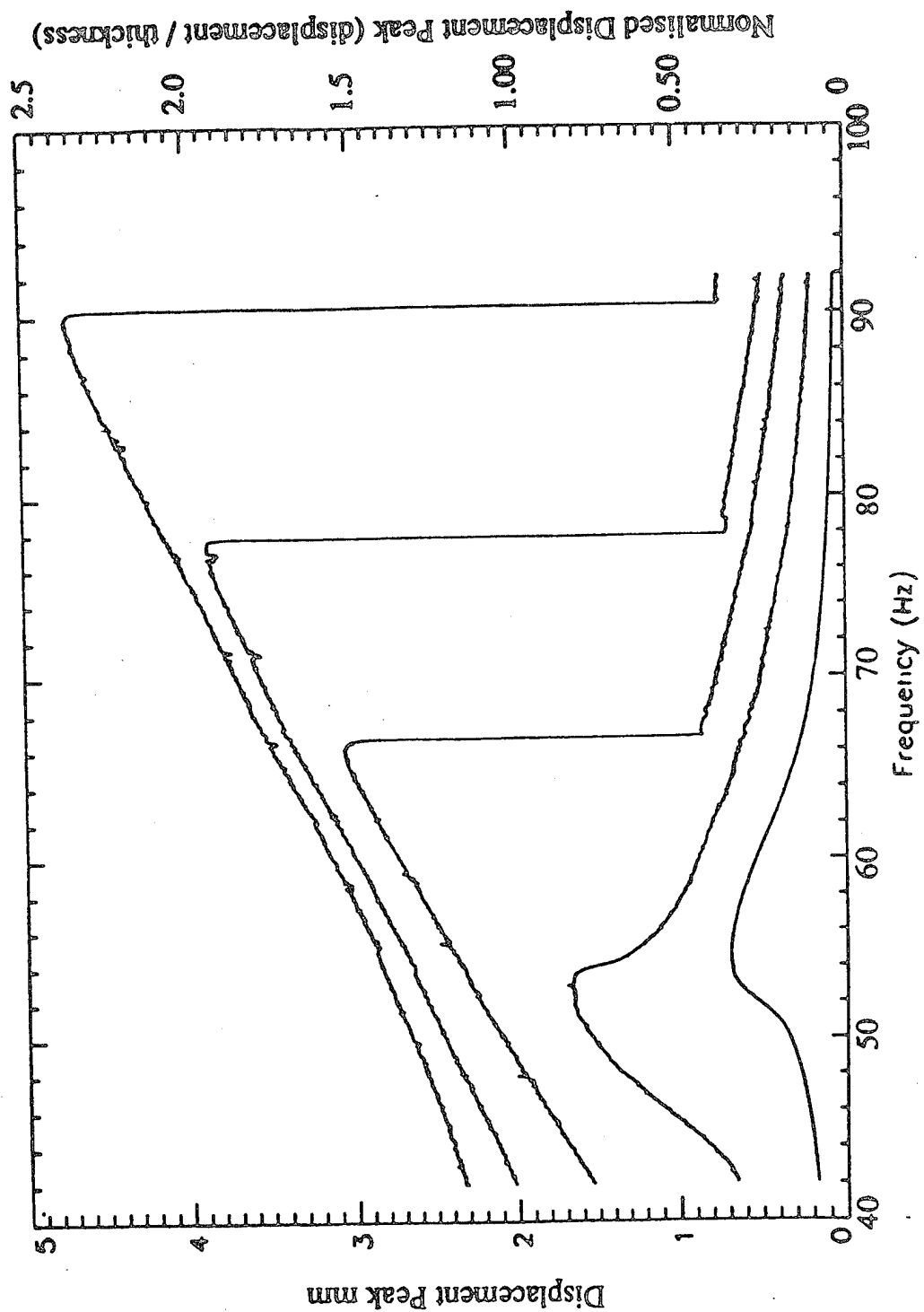


Fig 2.36 Slow sine sweeps, increasing 40-90 Hz, C-C CFRP beam.

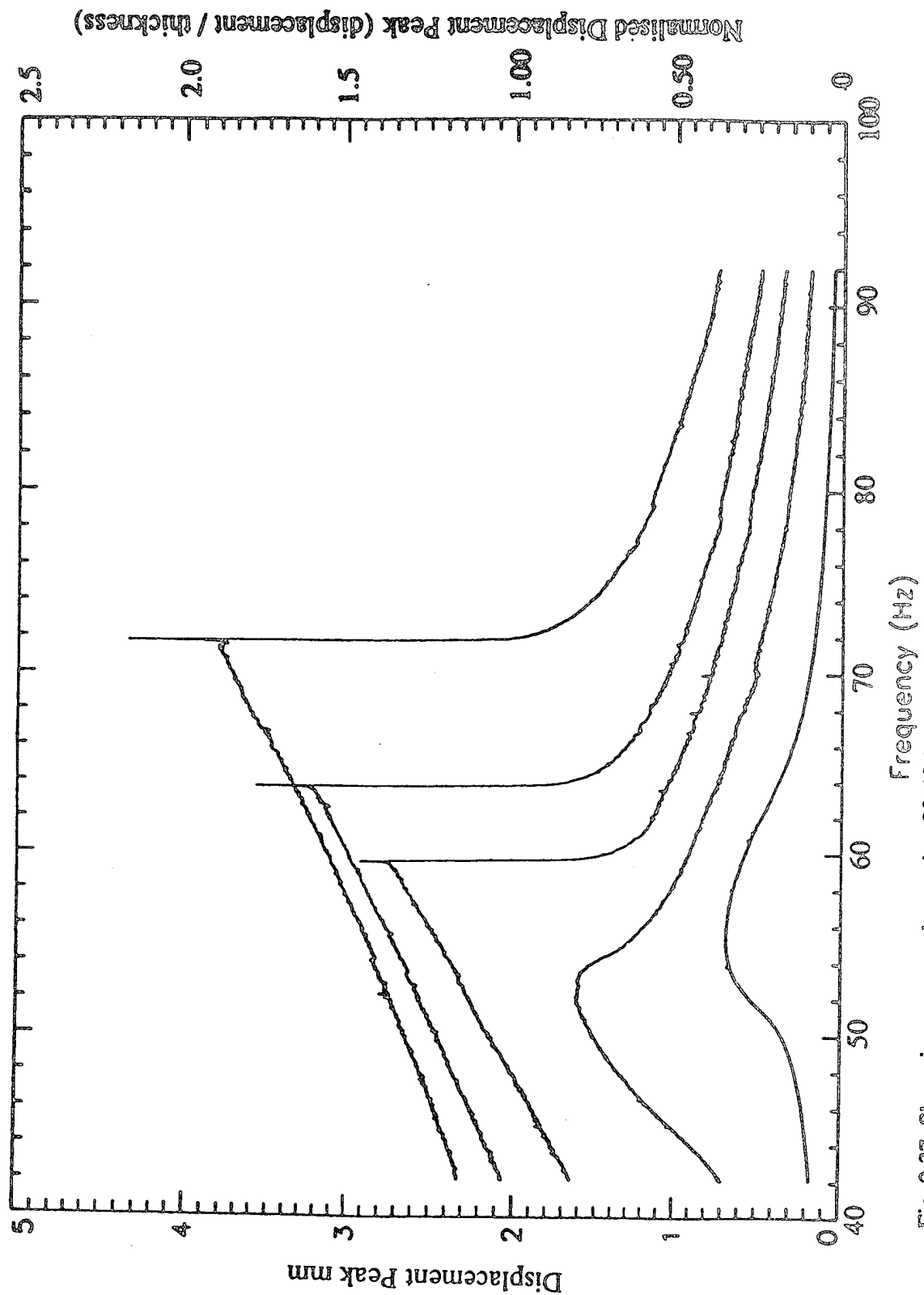


Fig 2.37 Slow sine sweeps, decreasing 90-40 Hz, C-C CFRP beam.

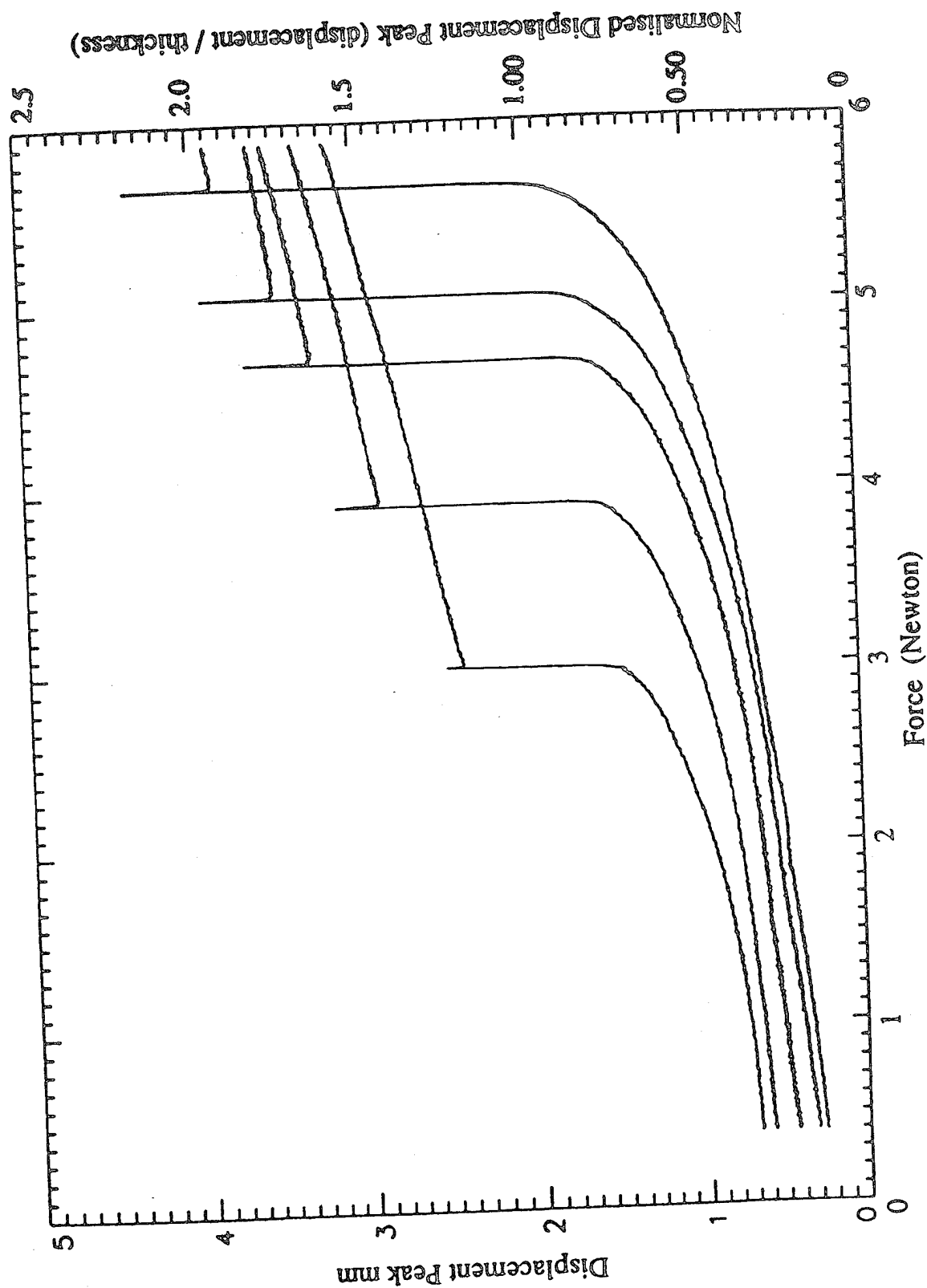


Fig 2.38 Slow amplitude sweeps, increasing excitation force 0.5-6N at constant frequency C-C CFRP beam.

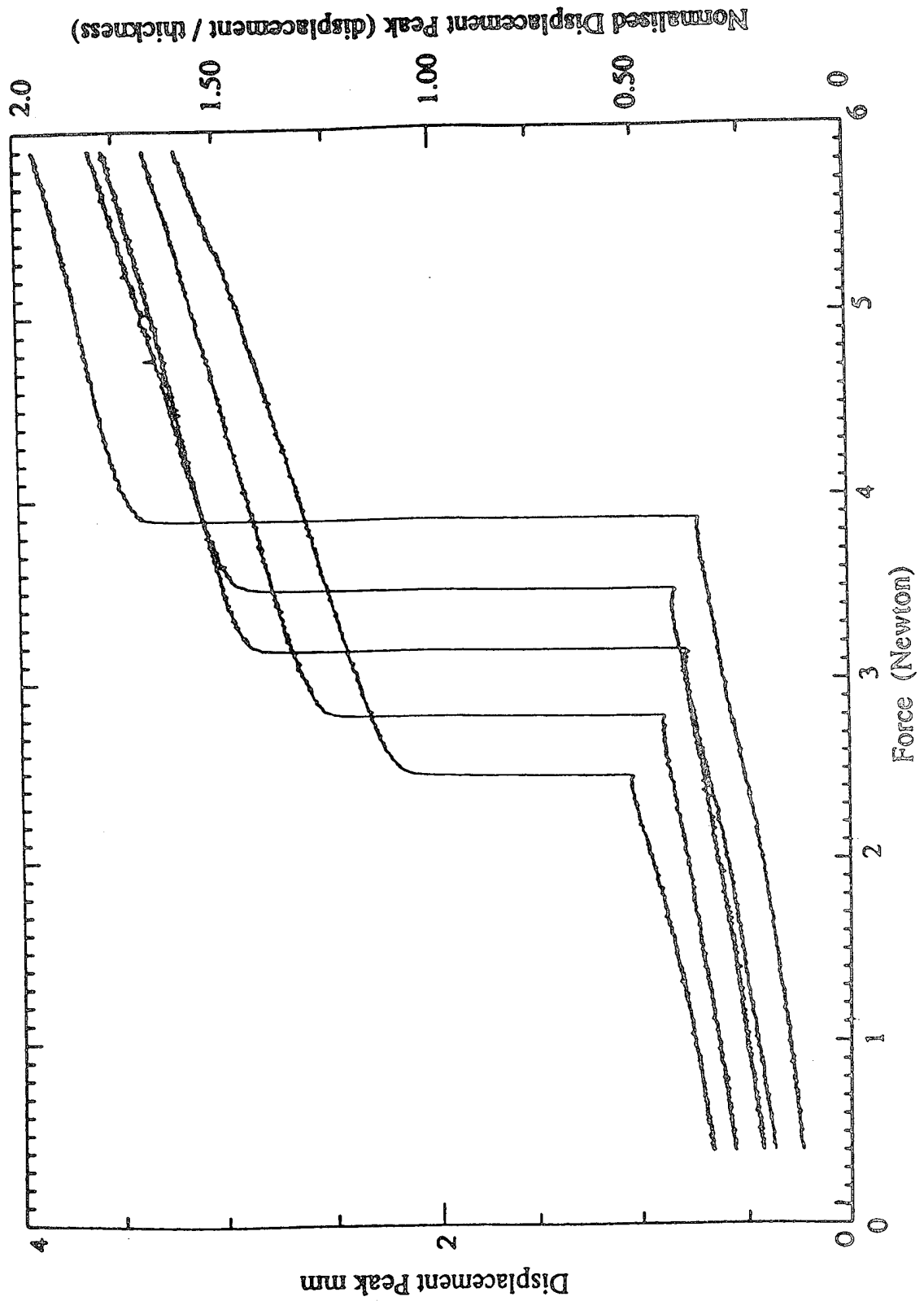


Fig 2.39 Slow amplitude sweeps, decreasing excitation force 0.5-6N at constant frequency C-C CFRP beam.

C-C CFRP BEAM SINE DWELL

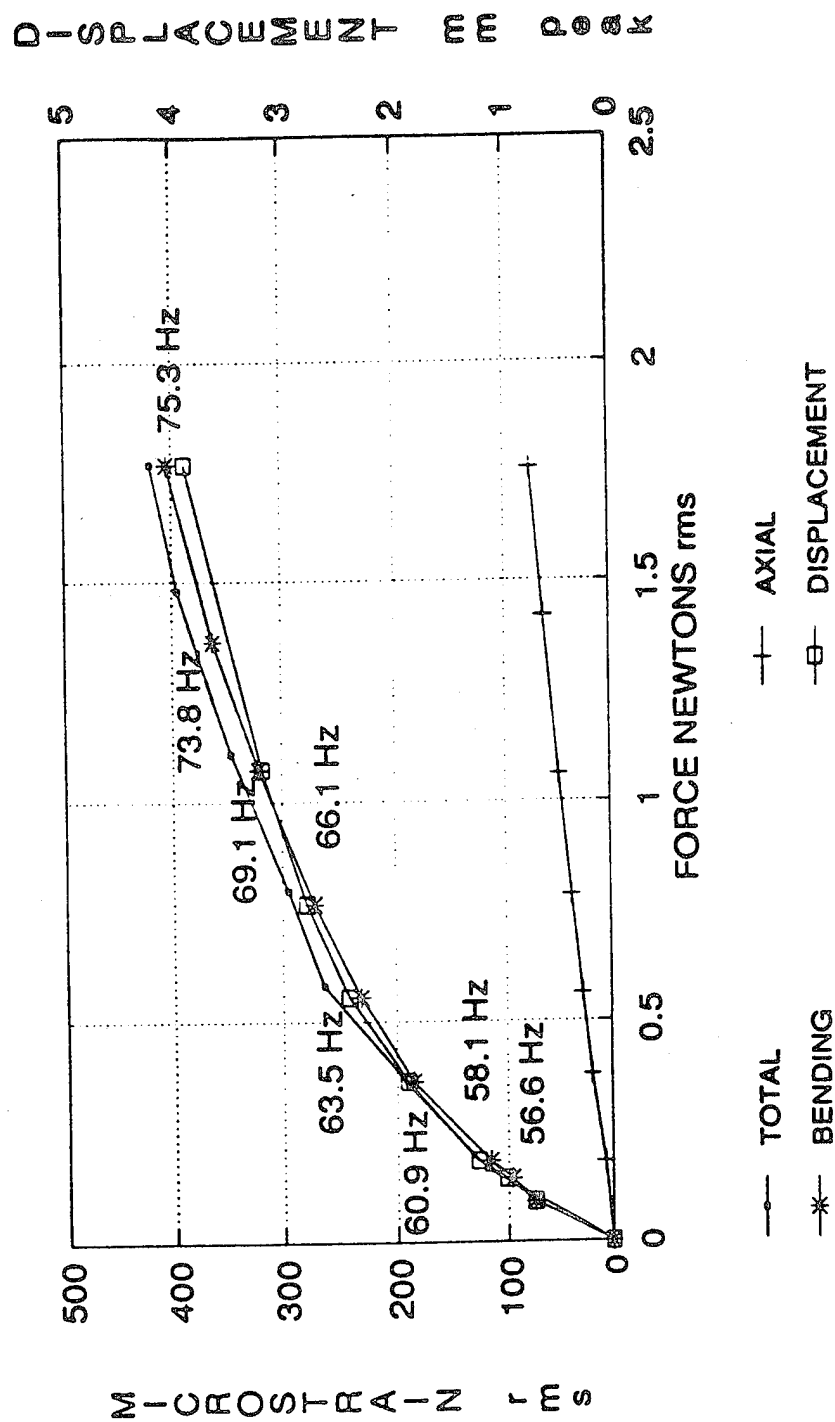


Fig 2.40 Total, axial and bending strains for sine dwell tests C-C CFRP beam.

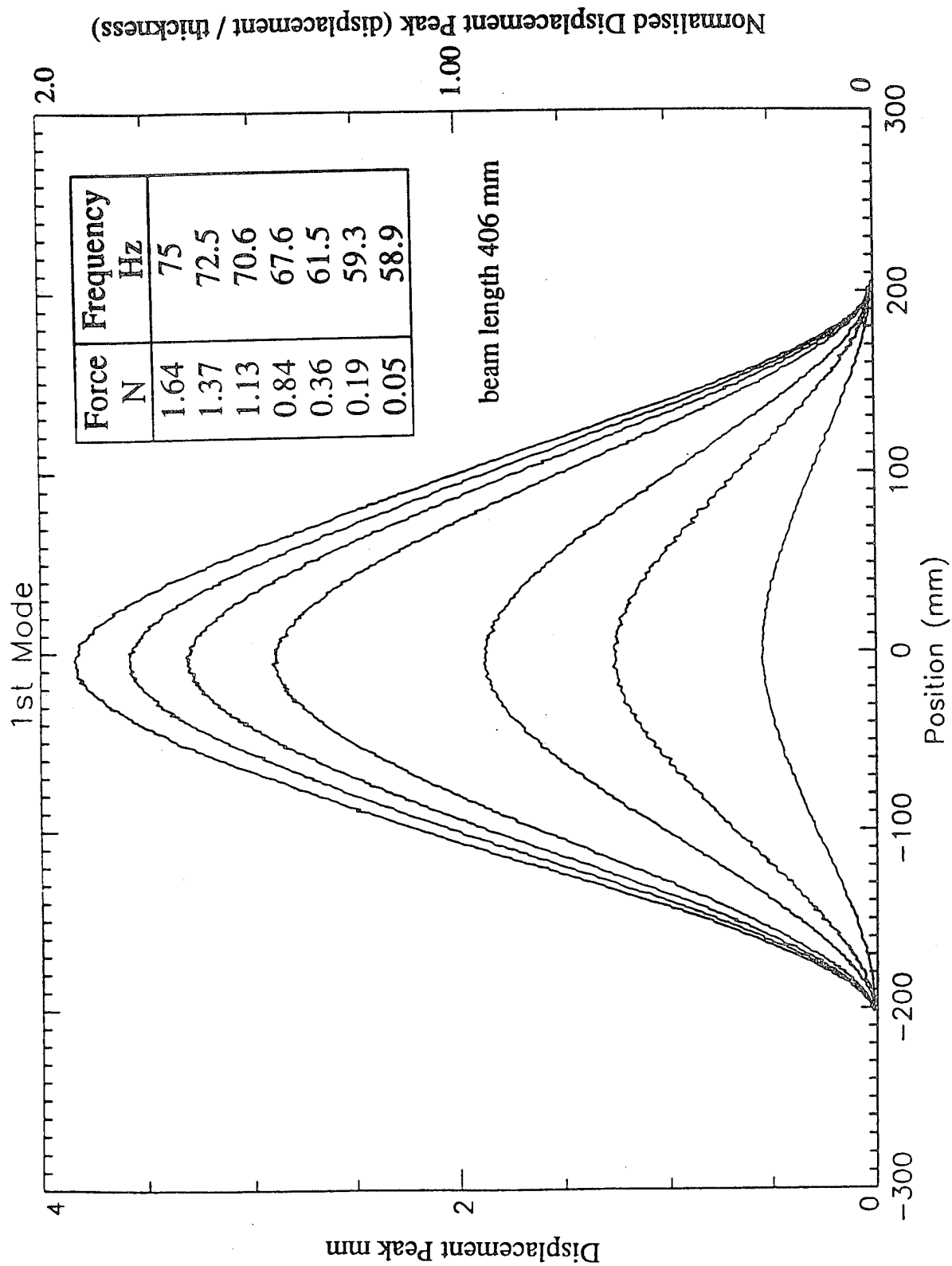


Fig 2.41 Nonlinear displacement shapes fundamental resonance, unsmoothed data, C-C CFRP beam.

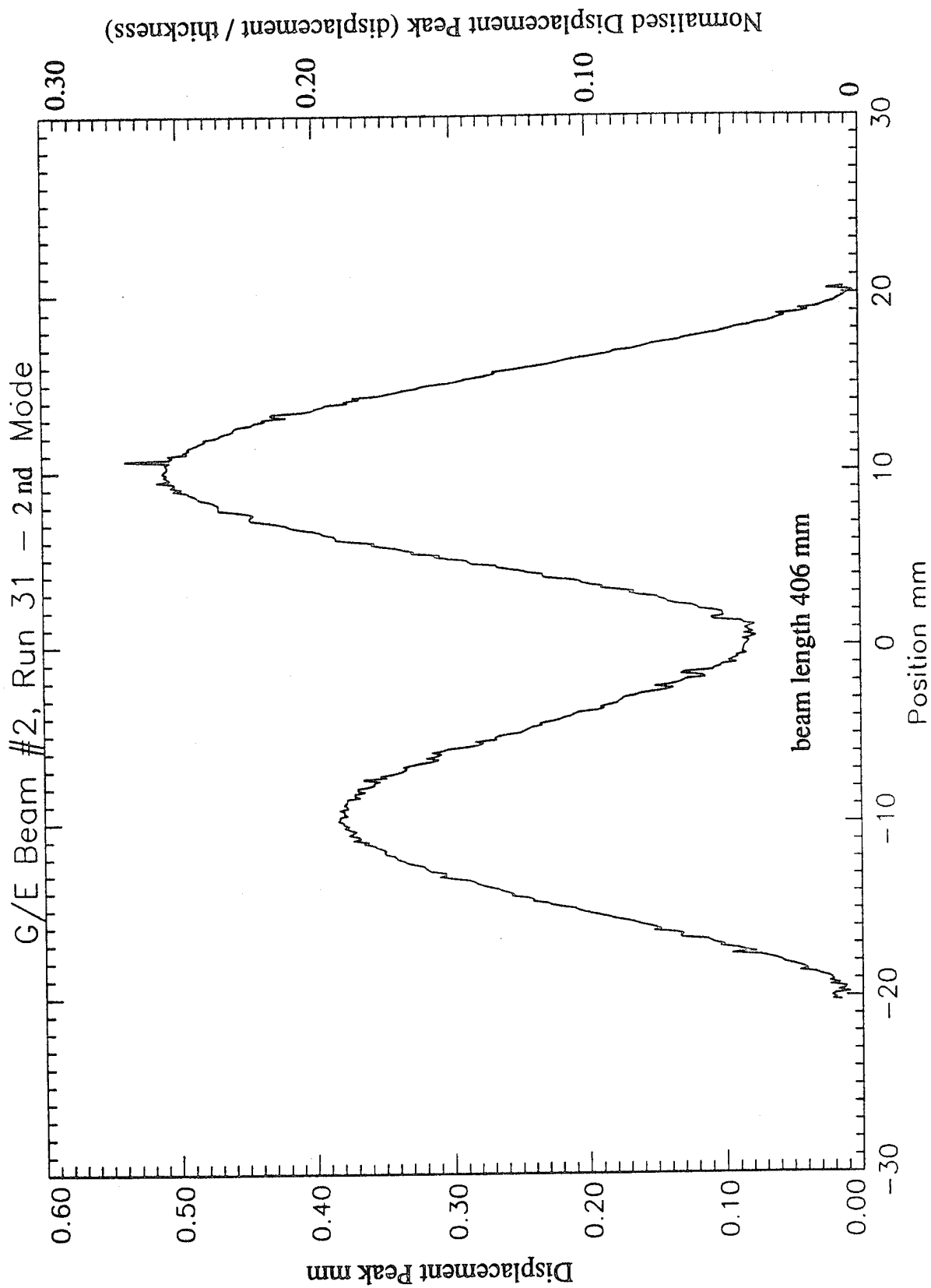


Fig 2.42 Nonlinear displacement shapes 2nd mode, 370 Hz, unsmoothed data, C-C CFRP beam.

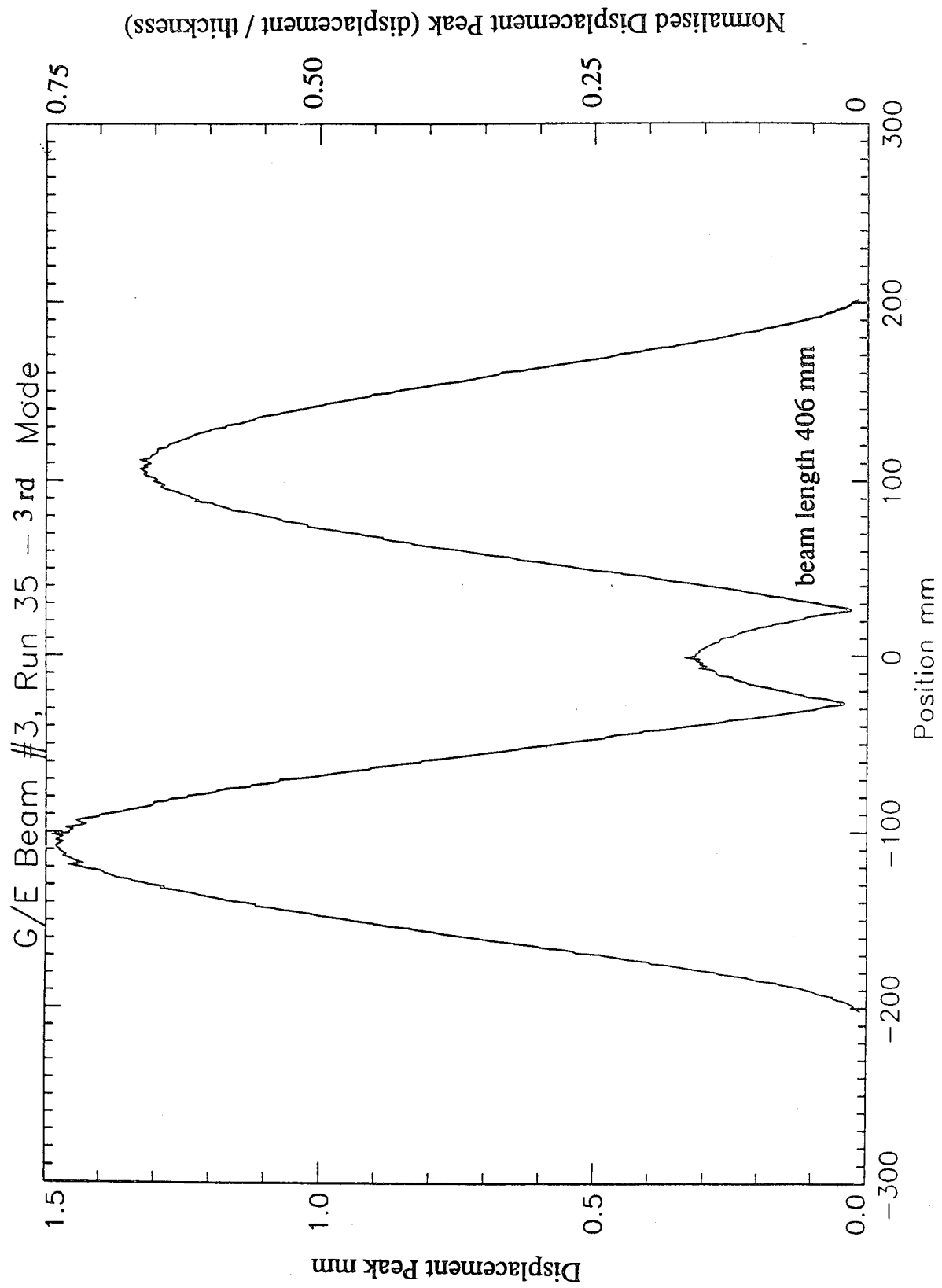


Fig 2.43 Nonlinear displacement shapes, 3rd mode, 389 Hz, unsmoothed data C-C CFRP beam.

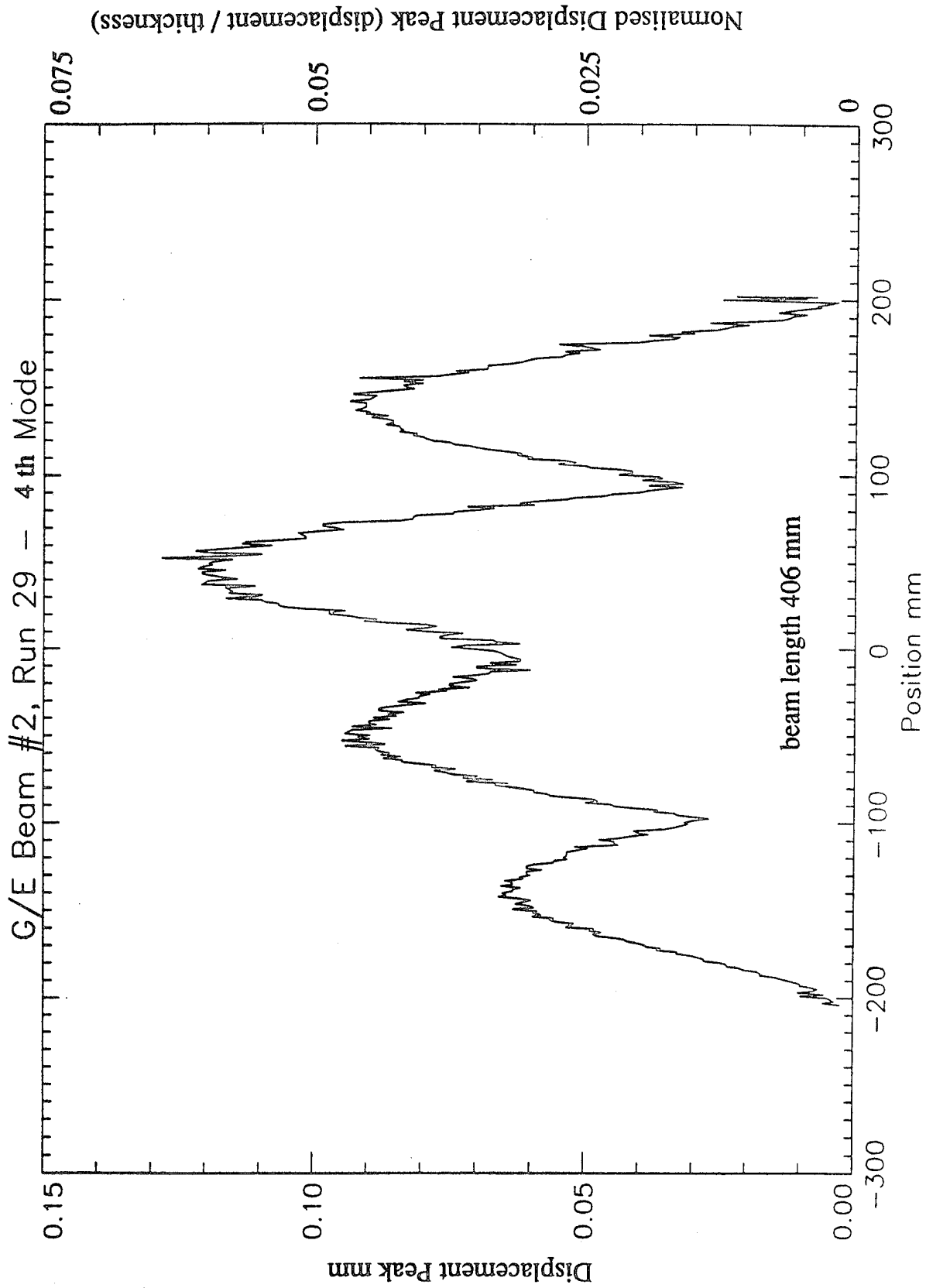


Fig 2.44 Nonlinear displacement shapes, 4th mode, 899 Hz, unsmoothed data C-C CFRP beam.

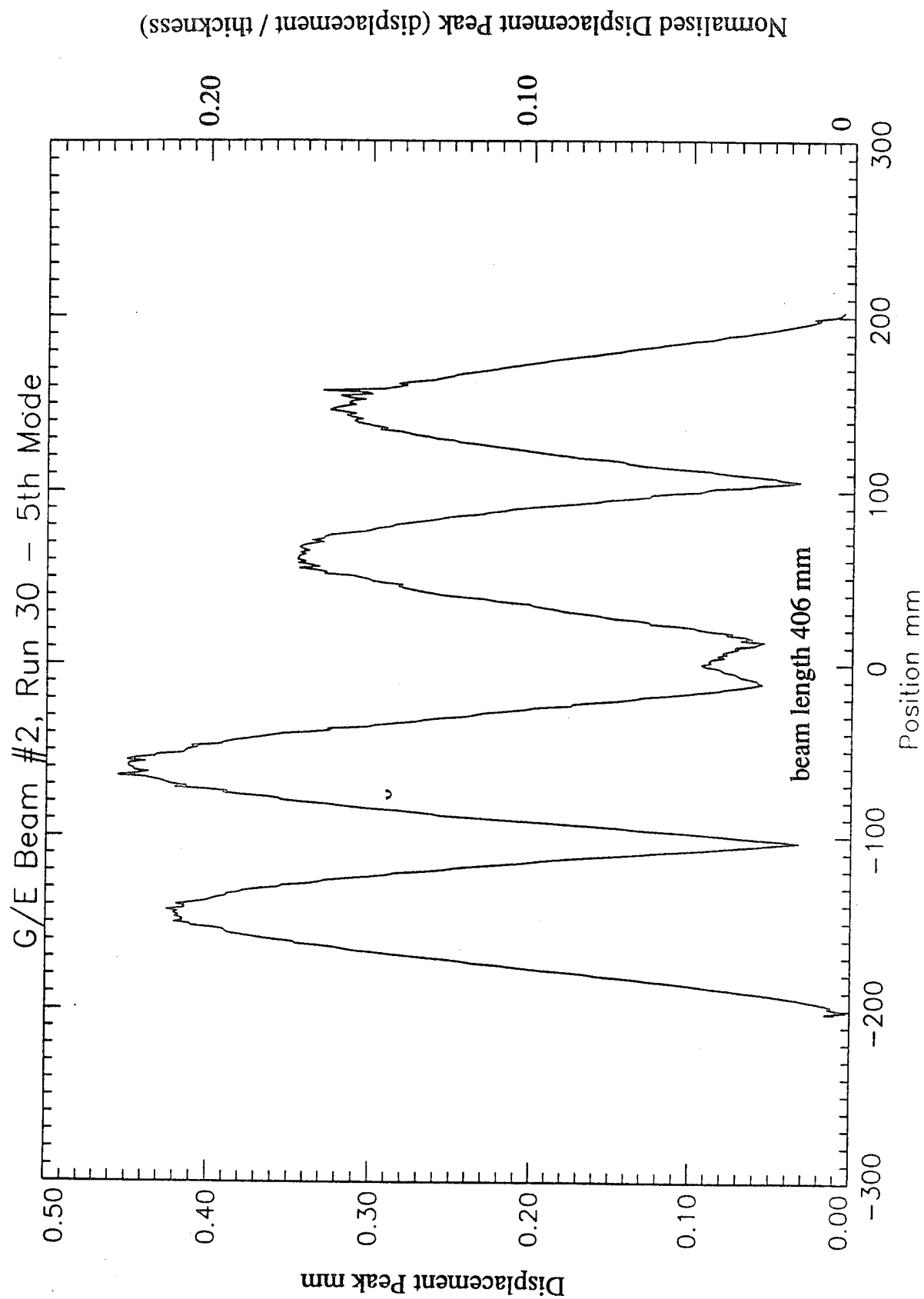


Fig 2.45 Nonlinear displacement shapes, fifth mode, 1028 Hz, unsmoothed data C-C CFRP beam.

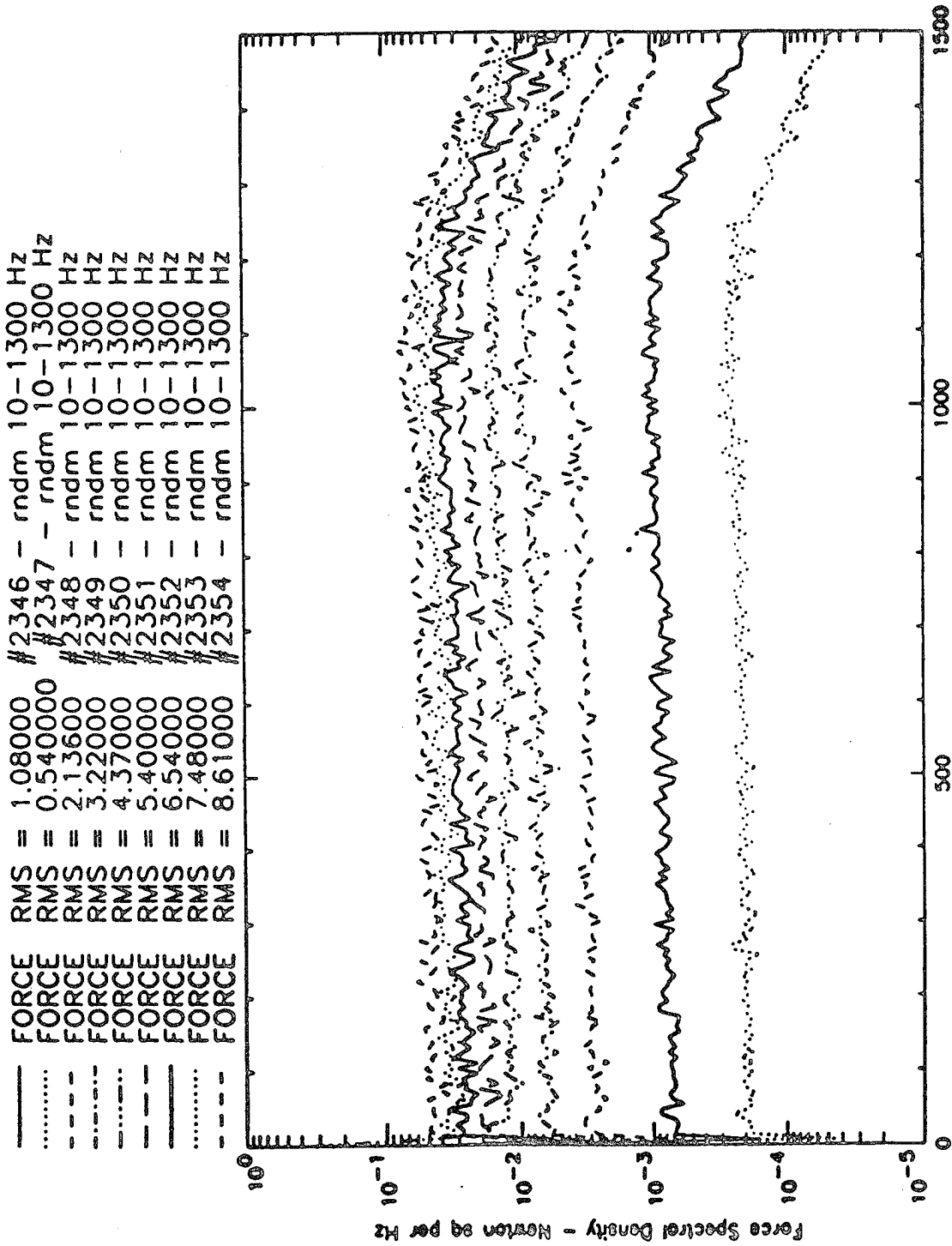


Fig 2.46 Force spectral densities, 10-130` Hz, random excitation, C-C CFRP beam.

WP CC G/E Beam

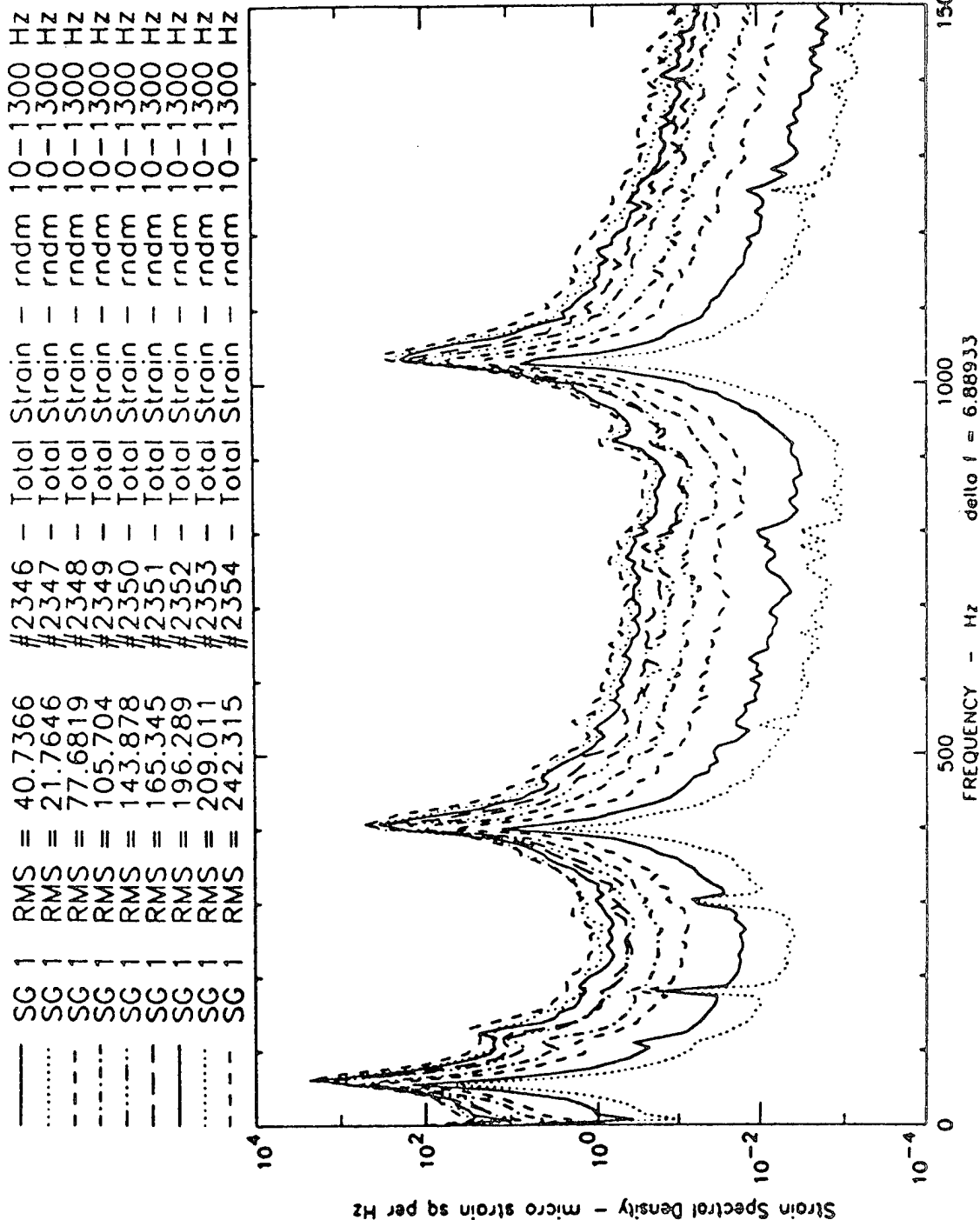


Fig 2.47 Strain spectral densities, 10-1300 Hz random excitation, SG 1, C-C CFRP beam.

WP CC G/E Beam

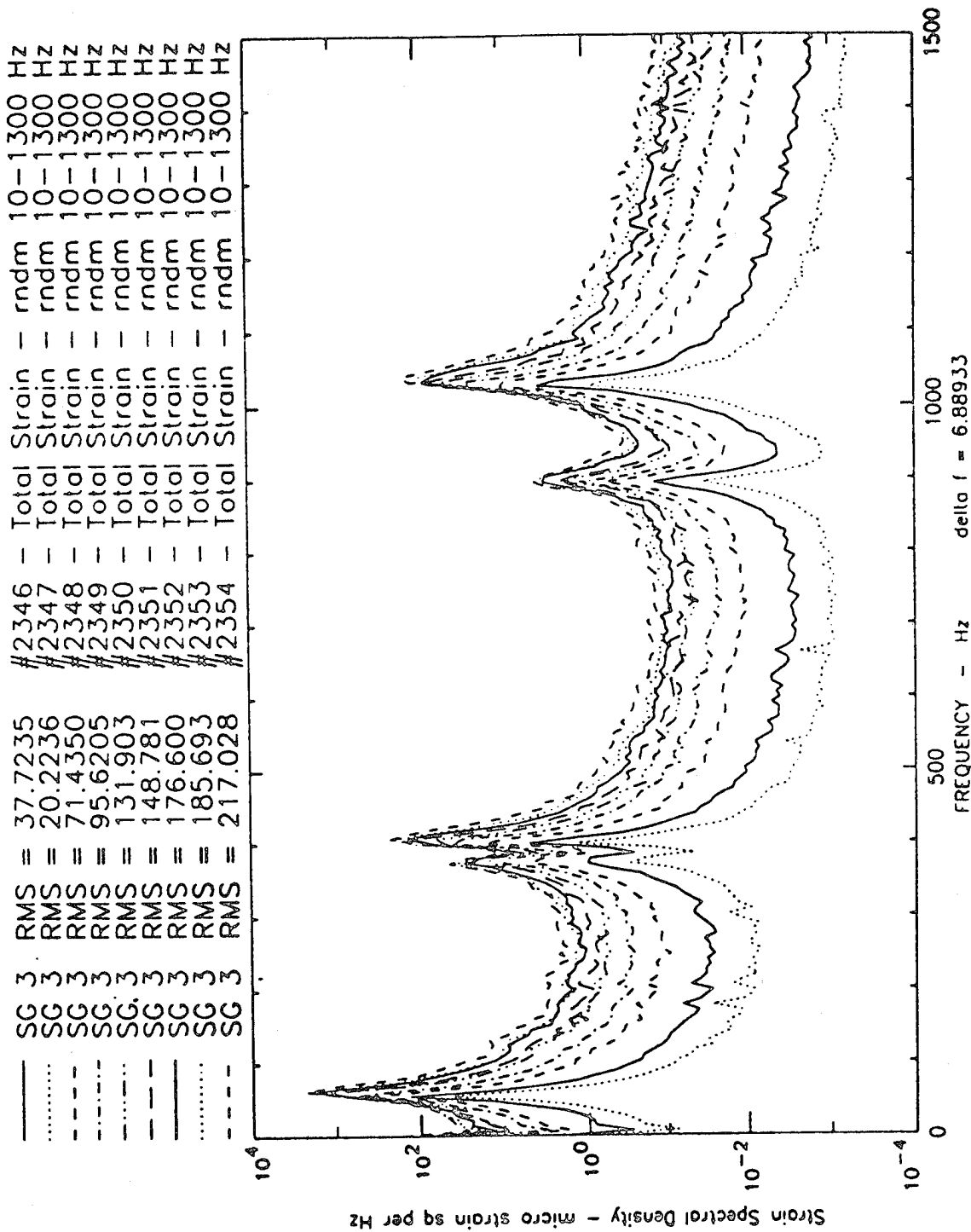


Fig 2.48 Strain spectral densities, 10-1300 Hz random excitation, SG 3, C-C CFRP beam.

WP CC G/E Beam

DISP	RMS	=	1.851820e-02	#2339	-	Total Strain	-	rndm	10-600	Hz
DISP	RMS	=	0.390063	#2340	-	Total Strain	-	rndm	10-600	Hz
DISP	RMS	=	0.726261	#2341	-	Total Strain	-	rndm	10-600	Hz
DISP	RMS	=	0.961595	#2342	-	Total Strain	-	rndm	10-600	Hz
DISP	RMS	=	1.20160	#2343	-	Total Strain	-	rndm	10-600	Hz
DISP	RMS	=	1.38456	#2344	-	Total Strain	-	rndm	10-600	Hz
DISP	RMS	=	1.51928	#2345	-	Total Strain	-	rndm	10-600	Hz

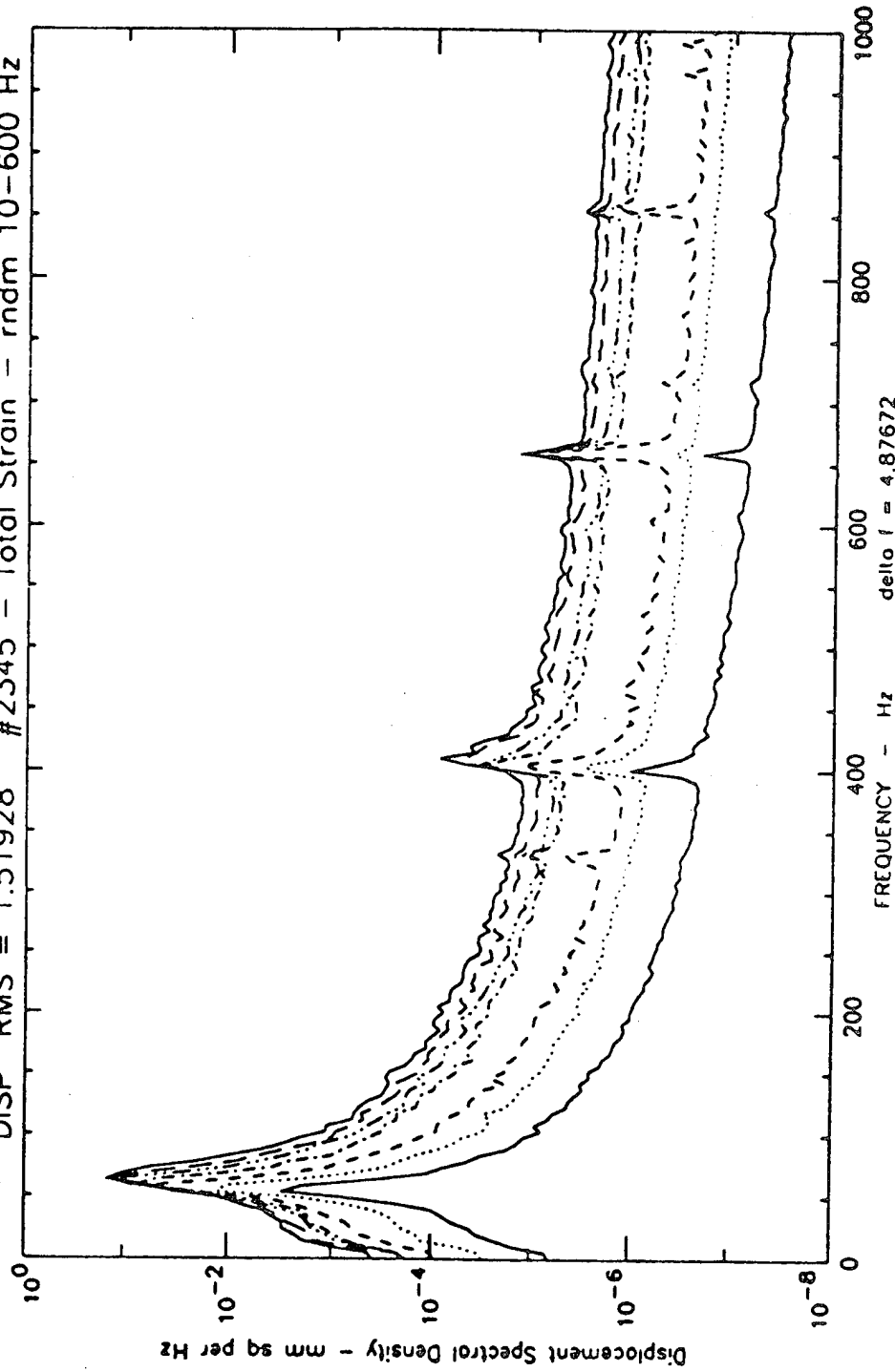


Fig 2.49 Displacement spectral densities, 10-1300 Hz random excitation, C-C CFRP beam.

C-C CFRP BEAM
10-600 HZ RANDOM

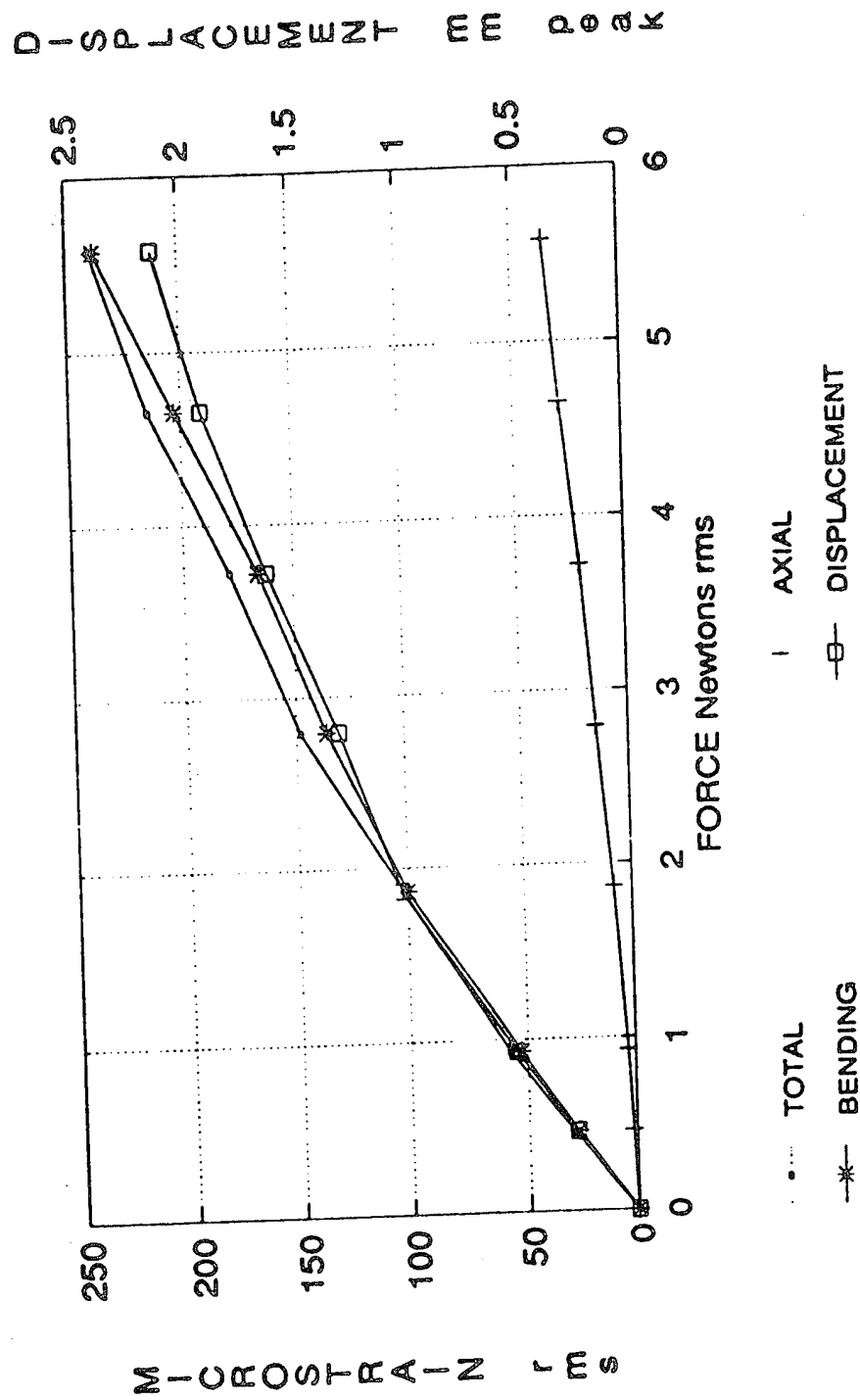


Fig 2.50 Total, axial and bending strains, 10-600 Hz, SG 3 and SG 3& 6, random excitation, C-C CFRP beam.

C-C CFRP BEAM
Amplitude PDF Force R2346, 2348, 2350, 2352, 2354

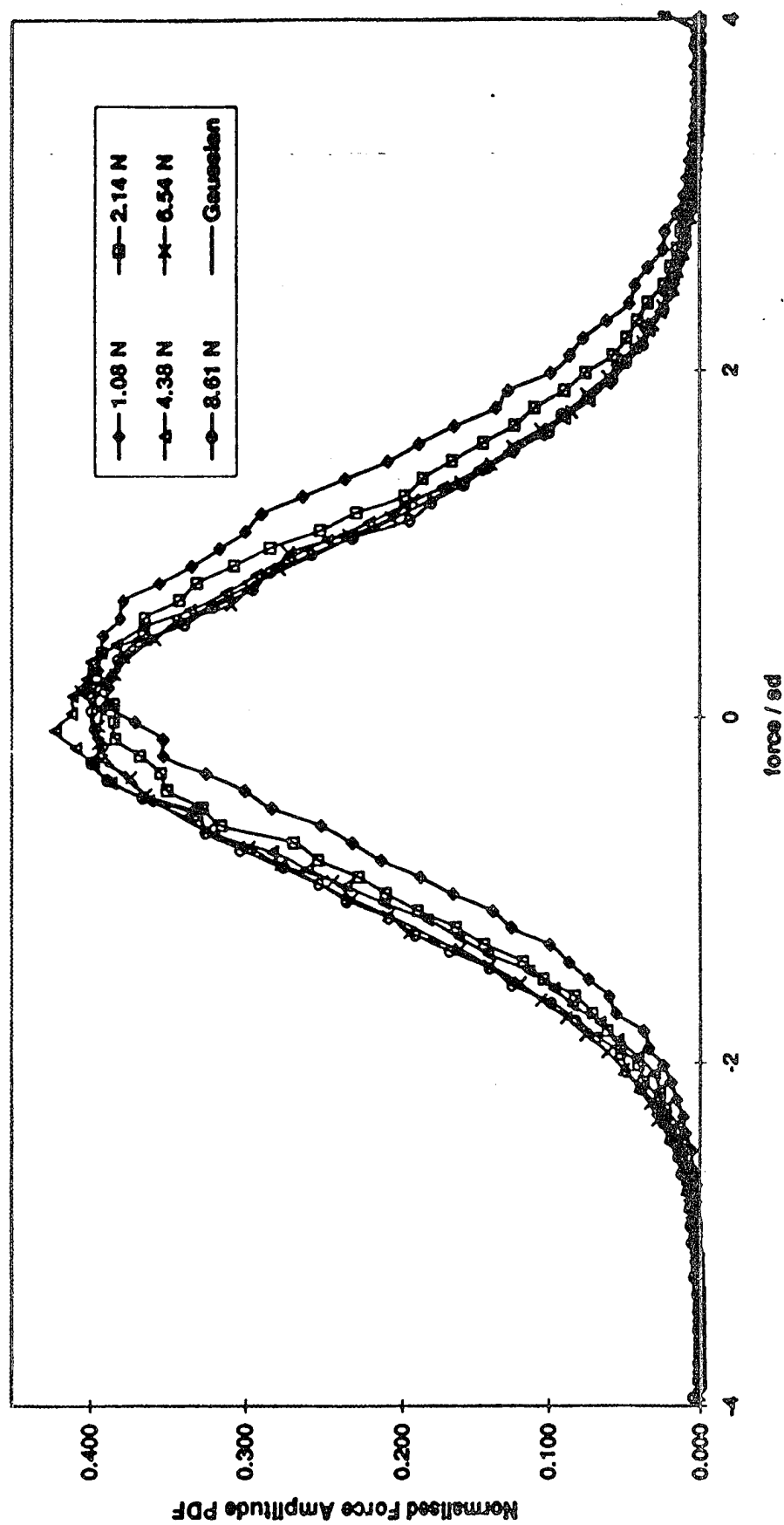


Fig 2.51 Normalised force amplitude PDFs, 10-600 Hz random excitation, C-C CFRP beam.

C-C CFRP BEAM
Amplitude PDF SG 1 R2346, 2348, 2350, 2352, 2354

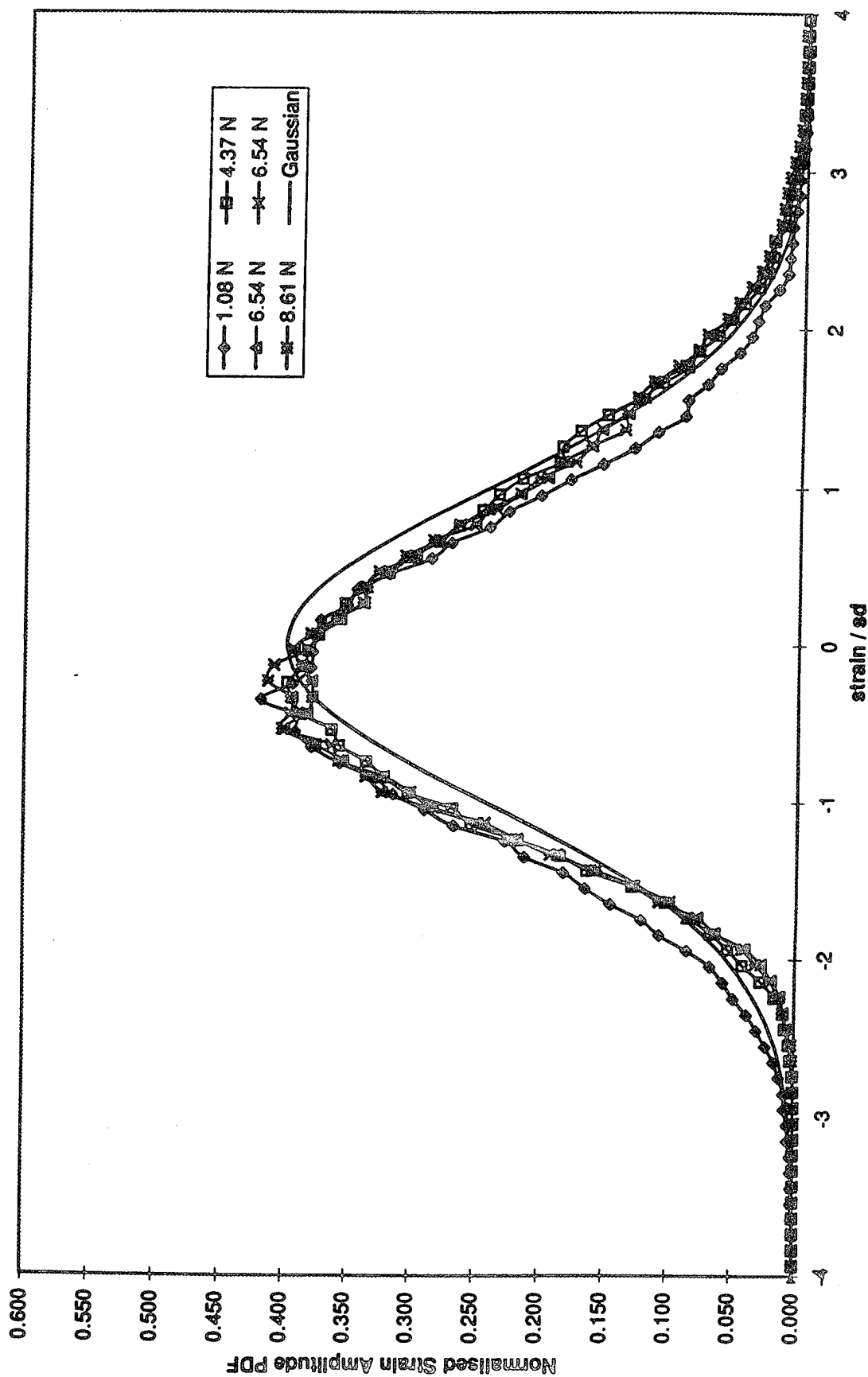


Fig 2.52 Normalised strain amplitude PDFs, 10-600 Hz random excitation, SG 1, C-C CFRP beam.

C-C CFRP BEAM
Amplitude PDF SG 1 R2346, 2348, 2350, 2352, 2354

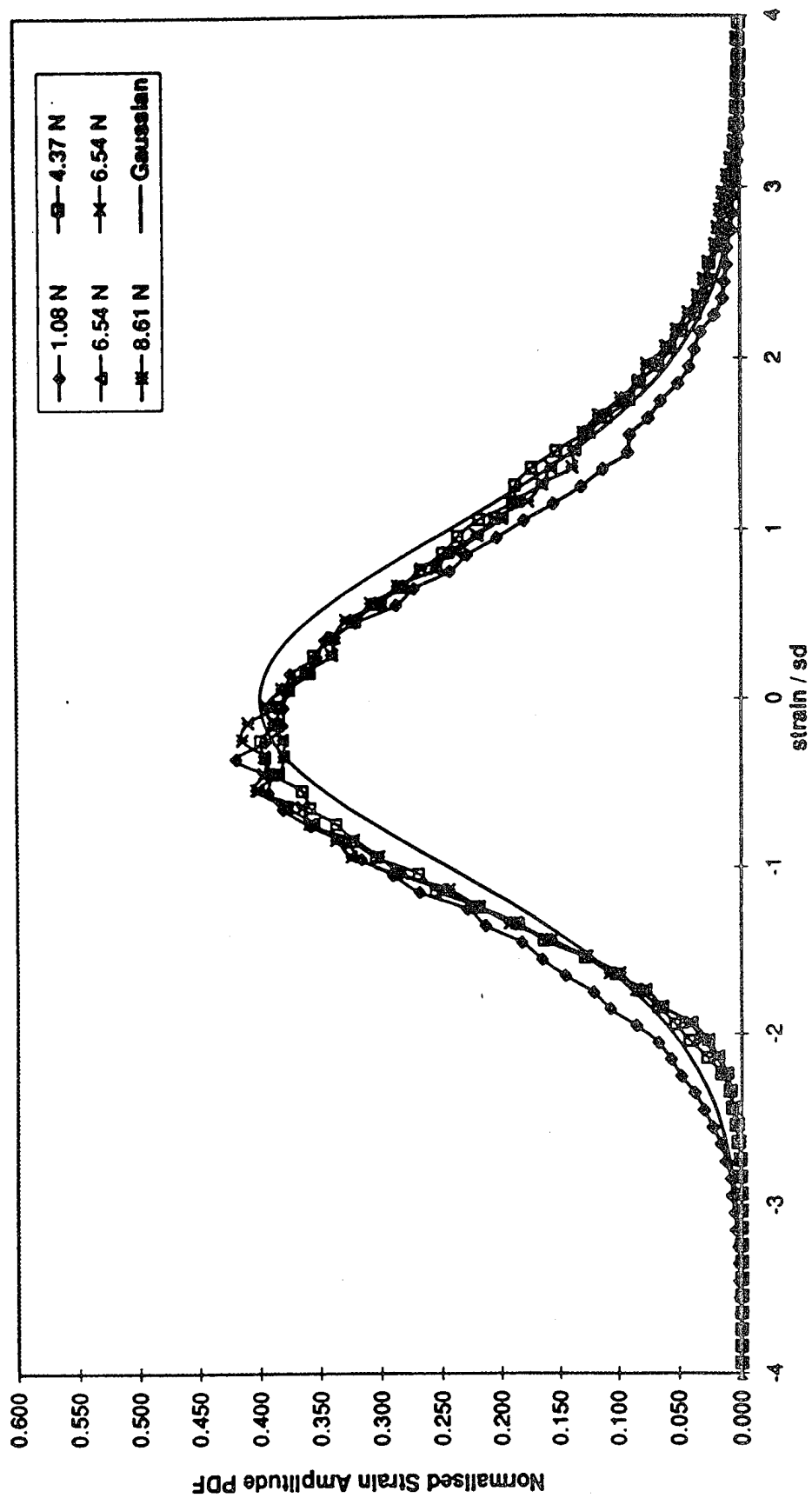


Fig 2.53 Normalised strain amplitude PDFs, 10-600 Hz random excitation, SG 3, C-C CFRP beam.

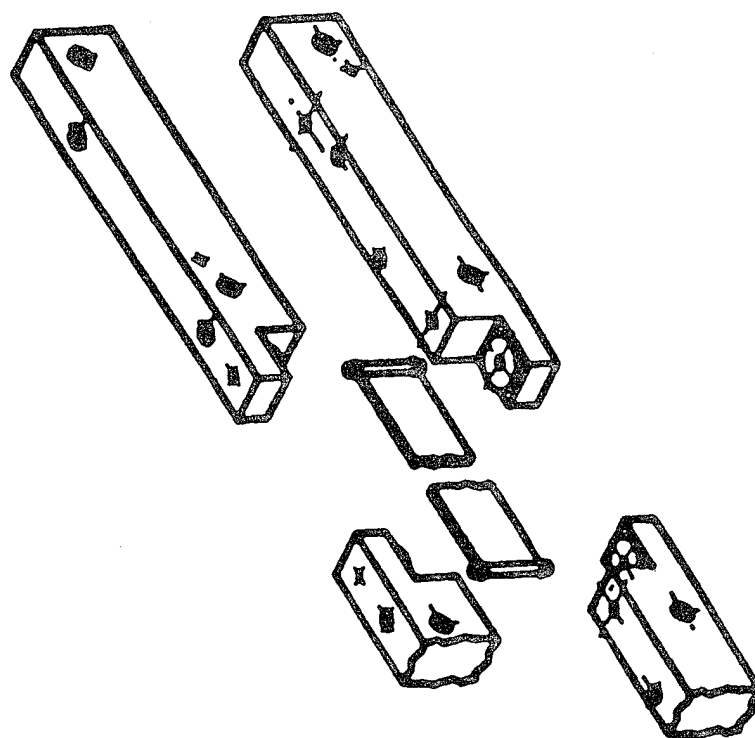


Fig 2.54 P-P aluminium alloy beam design.

P-P AL BEAM
STATIC BENDING (COIL-OUTWARD)

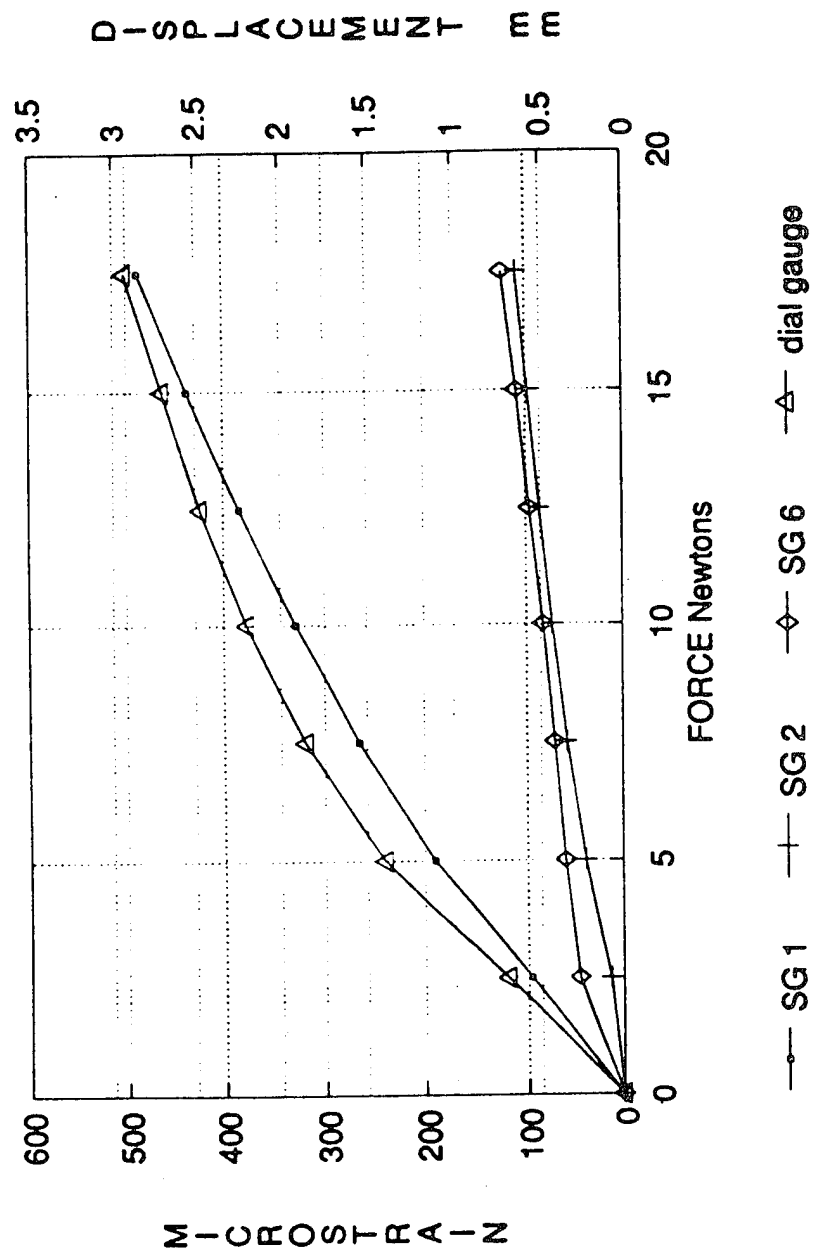


Fig 2.55 Total static strains and displacements, P-P aluminium beam.

WP P-P AL BEAM
STATIC BENDING (COIL-OUTWARD)

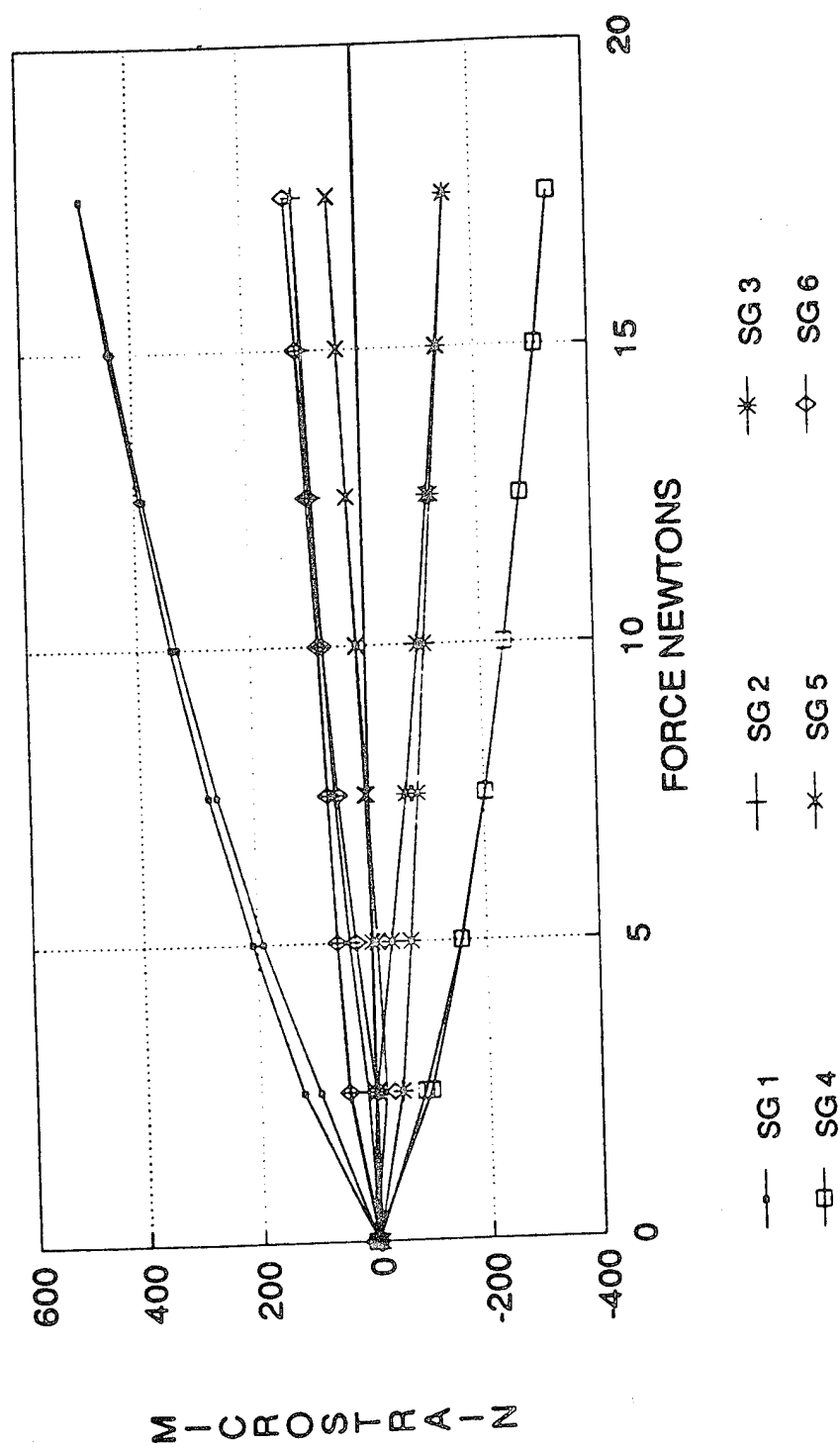


Fig 2.56 Total static strains, P-P aluminium beam.

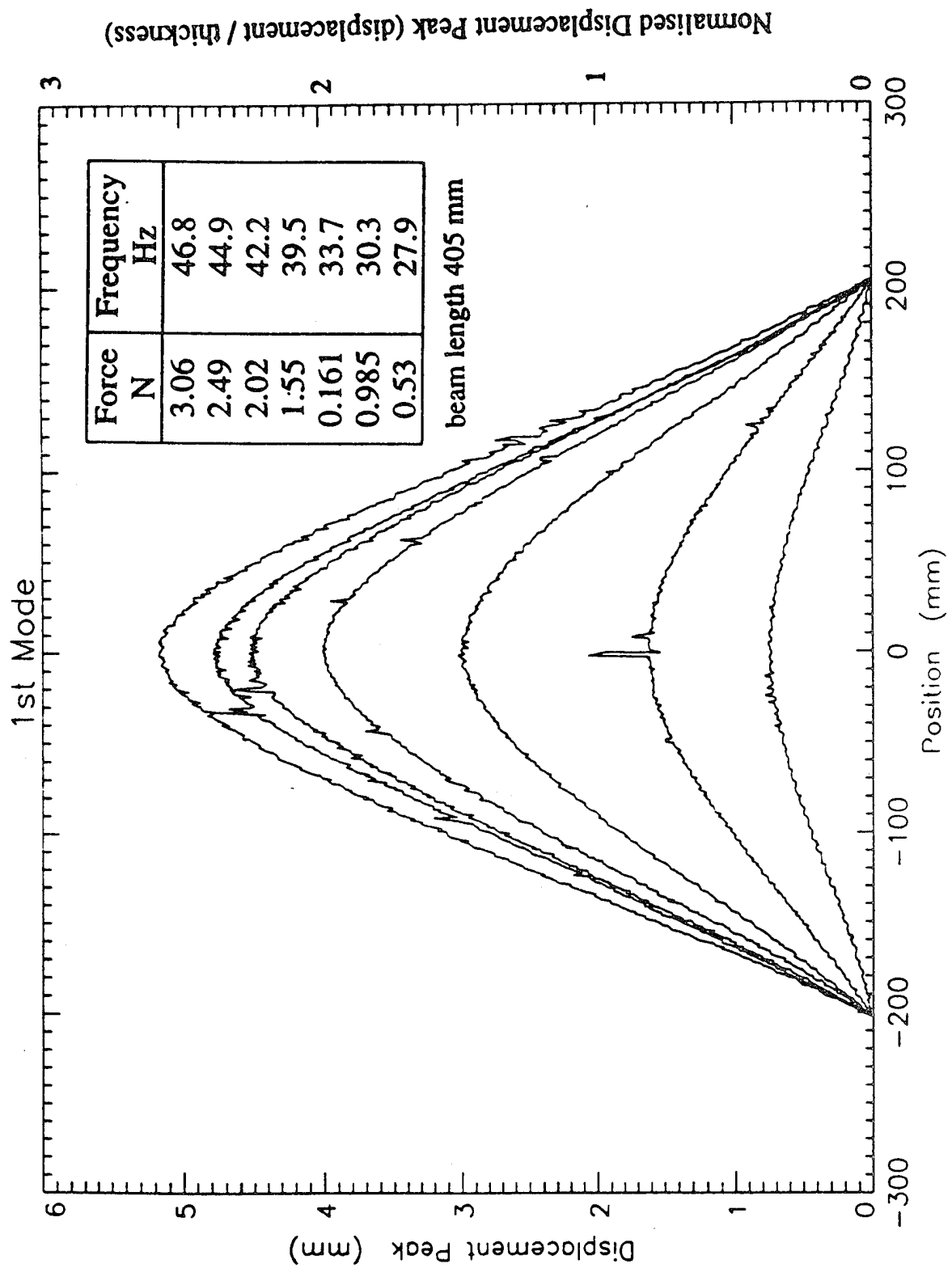


Fig 2.57 Nonlinear displacement shapes fundamental resonance unsmoothed data, P-P aluminium beam.

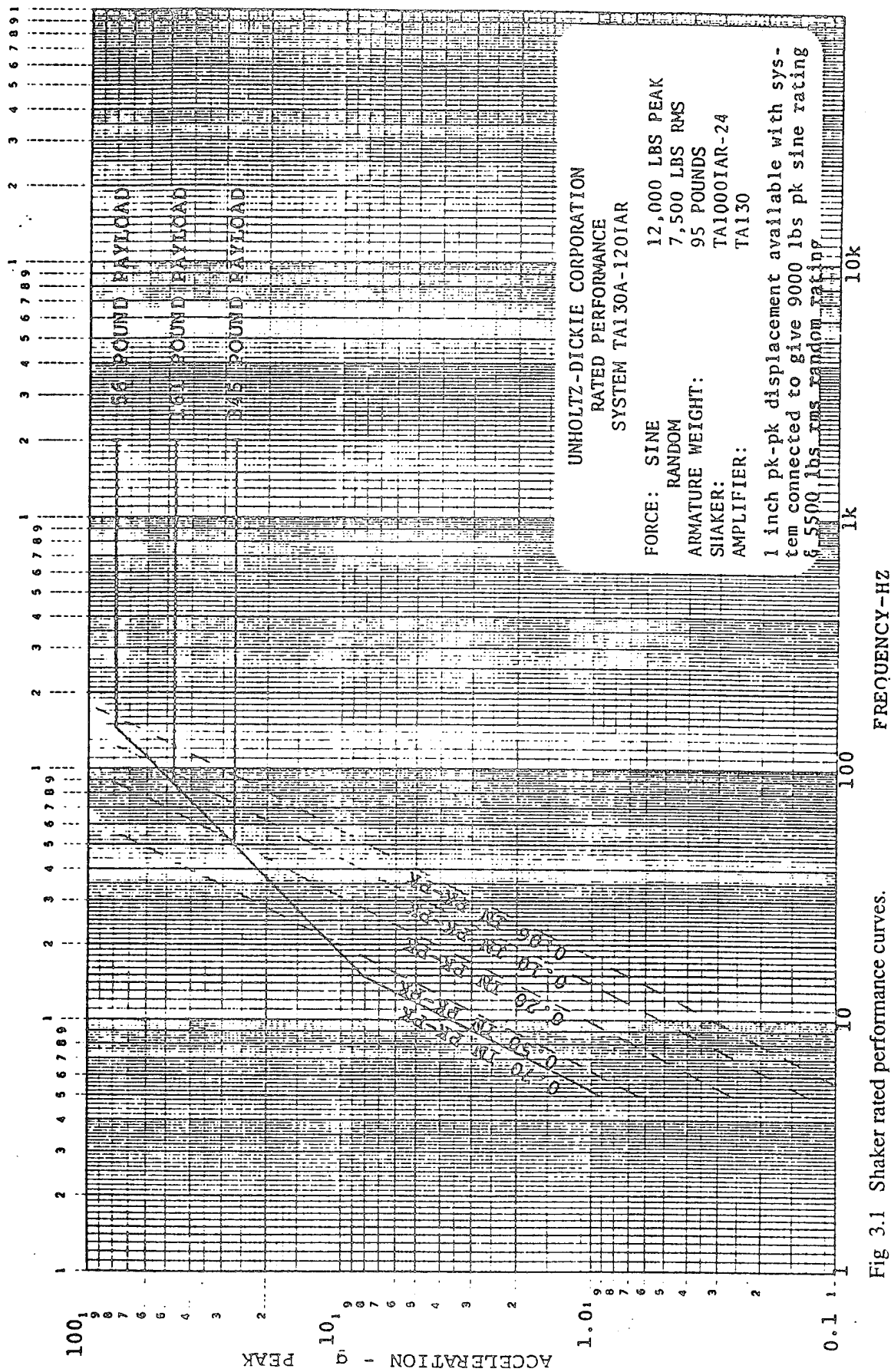


Fig 3.1 Shaker rated performance curves.

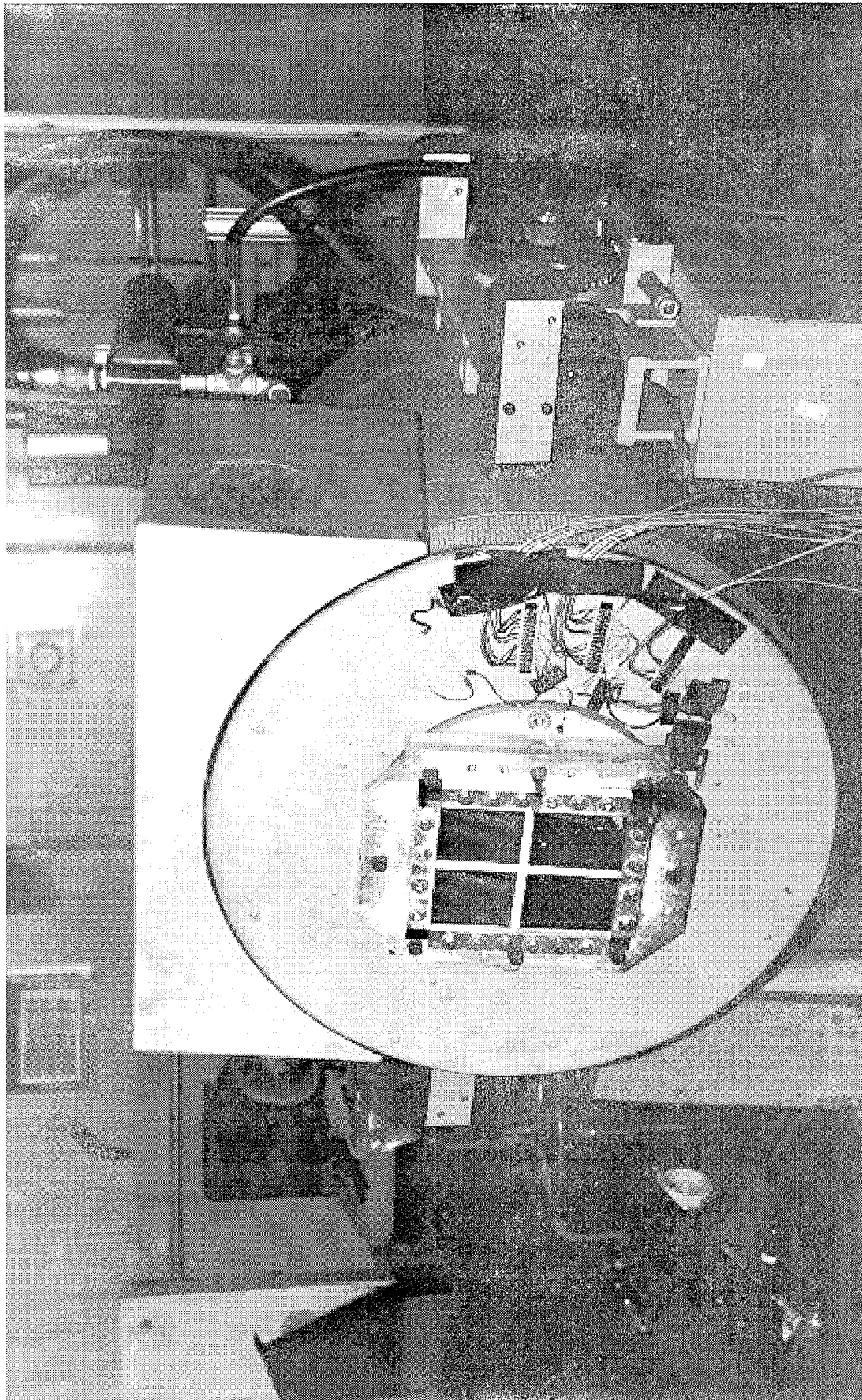


Fig 3.2 Photograph of shaker base excitation testing arrangement.

Technical drawing of a rectangular panel with dimensions and labels:

- Overall width: 267 mm
- Overall height: 318 mm
- Panel width: 254 mm
- Panel height: 209 mm
- Label: CLAMPING FRAME OPENING (with arrow pointing to the top edge)
- Label: PANEL CENTRE (with arrow pointing to the center of the panel)
- Label: SG 4.9 (with arrow pointing to the top edge)
- Label: SG 3.8 (with arrow pointing to the top edge)
- Label: SG 2.7 (with arrow pointing to the top edge)
- Label: SG 1.6 (with arrow pointing to the top edge)
- Label: SG 5.10 (with arrow pointing to the top edge)
- Label: 1/2 W 102 mm (with arrow pointing to the top edge)
- Label: 1/2 L 127 mm (with arrow pointing to the top edge)
- Label: 1/6 L 42.3 mm (with arrow pointing to the top edge)

STRAIN GAUGE PAIRS ARE BACK-TO-BACK
EDGE STRAIN GAUGES 1 mm FROM CLAMP
ALUMINUM THICKNESS = 1.30 mm
CFRP THICKNESS = 1.09 mm

SG# 1, 2, 3, 4, 5 FRONT SIDE
SG# 6, 7, 8, 9, 10 BACK SIDE
L = LENGTH
W = WIDTH

Fig 3.3 Shaker flat plate size and strain gauge locations.

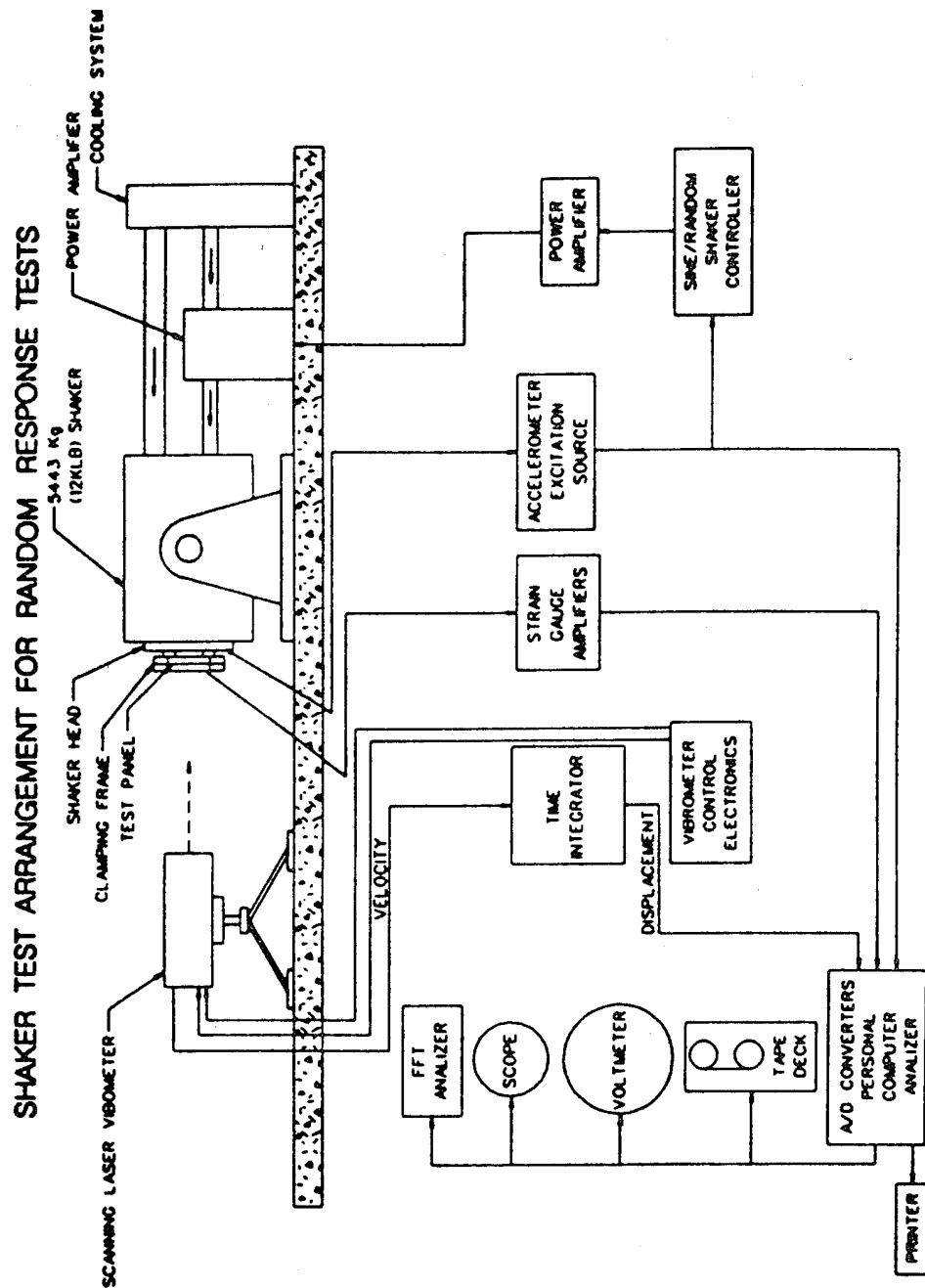


Fig 3.4 Schematic of shaker test arrangement.

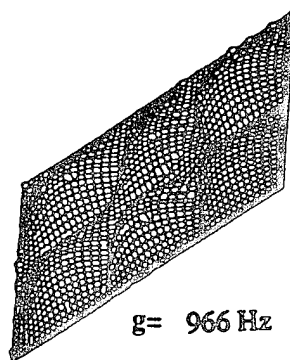
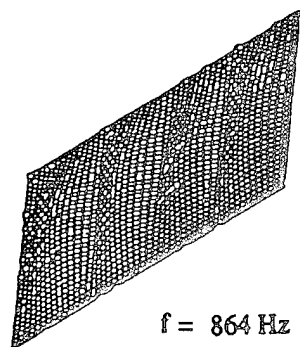
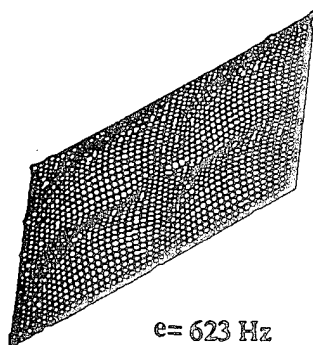
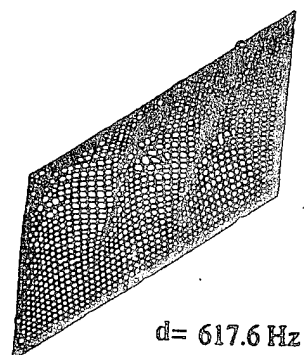
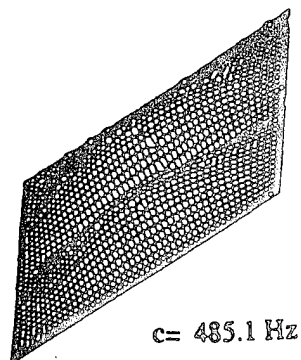
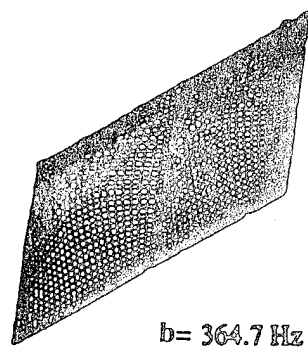
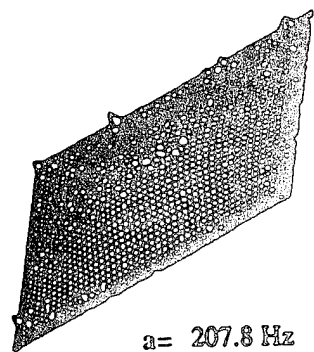


Fig 3.5 Mode shapes using video holography, a=208 Hz, b=365 Hz, c=485 Hz, d=618 Hz, e=623 Hz, f=864 Hz and g=966 Hz , C-C-C-C aluminium alloy shaker plate.

AL PLATE SHAKER TEST SINE DWELL SG #7

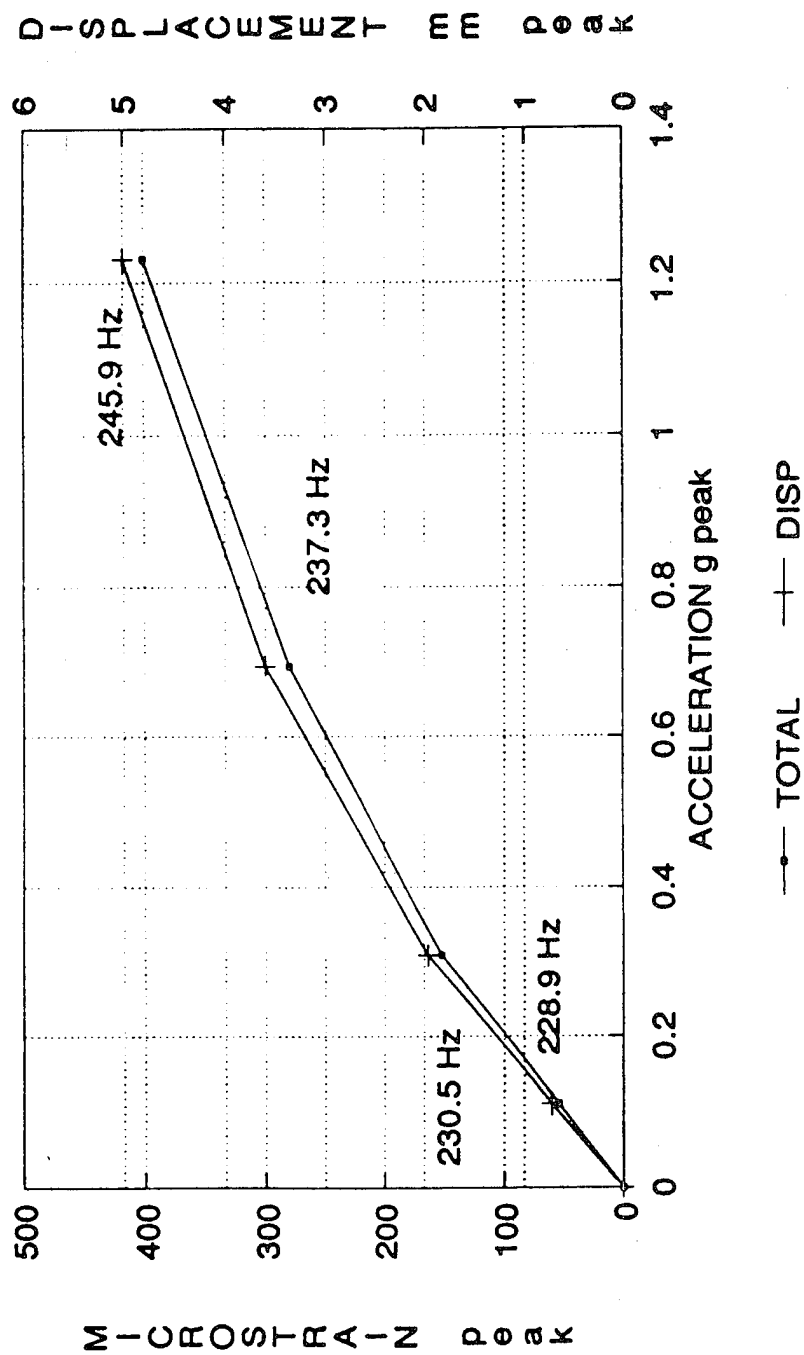


Fig 3.6 Total strains and displacements for sine dwell tests, C-C-C aluminium shaker plate.

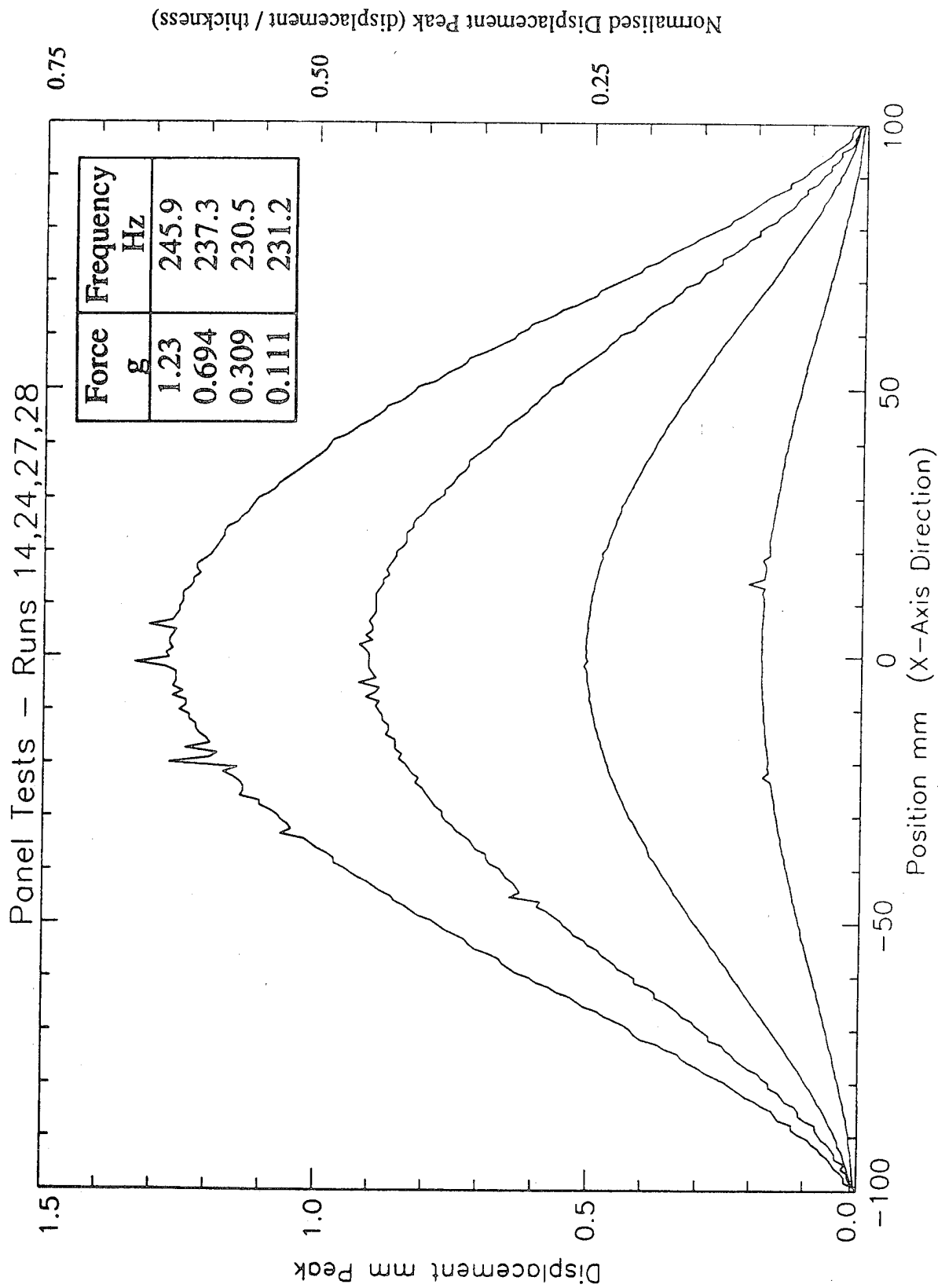


Fig 3.7 Nonlinear displacement shapes, fundamental resonance width direction, unsmoothed data, C-C-C-C aluminium shaker plate.

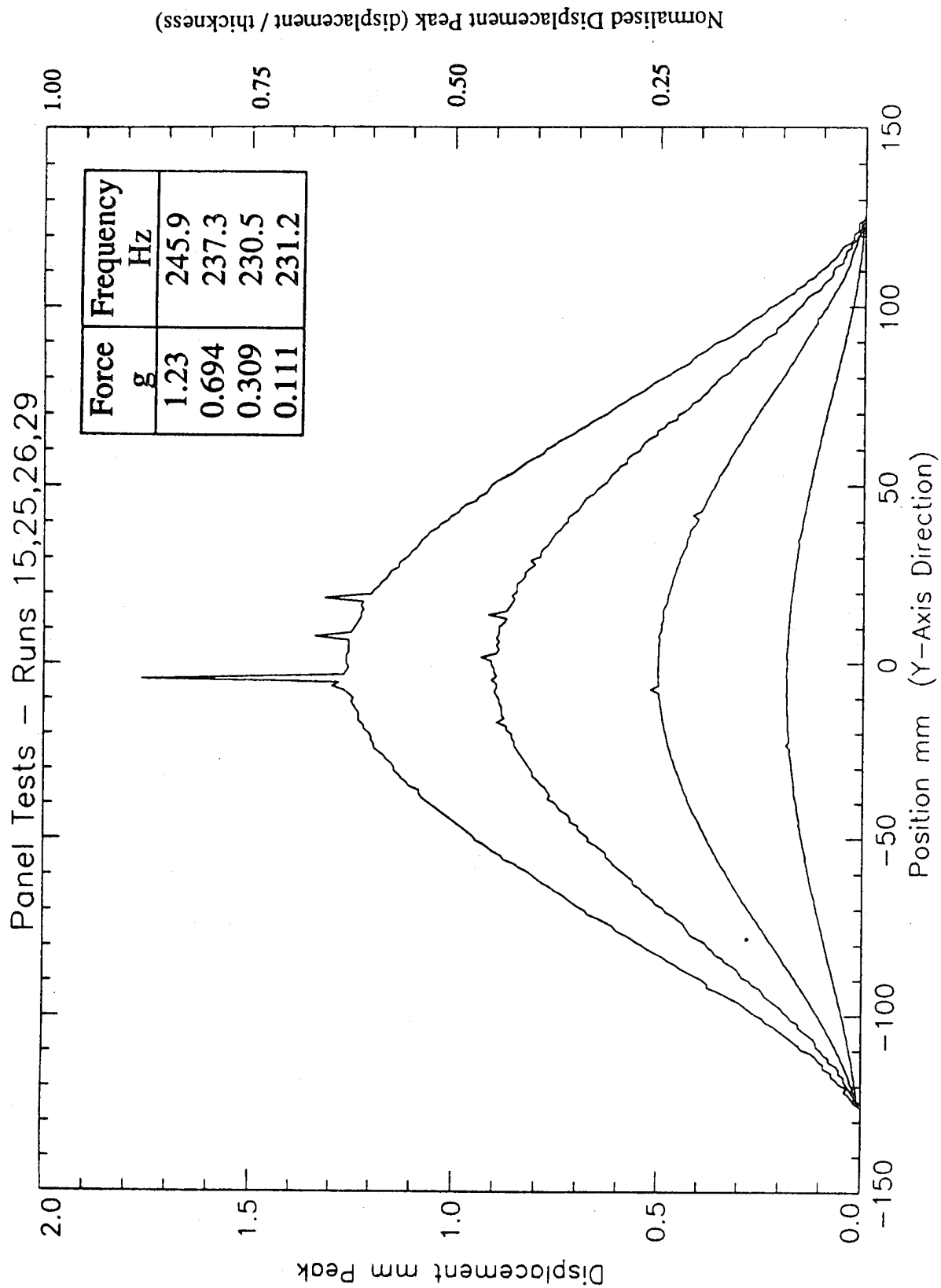


Fig 3.8 Nonlinear displacement shapes, fundamental resonance length direction, unsmoothed data, C-C-C-C aluminium shaker plate.

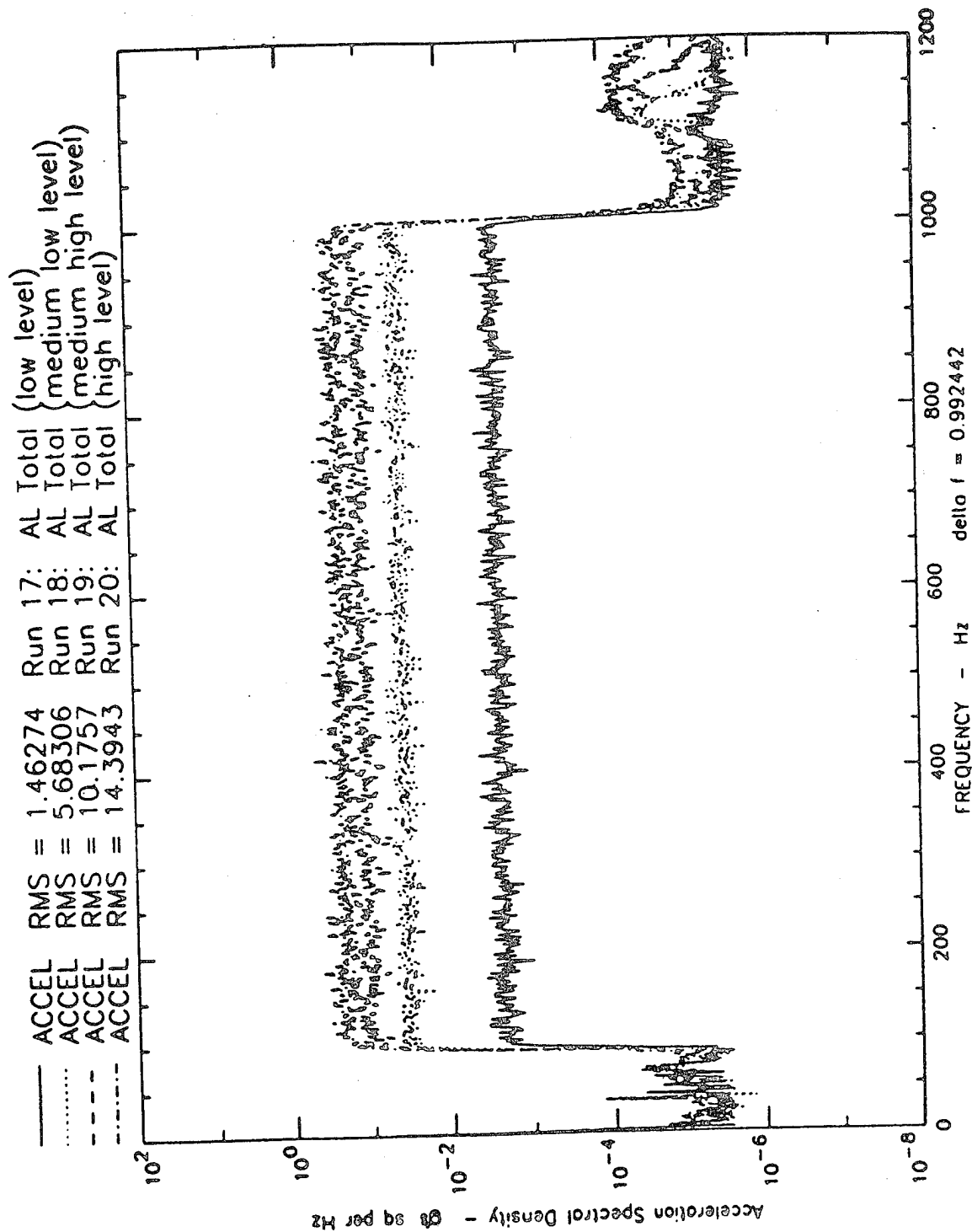


Fig 3.9 Excitation spectral densities, 100-1000 Hz, C-C-C-C aluminium shaker plate.

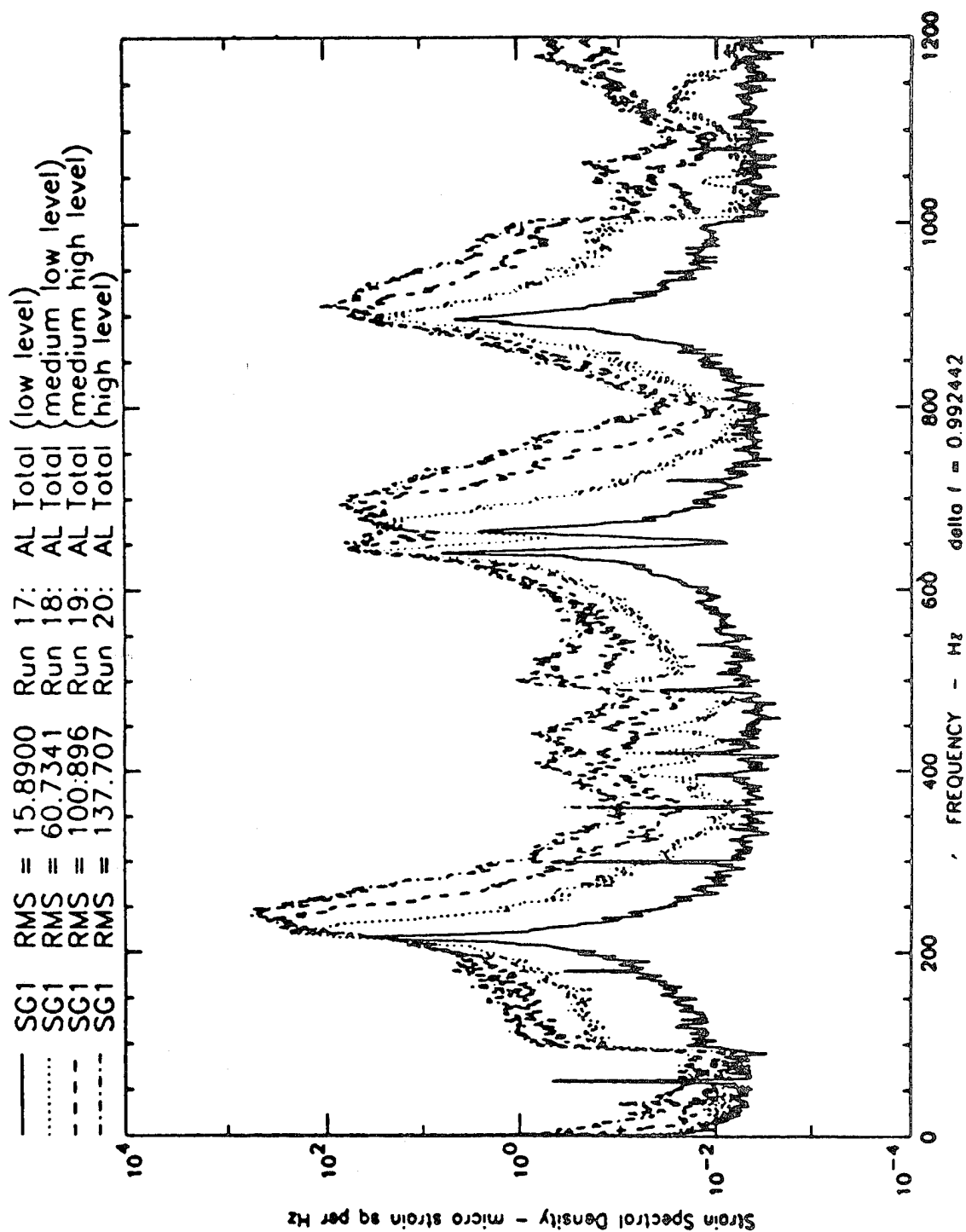


Fig 3.10 Strain spectral densities, 100-1000 Hz, SG 1, C-C-C-C aluminum shaker plate.

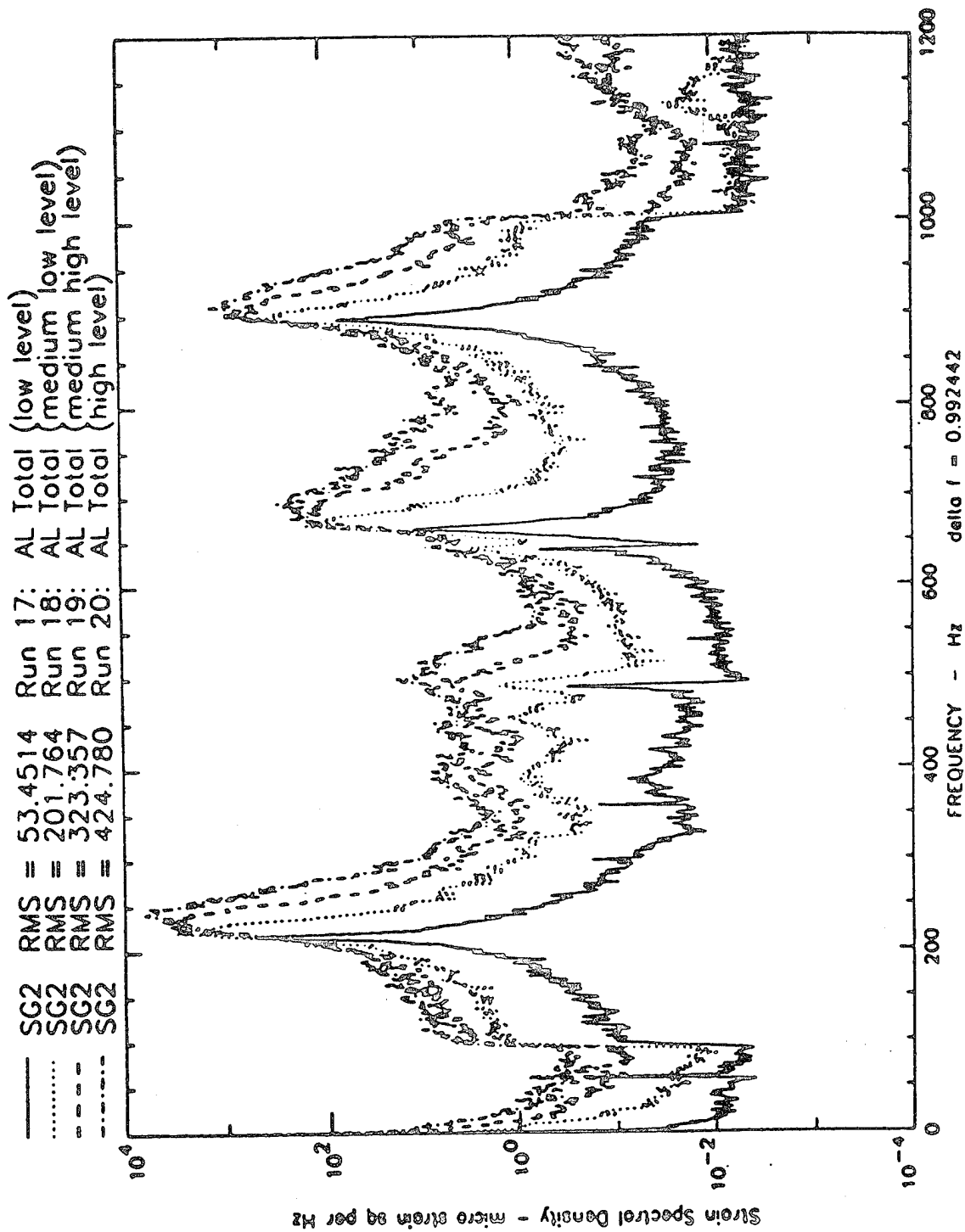


Fig 3.11 Strain spectral densities, 100-1000 Hz, SG 2, C-C-C-C aluminium shaker plate.

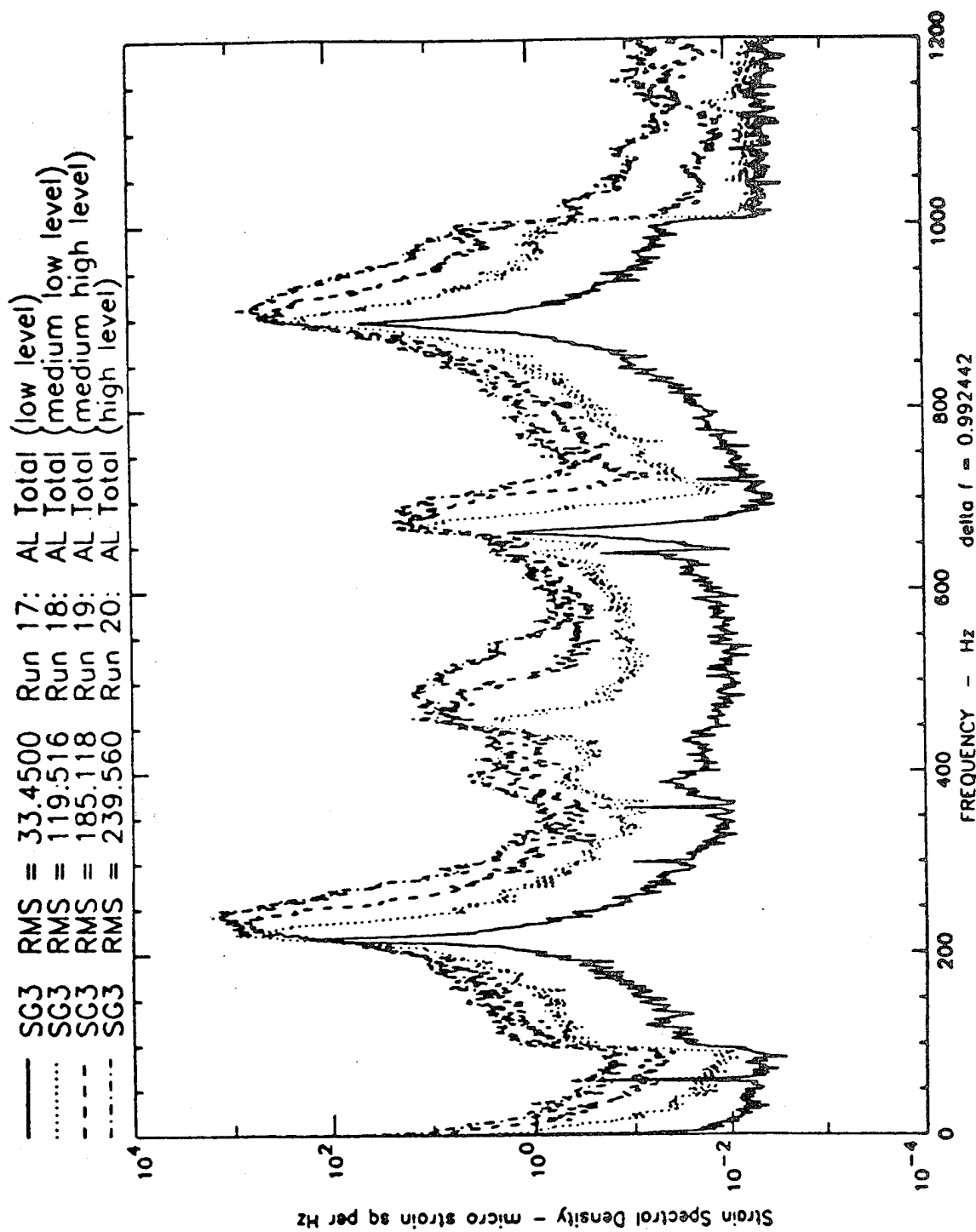


Fig 3.12 Strain spectral densities, 100-1000 Hz, SG 3, C-C-C-C aluminium shaker plate.

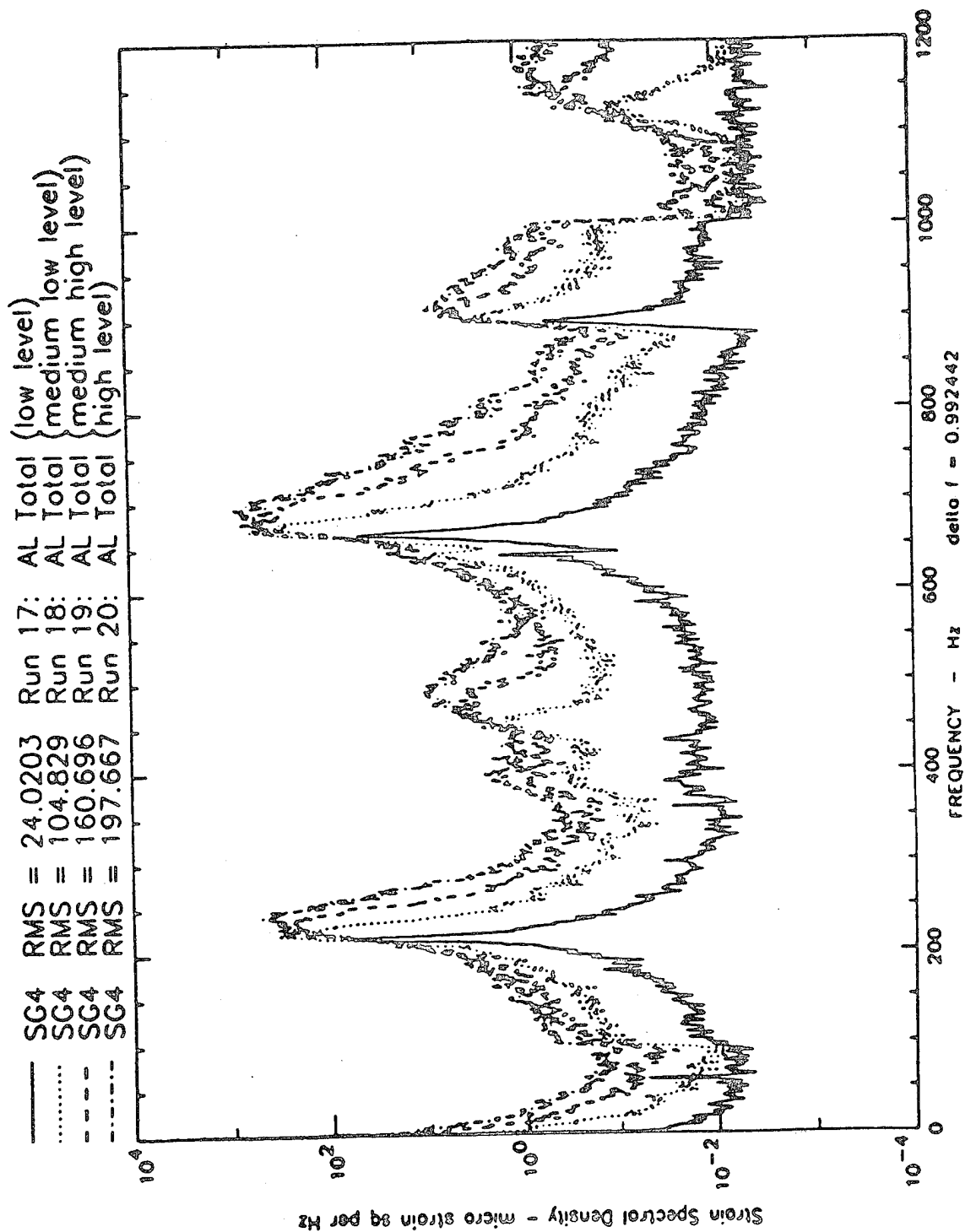


Fig 3.13 Strain spectral densities, 100-1000 Hz, SG 4, C-C-C-C aluminium shaker plate.

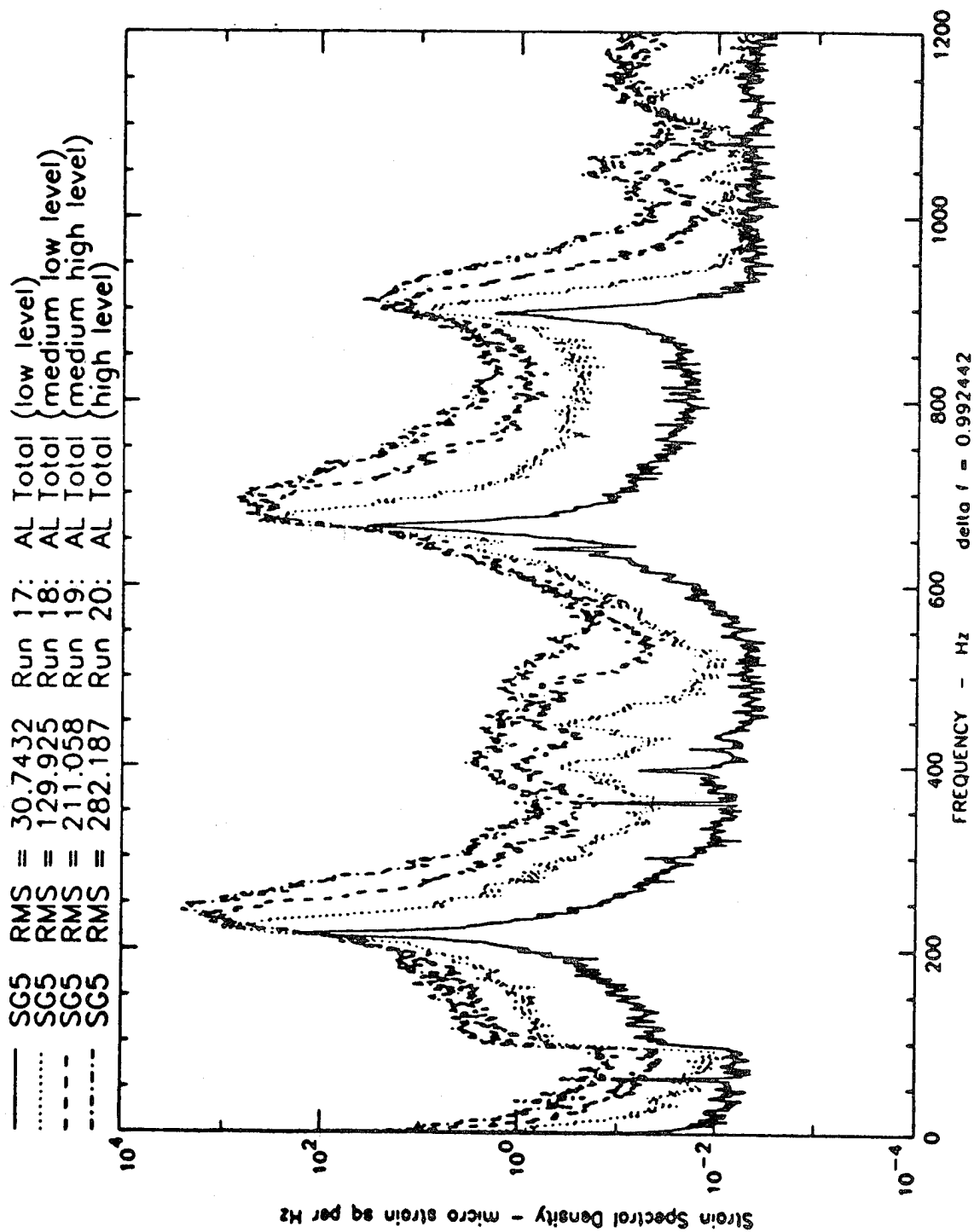


Fig 3.14 Strain spectral densities, 100-1000 Hz, SG 5, C-C-C aluminium shaker plate.

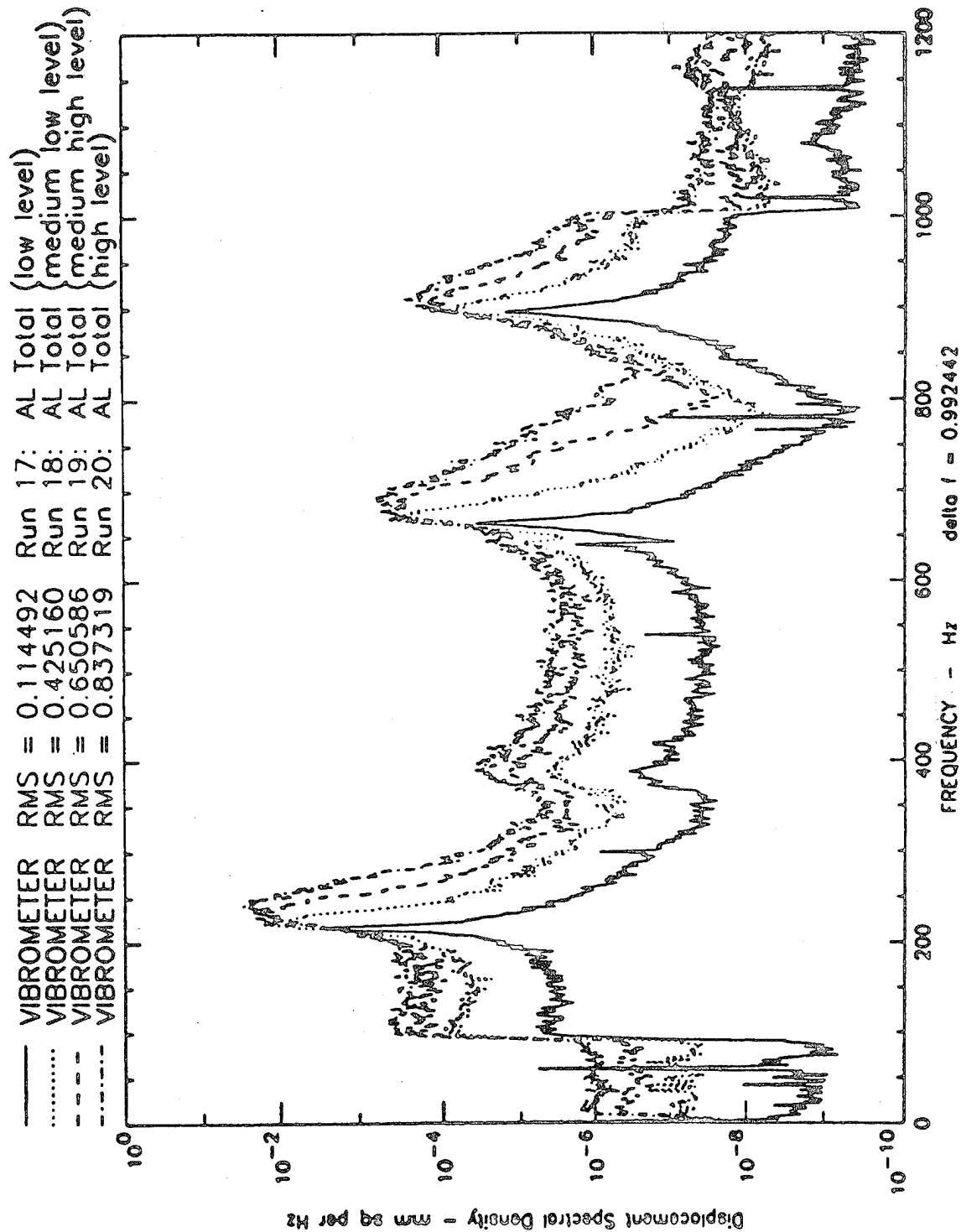


Fig 3.15 Displacement spectral densities, 100-1000 Hz, C-C-C aluminium shaker plate.

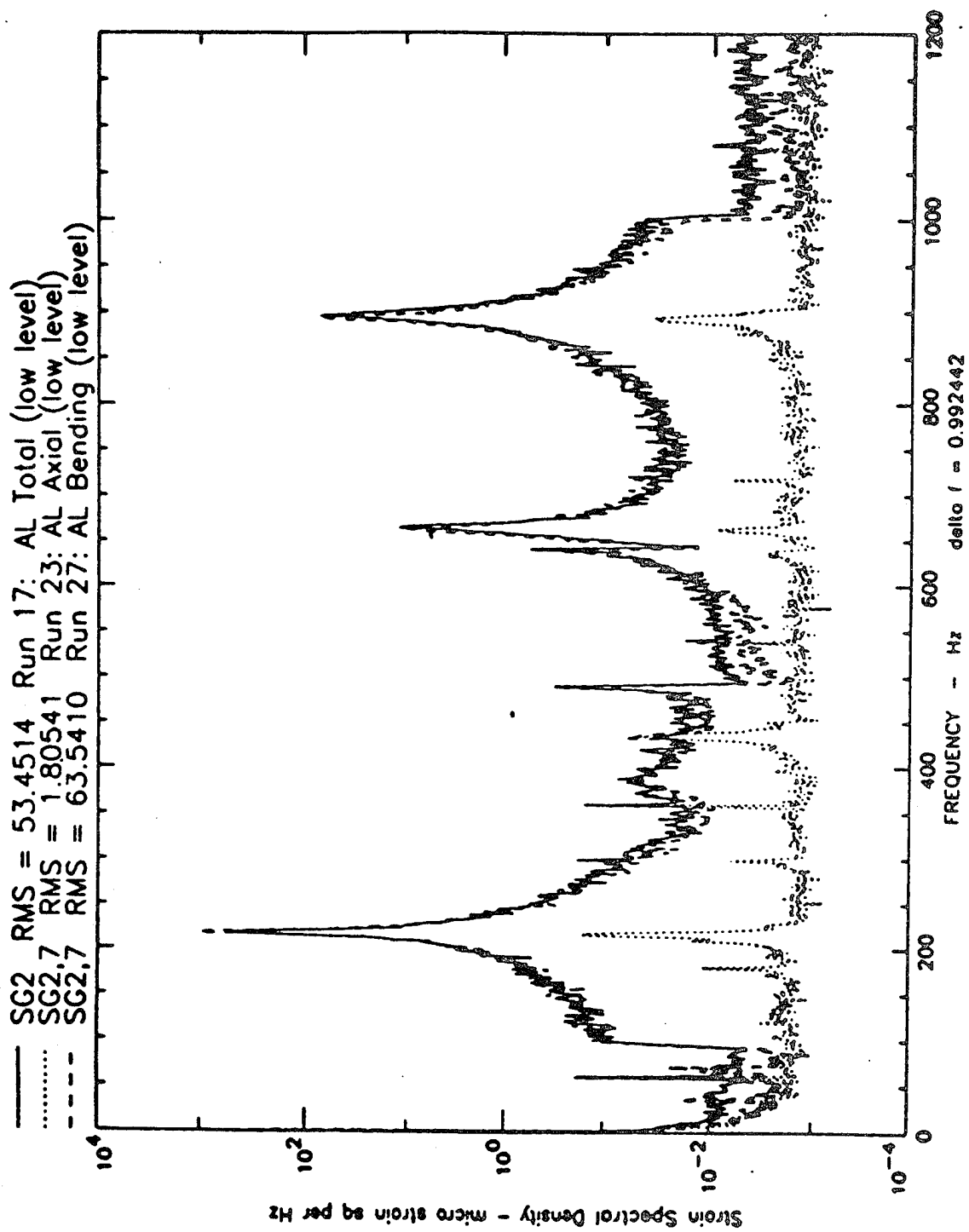


Fig 3.16 Total, axial, bending strain spectral densities, 1.46g random excitation, C-C-C-C aluminium shaker plate.

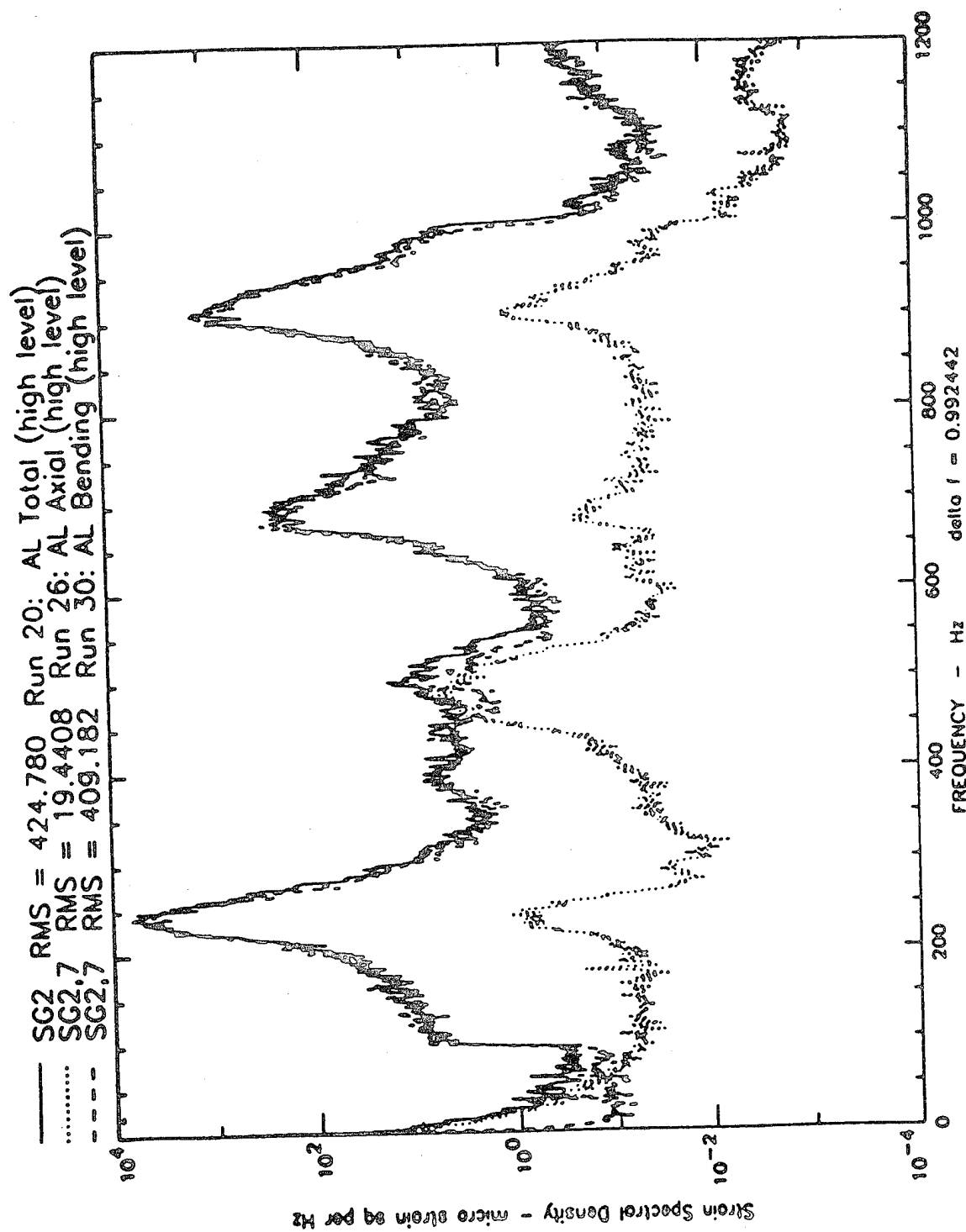


Fig 3.17 Total, axial, bending strain spectral densities, 14.4g random excitation, C-C-C-C aluminium shaker plate.

C-C-C-C AL SHAKER PLATE
100 - 1000 Hz RANDOM TOTAL STRAIN

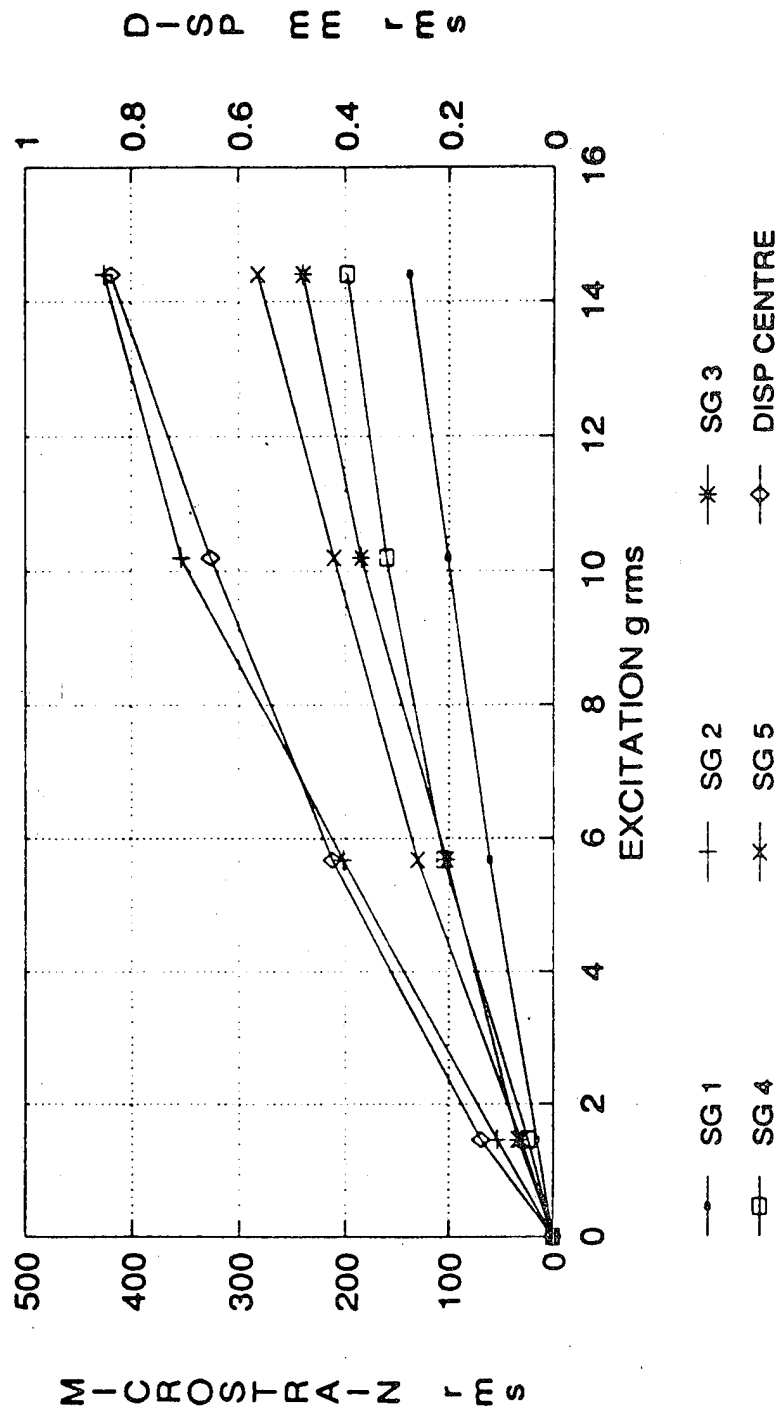


Fig 3.18 Total strains and displacements, C-C-C-C aluminium shaker plate.

C-C-C-C AL SHAKER PLATE
100 - 1000 Hz RANDOM TOTAL STRAIN

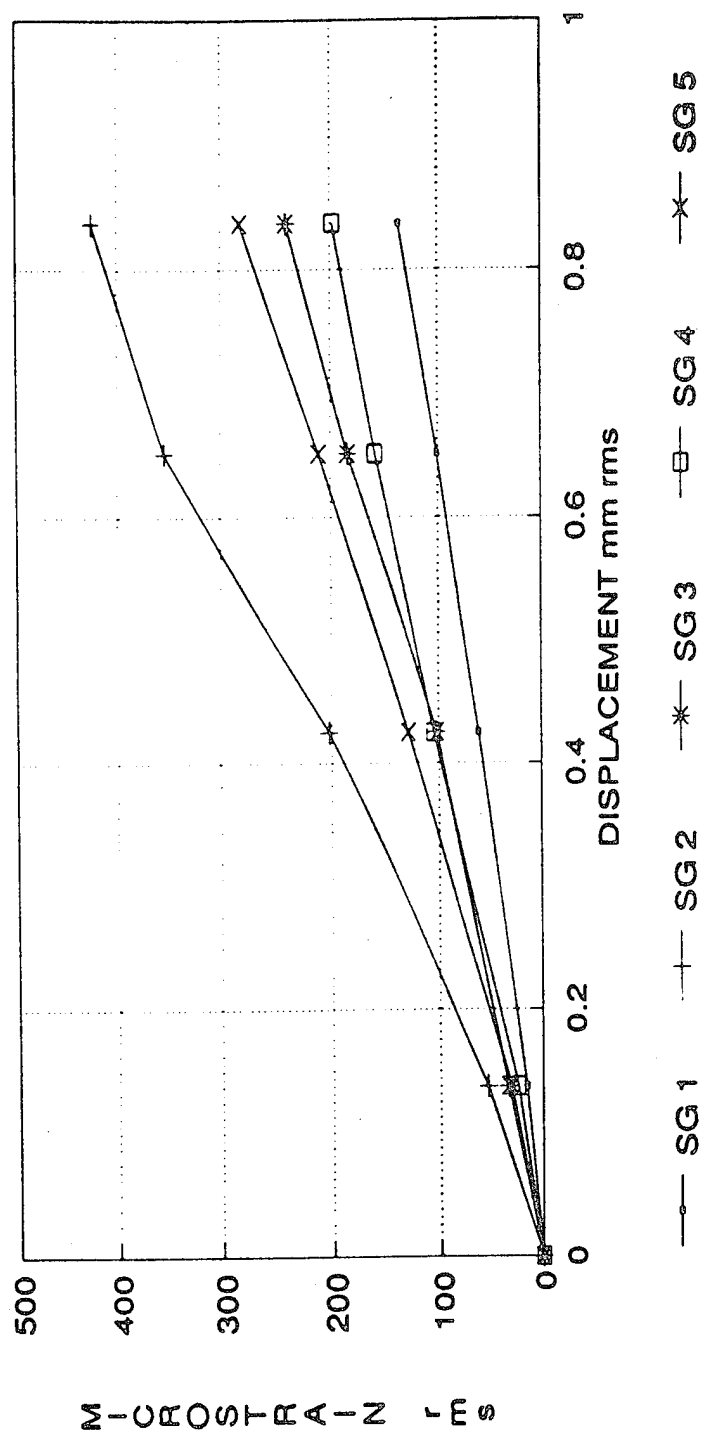


Fig 3.19 Total strain vs displacement, C-C-C-C aluminium shaker plate.

C-C-C-C AL SHAKER PLATE AXIAL STRAIN - RANDOM

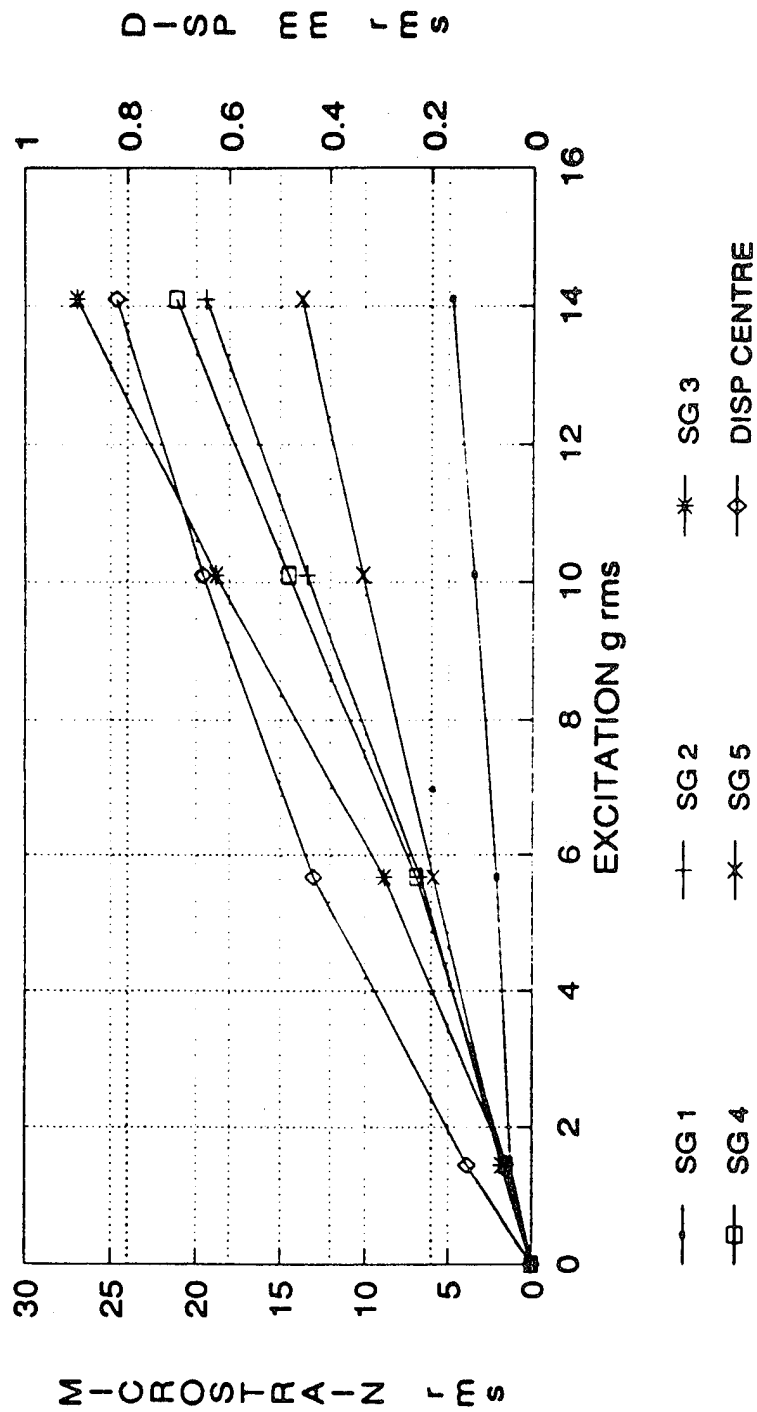


Fig 3.20 Axial strains and displacements, C-C-C-C aluminium shaker plate.

C-C-C-C AL SHAKER PLATE BENDING STRAIN - RANDOM

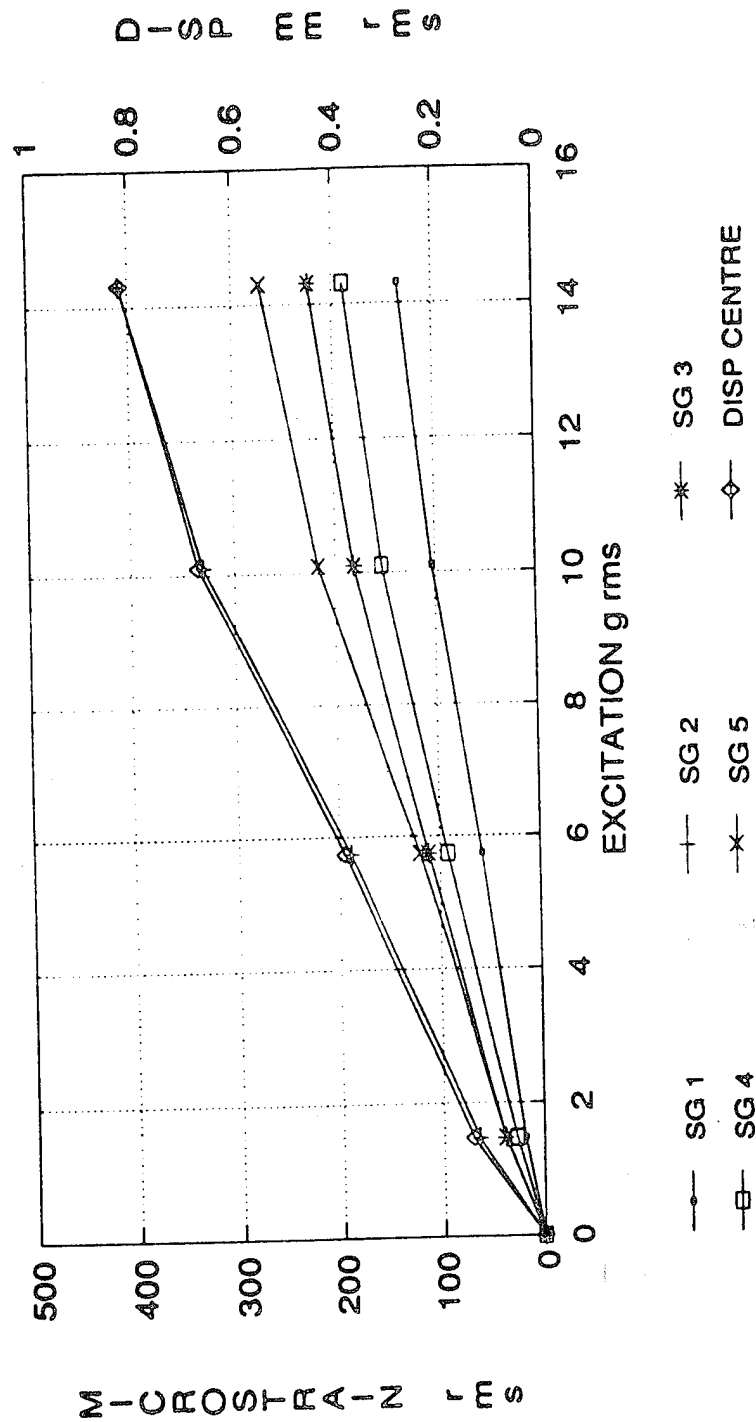


Fig 3.21 Bending strains and displacements, C-C-C-C aluminium shaker plate.

C-C-C-C AL SHAKER PLATE RANDOM SG 1 1&6

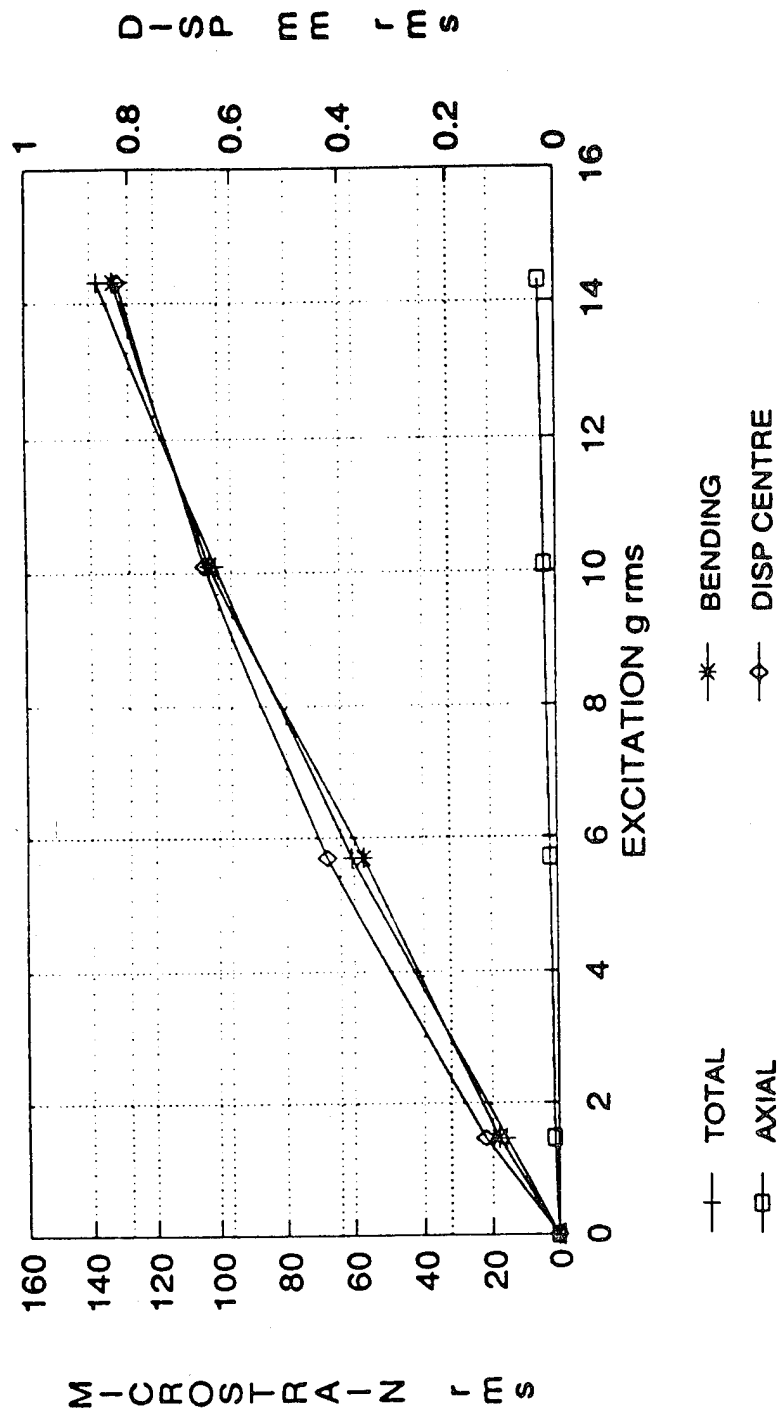


Fig 3.22 Total, axial and bending strains and displacements, SG 1 and 1 & 6, C-C-C-C aluminium shaker plate.

C-C-C-C AL SHAKER PLATE RANDOM SG 2 2&7

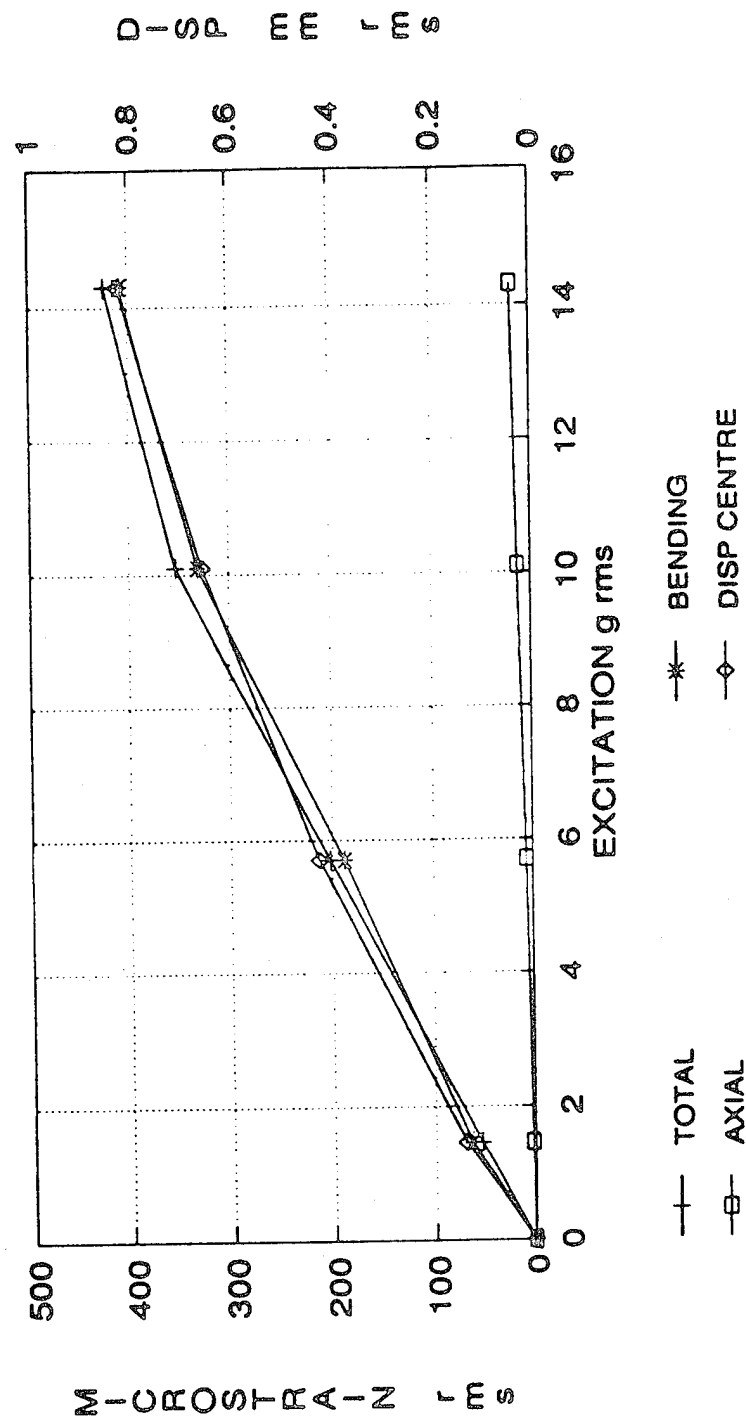


Fig 3.23 Total, axial and bending strains and displacements, SG 2 and 2 & 7 C-C-C-C aluminium shaker plate.

C-C-C-C AL SHAKER PLATE
RANDOM SG 3 3&8

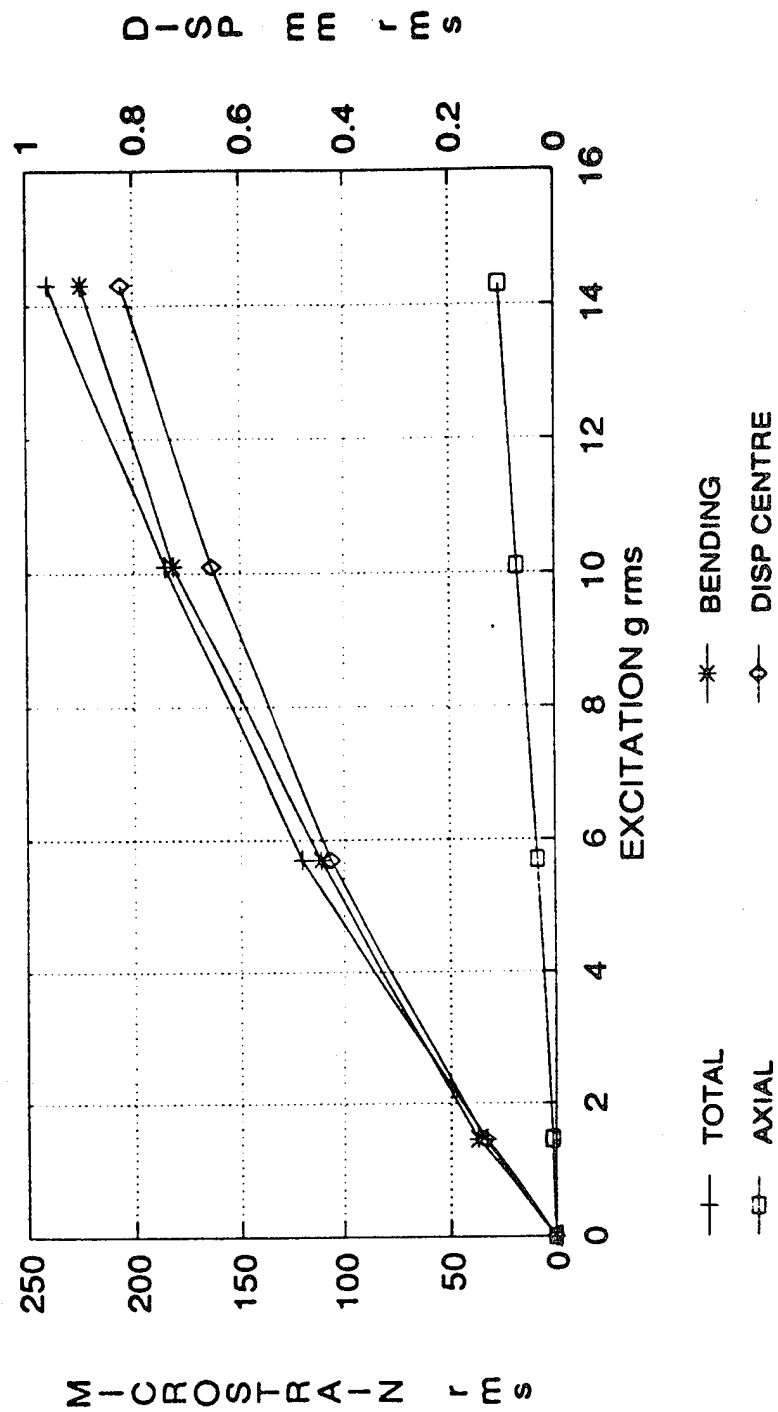


Fig 3.24 Total, axial and bending strains and displacements, SG 3 and 3 & 8 C-C-C-C aluminium shaker plate.

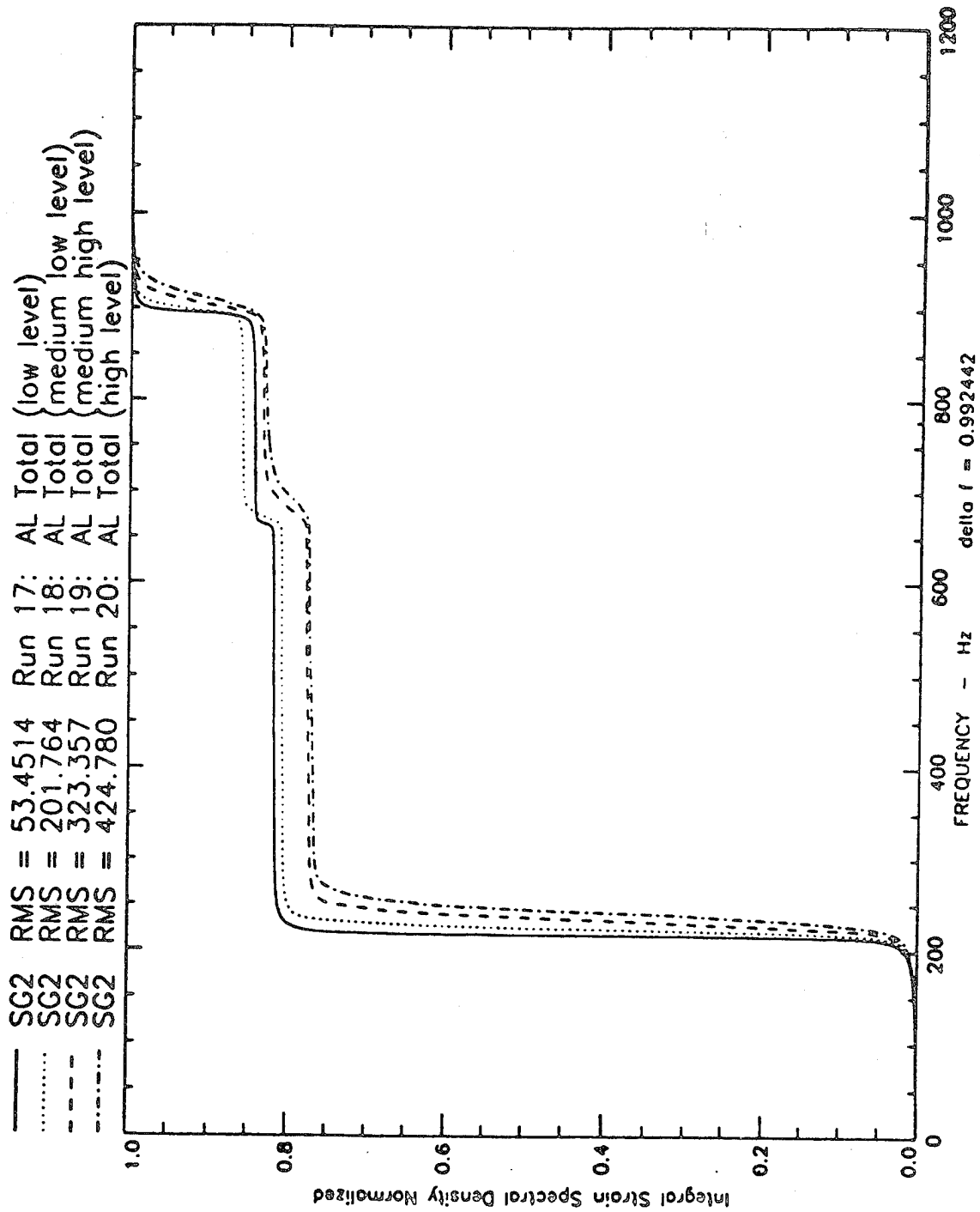


Fig 3.25 Normalised integrals of strain PSDs, SG 2, C-C-C-C aluminium shaker plate.

C-C-C-C AL SHAKER PLATE
Amplitude PDF ACCEL Rec 17 - 20

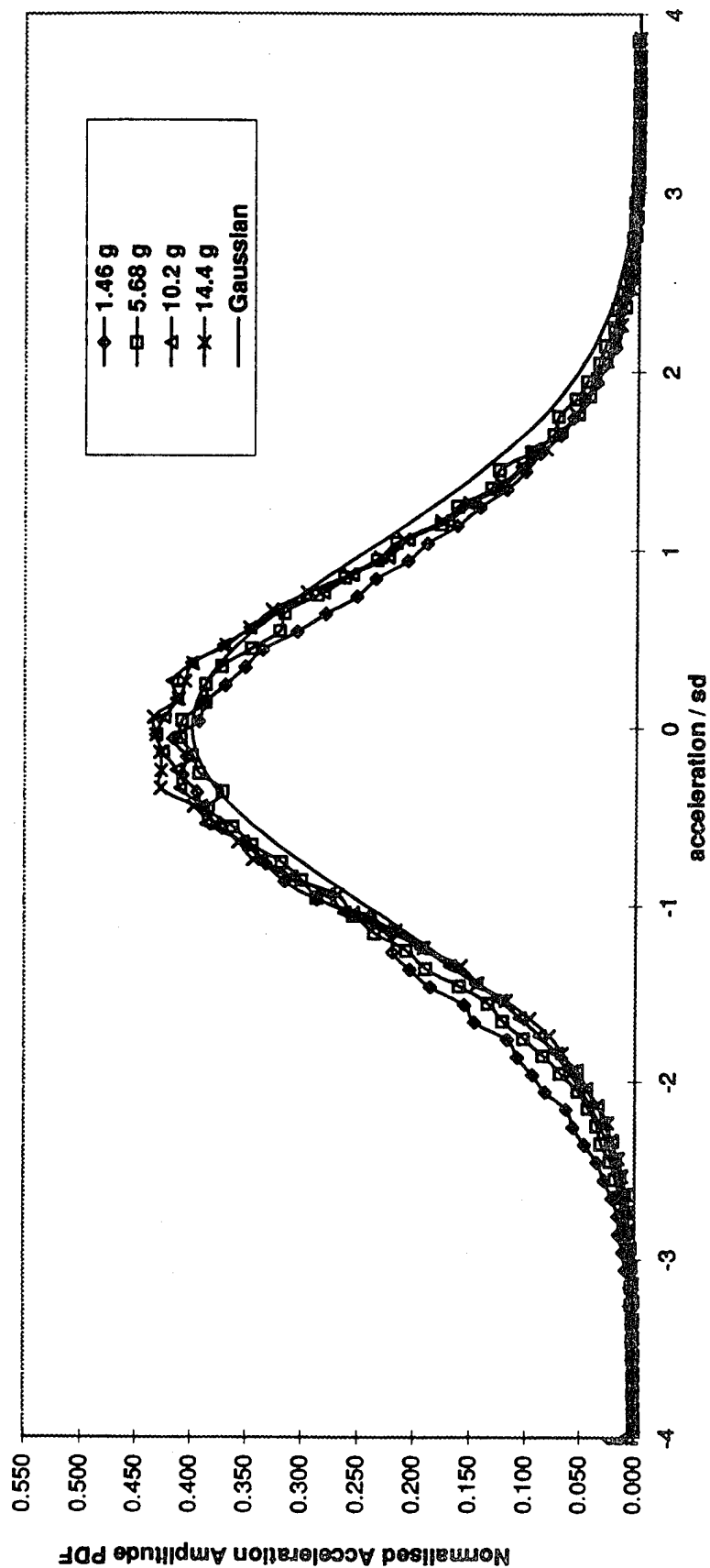


Fig 3.26 Normalised excitation amplitude PDFs, 100-1000 Hz random, C-C-C-C aluminium shaker plate.

C-C-C-C AL SHAKER PLATE
Amplitude PDF SG 2 Rec 17 - 20

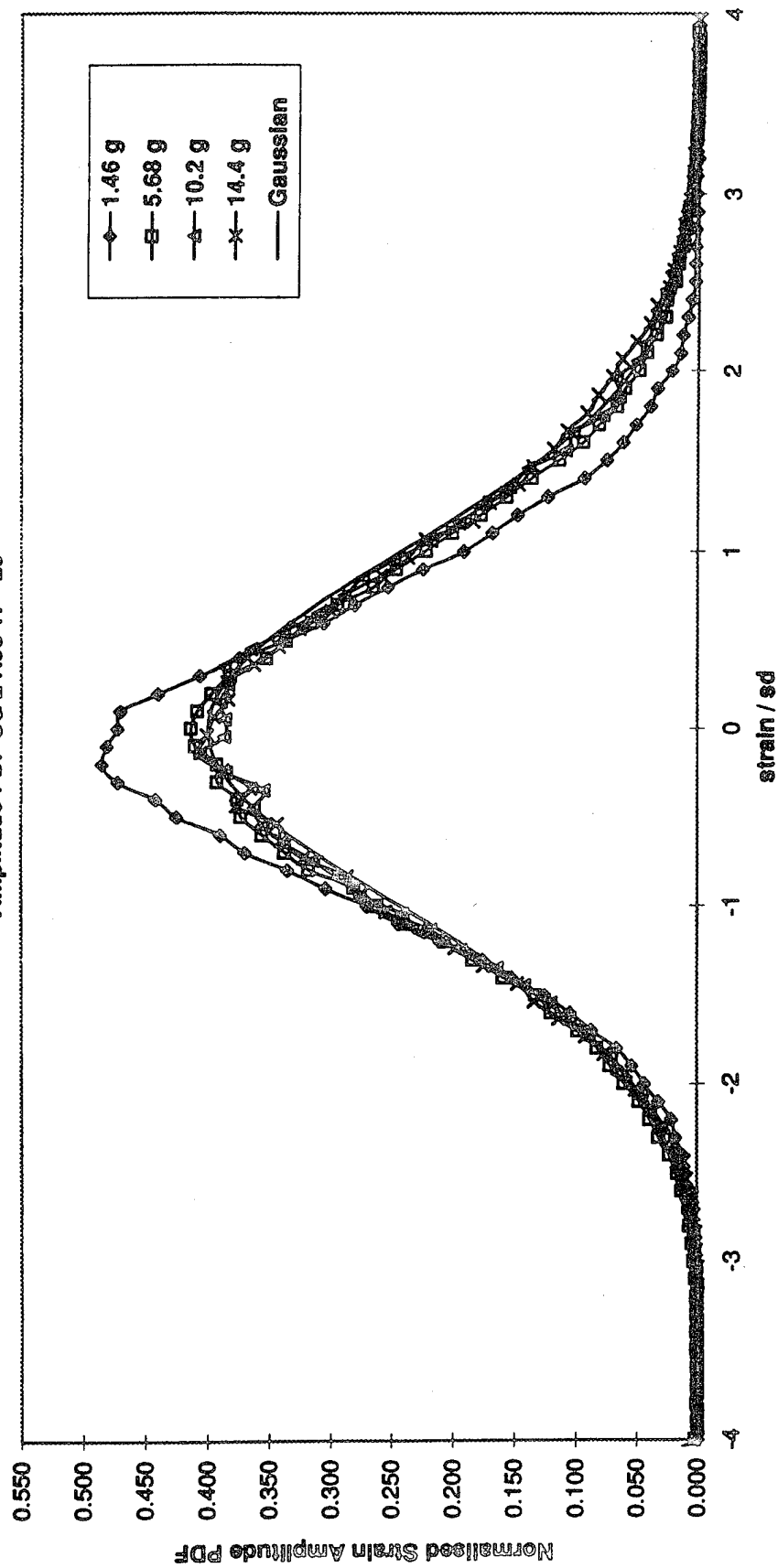


Fig 3.27 Normalised strain amplitude PDFs, 100-1000 Hz random, SG 2, C-C-C-C aluminium shaker plate.

C-C-C-AL SHAKER PLATE
Amplitude PDF 14.4 g SG 2 Rec 20

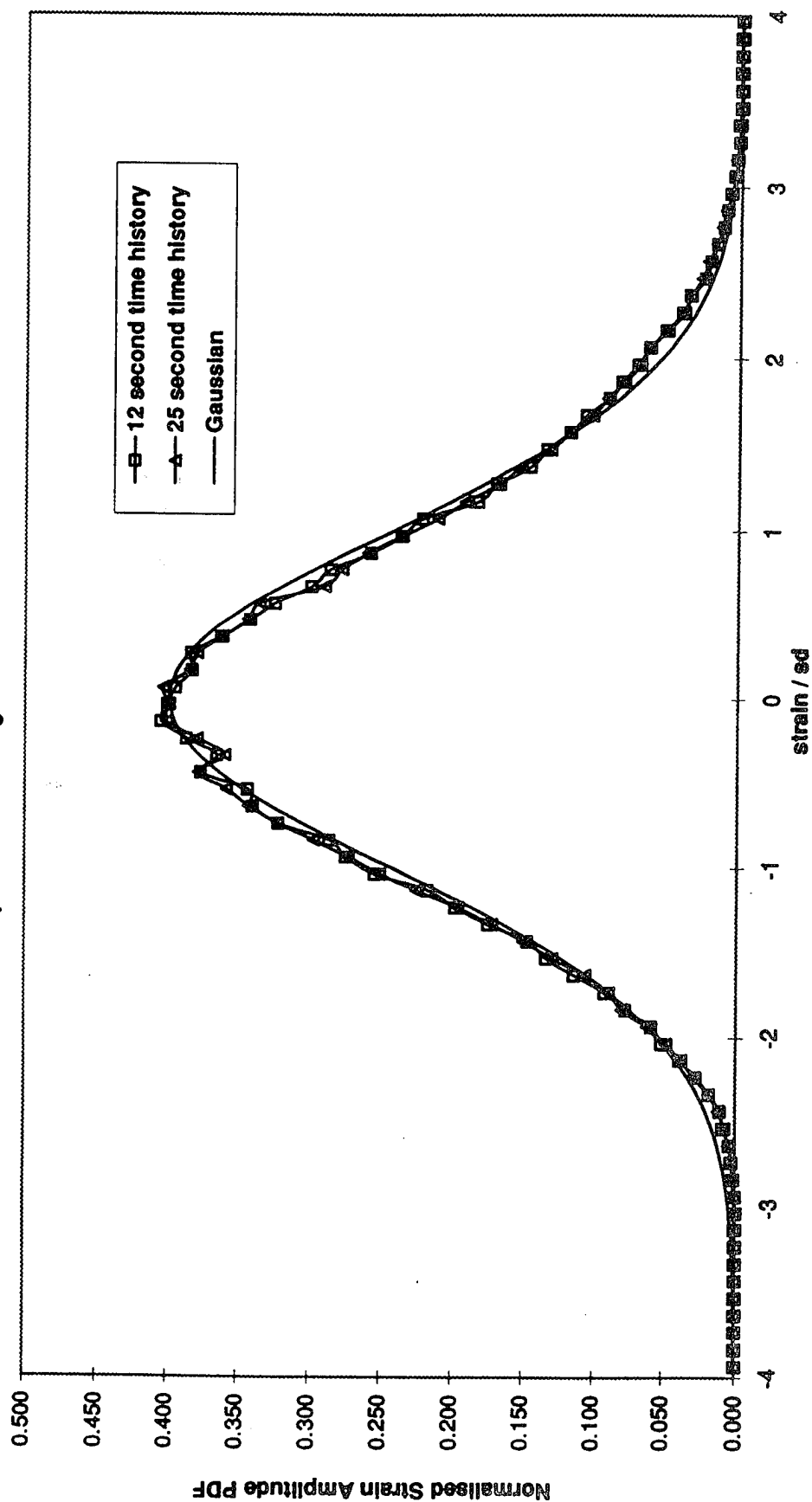
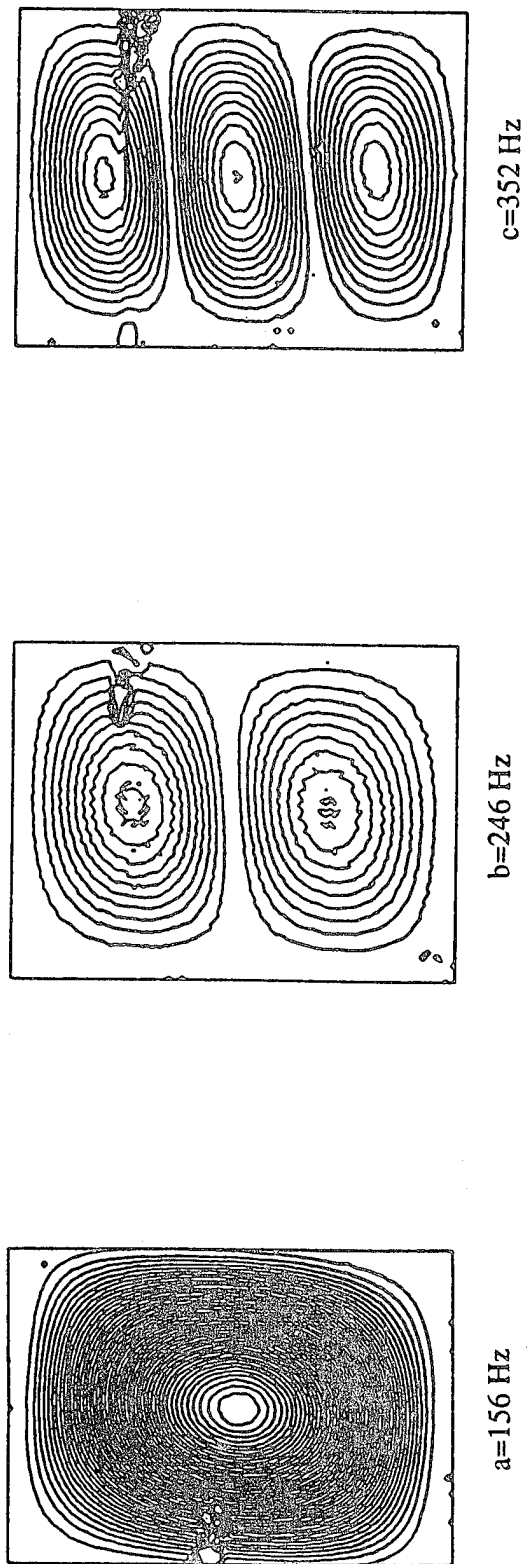


Fig 3.28 Normalised strain amplitude PDFs, 100-1000 Hz random, SG 2, 12 s and 25 s time histories, C-C-C-AL aluminium shaker plate.



$c=352\text{ Hz}$

$e=535\text{ Hz}$

$d=449\text{ Hz}$

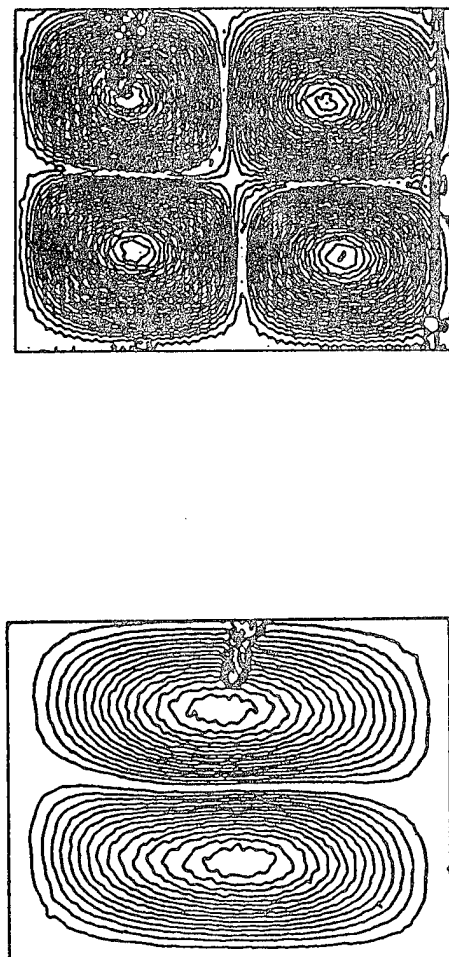
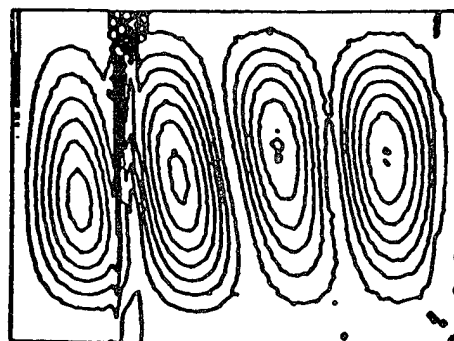
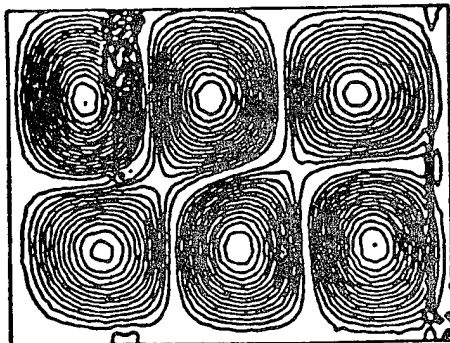


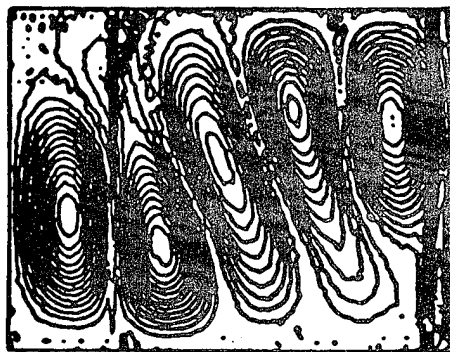
Fig 3.29 Mode shape, video holography method, $a=156\text{ Hz}$, $b=246\text{ Hz}$, $c=352\text{ Hz}$, $d=449\text{ Hz}$ and $e=535\text{ Hz}$, C-C-C-C CFRP shaker plane.



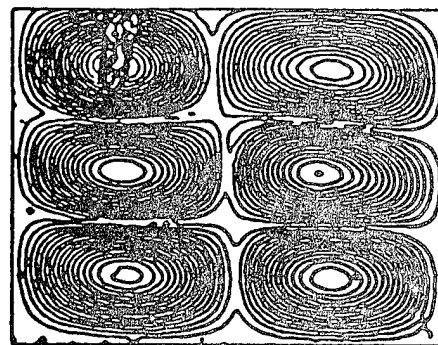
a=587 Hz



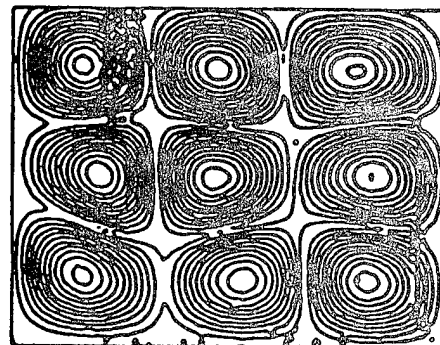
b=674 Hz



c=825 Hz



d=981 Hz



e=1110 Hz

Fig 3.30 Mode shape, video holography method, a=587 Hz, b=674 Hz, c=825 Hz, d=981 Hz and e=1110 Hz, C-C-C-C CTRP ~~shar~~ pin.

C-C-C-C CFRP SHAKER PLATE SINE DWELL

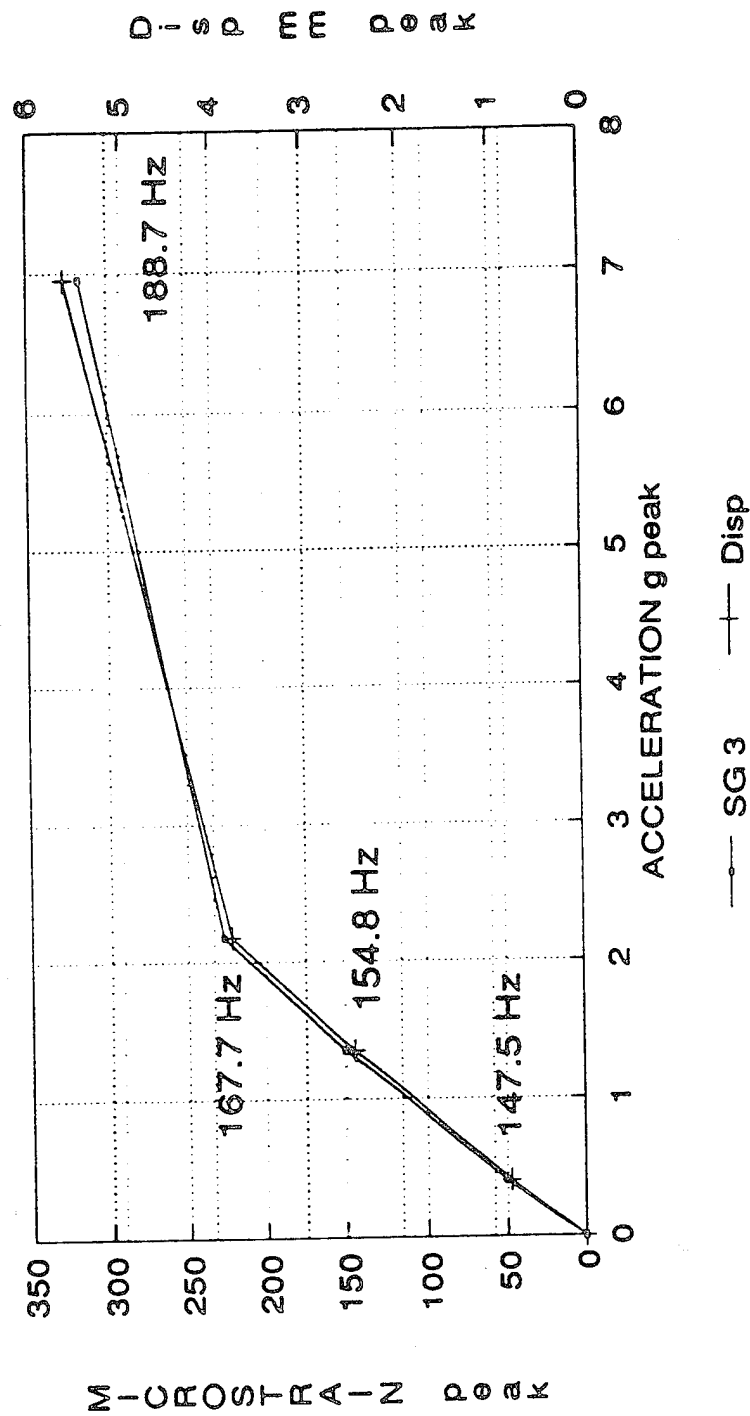


Fig 3.31 Total strains and displacements, SG 3, sine dwell tests, C-C-C-C CFRP shaker plate.

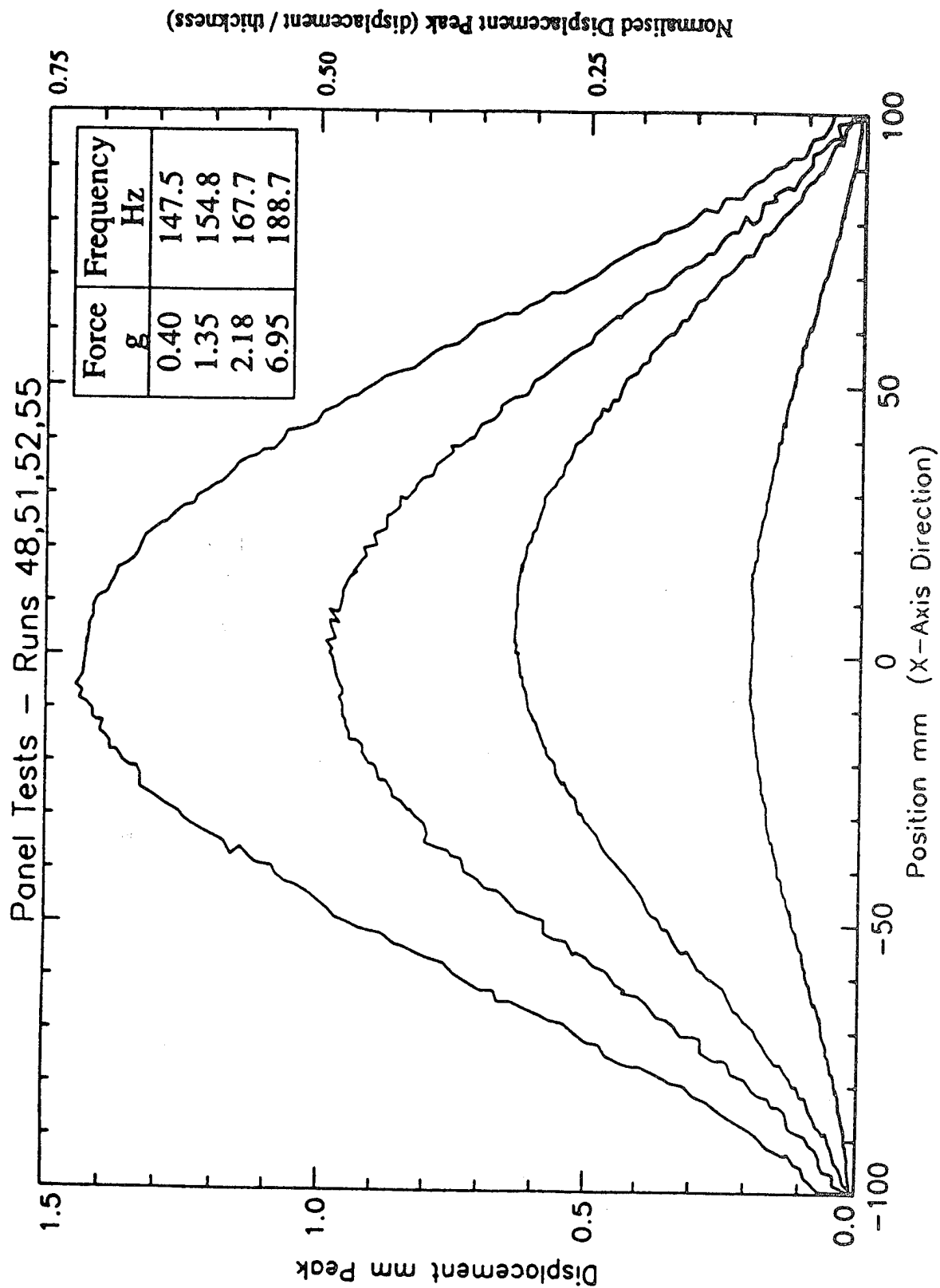


Fig 3.32 Nonlinear displacement shapes, fundamental resonance width direction, unsmoothed data, C-C-C-C CFRP shaker plate.

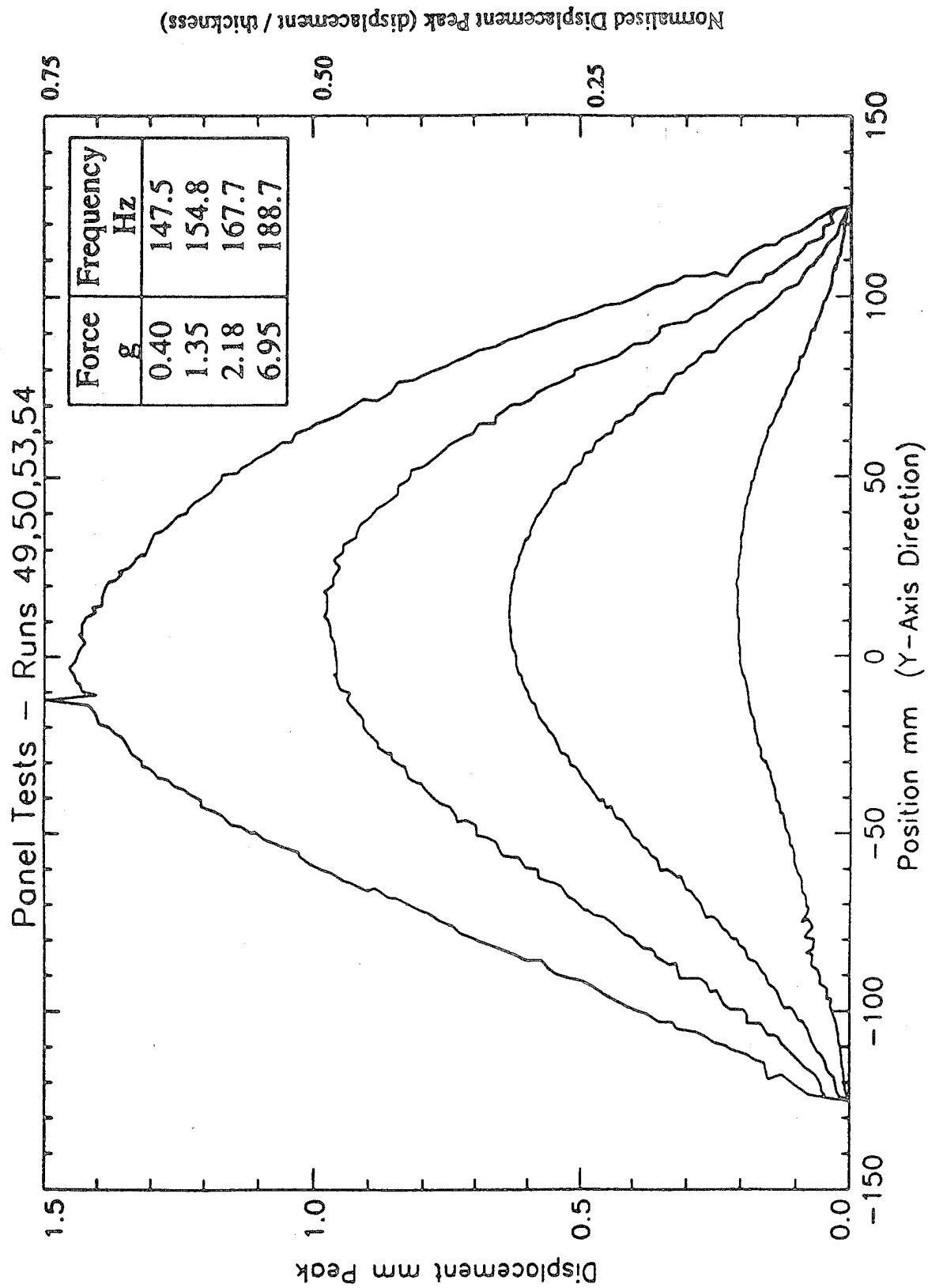


Fig 3.33 Nonlinear displacement shapes, fundamental resonance length direction, unsmoothed data, C-C-C-C CFRP plate.

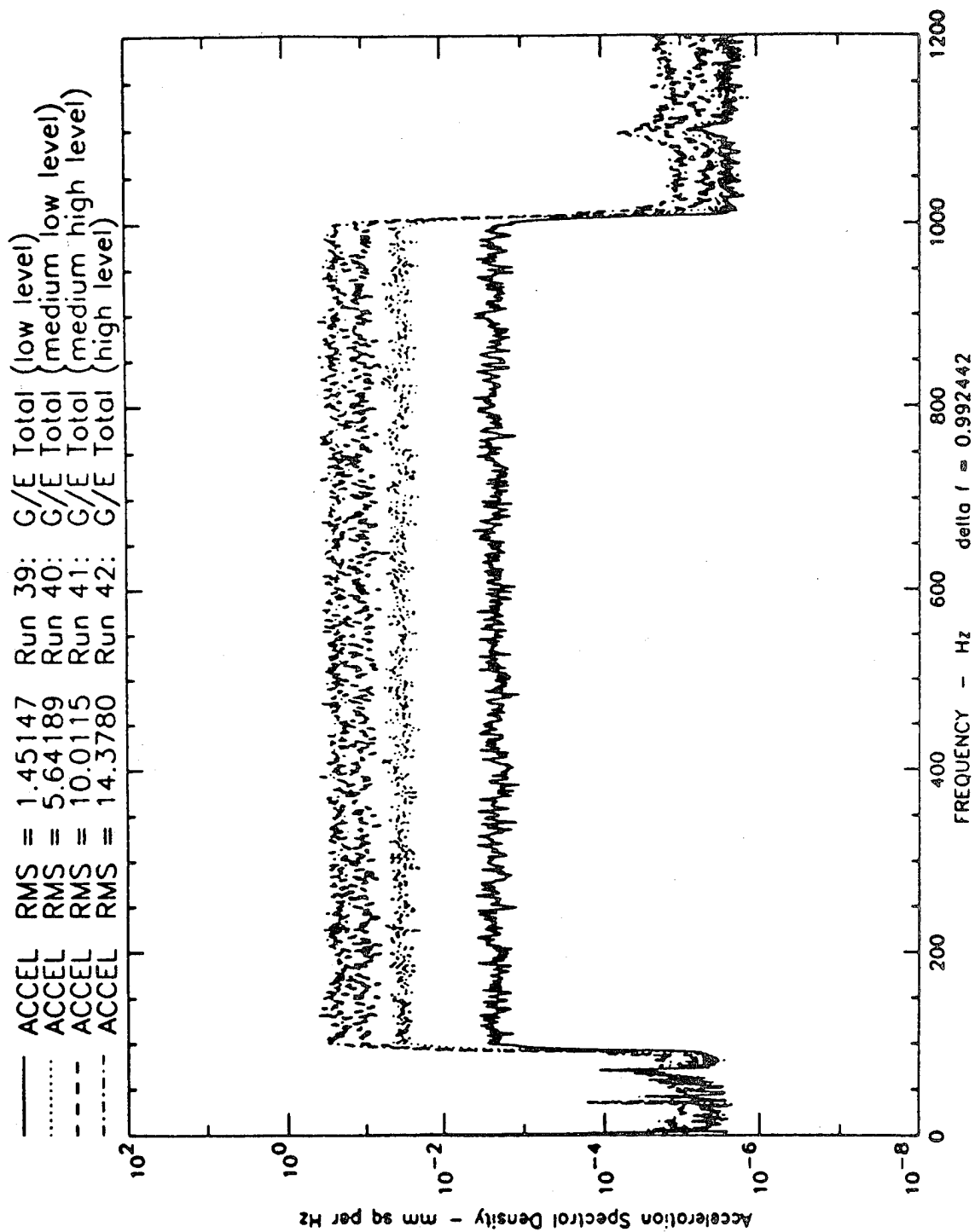


Fig 3.34 Excitation spectral densities, 100-1000 Hz, C-C-C-C CFRP shaker plate.

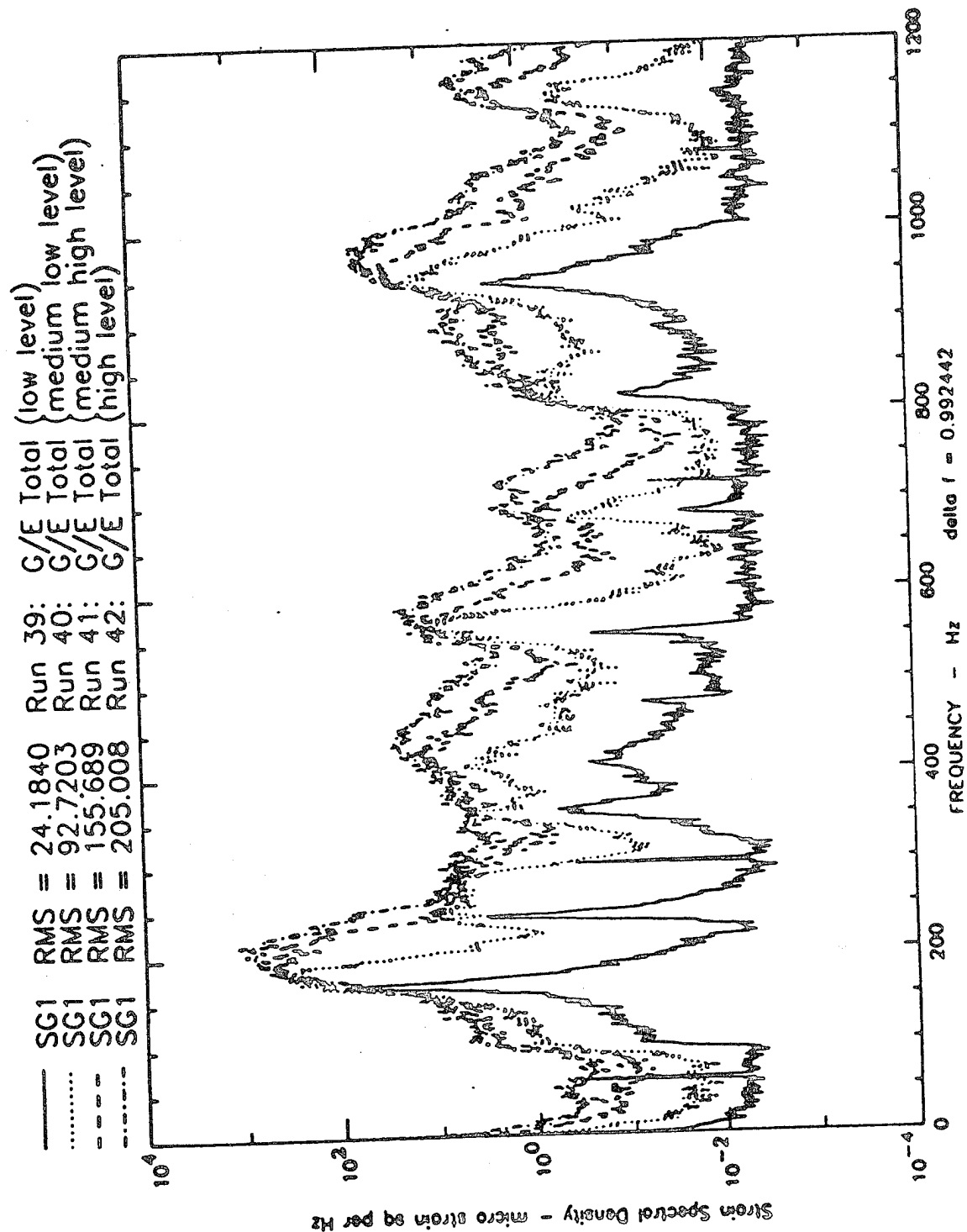


Fig 3.35 Strain spectral densities, 100-1000 Hz, SG 1, C-C-C-C CFRP shaker plate.

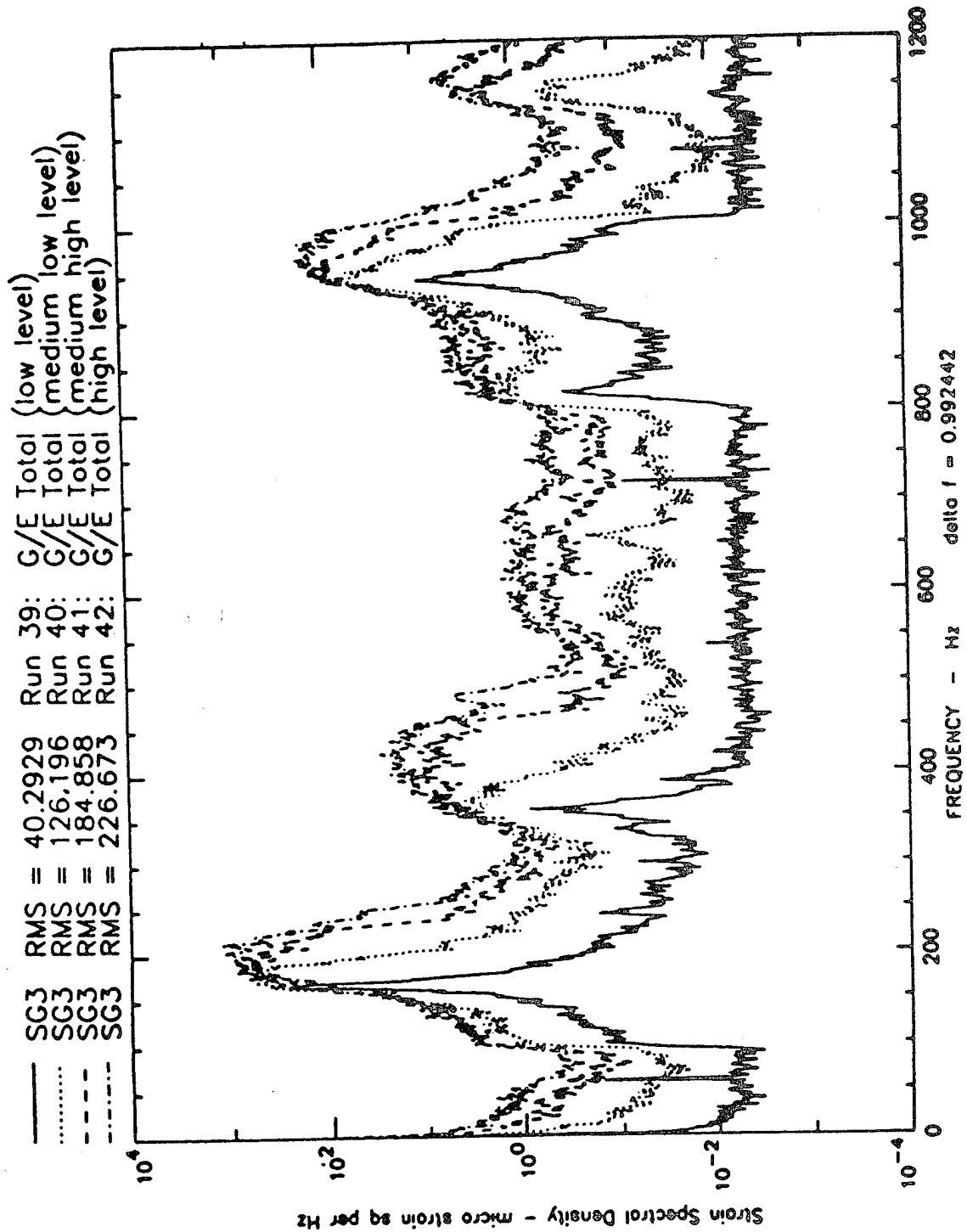


Fig 3.36 Strain spectral densities, 100-1000 Hz, SG 3, C-C-C-C CFRP shaker plate.

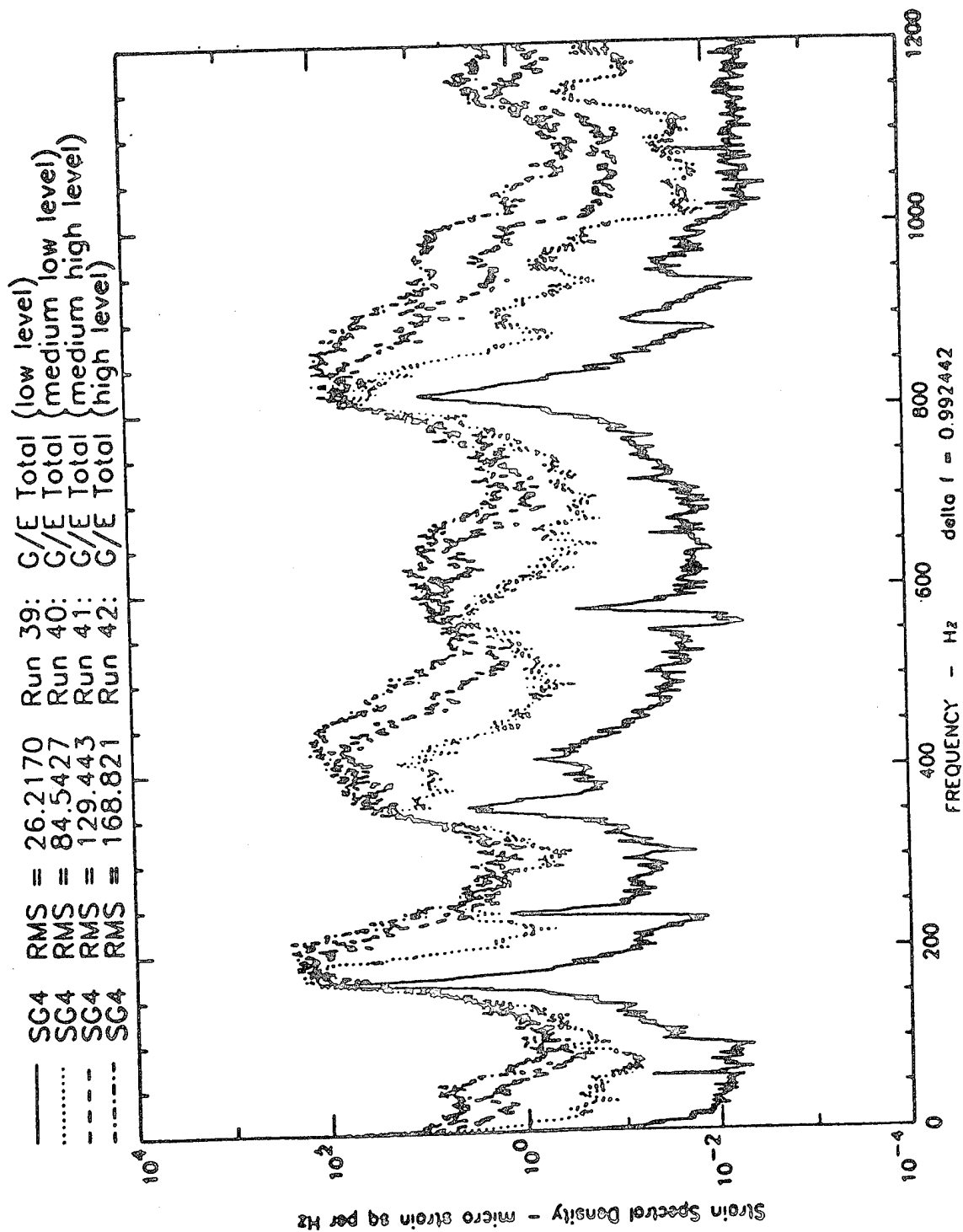


Fig 3.37 Strain spectral densities, 100-1000 Hz, SG 4, C-C-C CFRP shaker plate.

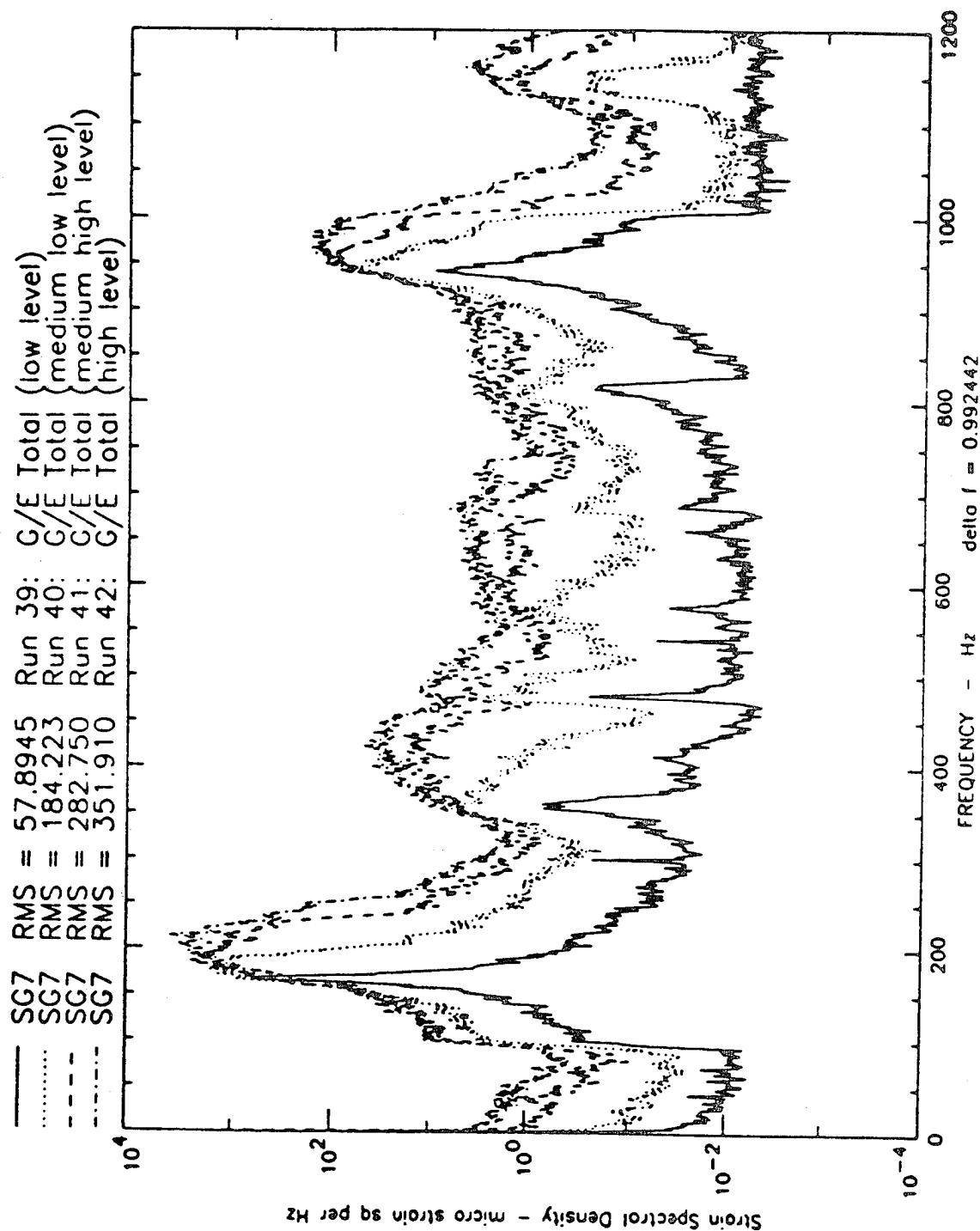


Fig 3.38 Strain spectral densities, 100-1000 Hz, SG 7, C-C-C-C FRP shaker plate.

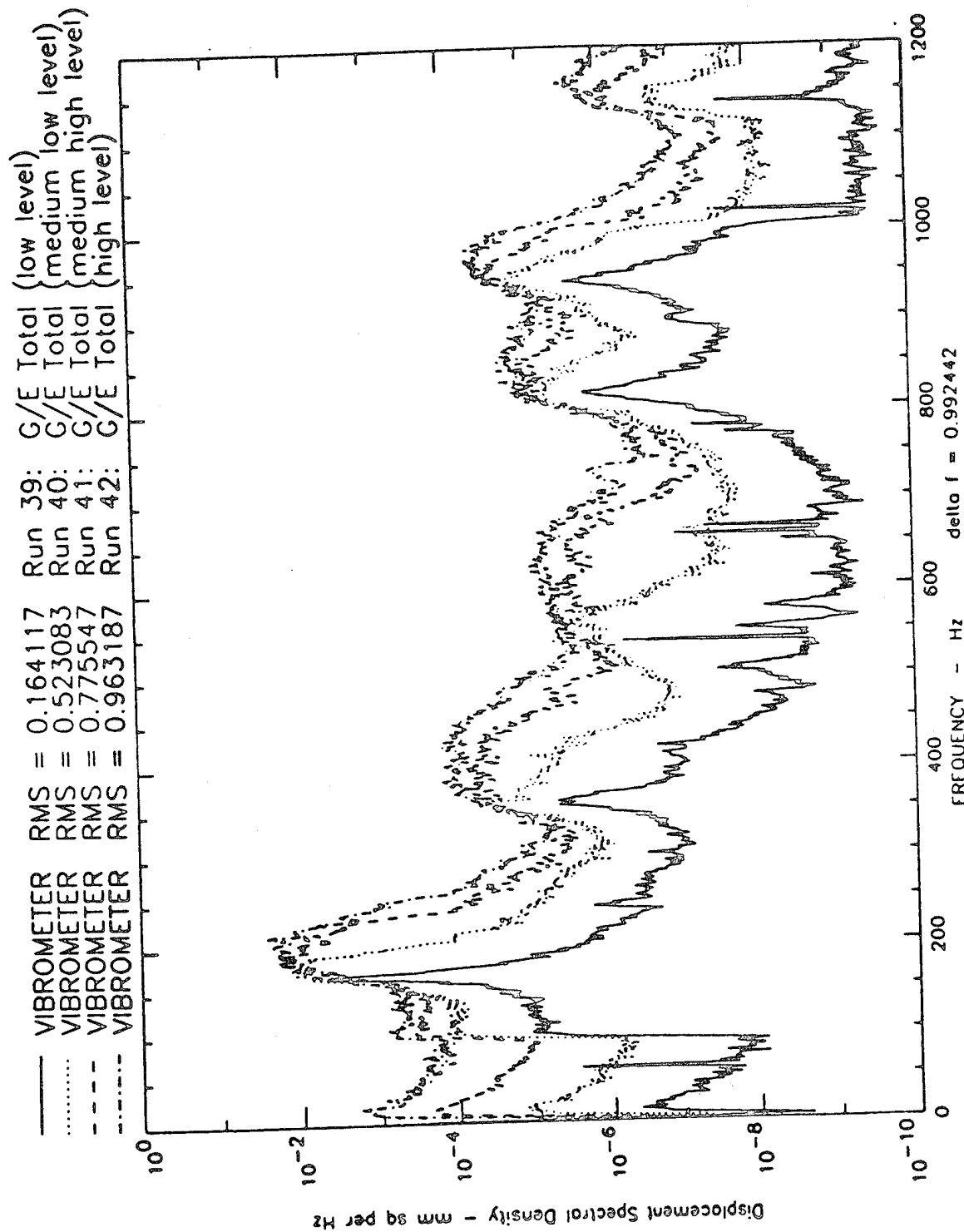


Fig 3.39 Displacement spectral densities 100-1000 Hz, C-C-C CFRP shaker plate.

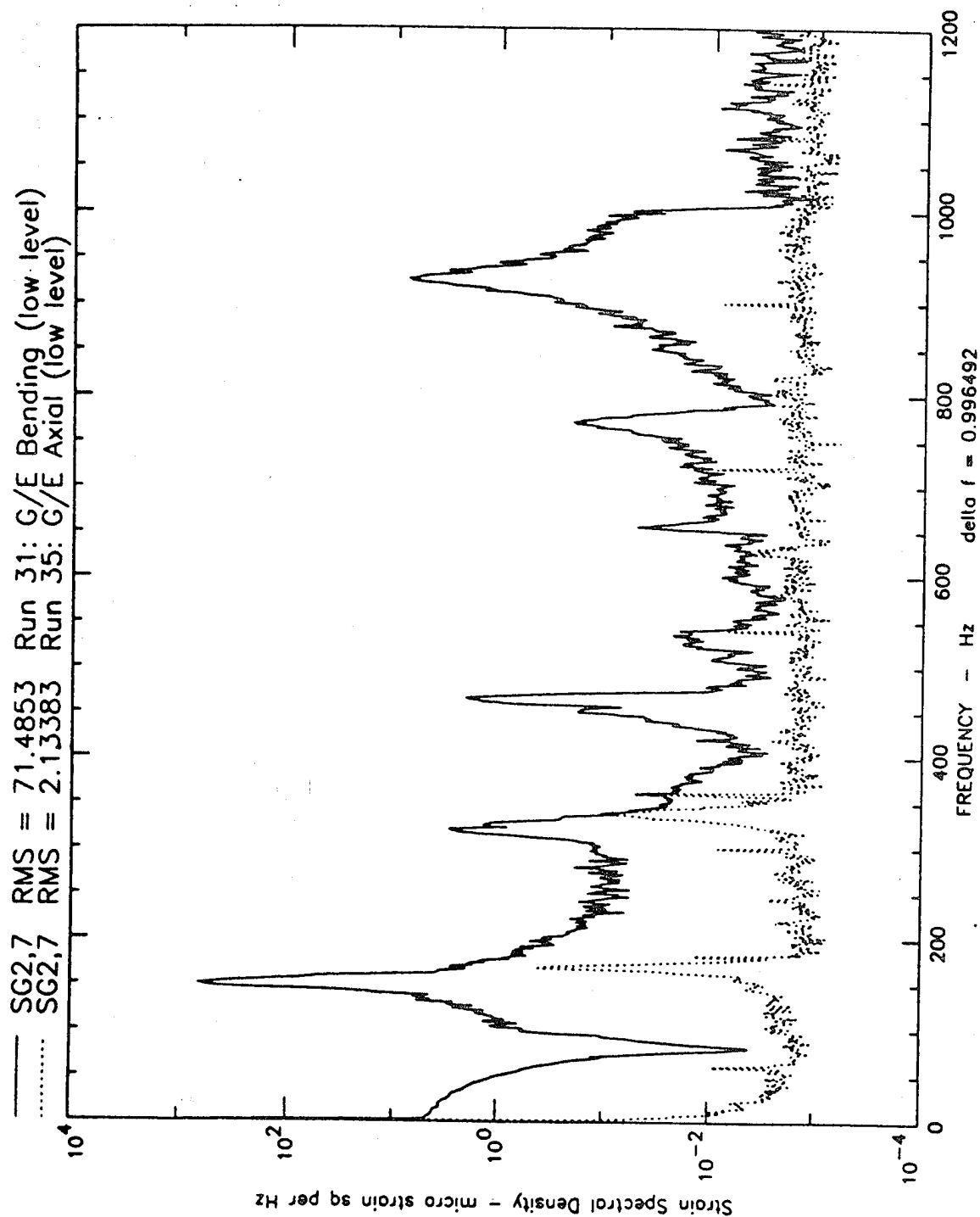


Fig 3.40 Axial and bending strain spectral densities, 1.45 g random excitation, C-C-C-C CFRP shaker plate.

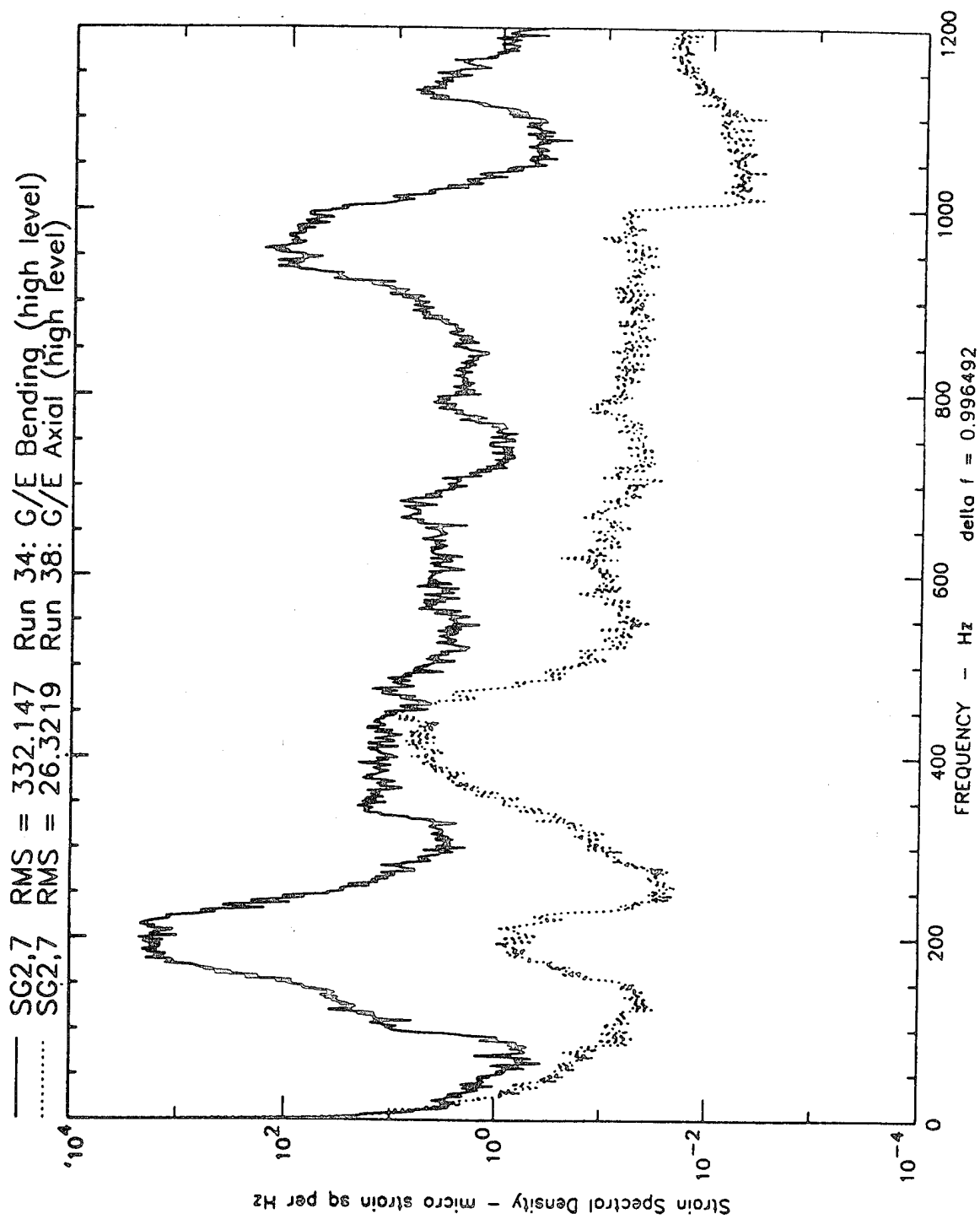


Fig 3.41 Axial and bending strain spectral densities, 14.4 g random excitation, C-C-C-C CFRP shaker plate.

C-C-C-C CFRP SHAKER PLATE
TOTAL STRAIN 100-1000 HZ RANDOM

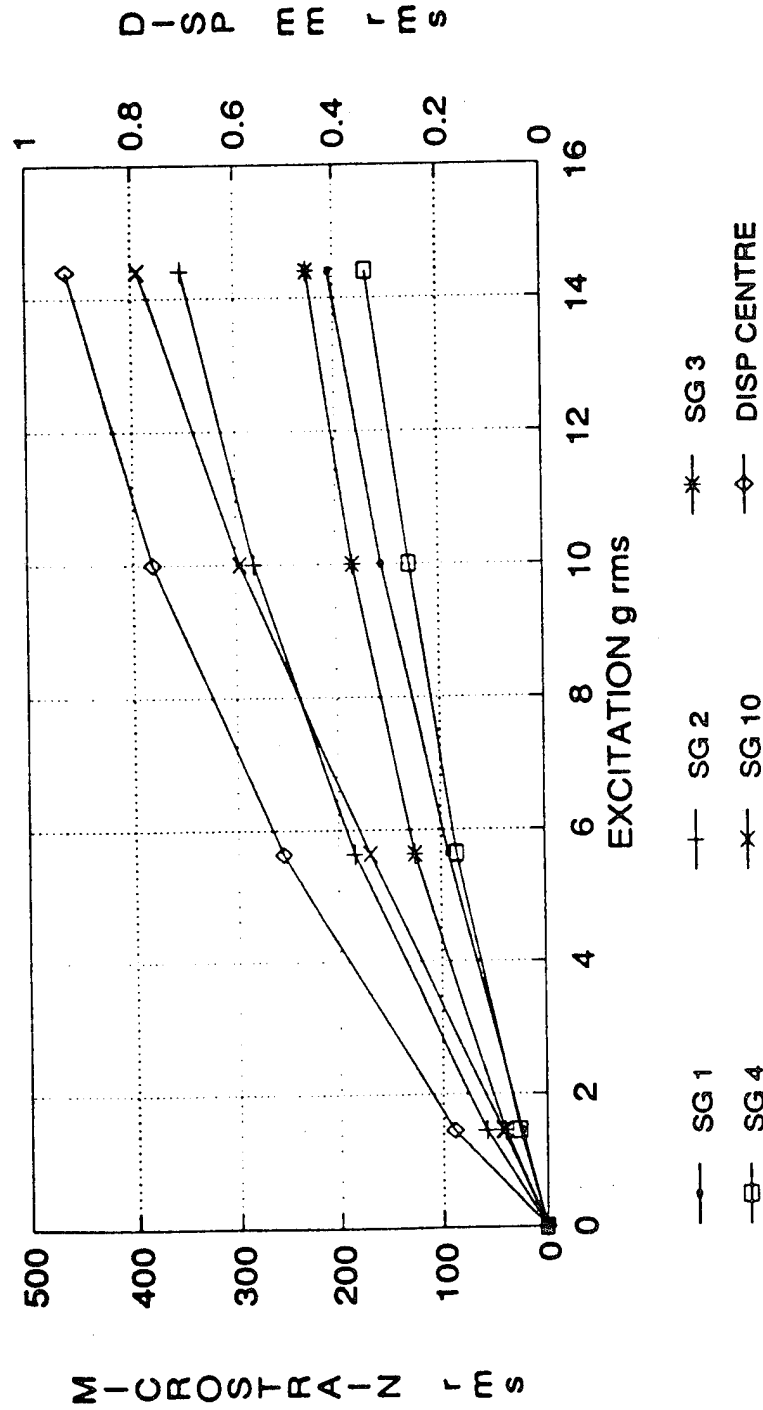


Fig 3.42 Total strains and displacements, C-C-C-C CFRP shaker plate.

C-C-C-C CFRP SHAKER PLATE TOTAL STRAIN

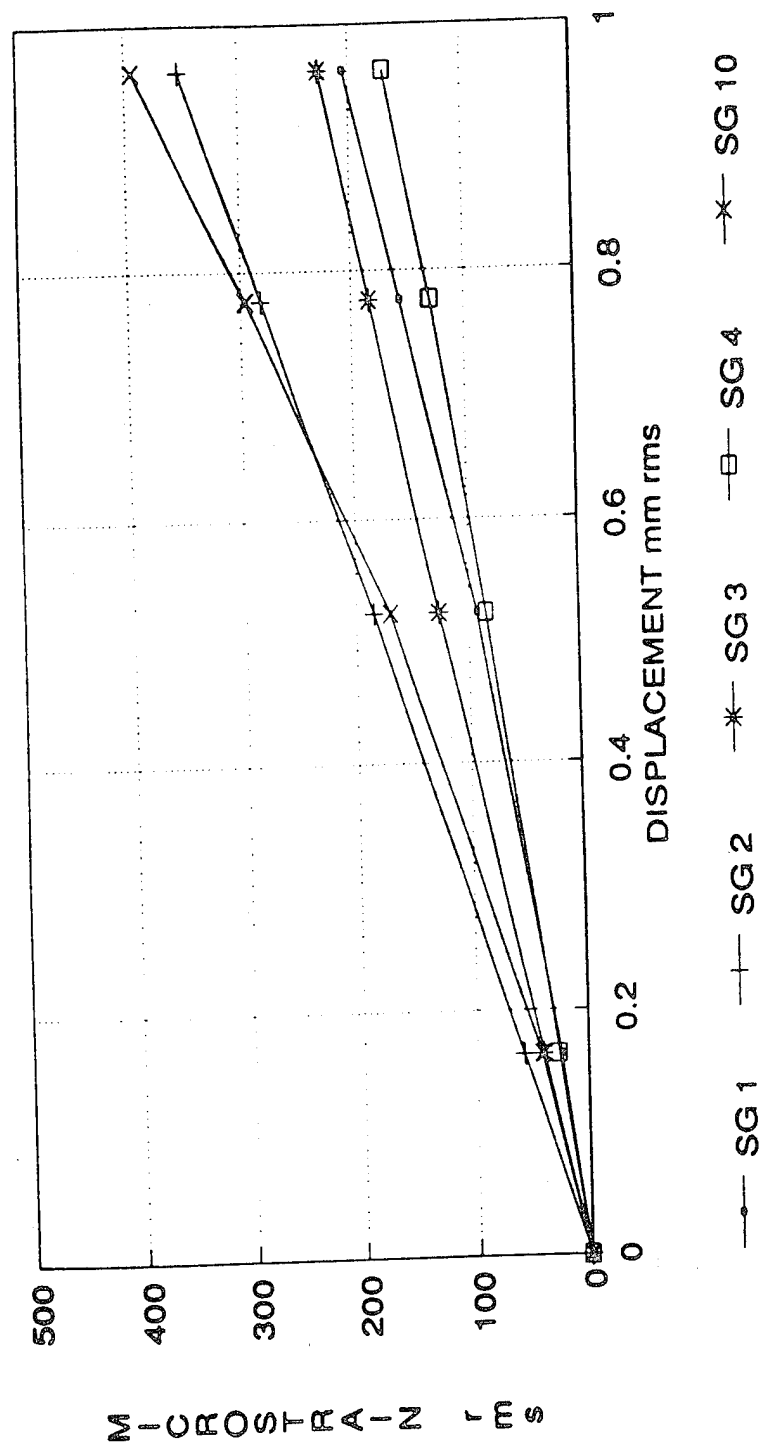


Fig 3.43 Total strain vs displacement, C-C-C-C CFRP shaker plate.

C-C-C-C CFRP SHAKER PLATE AXIAL STRAIN

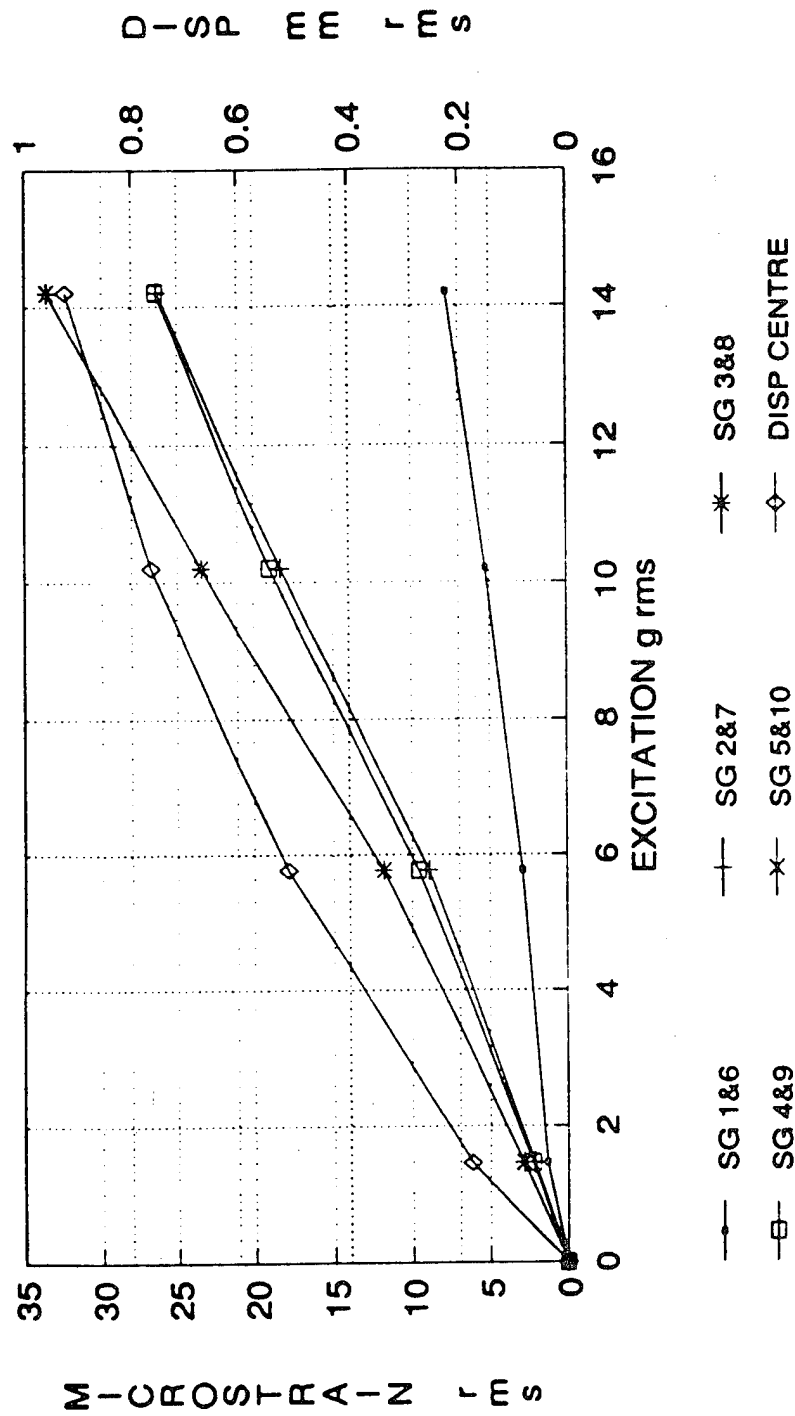


Fig 3.44 Axial strains and displacements, C-C-C-C CFRP shaker plate.

C-C-C-C CFRP SHAKER PLATE BENDING STRAIN

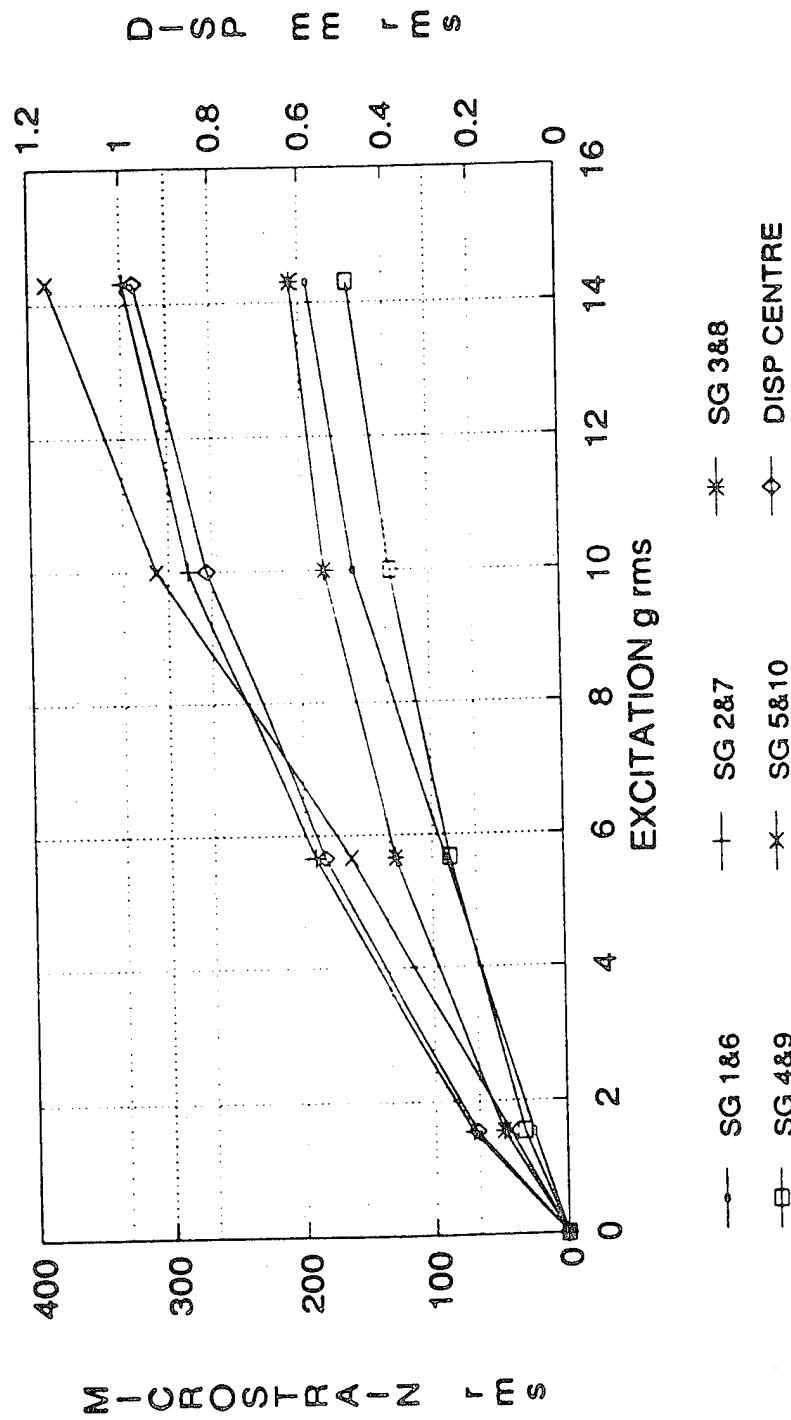


Fig 3.45 Bending strains and displacements, C-C-C-C CFRP shaker plate.

C-C-C-C CFRP SHAKER PLATE TOTAL BENDING AXIAL STRAIN SG 1 1&6

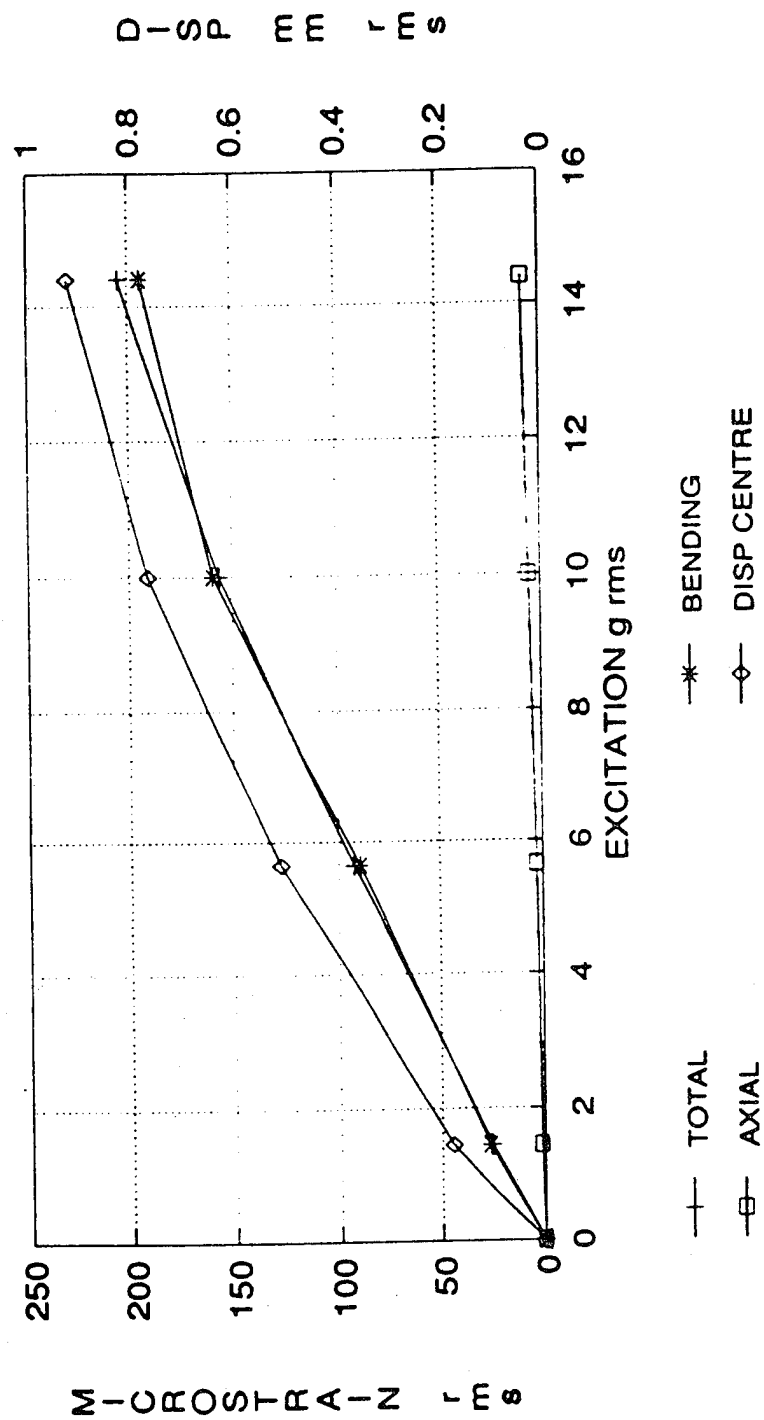


Fig 3.46 Total, axial and bending strains and displacements, SG 1 and 1 & 6, C-C-C-C CFRP shaker plate.

C-C-C-C CFRP SHAKER PLATE
TOTAL BENDING AXIAL STRAIN SG 2 2&7

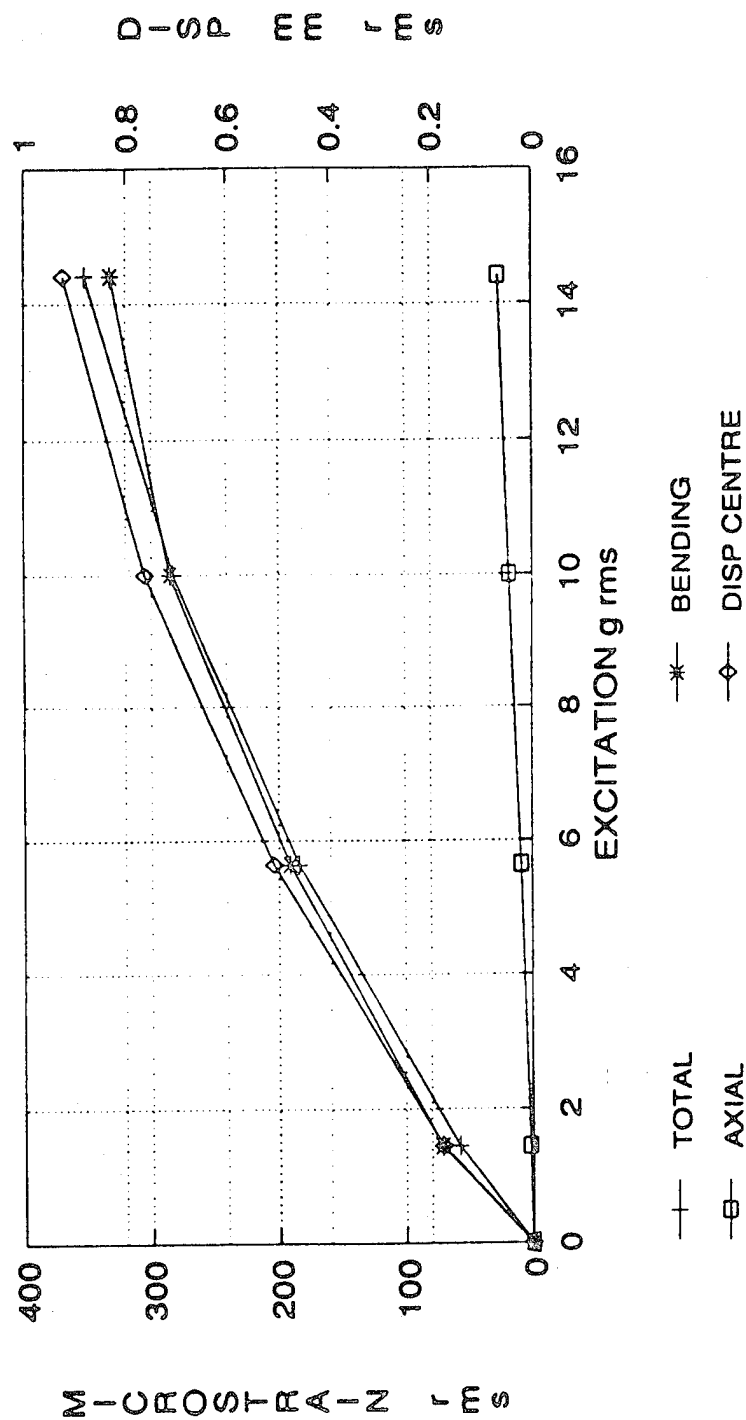


Fig 3.47 Total, axial and bending strains and displacements, SG 2 and 2 & 7, C-C-C-C CFRP shaker plate.

C-C-C-C CFRP SHAKER PLATE
TOTAL BENDING AXIAL STRAIN SG 3 3&8

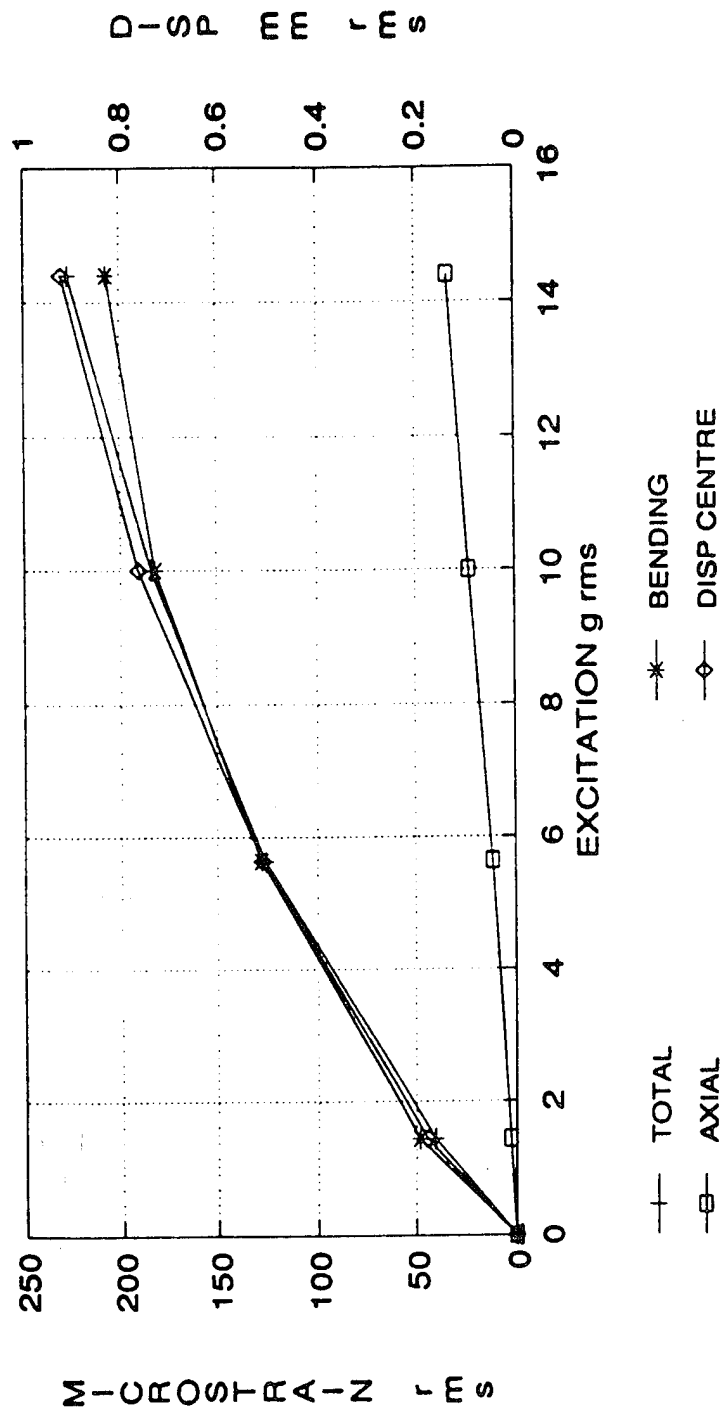


Fig 3.48 Total, axial and bending strains and displacements, SG3 and 3 & 8, C-C-C-C CFRP shaker plate.

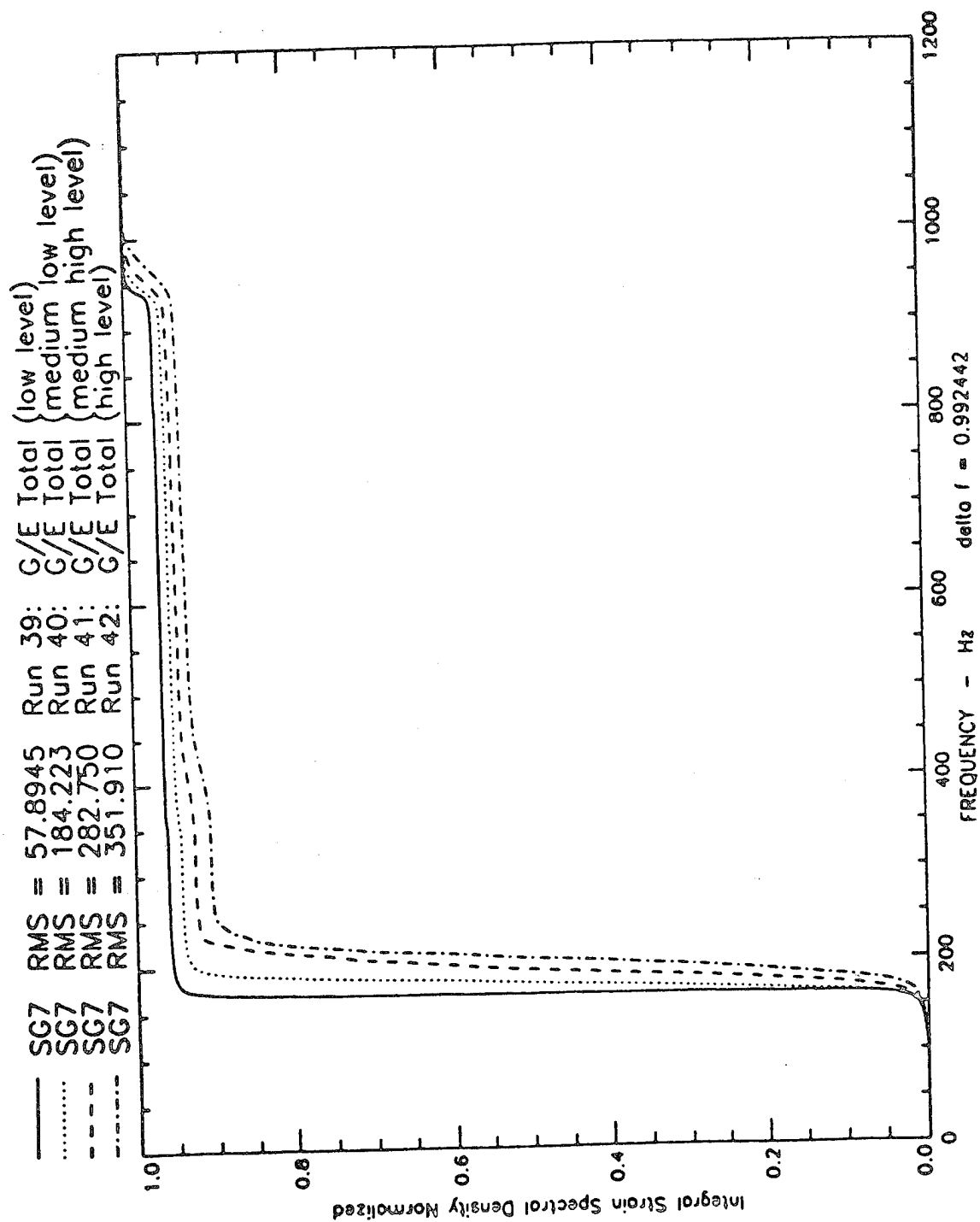


Fig 3.49 Normalised integrals of strain PSDs, SG 7, C-C-C-C CFRP shaker plate.

C-C-C-C CFRP SHAKER PLATE
Amplitude PDF Acceleration Rec 39 - 42

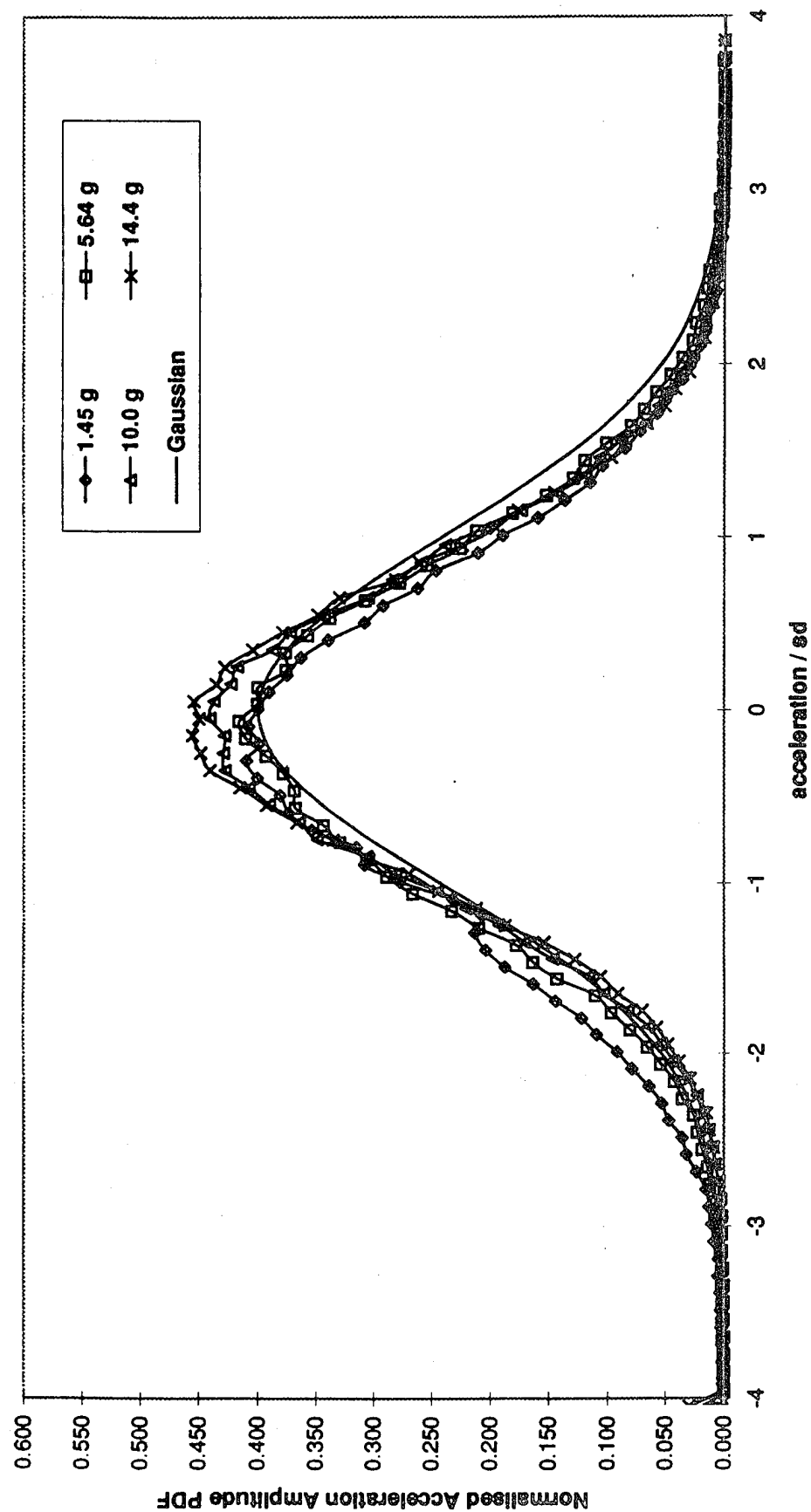


Fig 3.50 Normalised excitation amplitude PDFs, 100-1000 Hz random, C-C-C-C CFRP shaker plate.

C-C-C-C SHAKER CFRP PLATE
Amplitude PDF SG 7 Rec 39 - 42

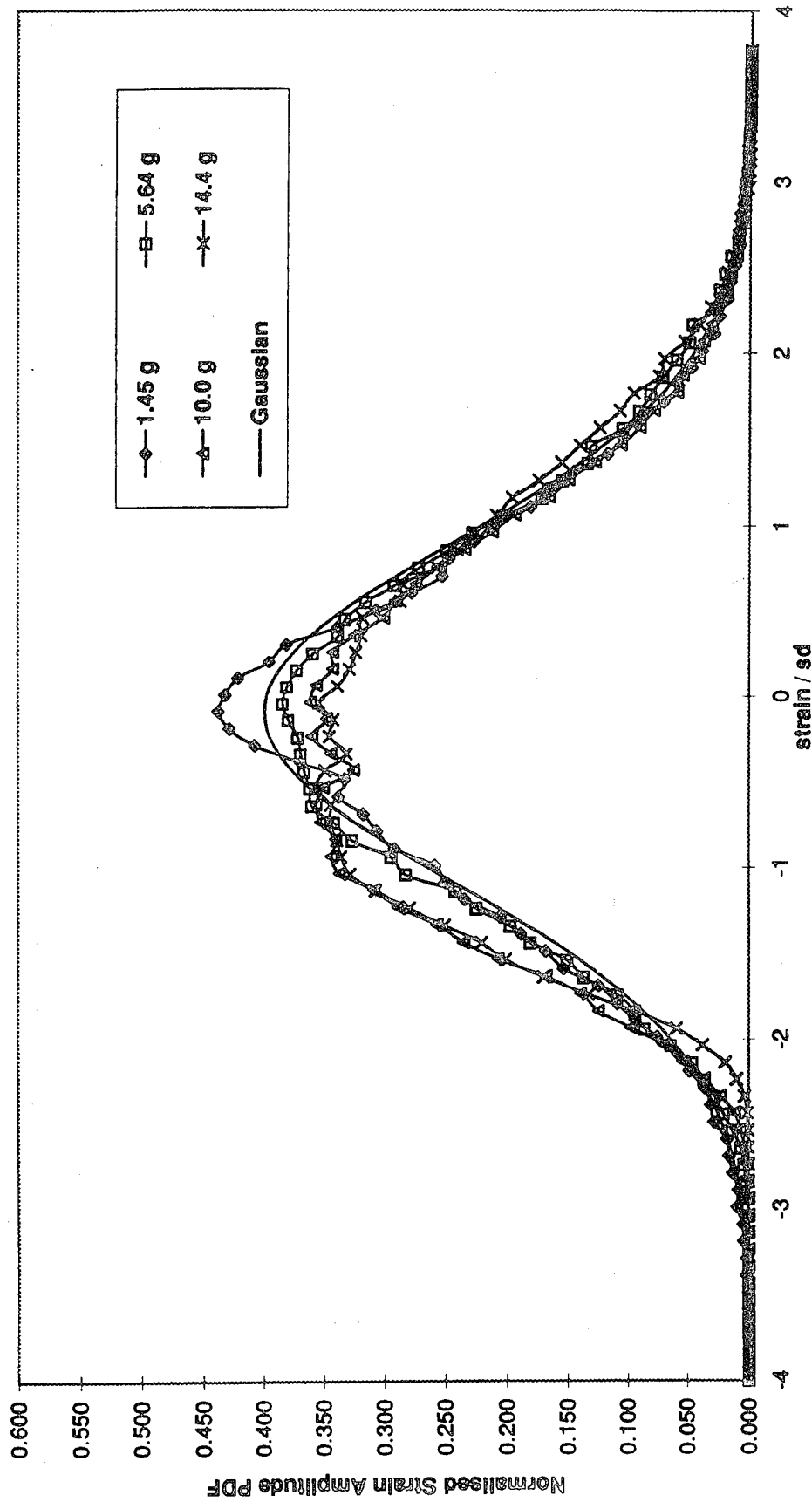


Fig 3.51 Normalised strain amplitude PDFs, 100-1000 Hz random, SG 7, C-C-C-C CFRP shaker plate.

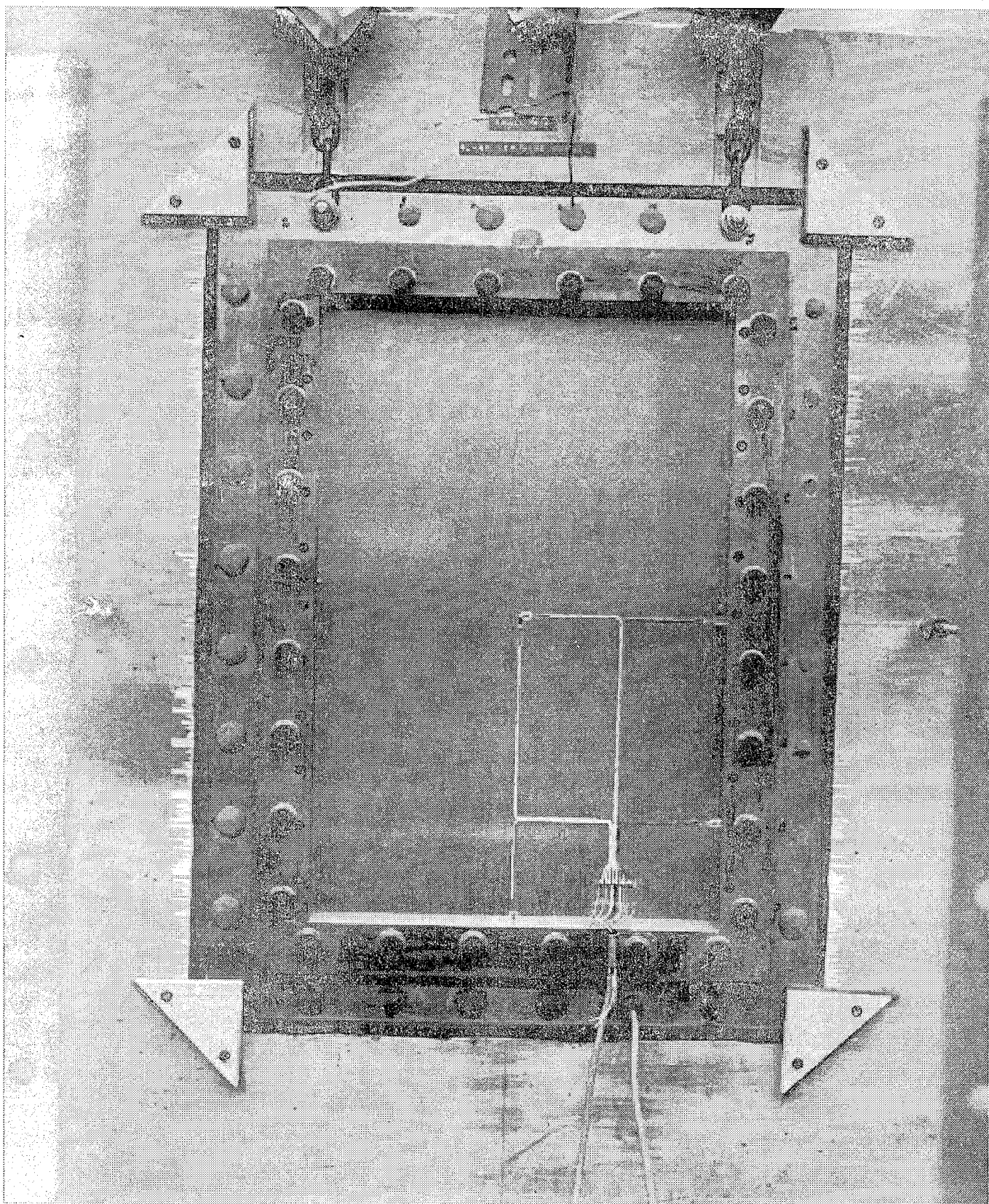


Fig 3.52 Photograph of C-C-C-C aluminum alloy plate installation in APWT.

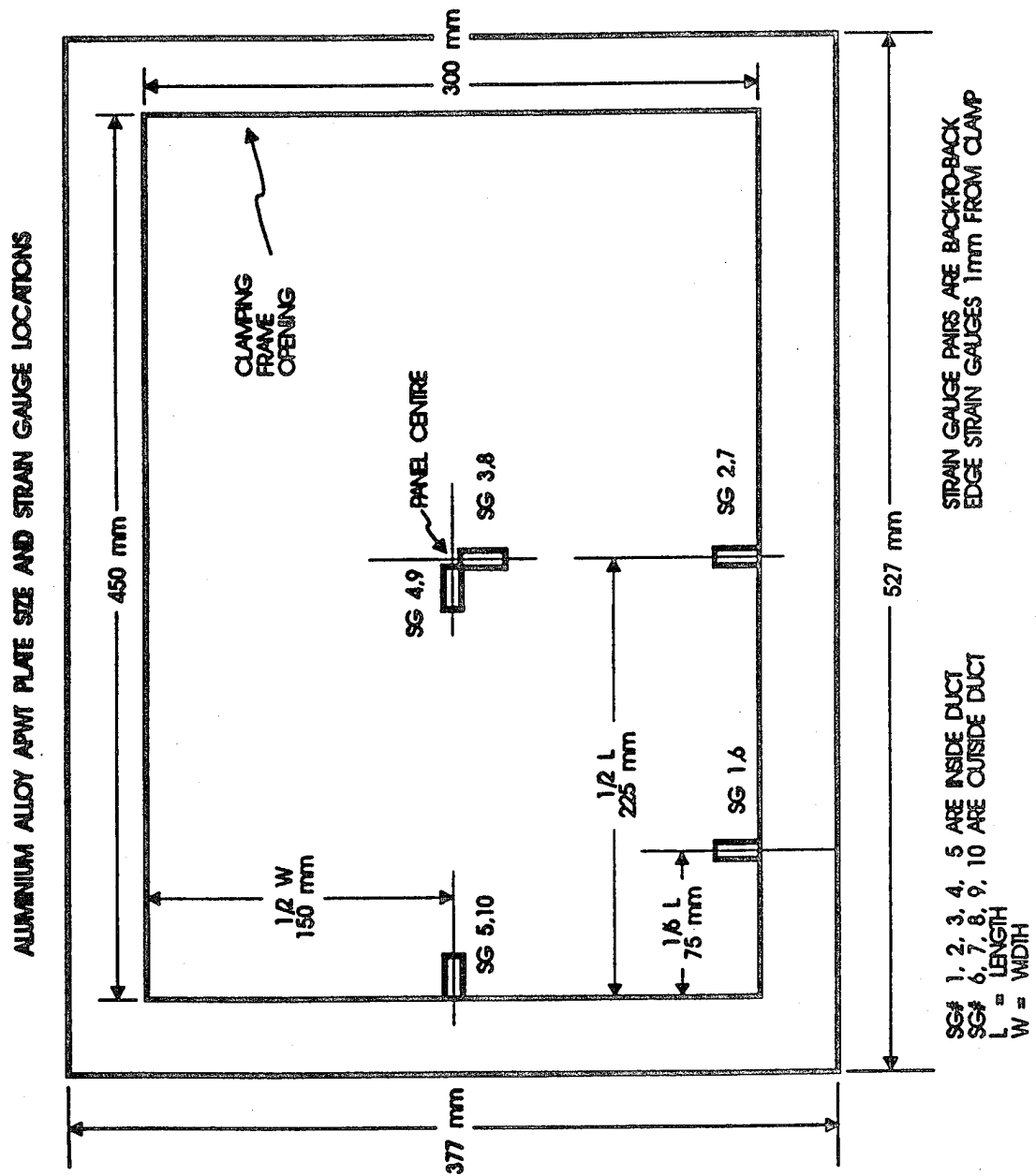


Fig 3.53 C-C-C-C aluminium APWT plate size and strain gauge location.

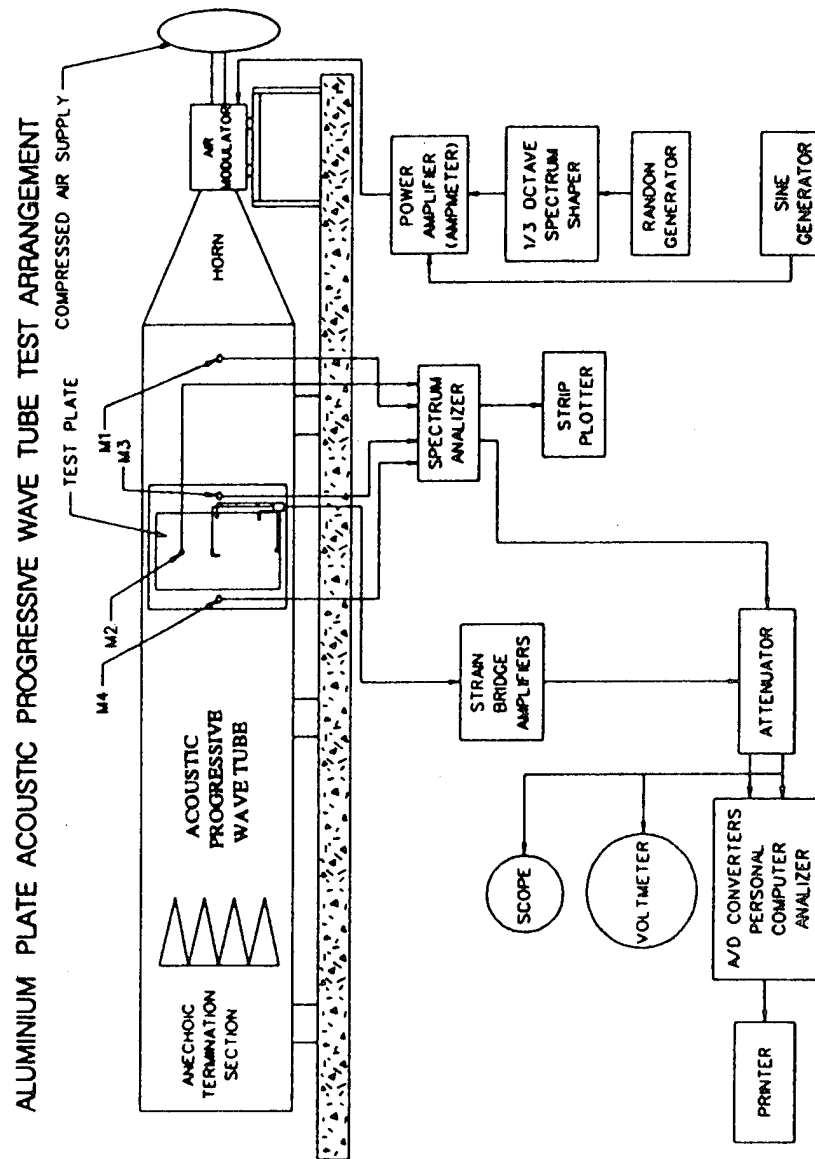


Fig 3.54 Schematic of C-C-C-C aluminium APWT plate testing arrangement.

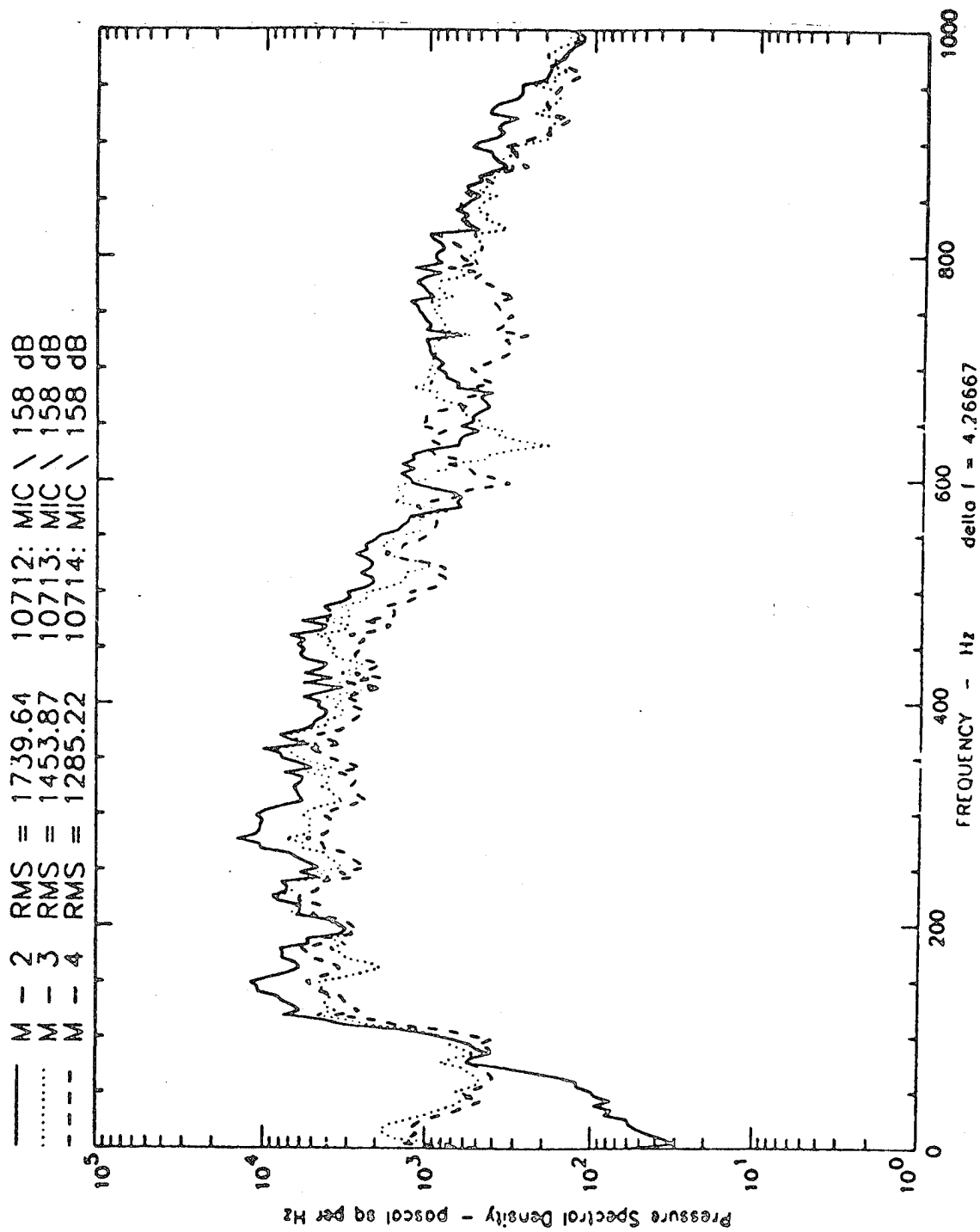


Fig 3.55 Pressure spectral density, C-C-C-C aluminium APWT plate testing arrangement.

C-C-C-C AL APWT
50-630 Hz RANDOM TOTAL STRAIN

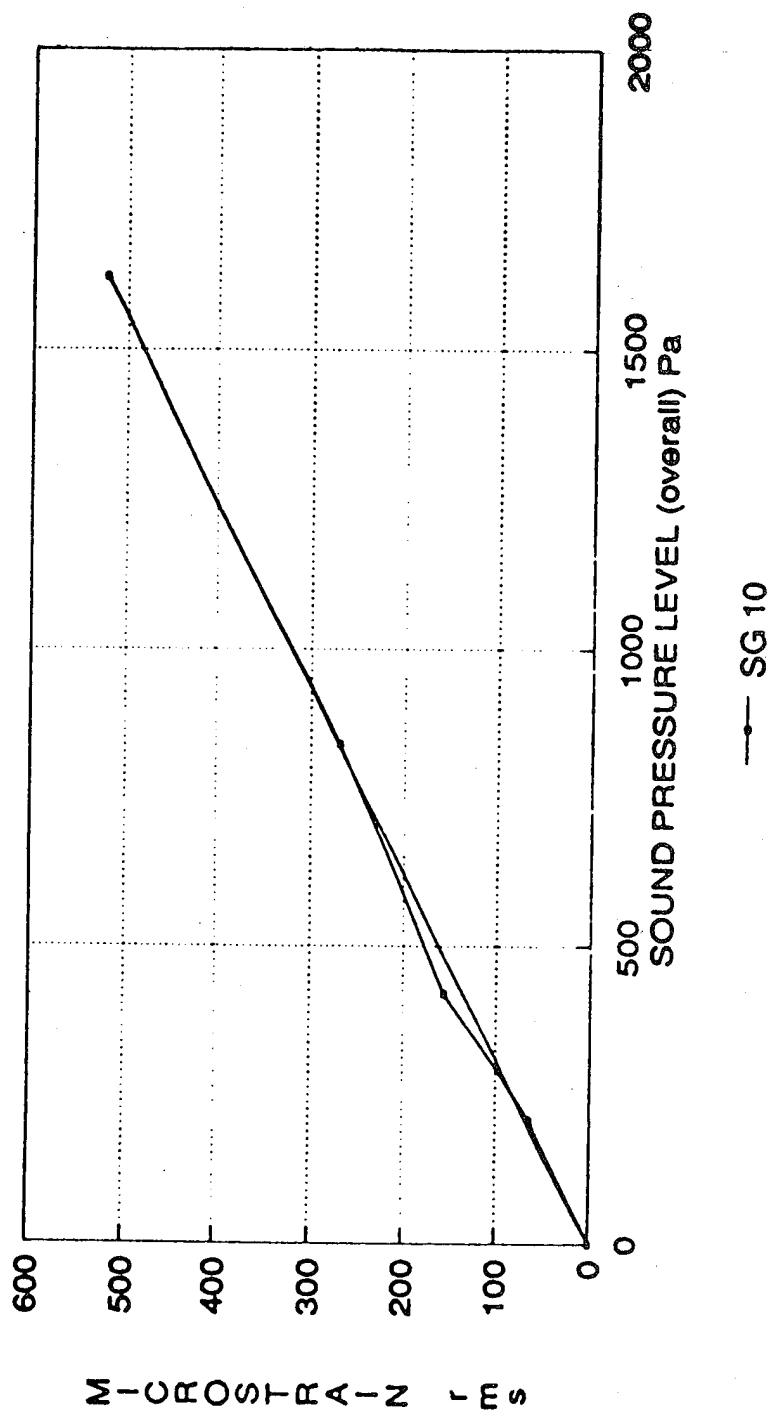


Fig 3.56 Total strain vs sound pressure level, C-C-C-C aluminium APWT plate testing arrangement.

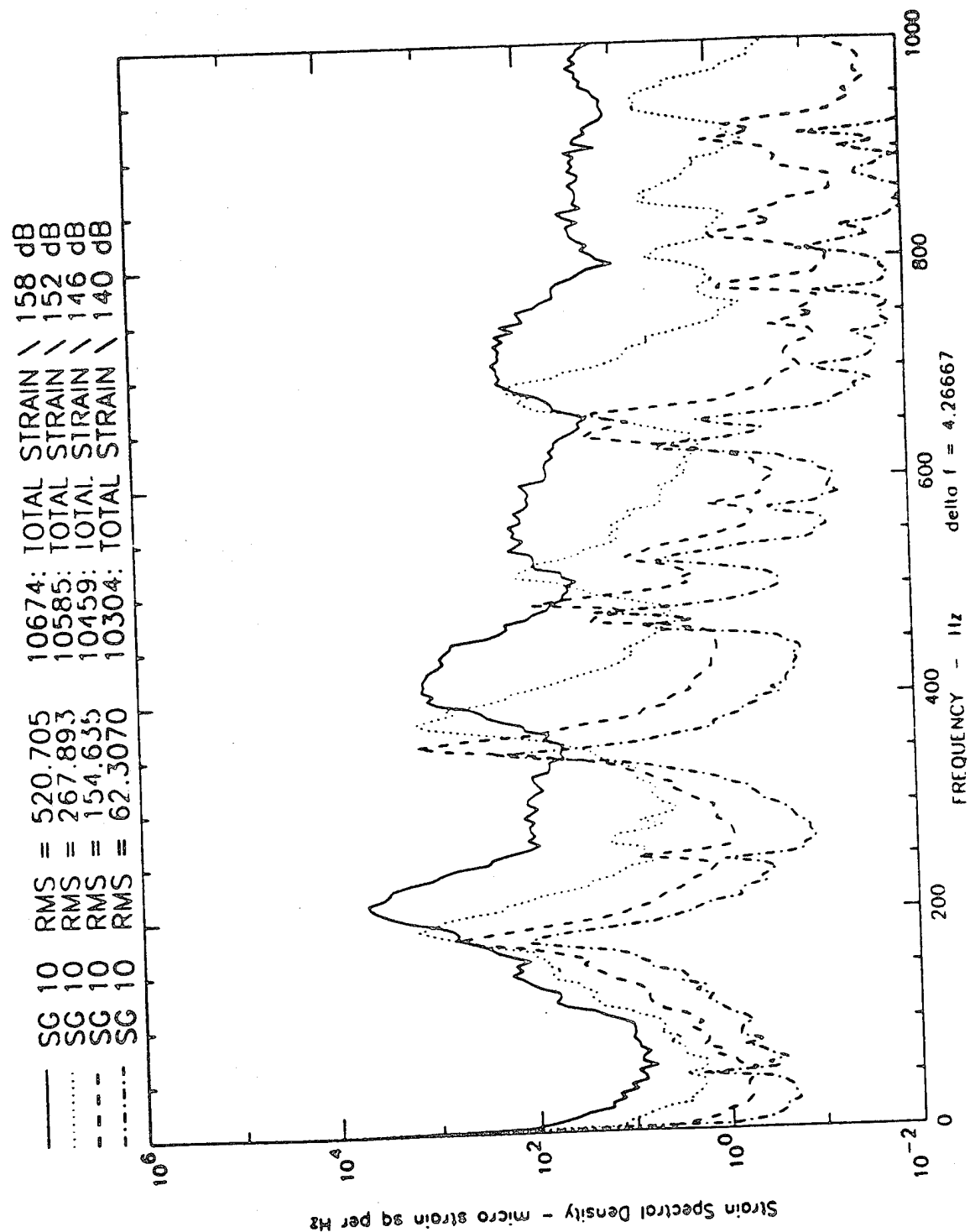


Fig 3.57 Strain spectral densities, four OSPLs, SG 10, C-C-C-C aluminium APWT plate.

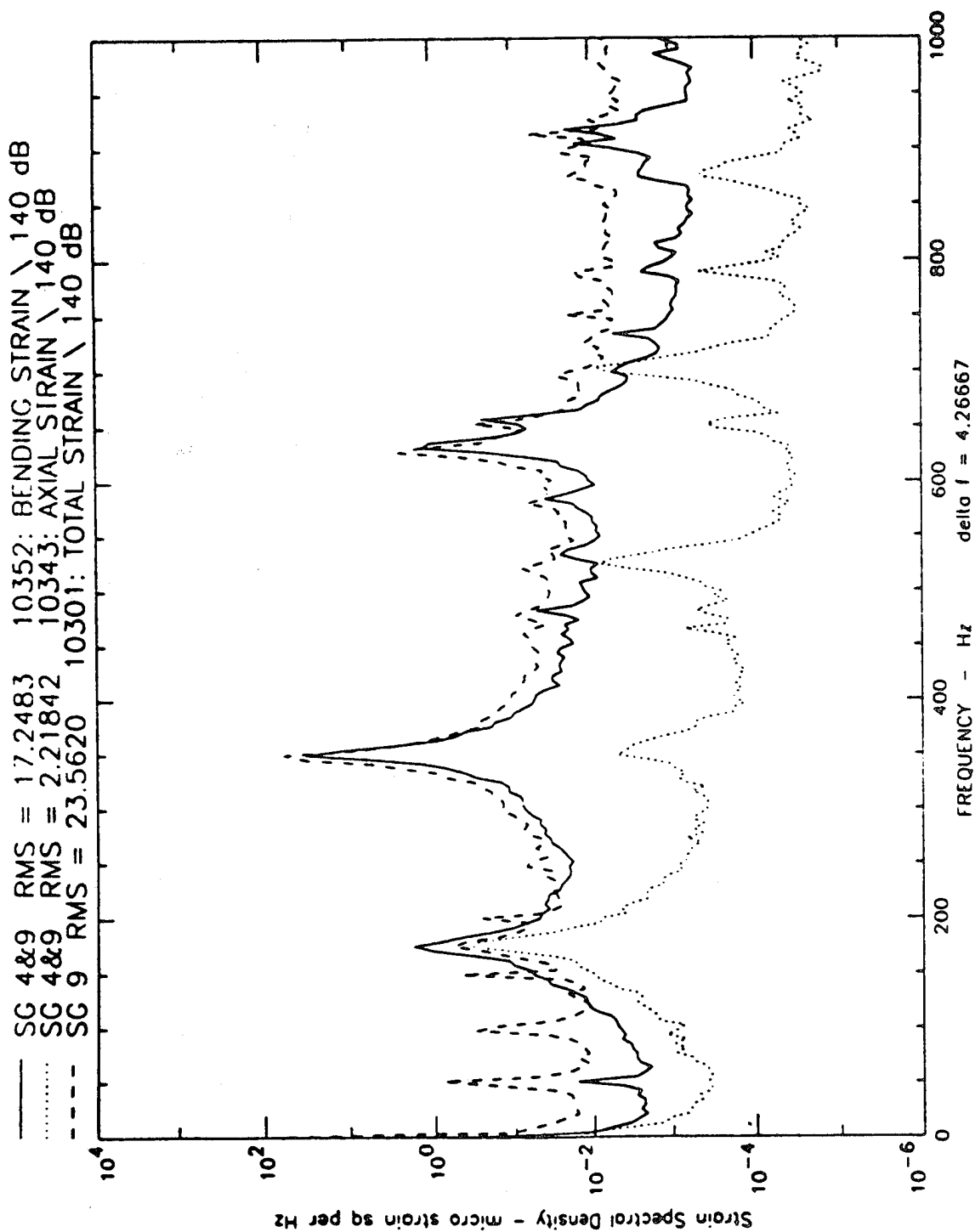


Fig 3.58 C-C-C-C Total, axial, bending strain spectral densities, 140 dB OSPL, SG 9 and 4&9, C-C-C-C aluminium APWT plate.

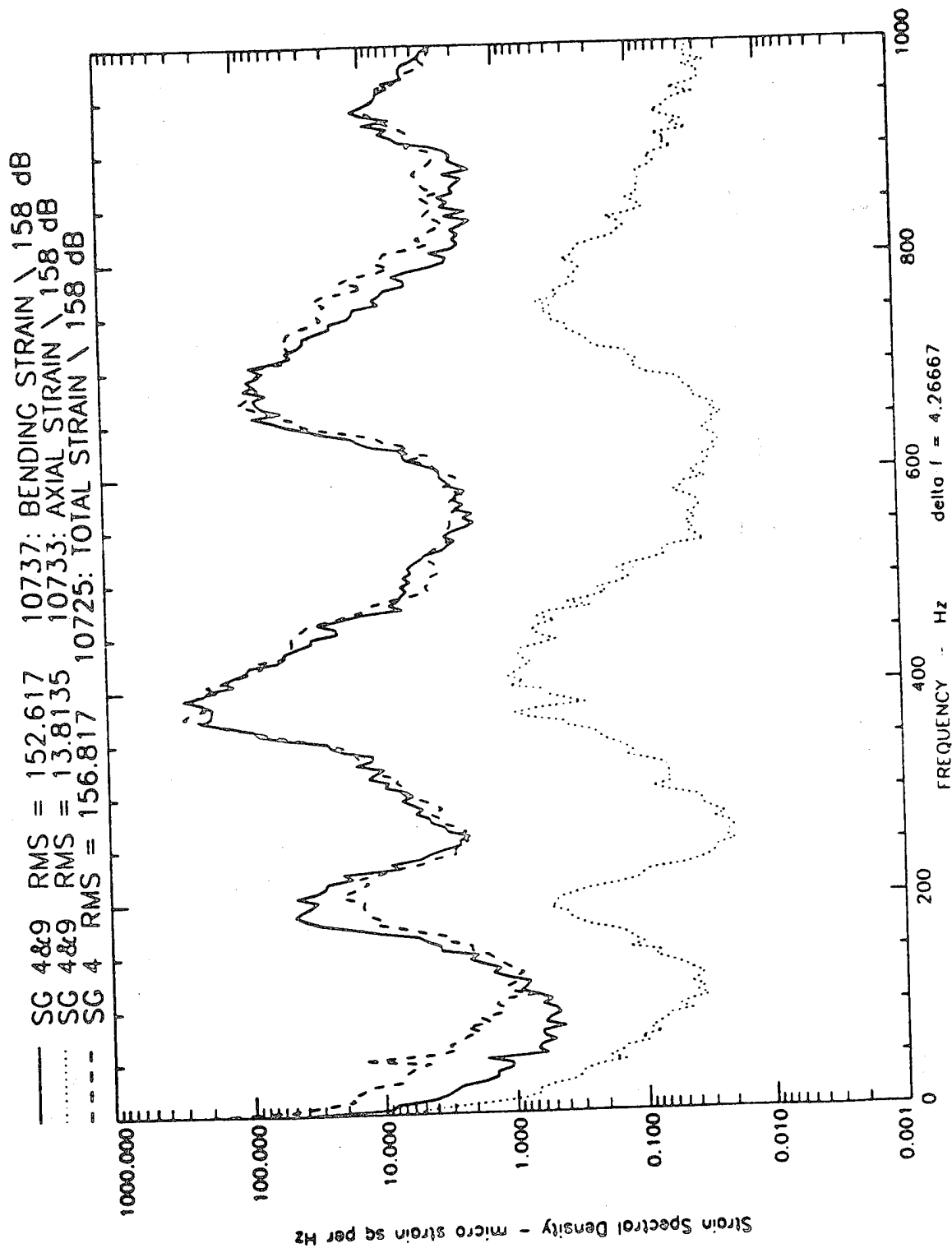


Fig 3.59 C-C-C-C Total, axial, bending strain spectral densities, 158 dB OSPL, SG 9 and 4&9, C-C-C-C aluminium APWT 1000.

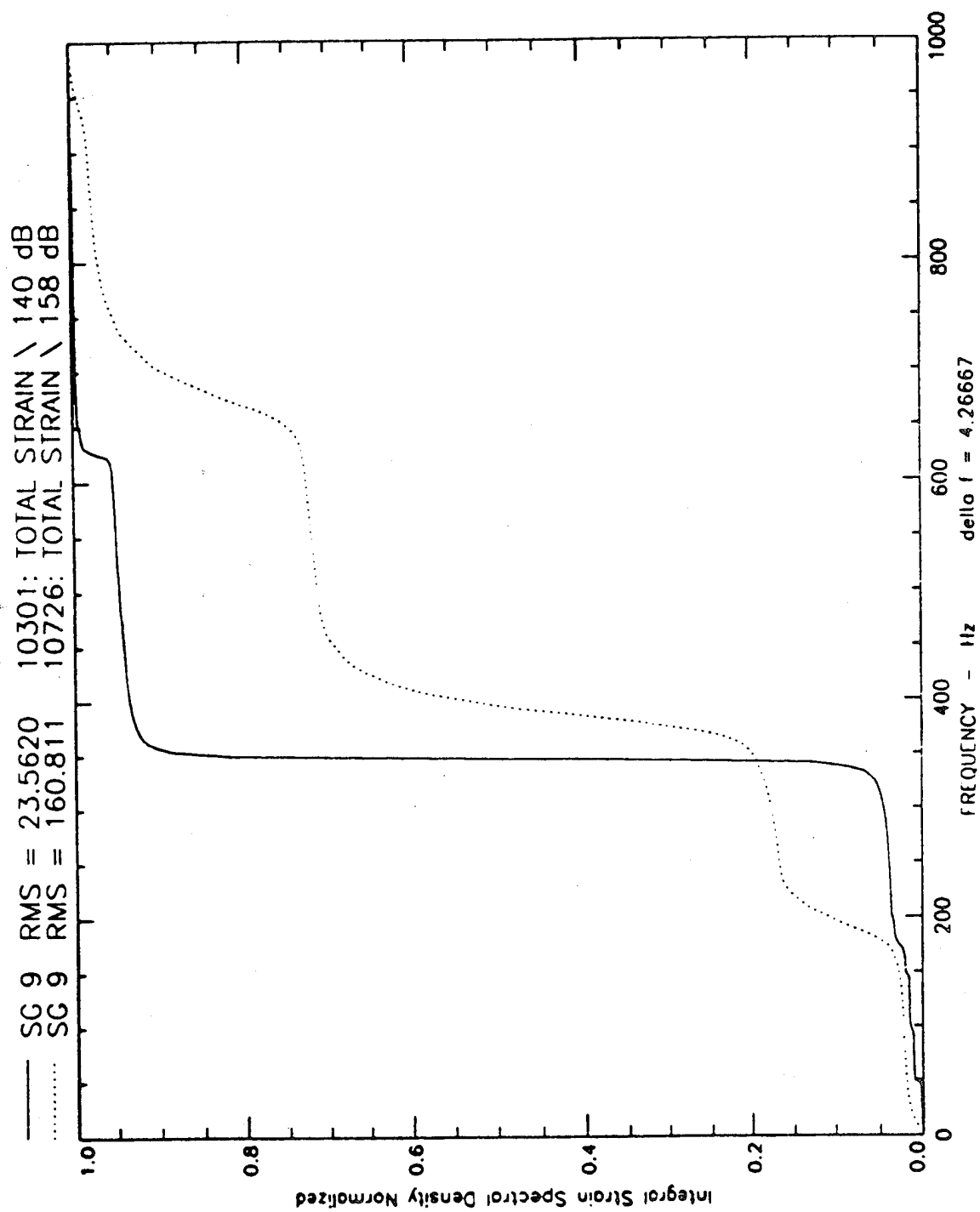


Fig 3.60 Normalised integrals of strain PSDs, SG 9, C-C-C-C aluminium APWT plate.

C-C-C-C AL PLATE APWT TEST
Amplitude PDF Microphone 2 R 10703,706,709,712

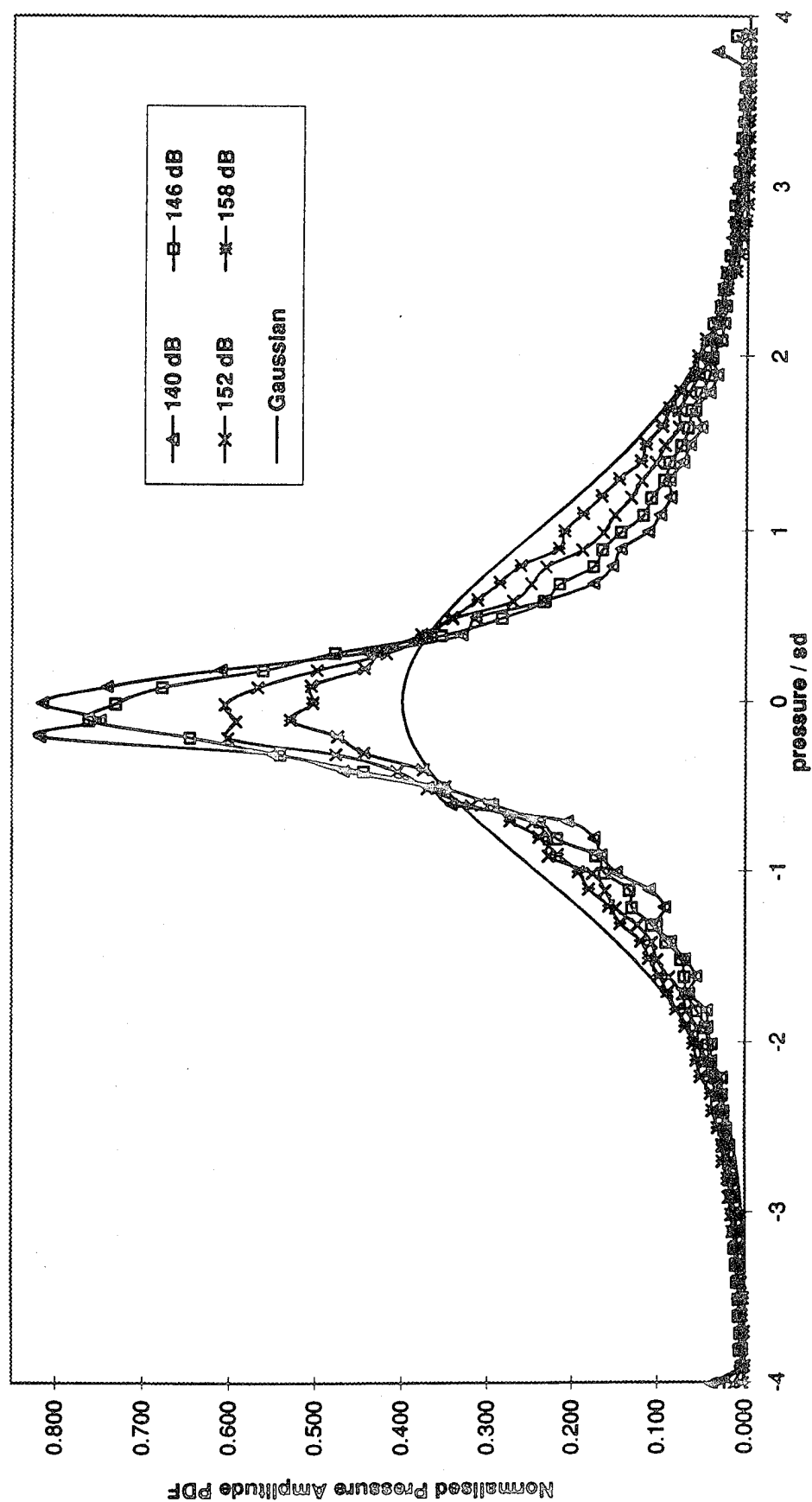


Fig 3.61 Normalised pressure amplitude PDFs, M 2, four OSPLs. C-C-C-C aluminium APWT plate.

C-C-C-C AL PLATE APWT TEST
Amplitude PDF 158 dB R 10712,713,714

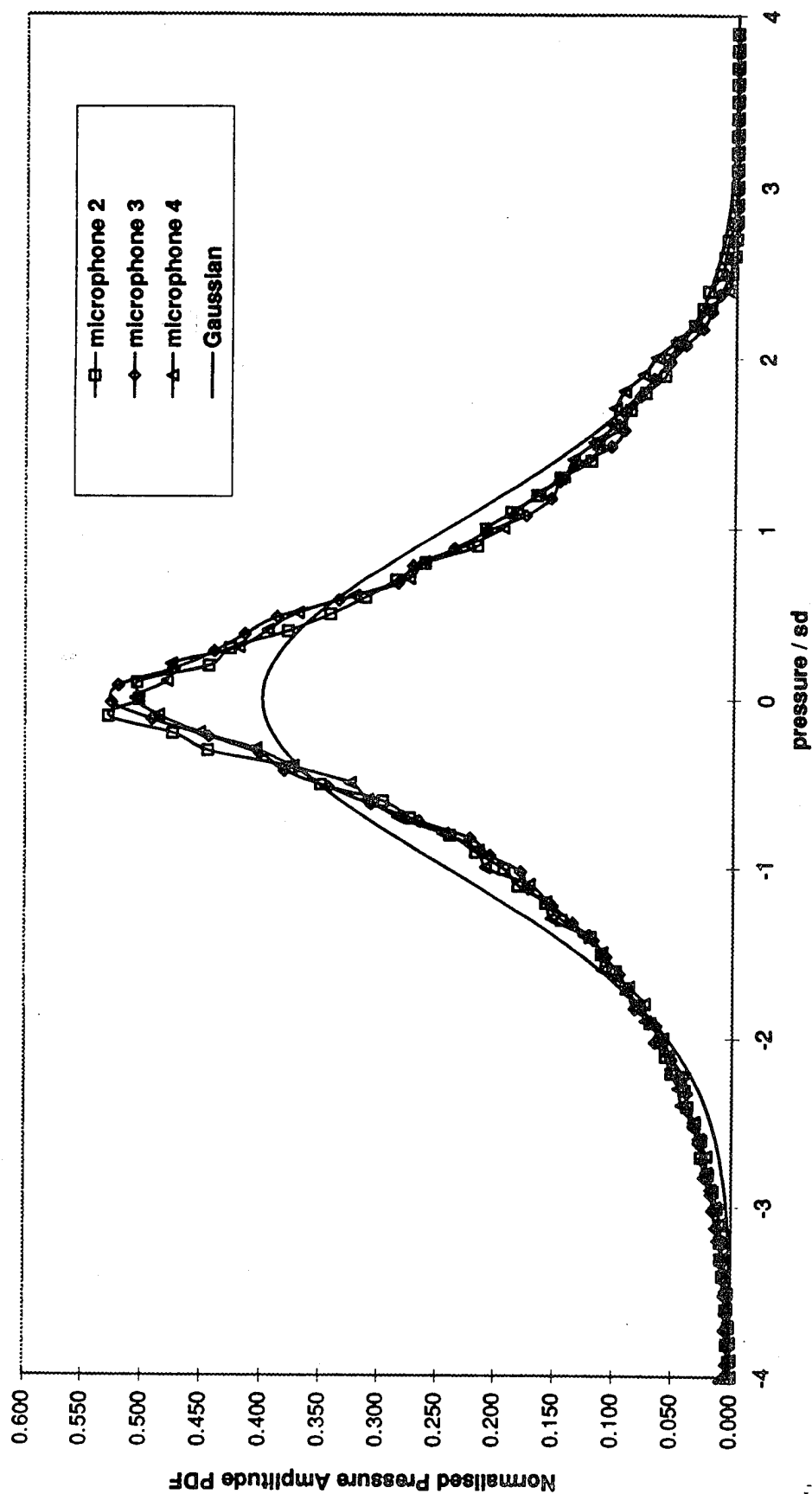


Fig 3.62 Normalised pressure amplitude PDFs, M 2, M 3, M 4, 158 dB OSPL, C-C-C-C aluminium APWT plate.

C-C-C-C AL PLATE APWT TEST
Strain PDF SG 9 R10301,725

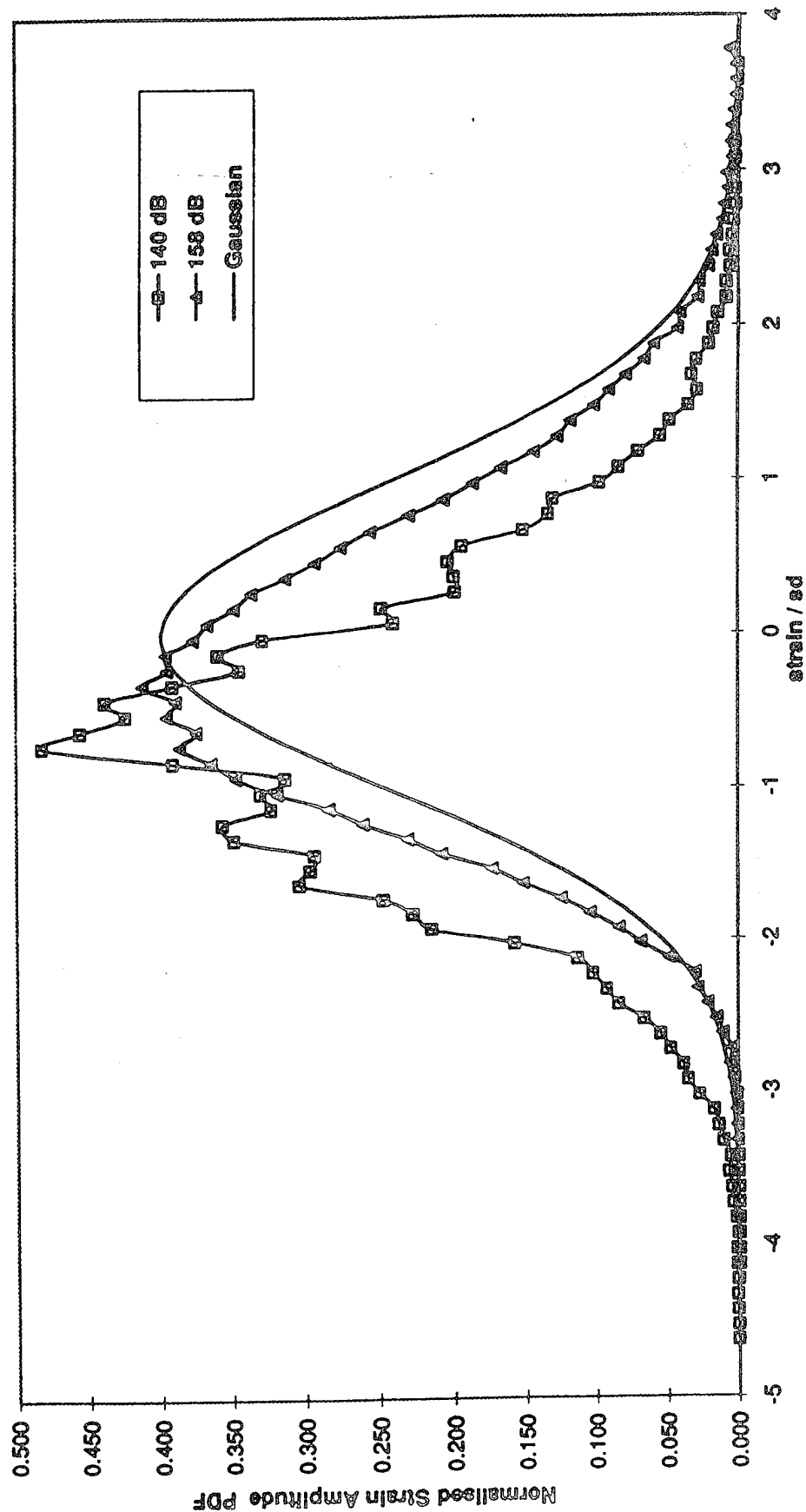


Fig 3.63 Normalised strain amplitude PDFs, SG 9, C-C-C-C aluminium APWT plate.

C-C-C-C AL PLATE APWT TEST
Strain PDF SG 10 R10304,585,459,674

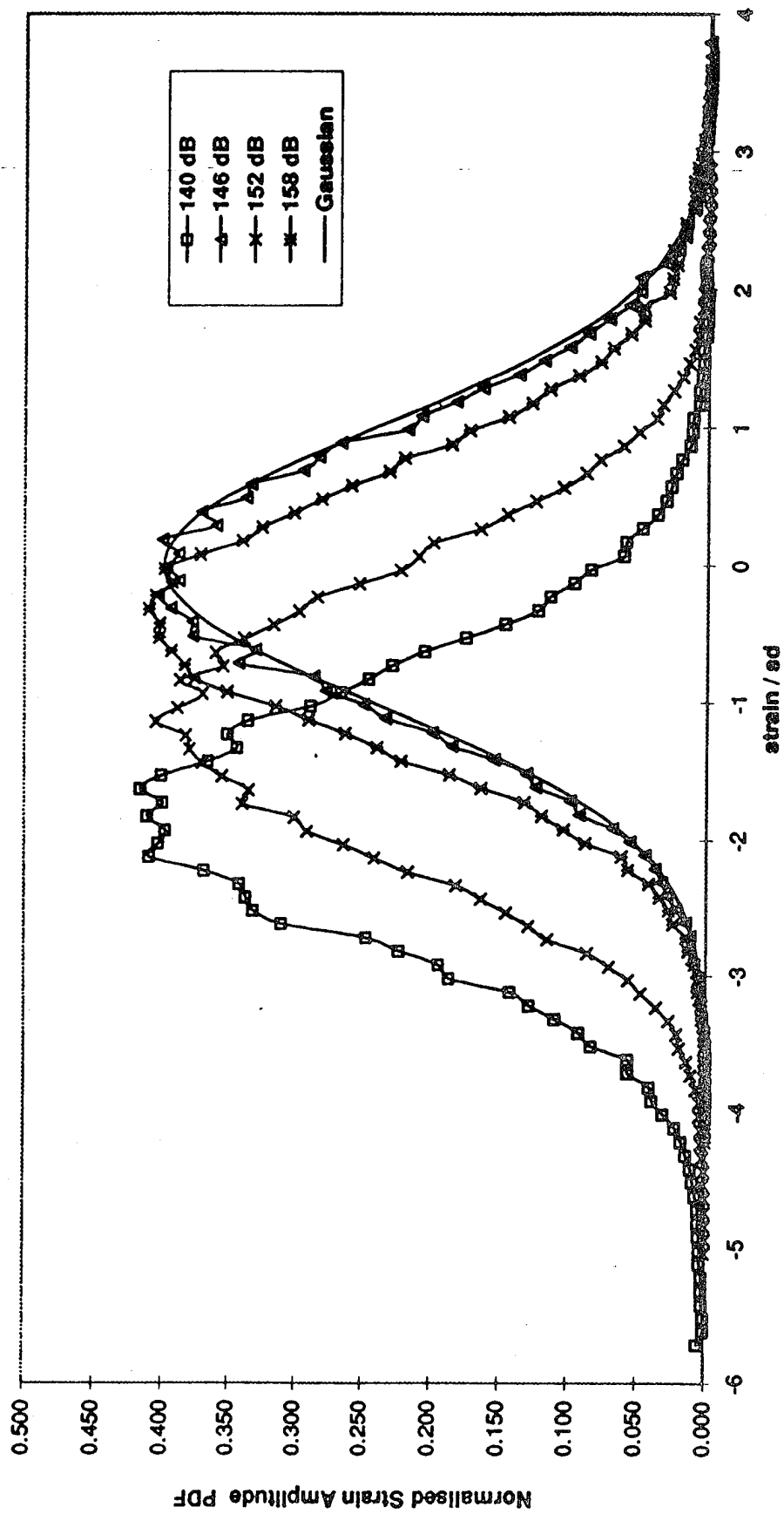


Fig 3.64 Normalised strain amplitude PDFs, SG 10, C-C-C-C aluminium APWT plate.

CFRP APWT PLATE SIZE AND STRAIN GAUGE LOCATIONS

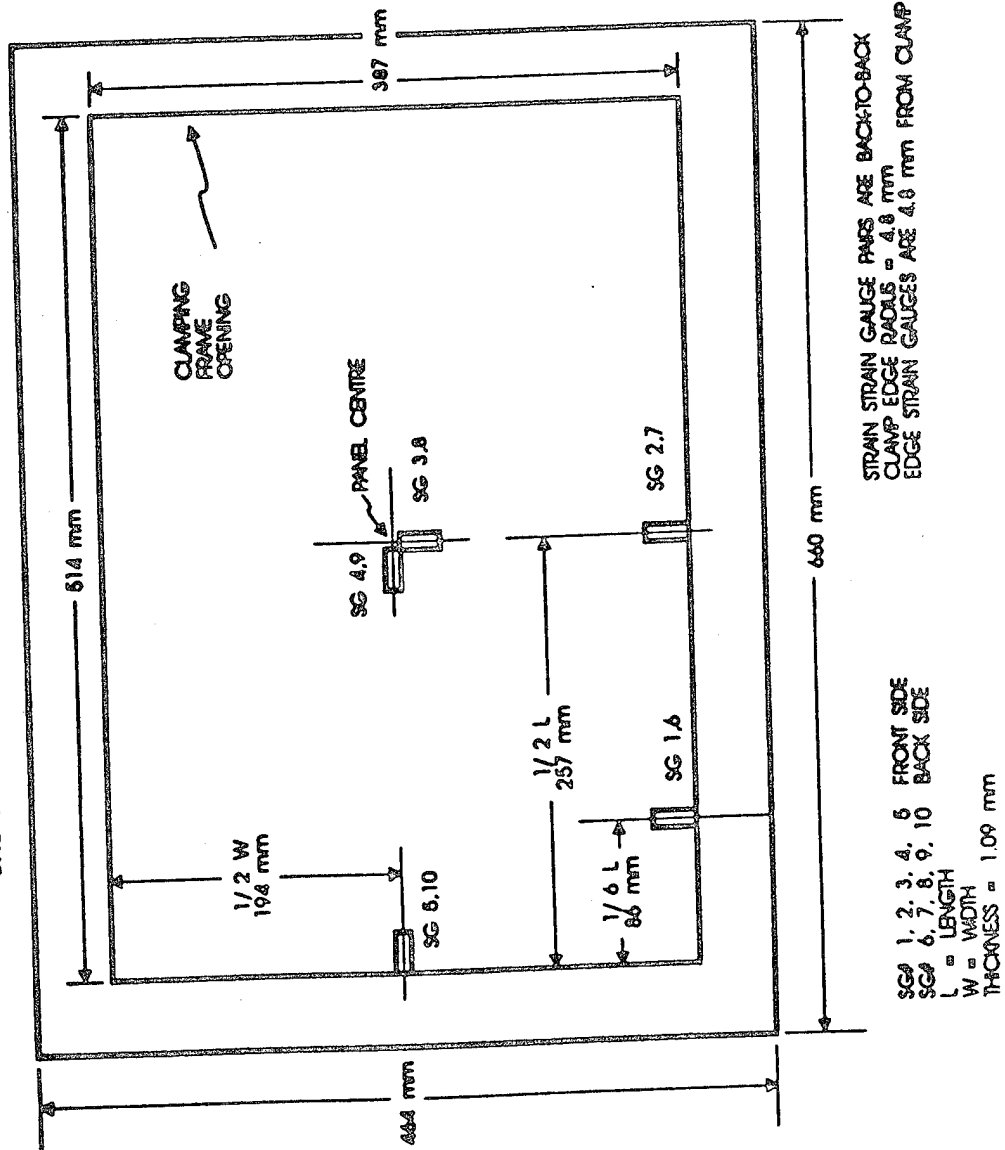


Fig 3.65 C-C-C-C CFRP APWT plate size and strain gauge location.

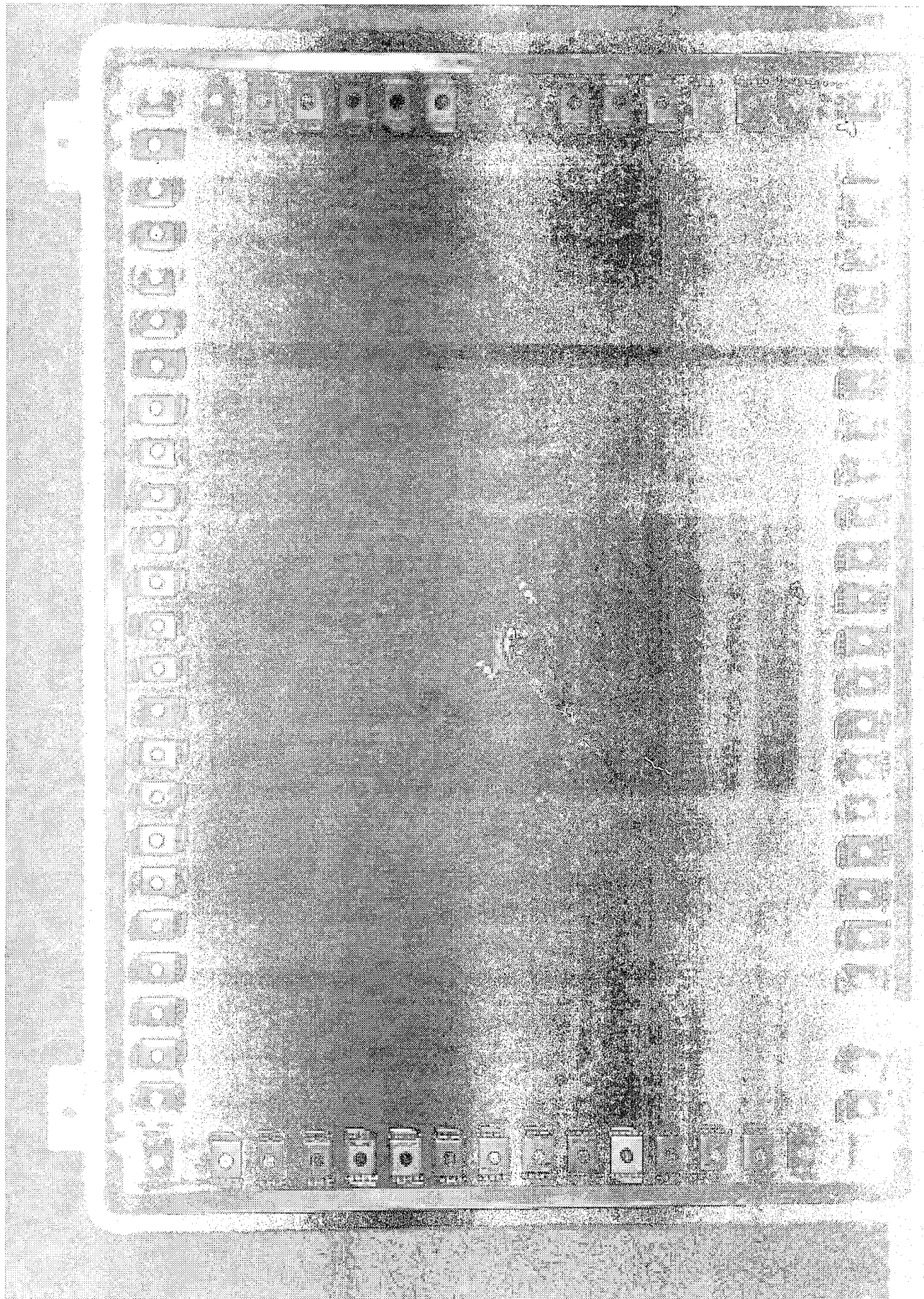


Fig 3.66 Photograph of C-C-C-C CFRP APWT plate claming arrangement.

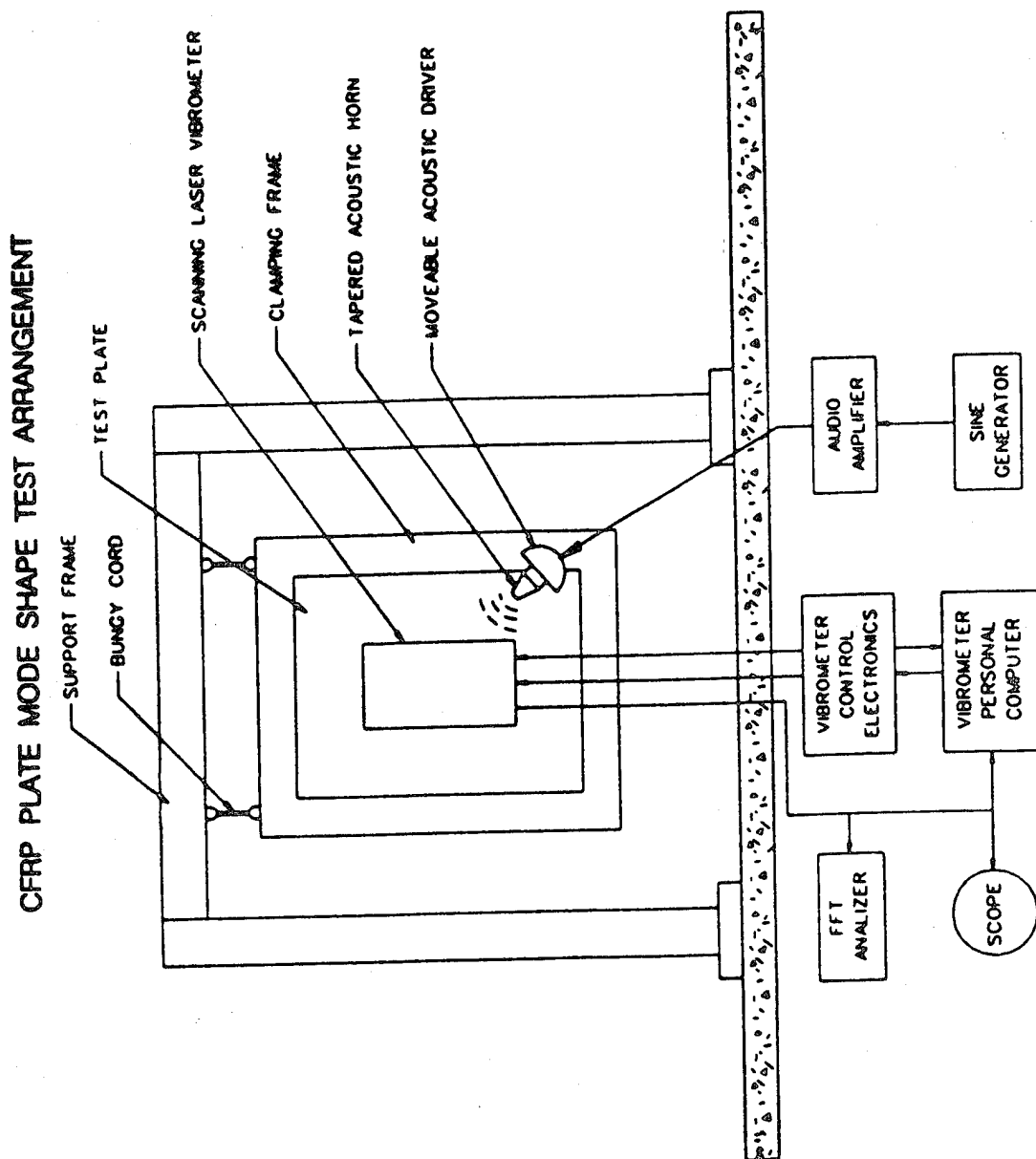
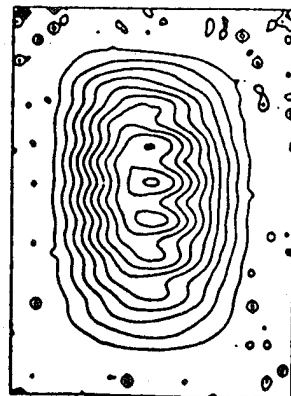
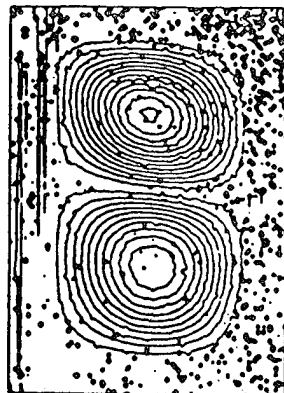


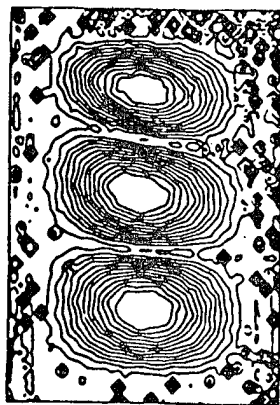
Fig 3.67 Schematic of C-C-C-C CFRP APWT plate mode shape testing arrangement.



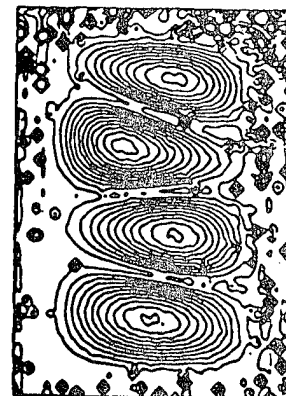
a=59 Hz



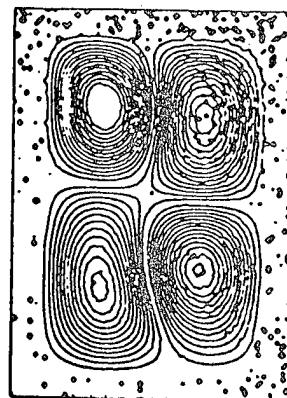
b=77 Hz



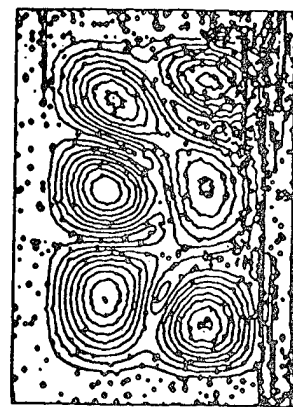
c=107 Hz



d=139 Hz

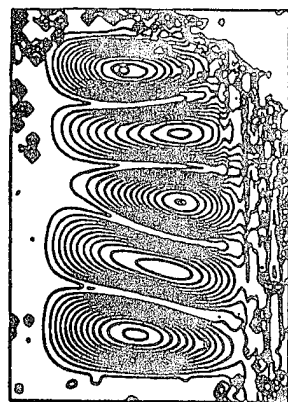


e=160 Hz

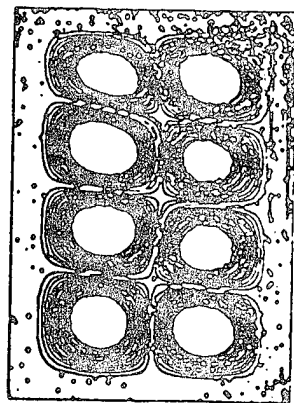


f=187 Hz

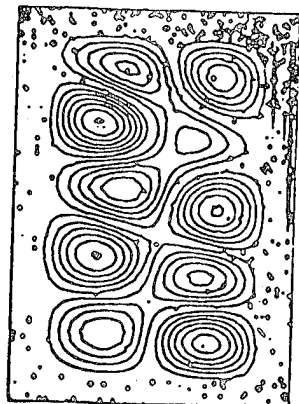
Fig 3.68 Mode shape, video holography method, a=59 Hz, b=77 Hz, c=107 Hz, d=139 Hz, e=160 Hz and f=187 Hz, C-C-C-C CFRP APWT plate.



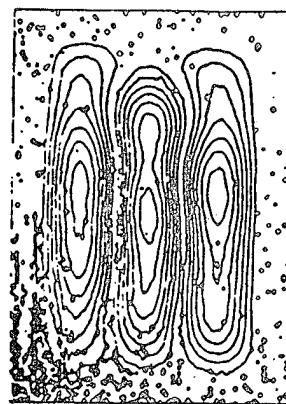
a=194 Hz



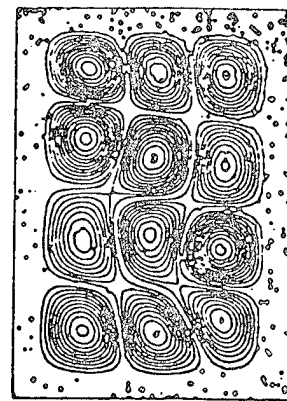
b=220 Hz



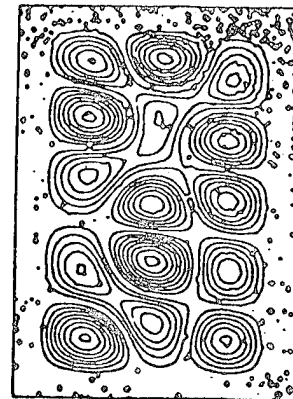
c=266 Hz



d=281 Hz



e=355 Hz



f=405 Hz

Fig 3.69 Mode shape, video holography method, a=194 Hz, b=220 Hz, c=266 Hz, d=281 Hz, e=355 Hz and f=405 Hz, C-C-C-C CFRP APWT plate.

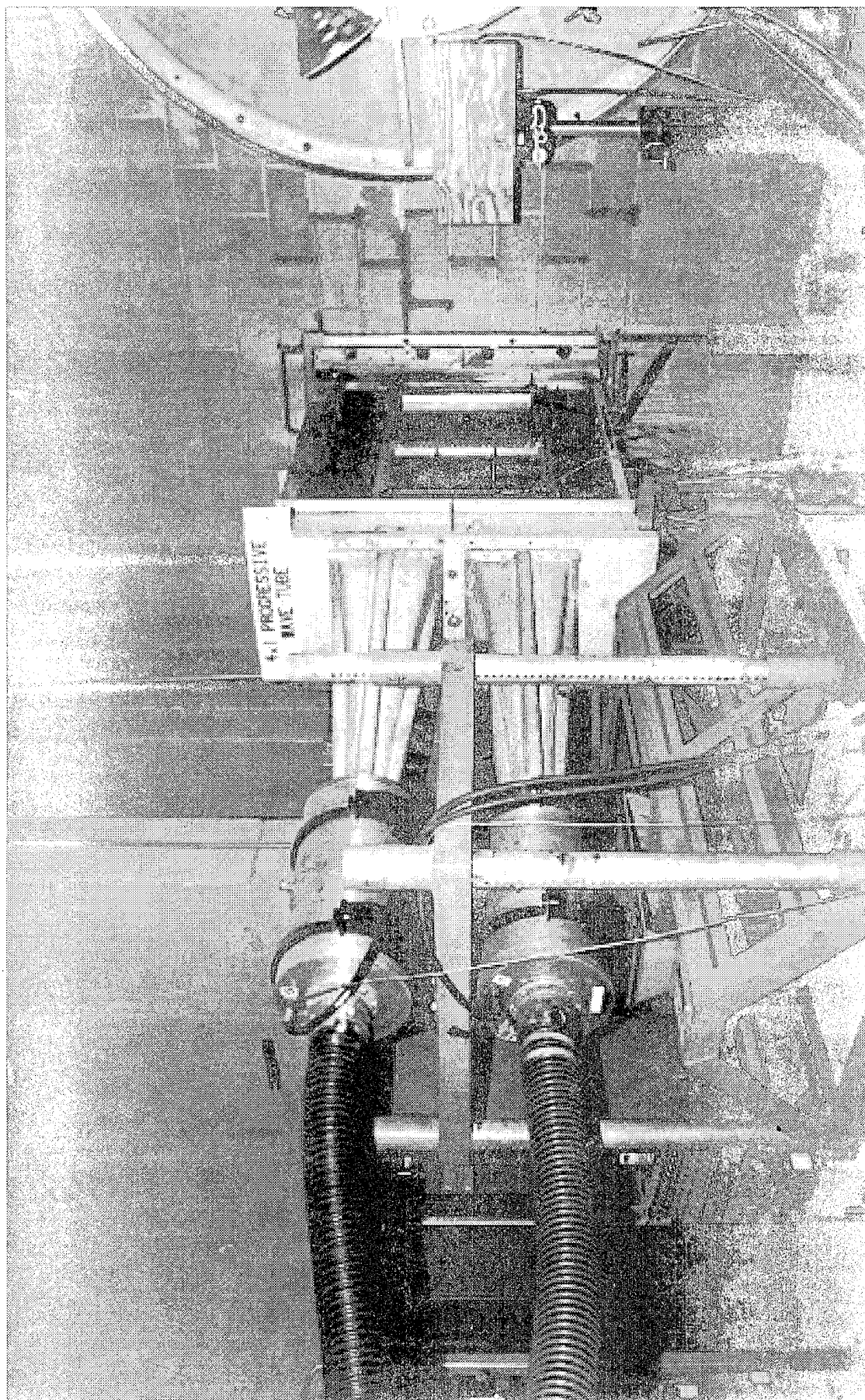


Fig 3.70 Photograph of C-C-C-C CFRP plate installation in APWT.

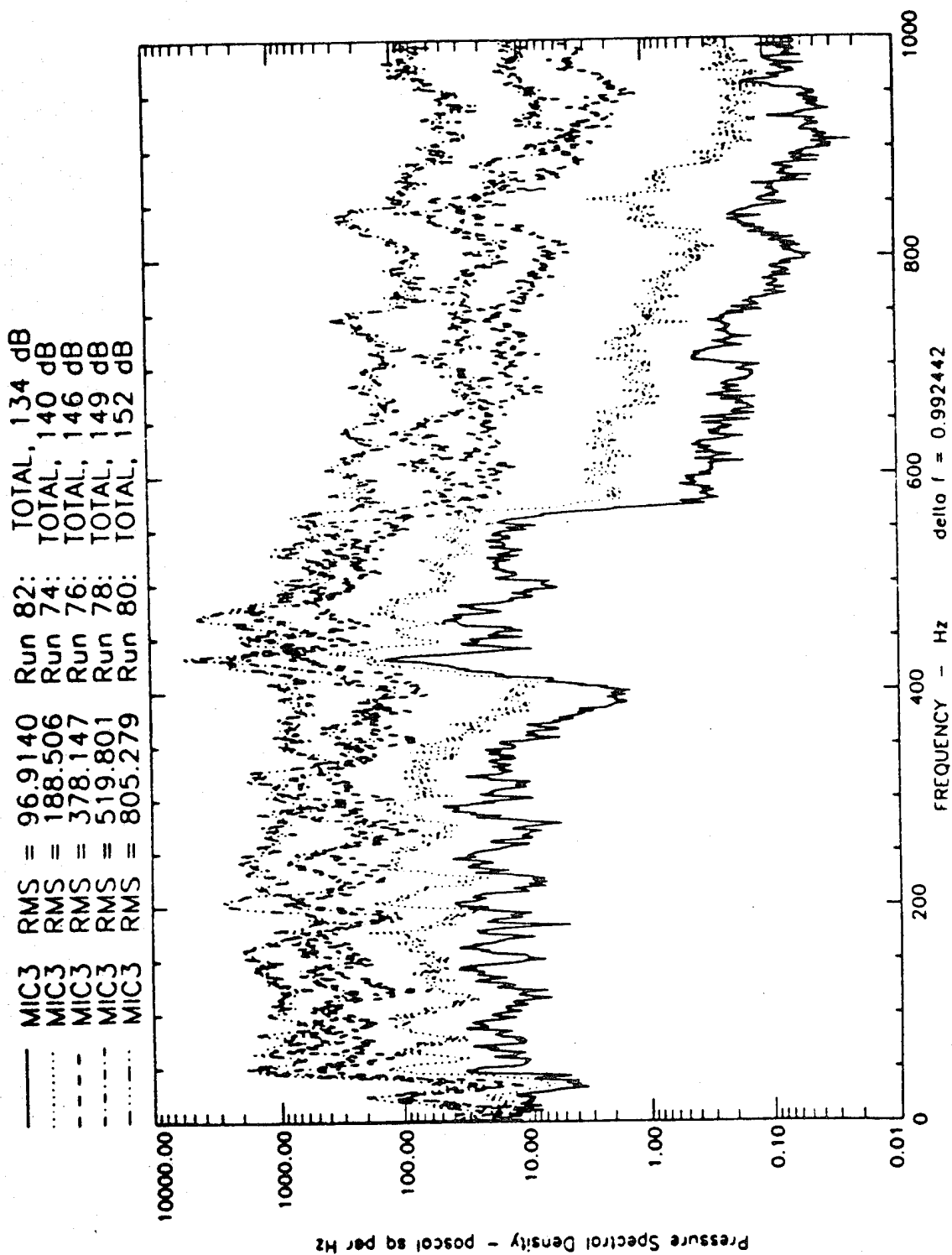


Fig 3.72 Pressure spectral densities, M 3, five OSPLs, C-C-C-C CFRP APWT plate.

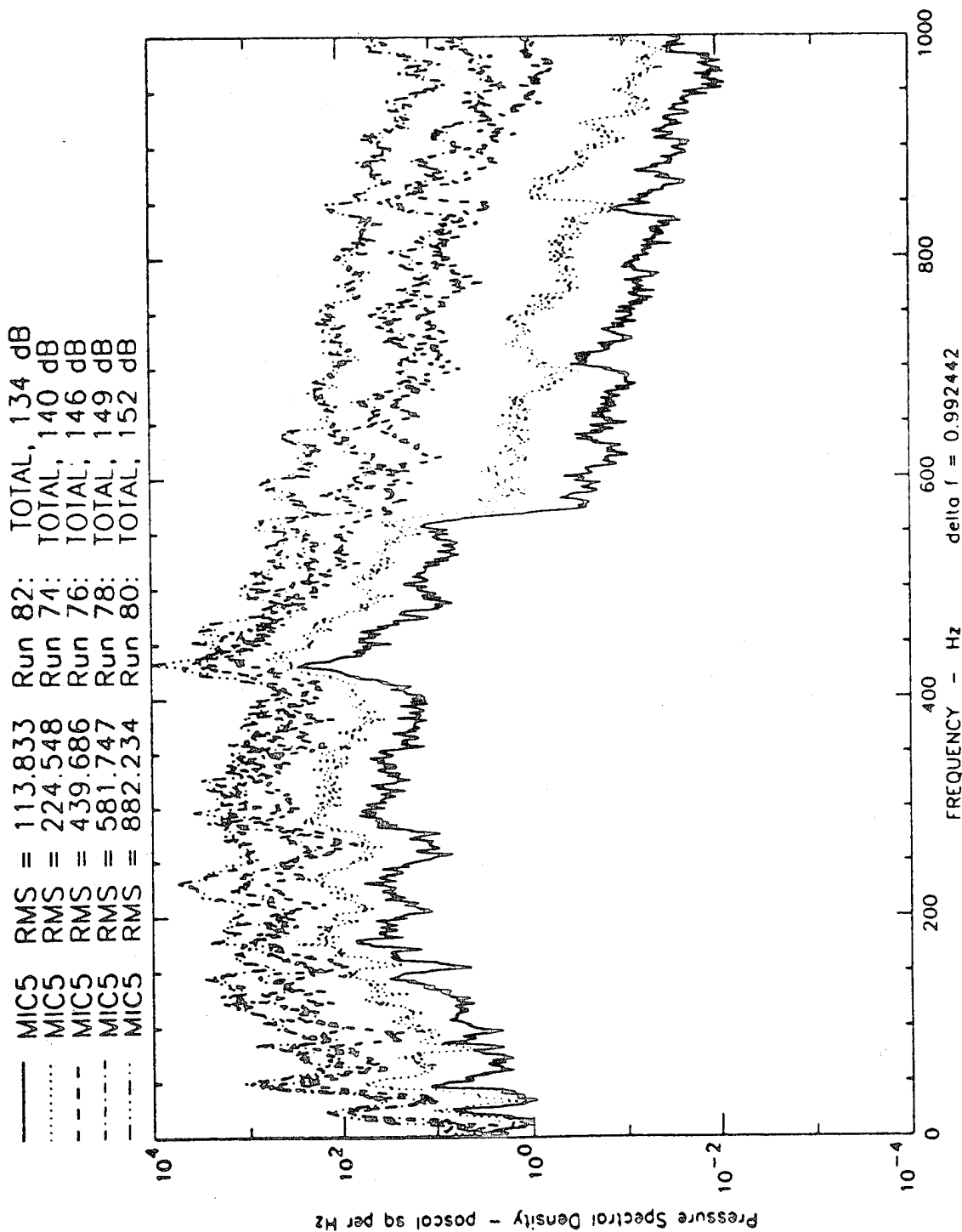


Fig 3.73 Pressure spectral densities, M 5, five OSPLs, C-C-C-C CFRP APWT plate.

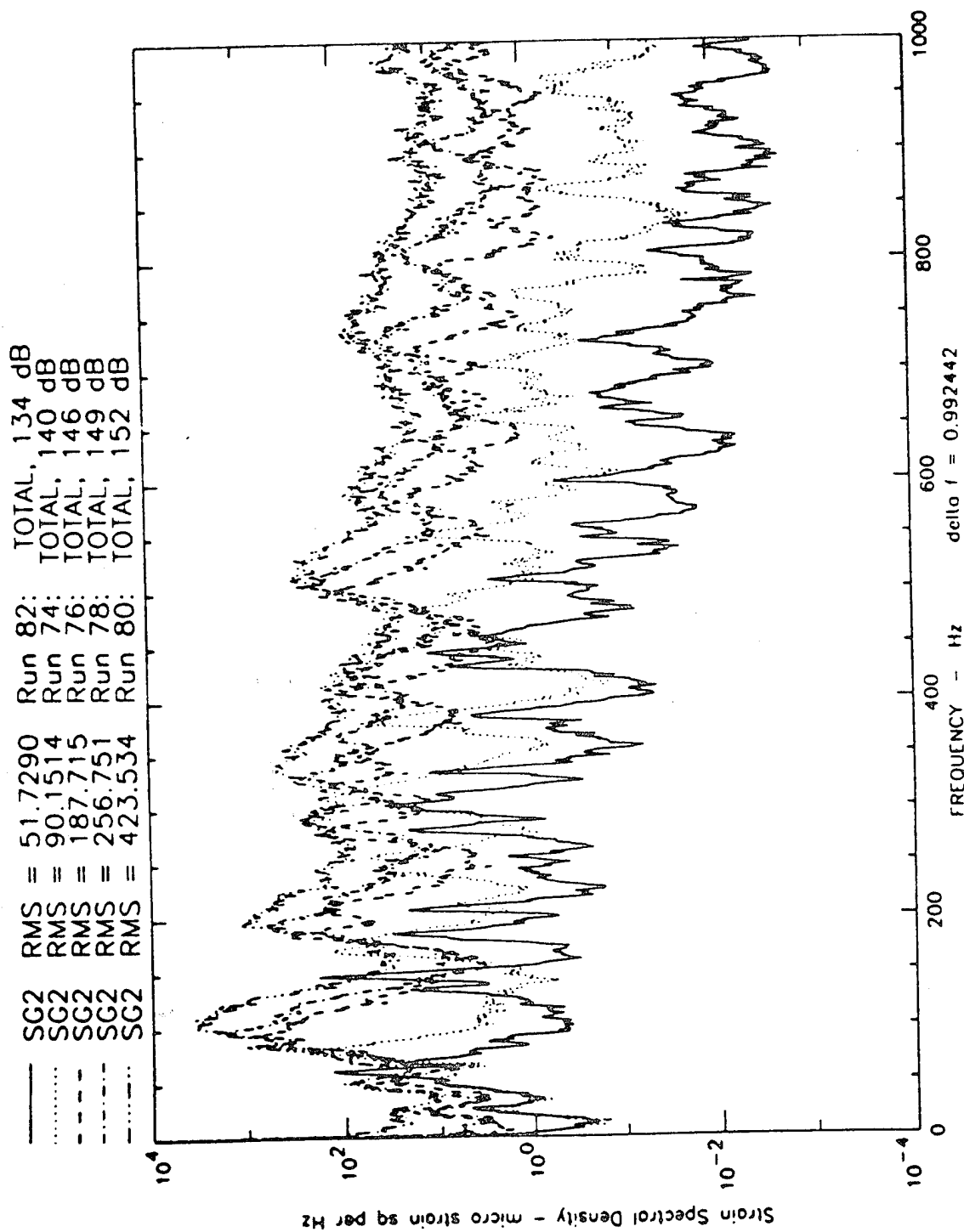


Fig 3.74 Total strain spectral densities, five OSPLs, SG 2, C-C-C-CFRP APWT plate.

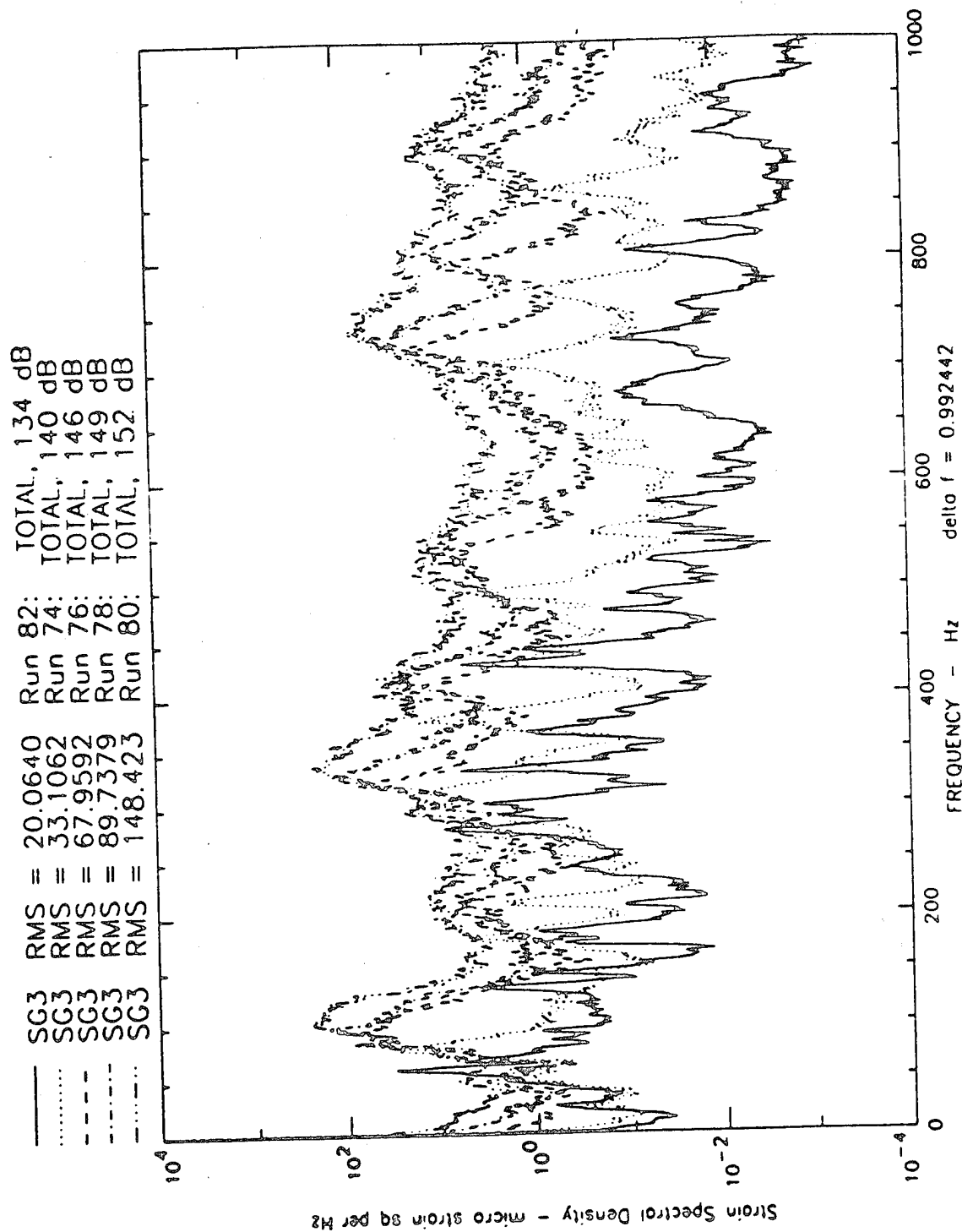


Fig 3.75 Total strain spectral densities, five OSPLs, SG 3, C-C-C-C CFRP APWT plate.

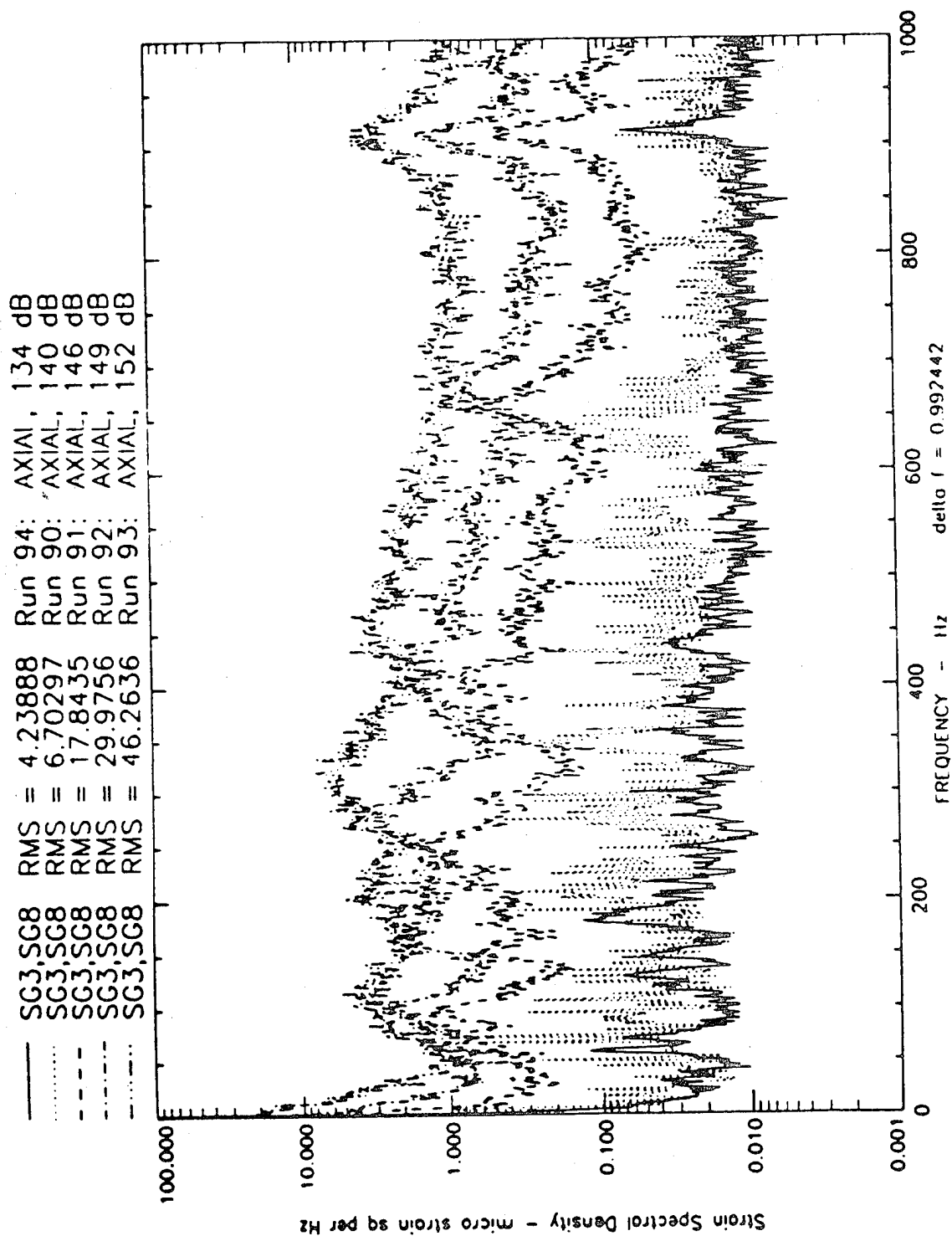


Fig 3.76 Axial strain spectral densities, five OSPLs, SG 3&8, C-C-C-C CFRP APWT plate.

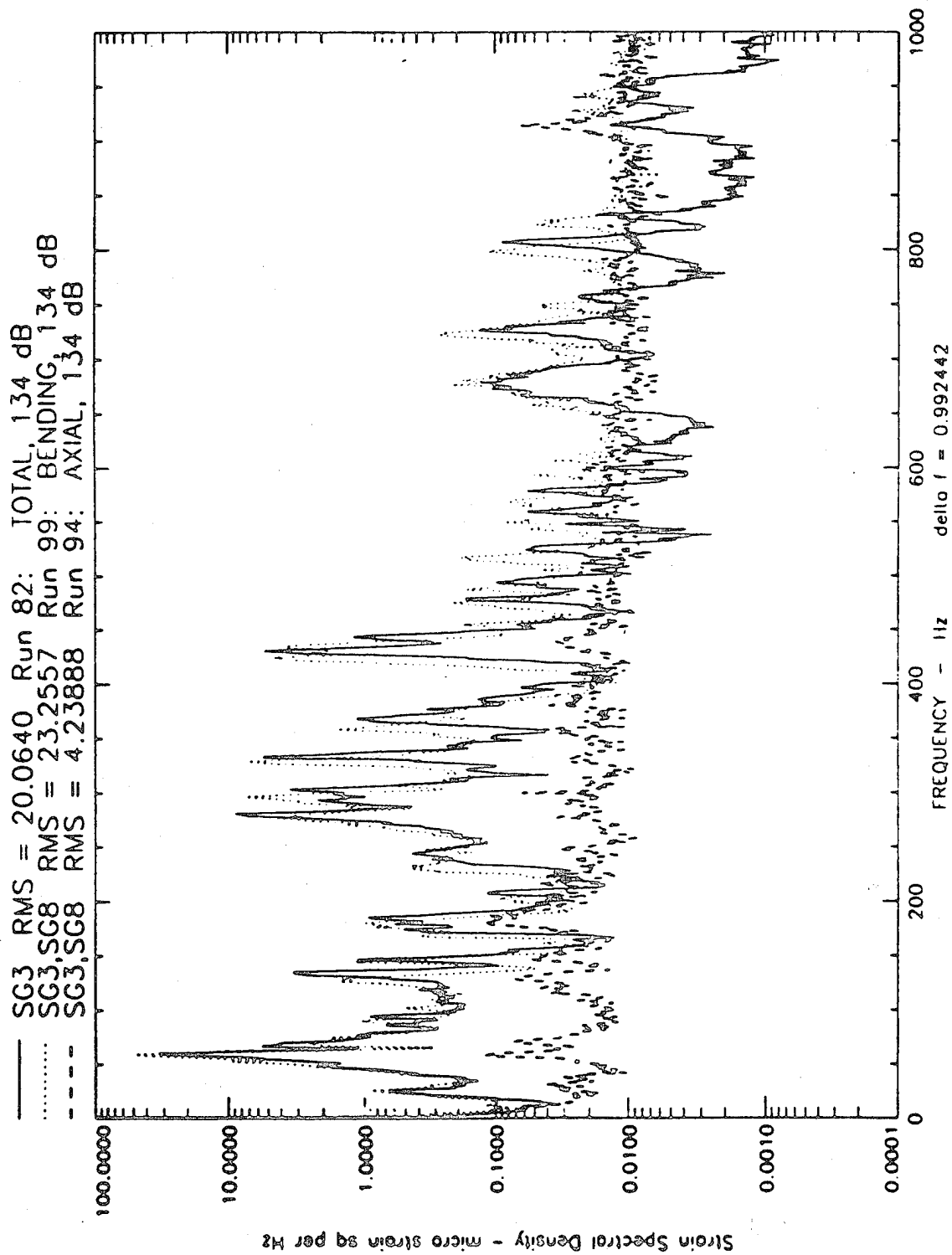


Fig 3.77 Total, axial and bending strain spectral densities, 134 dB OSPL, SG 3 and 3&8, C-C-C-C CFRP APWT plate.

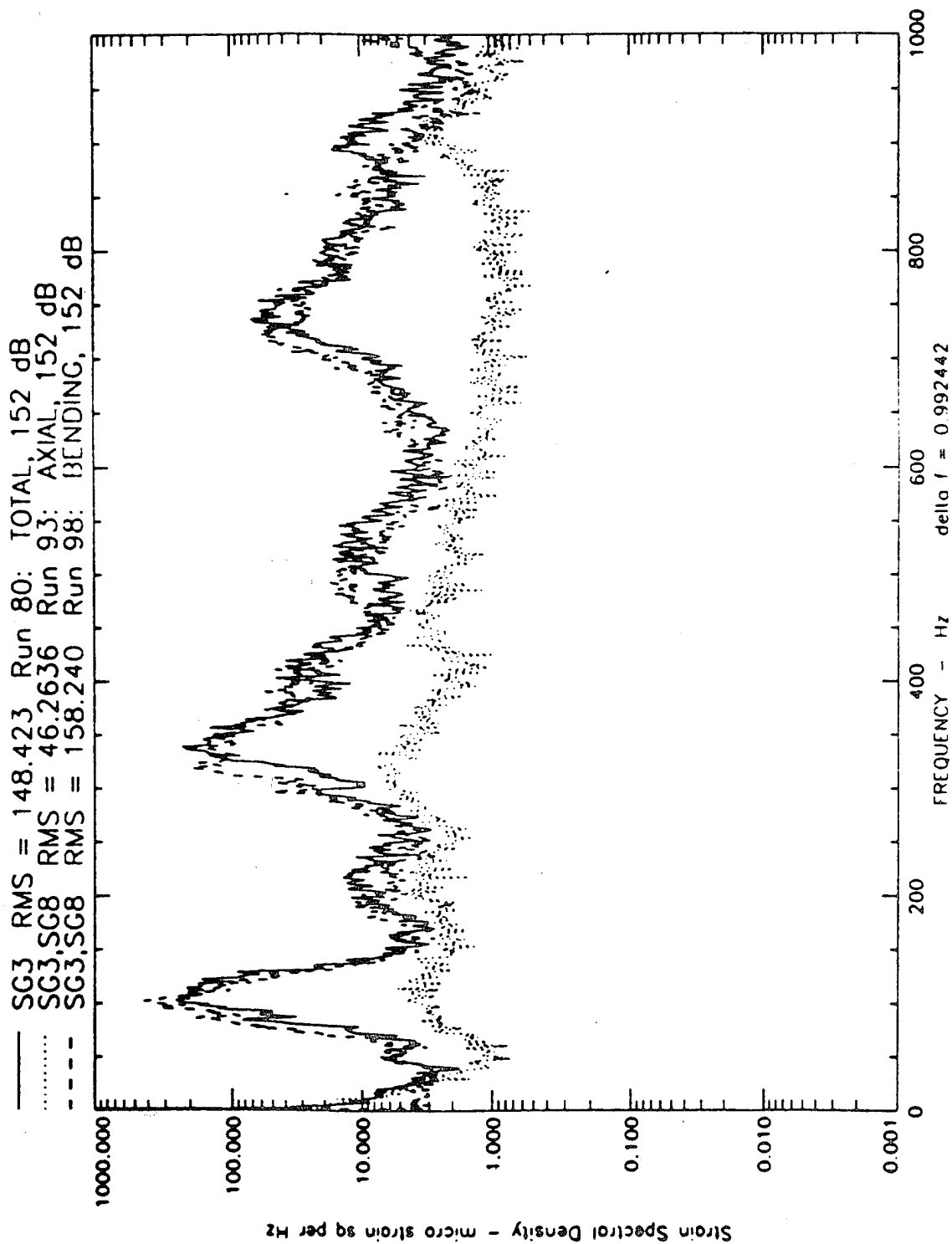


Fig 3.78 Total, axial and bending strain spectral densities, 152 dB OSPL, SG 3 and 3&8, C-C-C CFRP APWT plate.

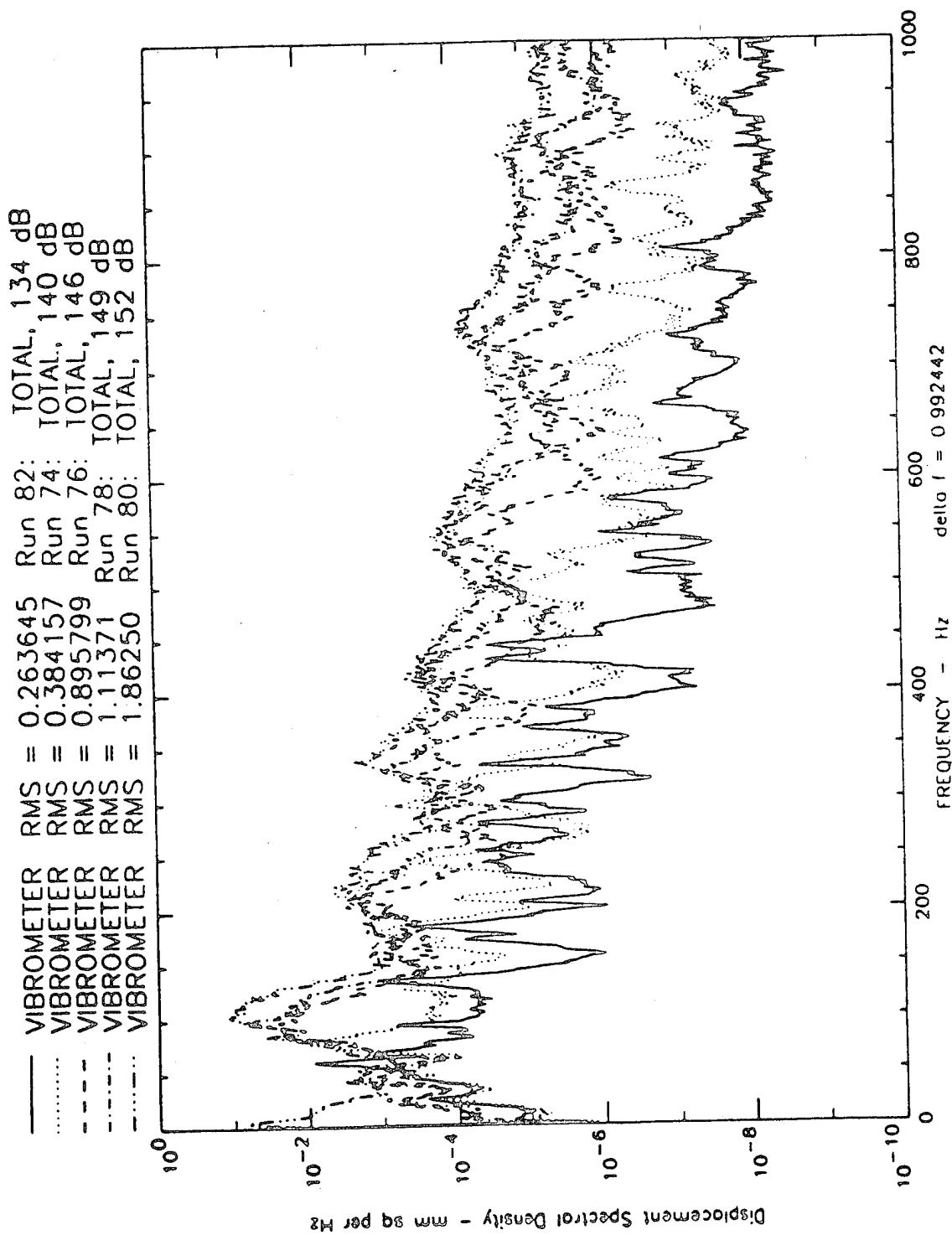


Fig 3.79 Displacement spectral densities, five OSPLs, C-C-C-C CFRP APWT plate.

C-C-C-C CFRP APWT
50-500 Hz RANDOM TOTAL STRAIN

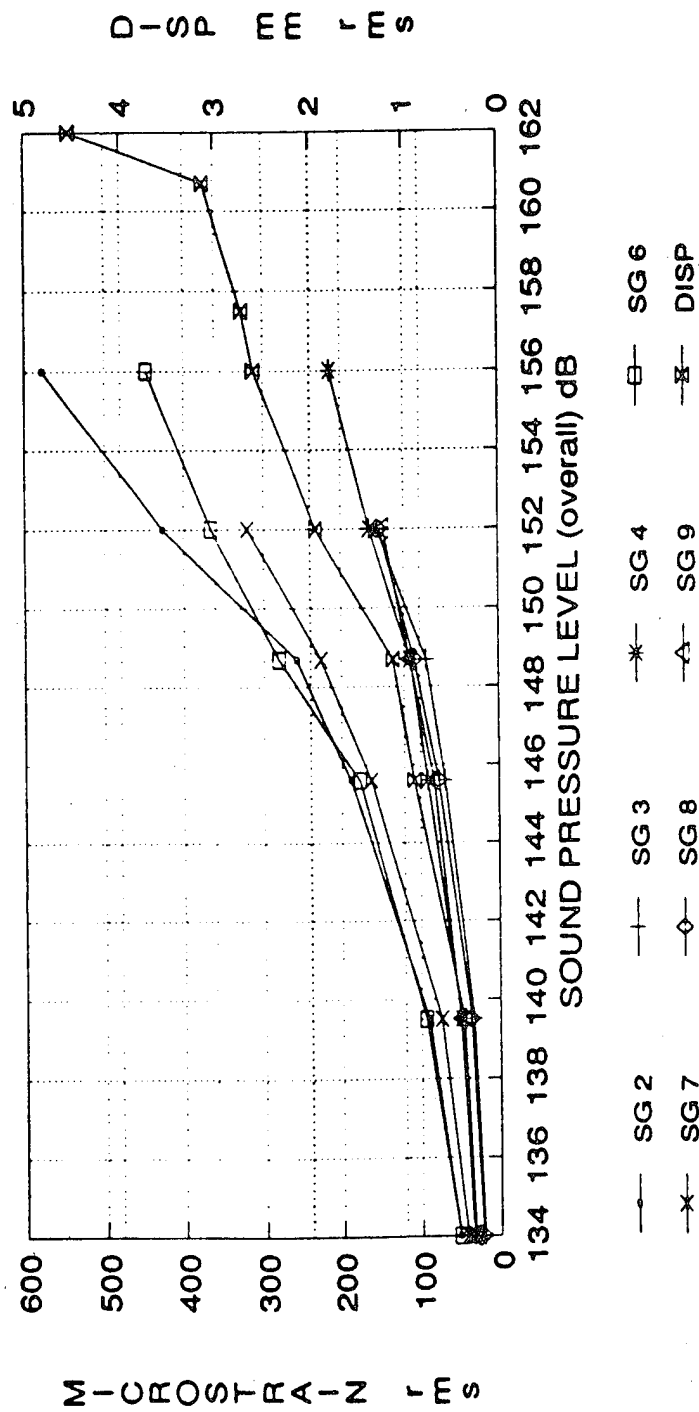


Fig 3.80 Total strains and displacements, C-C-C-C CFRP APWT plate.

C-C-C-C CFRP APWT
50-500 Hz RANDOM TOTAL STRAIN

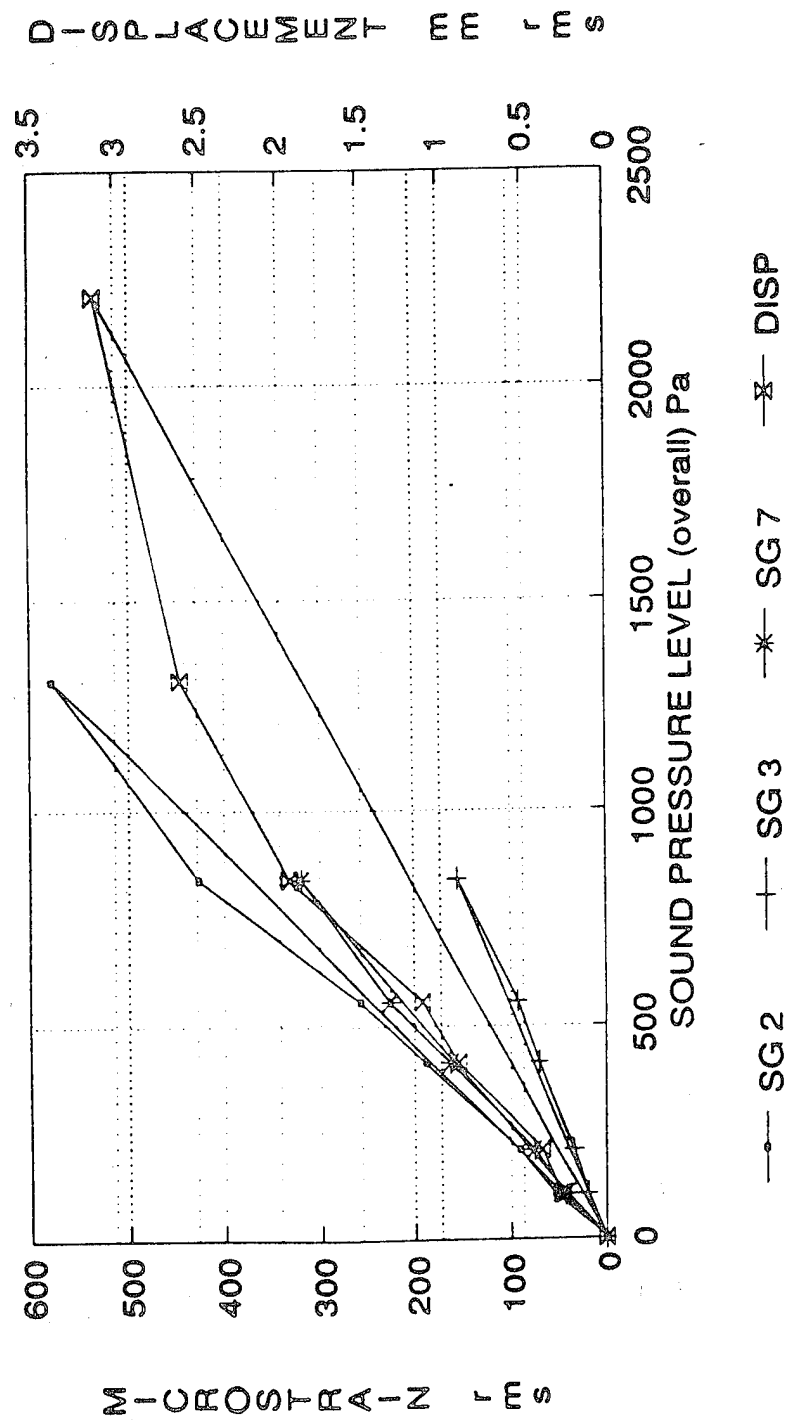


Fig 3.81 Total strains and displacements vs pressure (Pa), C-C-C-C CFRP APWT plate.

C-C-C-C CFRP APWT
50-500 Hz RANDOM AXIAL STRAIN

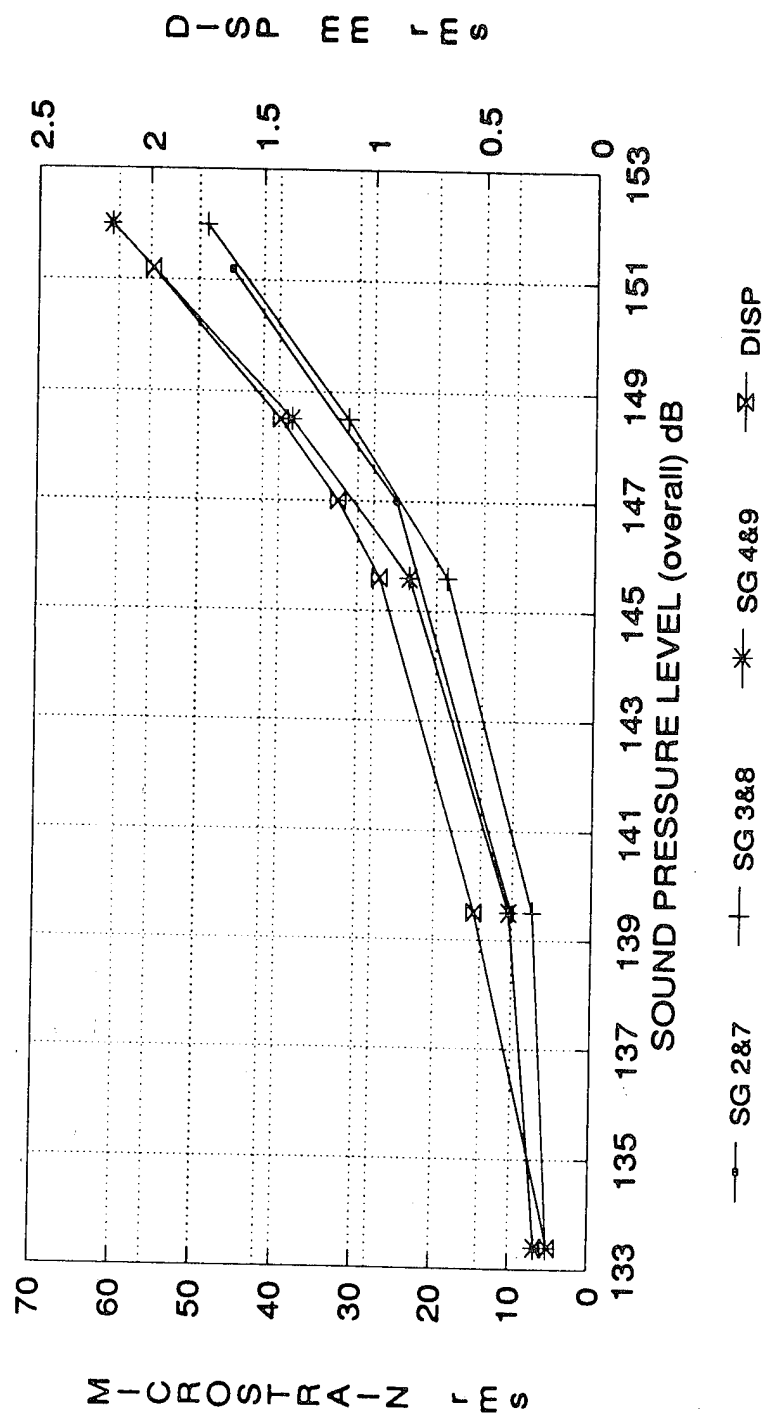


Fig 3.82 Axial strains and displacements, C-C-C-C CFRP APWT plate.

C-C-C-C CFRP APWT
50-500 Hz RANDOM BENDING STRAIN

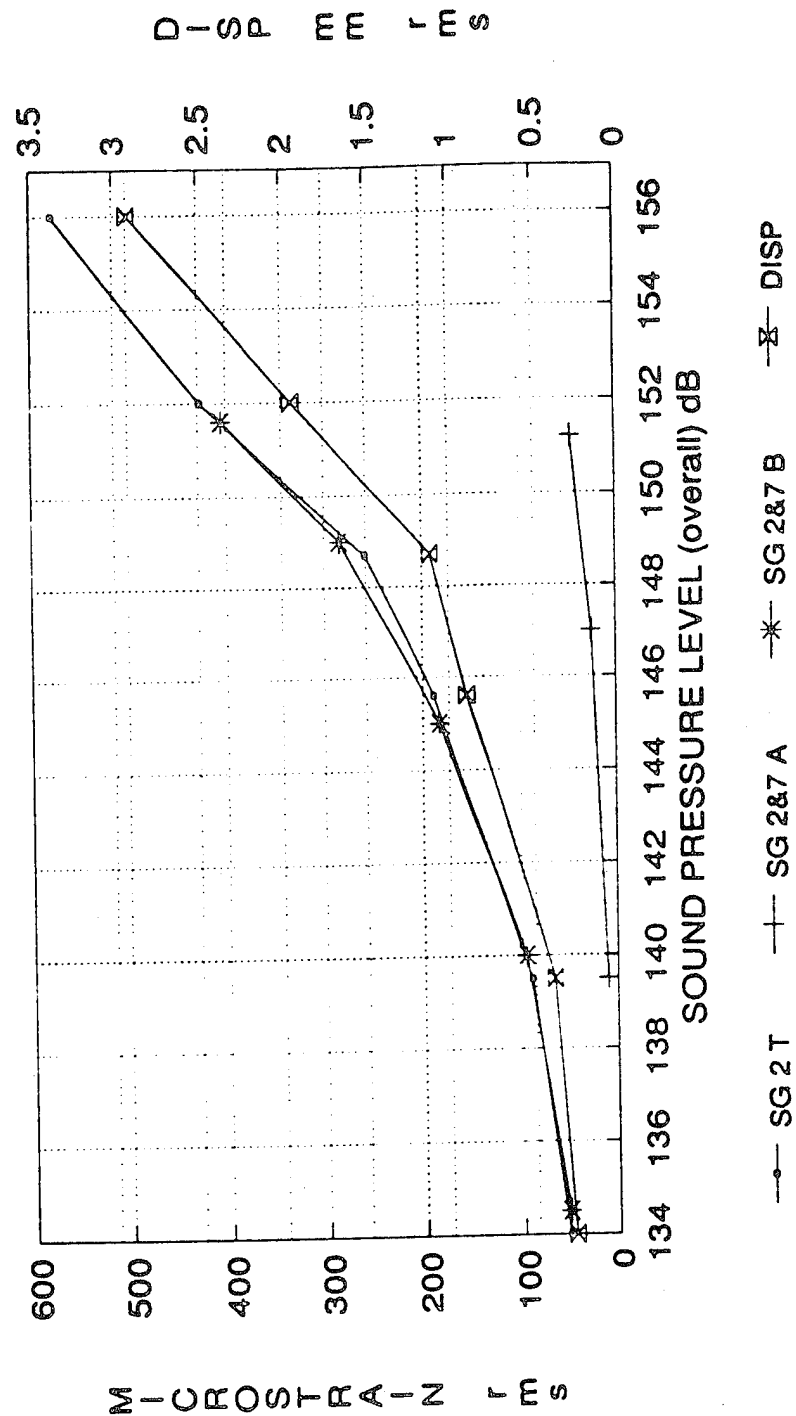


Fig 3.83 Bending strains and displacements, C-C-C-C CFRP APWT plate.

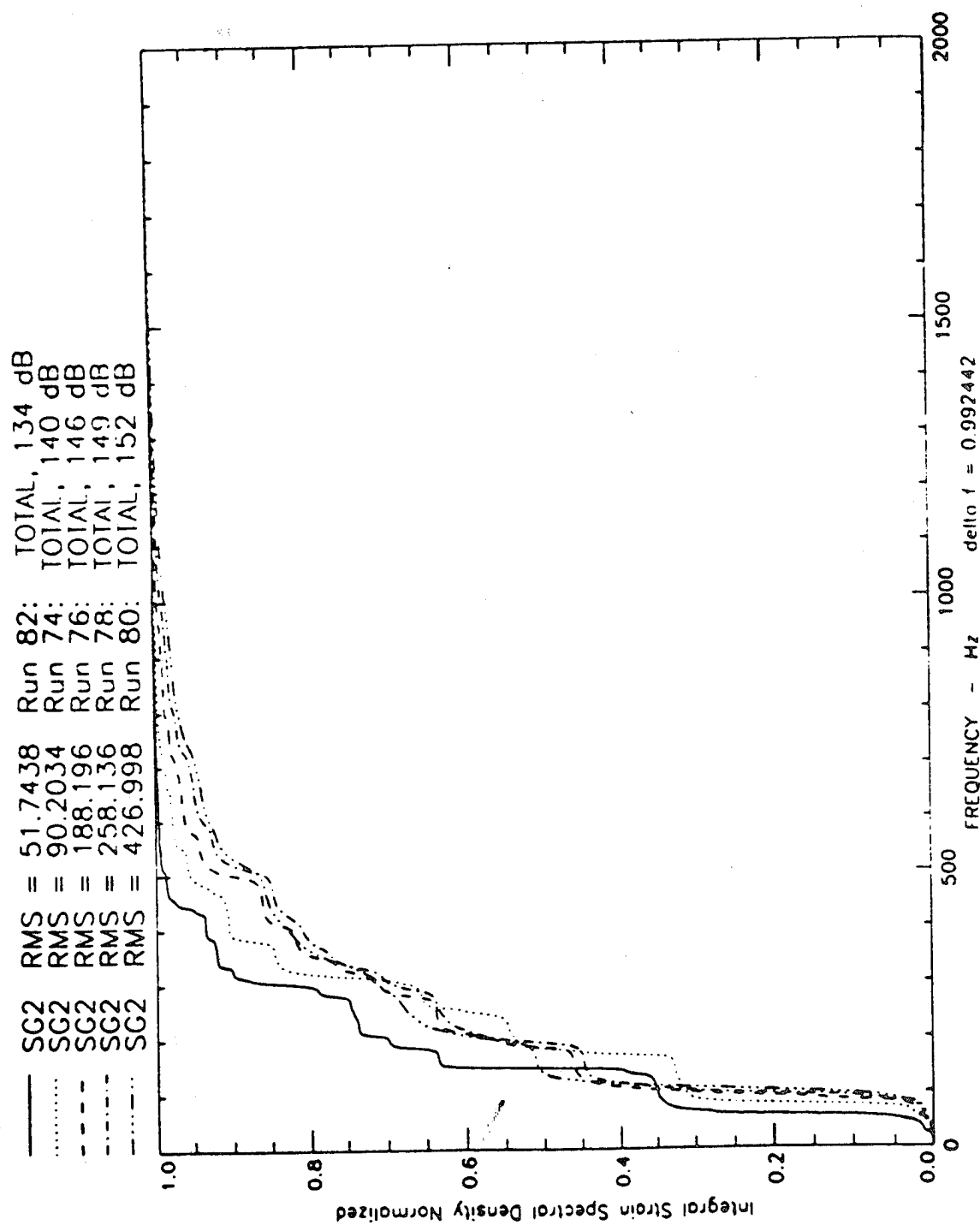


Fig 3.84 Normalised integrals of total strain spectral densities, SG 2, C-C-C-C FRP APWT plate.

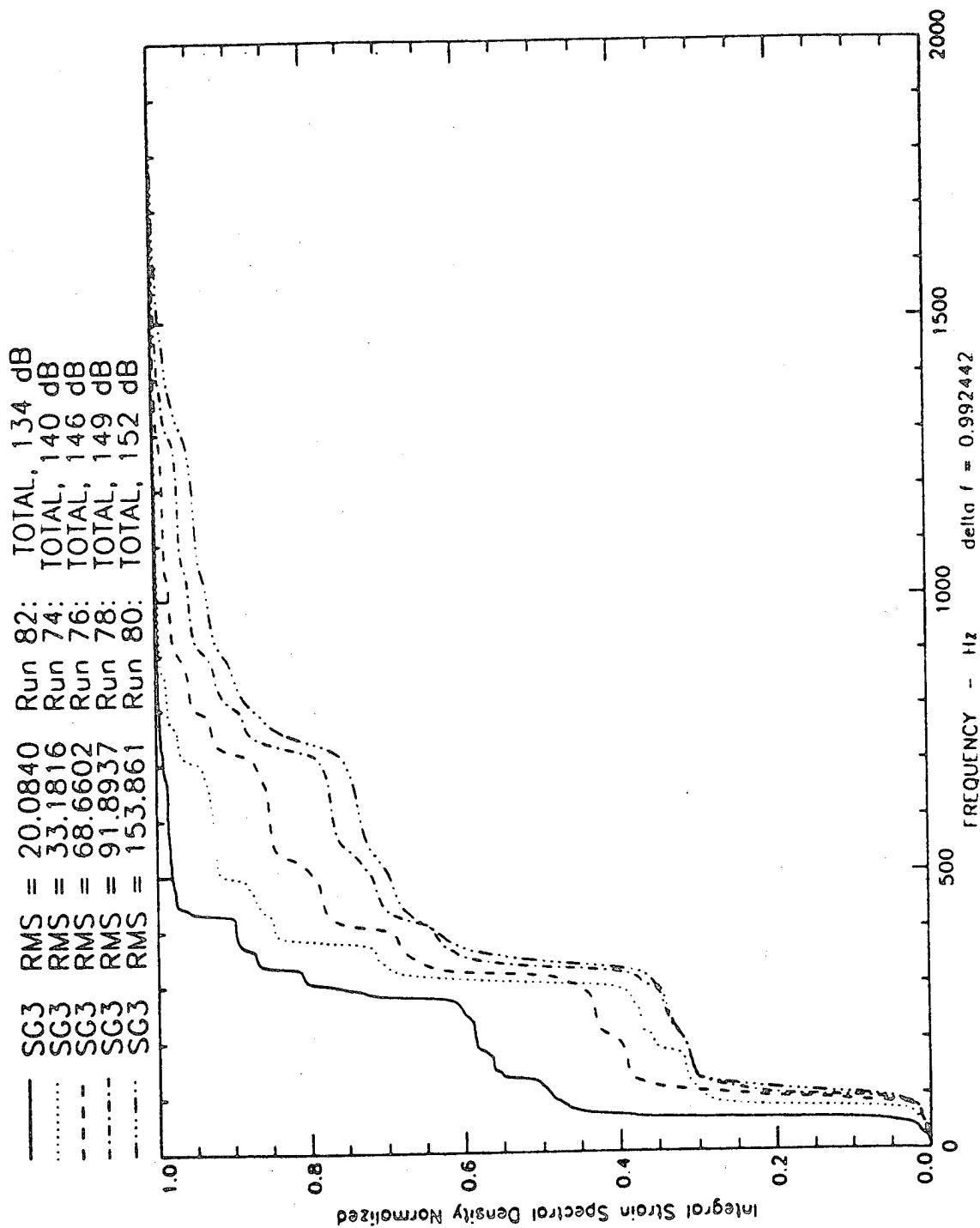


Fig 3.85 Normalised integrals of total strain spectral densities, SG 3, C-C-C-C CFRP APWT plate.

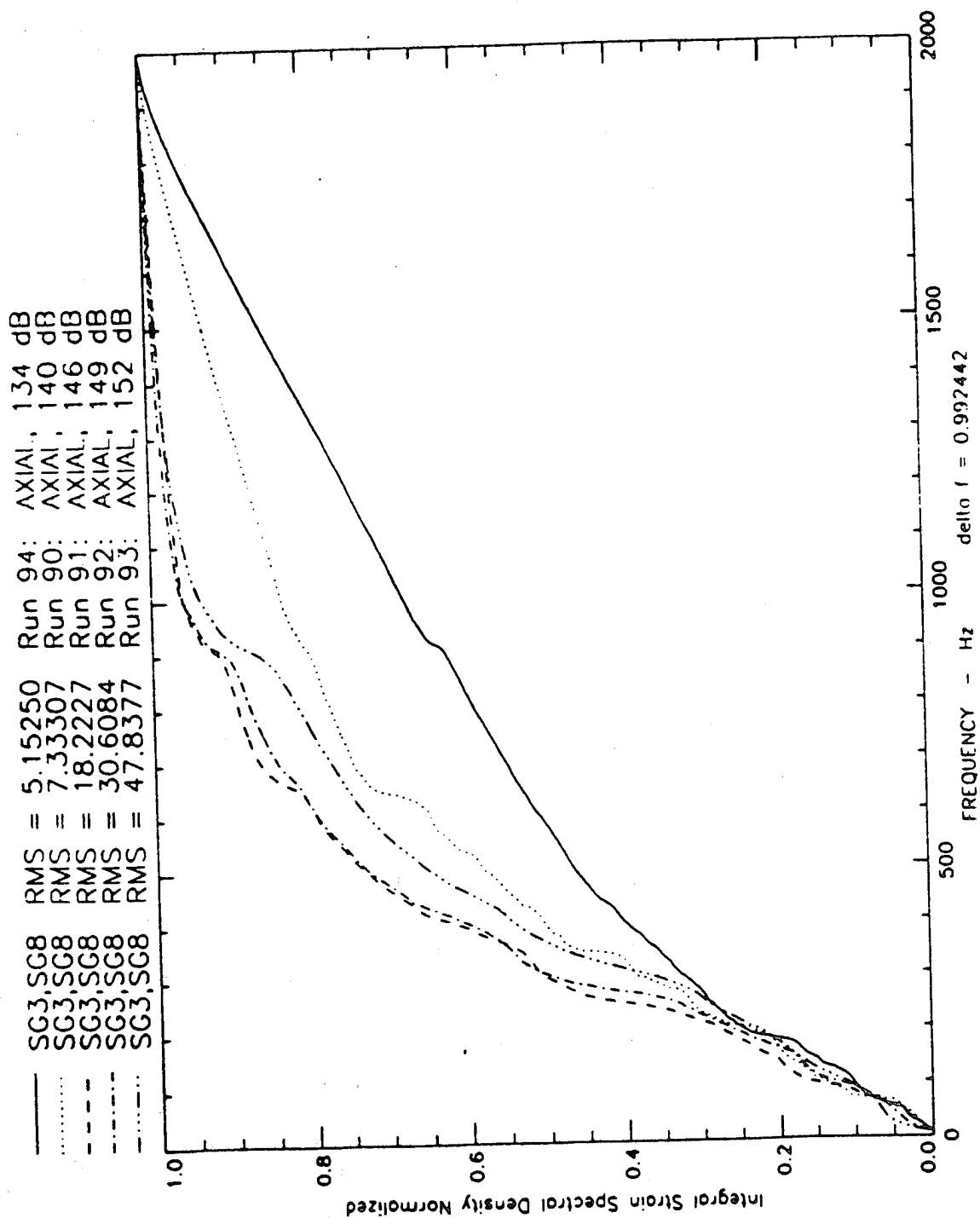


Fig 3.86 Normalised integrals of axial strain spectral densities, SG 3, C-C-C CFRP APWT plate.

C-C-C-C CFRP APWT
Amplitude PDF MIC 3 Rec 74, 76, 78, 80, 82

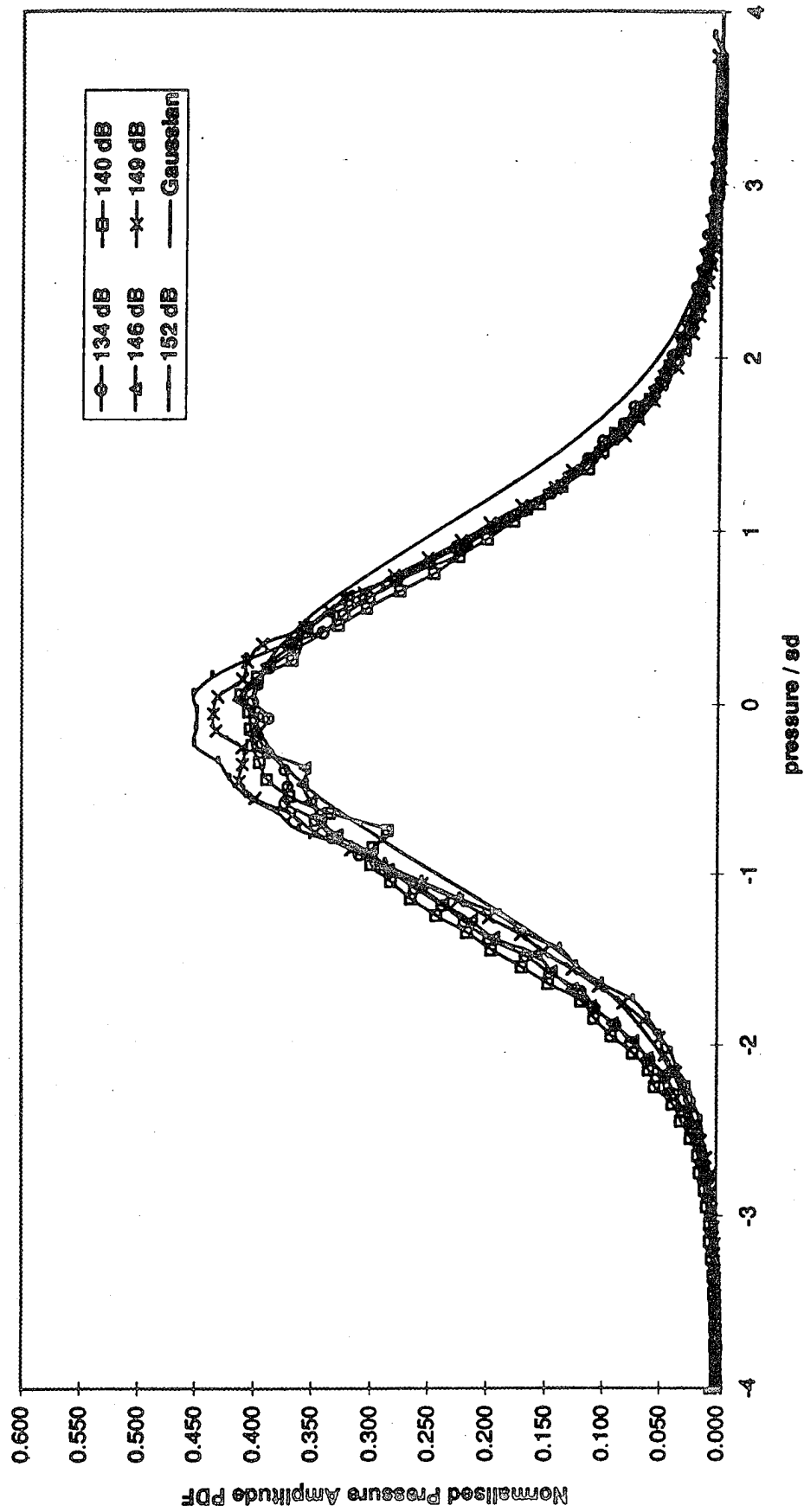


Fig 3.87 Normalised pressure amplitude PDFs, M 3, C-C-C-C CFRP APWT.

C-C-C-C CFRP APWT
Amplitude PDF SG 2 Rec 74, 76, 78, 80, 82

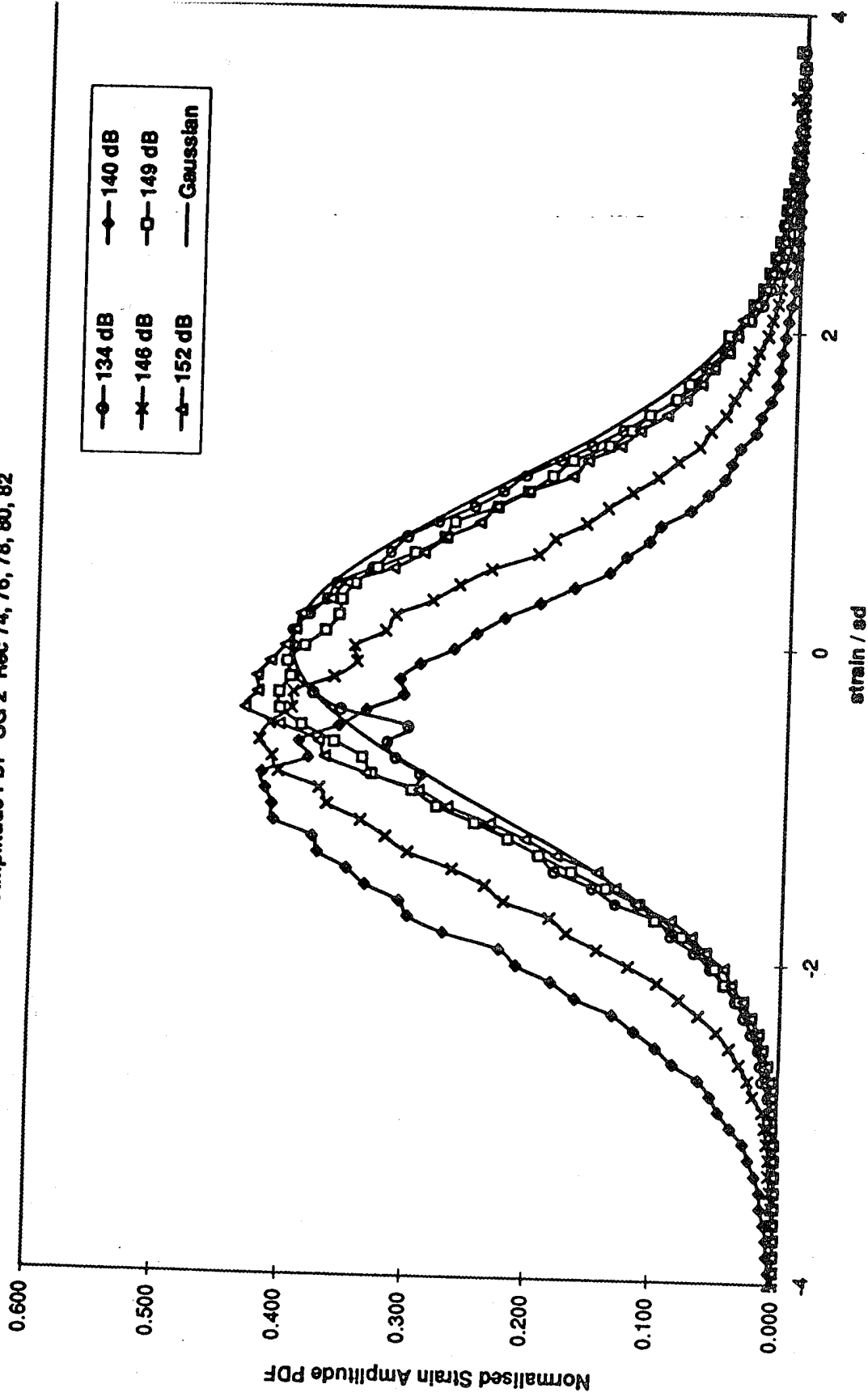


Fig 3.88 Normalised strain amplitude PDFs, SG 2, C-C-C-C CFRP APWT.

C-C ALUM BEAM STATIC TEST - BENDING

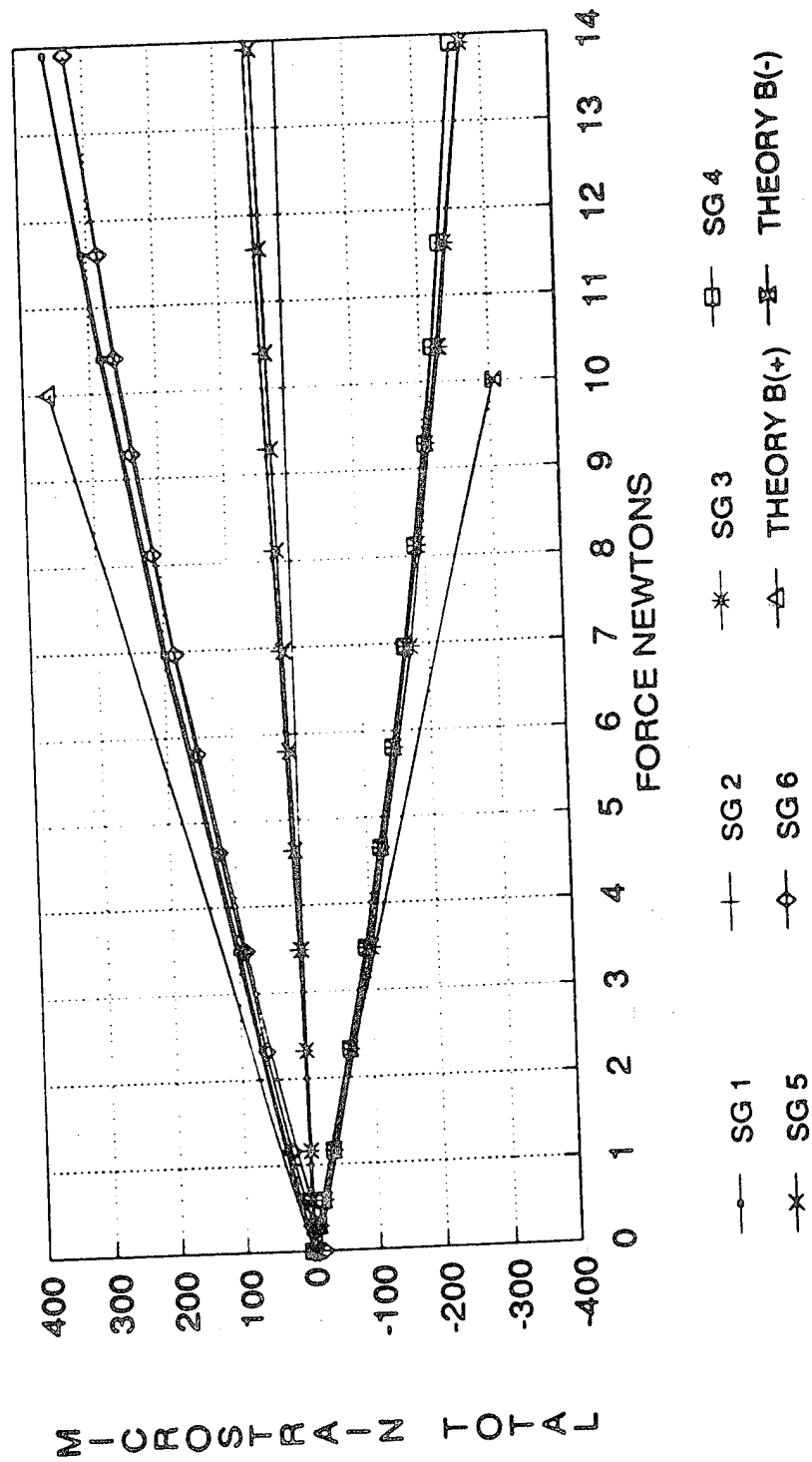


Fig 4.1 Static total strains compared with a second linear bending theory, C-C aluminium beam.

C-C AL BEAM STATIC TESTS- 2.5 Newtons

Rank 1 Eqn 8007 $y=a+b \cdot 4n/(1+n)^2$ $n=\exp(-(x-c)/d)$ (Logistic)

$a=-0.044152943$ $b=0.27187834$

$c=203.02861$ $d=62.835049$

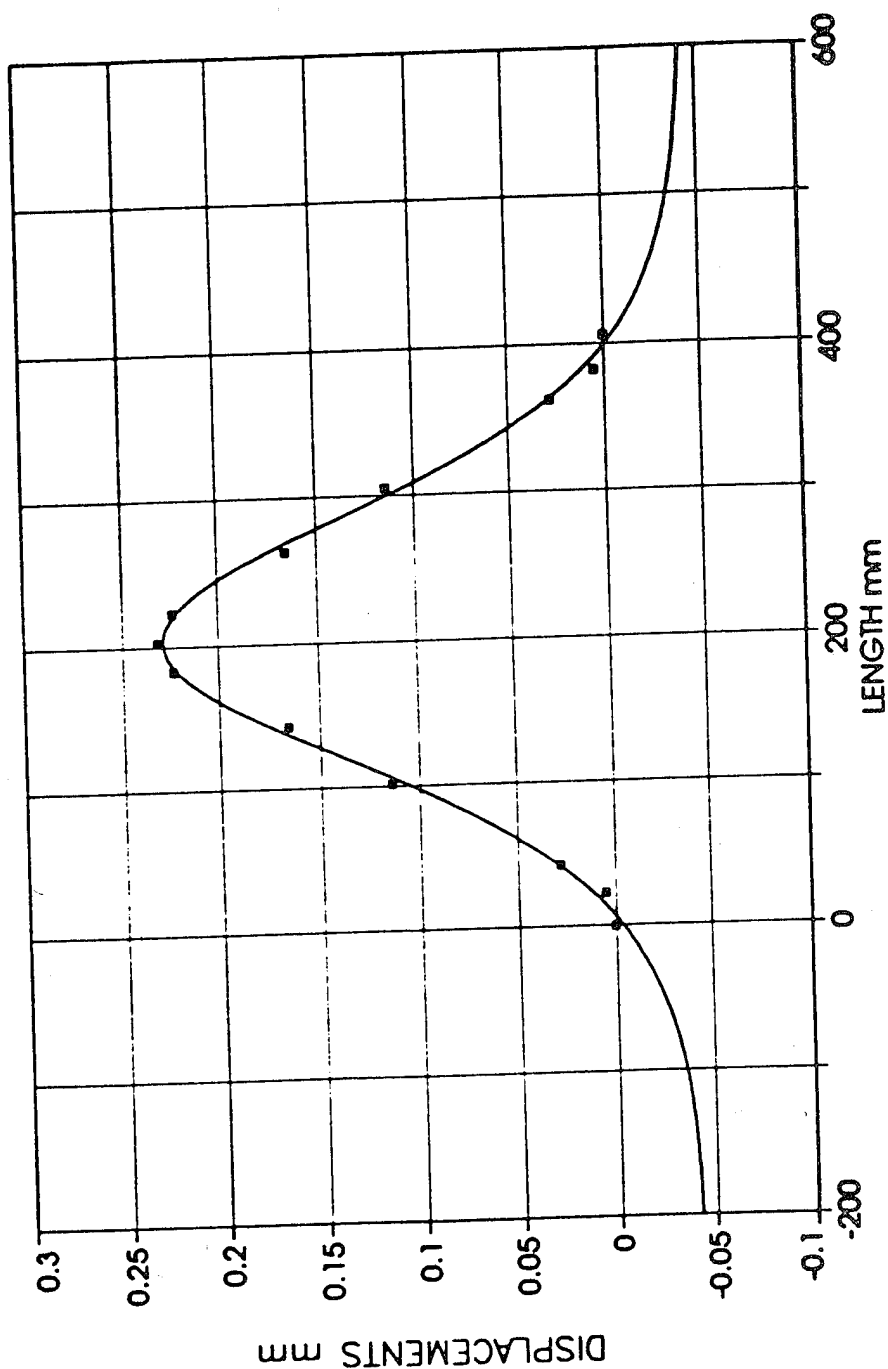


Fig 4.2 Rank 1, logistic curve fit of displacement shape, 2.5 N static test, C-C aluminium beam.

C-C AL BEAM STATIC TESTS- 2.5 Newtons

Rank 2 Eqn 8003 $y=a+b\exp(-0.5((x-c)/d)^2)$ (Gaussian)

$a=-0.020629906$ $b=0.24700817$

$c=203.0417$ $d=68.363712$

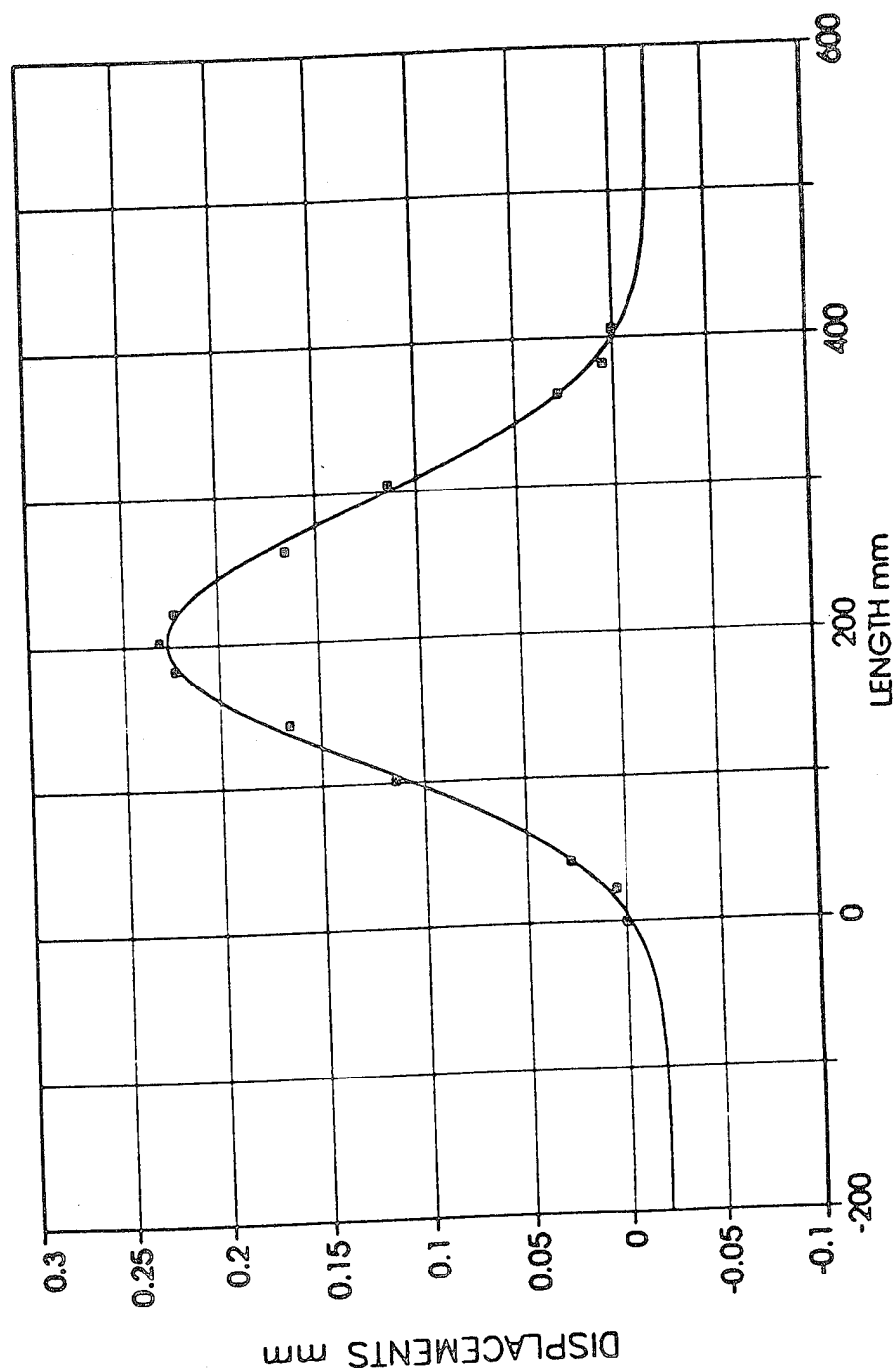


Fig 4.3 Rank 2, Gaussian curve fit of displacement shape, 2.5 N static test, C-C aluminium beam.

C-C AL BEAM STATIC TESTS- 2.5 Newtons

Rank 3 Eqn 8004 $y=a+b/(1+((x-c)/d)^2)$ (Lorentzian)

$a=0.10761974$ $b=0.33649817$

$c=203.01671$ $d=133.71386$

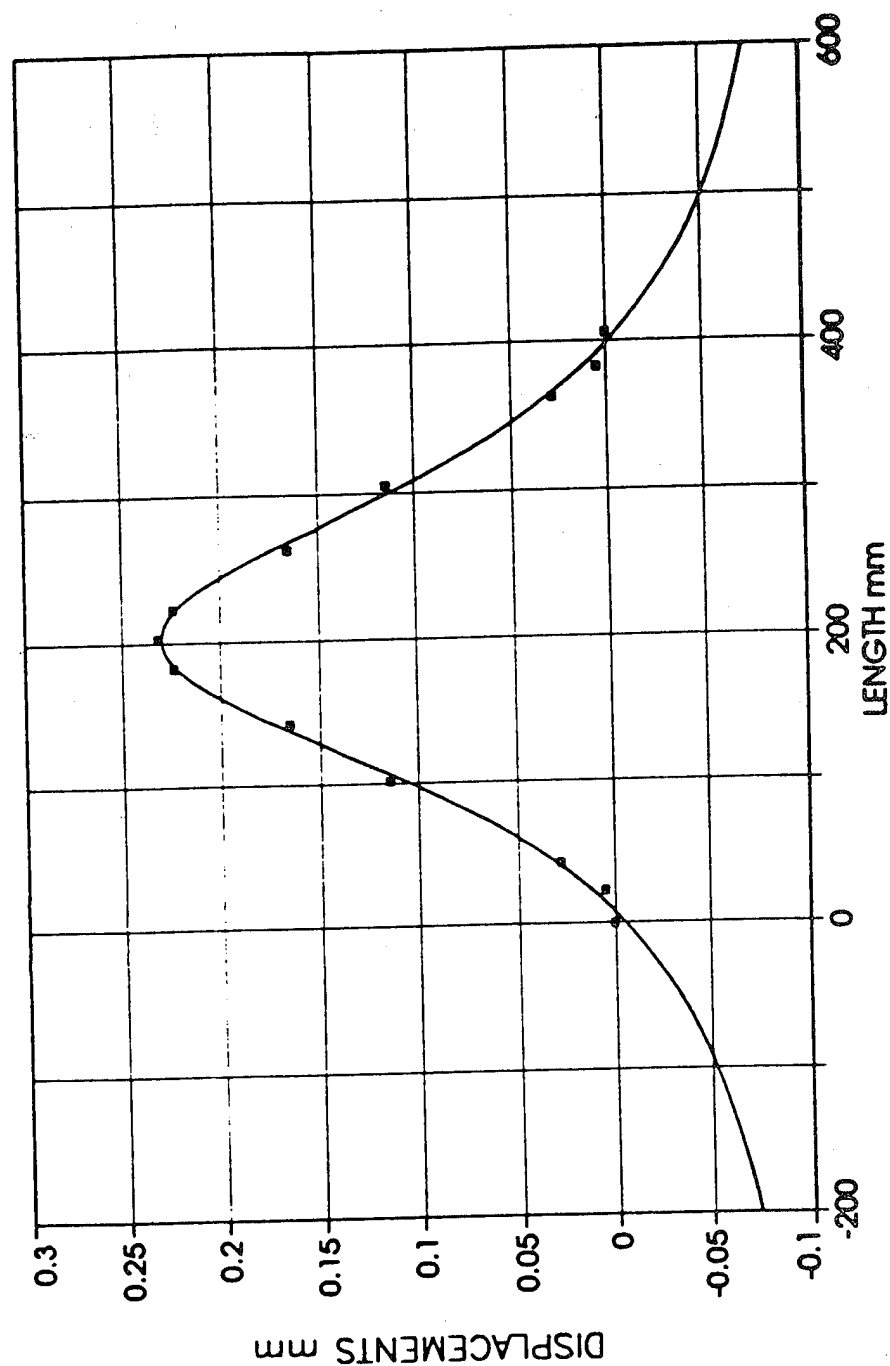


Fig 4.4 Rank 3, Lorentzian curve fit of displacement shape, 2.5 N static test, C-C aluminium beam.

C-C AL BEAM STATIC TESTS- 2.5 Newtons

Rank 7 Eqn 8014 $y=a+b\sin(2\pi x/d+c)$ (Sine)

$a=0.11206426$ $b=0.11128491$

$c=4.6981946$ $d=404.2942$

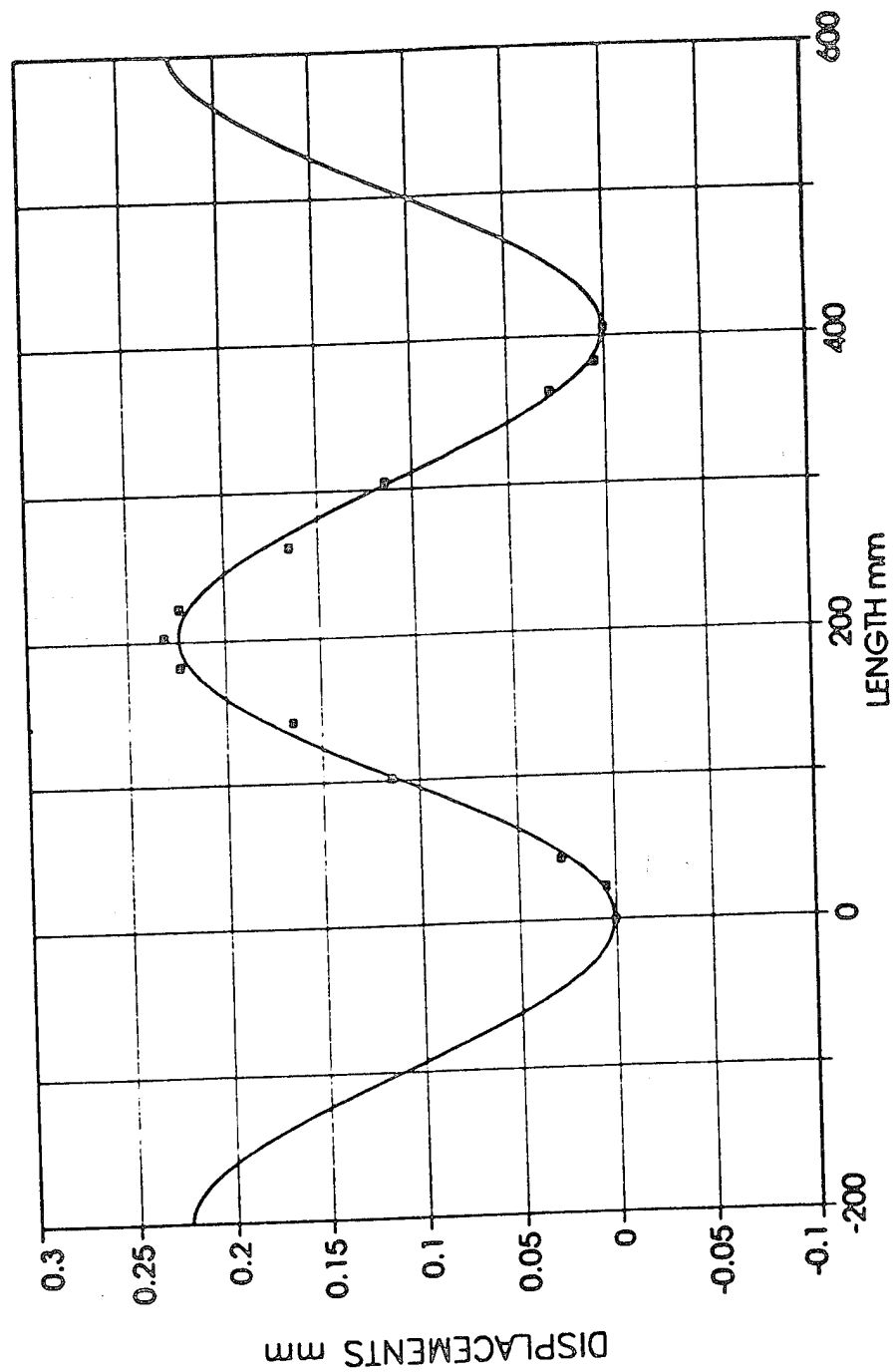


Fig 4.5 Rank 7, sine curve fit of displacement shape, 2.5 N static test, C-C aluminium beam.

C-C AL BEAM STATIC TESTS- 0.25 N

RANK 15 Eqn 8001 $y=a(\cos(bx)-\cos(bx))-c(\sinh(bx)-\sinh(bx))$

$a=0.13806736$ $b=0.011721076$

$c=0.98261627$

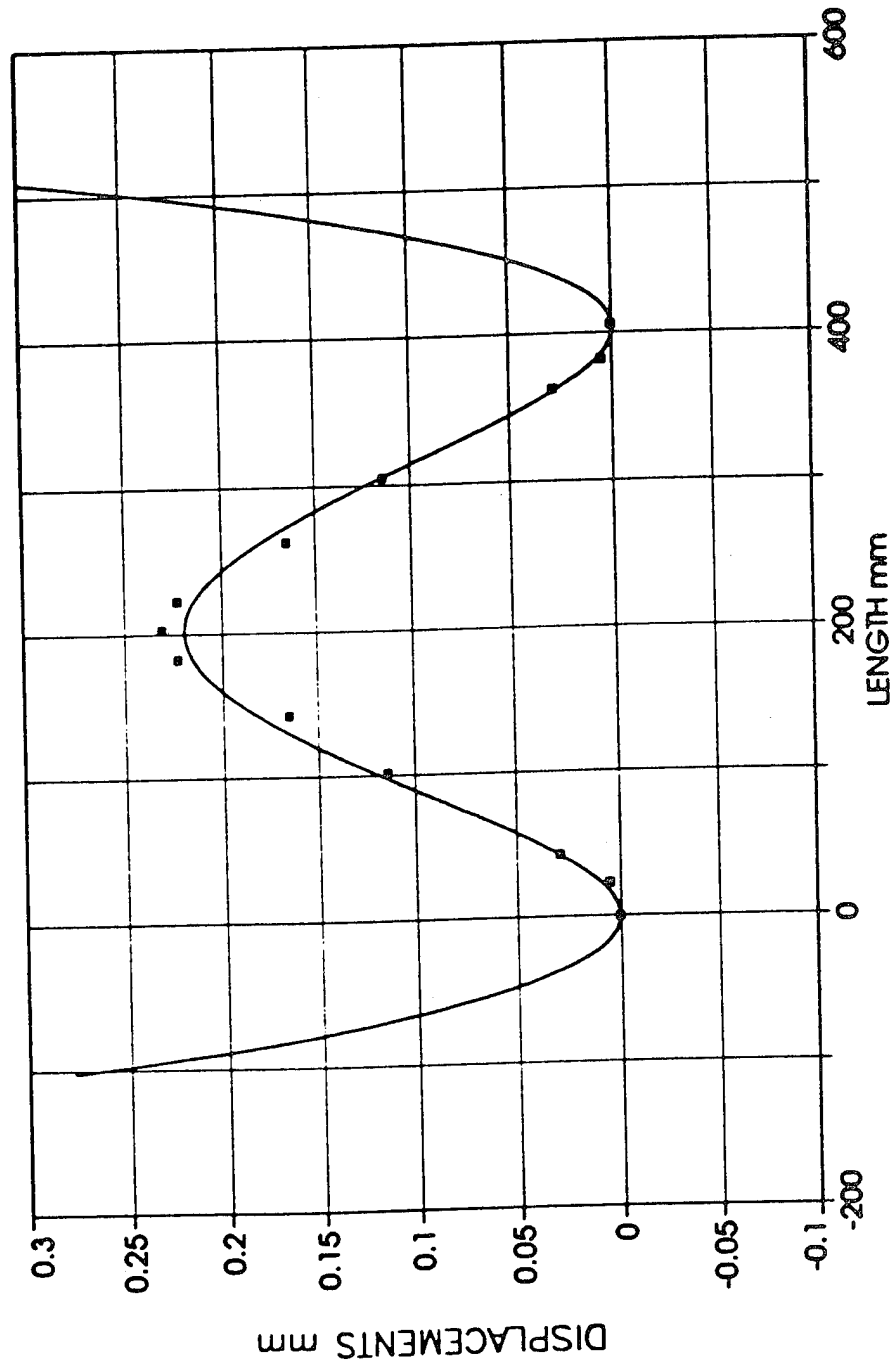


Fig 4.6 Rank 15 classical curve fit of displacement shape, 2.5N static test, C-C aluminium beam.

C-C AL BEAM STATIC TESTS- 2.5 Newtons

Rank 20 Eqn 6001 $y = a + bx + cx^2 + dx^3 + ex^4$

$a = 2.4095895e-09$ $b = 2.6105293e-07$ $c = 2.1472112e-05$

$d = -1.066853e-07$ $e = 1.3245813e-10$

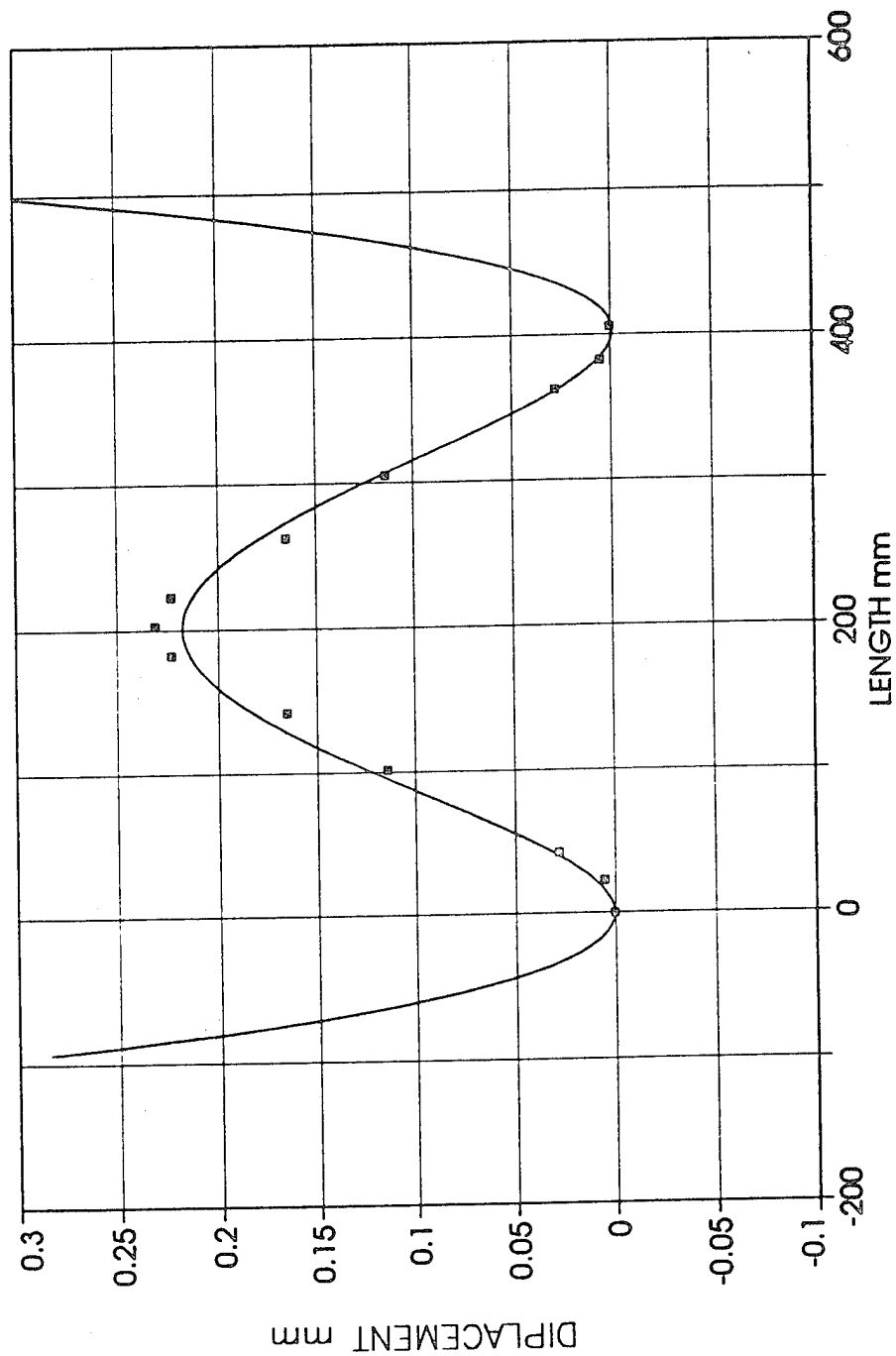


Fig 4.7 Rank 20 fourth order polynomial curve fit of displacement shape, 2.5 N static test, C-C aluminium beam.

C-C AL BEAM STATIC TESTS-13.7N

Rank 1 Eqn 8003 $y=a+b\exp(-0.5((x-c)/d)^2)$ (Gaussian)

$a=0.14027803$ $b=1.3173225$

$c=203.03098$ $d=93.867503$

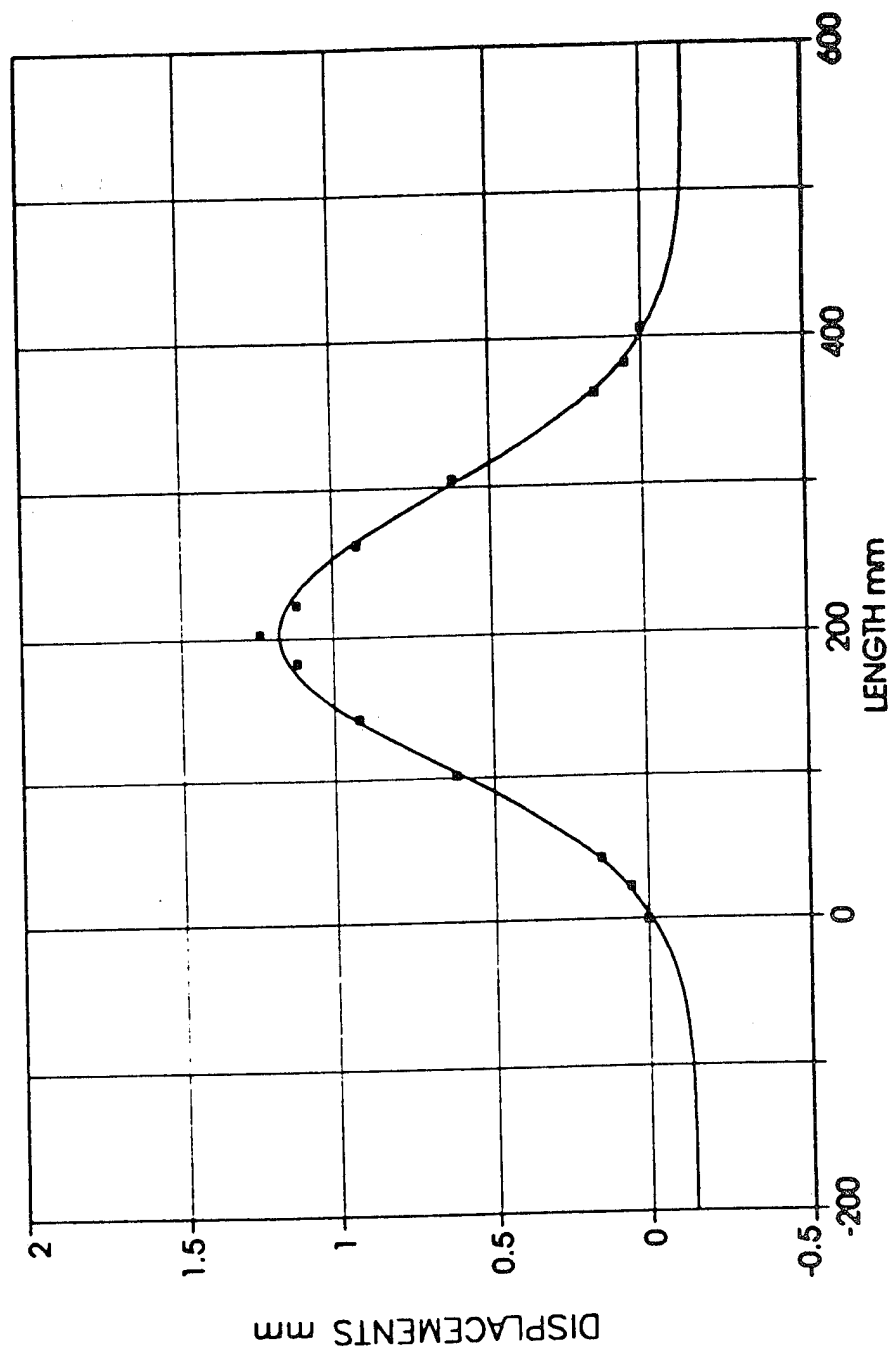


Fig 4.8 Rank 1 Gaussian curve fit of displacement shape, 13.7 N static test, C-C aluminium beam.

C-C AL BEAM STATIC TESTS-13.7N

Rank 2 Eqn 8014 $y=a+b\sin(2\pi x/d+c)$ (Sine)

$a=0.58362262$ $b=0.58199233$

$c=4.6009187$ $d=417.66598$

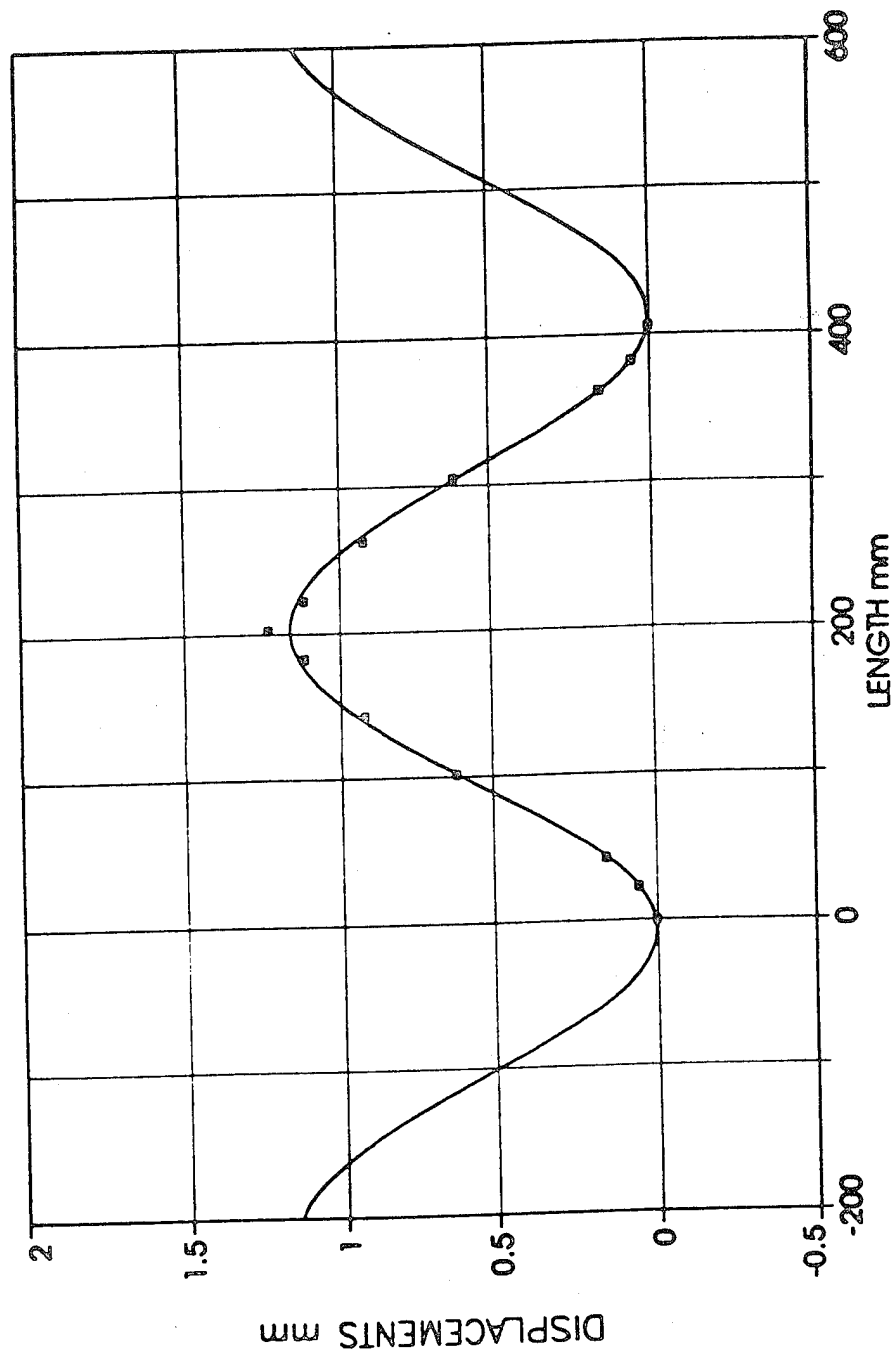


Fig 4.9 Rank 2 sine curve fit of displacement shape, 13.7 N static test, C-C aluminium beam.

C-C AL BEAM STATIC TESTS-13.7N

Rank 5 Eqn 8007 $y=a+b \cdot 4n/(1+n)^2$ $n=\exp(-(x-c)/d)$ (Logistic)

$a=-0.28808977$ $b=1.4694655$

$c=203.02056$ $d=67.856723$

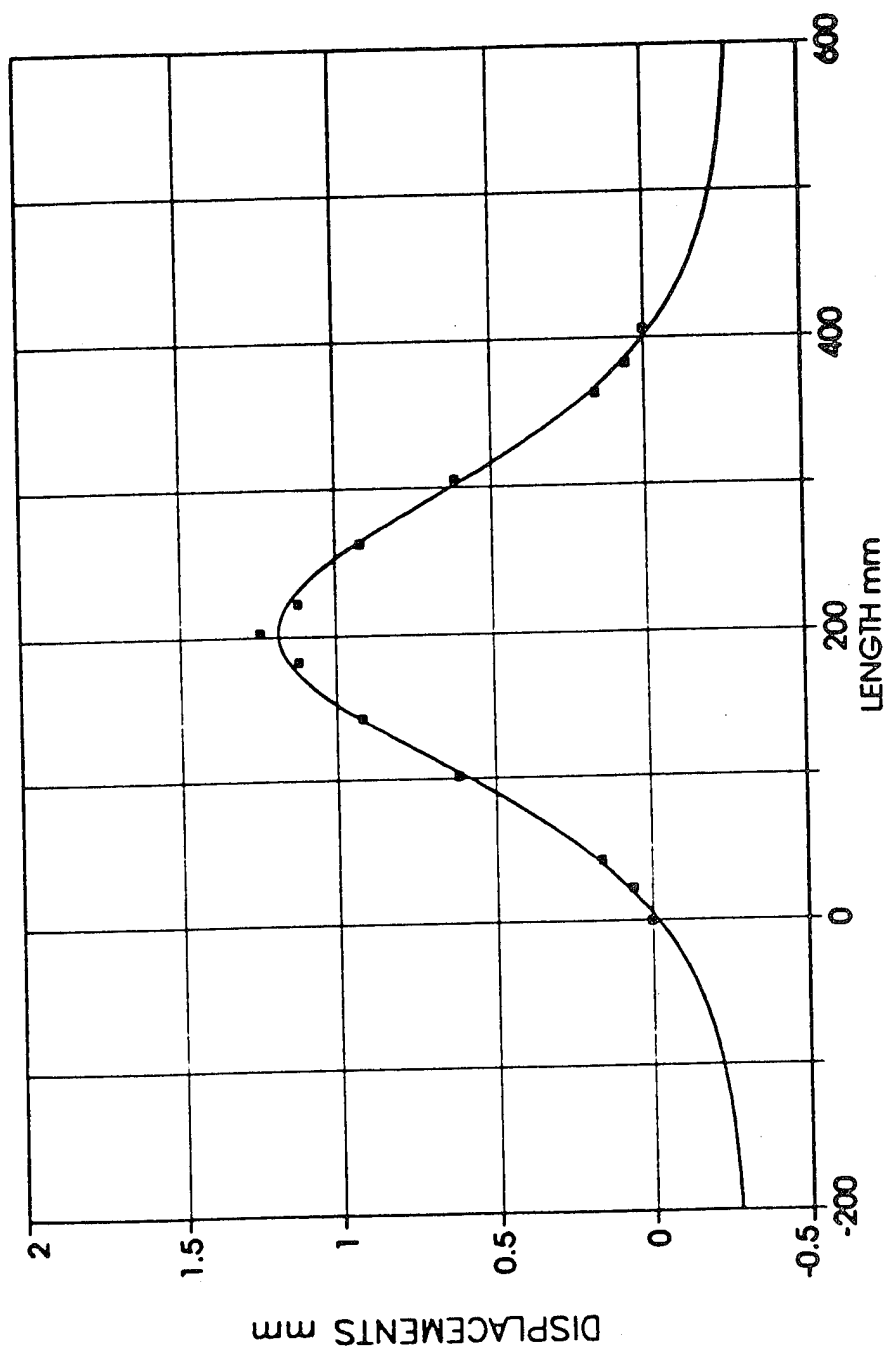


Fig 4.10 Rank 5 logistic curve fit of displacement shape, 13.7 N static test, C-C aluminium beam.

C-C AL BEAM STATIC TESTS-13.7N

Rank 6 Eqn 8001 $y = a(\cosh(bx) - \cos(bx)) - c(\sinh(bx) - \sin(bx))$

$a=0.72697339$ $b=0.01167264$

$c=0.98237469$

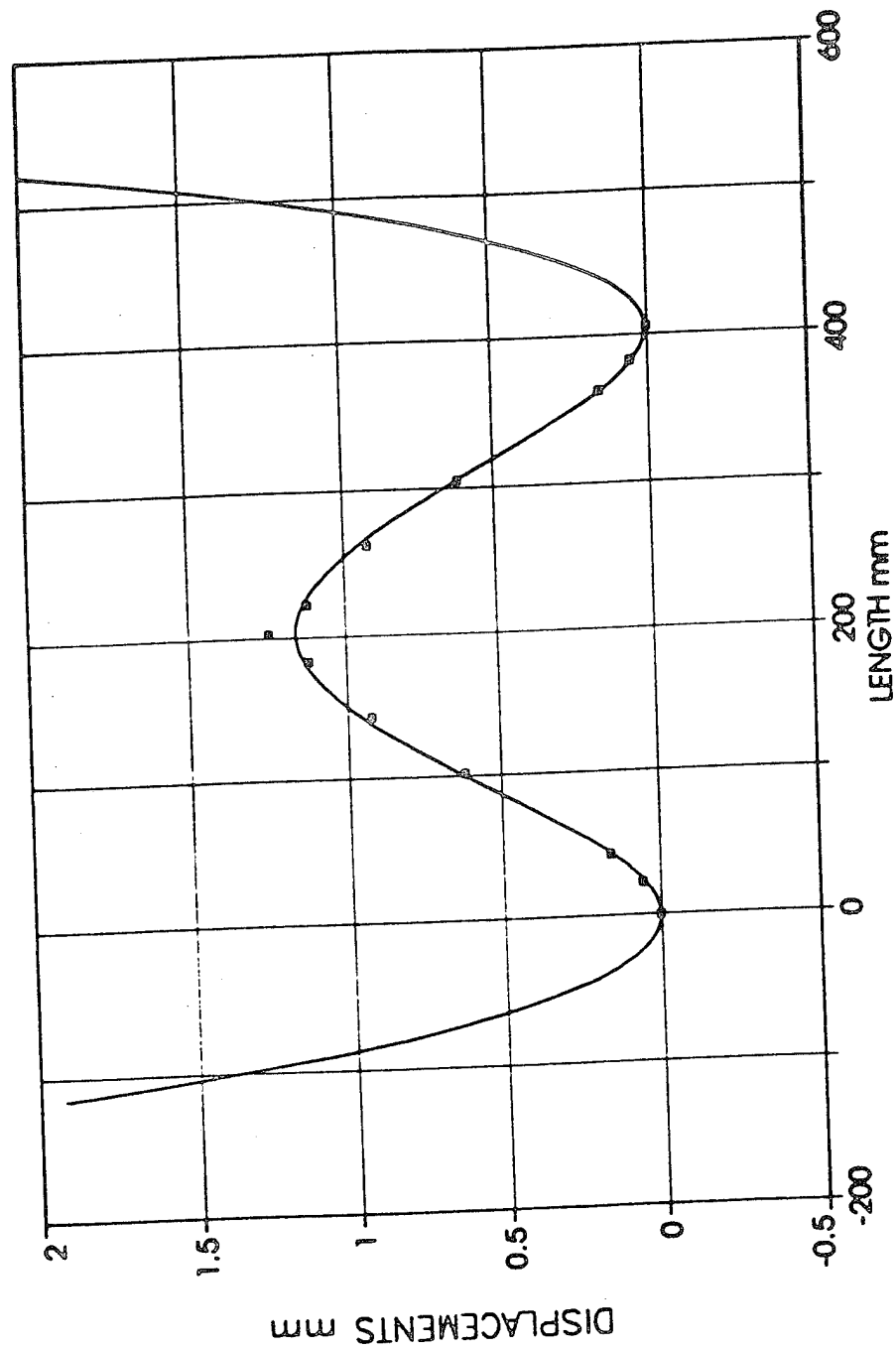


Fig 4.11 Rank 6 classical curve fit of displacement shape, 13.7 N static test, C-C aluminium beam.

C-C AL BEAM STATIC TESTS-13.7N

Rank 7 Eqn 8004 $y=a+b/(1+((x-c)/d)^2)$ (Lorentzian)

a=0.66777439 b=1.8527896

c=203.01104 d=147.50818

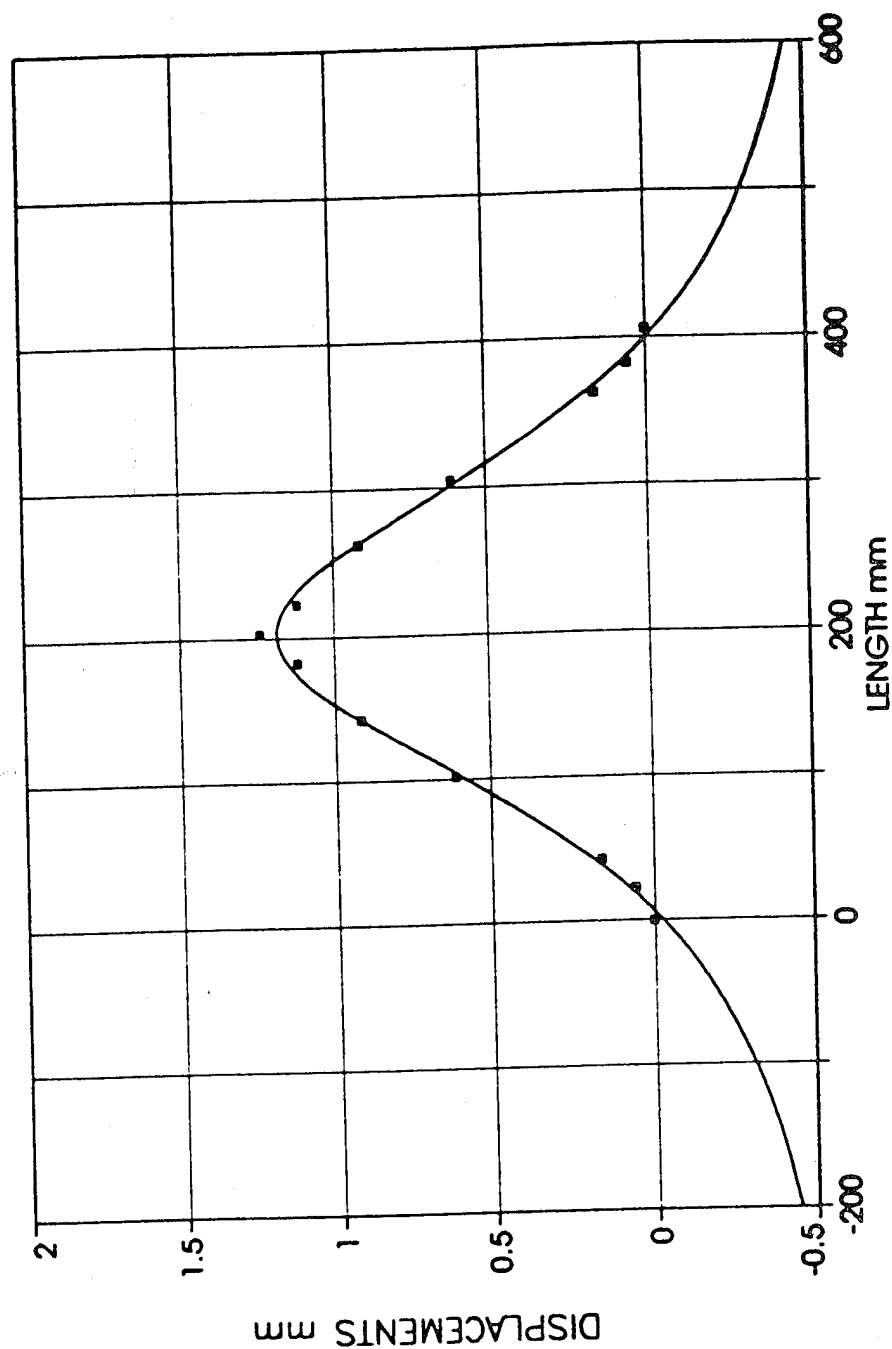


Fig 4.12 Rank 7 Lorentzian curve fit of displacement shape, 13.7 N static test, C-C aluminium beam.

C-C AL BEAM STATIC TESTS-13.7N

Rank 13 Eqn 6001 $y=a+bx+cx^2+dx^3+ex^4$

$a=1.2589504e-08$ $b=1.3639365e-06$ $c=0.00011218644$

$d=-5.5515275e-07$ $e=6.868641e-10$

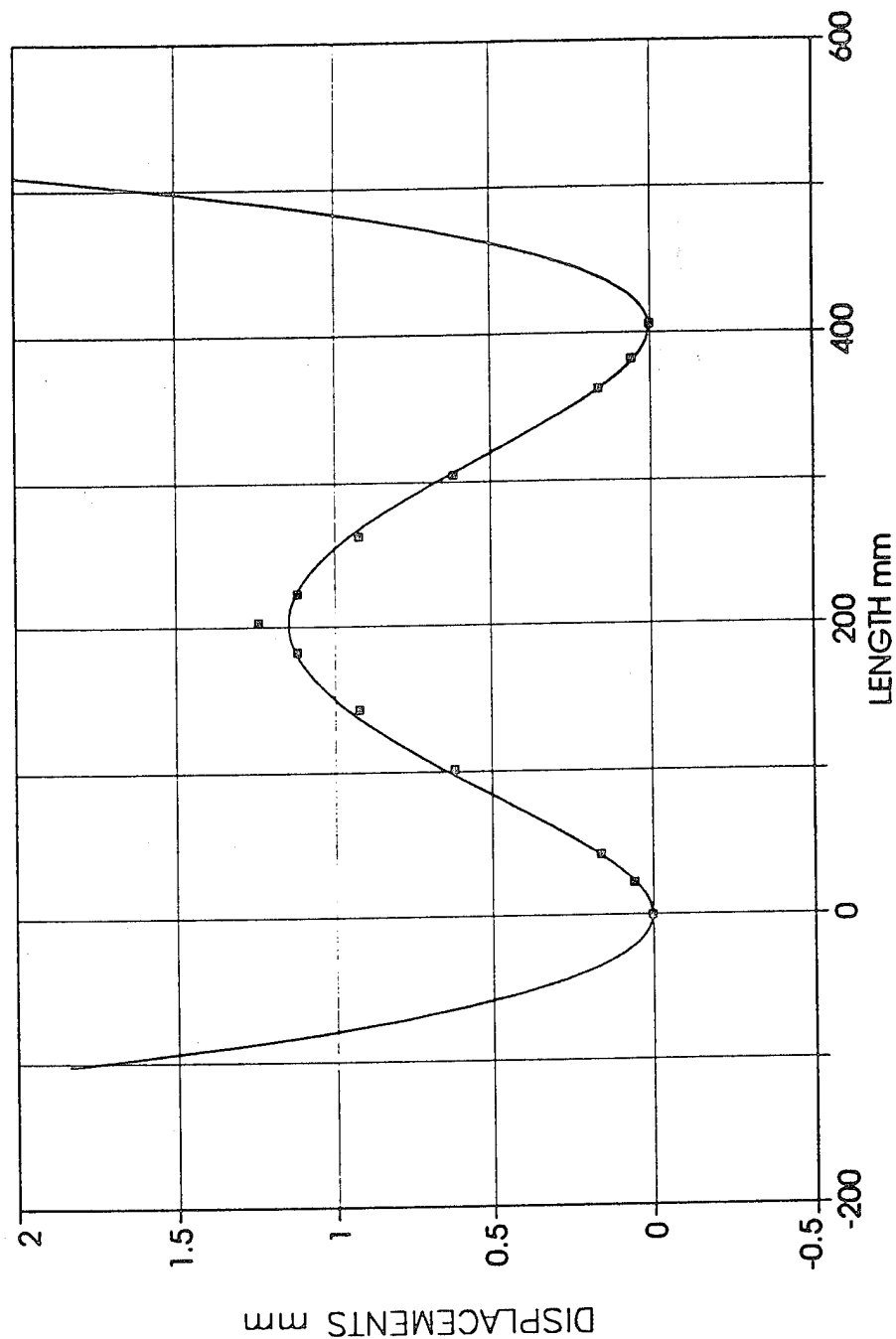


Fig 4.13 Rank 13 fourth order polynomial curve fit of displacement shape, 13.7 N static test, C-C aluminium beam.

C-C AL BEAM STATIC TESTS 0.25 N

Rank 20 Eqn 6001 $y=a+bx+cx^2+dx^3+ex^4$

$a=2.4095895e-09$ $b=2.6105293e-07$ $c=2.1472112e-06$

$d=1.066853e-07$ $e=1.3245813e-10$

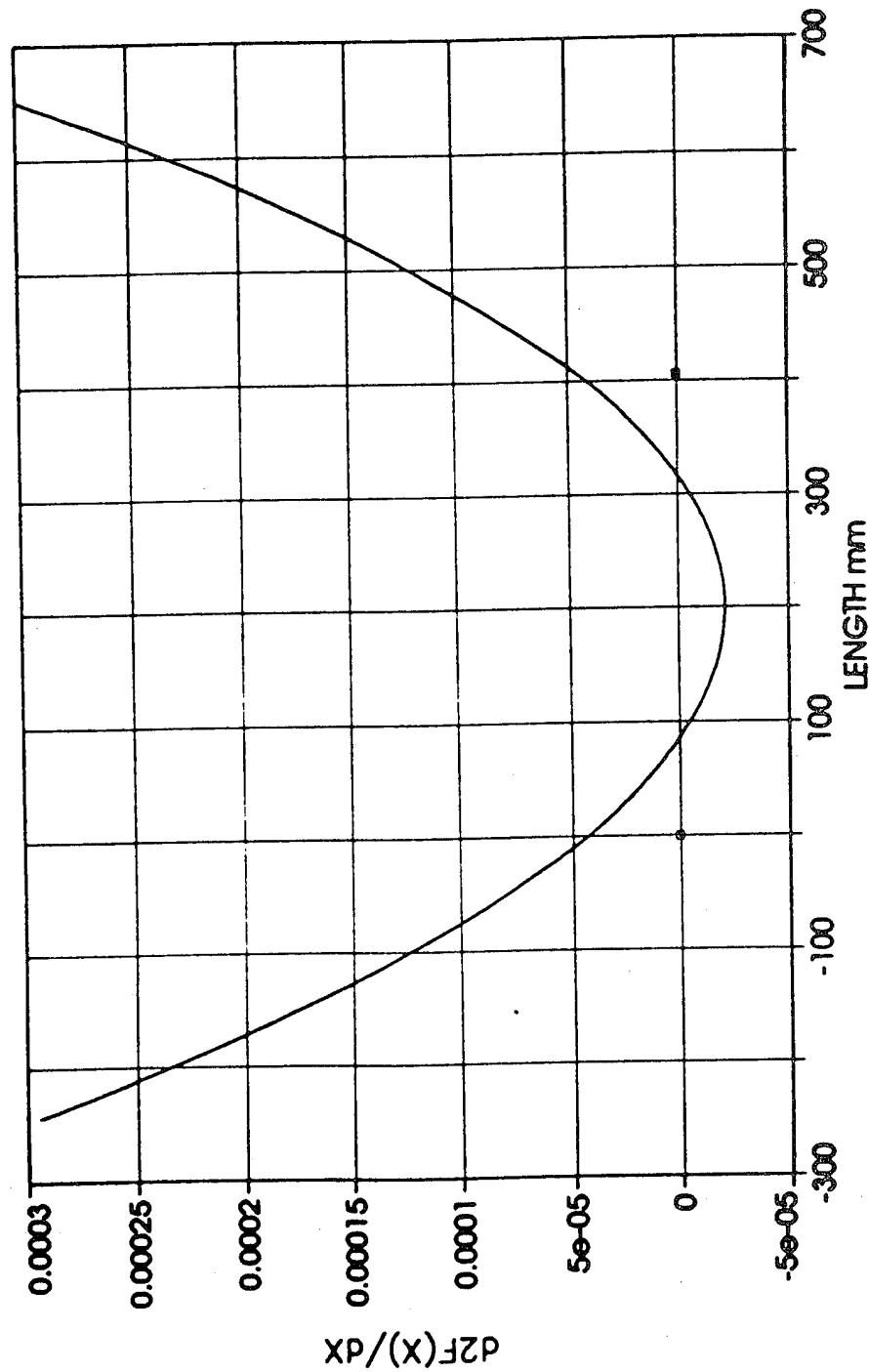


Fig 4.14 Second derivative of Fig 4.2, 2.5 N static test, C-C aluminium beam.

C-C AL BEAM STATIC TESTS- 0.25 N

RANK 15 Eqn 8001 $y=a[\cos(bx)-\cos(bx)-c(\sinh(bx)-\sinh(bx))]$

$a=0.13806736$ $b=0.011721075$

$c=0.98261627$

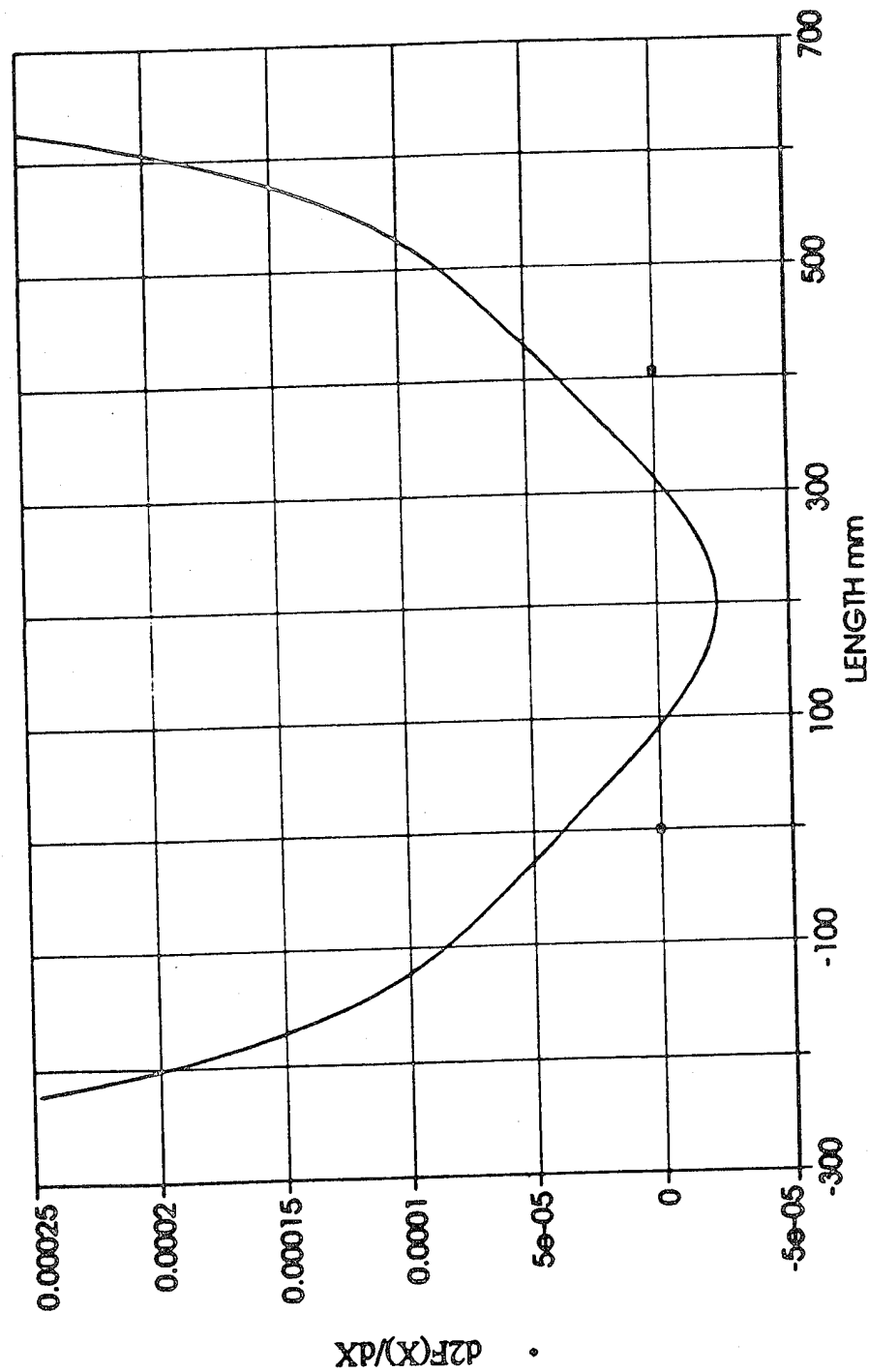


Fig 4.15 Second derivative of Fig 4.3, 2.5 N static test, C-C aluminium beam.

C-C AL BEAM STATIC TESTS- 2.5 Newtons

Rank 7 Eqn 8014 $y=a+b\sin(2\pi x/d+c)$ (Sine)

$a=0.11206426$ $b=0.11128491$

$c=4.6981946$ $d=404.2942$

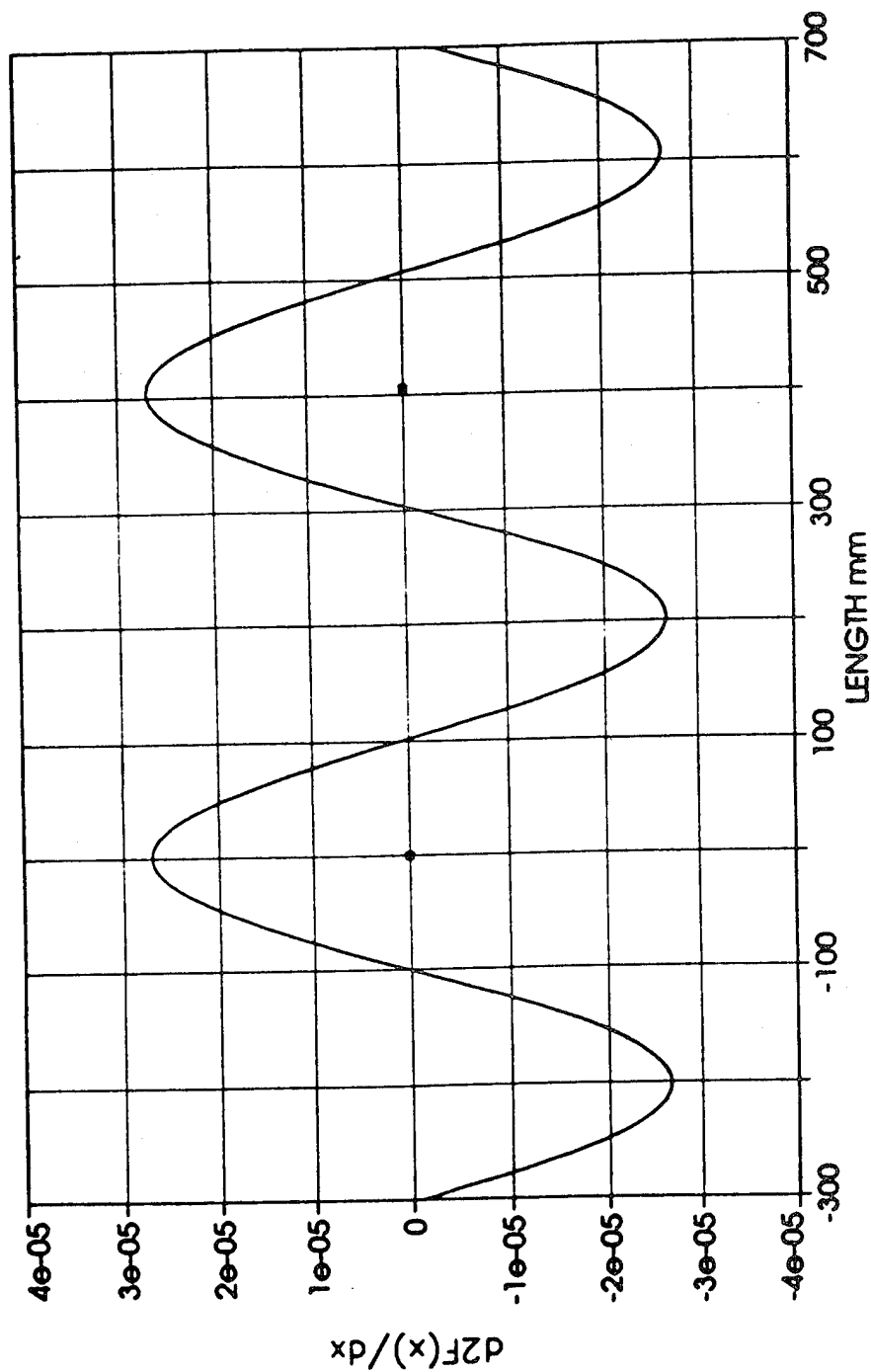


Fig 4.16 Second derivative of Fig 4.4, 2.5 N static test, C-C aluminium beam.

C-C AL BEAM STATIC TESTS- 2.5 Newtons

Rank 3 Eqn 8004 $y=a+b/(1+((x-c)/d)^2)$ (Lorentzian)

$a=0.10761974$ $b=0.33649817$

$c=203.01671$ $d=133.71386$

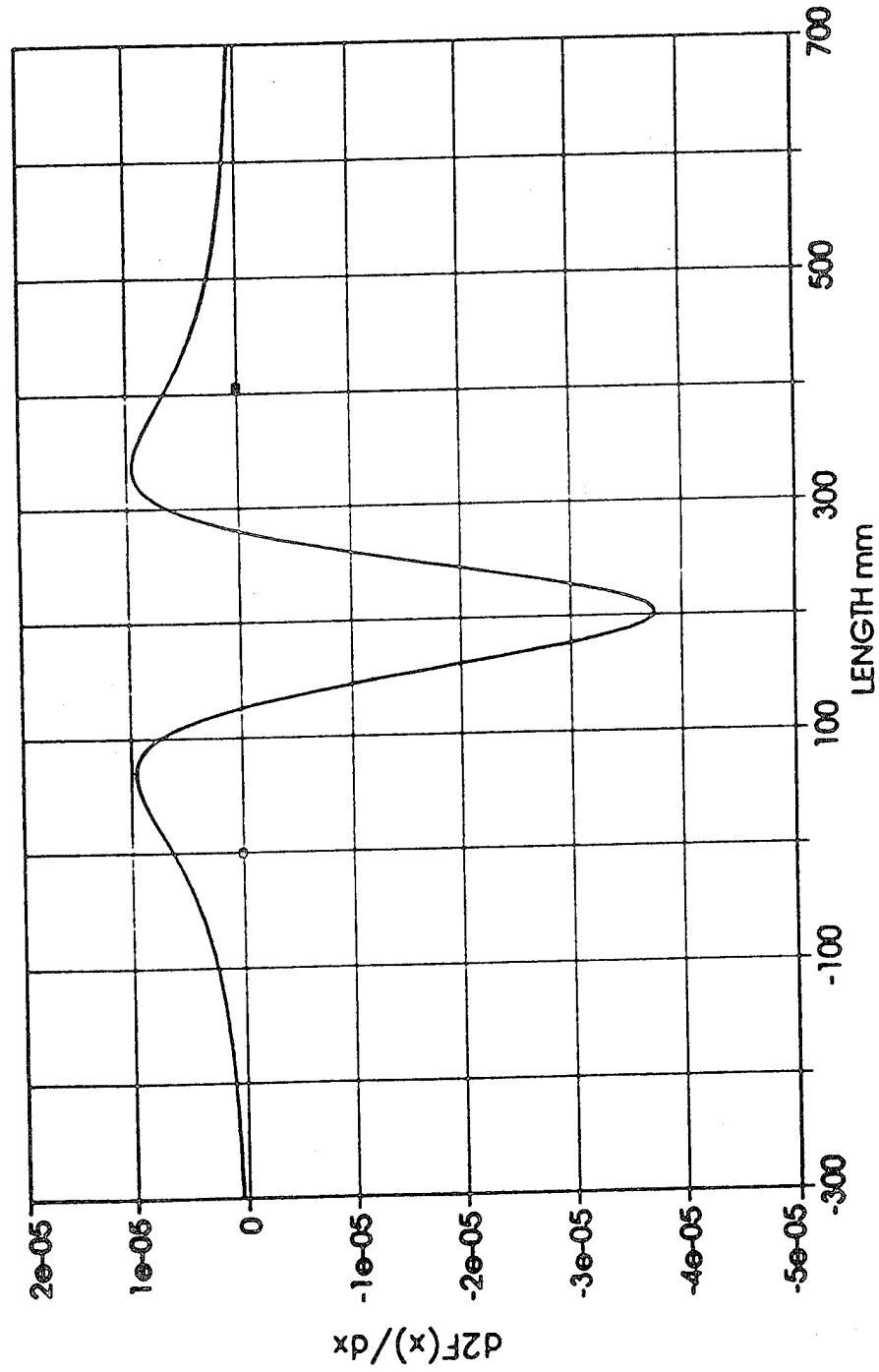


Fig 4.17 Second derivative of Fig 4.5, 2.5 N static test, C-C aluminium beam.

C-C AL BEAM STATIC TESTS- 2.5 Newtons

Rank 2 Eqn 8003 $y=a+b\exp(-0.5((x-c)/d)^2)$ (Gaussian)

$a=0.020629906$ $b=0.24700817$

$c=203.0417$ $d=88.363712$

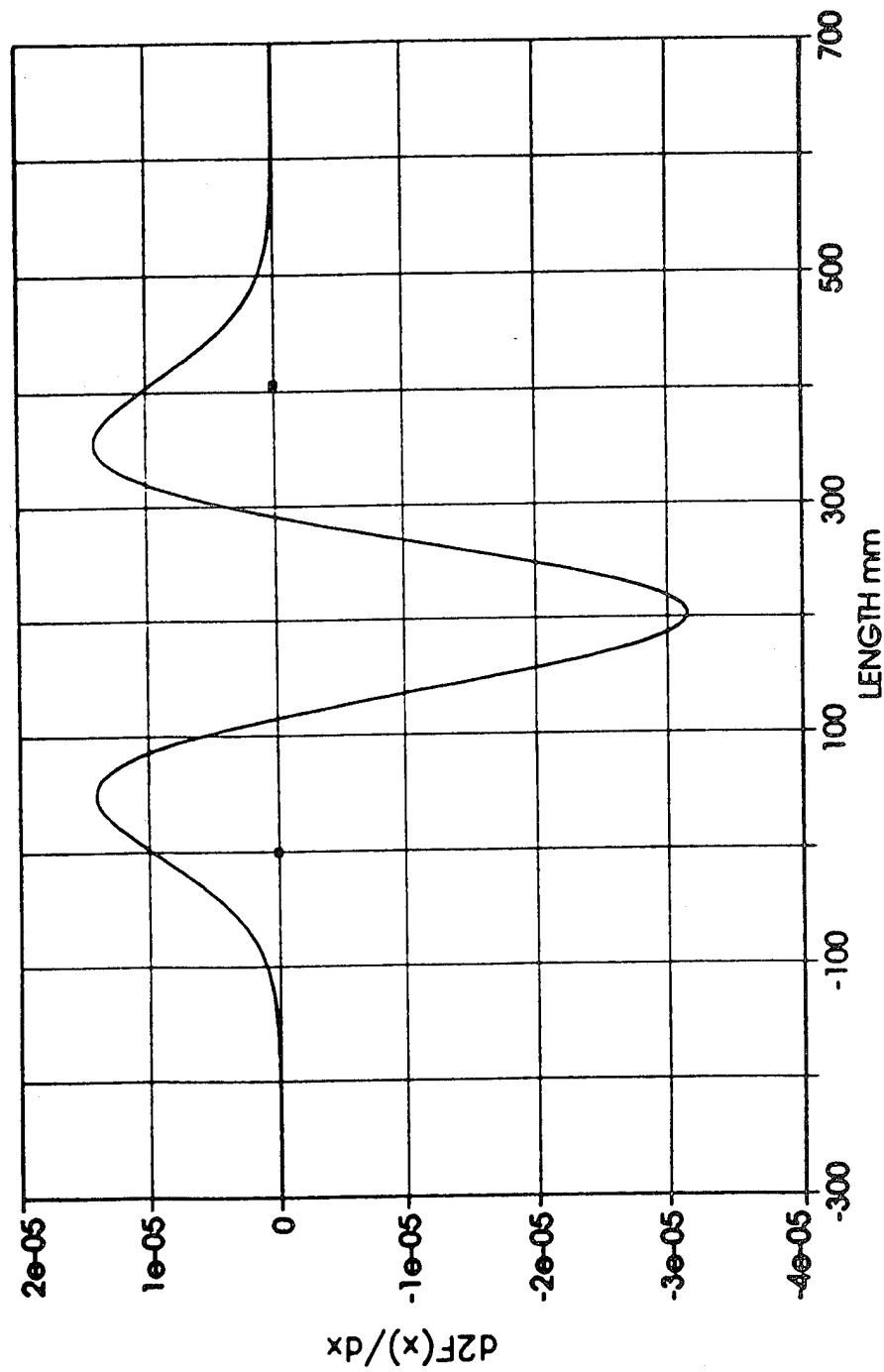


Fig 4.18 Second derivative of Fig 4.6, 2.5 N static test, C-C Aluminium beam.

C-C AL BEAM STATIC TESTS- 2.5 Newtons

Rank 1 Eqn 8007 $y=a+b \cdot 4n/(1+n)^2$ $n=\exp(-(x-c)/d)$ (Logistic)

$a=-0.044152943$ $b=0.27167634$

$c=203.02861$ $d=62.835049$

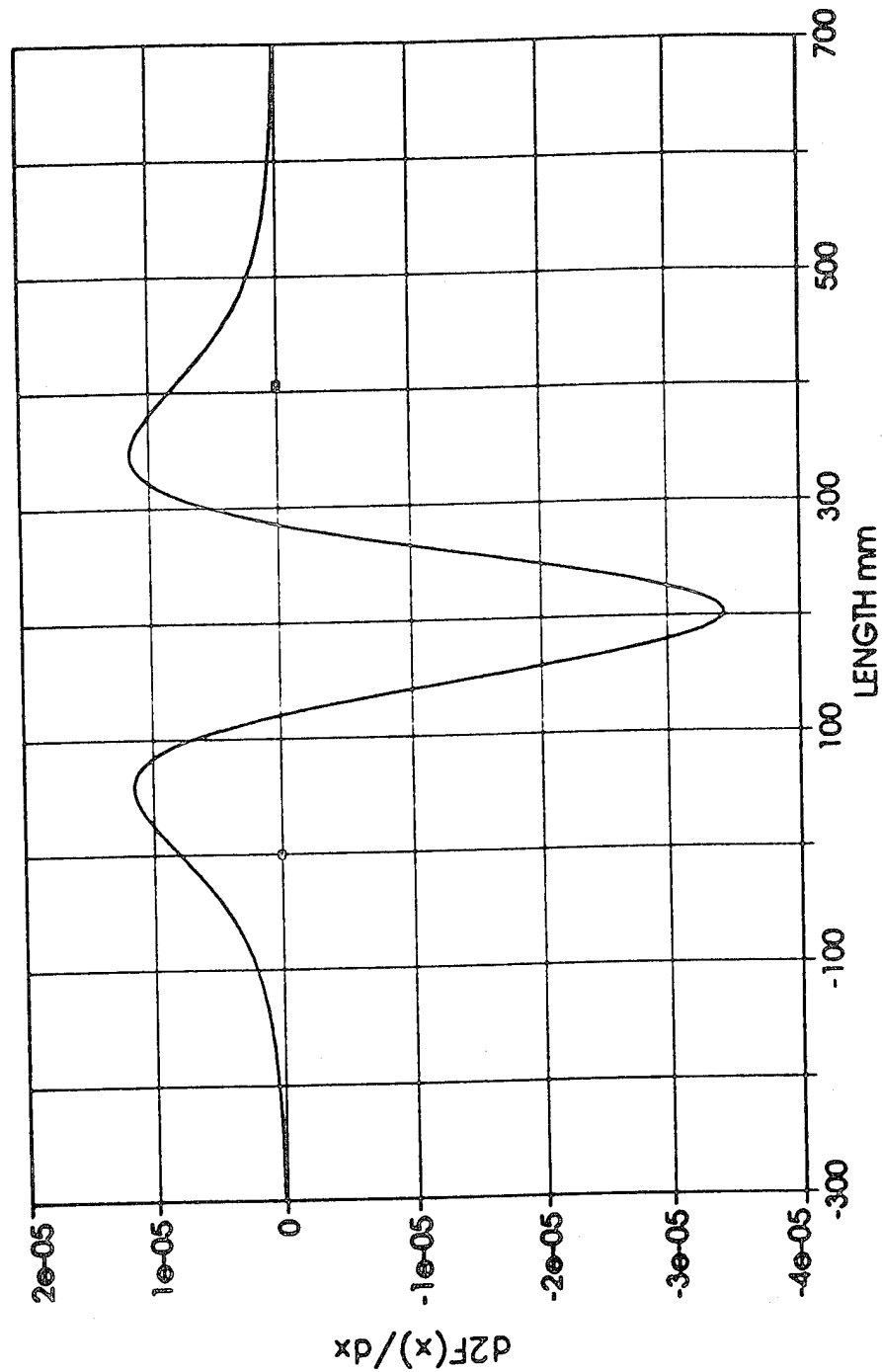


Fig 4.19 Second derivative of Fig 4.7, 2.5 N static test, C-C aluminium beam.

C-C AL BEAM STATIC TESTS-13.7N

Rank 1 Eqn 8003 $y=a+b\exp(-0.5(x-c)/d)^2$ (Gaussian)

a=-0.14027803 b=1.3173225

c=203.03098 d=93.887503

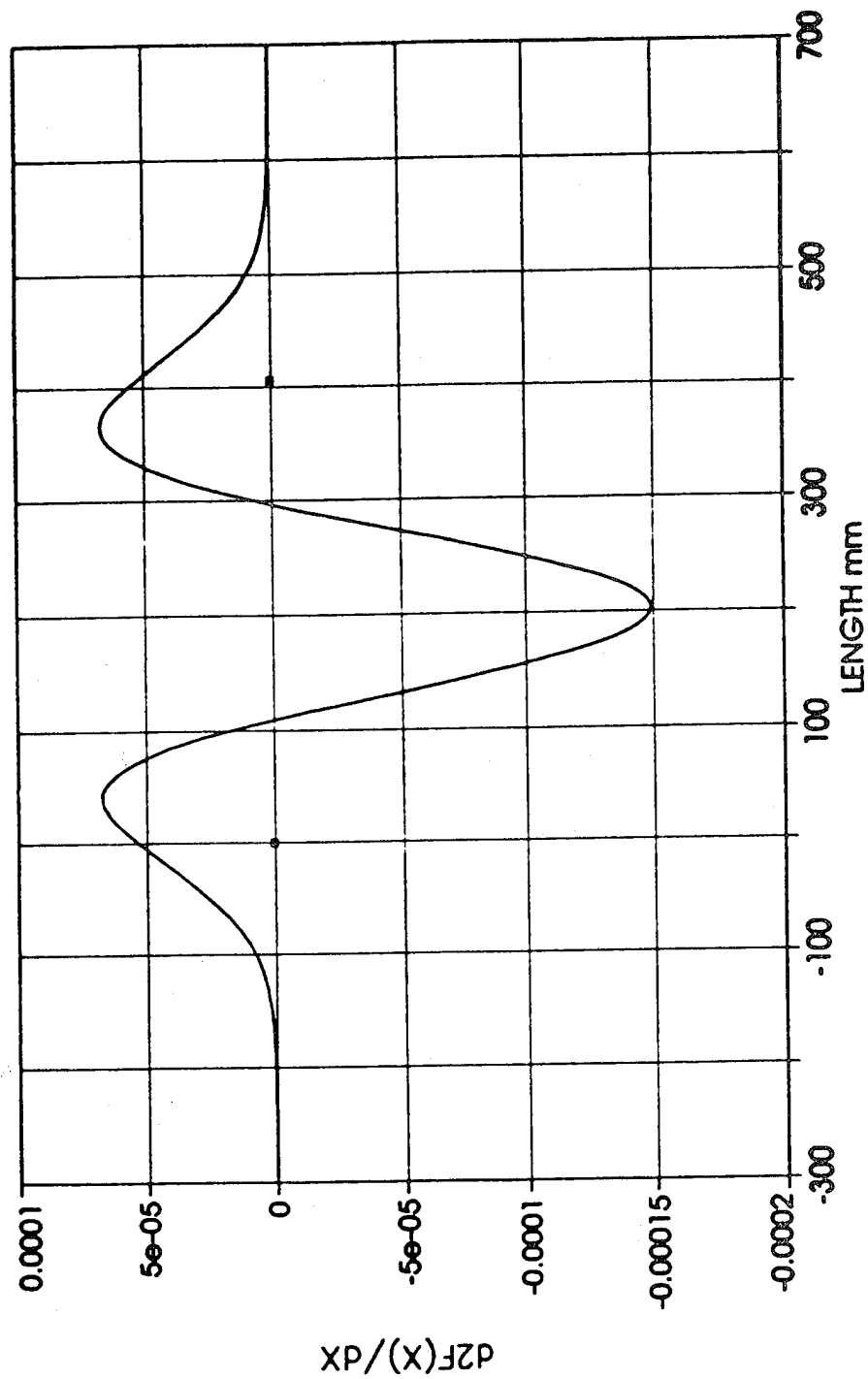


Fig 4.20 Second derivative of Fig 4.8, 13.7 N static test, C-C aluminium beam.

C-C AL BEAM STATIC TESTS-13.7N

Rank 2 Eqn 8014 $y=a+b\sin(2\pi x/d+c)$ (Sine)

$a=0.58362262$ $b=0.58199233$

$c=4.8009167$ $d=417.86598$

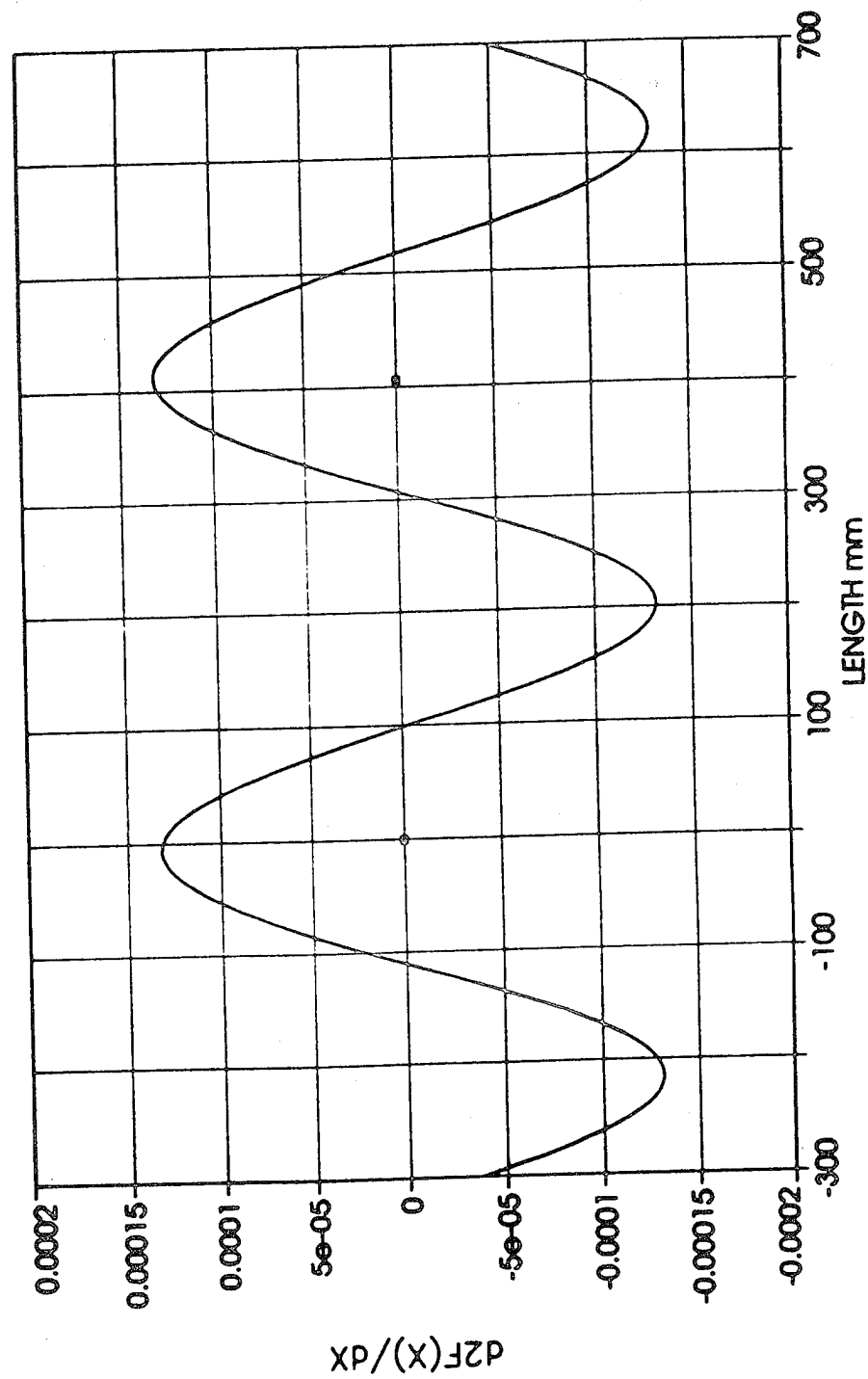


Fig 4.21 Second derivative of Fig 4.9, 13.7 N static test, C-C aluminium beam.

C-C AL BEAM STATIC TESTS-13.7N

Rank 5 Eqn 8007 $y=a+b \cdot 4n/(1+n)^2$ $n=\exp(-(x-c)/d)$ (Logistic)

$a=-0.28808977$ $b=1.4694655$

$c=203.02056$ $d=67.856723$

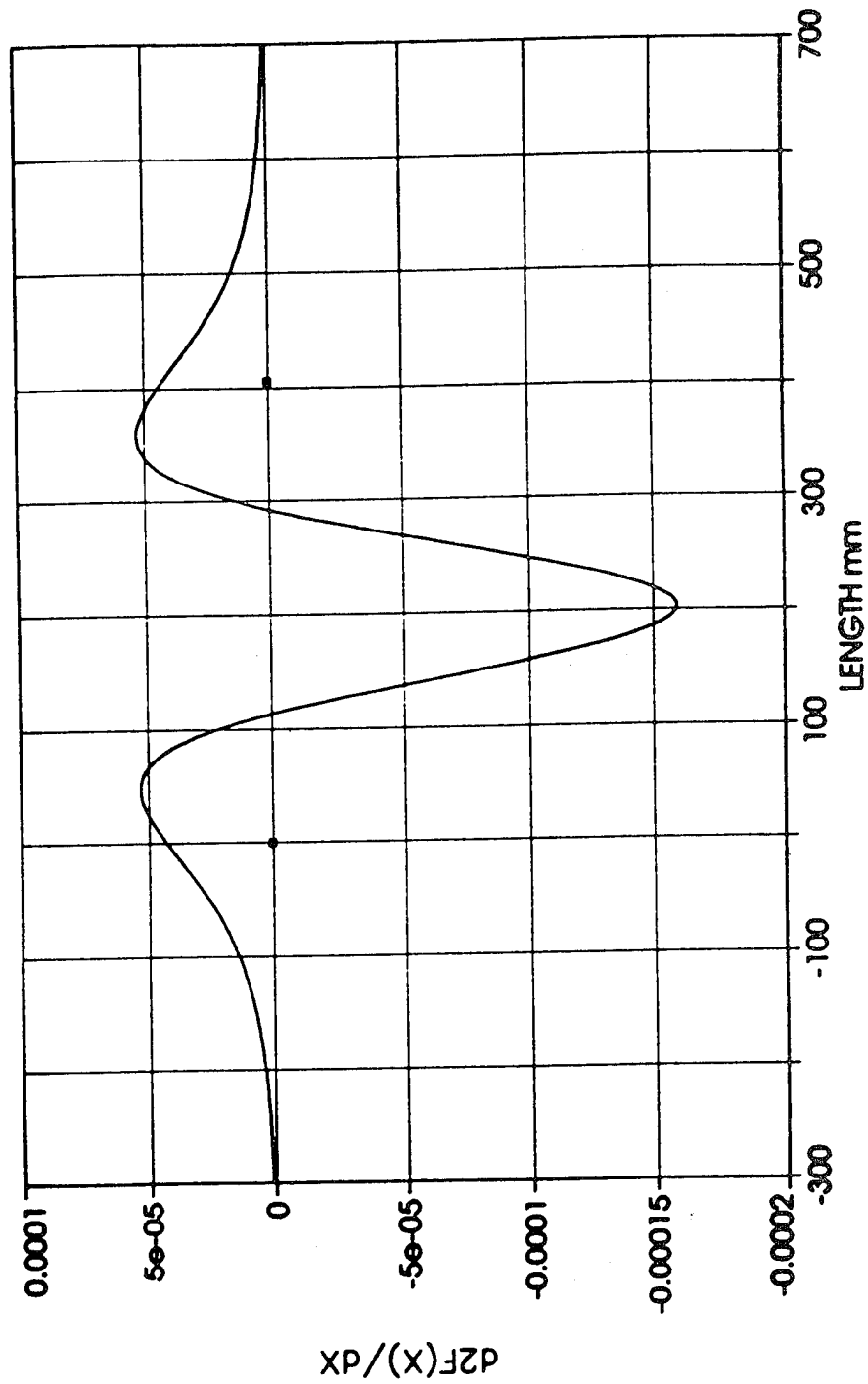


Fig 4.22 Second derivative of Fig 4.10, 13.7 N static test, C-C aluminium beam.

C-C AL BEAM STATIC TESTS-13.7N

Point 6 Eqn 8001 $y=a[\cos(bx)-\cos(bx)]-c[\sinh(bx)-\sinh(bx)]$

$a=0.72697339$ $b=0.01167254$

$c=0.98237449$

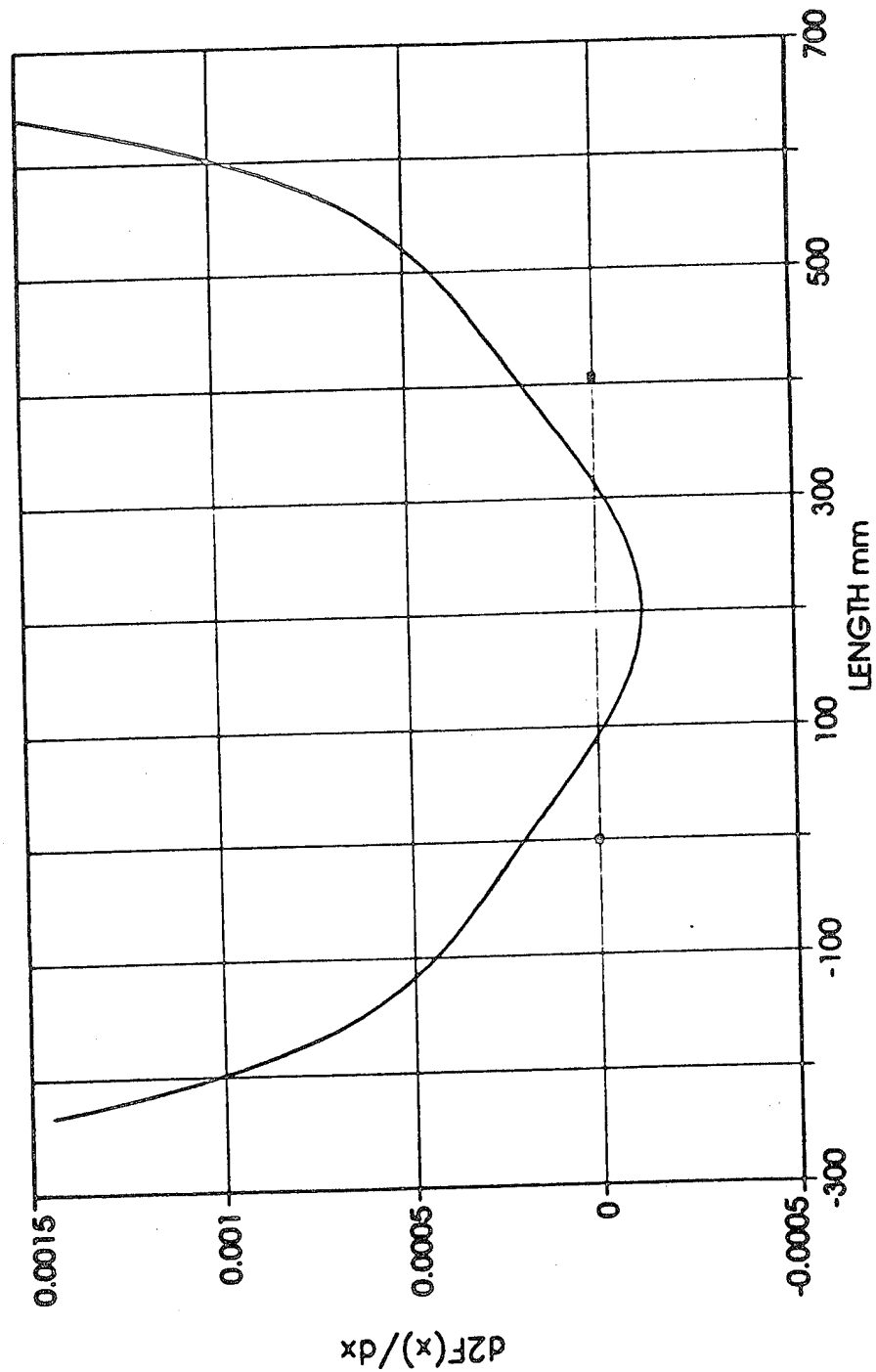


Fig 4.23 Second derivative of Fig 4.11, 13.7 N static test, C-C aluminium beam.

C-C AL BEAM STATIC TESTS-13.7N

Rank 7 Eqn 8004 $y=a+b/(1+((x-c)/d)^2)$ (Lorentzlon)

$a=0.66777439$ $b=1.8527896$

$c=203.01104$ $d=147.50618$

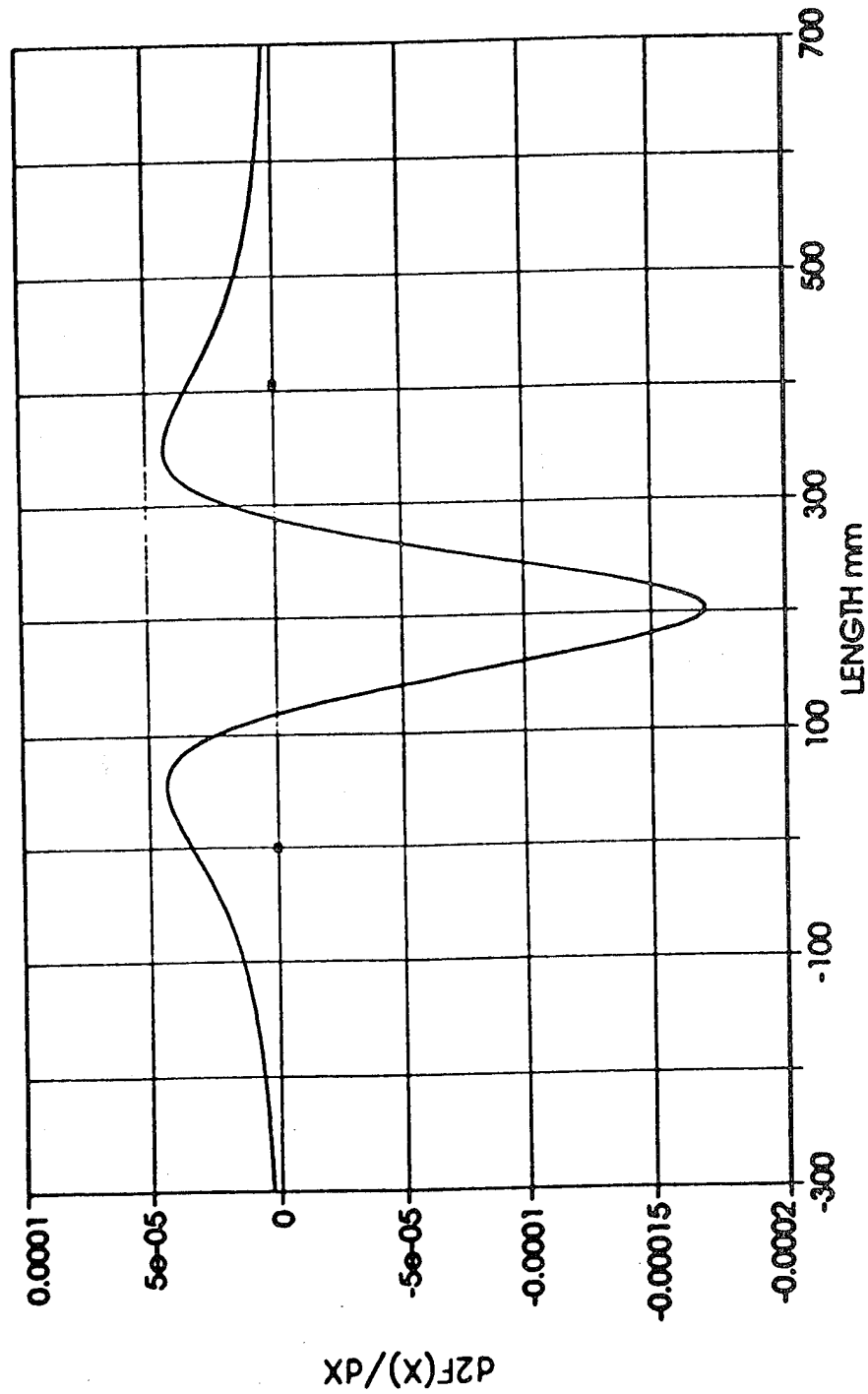


Fig 4.24 Second derivative of Fig 4.12, 13.7 N static test, C-C aluminium beam.

C-C AL BEAM STATIC TESTS-13.7N

Rank 13 Eqn 6001 $y=a+bx+cx^2+dx^3+ex^4$

$a=1.2589504e-08$ $b=1.3639365e-06$ $c=0.00011216444$

$d=-5.5516275e-07$ $e=-0.848641e-10$

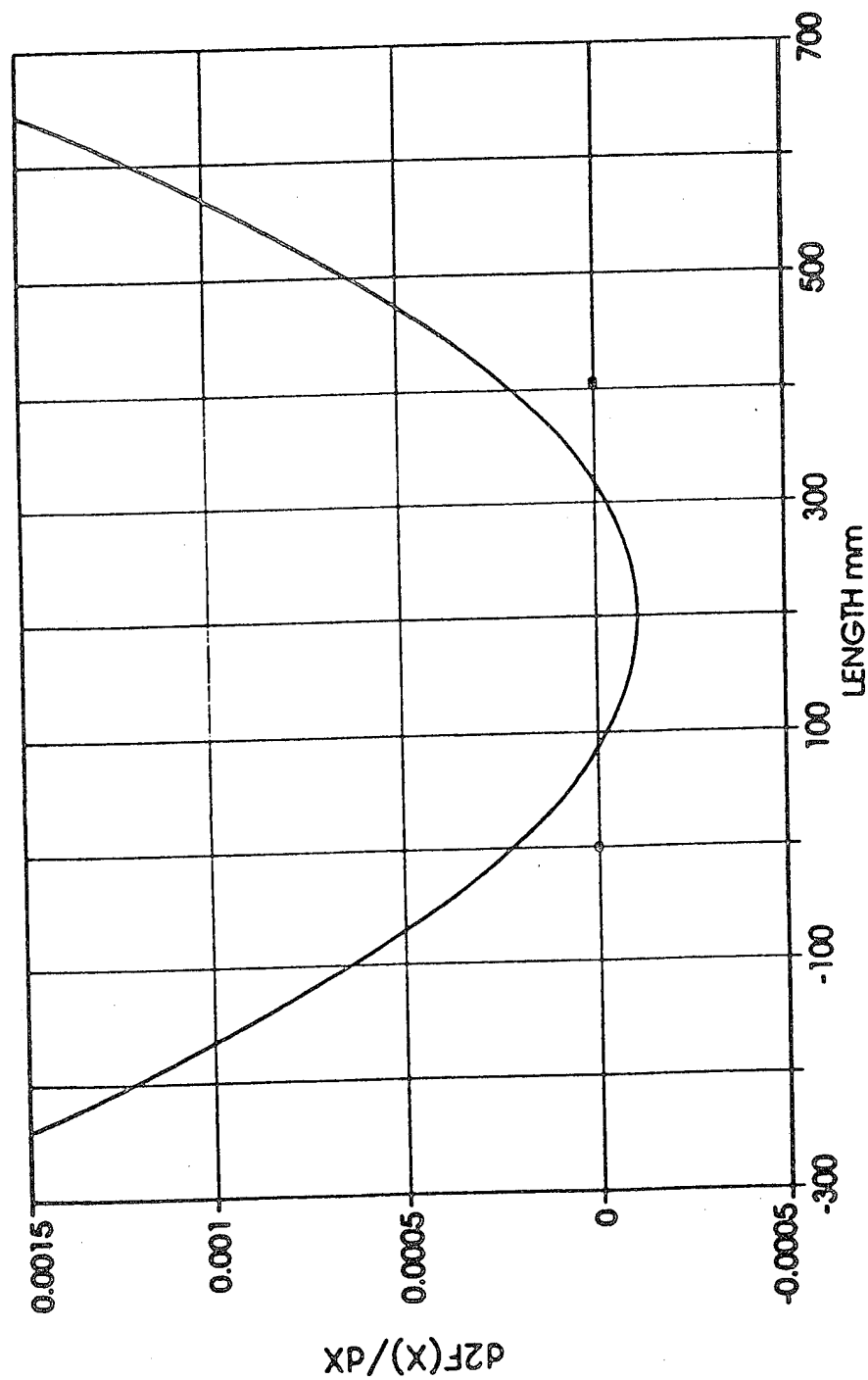


Fig 4.25 Second derivative of Fig 4.13, 13.7 N static test, C-C aluminium beam.

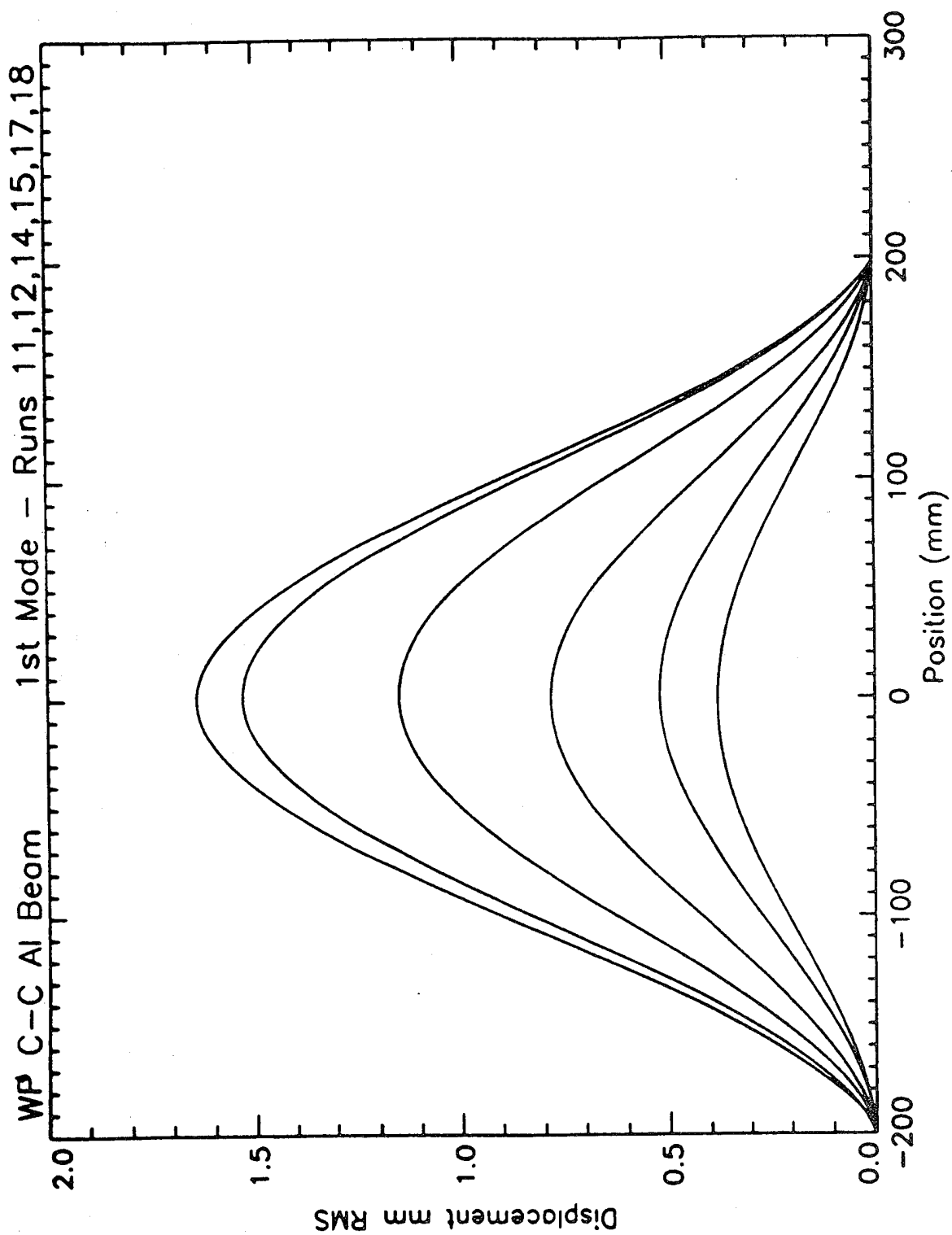


Fig 4.26 Seventh order polynomial fit of displacement shapes, sine excitation, C-C Aluminium beam.

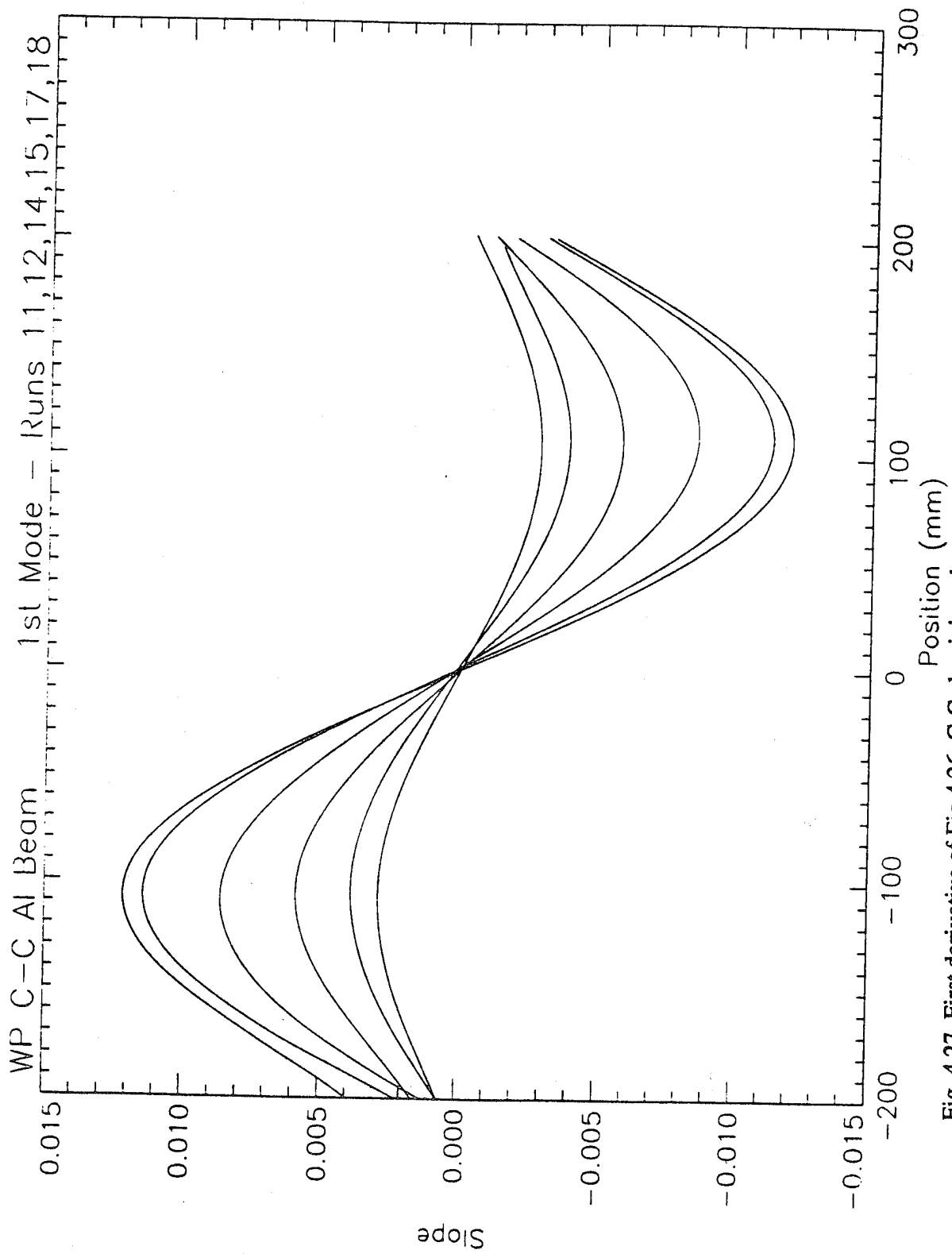


Fig 4.27 First derivative of Fig 4.26, C-C aluminium beam.

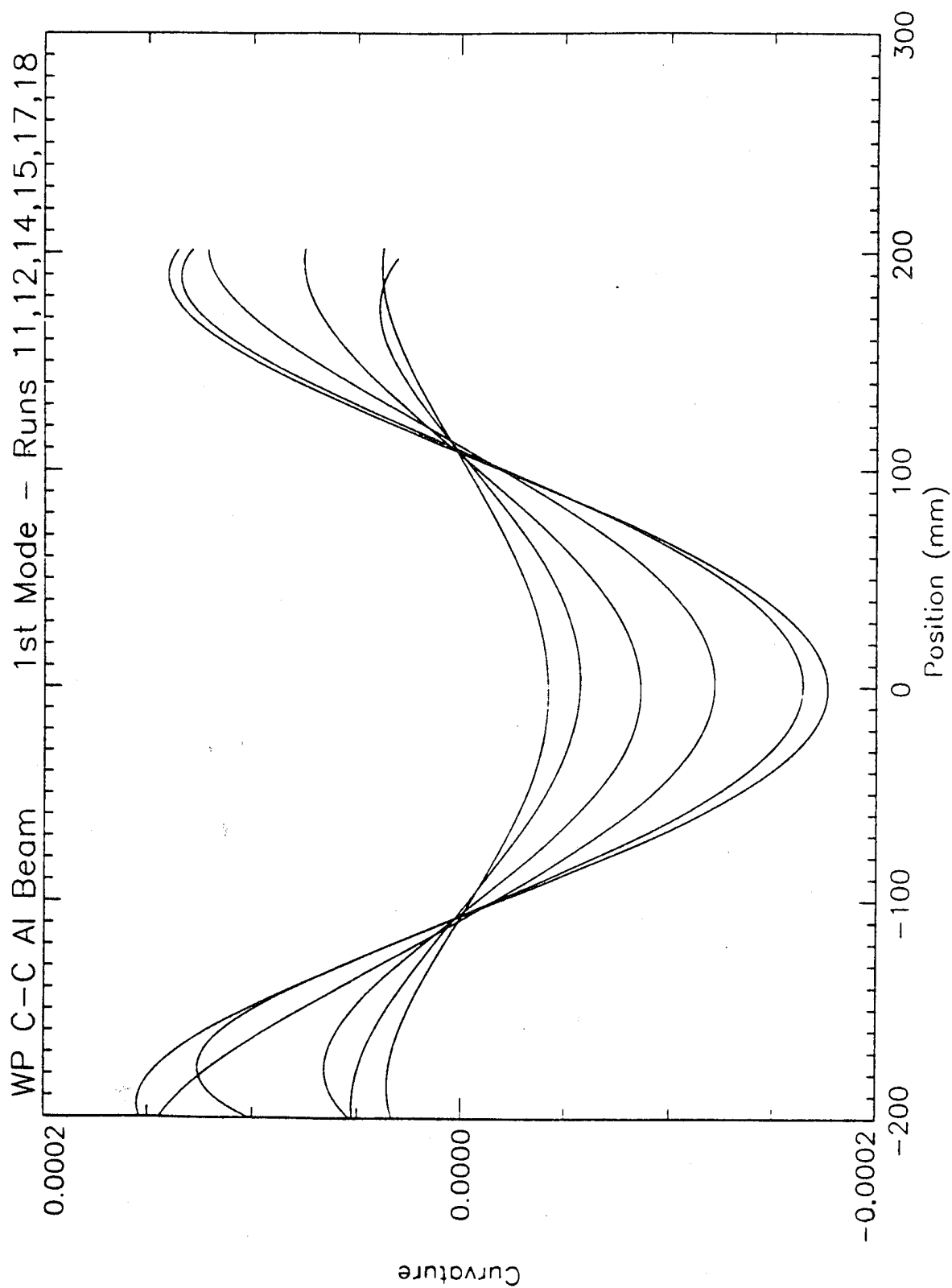


Fig 4.28 Second derivative of Fig 4.26, C-C aluminium beam.

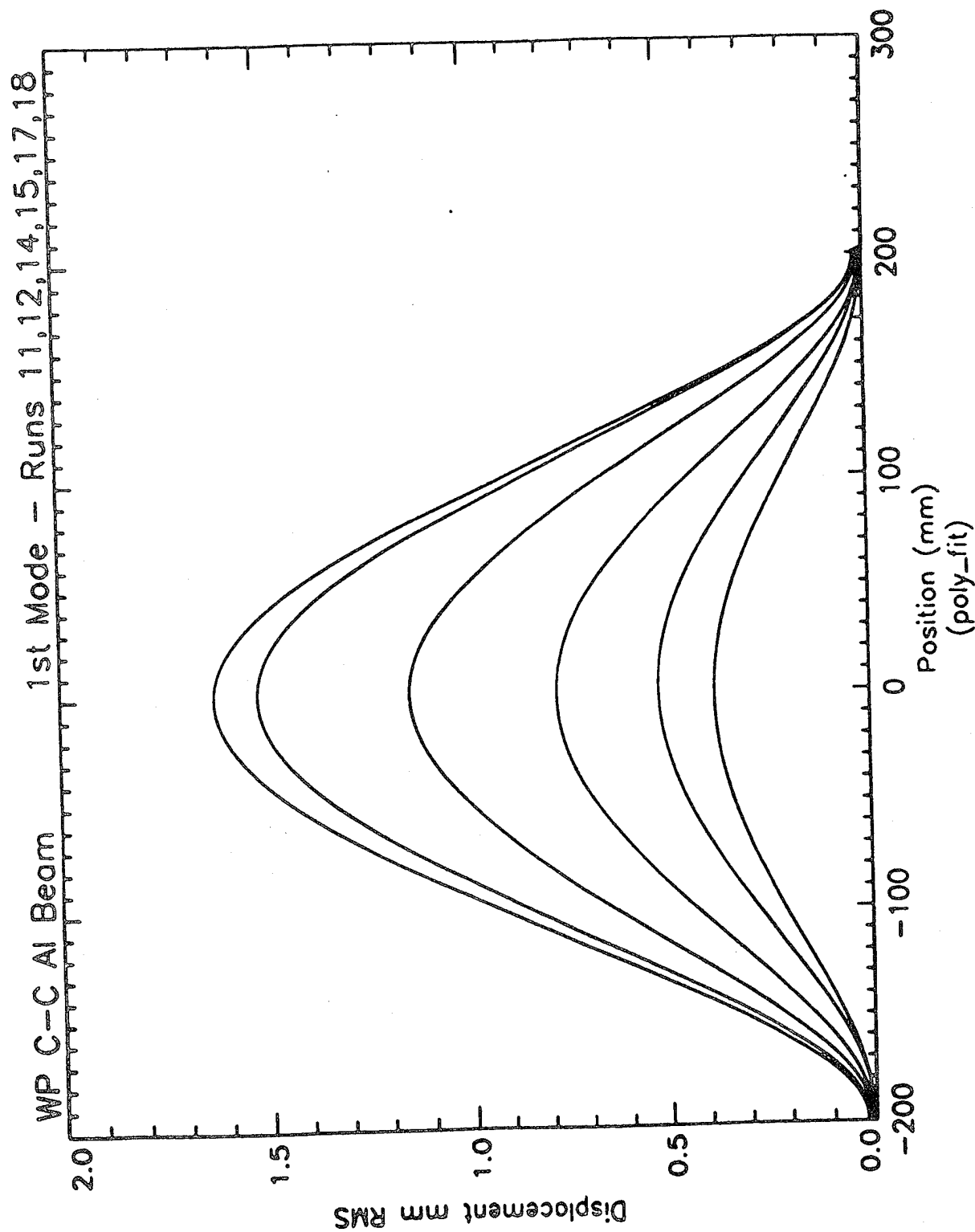


Fig 4.29 Fourth order of polynomial fit of displacement shapes, sine excitation, C-C aluminium beam.

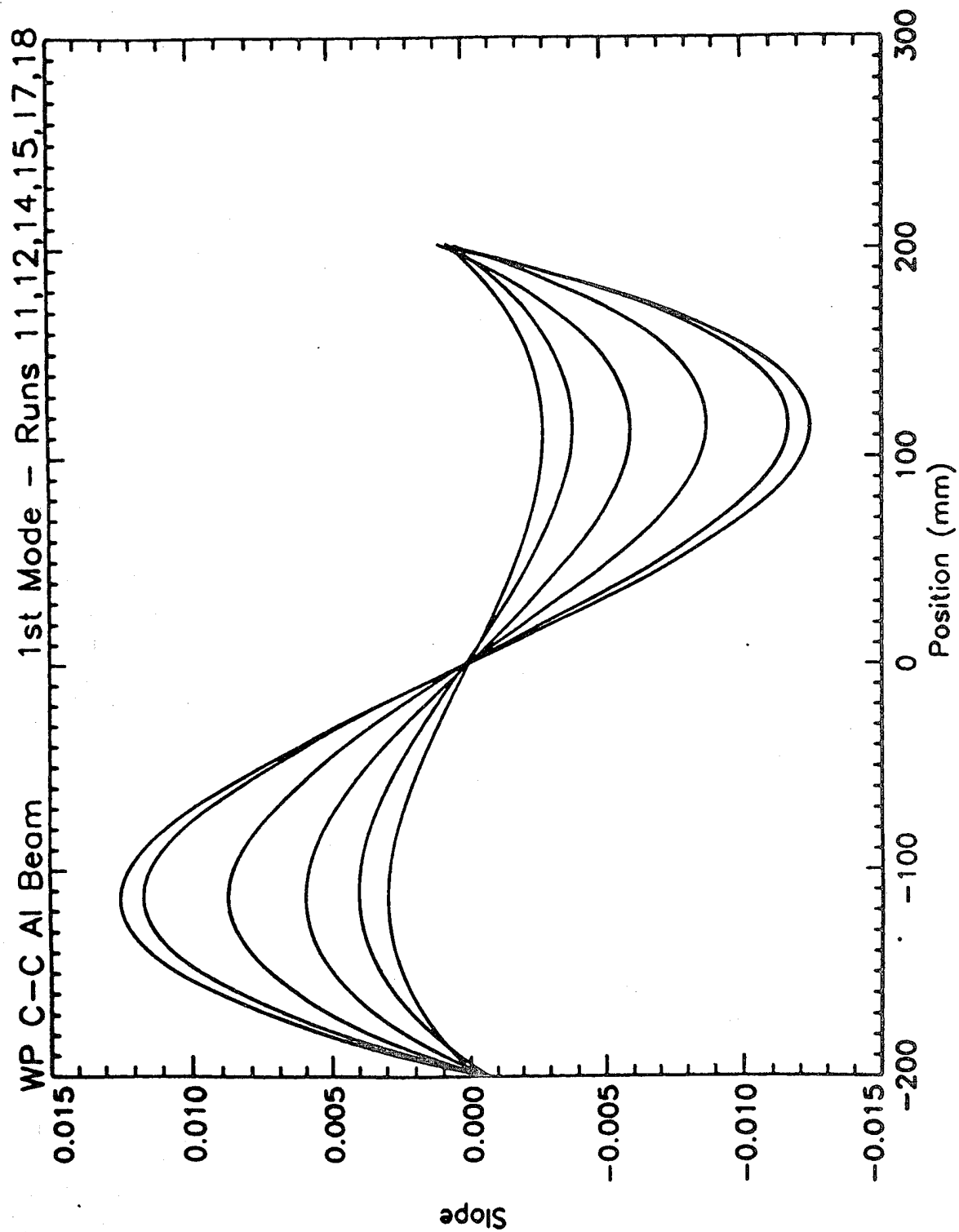


Fig 4.30 First derivative of Fig 4.30, C-C aluminium beam.

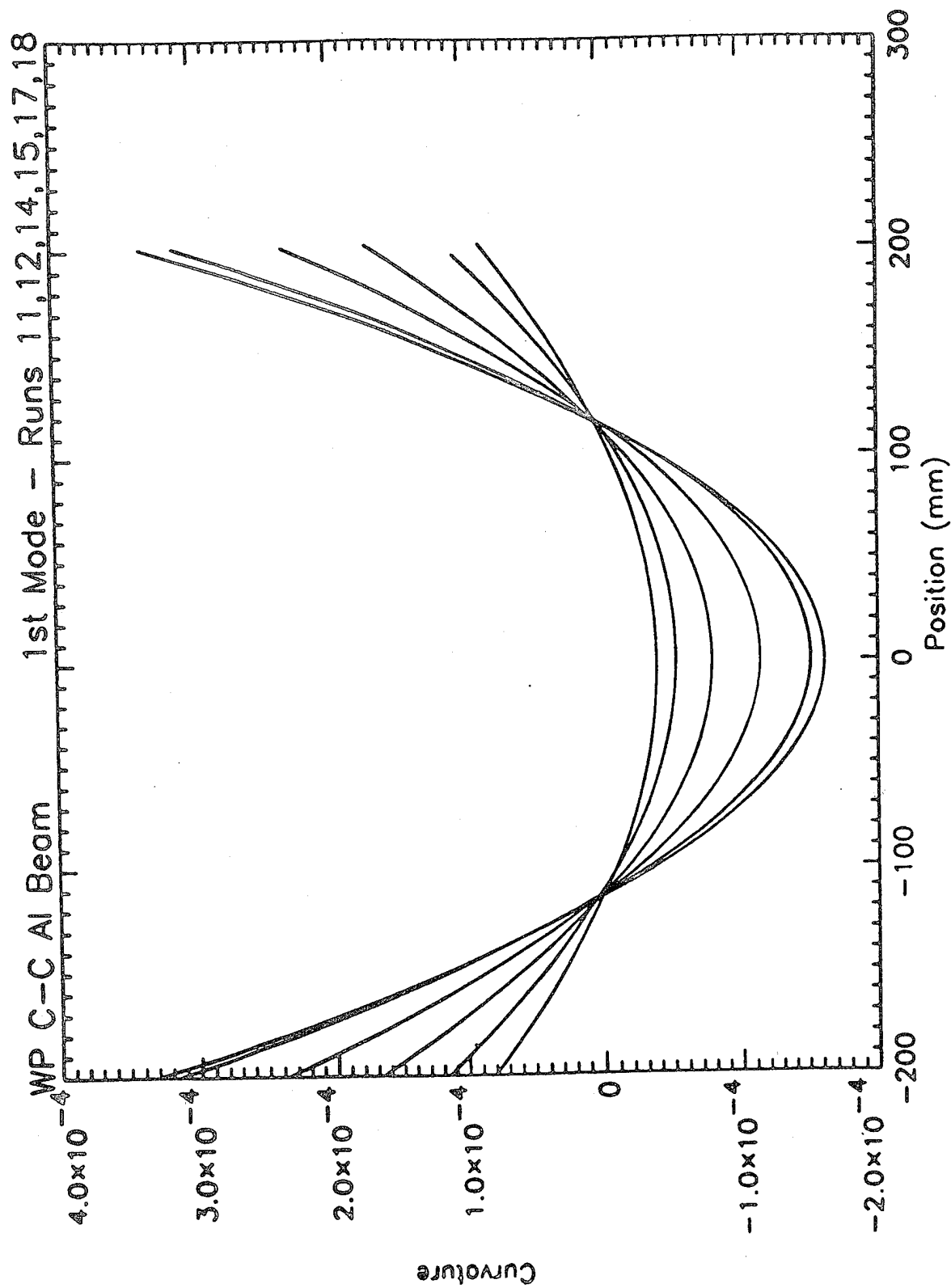


Fig 4.31 Second derivative of Fig 4.30, C-C aluminium beam.

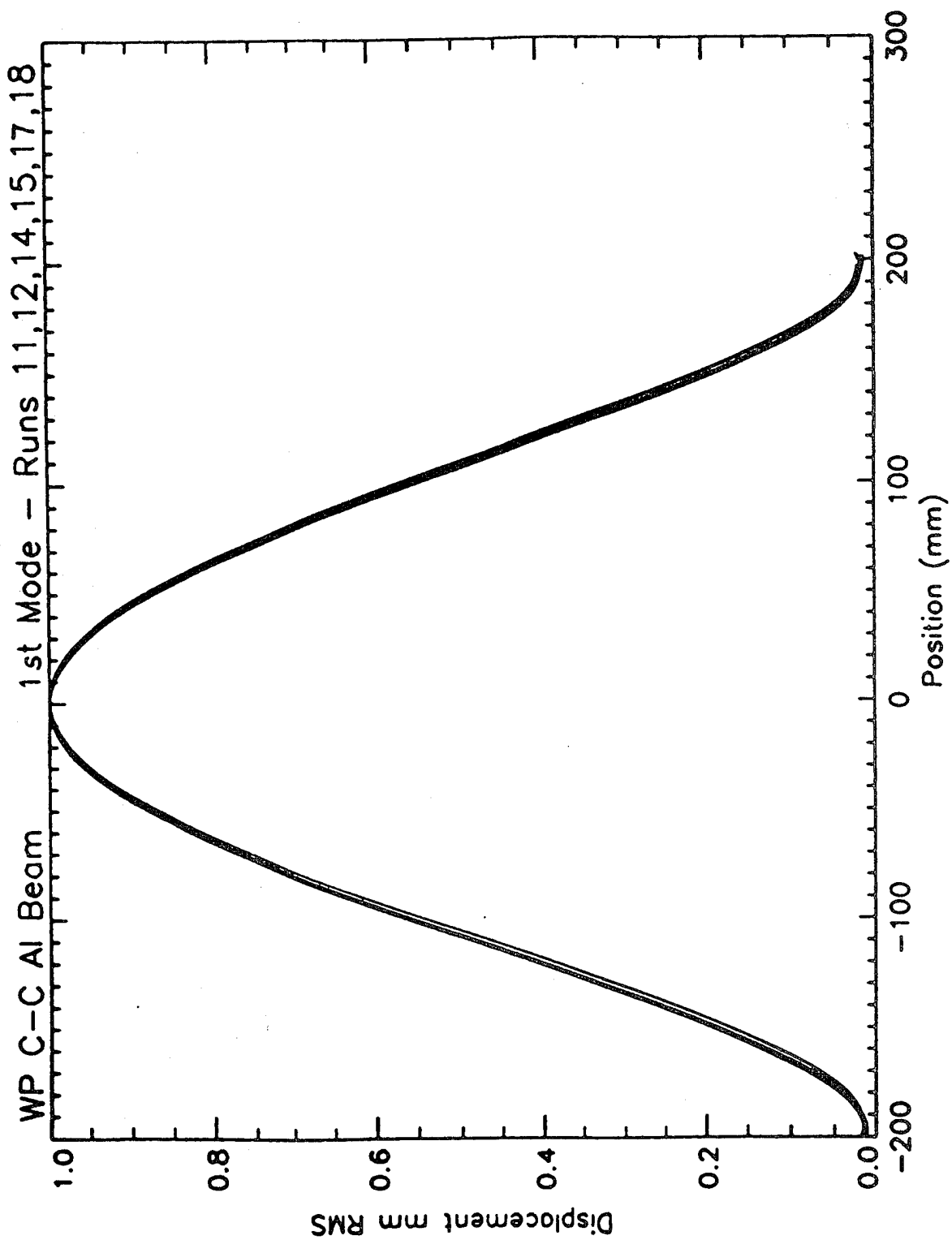


Fig 4.32 Normalised displacement shapes from Fig 4.29, C-C aluminium beam.

C-C AL BEAM R 1st 11h

Rank 1 Eqn 8014 $y=a+b\sin(2\pi x/d+c)$ (Sine)

$r^2=0.999865283$ DF Adj $r^2=0.999853309$ FMSideIn=0.00161638849 FMSide=113803.79

$a=0.18708723$ $b=0.19172892$

$c=4.8198187$ $d=420.02815$

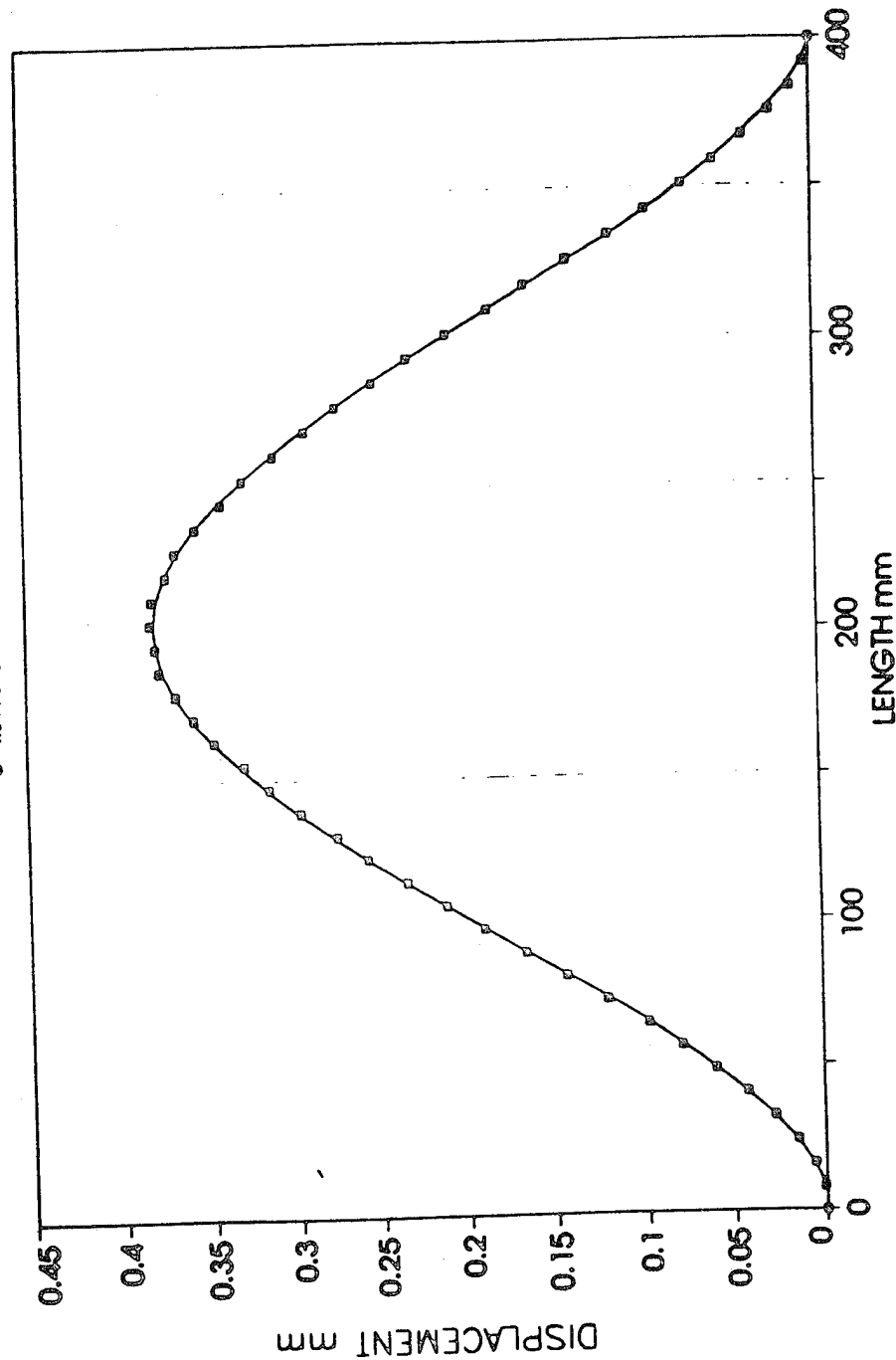


Fig 4.33 Rank 1, sine curve fit of 0.086N sine excitation, C-C aluminium beam.

C-C AL BEAM R 1st11h

Rank 2 Eqn 8015 $y=a+b\sin^2(2\pi x/d+c)$ (Sine²)

$r^2=0.999665283$ Df Adj $r^2=0.999653309$ FHSide $m=0.00161538869$ Fstch $=113803.79$

$a=0.0046416899$ $b=0.38345783$

$c=3.1953076$ $d=840.0663$

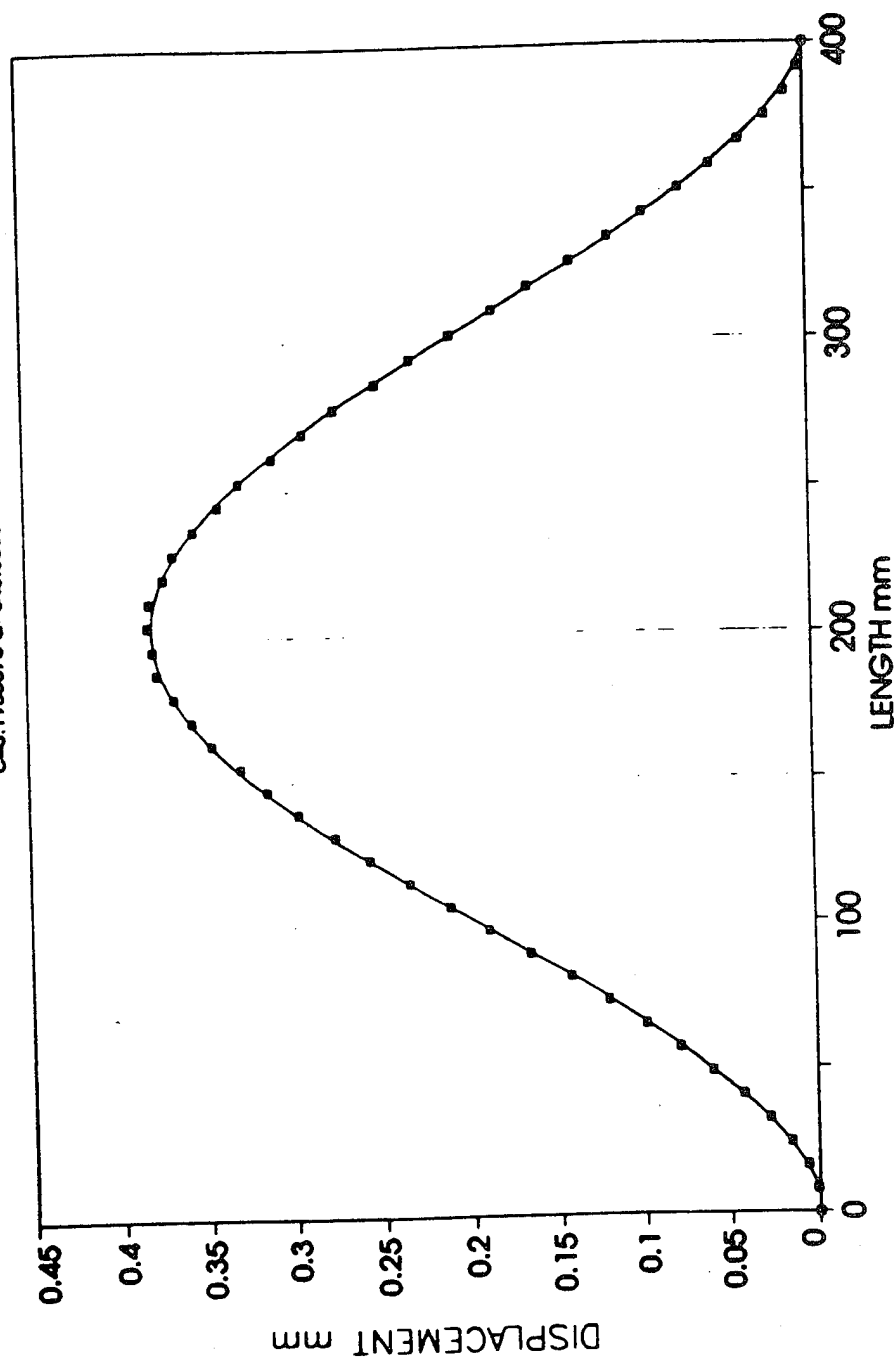


Fig 4.34 Rank 2, sine squared fit of 0.086N sine excitation, C-C aluminium beam.

C-C AL BEAM R 1st11h

Rank 5 Eqn 8009 $y=4thpolyfit0$

$r^2=0.999419989$ DF Adj $r^2=0.999354079$ F1StdErr=0.0033888675 Fstat=12384.9416

$a=0.0053915115$ $b=-0.00065707105$ $c=4.4073816e-05$

$d=-2.093421e-07$ $e=2.580811e-10$

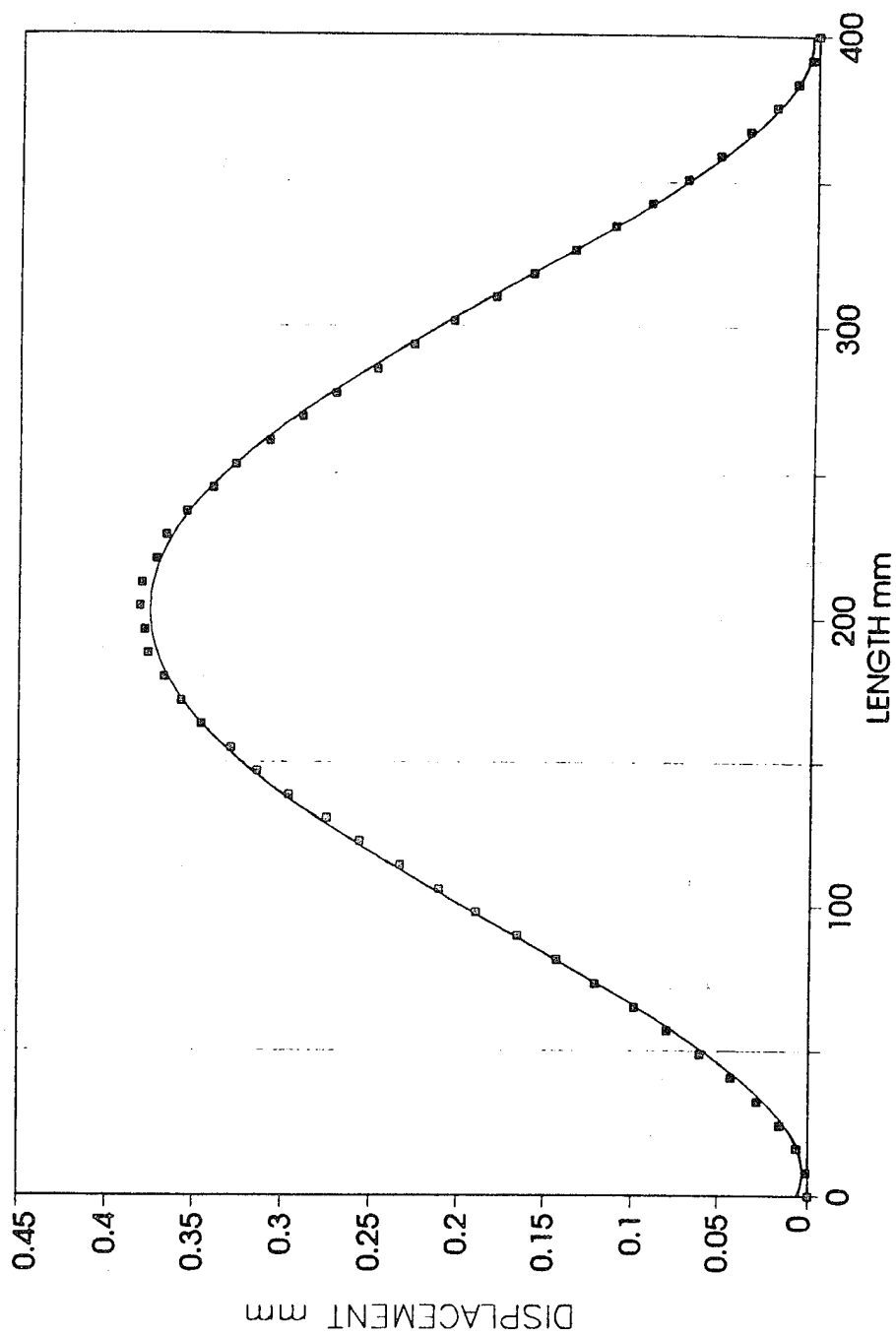


Fig 4.35 Rank 5, fourth order polynomial fit of 0.086N sine excitation, C-C aluminium beam.

C-C AL BEAM R 1st11h

Rank 8 Eqn 8001 $y=fcosh(x)$

$r^2=0.99922265$ Df Adj $r^2=0.999171543$ Fitted $r^2=0.00383983257$ Fitted $r^2=0.01924322$

$a=0.23564298$ $b=0.011675587$

$c=0.98279647$

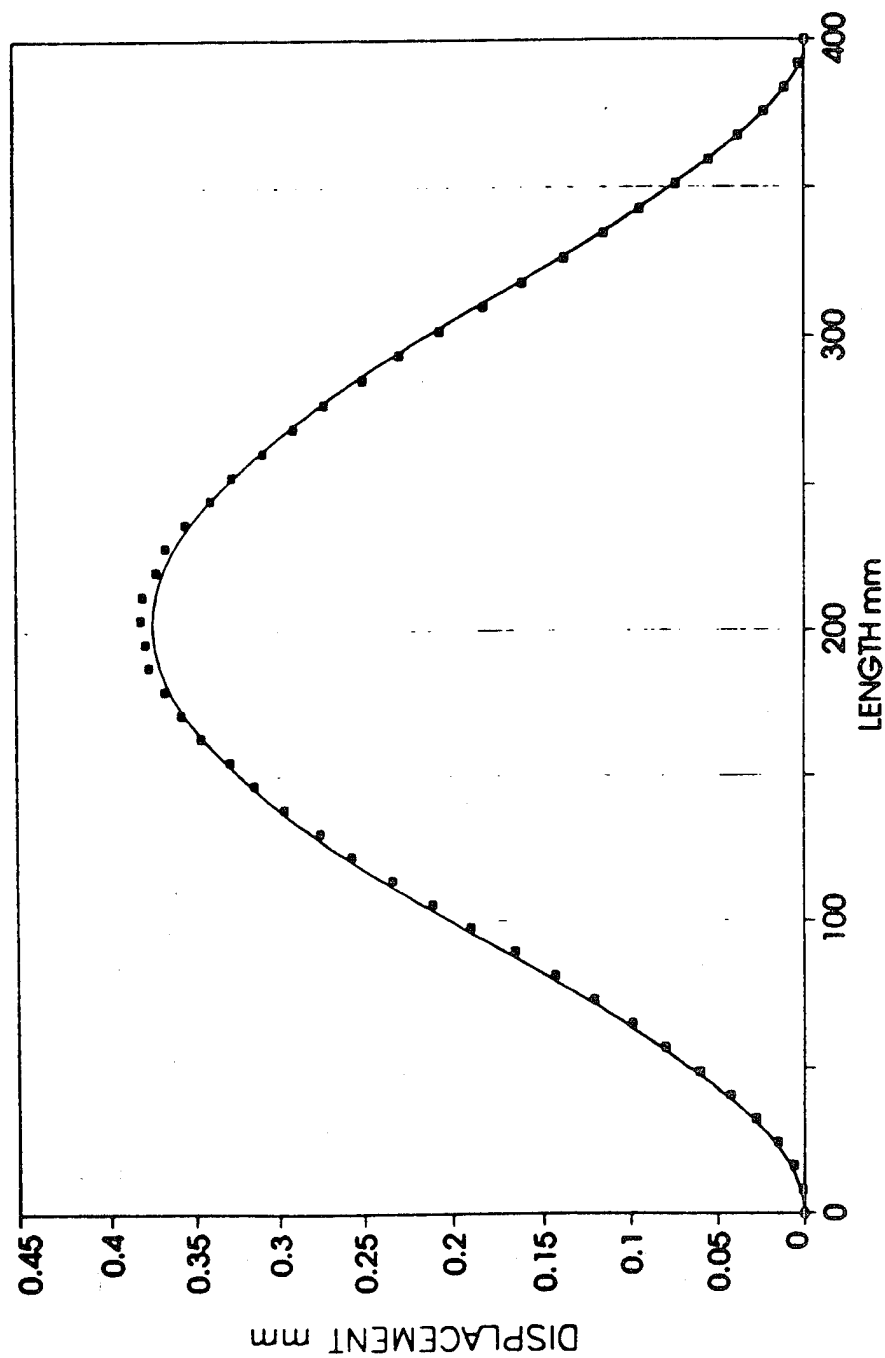


Fig 4.36 Rank 8, classical fit of 0.086N sine excitation, C-C aluminium beam.

C-C AL BEAM R 1st18h

Rank 1 $y = a + bx + cx^2 + dx^3 + ex^4$
 $r^2=0.999750037$ Df Adj $r^2=0.999741688$ FHSIdE $\pi=0.000442521621$ Fst $\sigma=77472.3928$
 $a=9.070052e-07$ $b=-0.002356989$ $c=0.00018967721$
 $d=-9.0597934e-07$ $e=1.1225435e-09$

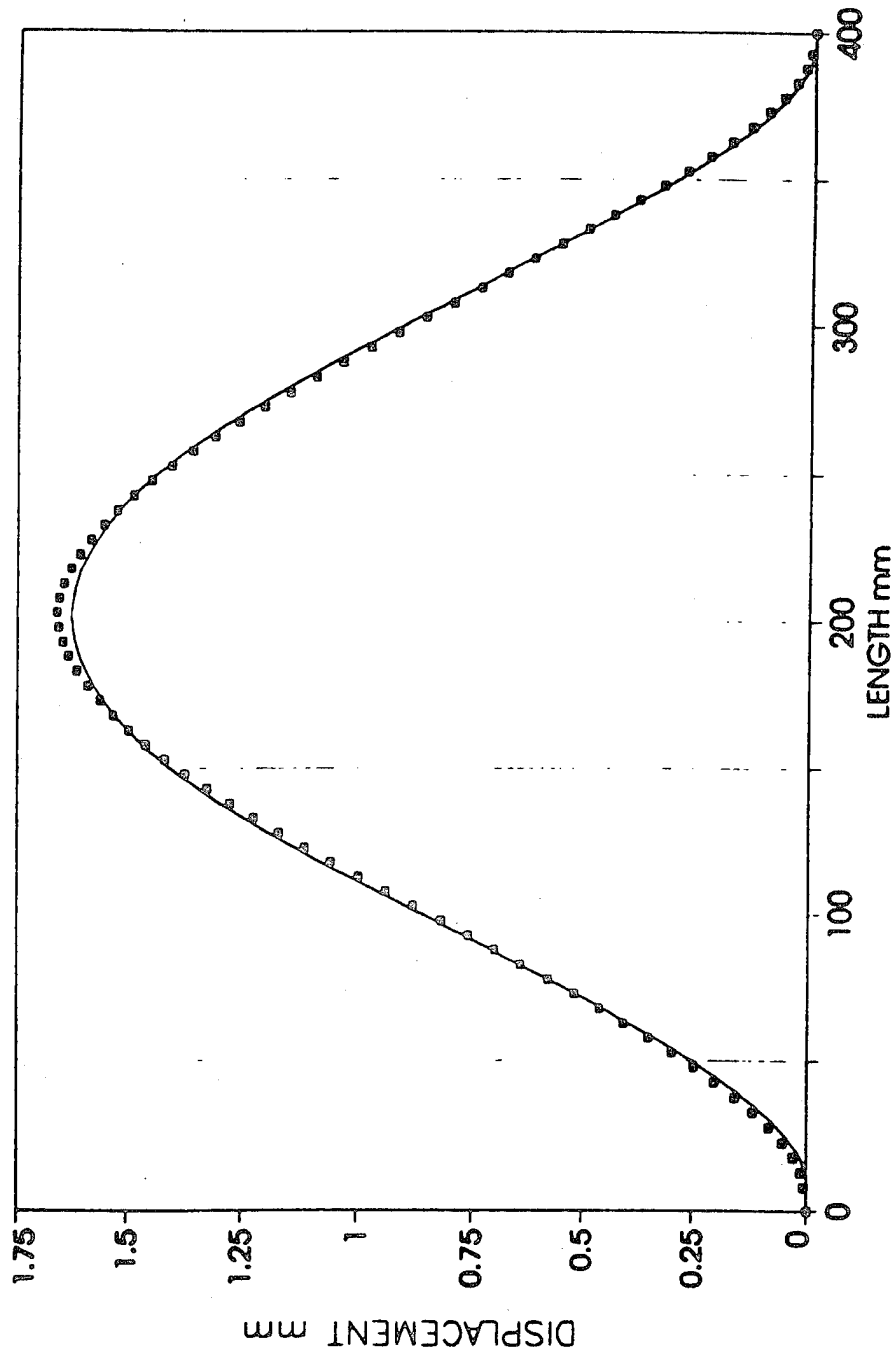


Fig 4.37 Rank 1, fourth fit of 0.60N sine excitation, C-C aluminium beam.

C-C AL BEAM R 1st18h

Rank 2 Eqn 8015 $y=a+bs\sin^2(2\pi x/d+c)$ (Sine²)

$r^2=0.999661057$ DF Adj $r^2=0.99964298$ FHSidErr=0.000520292013 Fstat=74716.7972

$a=-0.0031386313$ $b=1.6486802$

$c=3.1848908$ $d=823.66104$

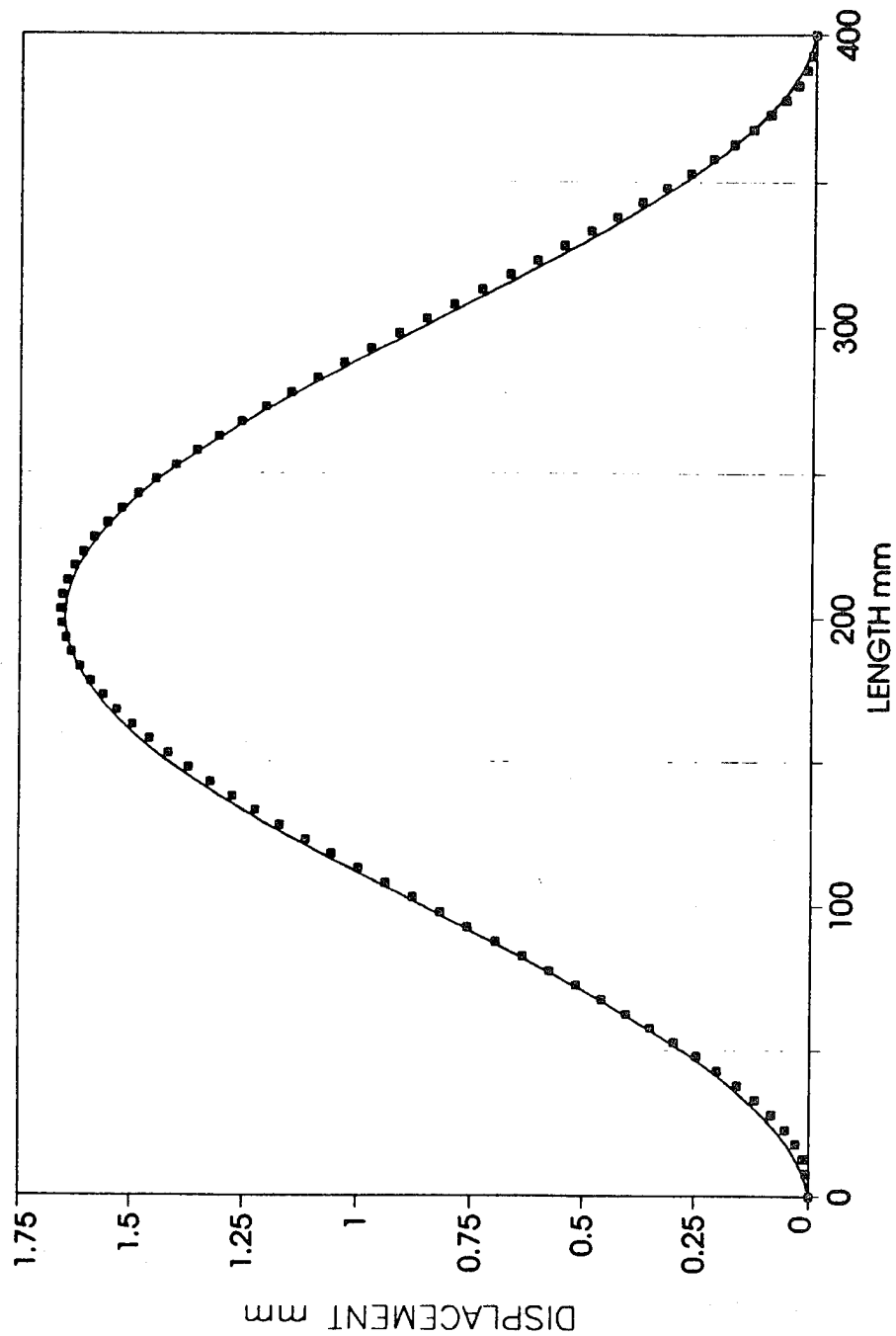


Fig 4.38 Rank 2, sine squared fit of 0.60N excitation, C-C aluminium beam.

C-C AL BEAM R 1st18h

Rank 3 Eqn 8014 $y=a+b\sin(2\pi x/d+c)$ (Sine)

$r^2=0.999661067$ DF Adj $r^2=0.99964298$ FMSIDE $m=0.000620292013$ FMSIG $=74716.7972$

$a=0.82120149$ $b=0.8243401$

$c=4.796985$ $d=411.83049$

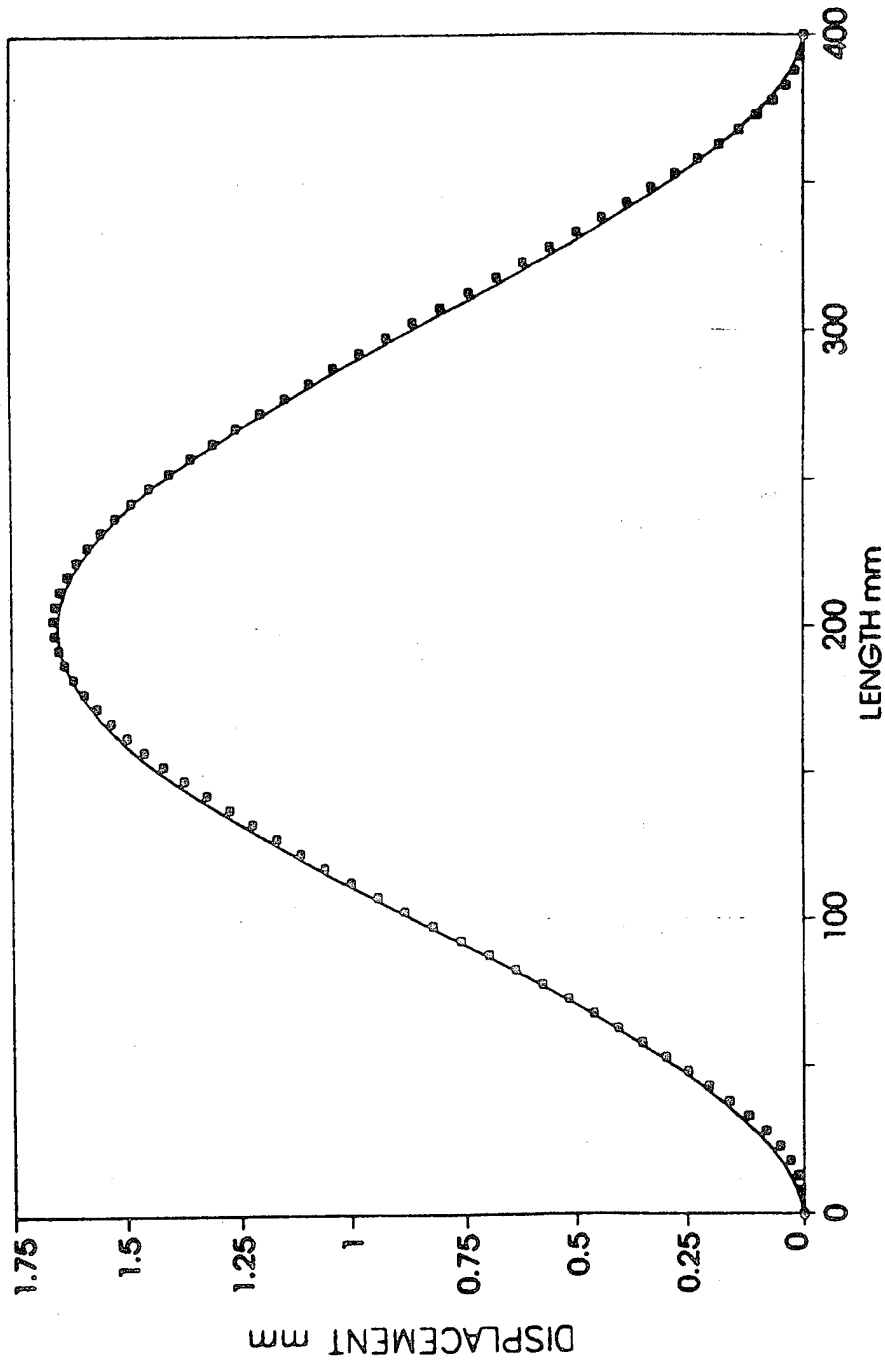


Fig 4.39 Rank 3, sine fit of 0.60N sine excitation, C-C aluminium beam.

C-C AL BEAM R 1st18h

Rank 4 Eqn 8001 $y=a\{\cosh(bx)-\cos(bx)-c[\sinh(bx)-\sin(bx)]\}$

$r^2=0.999623992$ DF Adj $r^2=0.999609149$ FHSIDE=0.000644432261 FATCH= 102352.868

$a=1.0169144$ $b=0.011755874$

$c=0.98251591$

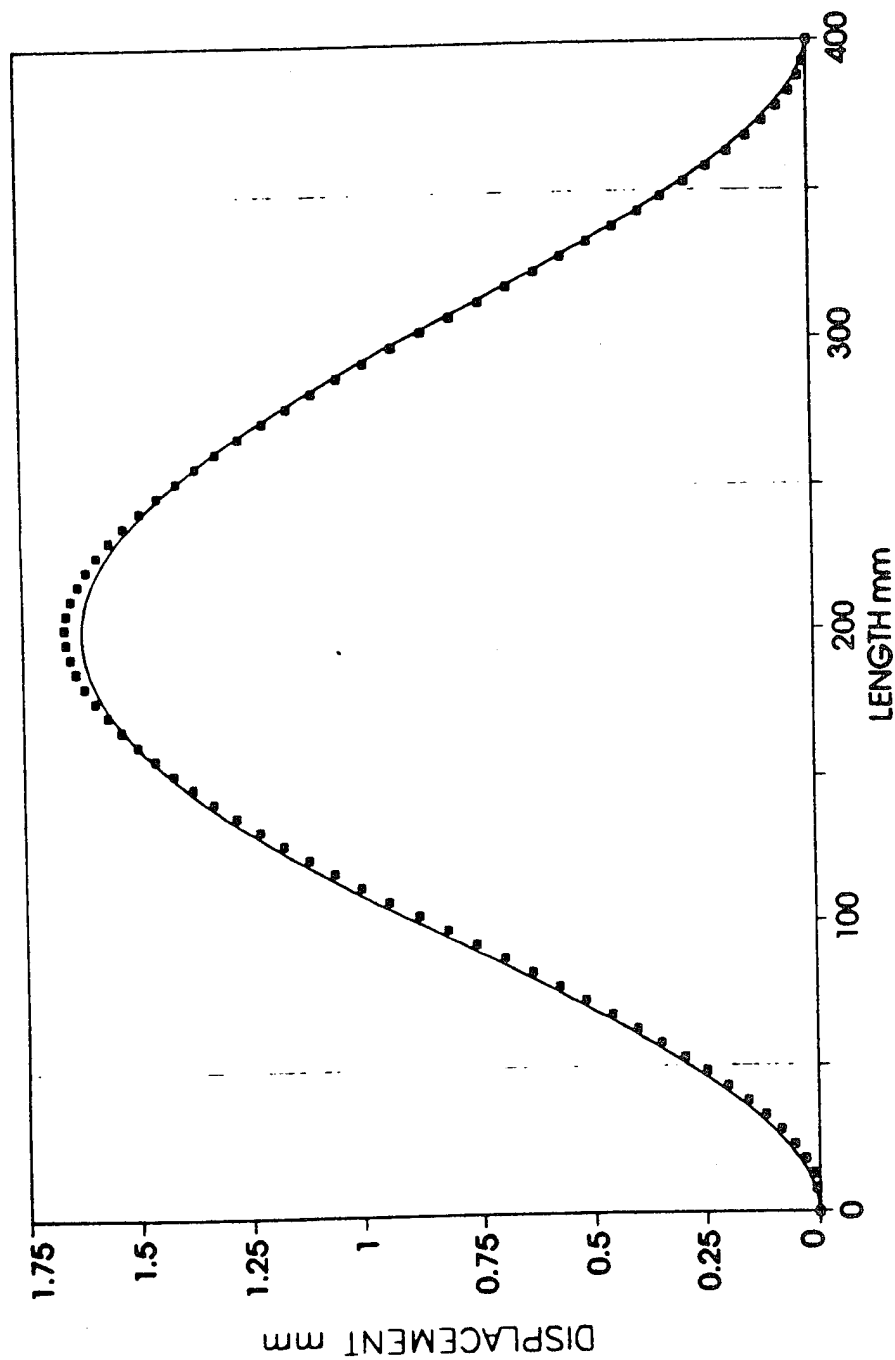


Fig 4.40 Rank 4, classical curve fit of 0.60N sine excitation, C-C aluminium beam.

C-C AL BEAM R 1st 11h

Rank 1 Eqn 8014 $y=a+b\sin(2\pi x/d+c)$ (Sine)

$r^2=0.999866283$ Df Adj $r^2=0.999853309$ F1StdErr=0.00161538869 F1std=113803.79

$a=0.18708723$ $b=0.19172892$

$c=4.8198187$ $d=420.02815$

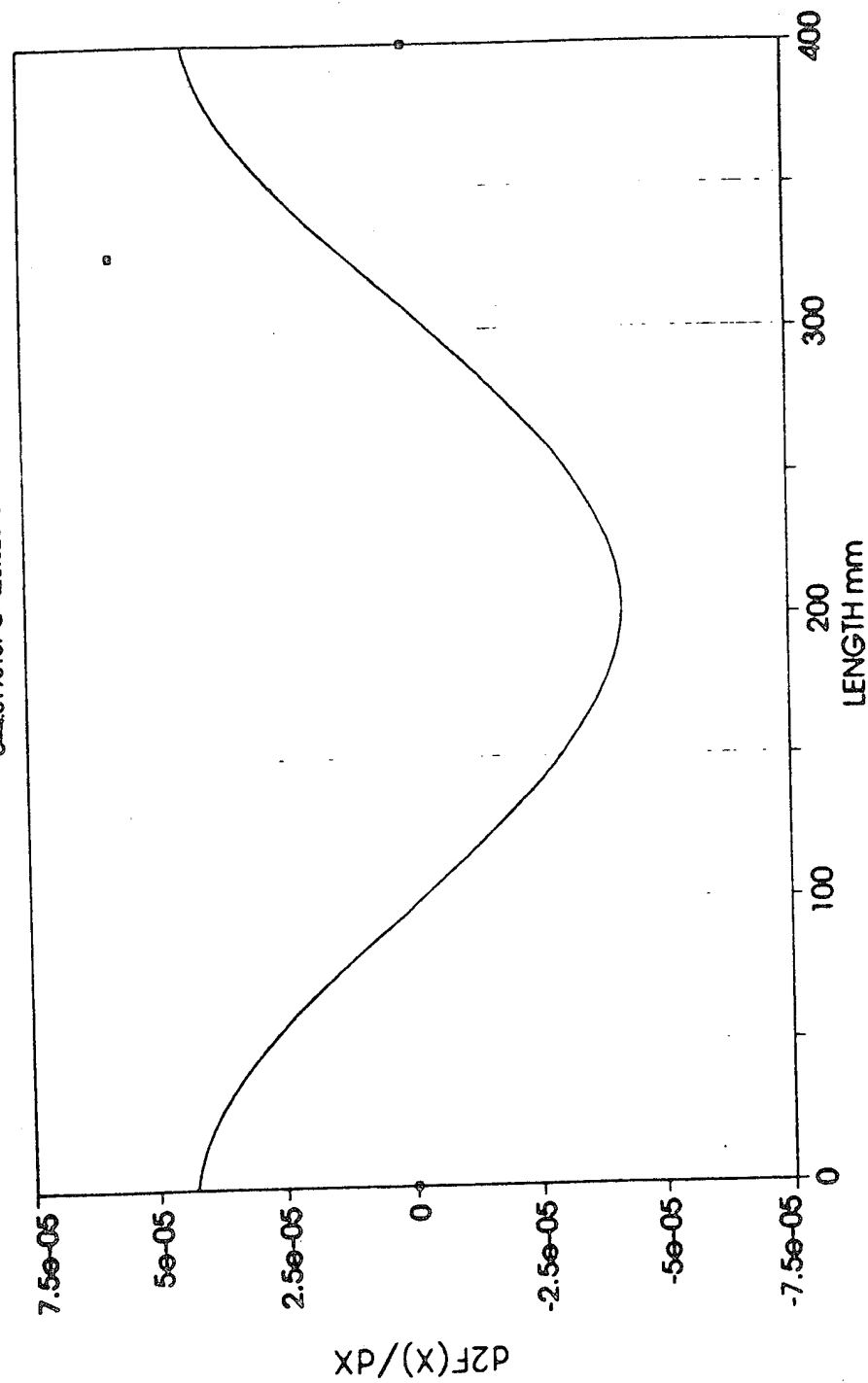


Fig 4.41 Second derivative of Fig 4.33, C-C aluminium beam.

C-C AL BEAM R 1st11h

Rank 2 Eqn 8015 $y = a + b \sin^2(2\pi x/d + c)$ (Sine²)

$r^2 = 0.999865283$ DF Adj $r^2 = 0.999863309$ F1stOfm = 0.00161638869 Fctch = 113803.79

$a = 0.0046416999$ $b = 0.38345783$

$c = 3.1953075$ $d = 840.0563$

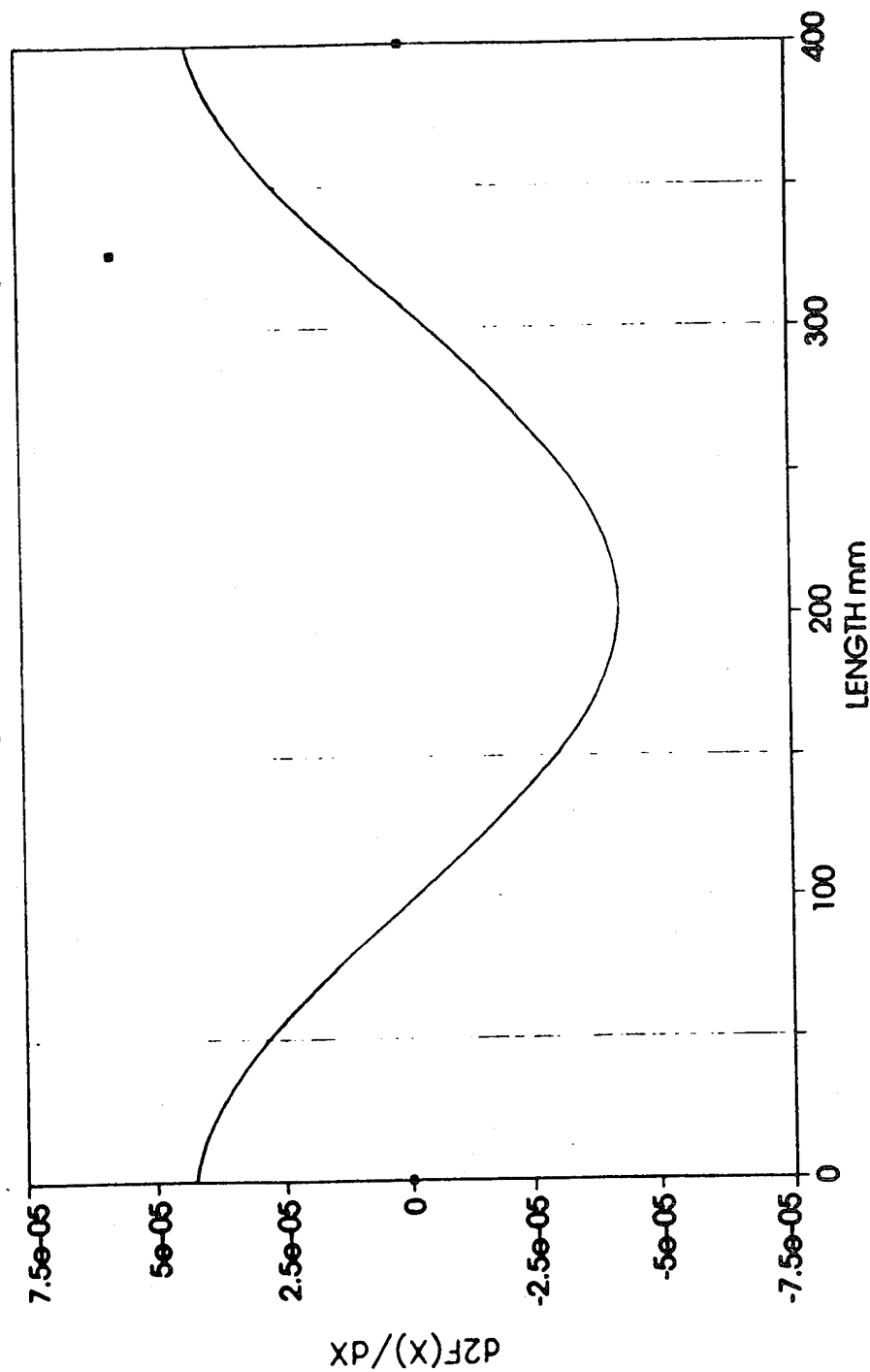


Fig 4.42 Second derivative of Fig 4.34, C-C aluminium beam.

C-C AL BEAM R 1st11h

Rank 5 Eqn 8009 $y = a + bx + cx^2 + dx^3 + ex^4$

$r^2=0.999419989$ Df Adj $r^2=0.999354079$ FstSdEm=0.00038886675 FstCfm=19384.9416

$a=0.0053915115$ $b=-0.0005707105$ $c=4.4073816e-05$

$d=-2.093421e-07$ $e=2.580811e-10$

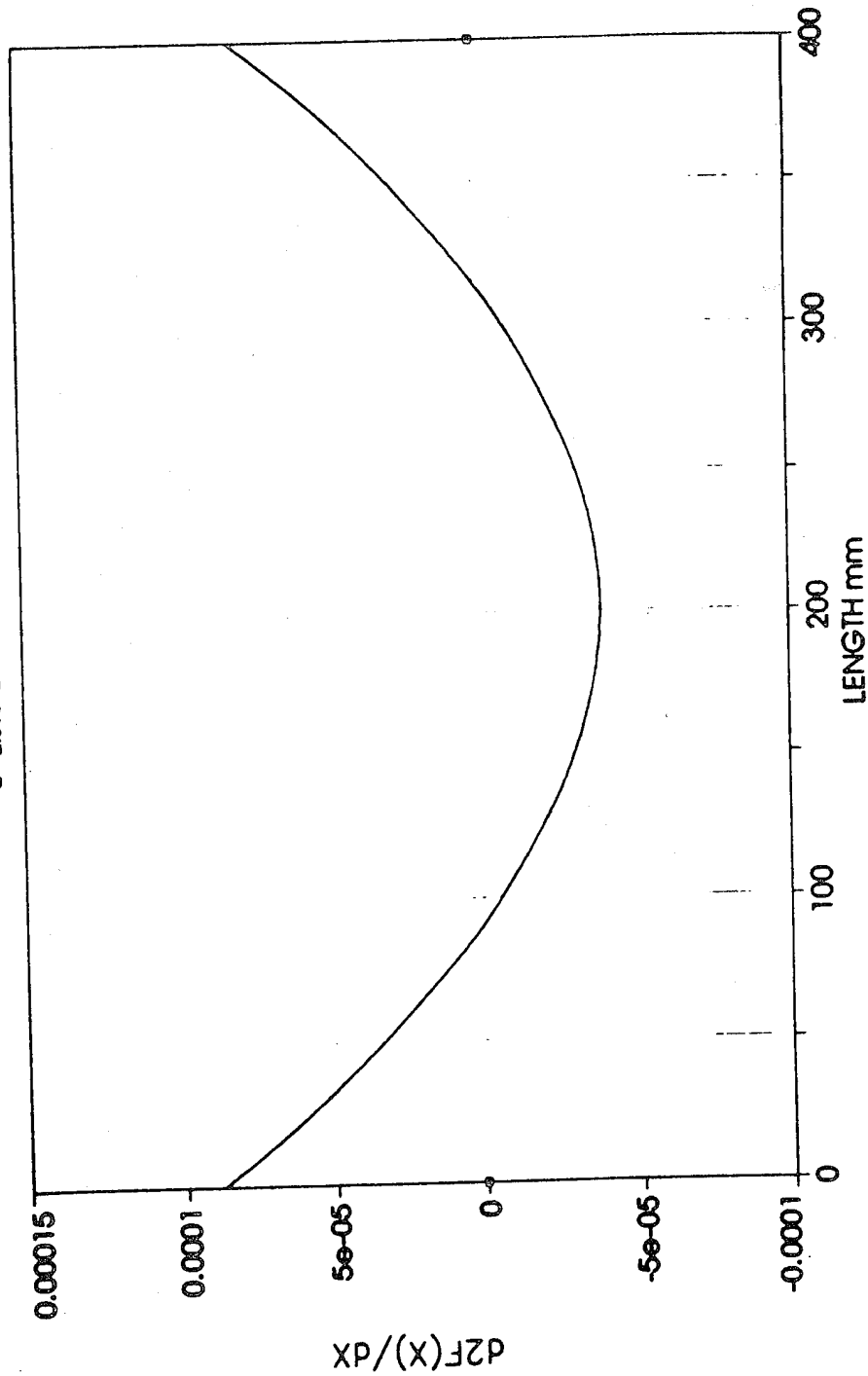


Fig 4.43 Second derivative of Fig 4.35, C-C aluminium beam.

C-C AL BEAM R 1st11h

Rank 8 Eqn 8001 $y=a[\cosh(bx)-\cos(bx)-c[\sinh(bx)-\sin(bx)]]$

$r^2=0.999222268$ DF Adj $r^2=0.999171643$ FstStdEm=0.00383983267 FstStd=30192.4322

$a=0.23564298$ $b=0.011675587$

$c=0.98279647$

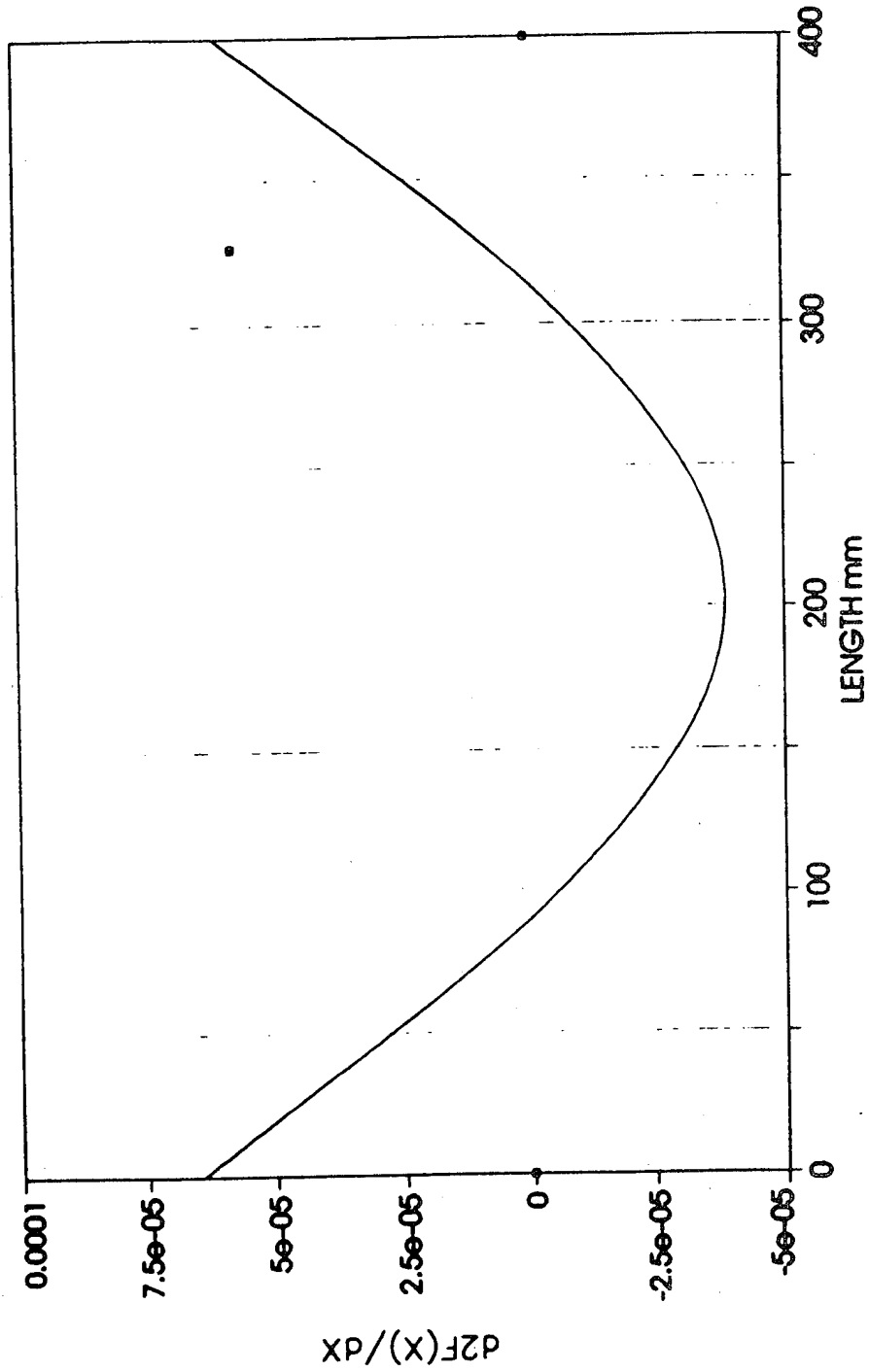


Fig 4.44 Second derivative of Fig 4.36, C-C aluminium beam.

C-C AL BEAM R 1st18h

Rank 1 Eqn 8009 $y = a + bx + cx^2 + dx^3 + ex^4$

$r^2=0.999756037$ DF Adj $r^2=0.999741688$ F1stIDE=0.000442621621 Ftotal=77472.3928

$a=9.070052e-07$ $b=-0.002356959$ $c=0.00018867721$

$d=-9.0597936e-07$ $e=1.1225435e-09$

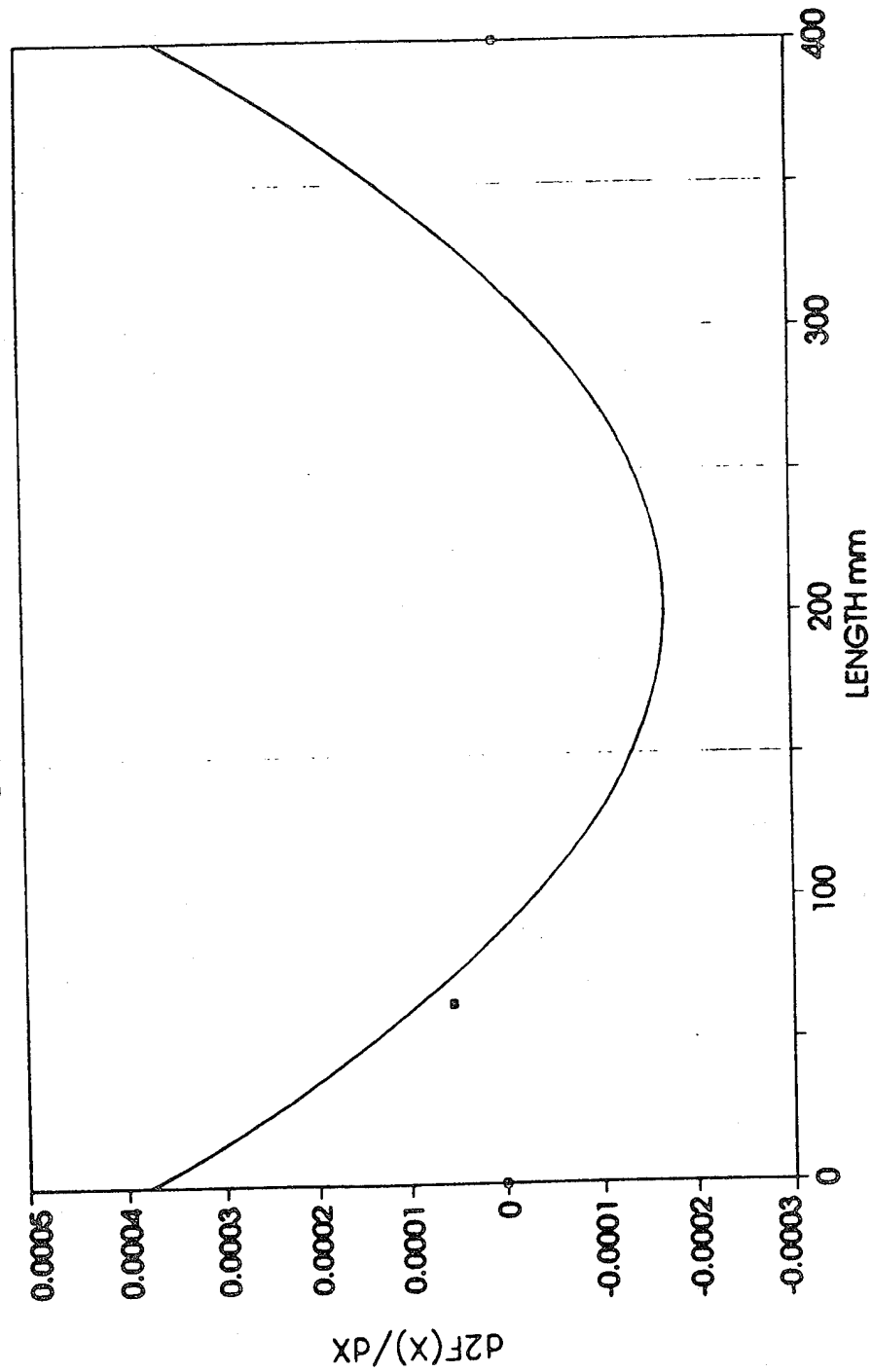


Fig 4.45 Second derivative of Fig 4.37, C-C aluminium beam.

C-C AL BEAM R 1st18h

Rank 2 Eqn 8015 $y=a+b\sin^2(2\pi x/d+c)$ (Sine²)

$r^2=0.999661067$ DF Adj $r^2=0.99964298$ FHSidErr=0.000620292013 Fstat=74716.7972

$a=-0.0001386313$ $b=1.6486802$

$c=3.1848908$ $d=823.66104$

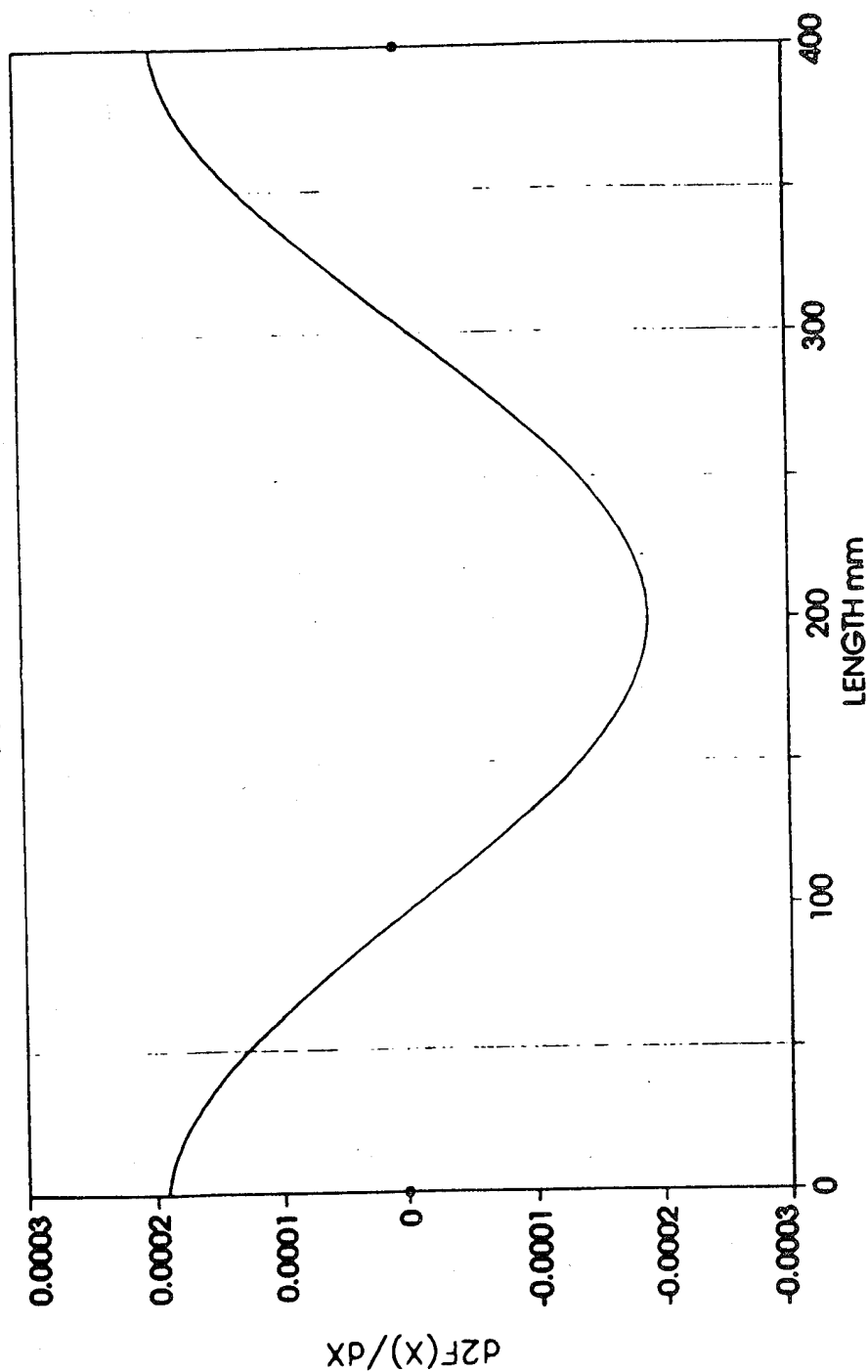


Fig 4.46 Second derivative of Fig 4.38, C-C aluminium beam.

C-C AL BEAM R 1st18h

Rank 3 Eqn 8014 $y=a+b\sin(2\pi x/d+c)$ (Sine)

$r^2=0.999661057$ DF Adj $r^2=0.99964298$ FHSide $n=0.000520292013$ Fstata $=74716.7972$

$a=0.82120149$ $b=0.8243401$

$c=4.798985$ $d=411.83049$

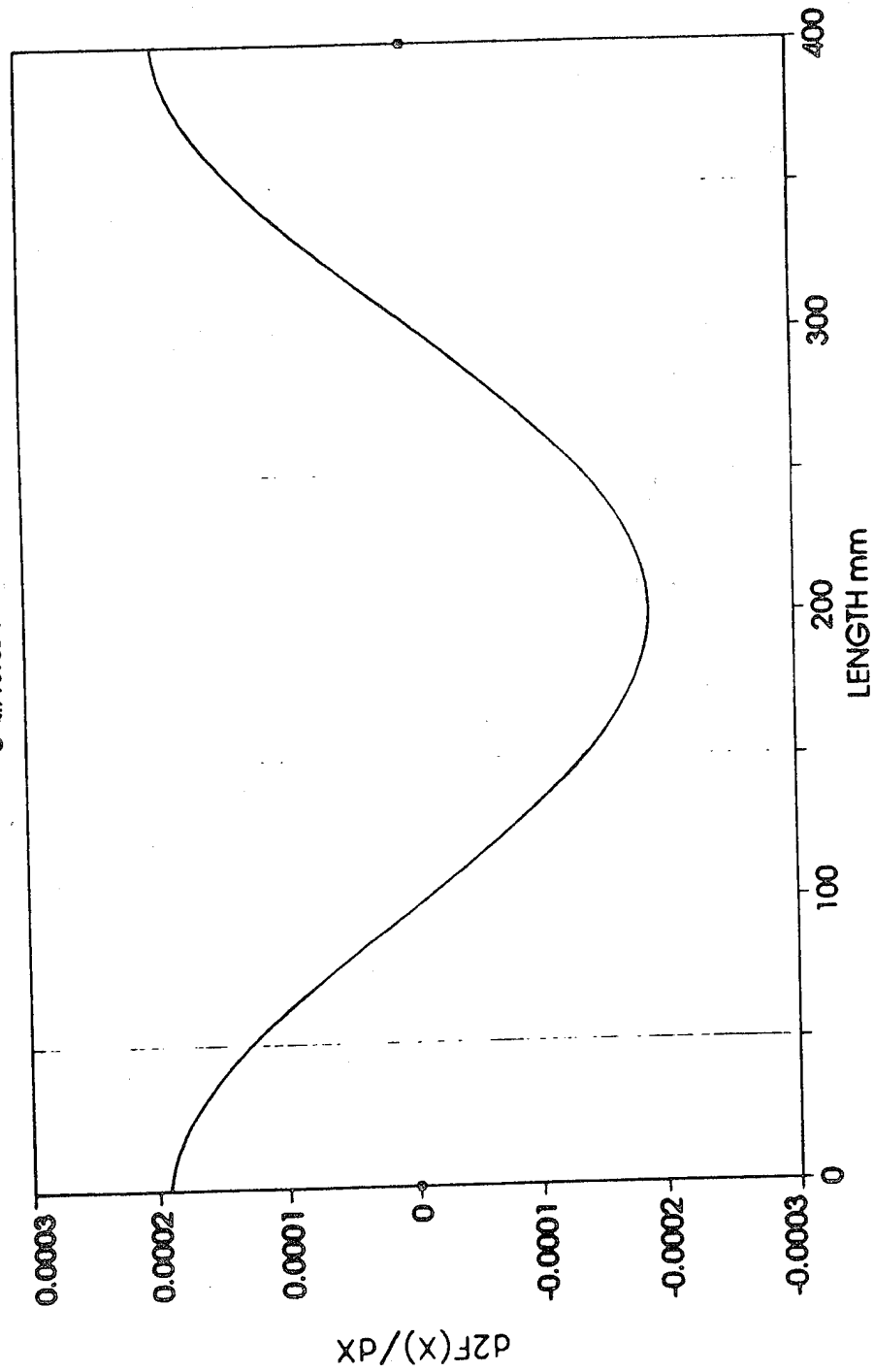


Fig 4.47 Second derivative of Fig 4.39, C-C aluminium beam.

C-C AL BEAM R 1st18h

Rank 4 Eqn 8001 $y=a\{\cosh(bx)-\cos(bx)-c[\sinh(bx)-\sin(bx)]\}$

$r^2=0.999623992$ DF Adj $r^2=0.999609149$ FHSIDE $r=0.000644432261$ Fstot $=102352.568$

$a=1.0189144$ $b=0.011755874$

$c=0.98251591$

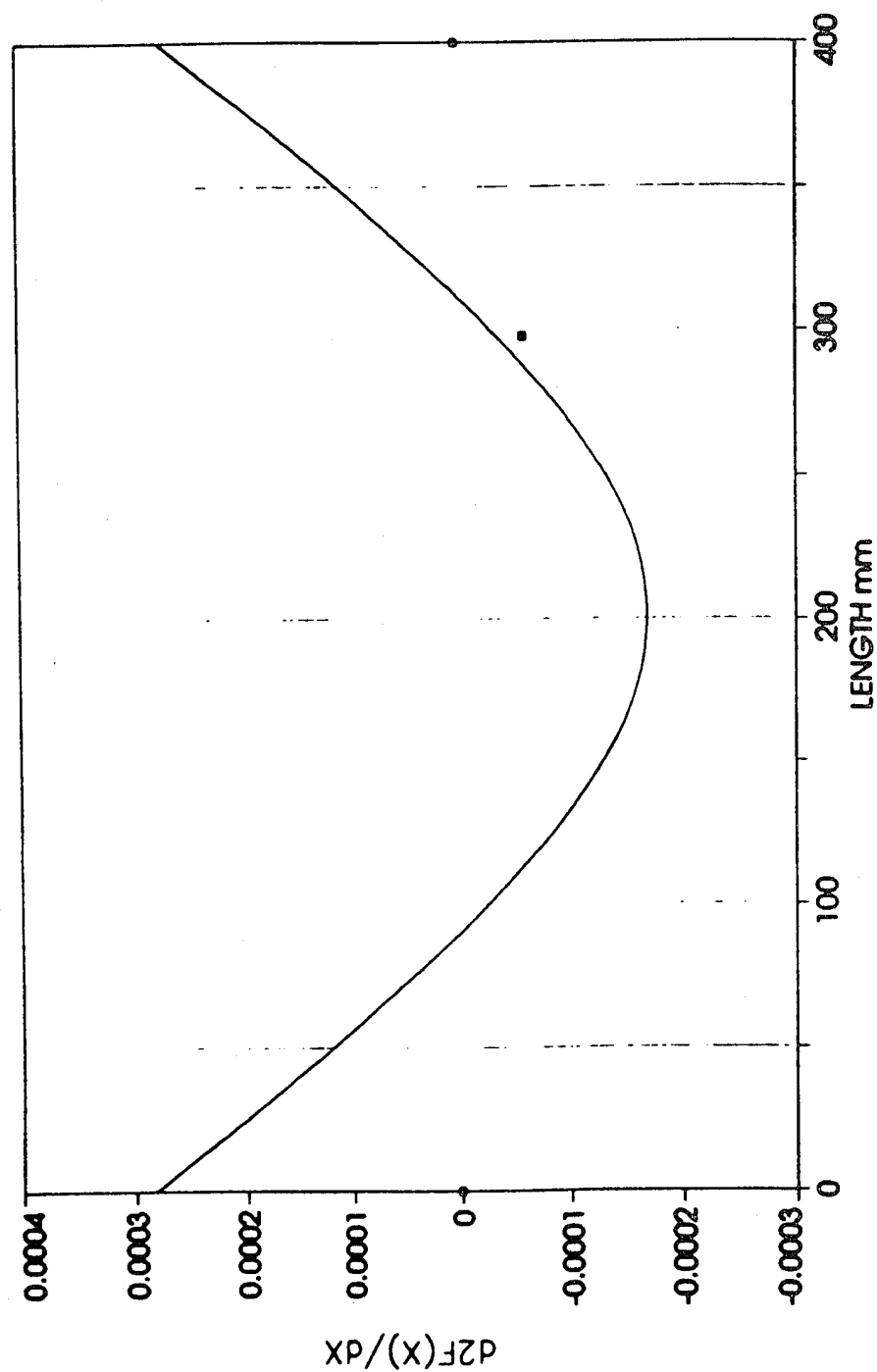


Fig 4.48 Second derivative of Fig 4.40, C-C aluminium beam.

C-C AL BEAM R 1st11

Rank 2 Eqn 800? $y=a\{\cosh(bx)-\cos(bx)-c[\sinh(bx)-\sin(bx)]\}$

$r^2=0.99996612$ Df Adj $r^2=0.999947298$ FittedEm=0.000504679369 Fctot=73788.2177

$a=0.0002191115$ $b=-0.00013490922$ $c=3.5199021e-05$

$d=1.6364317e-07$ $e=1.9123056e-10$

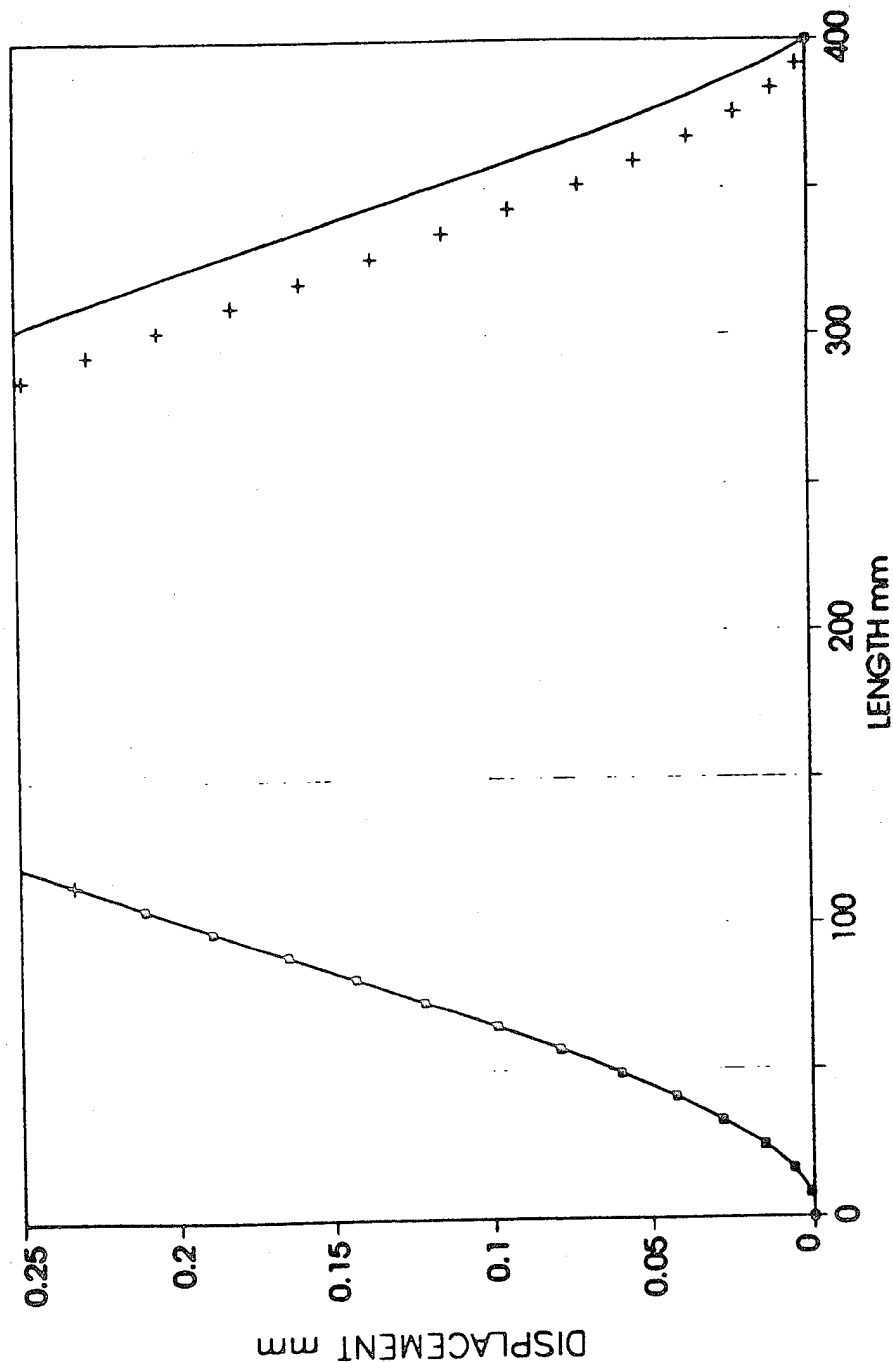


Fig 4.49 Rank 2 curve fit of data near clamp, fourth order polynomial, C-C aluminium beam.

C-C AL BEAM R 1st11j

Rank 2 Eqn 8009 $y = a + bx + cx^2 + dx^3 + ex^4$

$r^2=0.99996612$ Df Adj $r^2=0.999947298$ F1StdErr=0.000604679369 FstCst=73768.2177

$a=-0.00021911115$ $b=-0.00013490922$ $c=3.5199021e-06$

$d=-1.6364317e-07$ $e=1.9123056e-10$

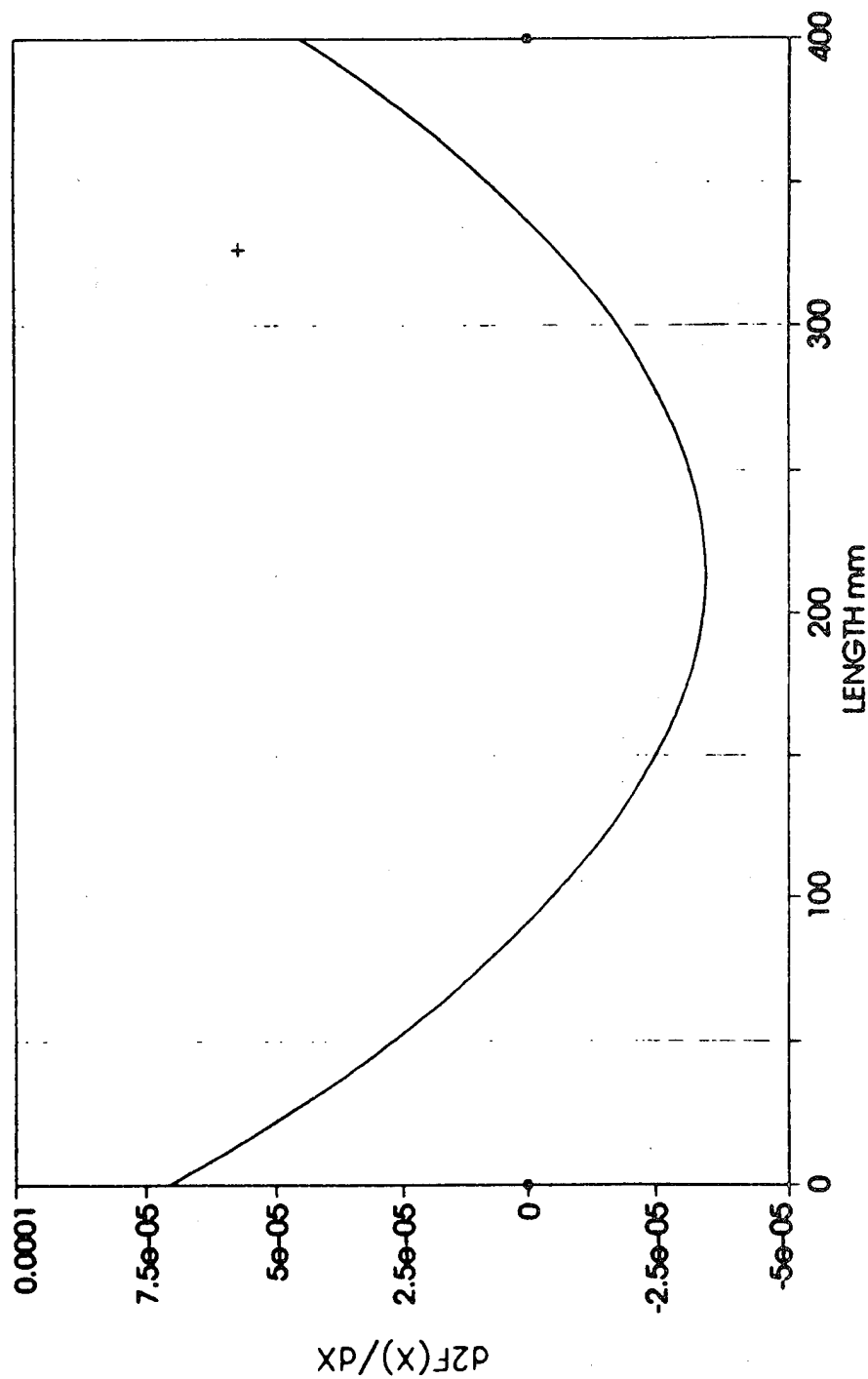


Fig 4.50 Second derivative of Fig 4.49, C-C aluminium beam.

BEAM NONLINEAR DISPLACEMENT SHAPES
4th ORDER POLYNOMIAL COEFFICIENTS 'a'

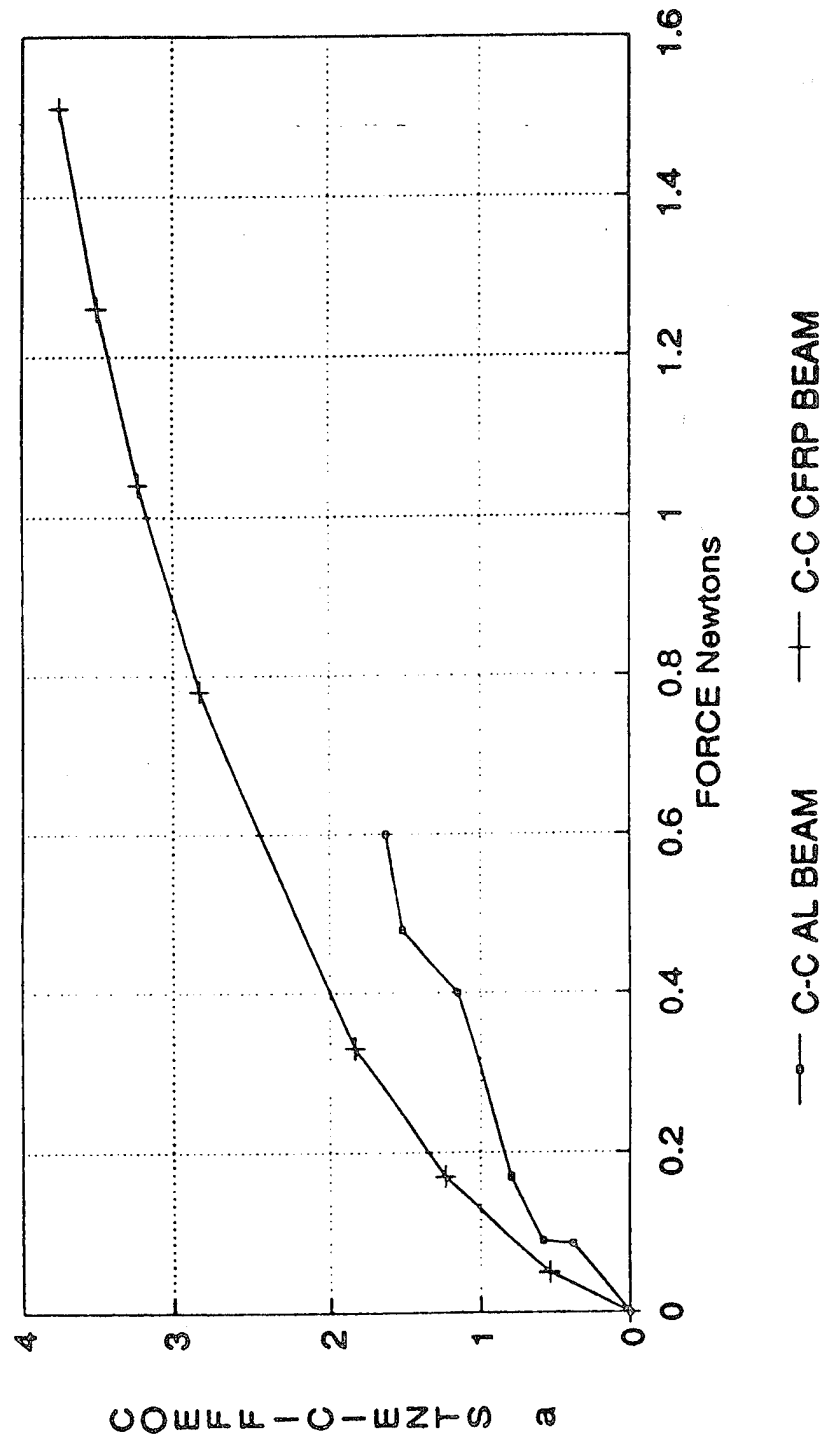


Fig 4.51 Coefficients 'a' for fourth order polynomial fits, C-C aluminium and CFRP beams.

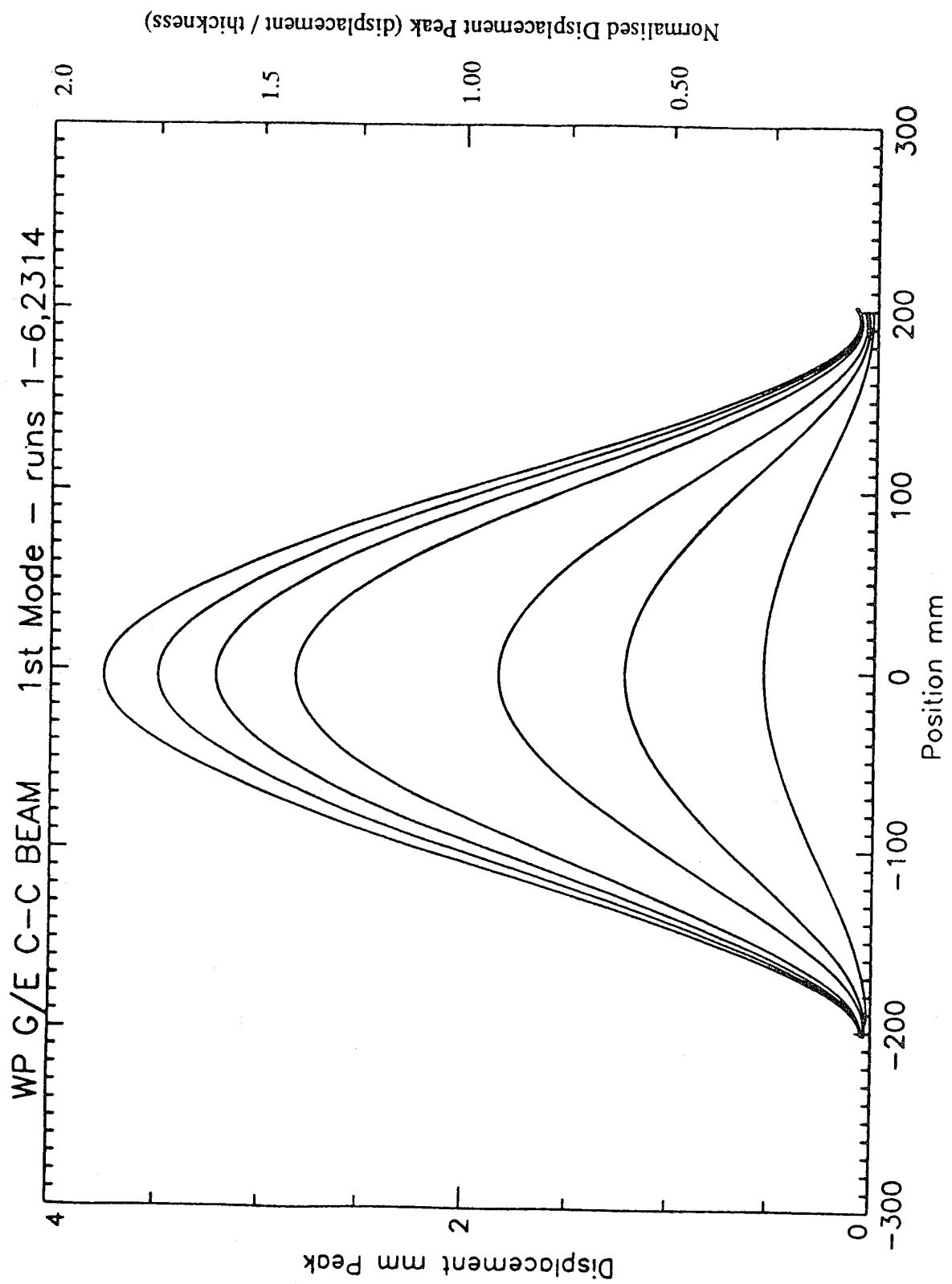


Fig 4.52 Fourth order polynomial fit of displacement shapes, sine excitation, C-C CFRP beam.

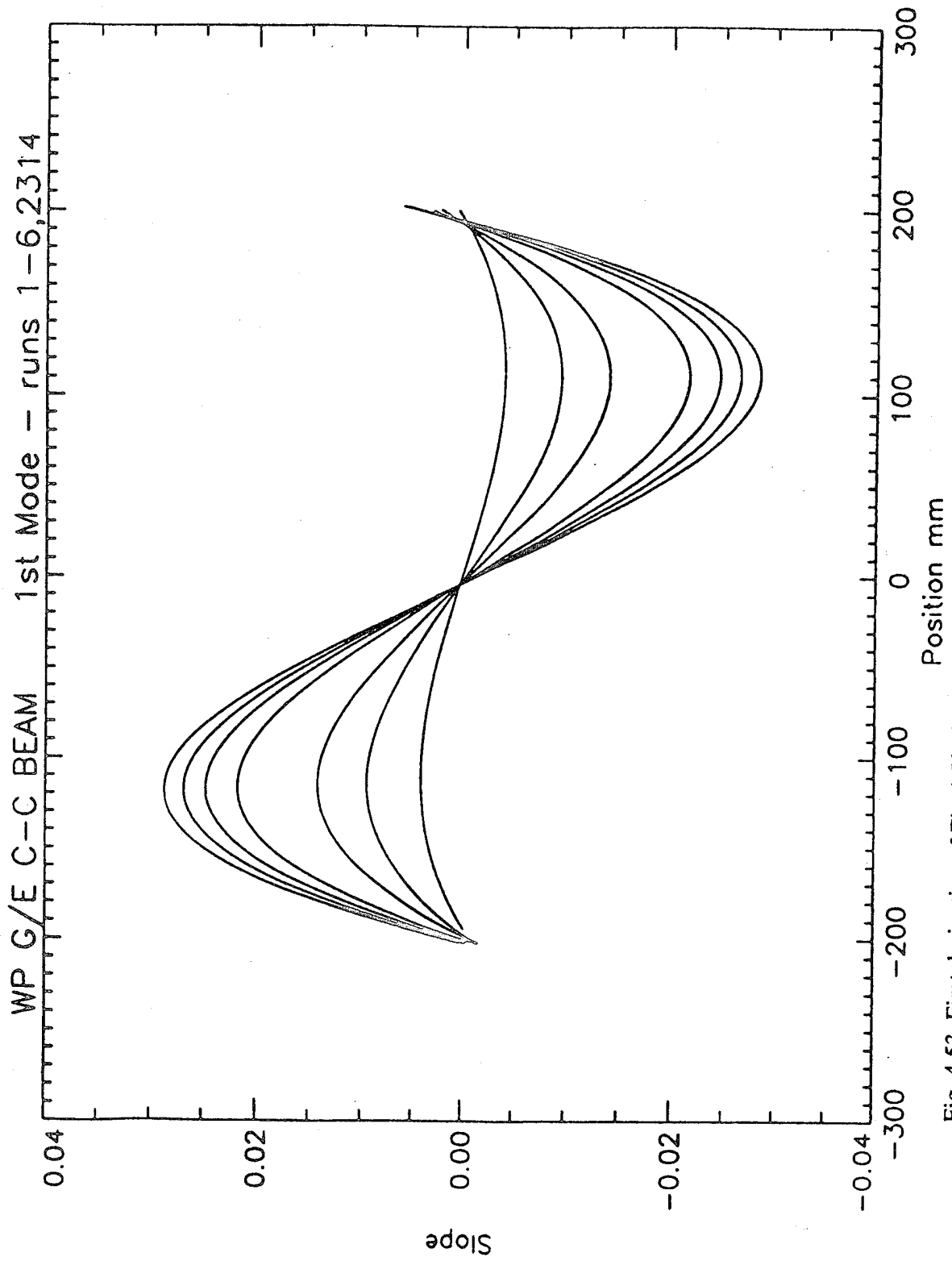


Fig 4.53 First derivative of Fig 4.52, CFRP beam.

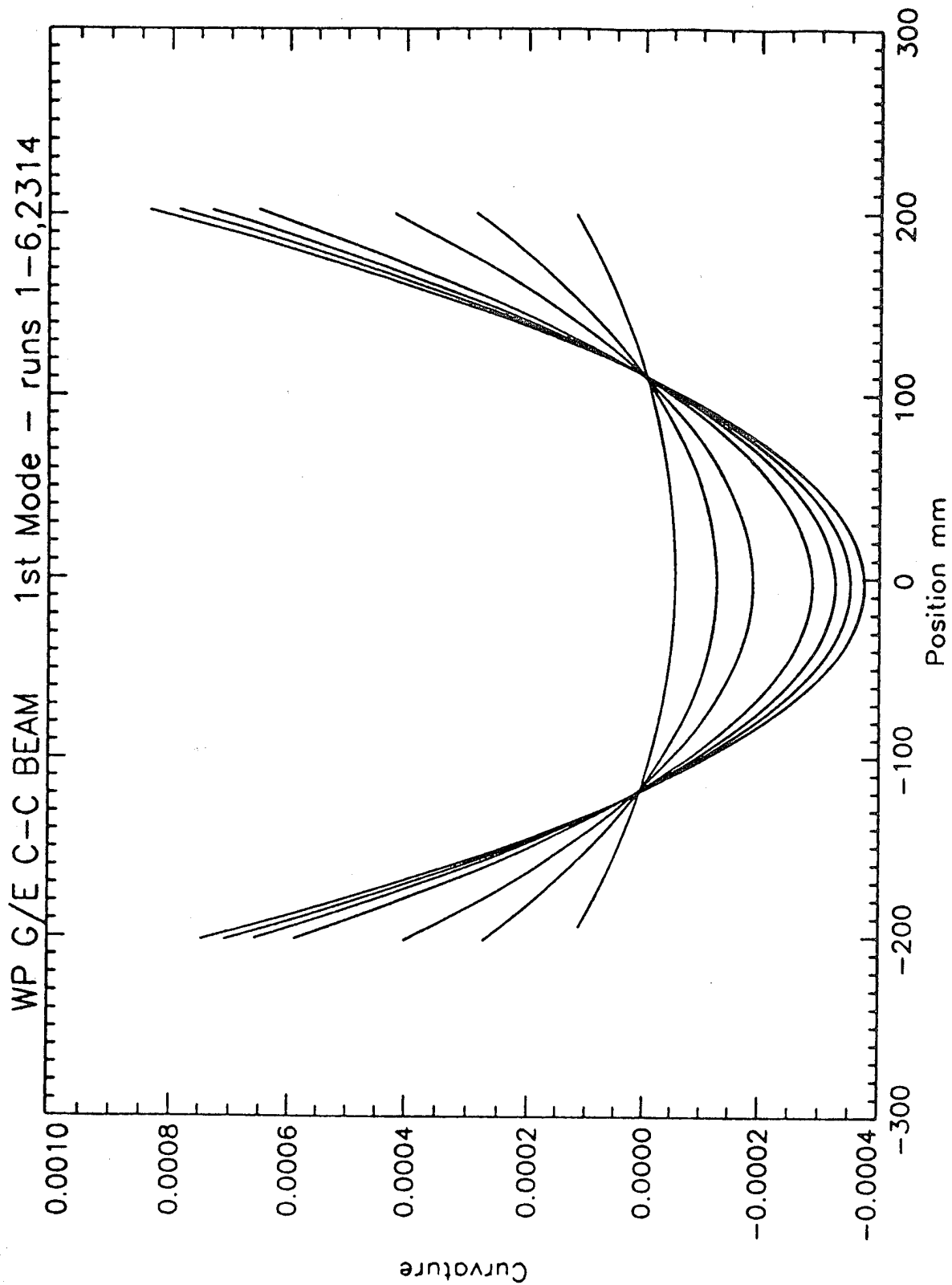


Fig 4.54 Second derivative of Fig 4.52, CFRP beam.

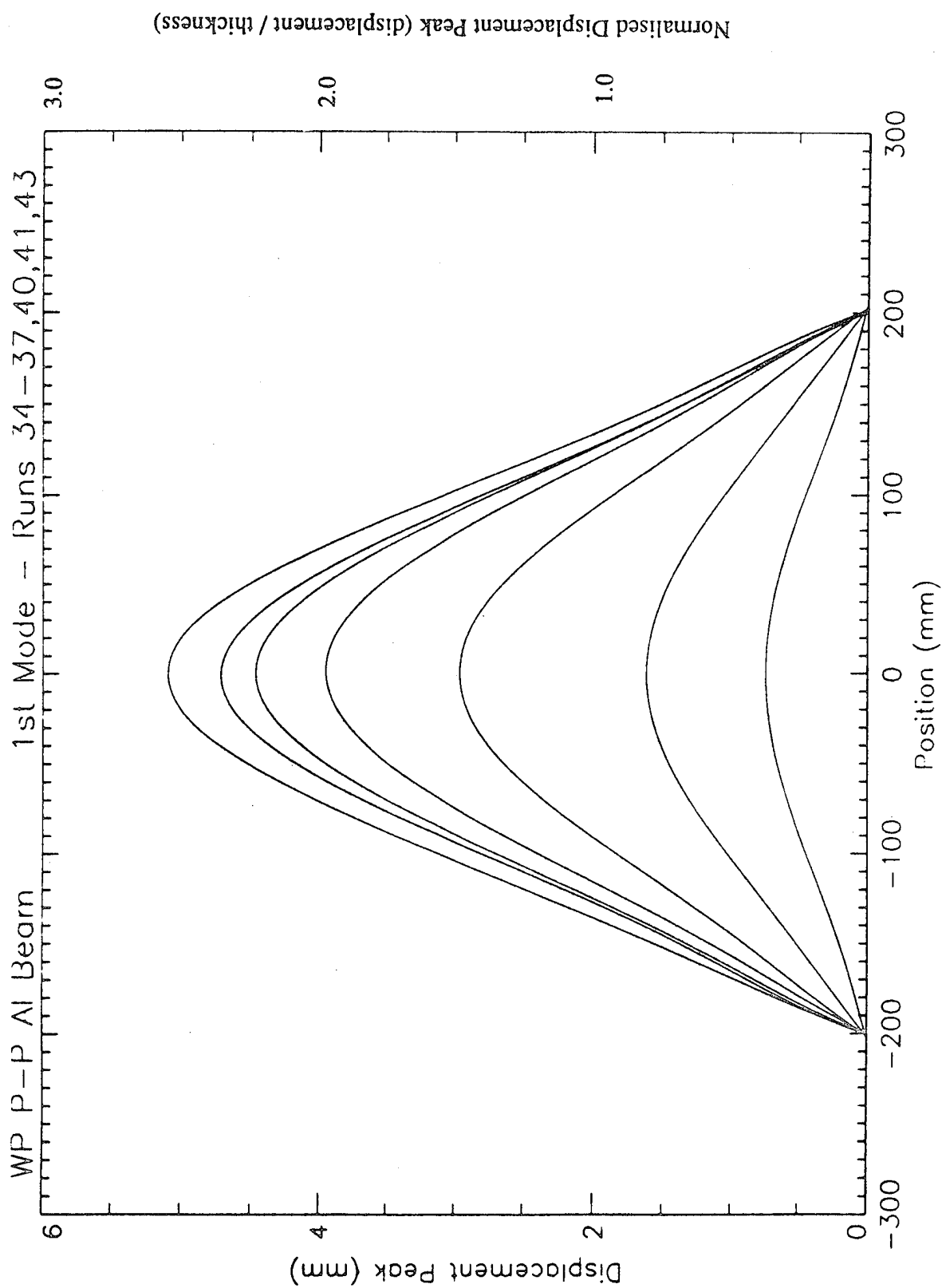


Fig 4.55 Fourth order polynomial fit of displacement shapes, sine excitation, P-P aluminium beam.

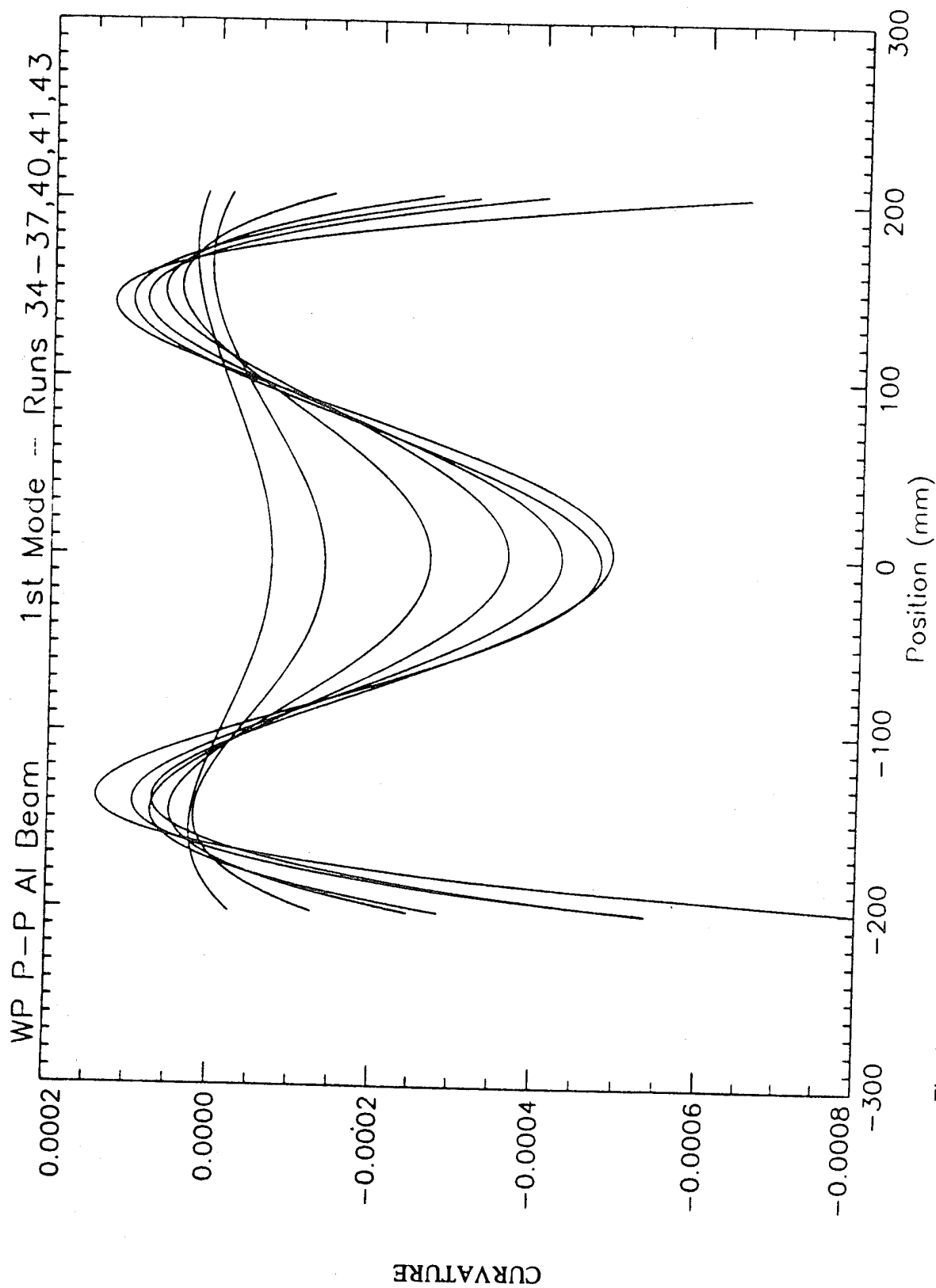


Fig 4.56 Second derivative of Fig 4.55, P-P aluminium beam.

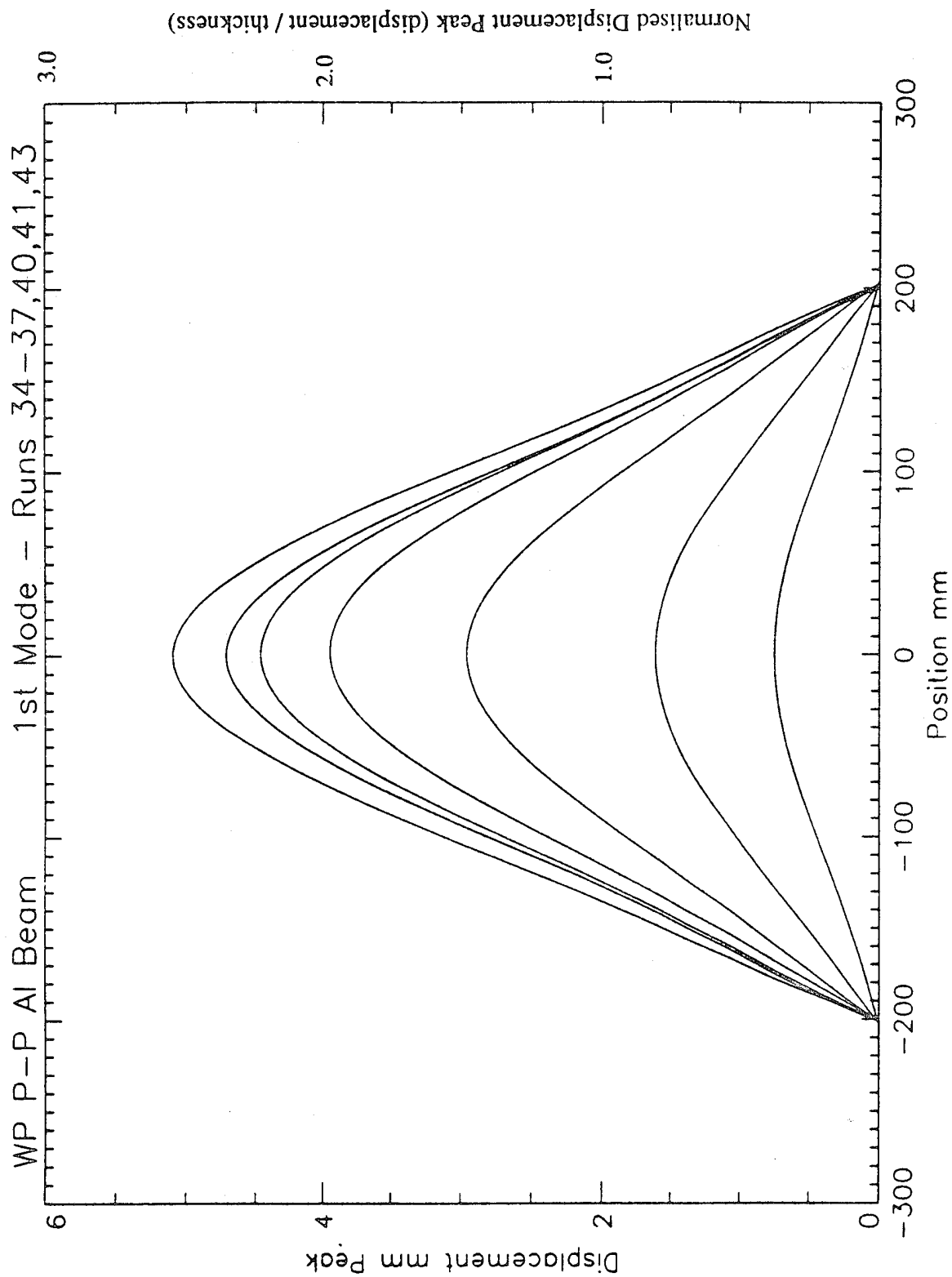


Fig 4.57 Sixth order polynomial fit of displacement shapes, sine excitation, P-P aluminium beam.

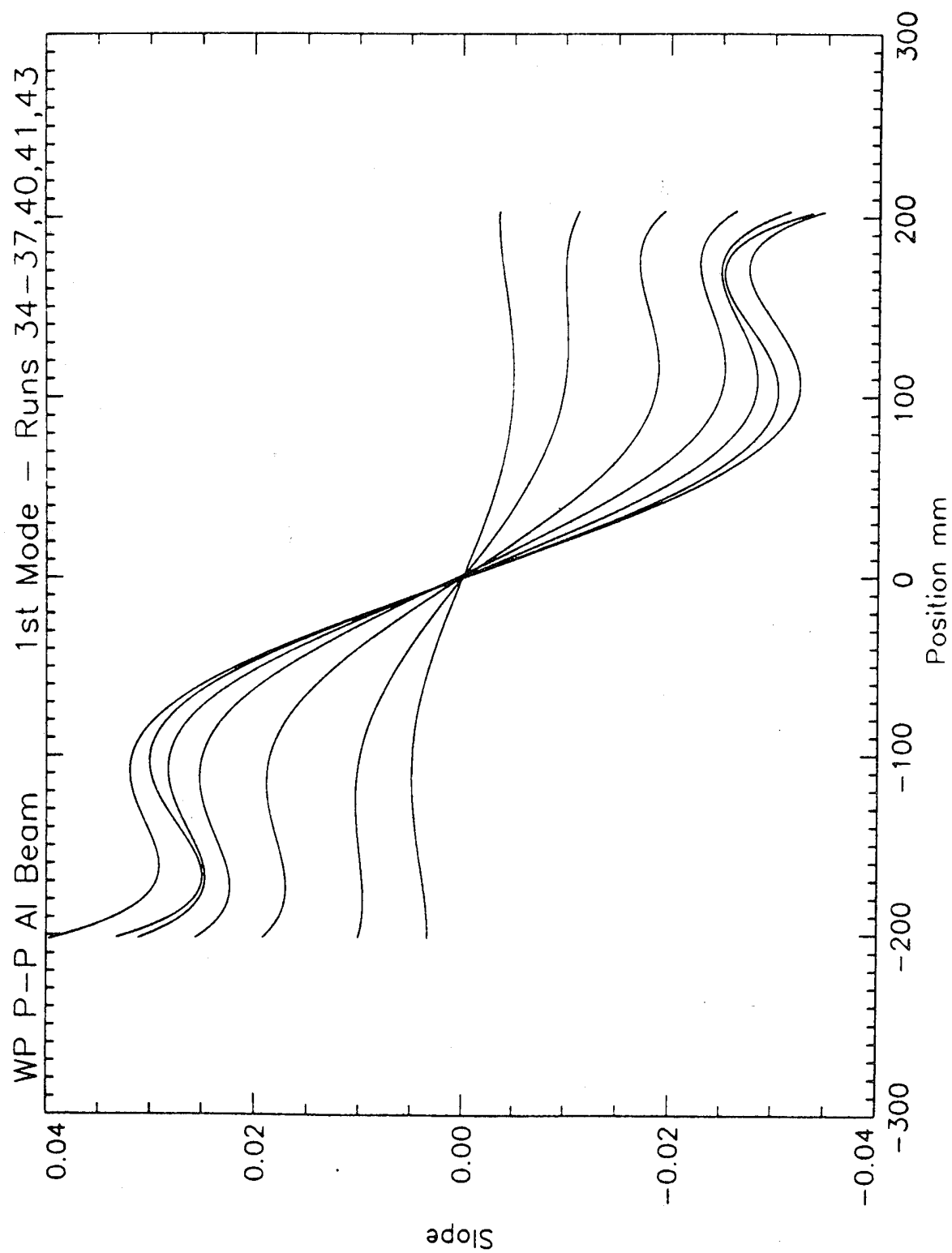


Fig 4.58 First derivative of Fig 4.57, P-P aluminium beam.

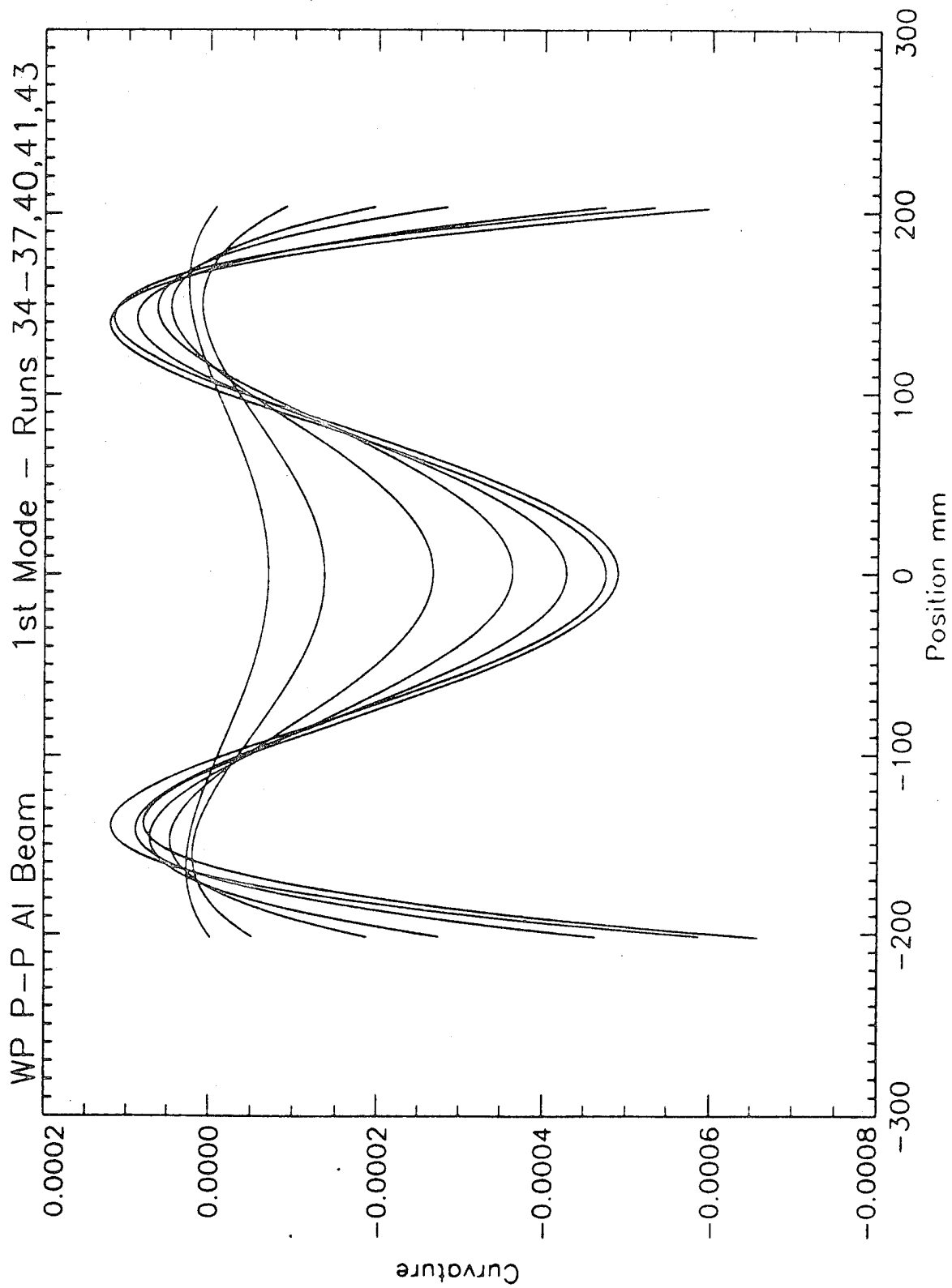


Fig 4.59 Second derivative of Fig 4.57, P-P aluminium beam.

P-P AL BEAM R23 30.3 Hz 0.61N

Rank 1 Eqn 8003 $y=a+b\exp(-0.5((x-c)/d)^2)$ (Gaussian)

$a=0.17969329$ $b=0.91700264$

$c=0.57544777$ $d=114.14576$

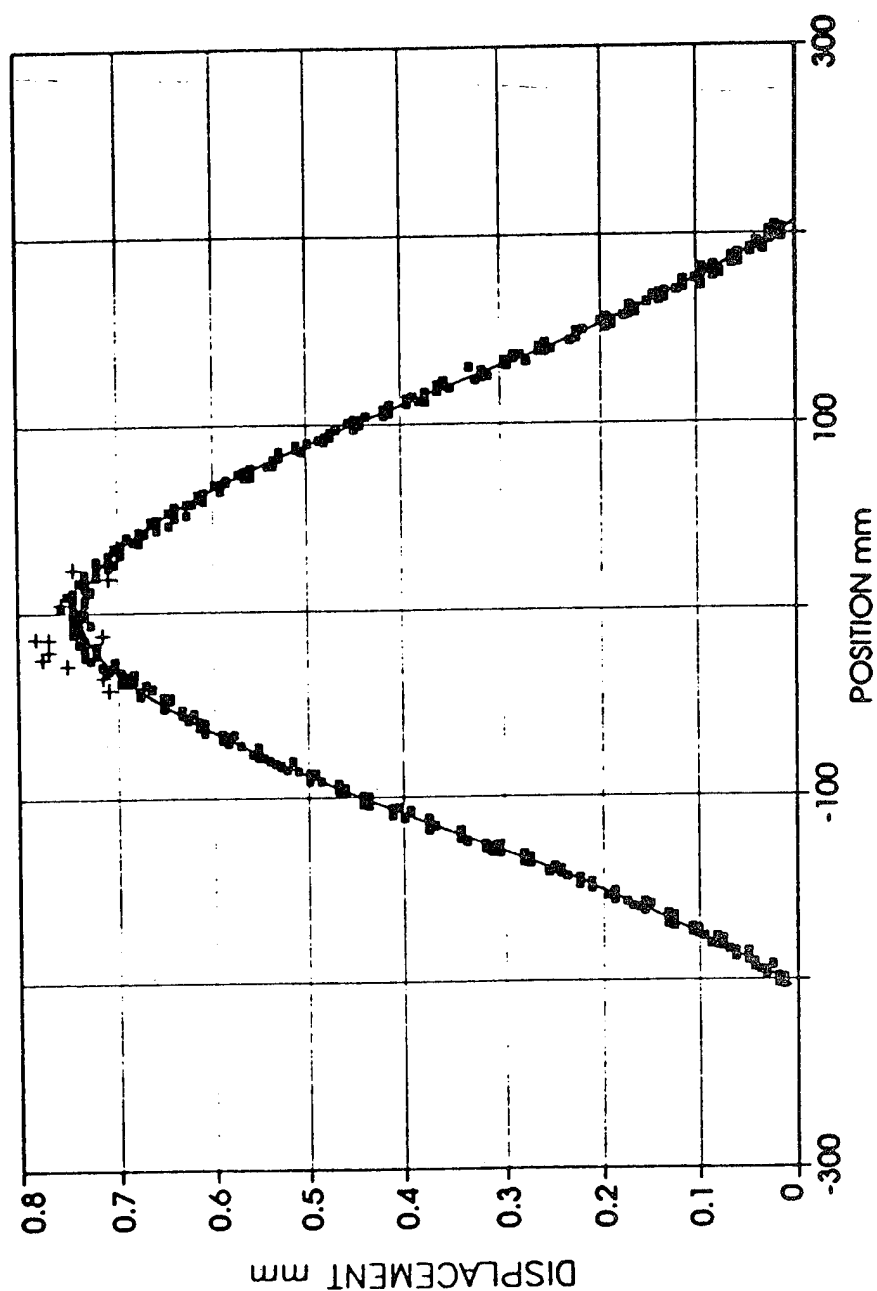


Fig 4.60 Gaussian fit of displacement shapes, sine excitation 0.61 N, P-P aluminium beam.

P-P AL BEAM R41 46.8 Hz 3.06 N

Rank 1 Eqn 8004 $y=a+b/(1+((x-c)/d)^2)$ (Lorentzian)

$a=4.8662696$ $b=9.9619014$

$c=-0.54660228$ $d=200.24917$

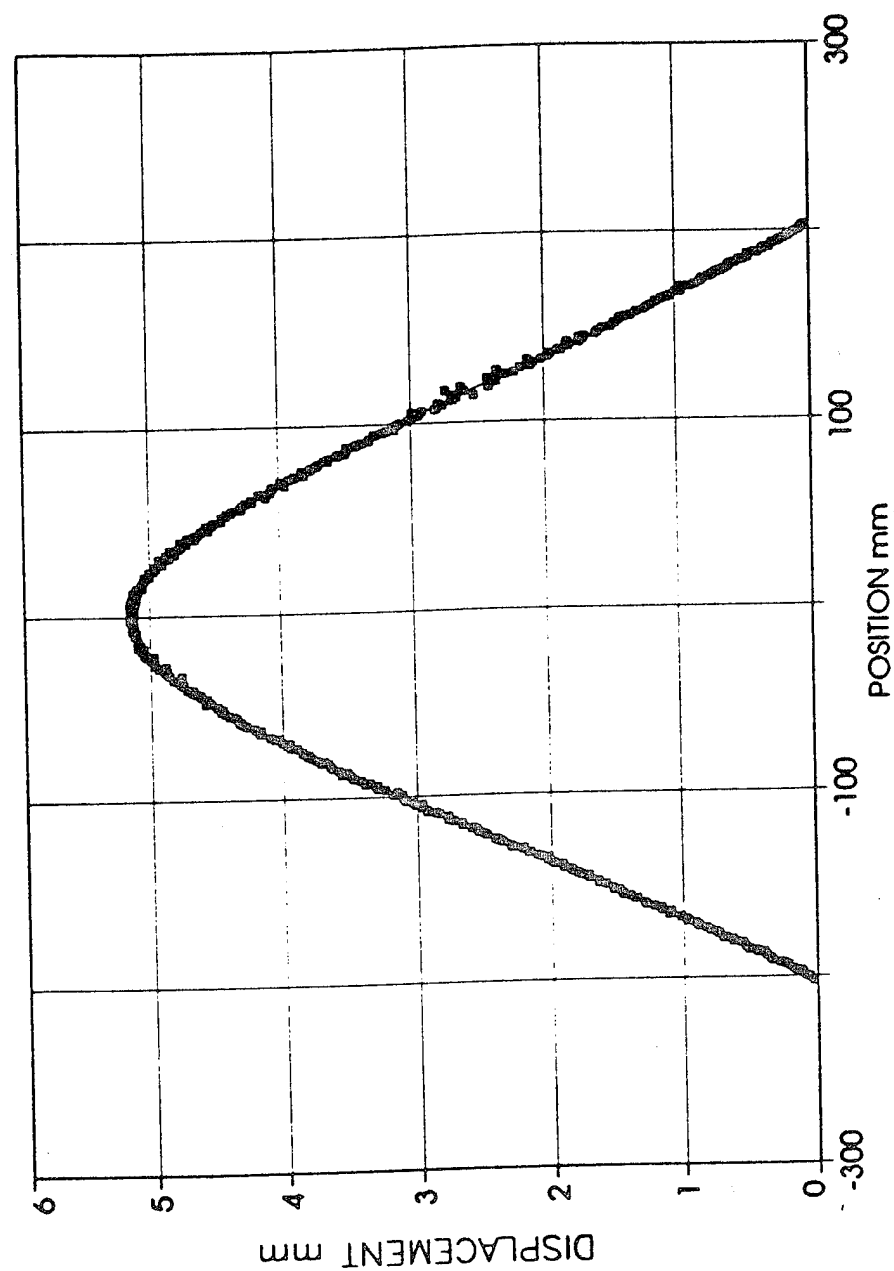


Fig 4.61 Lorentzian fit of displacement shapes, sine excitation 3.06 N, P-P aluminium beam.

P-P AL BEAM R23 30.3 Hz 0.61N

Rank 1 Eqn 8003 $y=a+b\exp(-0.5(x-c)/d)^2$ (Gaussian)

$a=-0.17969329$ $b=0.91700264$

$c=0.57544777$ $d=114.14576$

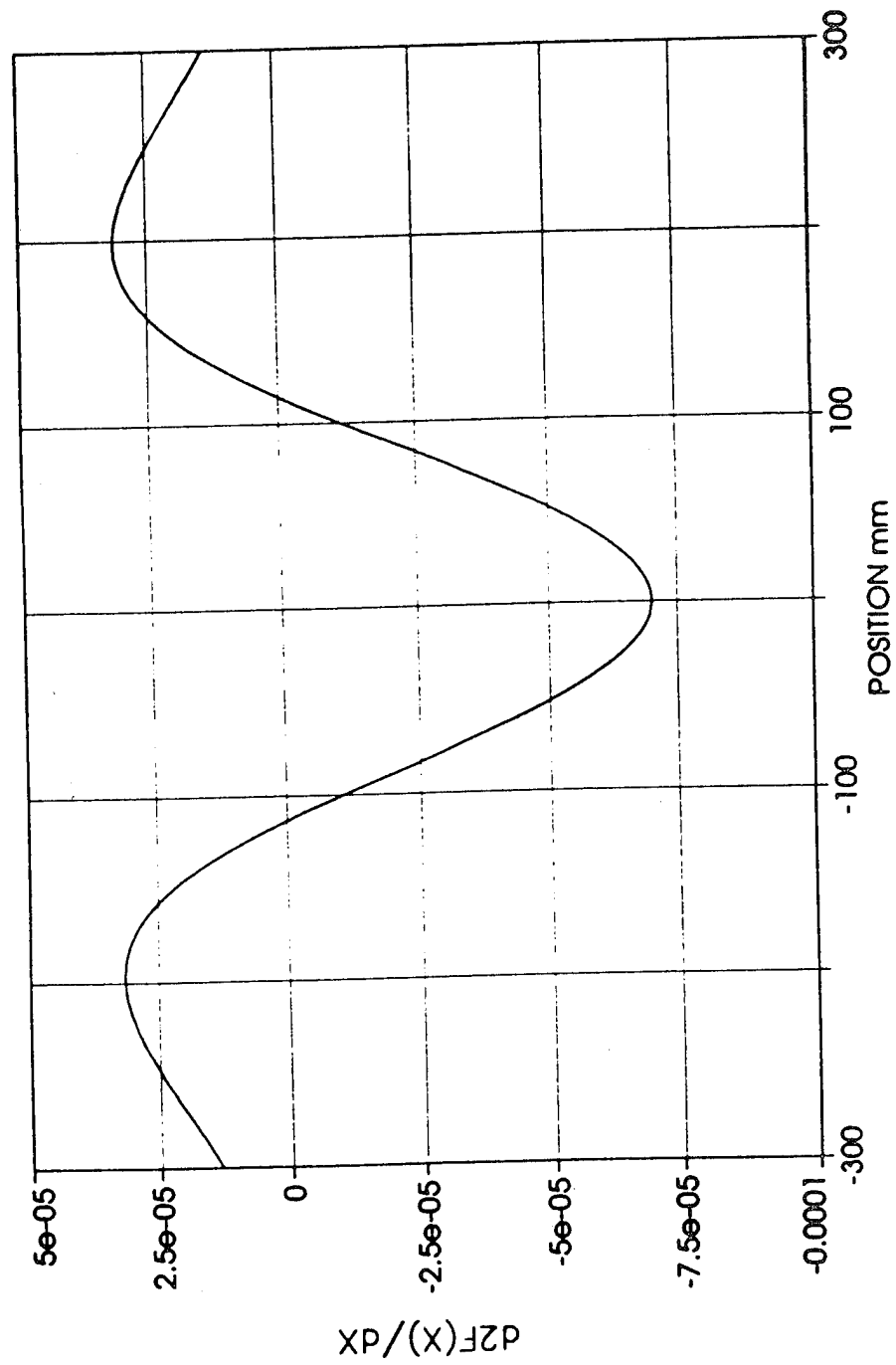


Fig 4.62 Second derivative of Fig 4.60, P-P aluminium beam.

Panel Tests - Runs 14, 24, 27, 28

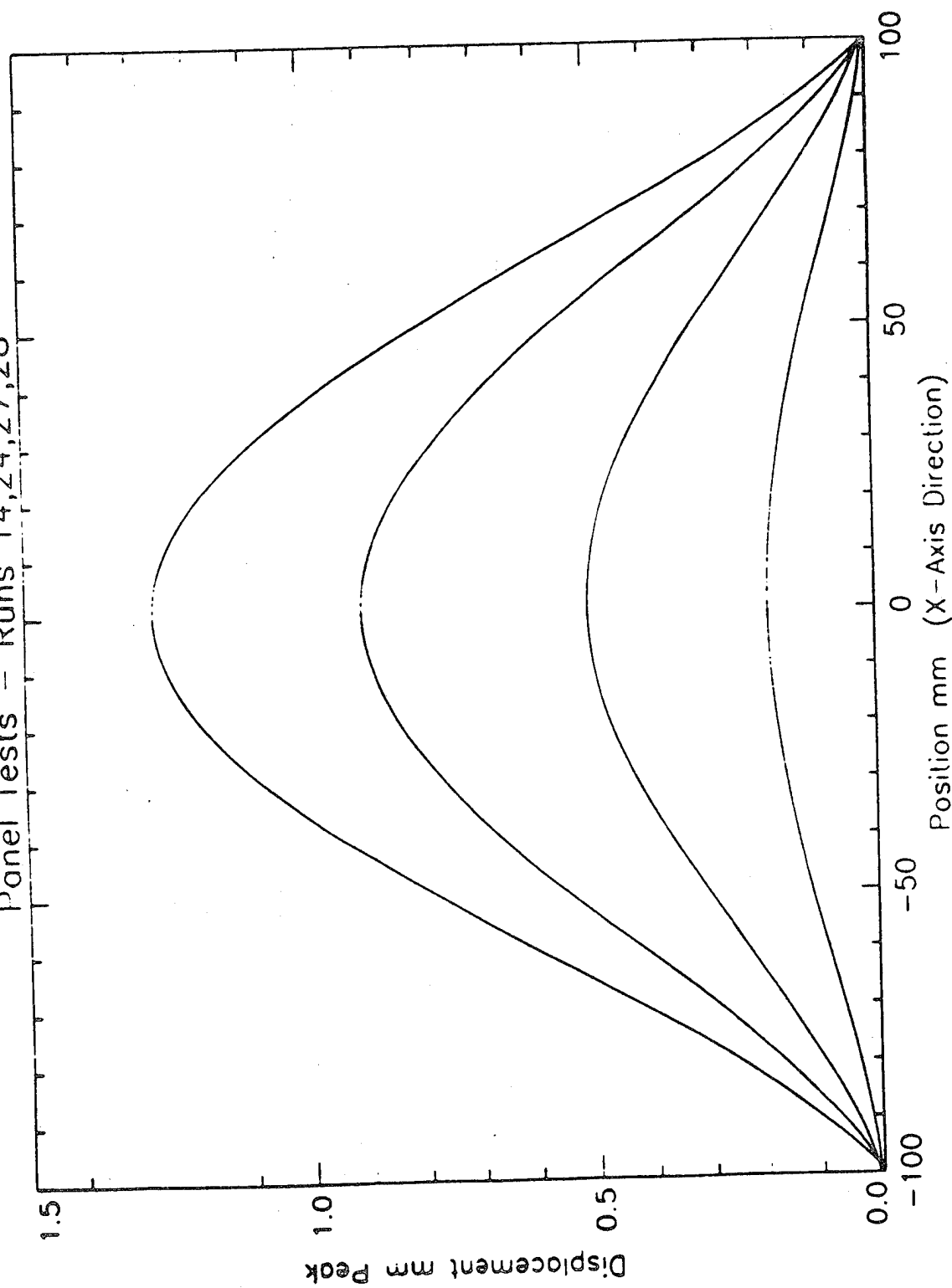


Fig 4.63 Fourth order polynomial fit of displacement shapes, width direction, C-C-C-C aluminium shaker plate.

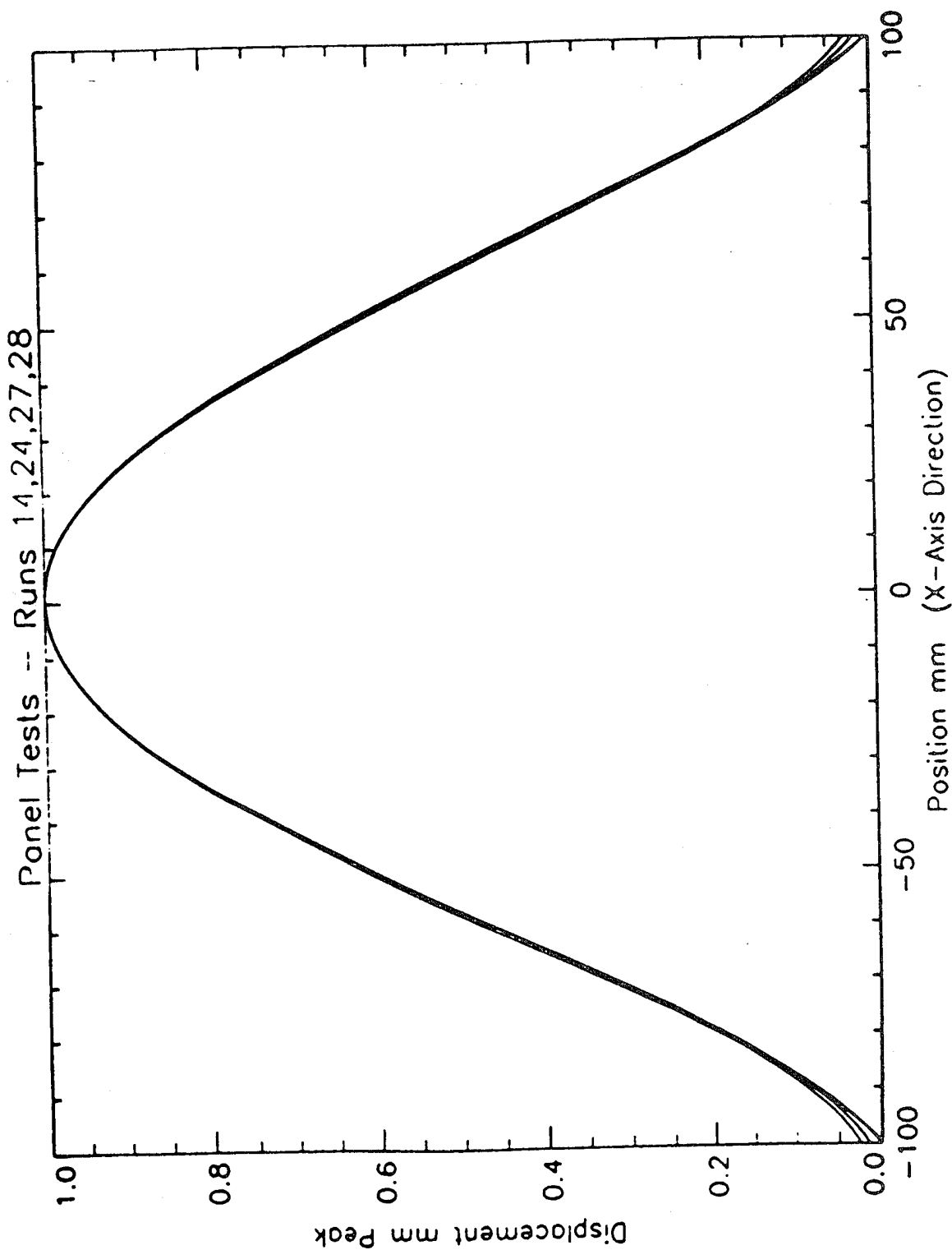


Fig 4.64 Normalised displacement shapes from Fig 4.63, C-C-C-C aluminium shaker plate.

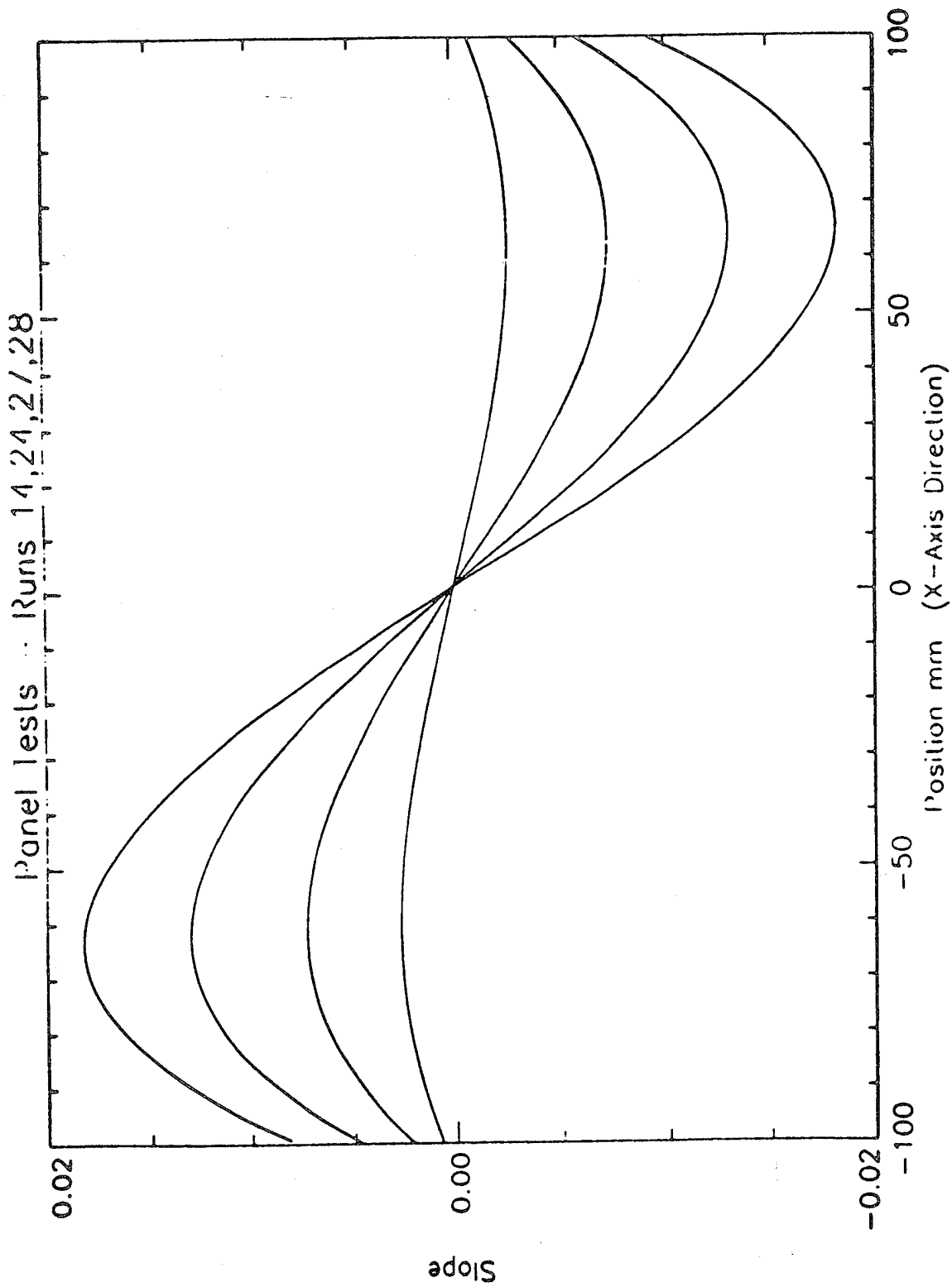


Fig 4.65 First derivatives of Fig 4.63, C-C-C-C aluminium shaker plate.

Panel Tests - Runs 14,24,27,28

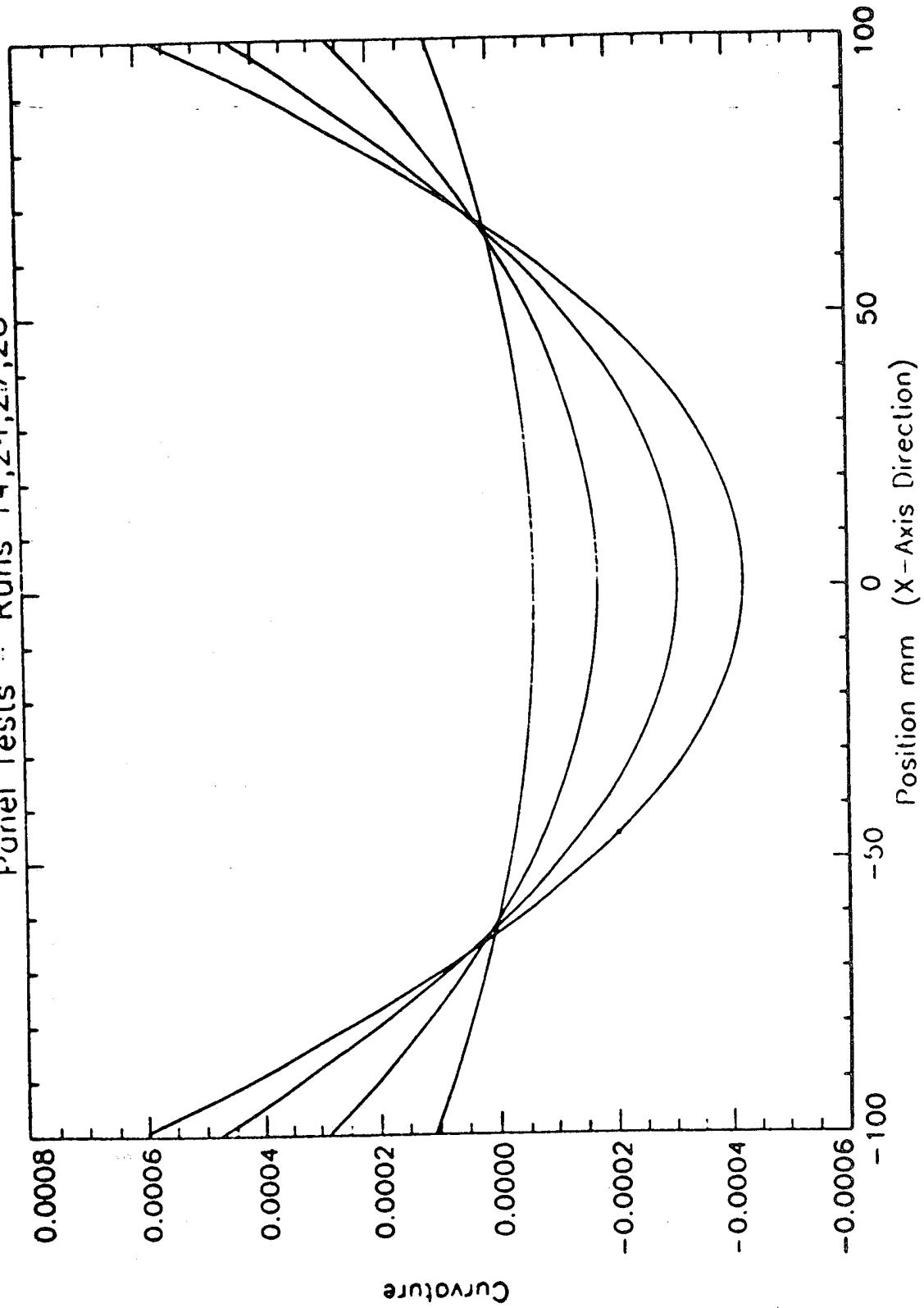


Fig 4.66 Second derivatives of Fig 4.63, C-C-C-C aluminium shaker plate.

Panel Tests - Runs 15,25,26,29

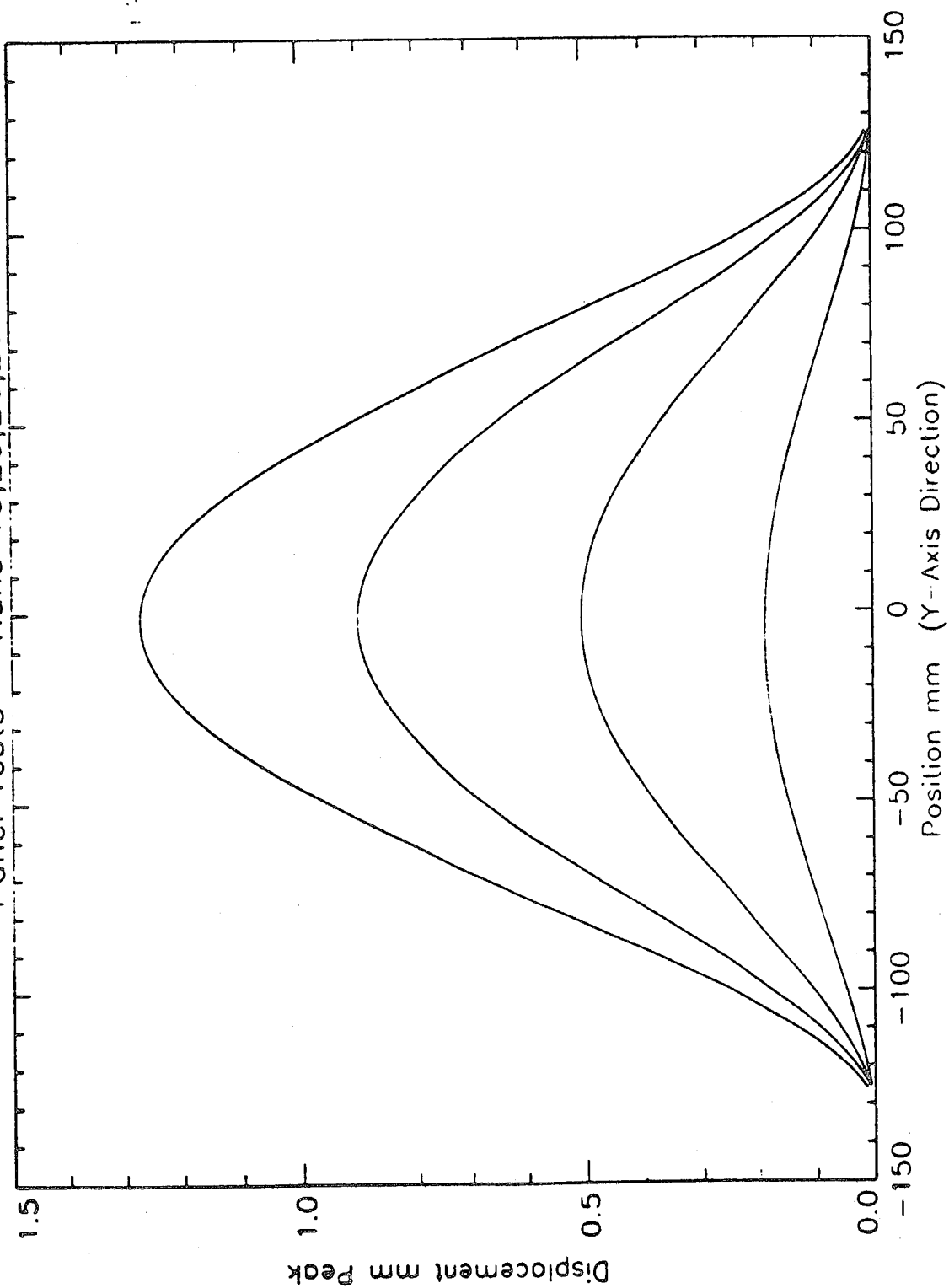


Fig 4.67 Fourth order polynomial fit of displacement shapes, length direction, C-C-C-C aluminium shaker plate.

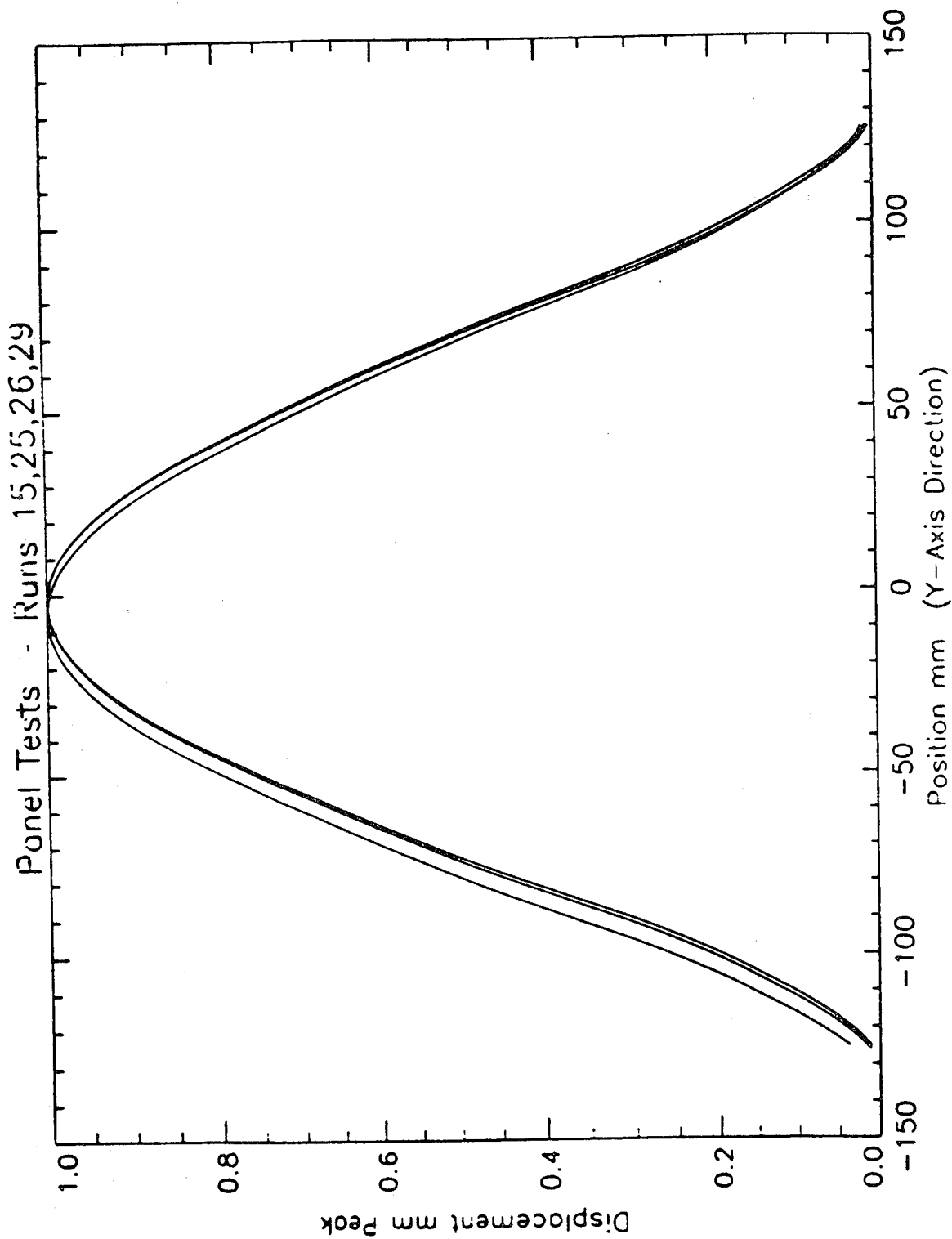


Fig 4.68 Normalised displacement shapes from Fig 4.67 C-C-C-C aluminium shaker plate.

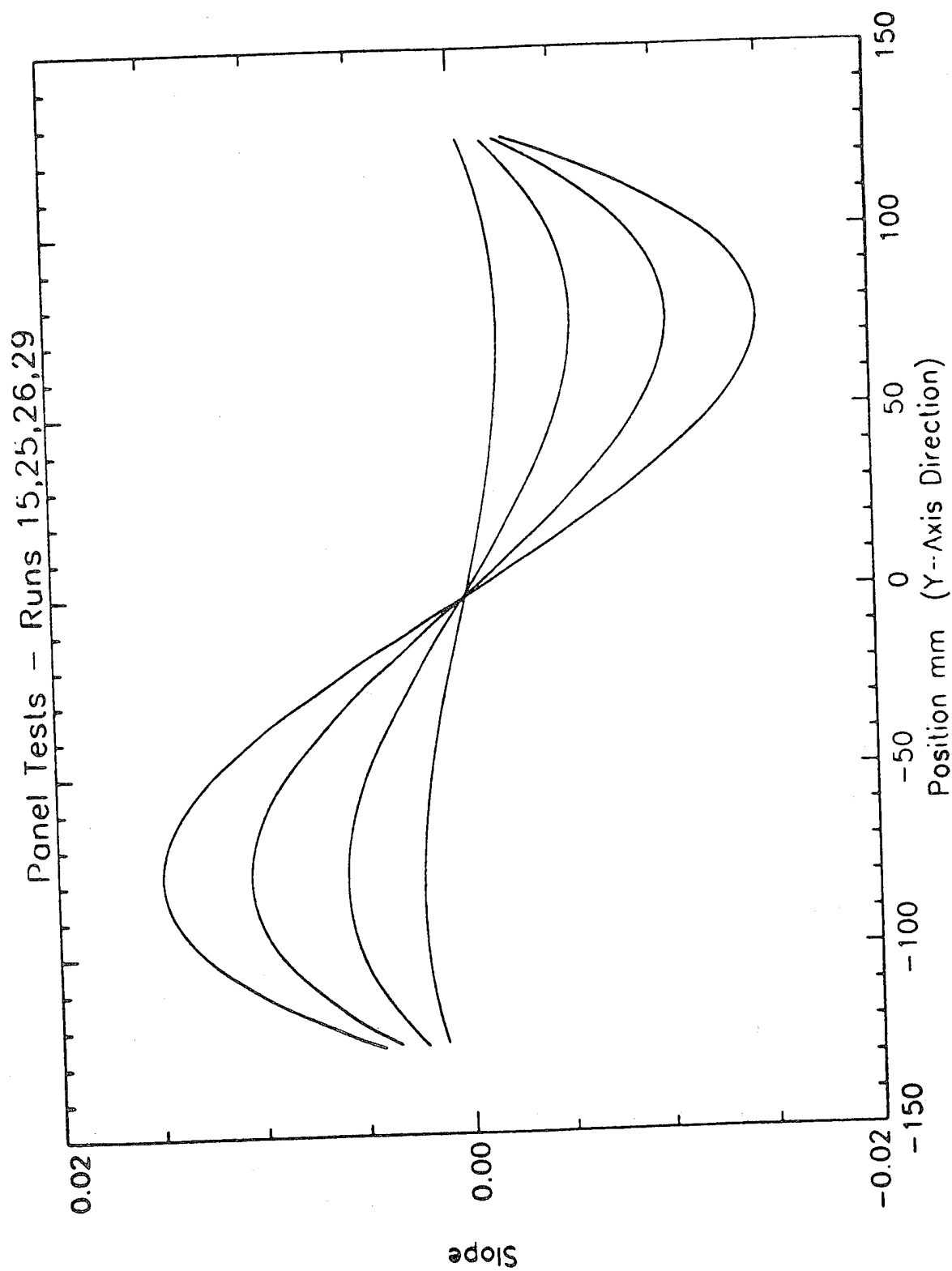


Fig 4.69 First derivative of Fig 4.67, C-C-C-C aluminium shaker plate.

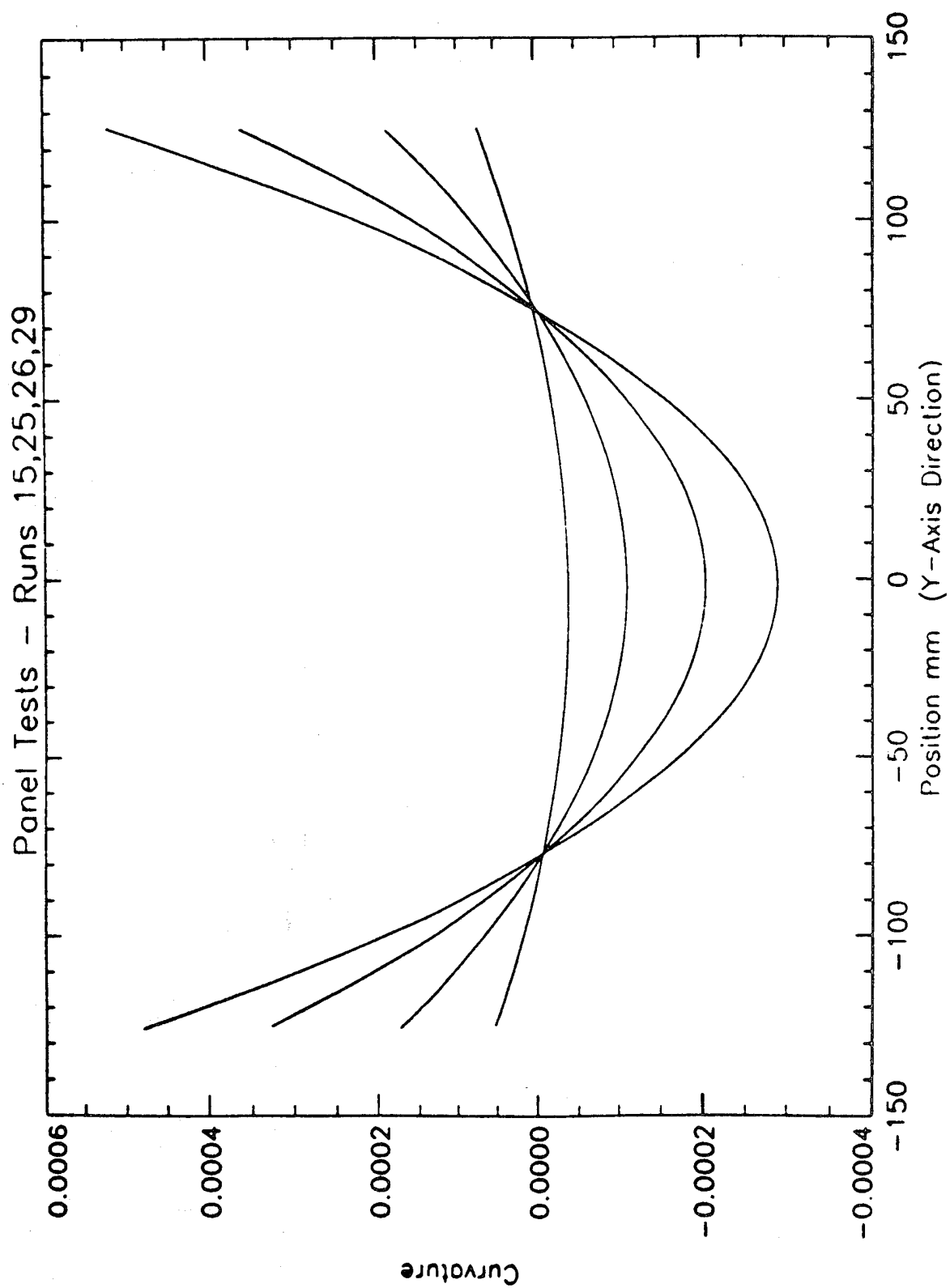


Fig 4.70 Second derivative of Fig 4.67, C-C-C-C aluminium shaker plate.

SHAKER PLATE NONLINEAR DISP SHAPES 4th ORDER POLYNOMIAL COEFFICIENTS 'a'

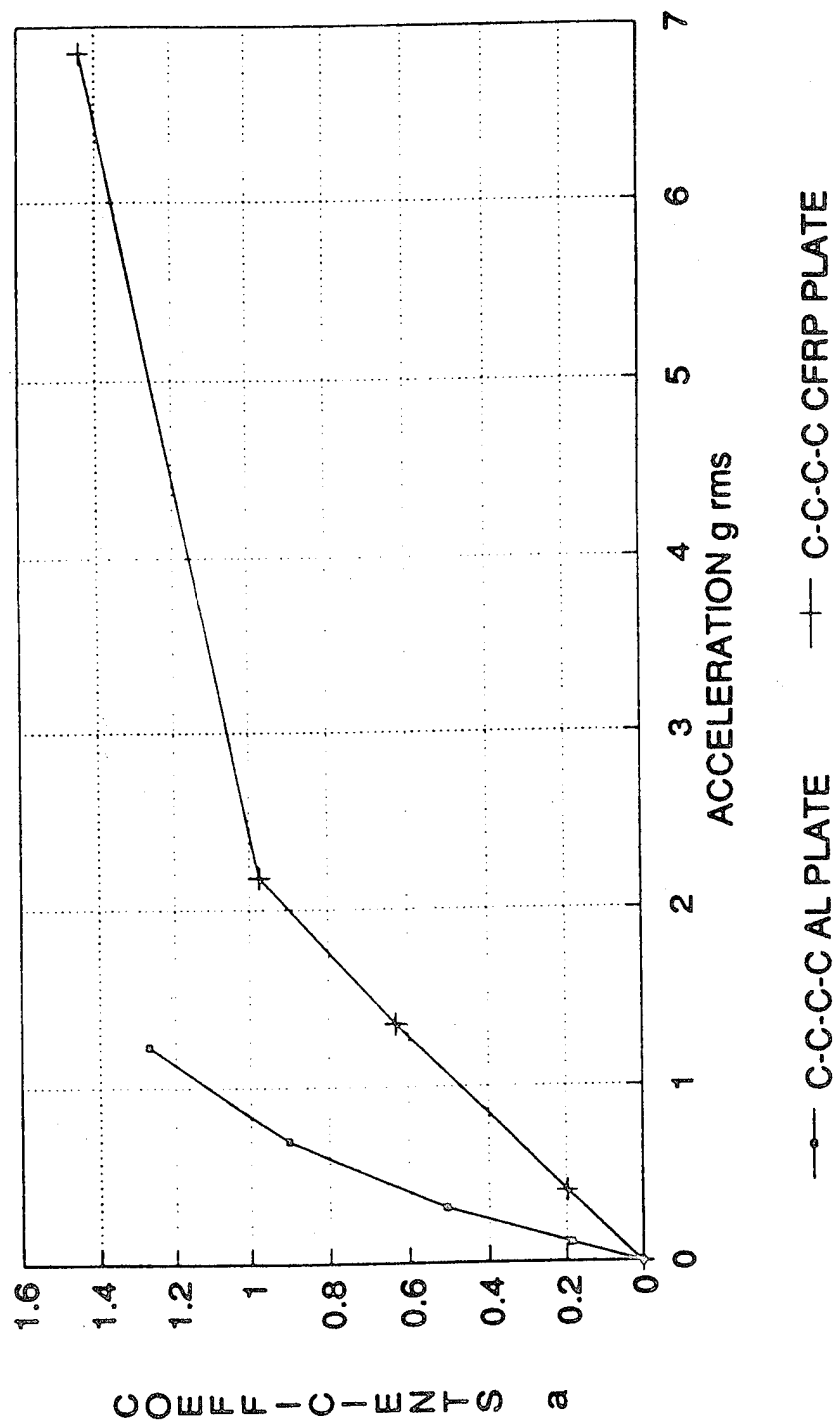


Fig 4.71 Coefficients 'a' for fourth order polynomial fits, C-C-C-C aluminium and CFRP shaker plates.

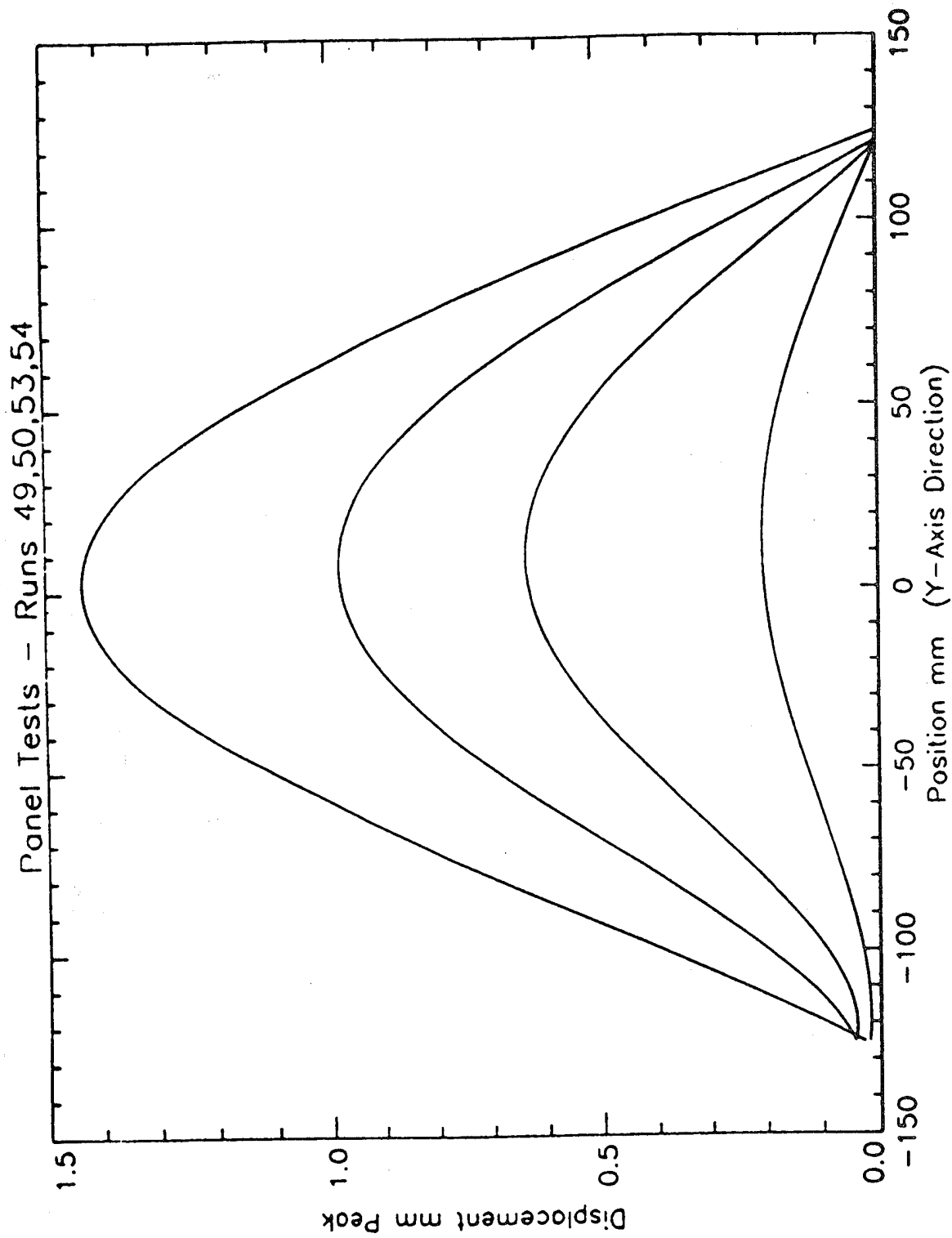


Fig 4.72 Fourth order polynomial fit of displacement shapes, length direction, C-C-C-C CFRP shaker plate.

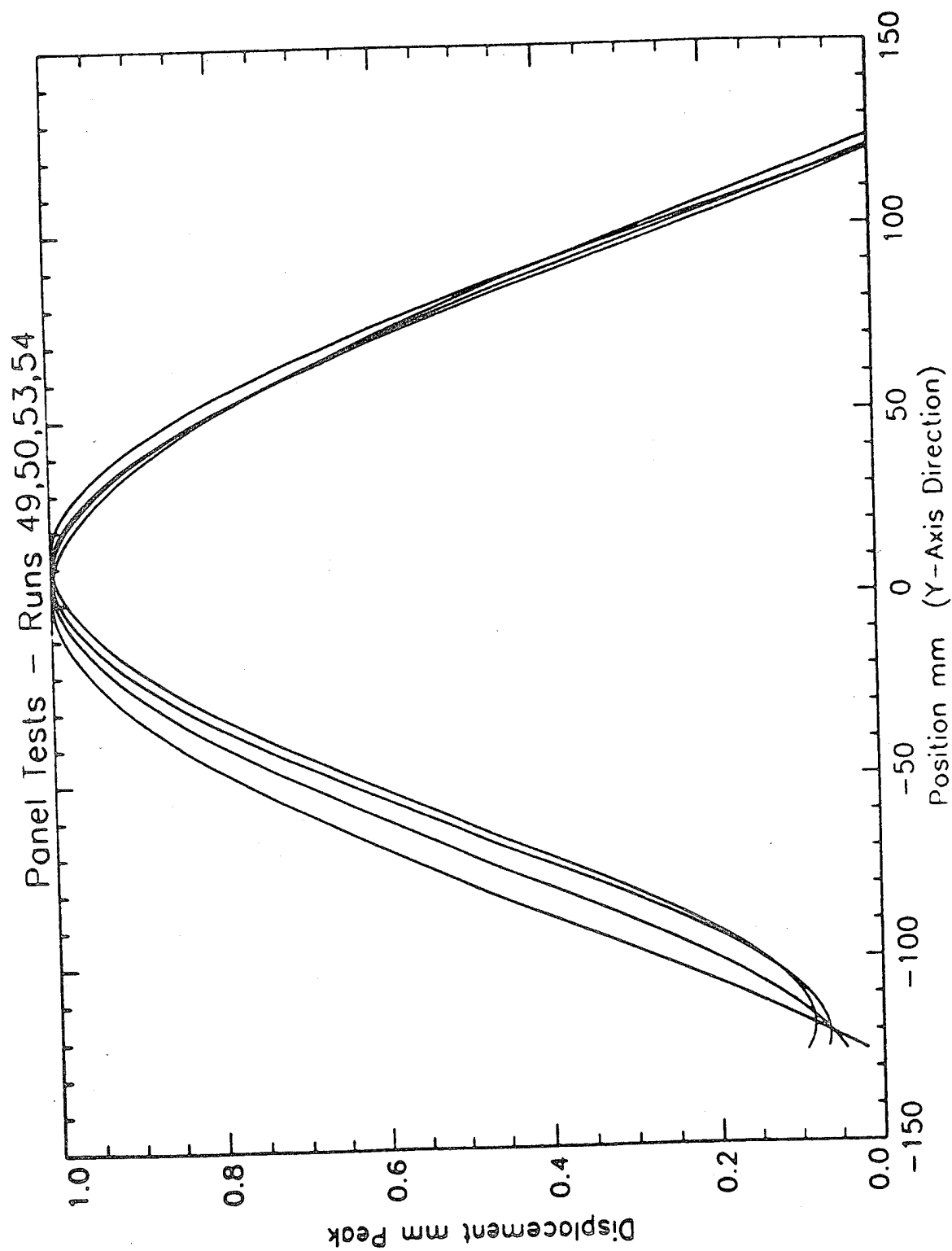


Fig 4.73 Normalised displacement shapes from Fig 4.72, C-C-C-C CFRP shaker plate.

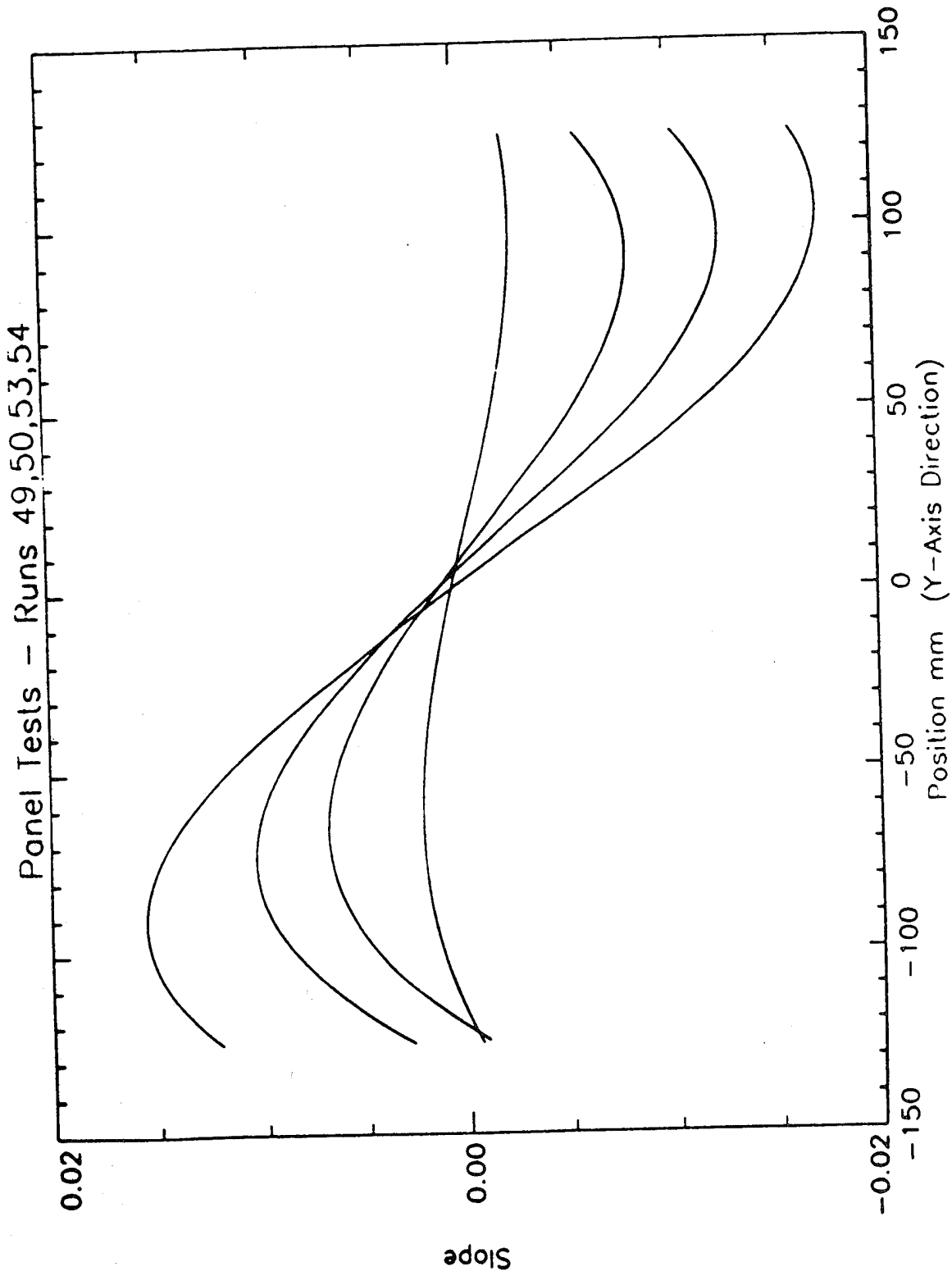


Fig 4.74 First derivative of Fig 4.72, C-C-C-C CFRP shaker plate.

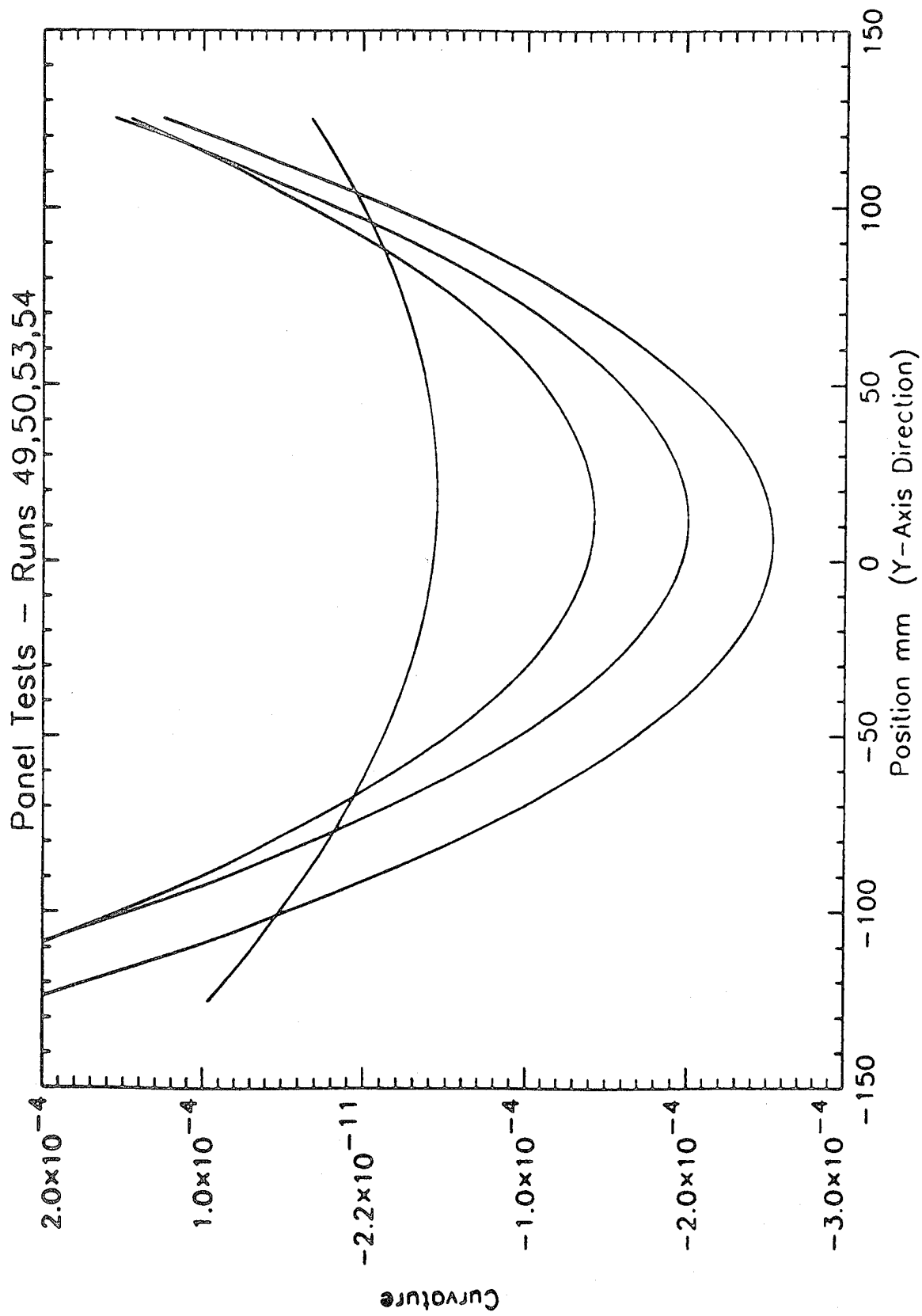


Fig 4.75 Second derivative of Fig 4.72, C-C-C-C CFRP shaker plate.

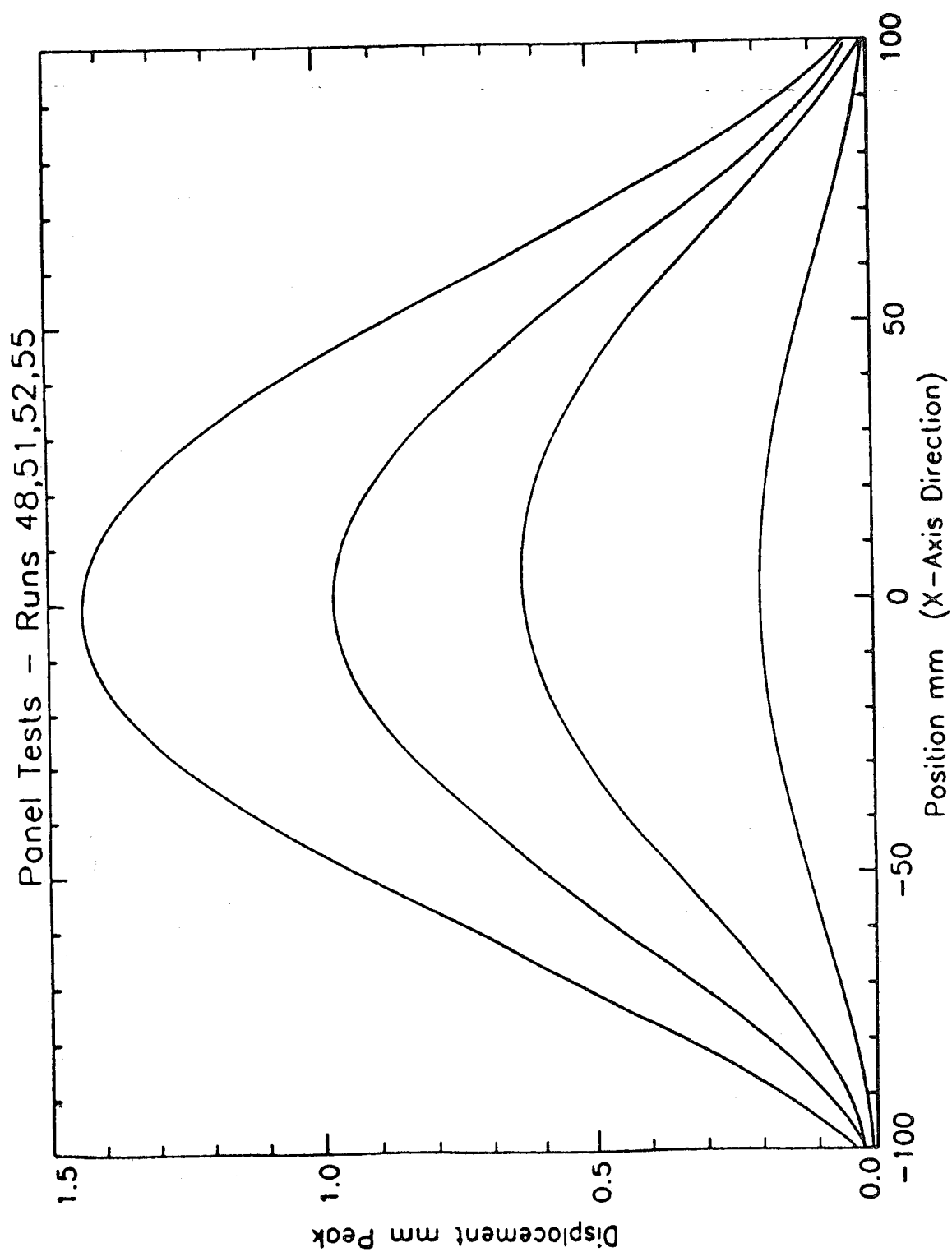


Fig 4.76 Fourth order polynomial fit of displacement shapes, width direction, C-C-C-C CFRP shaker plate.

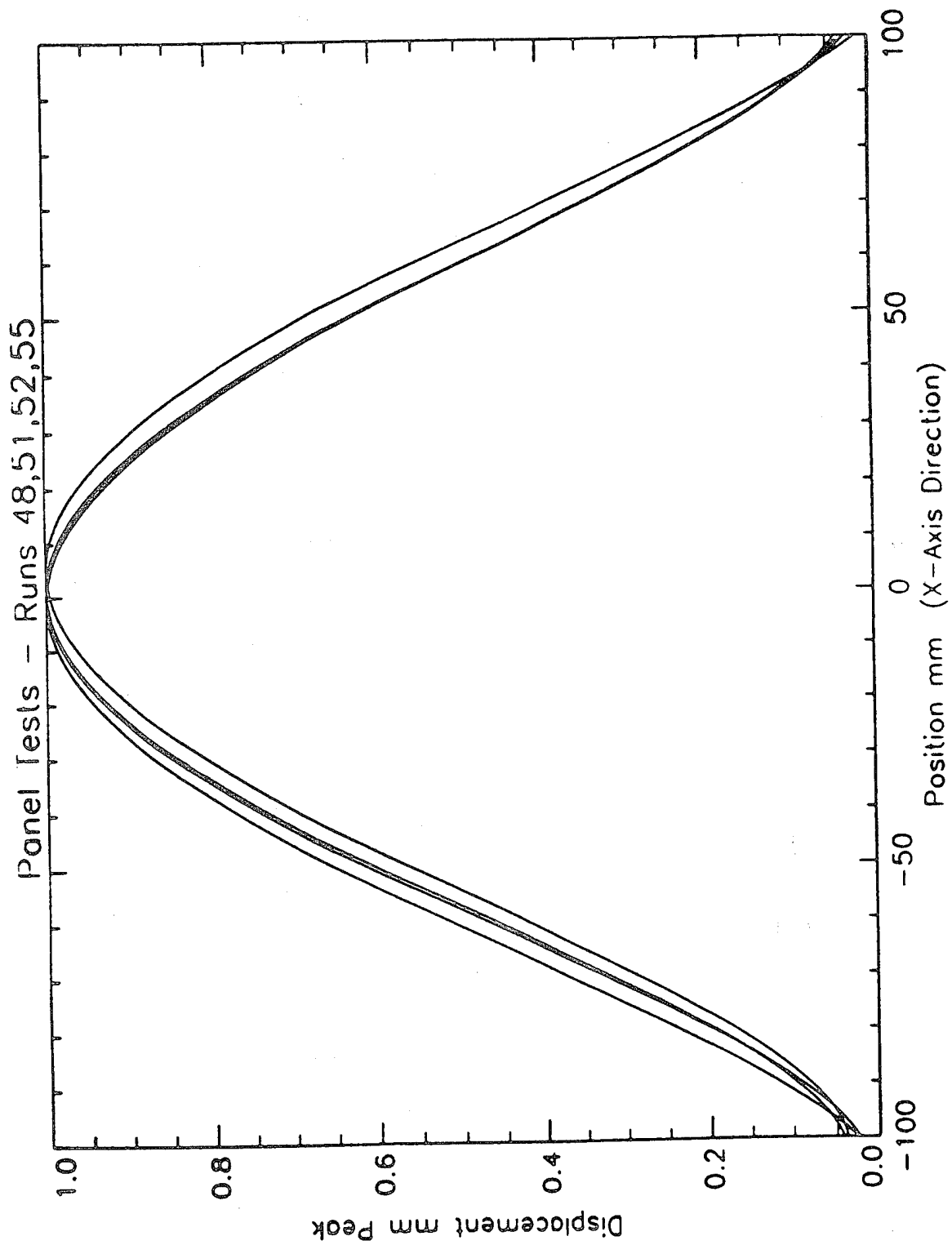


Fig 4.77 Normalised displacement shapes of Fig 4.76, C-C-C-C CFRP shaker plate.

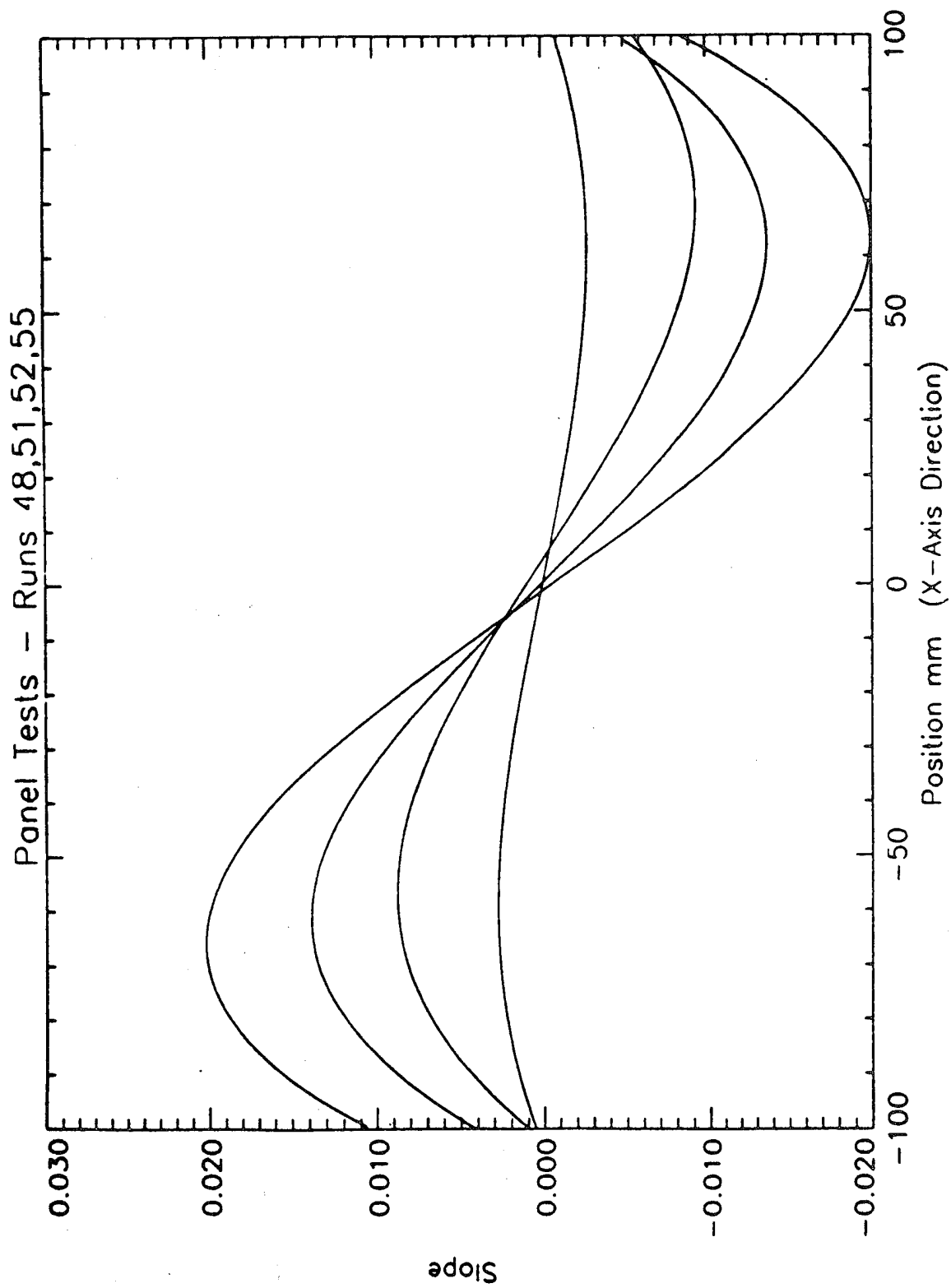


Fig 4.78 First derivative of Fig 4.76, C-C-C-C CFRP shaker plate.

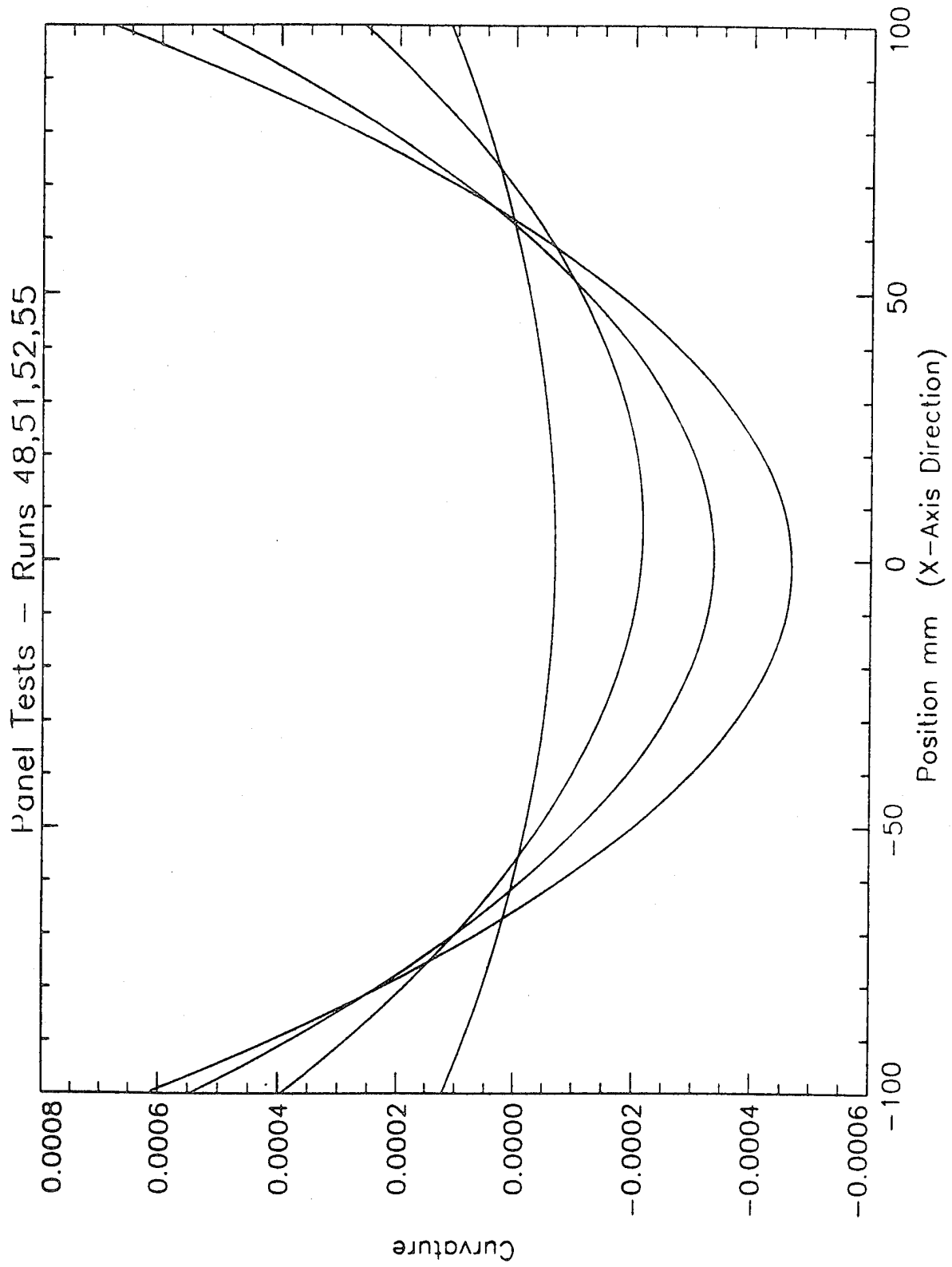


Fig 4.79 Second derivative of Fig 4.76, C-C-C-C CFRP shaker plate.

COMPARISONS OF THE FUNDAMENTAL RESONANCE CONTRIBUTION WITH INCREASING STRAIN LEVELS

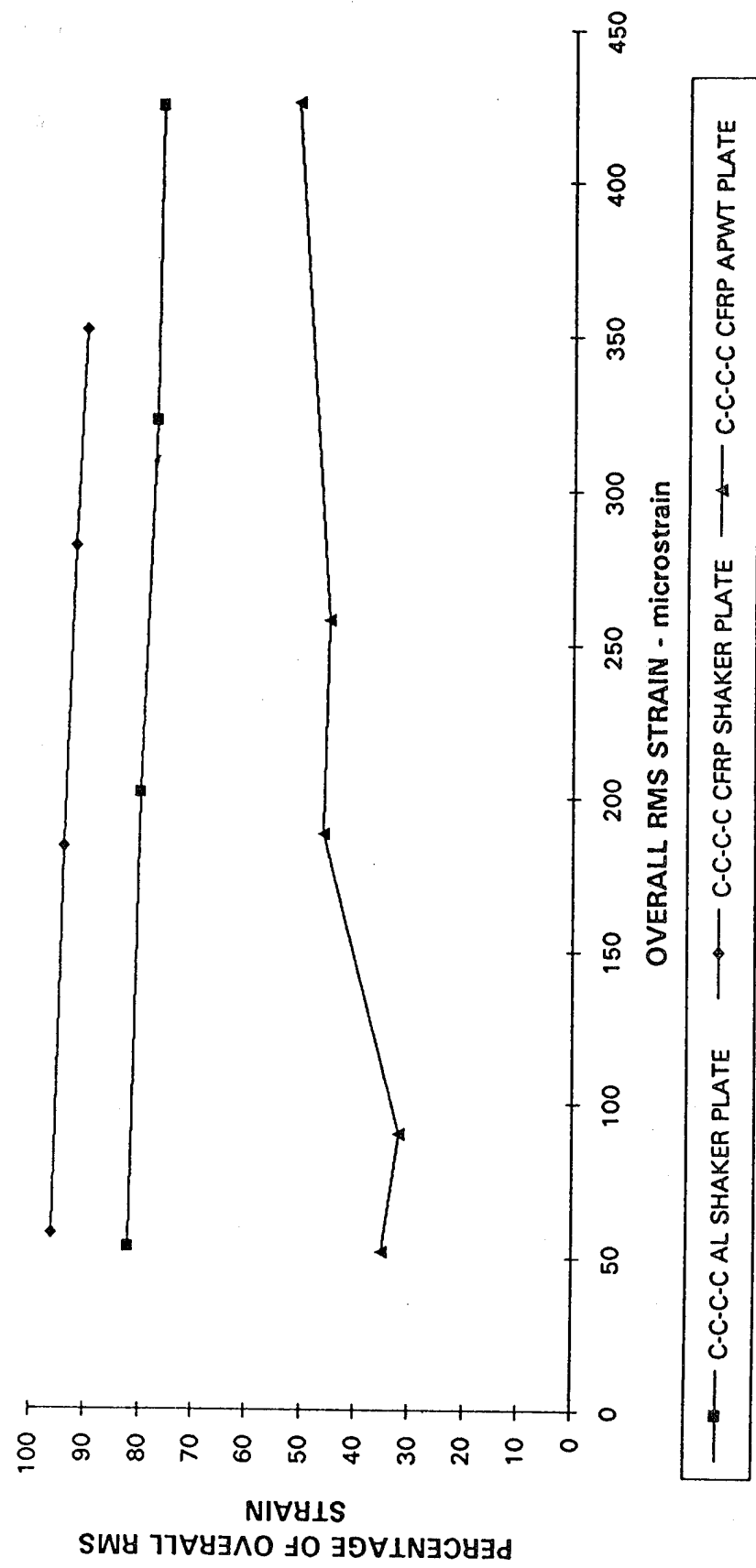


Fig 4.80 Comparison of the fundamental resonance contribution with increasing strain levels.

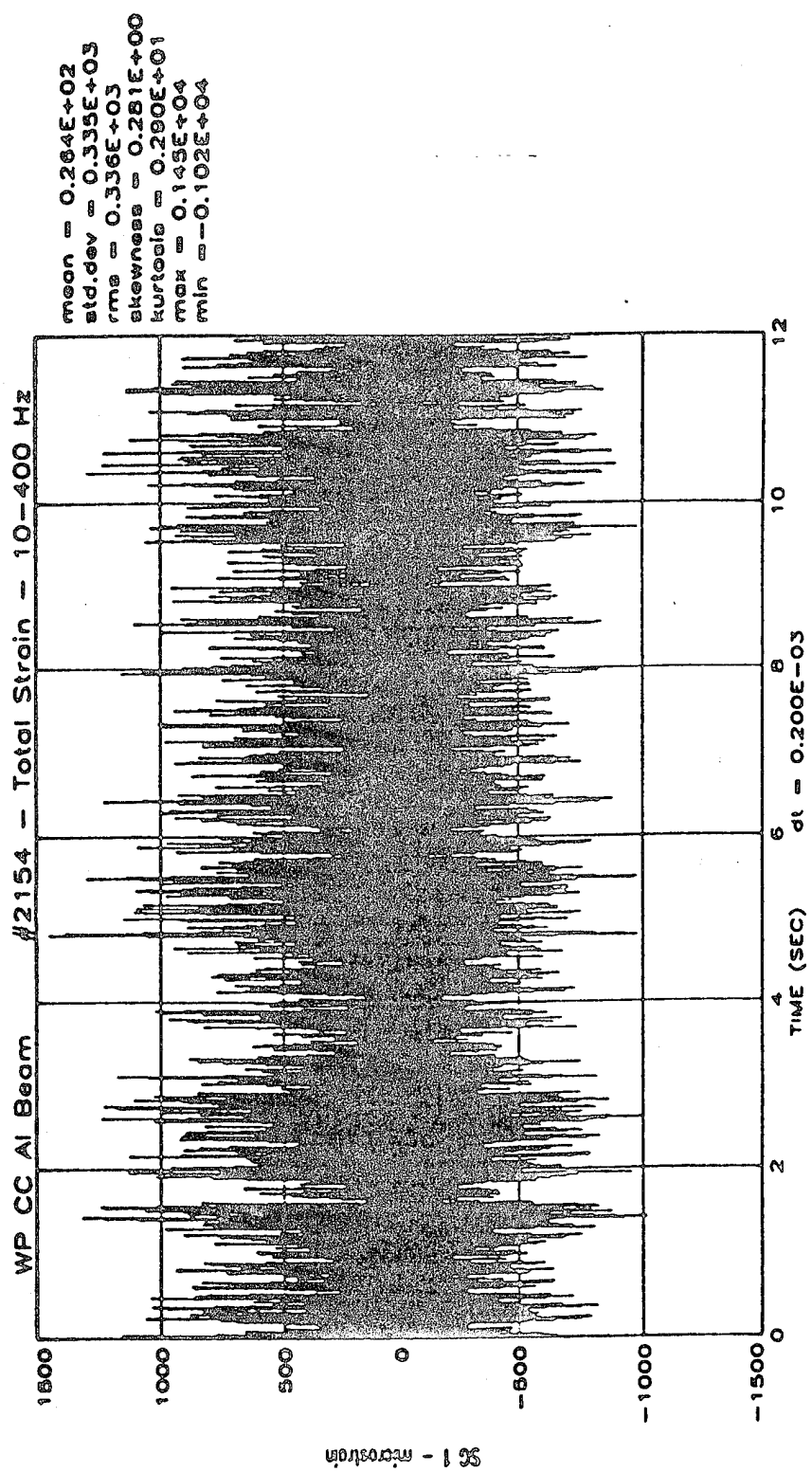


Fig 5.1 Strain time history, 0 to 12 seconds, 10-400 Hz random excitation, C-C aluminium beam.

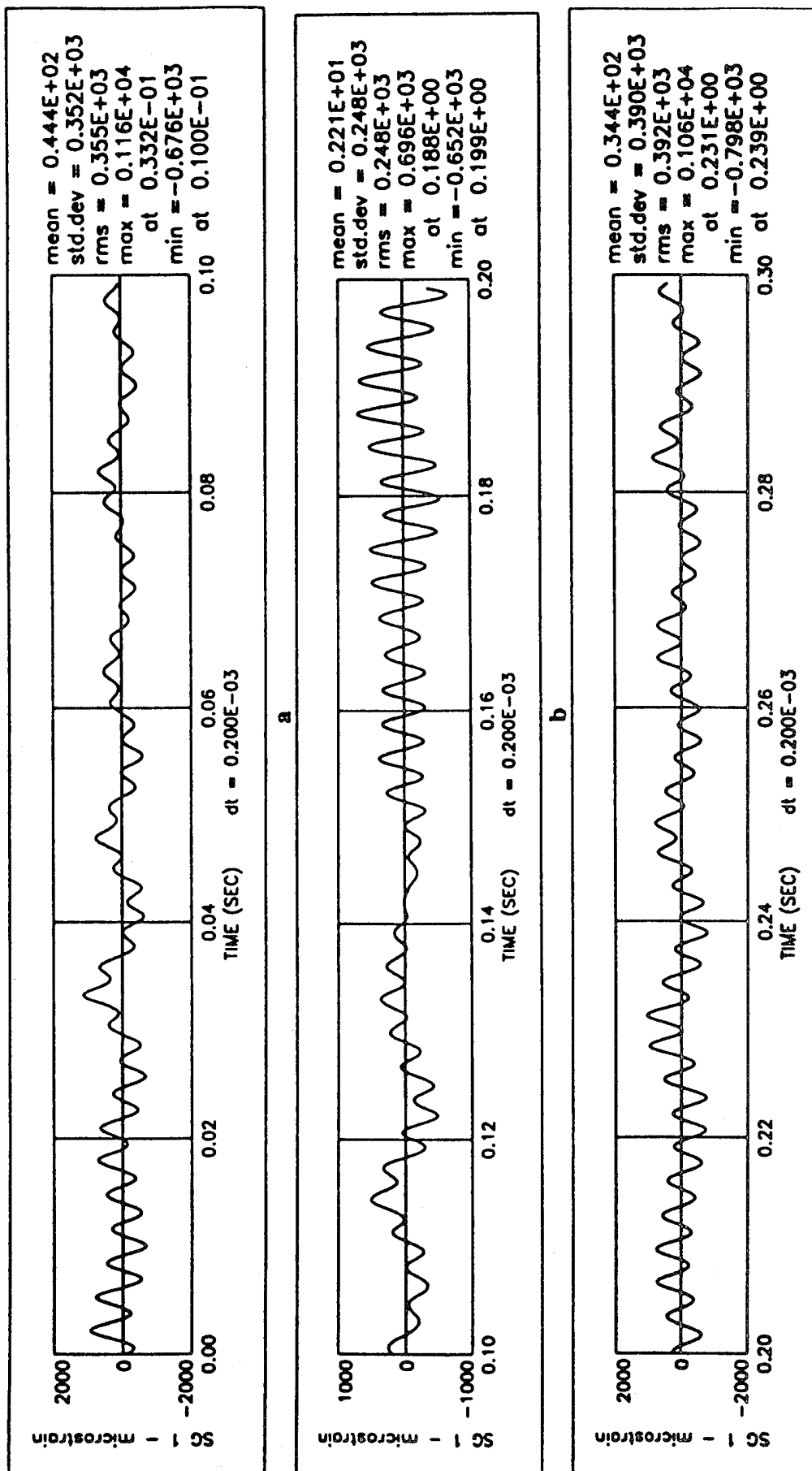


Fig 5.2 Expanded time history from Fig 5.1, a= 0-0.1 s, b=0.1-0.2 s, c=0.2-0.3 s.

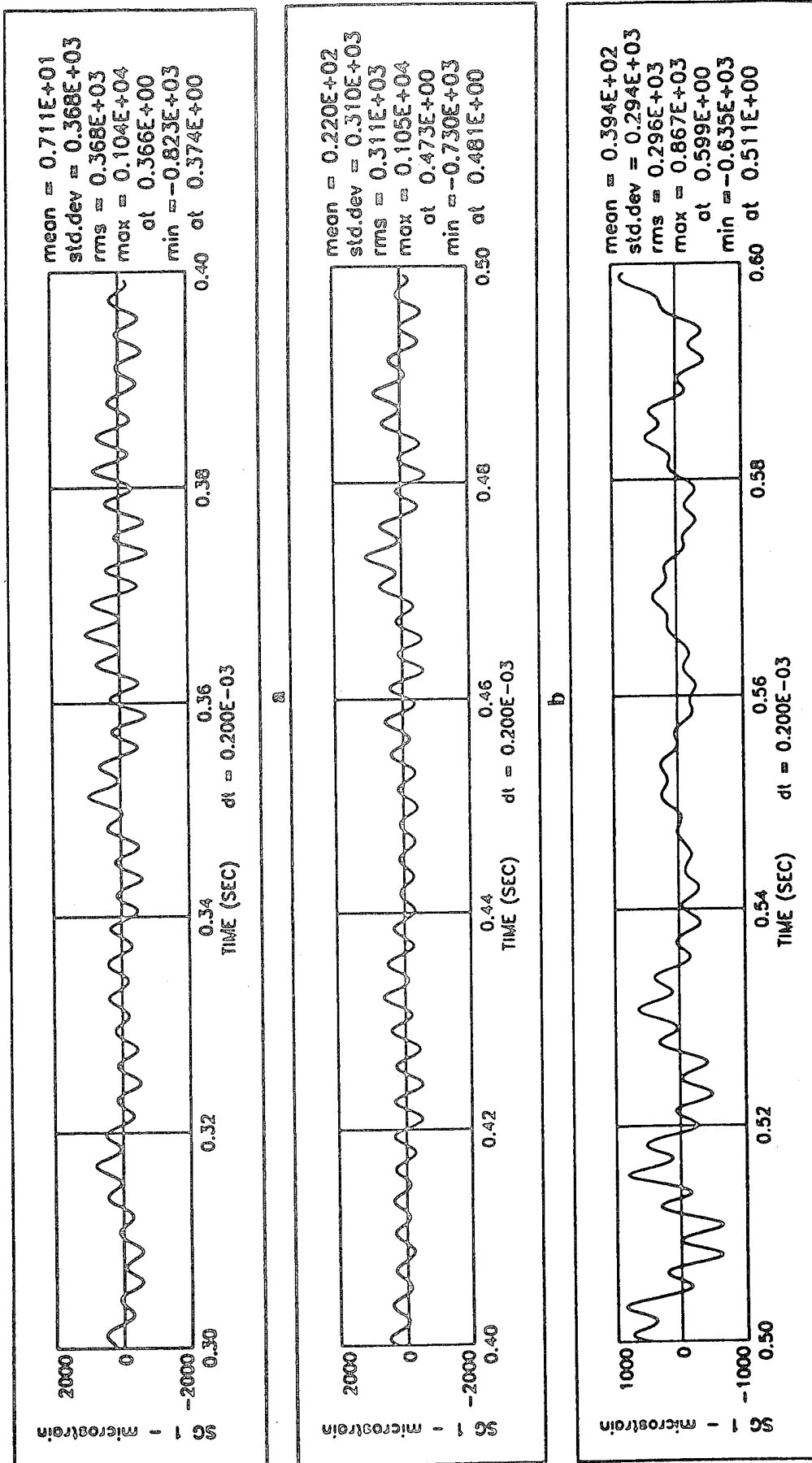


Fig 5.3 Expanded time history from Fig 5.1, a=0.3-0.4 s, b=0.4-0.5 s, c=0.5-0.6 s.

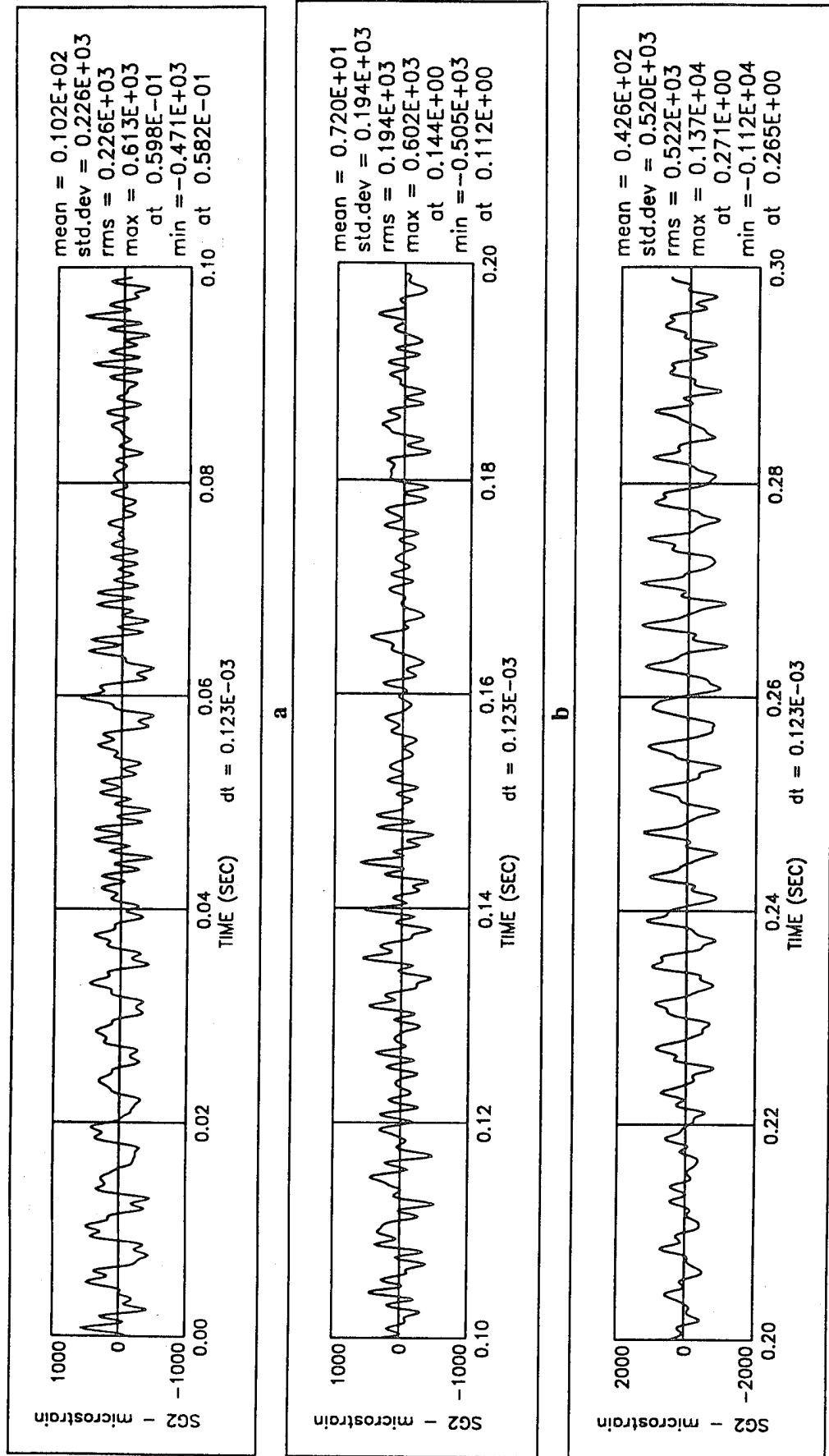


Fig 5.4 Clamped aluminium shaker plate , time histories, 10-1000 Hz random excitation, $a=0.1$ s, $b=0.1-0.2$ s, $c=0.2-0.3$ s.

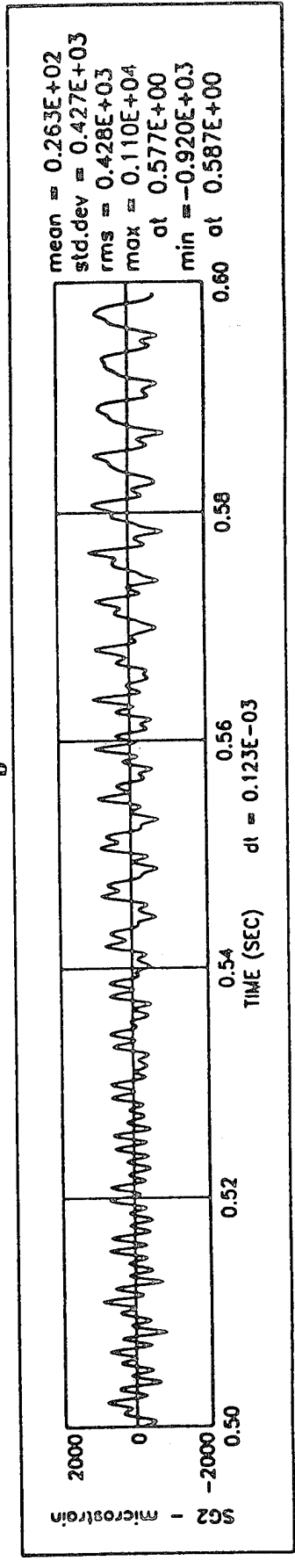
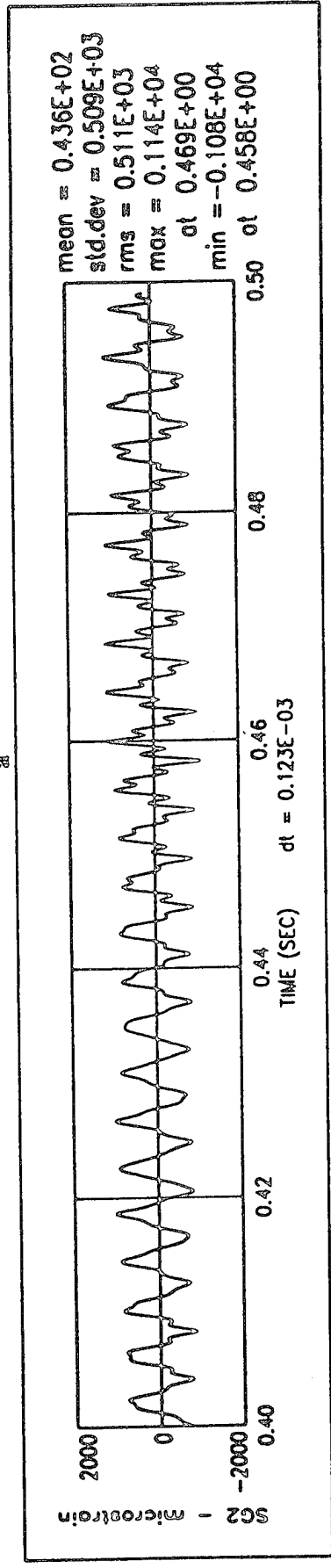
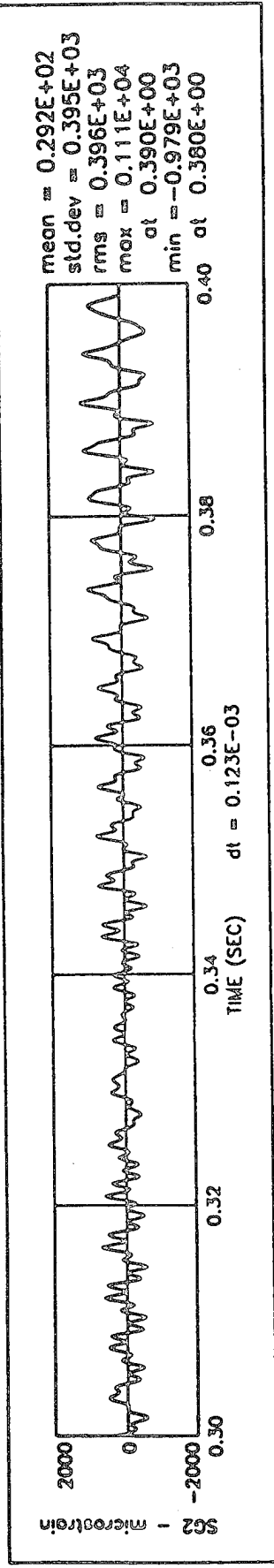


Fig 5.5 Clamped aluminium shaker plate, time histories, 10-1000 Hz random excitation, a=0.3-0.4 s, b=0.4-0.5 s, c=0.5-0.6 s.

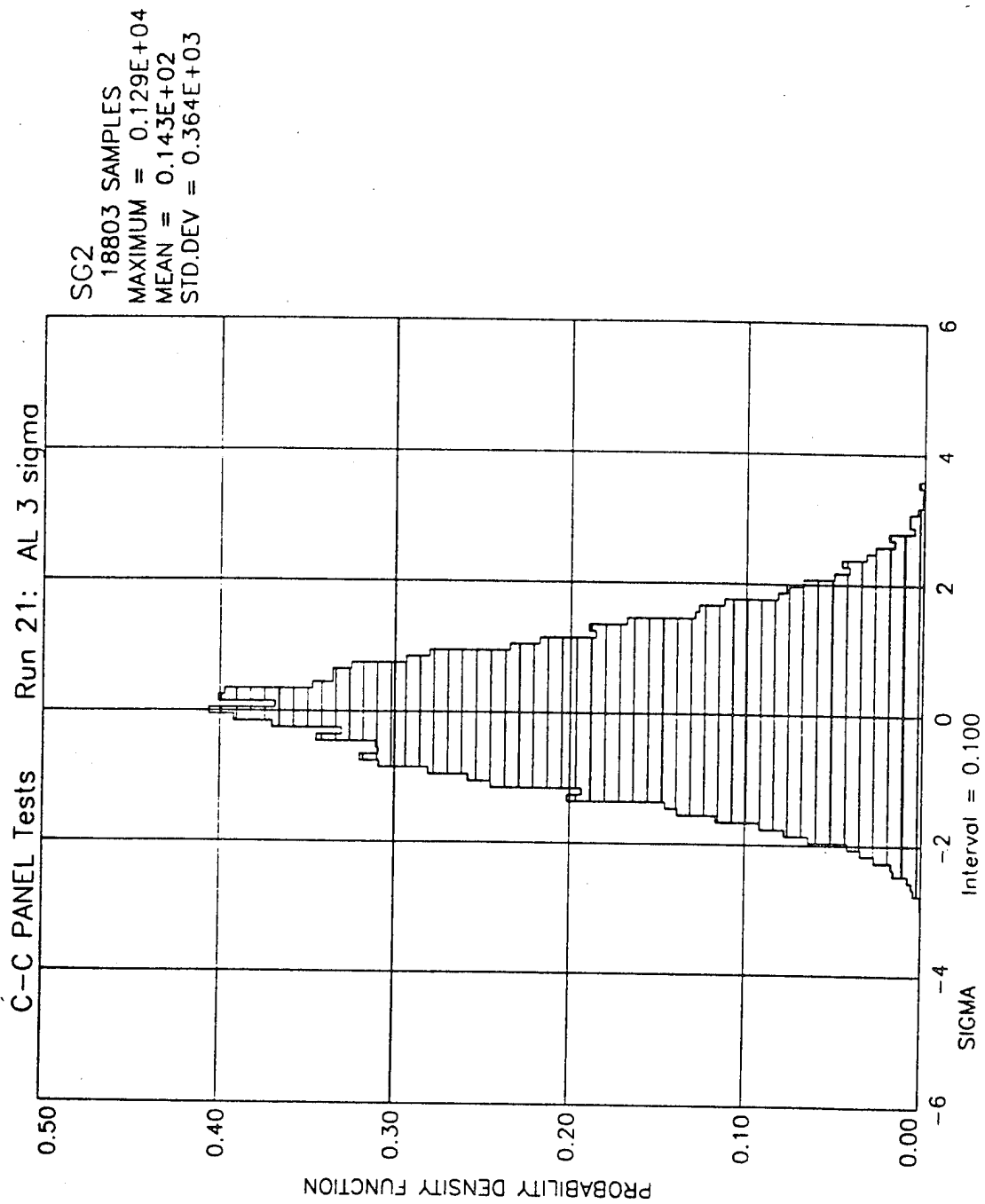


Fig 5.6 Minor peaks, PPDF, run 21, SG2, C-C-C-C aluminium shaker plate.

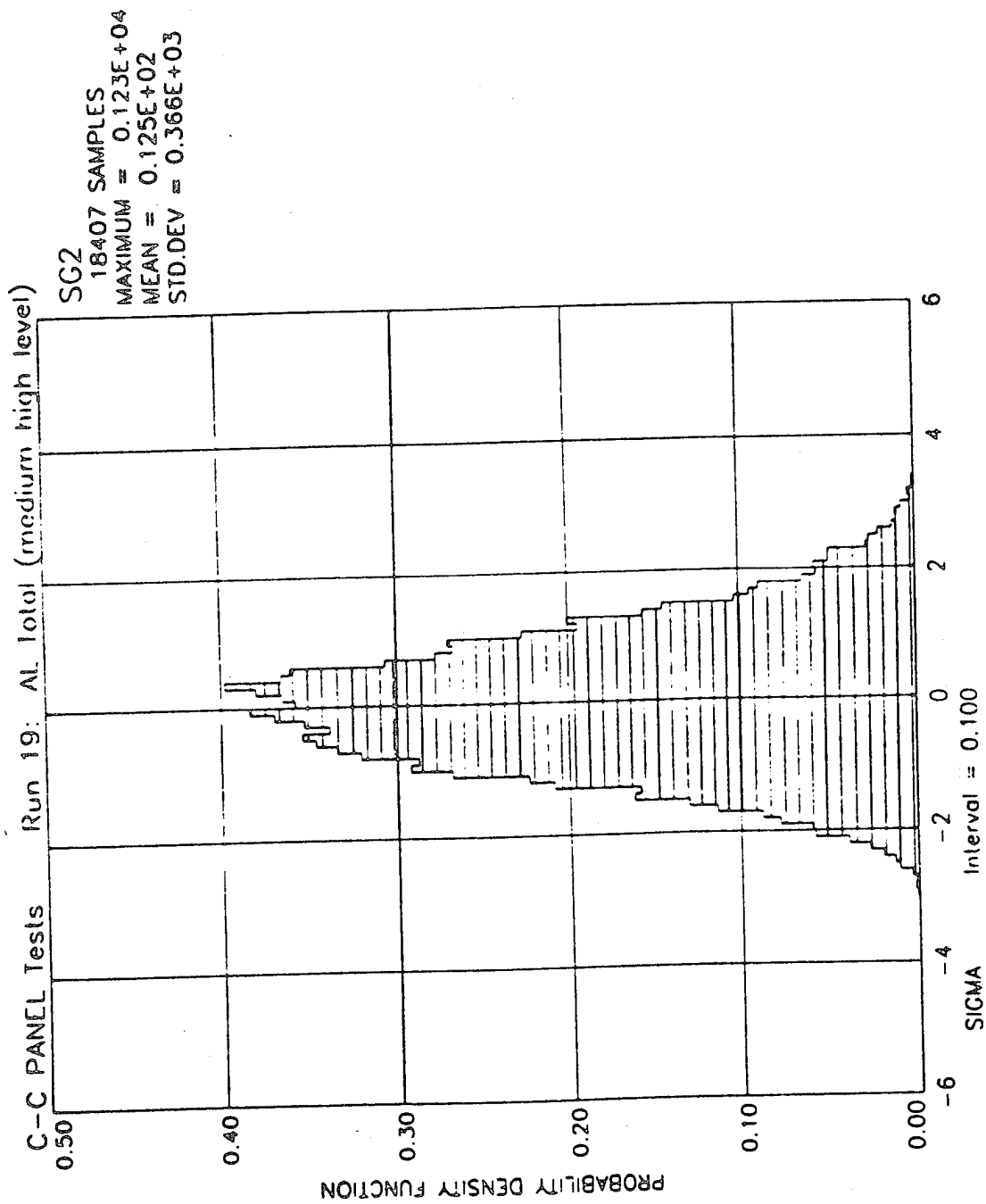


Fig 5.7 Major peaks, PPDF, run 19, SG2, C-C-C-C aluminium shaker plate.

C-C ALUM BEAM 10-400Hz
Peak PDF SG1 Rec 2148, 2154

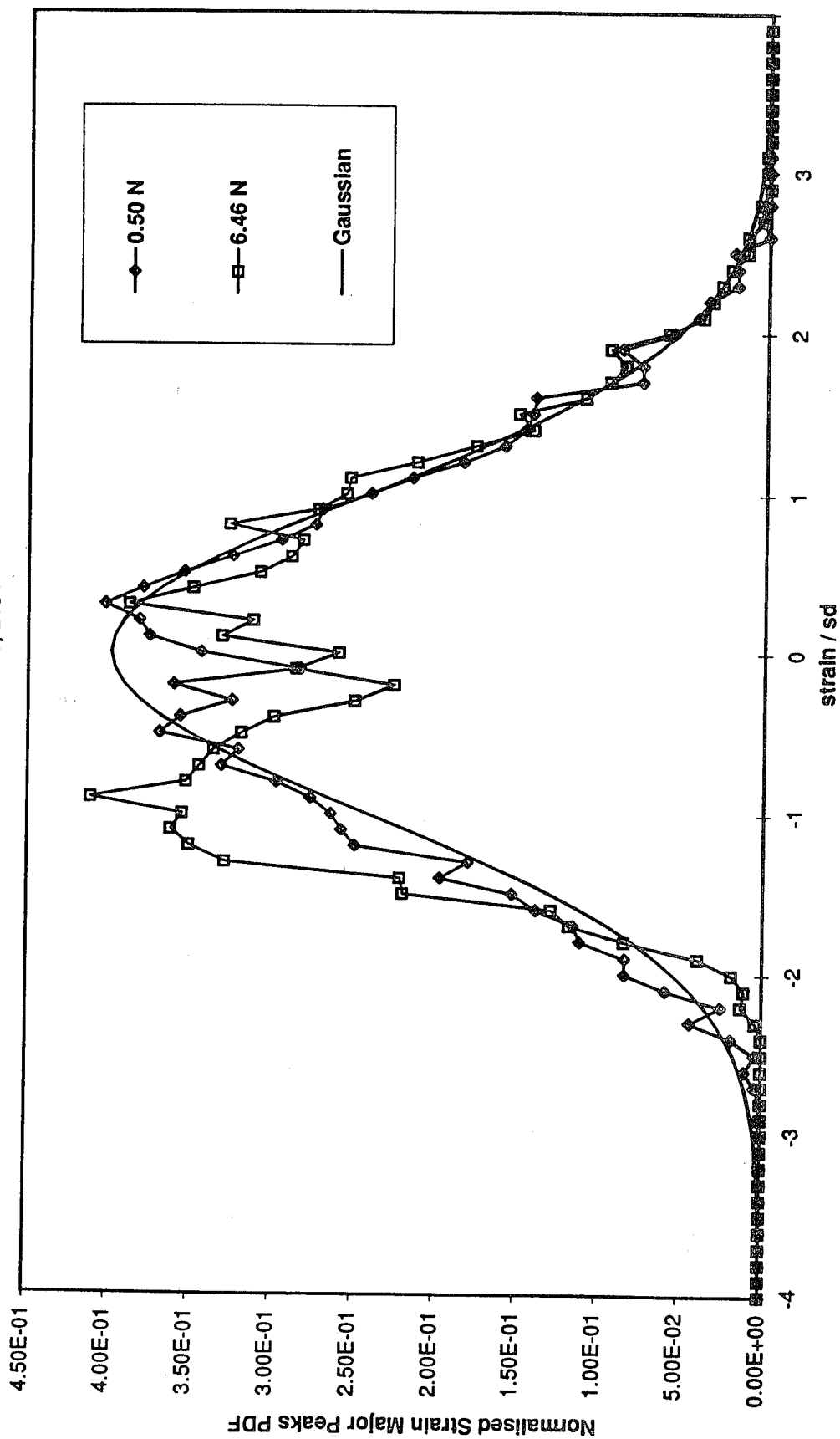


Fig 5.8 Normalised strain major peaks, PPDF, SG1, 10-400 Hz random, 0.50 and 6.46N comparison with Gaussian, C-C aluminium beam

C-C ALUM BEAM 10-400Hz
Peak PDF SG3 Rec 2148, 2154

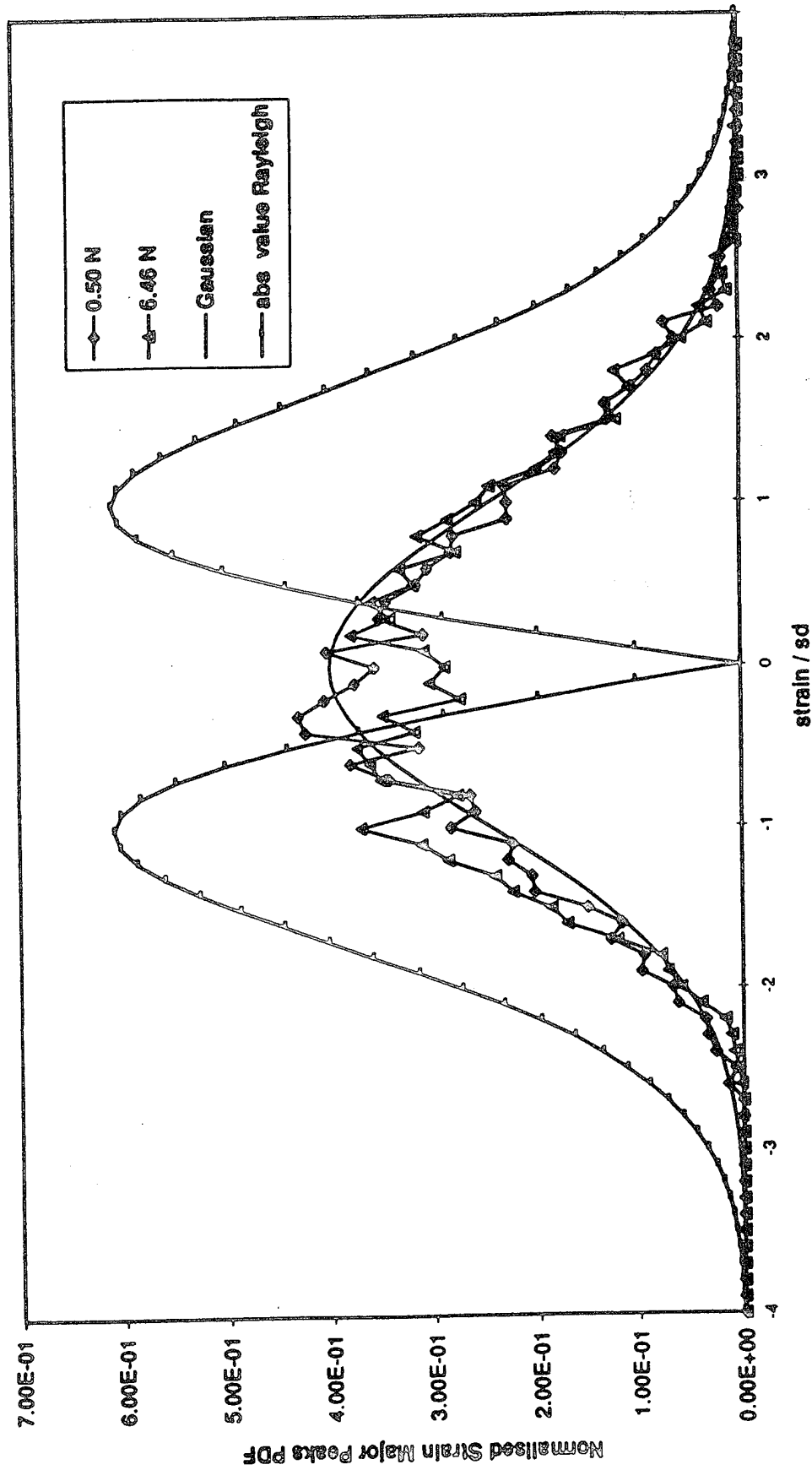


Fig 5.9 Normalised strain major peaks, PPDF, SG3, 10-400 Hz random, 0.50 and 6.46N comparison with Gaussian and Rayleigh C-C aluminium beam.

C-C ALUM BEAM 10-1000 Hz
Peak PDF SG 3 R2155,2162

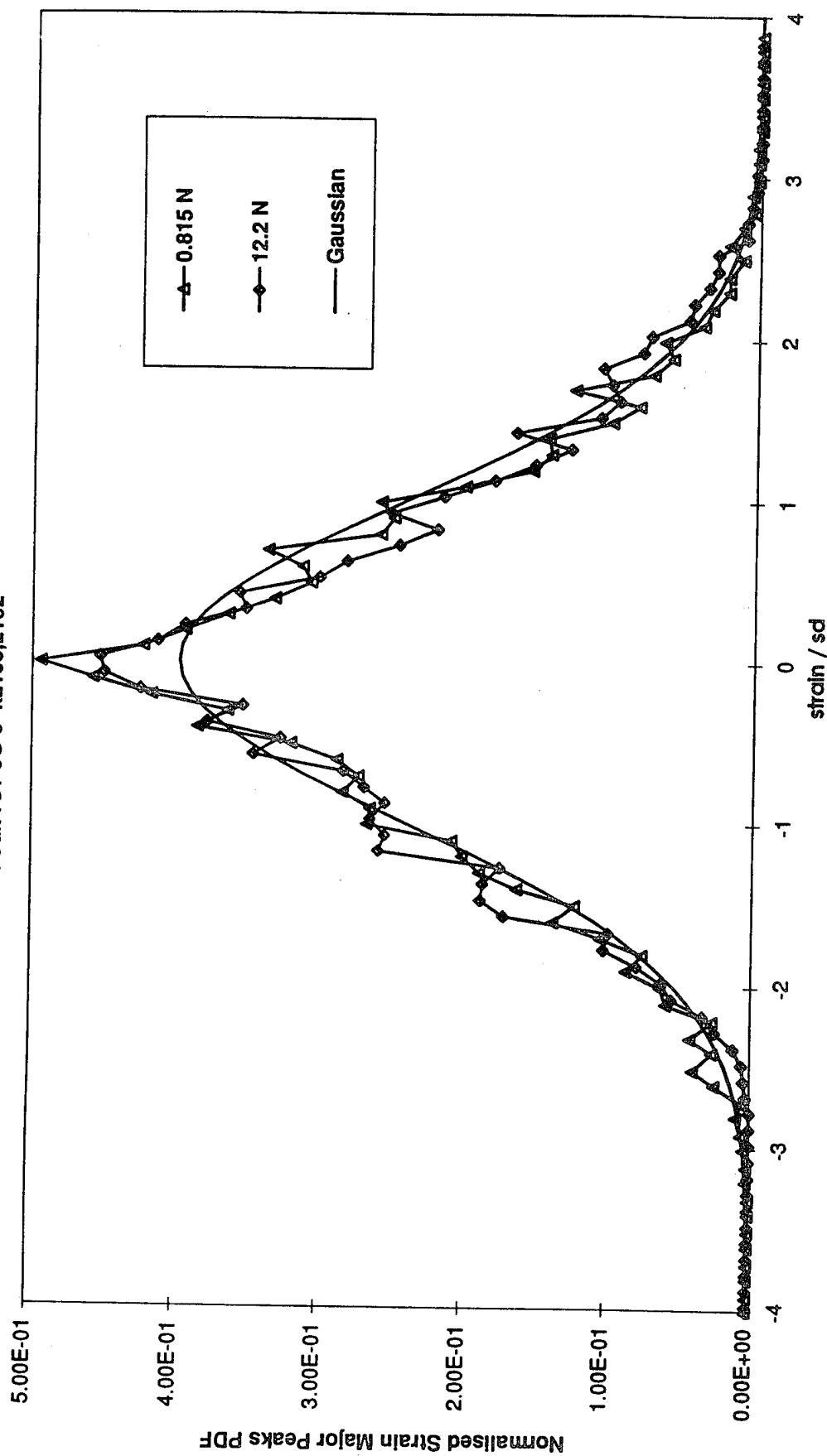


Fig 5.10 Normalised strain major peaks, PPDF, SG3, 10-1000 Hz random, 0.815 and 12.2N compared with Gaussian, C-C aluminium beam.

C-C-C ALUM SHAKER PLATE
Peak PDF SG 2 Rec 17, 20

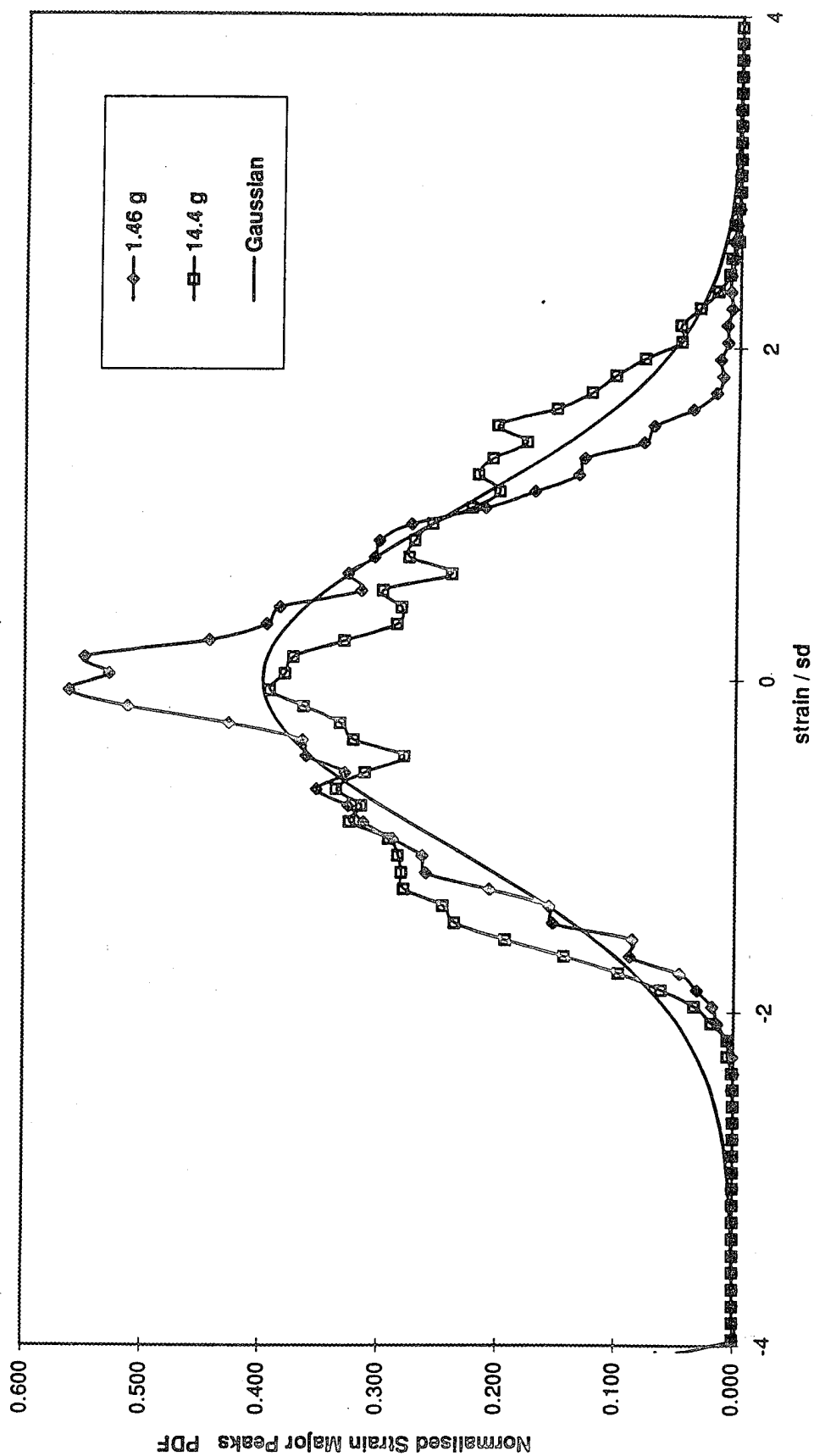


Fig 5.11 Normalised strain major peaks, PPDF, SG2, 10-1000 Hz random, 1.46 and 14.4g compared with Gaussian, C-C-C-C aluminium shaker plate.

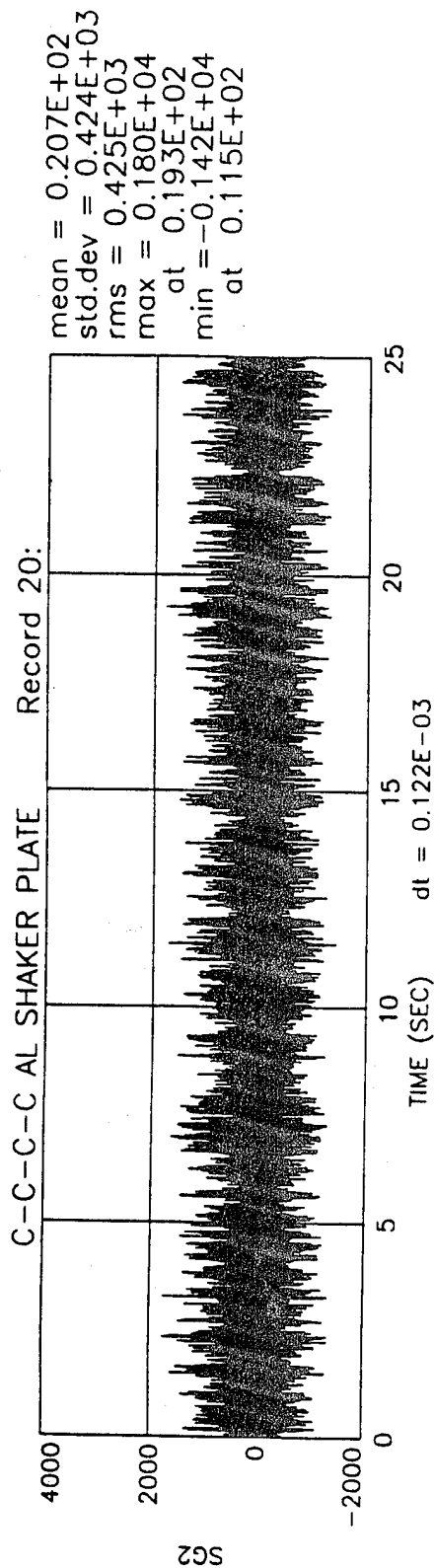


Fig 5.12 Strain time history, 0 to 25 seconds, 10-1000 Hz random excitation, C-C-C-C aluminium shaker plate.

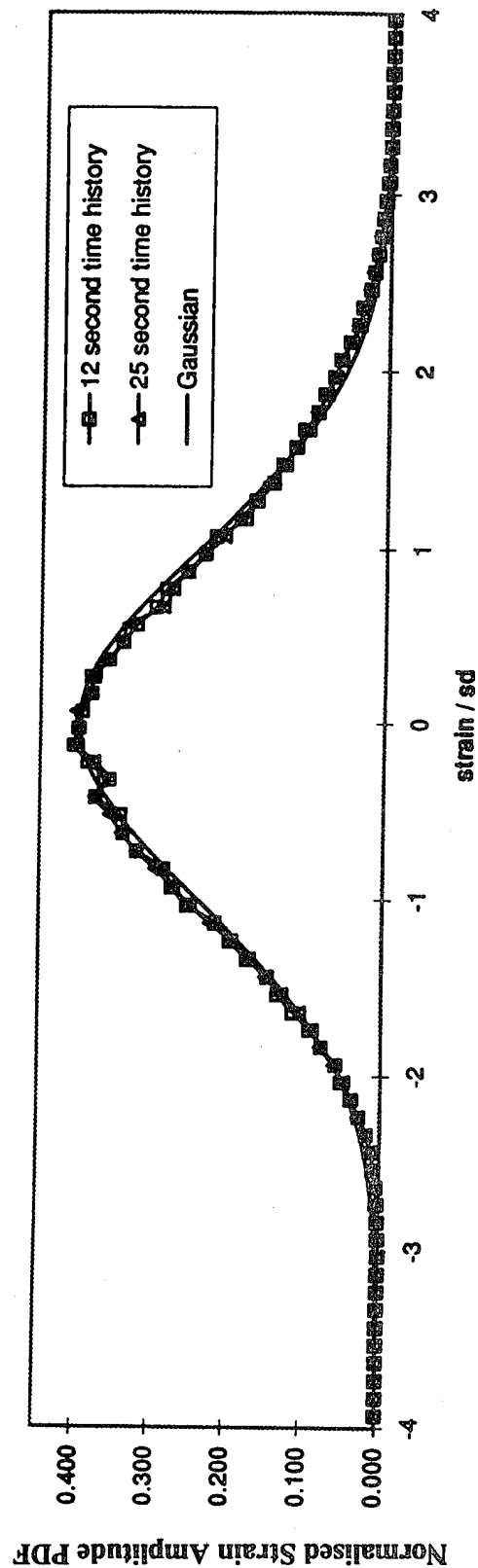


Fig 5.13 Normalised strain APDF comparisons, from 12 and 25 seconds time histories with Gaussian, C-C-C-C aluminium shaker plate.

C-C-C-C CFRP SHAKER PLATE
Peak PDF SG 7 R 39, 40, 41, 42

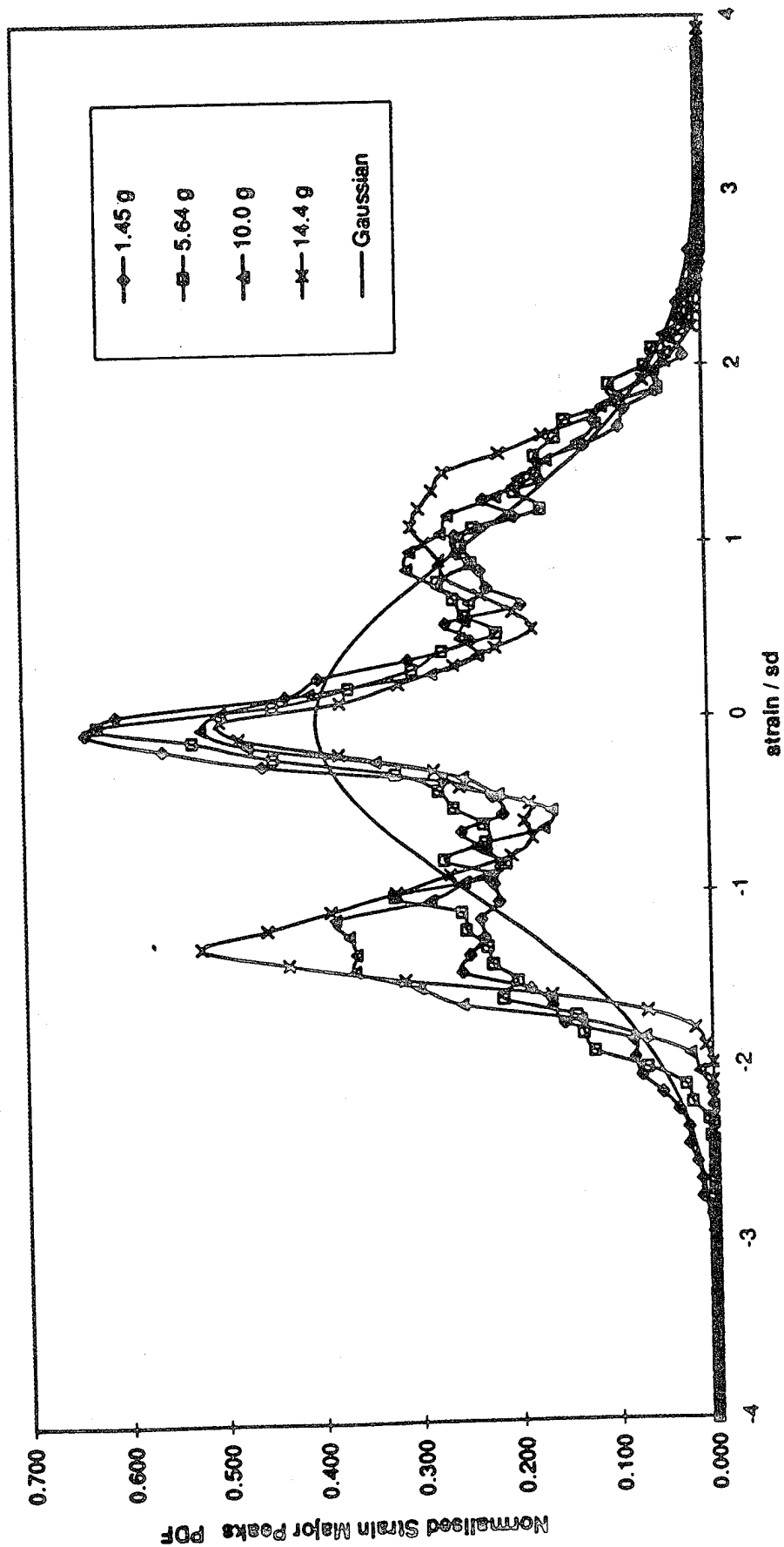


Fig 5.14 Normalised strain PPDF comparison with Gaussian, SG 7, C-C-C-C CFRP shaker plate.

C-C-C-C AL PLATE APWT TEST
Strain PDF SG 10 R10304,459,585,674

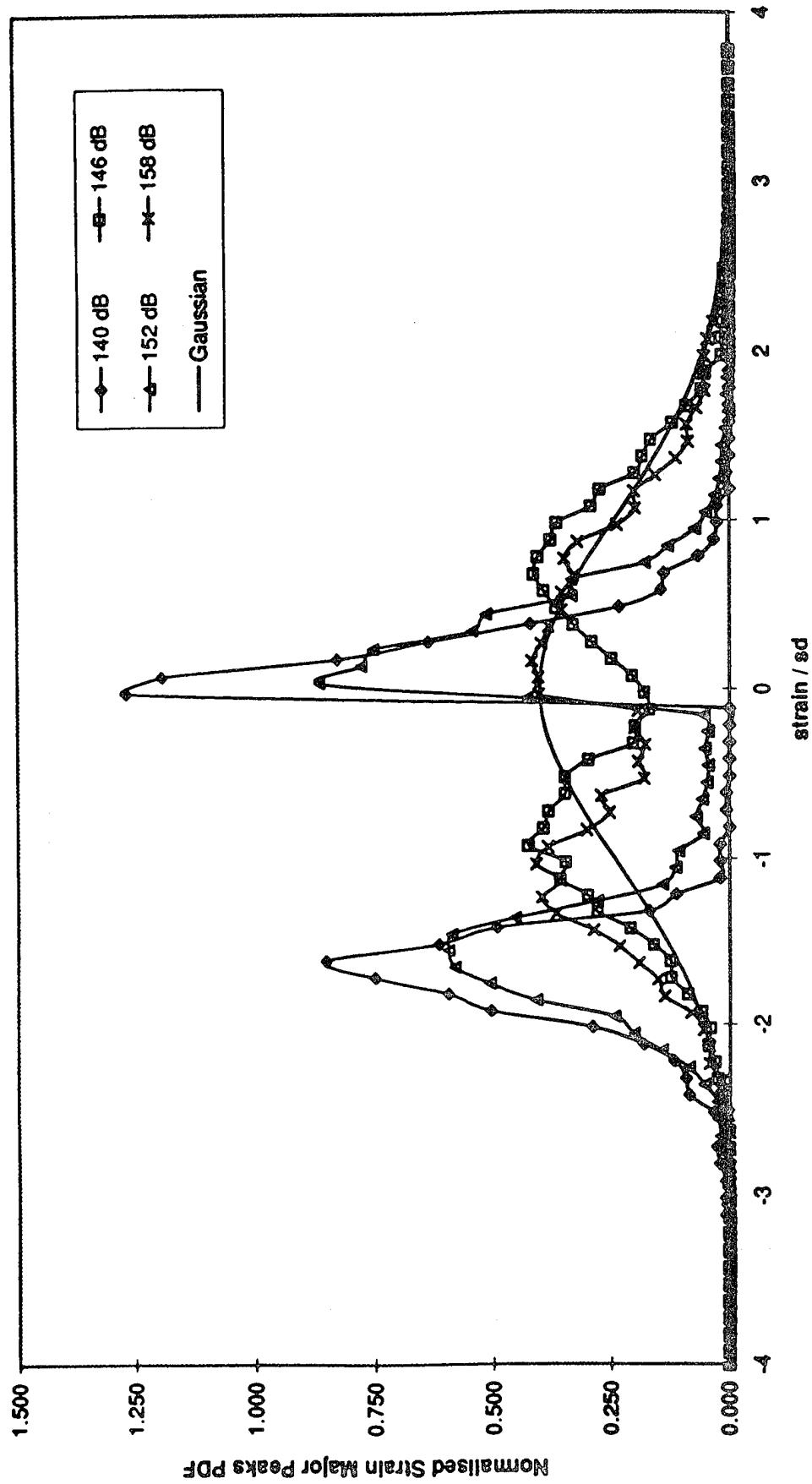


Fig 5.15 Normalised strain PPDF comparison with Gaussian, SG10, C-C-C-C aluminium APWT plate.

C-C-C-C AL PLATE APWT TEST
Strain PDF SG 9 & 10 R10301,725

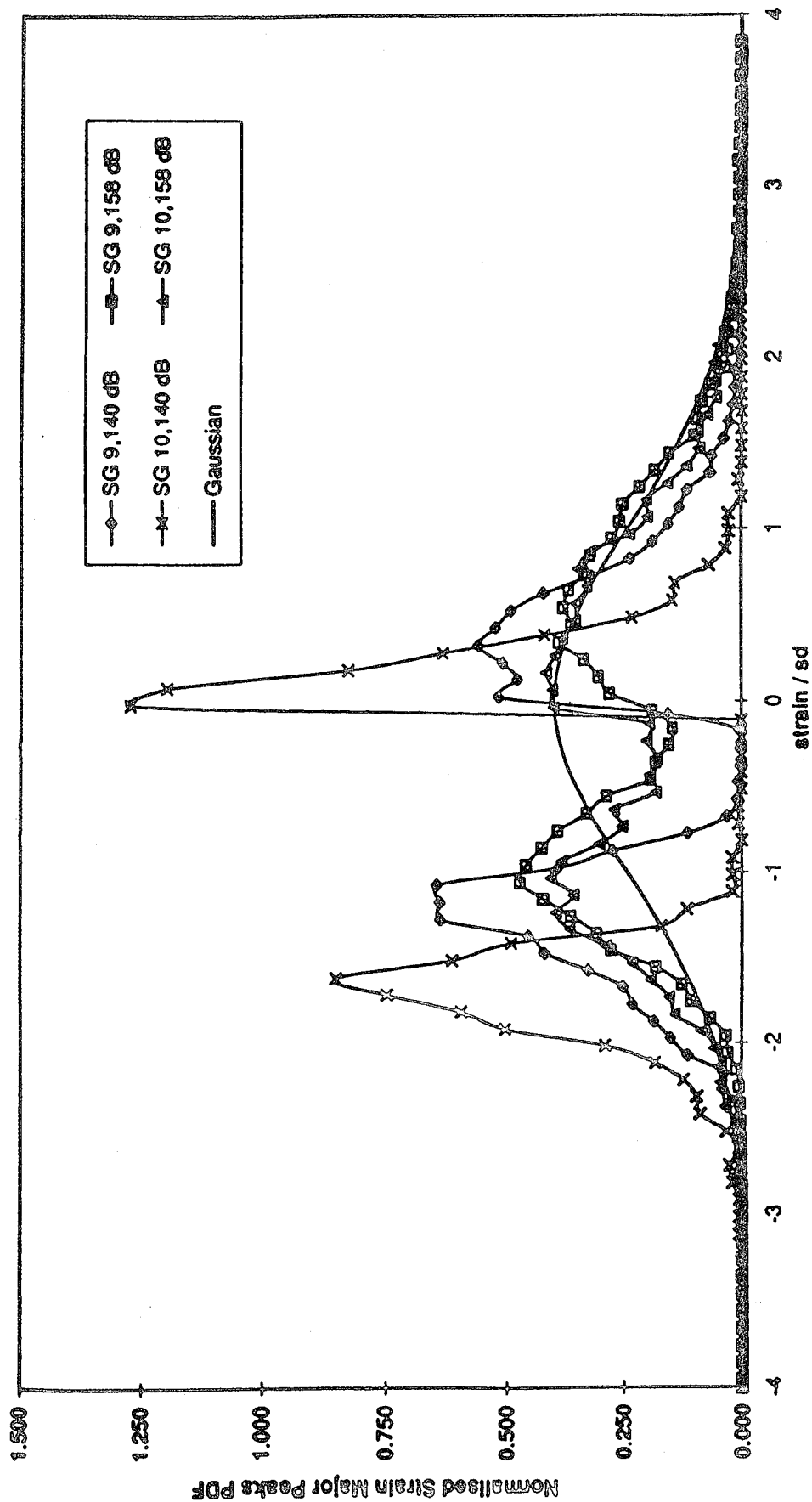


Fig 5.16 Normalised strain PPDF comparison with Gaussian, SG 9 and 10, C-C-C-C aluminium APWT plate.

C-C-C-C CFRP APWT
Peak PDF SG 2 Rec 74, 76, 78, 80, 82

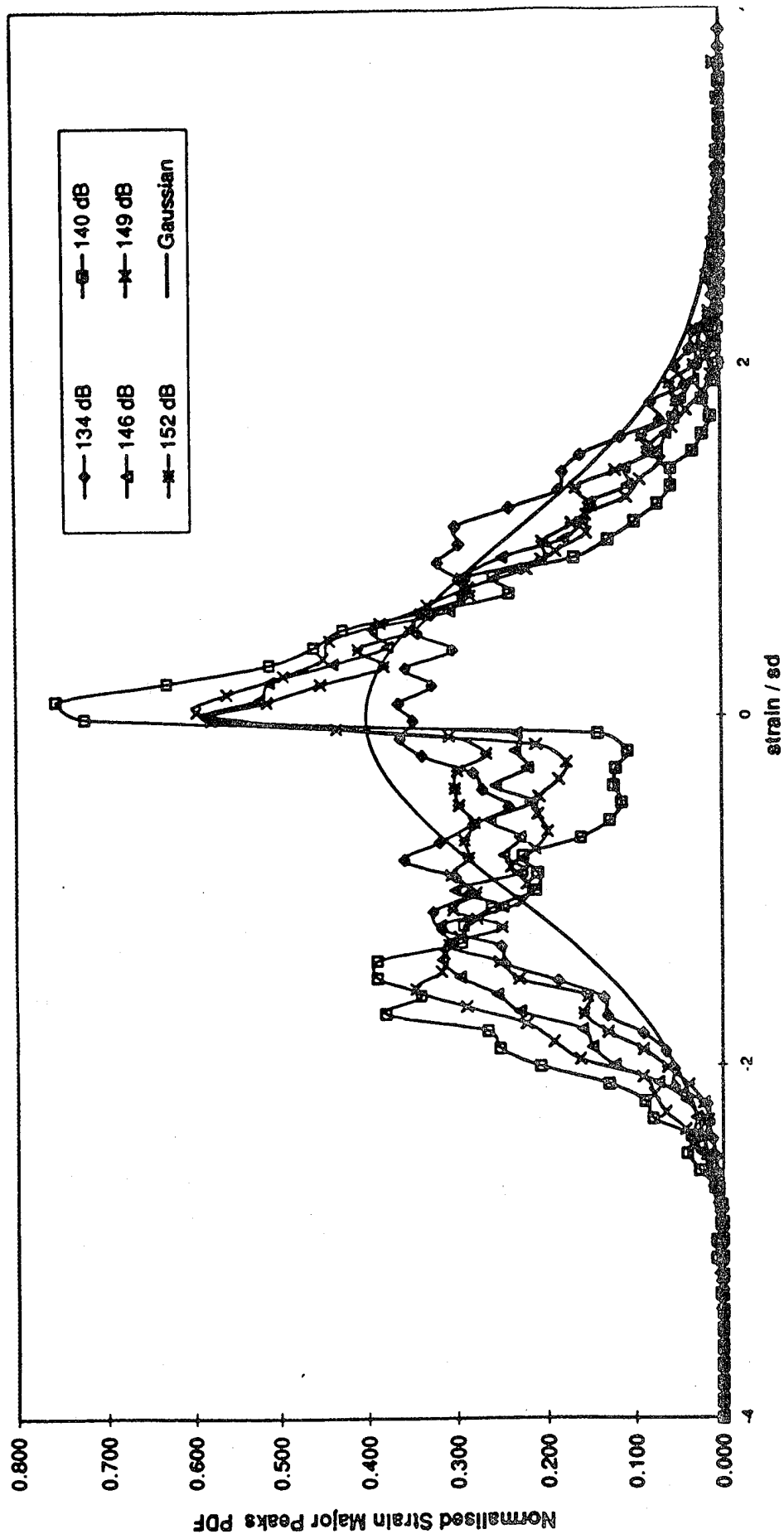


Fig 5.17 Normalised strain PPDF comparison with Gaussian, SG 2, C-C-C-C CFRP APWT plate.

DTD 5070 coupon

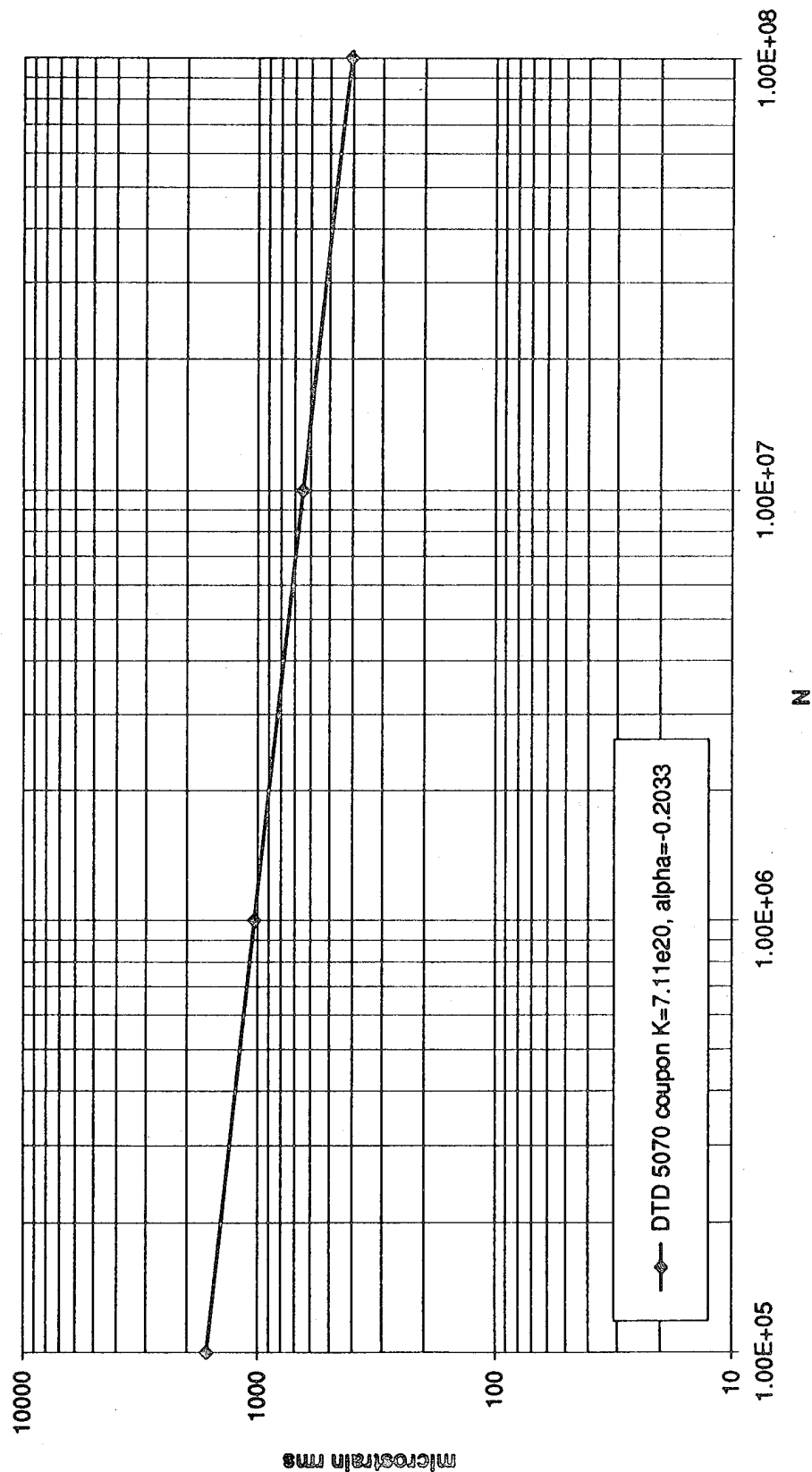


Fig 5.18 Characterization of S-N curve, DTD 5070 aluminium alloy.

microstrain vs cycles

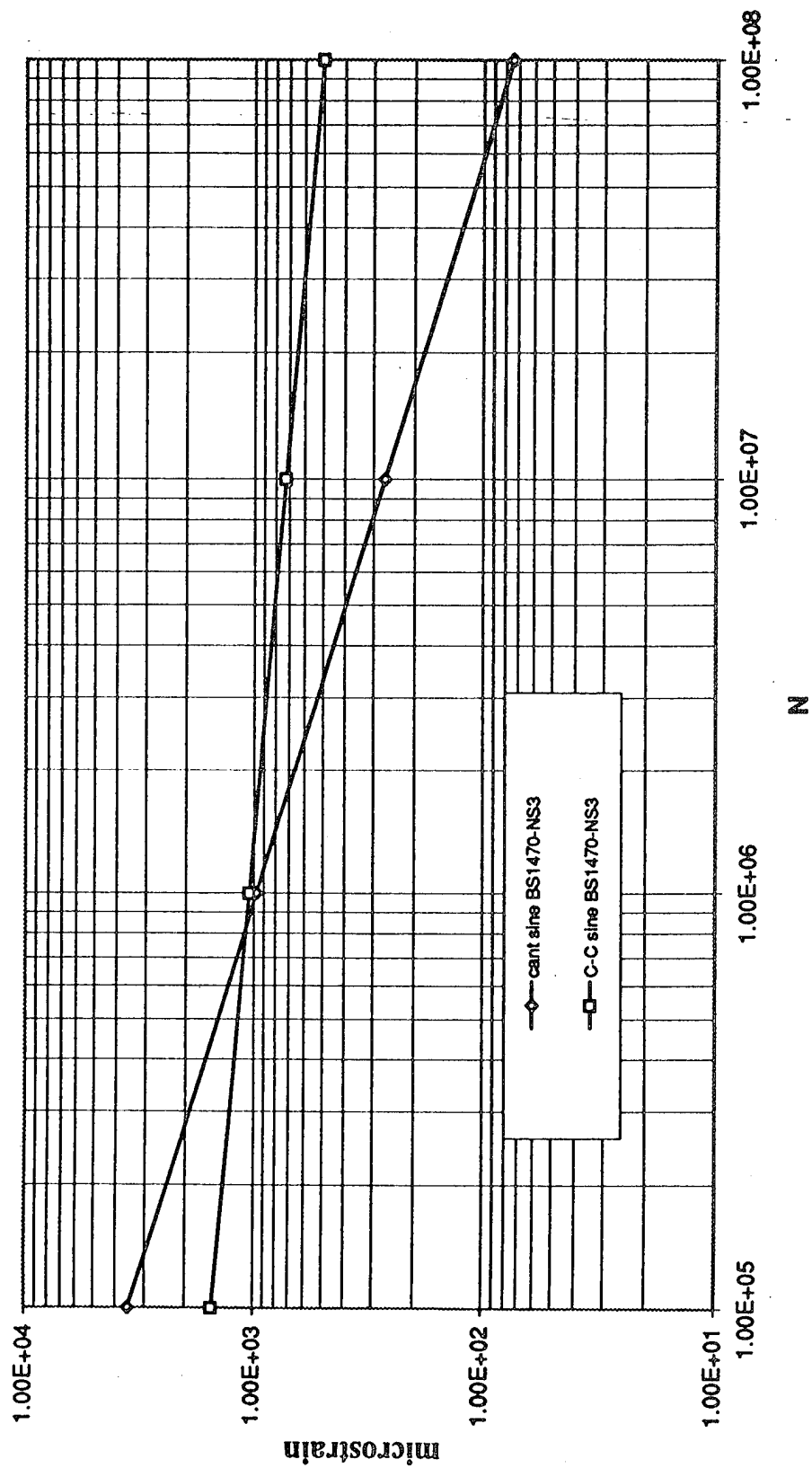


Fig 5.19 e-N curves for BS 1470-NS3, aluminium alloy.

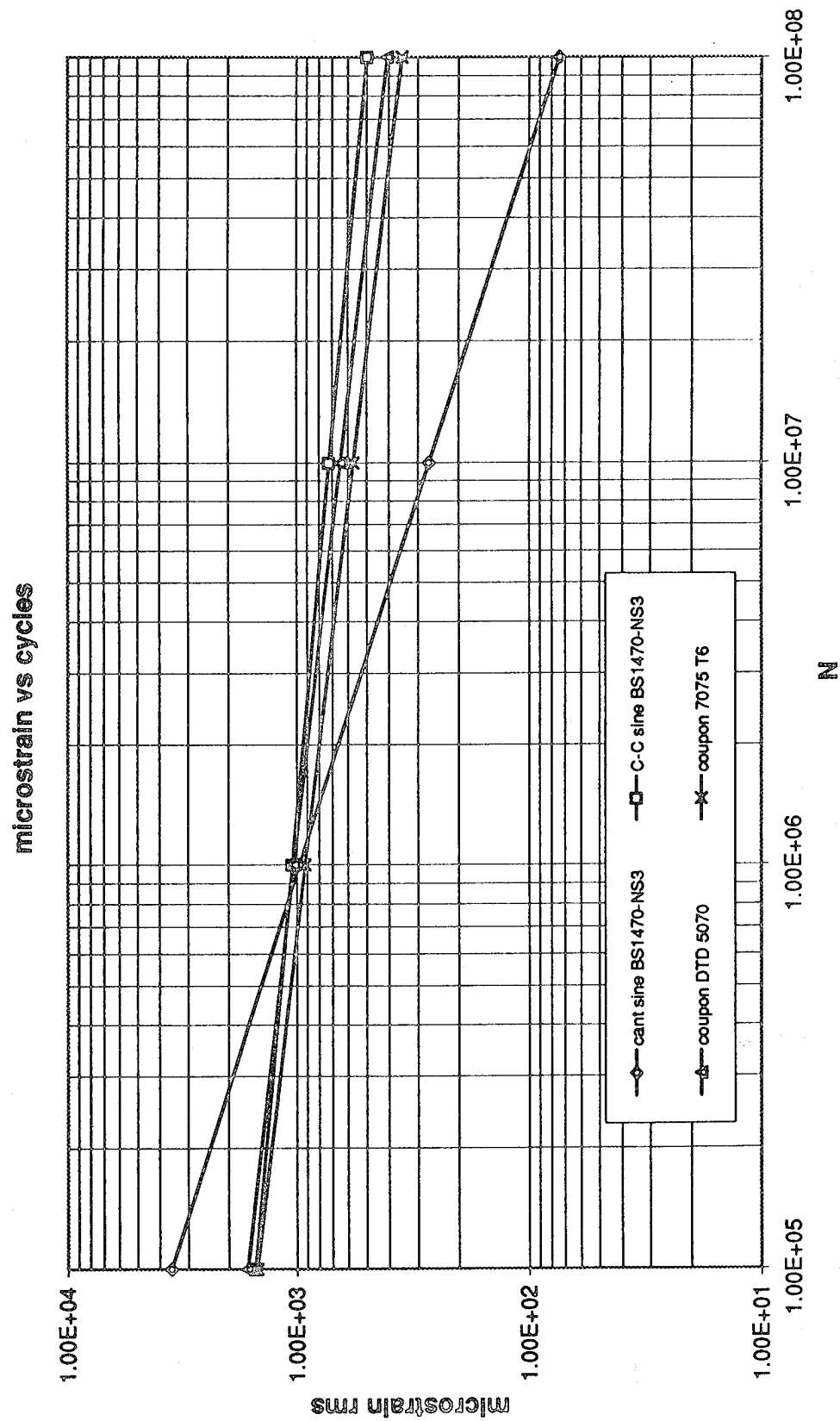


Fig 5.20 ϵ -N curve comparisons.

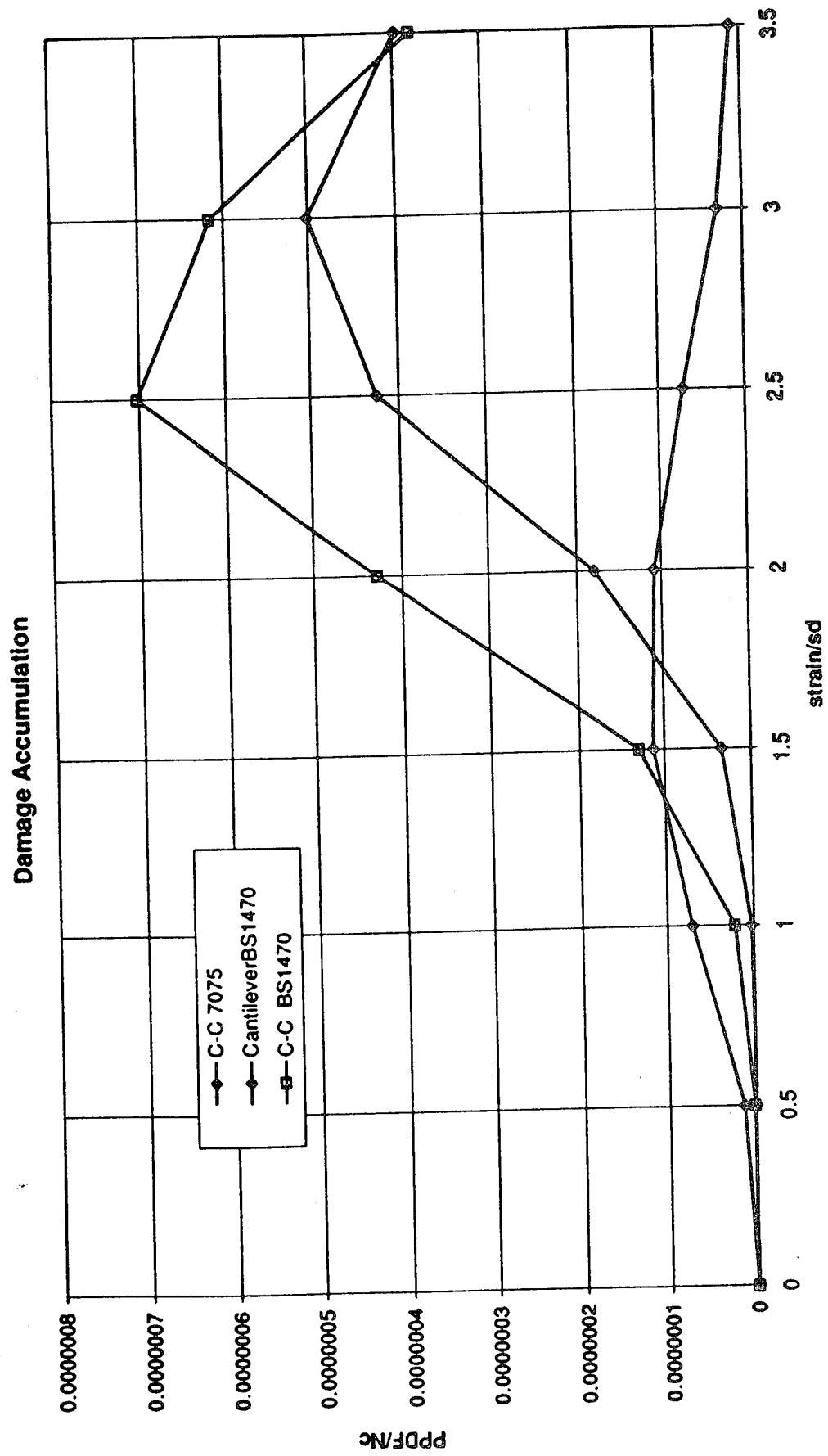


Fig 5.21 Damage accumulation for cantilevered and clamped beams.

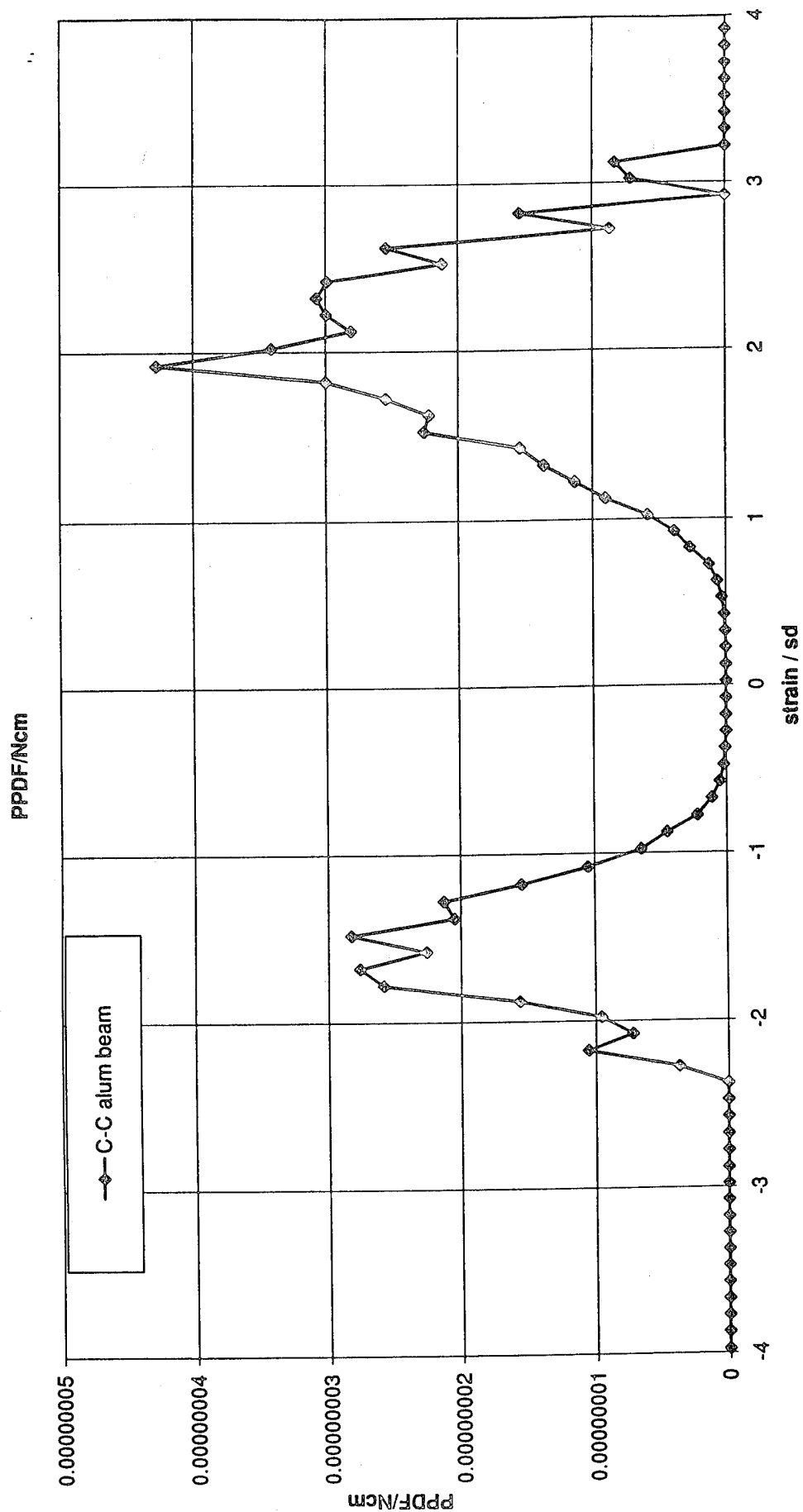


Fig 5.22 Damage accumulation for C-C aluminium beam.

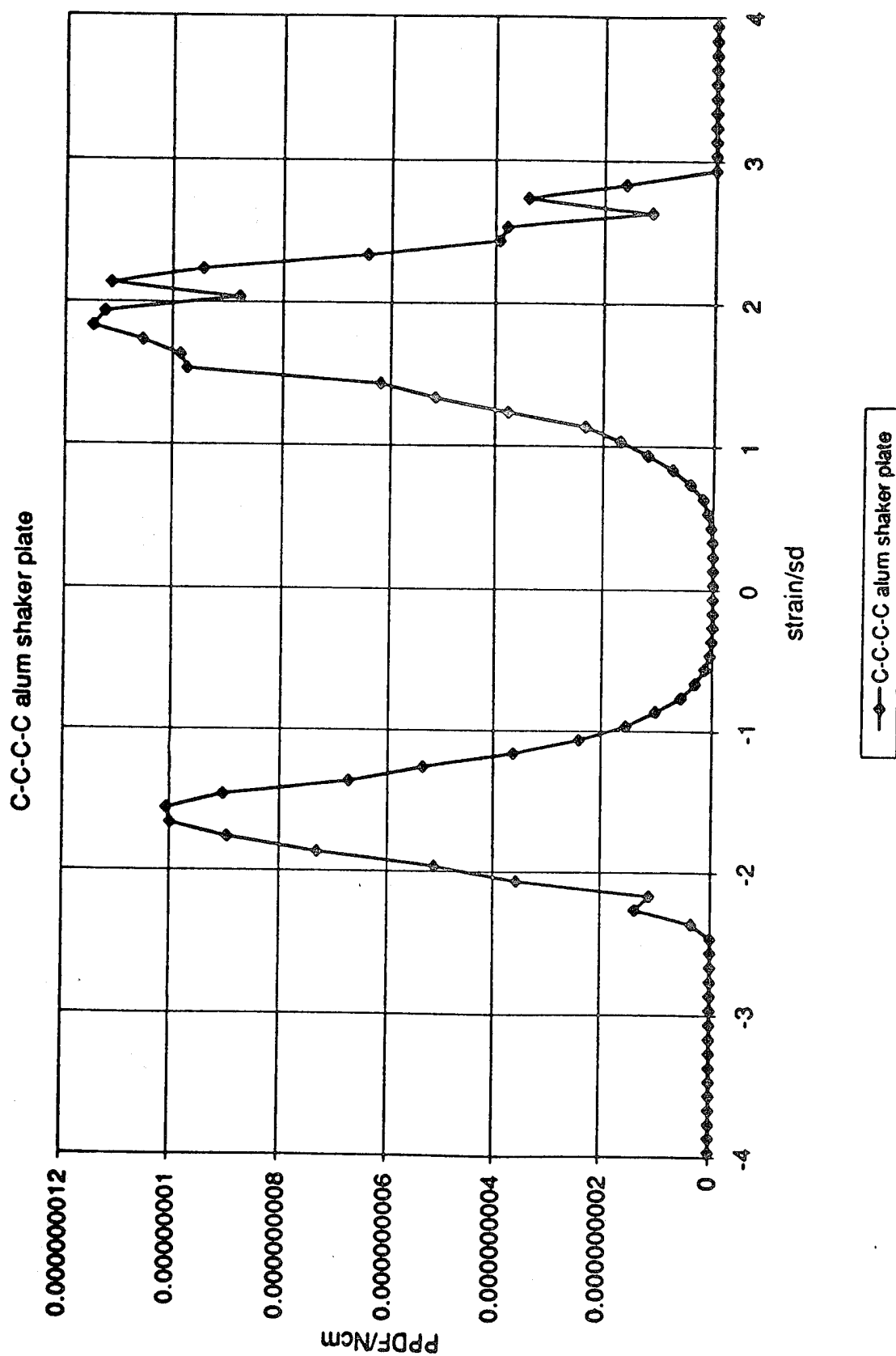


Fig 5.23 Damage accumulation for C-C-C-C aluminium shaker plate.

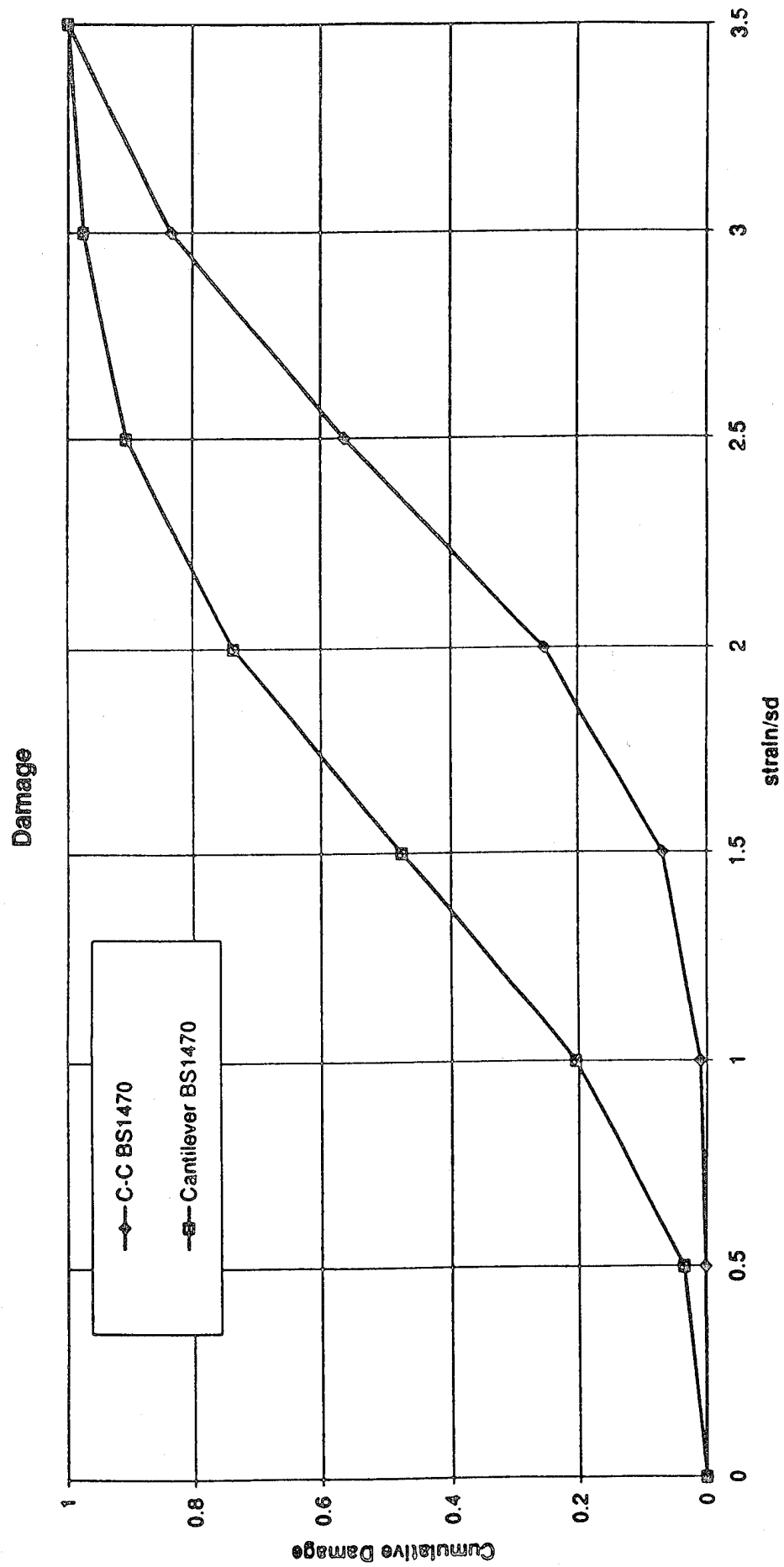


Fig 5.24 Cumulative damage comparison, cantilevered and C-C beams.

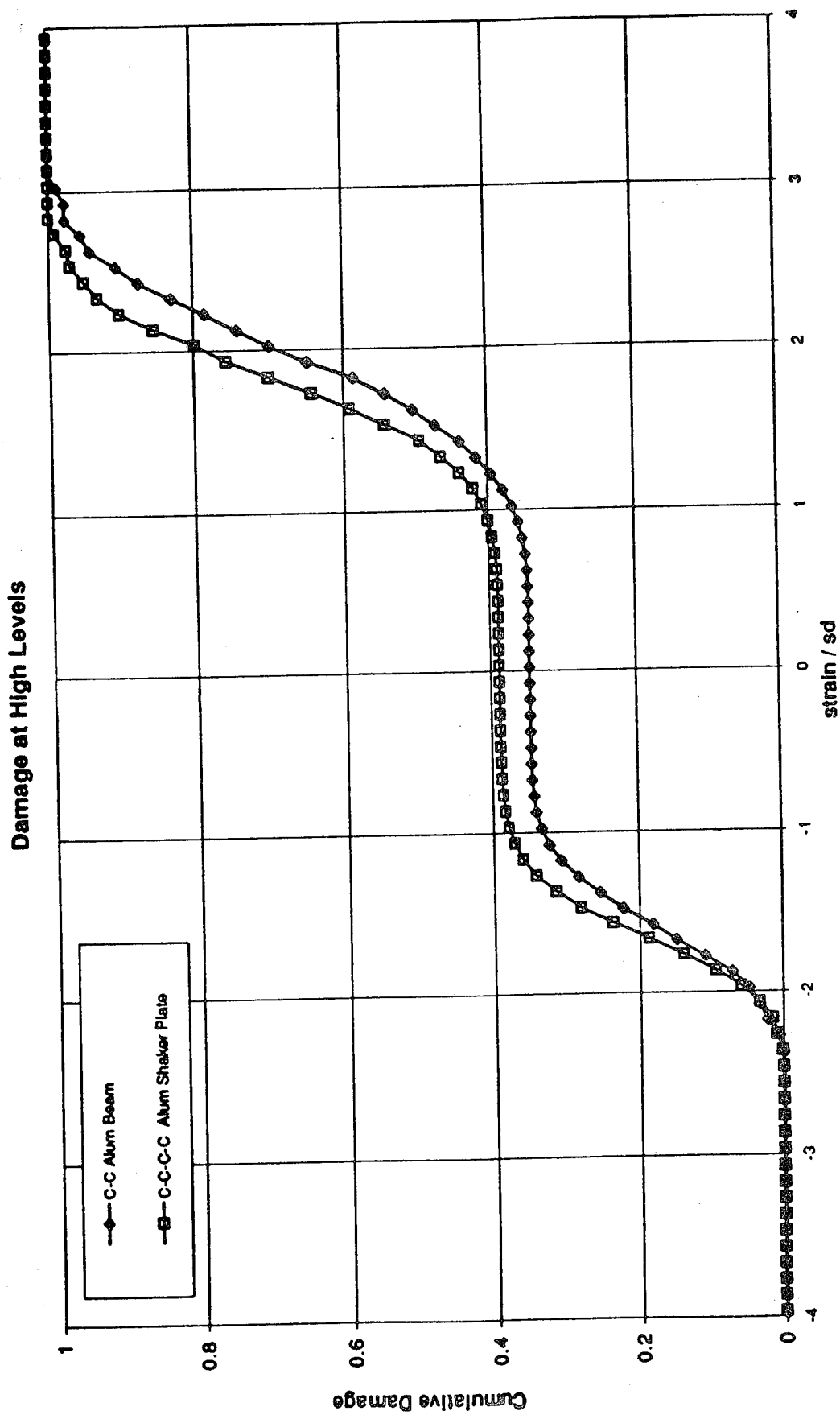


Fig 5.25 Cumulative damage comparison, C-C aluminium beam and C-C-C-C aluminium shaker plate.

C-C-C-C Al Shaker R 20 14.4 g SG2

Rank 1 Eqn 6007 $y=a+bx+cx^2+dx^3+ex^4+fx^5+gx^6+hx^7+ix^8+jx^9+kx^{10}$

$a=0.34584102$ $b=-0.014767117$ $c=-0.13719843$ $d=-0.053935173$ $e=0.0896655687$ $f=0.043278377$

$g=-0.040363172$ $h=-0.0097647634$ $i=0.0072221439$ $j=0.00068484792$ $k=-0.00043557573$

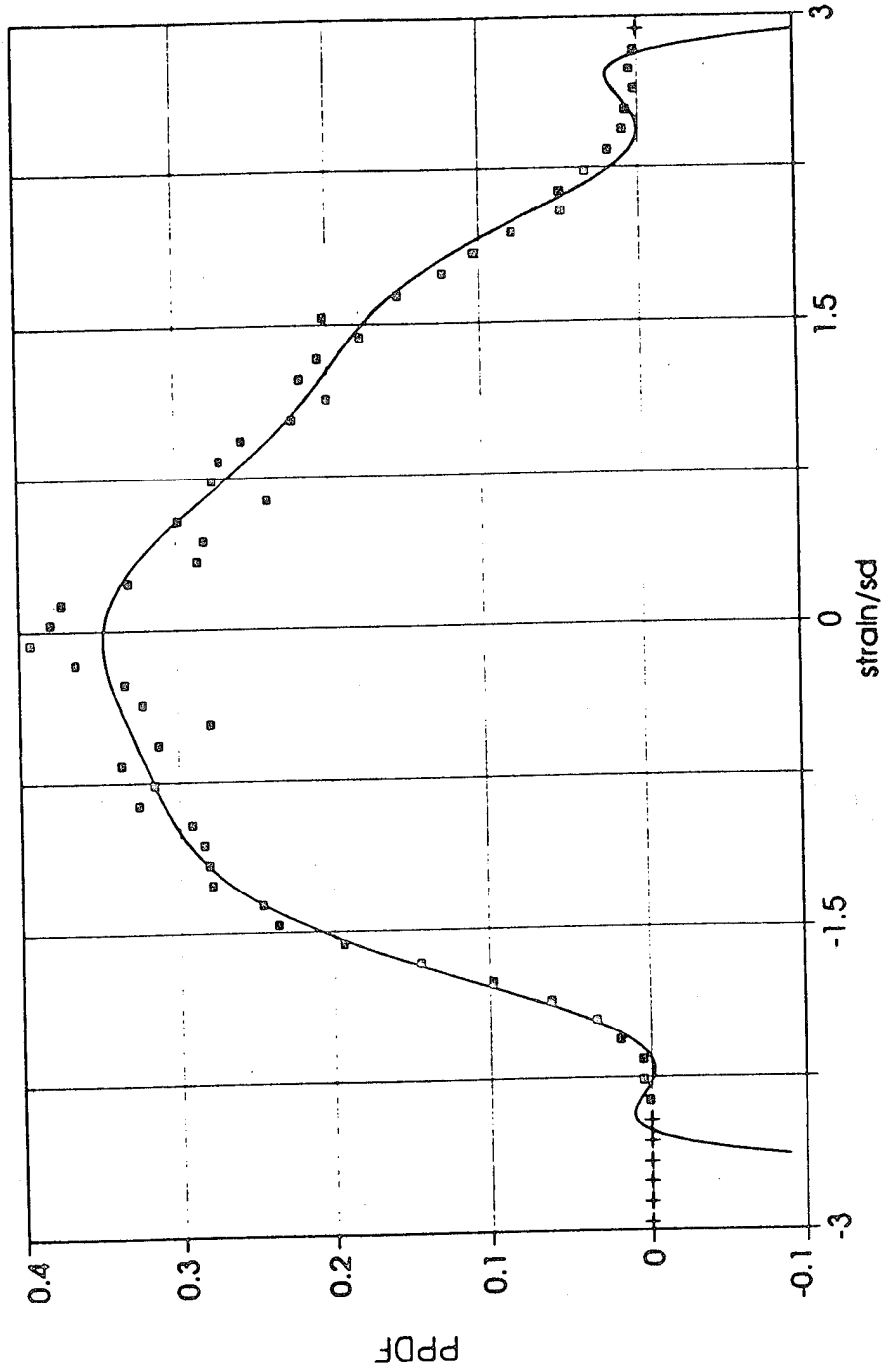


Fig 5.26 Rank 1, curve fit of PPDF, SG 2, C-C-C-C aluminium shaker plate.

C-C-C-C Al Shaker R 20 14.4 g SG2

Rank 41 Eqn 8003 $y=a+b\exp(-0.5((x-c)/d)^2)$ (Gaussian)

$a=0.096825788$ $b=0.44854937$

$c=-0.050441616$ $d=1.4526096$

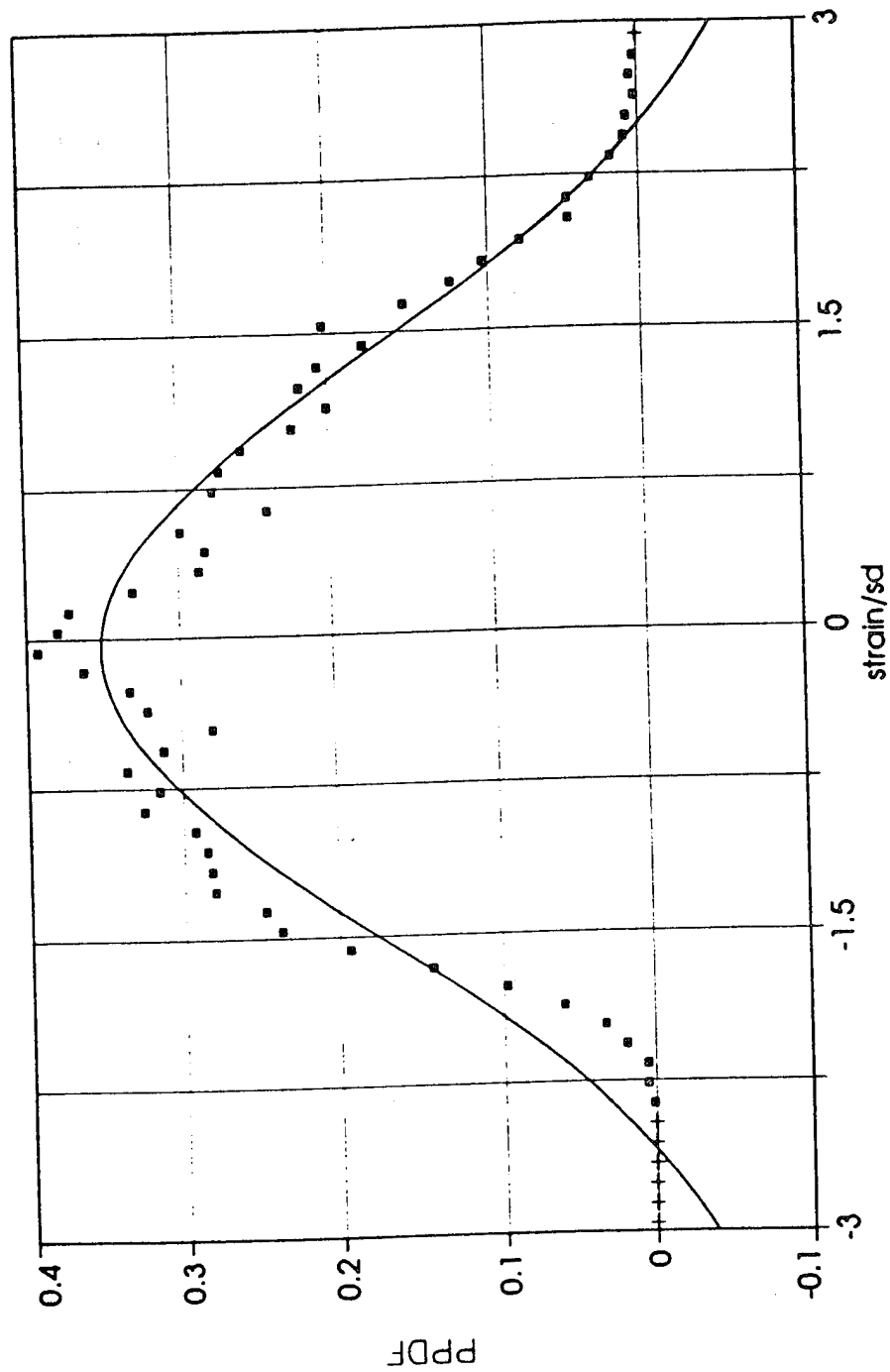


Fig 5.27 Rank 41, curve fit of PPDF, SG 2, C-C-C-C aluminium shaker plate.

C-C-C-C Alum Shaker Plate R20 SG2

Rank 1 Eqn 26 $\ln y = a + bx^2 \ln x$

$r^2 = 0.98344454$ DF Adj $r^2 = 0.982340842$ Fitted $r^2 = 0.0129466699$ Fitted $r^2 = 1841.49998$

$a = -1.3833926$

$b = 0.42747842$

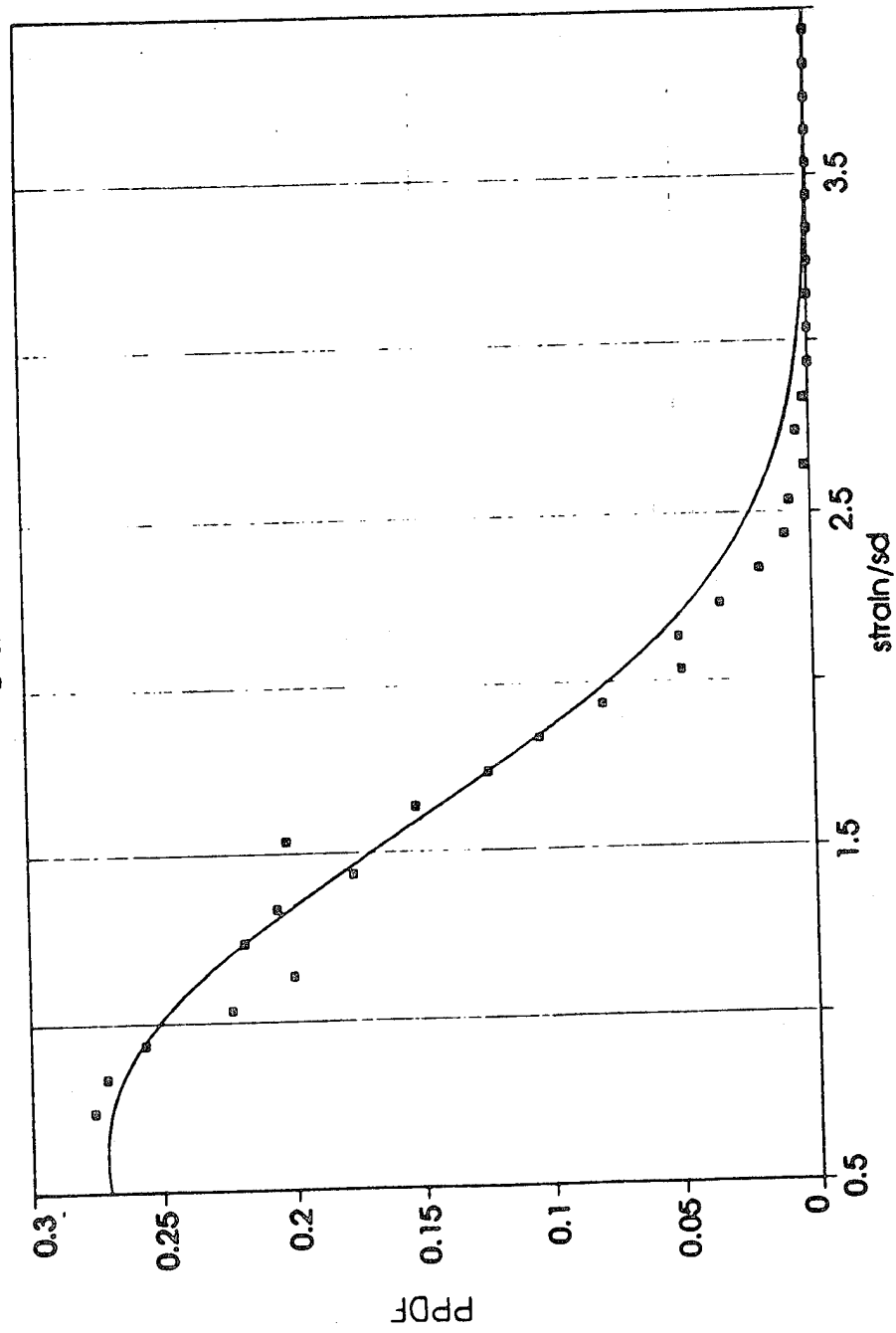


Fig 5.28 Rank 1 curve fit, part of PPDF data, SG 2, C-C-C-C aluminium shaker plate.

LINEAR MODE SHAPES

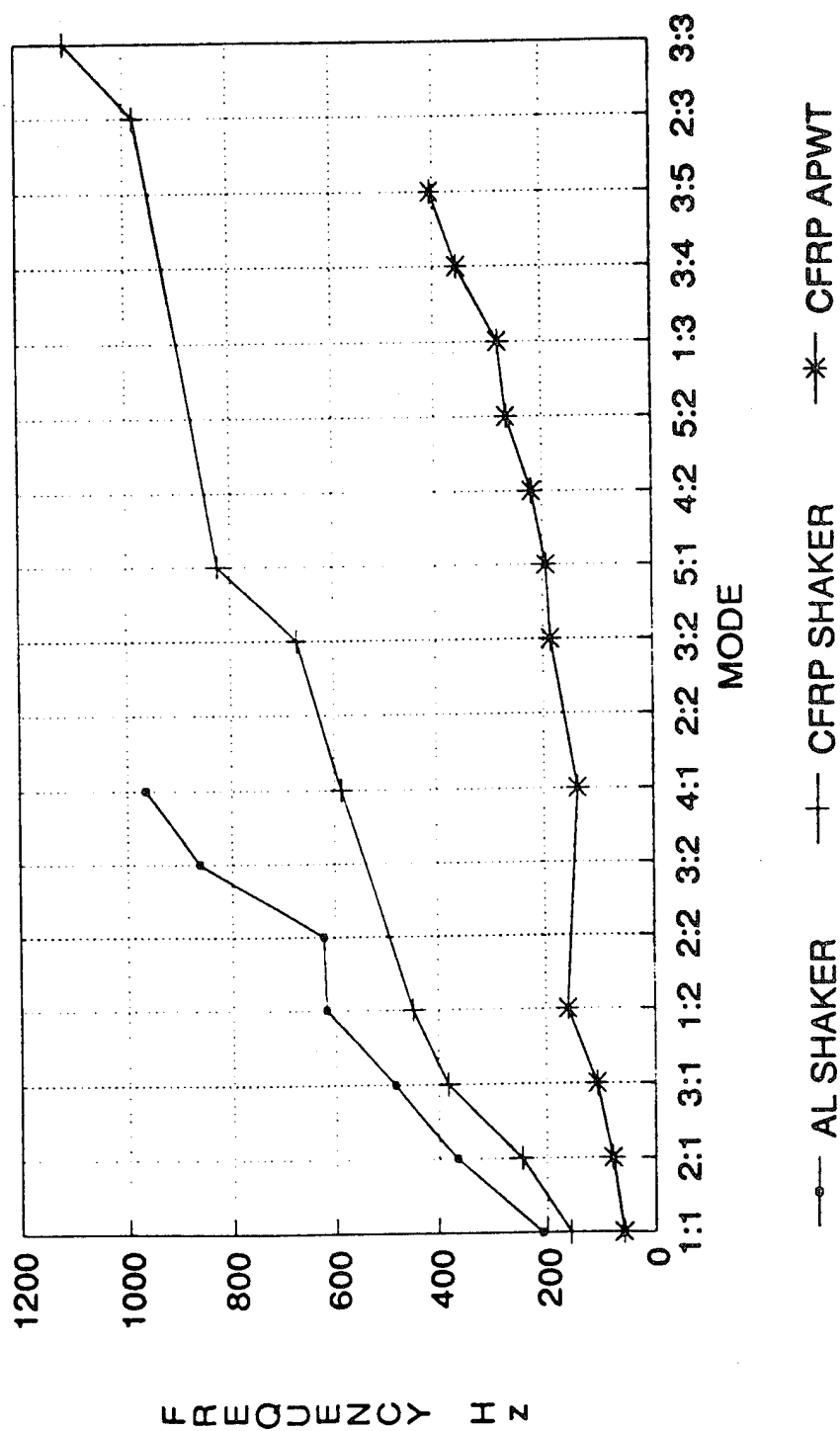


Fig 5.29 Linear mode shape comparison of C-C-C-C aluminium and CFRP shaker plates and CFRP APWT plate.

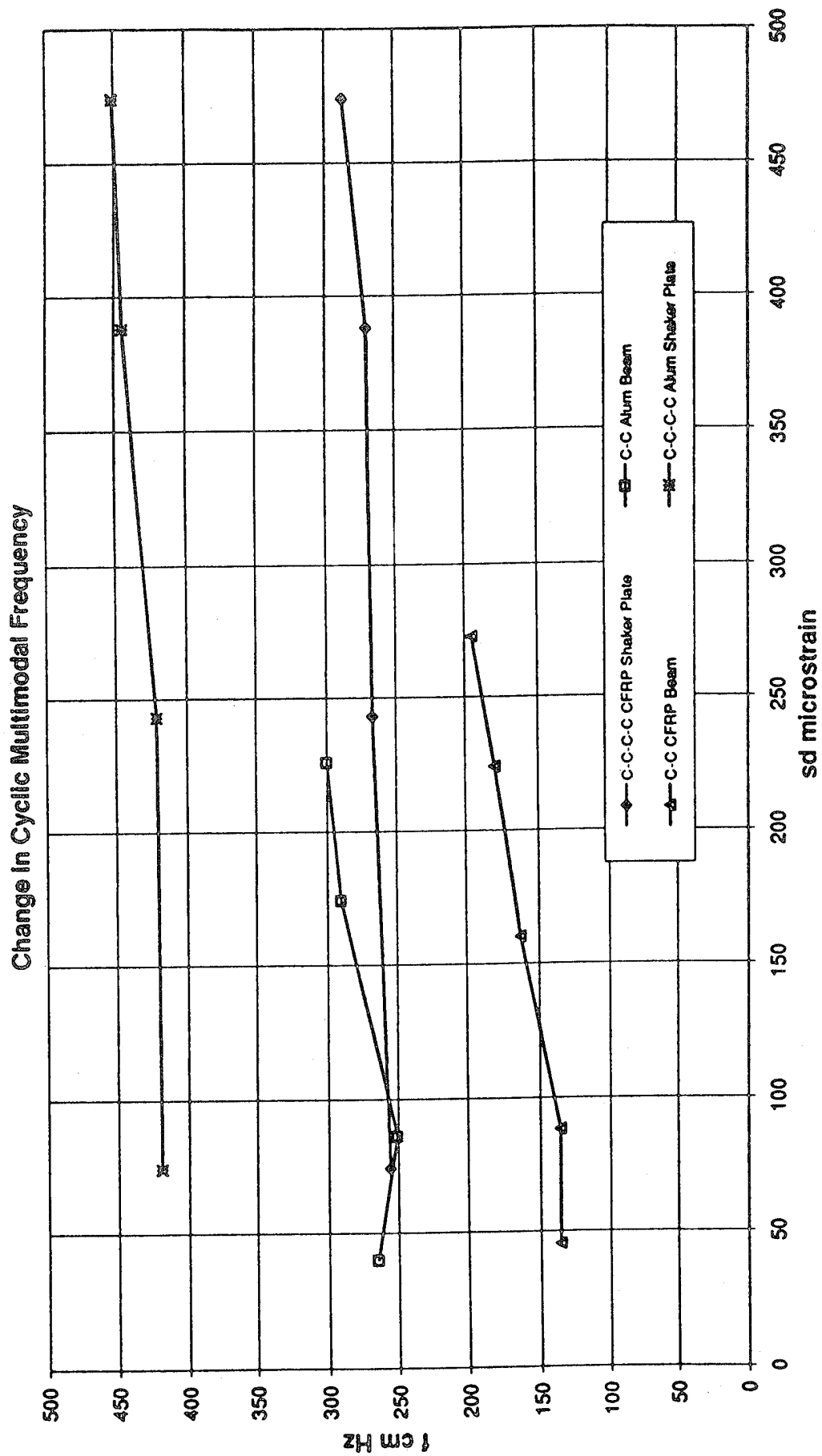


Fig 5.30 Comparison of changes in cyclic multimodal frequencies.